Magnetic polyion complex micelles as therapy and diagnostic agents

Vo Thu An Nguyen

A THESIS PRESENTED IN FULFILLMENT OF THE
THESIS REQUIREMENT FOR THE DEGREE OF

DOCTOR OF PHILOSOPHY

FROM UNIVERSITÉ DE BORDEAUX
AND FROM UNIVERSITY OF WATERLOO

ÉCOLE DOCTORALE DES SCIENCES CHIMIQUES UBX

DEPARTMENT OF CHEMISTRY

SPECIALIZED IN POLYMER SCIENCE

By **Vo Thu An NGUYEN**

MAGNETIC POLYION COMPLEX MICELLES AS THERAPY AND DIAGNOSTIC AGENTS

Under the supervision of: Dr. Olivier SANDRE, Prof. Mario GAUTHIER,
and Dr. Marie-Claire DE PAUW-GILLET

Defense date: September 16, 2015

Jury members:

Mr. Étienne DUGUET	Professor, Université de Bordeaux	President
Mrs. Nguyen Thi Kim THANH	Professor, University College London	Reviewer
Mr. Harald STÖVER	Professor, McMaster University	Reviewer
Mr. Olivier SANDRE	Research Director, CNRS	Examiner
Mr. Mario GAUTHIER	Professor, University of Waterloo	Examiner
Mrs. Marie-Claire DE PAUW-GILLET	Associate Professor, Université de Liège	Examiner
Mr. Xiaosong WANG	Associate Professor, University of Waterloo	Examiner
Mrs. Caroline ROBIC	Research Engineer, Guerbet Group	Examiner

Magnetic Polyion Complex Micelles as Therapy and Diagnostic Agents

by

Vo Thu An Nguyen

A thesis

presented to the University of Waterloo

in fulfillment of the

thesis requirement for the degree of

Doctor of Philosophy

in

Chemistry

Waterloo, Ontario, Canada, 2015

AUTHOR'S DECLARATION

I hereby declare that I am the sole author of this thesis. This is a true copy of the thesis, including any required final revisions, as accepted by my examiners.

I understand that my thesis may be made electronically available to the public.

Résumé / Abstract

Ce manuscrit de thèse présente la synthèse de nanoparticules d'oxyde de fer superparamagnétiques couramment appelées SPIONs servant d'agents de contraste pour l'imagerie par résonance magnétique (IRM) et la génération de chaleur pour la thérapie cellulaire par hyperthermie induite par champ magnétique radiofréquence (HMRF). Le contrôle des tailles et de la distribution en tailles des SPIONs et donc de leurs propriétés magnétiques a été obtenu en utilisant un copolymère arborescent G1 (substrat de polystyrène branché en peigne noté G0, greffé avec des groupements pendants poly(2-vinyle pyridine)) comme milieu « gabarit », tandis que la stabilité colloïdale et la biocompatibilité des SPIONs ont été apportées par un procédé de poly-complexation ionique grâce à un copolymère double-hydrophile acide polyacrylique-*bloc*-poly(acrylate de 2-hydroxyéthyle) PAA-*b*-PHEA.

La complexation des segments de PAA-*b*-PHEA avec des nanostructures préformées contenant de la poly(2-vinyle pyridine) (P2VP) a été conduite dans l'eau afin de produire des micelles dynamiques unimoléculaires par poly-complexation ionique (PIC), par ajustement du pH dans une gamme étroite. Une fois formées, ces micelles PIC sont stables dans des tampons à pH neutre tels que des milieux de culture cellulaire. Le contrôle de la taille et de la structure des micelles PIC, allant d'espèces larges floculées à des entités stables unimoléculaires avec des diamètres hydrodynamiques entre 42 et 67 nm, a été accompli par l'ajustement de la densité de la couche polymère stabilisante autour du cœur G1. La preuve de l'unimolécularité par rapport à la formation de structures multimoléculaires a été apportée par des techniques de diffusion dynamique et statique de la lumière, tandis que la nature cœur–écorce des micelles PIC a été révélée par des images du signal de phase en microscopie de force atomique (AFM) ainsi que par la variation de la déflexion et de l'amplitude de vibration de la pointe AFM.

Notre revue de la littérature a rapporté les tentatives et les succès dans le contrôle des tailles et des formes dans la synthèse de nanoparticules magnétiques grâce à la variation de la

taille et de la géométrie des gabarits polymères, dont il a été présagé qu'ils puissent servir de moules à l'échelle nanométrique. Bien que ces micelles PIC se soient révélées d'usage limité pour la synthèse directement *in situ* de nanoparticules magnétiques, le copolymère arborescent G1 (G0PS-*g*-P2VP) a été utilisé pour la première fois comme gabarit polymère pour contrôler les tailles et améliorer la distribution en tailles de nanoparticules d'oxyde de fer, comme prouvé par microscopie électronique en transmission (MET). La stabilité colloïdale à pH 7 des nanoparticles magnétiques, notées G1@Fe_3O_4, a aussi été améliorée par poly-complexation ionique avec le PAA-*b*-PHEA, produisant des micelles poly-complexes ioniques magnétiques (MPIC) de diamètre hydrodynamique $D_h \approx 130$ nm et d'indice de polydispersité PDI ≈ 0.136.

Le superparamagnétisme des nanoparticules de Fe_3O_4 a été révélé par magnétométrie par vibration de l'échantillon, une technique aussi employée pour étudier l'influence de paramètres variés : stœchiométrie de complexation fer/azote, température, et nature du matériau de la couronne sur les propriétés magnétiques et relaxométriques des nanoparticules de Fe_3O_4, confirmant l'idée de pouvoir moduler les propriétés magnétiques et relaxométriques *via* les conditions de synthèse. On a effectué des tentatives pour comparer les résultats à des ajustements théoriques, pour discuter des différences entre échantillons (micelles nues ou recouvertes de copolymère dibloc), entre les échantillons et d'autres issus de la littérature, et entre les différentes mesures (taille relaxométrique, taille magnétique et taille issue d'images MET). Au final on a réussi à synthétiser des SPIONs présentant de fortes valeurs de relaxivité transverse $r_2 = 335\ s^{-1}\ mM^{-1}$ et de rapport de relaxivité transverse sur relaxivité longitudinale $r_2/r_1 = 31.4$ (sous 1.47 T et à 37 °C), comparables ou même supérieurs aux produits de contraste commerciaux, suggérant leur efficacité comme agents de contraste négatifs pour les séquences IRM pondérées en T_2. La fraction volumique intra-agrégat de Fe_3O_4 à l'intérieur des micelles polymères a été estimée, et a mené à un nombre de 12 cristallites magnétiques par micelle, compatible avec les observations par AFM et MET. Par ailleurs, une efficacité de chauffage magnéto-induite (SAR) jusqu'à 55.6 $W \cdot g^{-1}$ a été mesurée par calorimétrie sous champ alternatif à la radiofréquence $f = 755$ kHz et l'amplitude

de champ H_{max} = 10.2 kA·m^{-1}. La dépendance des valeurs de SAR avec H_{max} et f a été examinée dans une vaste gamme de ces deux paramètres.

L'internalisation cellulaire et la cytotoxicité des micelles PIC et MPIC ont été évaluées par des expériences *in vitro*. L'internalisation cellulaire a été visualisée par microscopie par balayage laser confocale et par une étude histologique en MET, et quantifiée par tri par cytométrie de flux et mesure de fluorescence. L'utilité des micelles MPIC pour le chauffage par champ magnétique radiofréquence a aussi été confirmée, comme l'a révélé l'effet dose-dépendant des micelles MPIC sur la viabilité cellulaire. C'est bien à la dose d'incubation maximale (1250 µg/mL d'oxyde de fer) que la viabilité cellulaire sous champ magnétique alternatif radiofréquence la plus faible a été observée : environ 46–57% après une heure-et-demi de traitement, et 30–35 % après trois heures pour la lignée cellulaire murine de fibroblastes L929. Nous avons vérifié l'hypothèse que l'excitation magnétique RF des nanoparticules internalisées dans les cellules était bien le facteur principal conduisant à la mort programmée (apoptose), même en l'absence de chauffage macroscopique.

Mots clés : SPION, copolymère arborescent, poly-complexation ionique, agents de contraste IRM, hyperthermie magnétique, relaxométrie des protons de l'eau

---

Laboratoire de Chimie des Polymères Organiques (LCPO) UMR5629

ENSCBP, 16 avenue Pey Berland 33607 Pessac Cedex, France

This Ph.D. dissertation describes the synthesis of superparamagnetic iron oxide nanoparticles (SPIONs) designed to serve as magnetic resonance imaging (MRI) contrast agents and for heat generation in cellular radiofrequency magnetic field hyperthermia (MFH) treatment. Control over the size and size distribution of the iron oxide nanoparticles (NPs), and thus over their magnetic properties, was achieved using a G1 arborescent copolymer (comb-branched (G0) polystyrene substrate grafted with poly(2-vinylpyridine) side chains, or G0PS-*g*-P2VP) as a template. Good colloidal stability and biocompatibility of the SPIONs were achieved via the formation of polyion complex (PIC) micelles with a poly(acrylic acid)-*block*-poly(2-hydroxyethyl acrylate) (PAA-*b*-PHEA) double-hydrophilic block copolymer.

The formation of SPIONs was first attempted using preformed PIC micelles as templates. Complexation of the PAA segment of PAA-*b*-PHEA with G0PS-*g*-P2VP was achieved in water over a narrow pH range to produce dynamic, unimolecular PIC micelles stable in neutral pH buffers such as cell growth media. Control over the size and structure of the PIC micelles, from large flocculated species to stable unimolecular entities with hydrodynamic diameters ranging from 42 to 67 nm, was accomplished by tuning the density of the polymer stabilizing layer surrounding the G1 core. Evidence for the formation of uni- vs. multimolecular structures was provided by dynamic and static light scattering measurements, while the core–shell morphology of the micelles was confirmed by atomic force microscopy (AFM) phase images. Unfortunately, the preformed PIC micelles did not perform well as templates for the *in situ* synthesis of SPIONs. An alternate procedure was developed using the G0PS-*g*-P2VP copolymer as a template to control the size and size distribution of the iron oxide NPs, as evidenced by transmission electron microscopy (TEM) imaging. The colloidal stability of the G1@Fe_3O_4 magnetic nanoparticles at pH 7 was improved by subsequent complexation with PAA-*b*-PHEA, to produce magnetic polyion complex (MPIC) micelles with a hydrodynamic diameter $D_h \approx 130$ nm and a polydispersity index PDI ≈ 0.136.

Vibrating sample magnetometry was employed to reveal the superparamagnetic character of the Fe_3O_4 NPs, but also to investigate the influence of the Fe/N templating ratio,

the temperature, and of the PAA-*b*-PHEA coating on their magnetic and relaxometric properties, and to demonstrate the possibility of tuning these properties via the synthetic conditions used. The results obtained were compared for samples in their bare state and after coating with the block copolymer, and with litterature values for relaxometric vs. magnetic and TEM measurements. The SPIONs synthesized in this work had values of transverse relaxivity of up to r_2 = 335 $s^{-1} \cdot mM^{-1}$, and a transverse-over-longitudinal relaxivity ratio r_2/r_1 = 31.4 (1.47 T, 37 °C), comparable with or even larger than for commercial products, suggesting their efficiency as negative contrast agents for T_2-weighted imaging. The estimation of the volume fraction of Fe_3O_4 inside the polymer micelles yielded a number of ca. 12 magnetite crystallites per micelle, comparable with the AFM and TEM observations. Moreover, a maximum SAR value of 55.6 $W \cdot g^{-1}$ was measured by alternating magnetic field (AMF) calorimetry at f = 755 kHz, H_{max} = 10.2 $kA \cdot m^{-1}$. The dependence of the SAR values on the magnetic field amplitude H and the frequency f was also examined.

The cytotoxicity and cell internalization of the PIC and MPIC micelles were evaluated *in vitro*. Cell internalization was visualized by confocal laser scanning microscopy and TEM, and quantified by fluorescence-activated cell sorting. The usefulness of MPIC micelles for cellular radiofrequency magnetic field hyperthermia was also confirmed, as the MPIC micelles had a dose-dependent effect on cell viability. At the maximum incubation dose (1250 µg/mL iron oxide), the lowest cell viabilities were observed with an applied AMF: about 46–57% after 1.5 h of treatment, and 30–35 % after 3 h for the L929 cell line. We verified the hypothesis that AMF excitation of the intracellular MNPs was the main factor leading to programmed cell death (apoptosis), even in the absence of macroscopic heating.

Keywords: SPION, arborescent copolymer, poly-ionic complexation, MRI contrast agents, magnetic hyperthermia, water proton relaxometry

Acknowledgements

I would like to express my sincere gratitude to many individuals who have offered their precious support and encouragements throughout my Ph.D. journey.

I am immensely grateful to Prof. Mario Gauthier, who introduced me to the world of polymer chemistry and to academic writing. He has always impressed me with his profound wisdom, interdisciplinary knowledge, massive support and endless patience. My heartfelt appreciation also goes to Dr. Olivier Sandre, who has patiently guided and unwaveringly supported me in my journey through the field of magnetic nanoparticles. I truly admire his interdisciplinary knowledge and his passionate enthusiasm for science. I am sincerely thankful to Prof. Marie-Claire De Pauw-Gillet, who introduced me to the world of cell culture; without her great encouragement and her generous support, I would not have had the chance to complete many of the valuable parts of my work.

I would also like to thank my defense committee members, Prof. Nguyen Thi Kim Thanh, Prof. Harald Stöver, Prof. Étienne Duguet, Prof. Xiaosong Wang, and Dr. Caroline Robic for accepting to read my work, for their fruitful discussion and their guidance provided at different stages of the work.

I wish to express my warm and sincere thanks to Prof. Sébastien Lecommandoux and everyone in the TH2 team and at LCPO, Bordeaux, France who have made my experience in the lab so much more valuable. Thank you Annie and Camille for teaching me how to work professionally, brightening my Ph.D. student life, and fulfilling it with English lessons, running, and a heartfelt friendship. My gratitude also goes to you, our magnetic nanoparticles team: Kevin, Hugo, Eneko and Gauvin for your solid support, and Colin for your drawings. Thank you Edgar for always caring, and Lise for being my running best friend. I appreciate Elisabeth, Elizabeth, Julie, Silvia, Cony, Charlotte, Pauline, Ariane, Deniz, Paul, and Winnie who have been very supportive, and kept me strong with the LCPO spirit. I am grateful to Manu (the AFM expert), Nico (the SEC and ALV master), Anne-Laure (NMR lady), Sabrina (TEM) and Cédric (TGA). I thank Prof. Neso Sojic and Mr. Patrick Garrigue (NSysA,

ENSCBP) for allowing me to use their AFM. My special appreciation goes to Madame Catherine Roulinat, who gave me her warm welcome and tremendous support. And also, thank you Ms. Bernadette, Ms. Corin, Ms. Nicol and Mr. Claude.

I would further like to thank my colleagues and friends in the Polymer Chemistry Laboratory at the University of Waterloo, Canada, who have shared my lab life and made it more interesting: Deepak, Toufic, Firmin, Joanne, Mosa, Ala, Ryan, Mehdi, Priscilla, Xiaozhou, Liying, Yan, and Timothy. Thank you Olivier Nguon, my ATRP mentor and Aklilu, my friend with whom I can discuss many topics. I am grateful to Prof. Jean Duhamel, for his knowledge and the fruitful discussions that helped me to strengthen my work. Thank you also to all the members of Prof. Duhamel's group, who have been helpful and welcoming. I am grateful to Prof. Michael Tam for inspiring me with his Nano-courses.

I wanted to thank Dr. Yi-Shiang, who mentored me to work with cells, Dr. Sandra Ormenese, who trained me to use confocal microscopy, Dr. Pierre Colson and Ms. Nicole Decloux , for their valuable help with TEM for cells, and Dr. Ji Liu, for sharing his experience and for his fruitful email discussions.

I am grateful to Prof. Sophie Laurent, Prof. Luce Vander Elst, Coralie Thirifays, Corinne Piérart, Adeline Hannecart, and my colleagues in the NMR and Molecular Imaging Laboratory (UMONS, Belgium) for their treasured help with relaxometry. Thank you, Prof. Yves Gossuin and Dr. Lam Quoc Vuong (Biomedical Physics Unit, UMONS, Belgium) for your precious support with magnetometry. I would like to thank Dr. Franck Couillaud and Coralie Genevois, at the Centre de Résonance Magnétique des Systèmes Biologiques, for allowing me to perform cellular hyperthermia in their lab and for being so helpful.

I sincerely thank Erin for helping me with my academic writing, Uyxing, Wiljan and Mylène for being my squash partners, Marie for allowing me to stay at her house when I was in Liège, Vusala, Mathilde Champeau, Mathield Weiss-Maurin, and Tuyen for your support. Thank you Varsity Squash team for a good practice time. Thank you Van U, Vi Beo, Thuy Vy, Vi Vi, Mien, and Thao for always listening. Thank you, Chi Phuong for sharing my brightest and darkest days.

I wish to thank the International Doctoral School in Functional Materials (IDS-FunMat), an Erasmus Mundus Program of the European Union, for financial support and for giving me the opportunity to work in six different labs, in three different countries, and allowing me to establish a solid network beneficial to my work. I also thank Prof. Mario Gauthier for funding my work during my 4th year, and the University of Waterloo Graduate Office for their financial support. I am grateful to Dr. Olivier Sandre for sponsoring my cellular hyperthermia work, and for giving me the chance to develop my work at the University of Mons. I sincerely appreciate Ms. Audrey Sidobre, Prof. Stéphane Carlotti, Ms. Marianne Delmas, Ms. Elodie Goury, Mr. Christopher Niesen, Ms. Catherine Van Esch, Ms. Susanna Fiorelli, and Ms. Marta Kucharska for their wonderful job as administrative coordinators.

Last but not least, I want to send my biggest and warmest thank you to my dearest Mother, whose love, passion, strength and bravery have enlightened everyday of my life. I am indebted to my Father, who sacrificed his life to love, to care and to ensure that we have the best education. I thank my brother who made me proud of him, and my Grandmothers and my Aunt Hang for always loving and trusting us.

I thank you all, a lot!

Vo Thu An Nguyen

Dedication

I dedicate this work to my dearest Mother, whose love, passion, strength and bravery have enlightened every day of my life and to my Father, who sacrificed his life to love, to care and to ensure that we have the best education.

Con kính tặng luận văn này cho Mẹ yêu dấu. Tình yêu thương, sức mạnh và sự can đảm của Mẹ thắp sáng cuộc đời con mỗi ngày. Con kính tặng luận văn này cho Bố, người đã dành cả cuộc đời để yêu thương, chăm sóc và đảm bảo cho chúng con nhận được sự giáo dục tốt nhất.

Some people dream of success while others wake up and work hard at it.

Winston Churchill

Logic will get you from A to B. Imagination will take you everywhere.

Albert Einstein

Table of Contents

AUTHOR'S DECLARATION ..... **II**

RÉSUMÉ / ABSTRACT ..... **III**

ACKNOWLEDGEMENTS ..... **VIII**

DEDICATION ..... **XI**

TABLE OF CONTENTS ..... **XII**

LIST OF FIGURES ..... **XVI**

LIST OF TABLES ..... **XXX**

LIST OF SCHEMES ..... **XXXII**

LIST OF ABBREVIATIONS AND SYMBOLS ..... **XXXIII**

CHAPTER 1 INTRODUCTION **1**

1.1 Overview 2

1.2 Research Objectives and Thesis Outline 3

CHAPTER 2 TEMPLATED SYNTHESIS OF MAGNETIC NANOPARTICLES THROUGH THE SELF-ASSEMBLY OF POLYMERS AND SURFACTANTS **7**

2.1 Overview 8

2.2 Introduction 9

2.3 *In Situ* Synthesis in Non-Polymeric Templates 10

2.3.1 Carboxylates *10*

2.3.2 Sulfonates and Sulfates *11*

2.4 *In Situ* Synthesis with Polymers in Solution or in the Bulk State 13

2.4.1 Dextran (DEX) and Polysaccharide Derivatives *13*

2.4.2 Synthetic Linear Homopolymers *18*

2.4.3 Synthetic Linear Copolymers *26*

2.5 Synthesis Templated by Preformed Structures 41

2.5.1 Microemulsions in an Organic Solvent *41*

2.5.2 Spherical Micelles in Water *45*
2.5.3 Cylindrical Multimolecular Micelles *51*
2.5.4 Lamellar Films *55*
2.5.5 Hexagonal Ordered Films *57*
2.5.6 Holey Membranes *60*
2.5.7 Tridimensional Scaffolds (Macroscopic Samples) *61*
2.5.8 Dispersed Colloids (Microscopic) *69*
2.5.9 Preformed Microspheres in Organic Solvents *76*
2.6 CONCLUSIONS 78

CHAPTER 3 POLYION COMPLEX MICELLES SYNTHESIS FROM ARBORESCENT POLYMERS 81

3.1 OVERVIEW 82
3.2 INTRODUCTION 83
3.2.1 Colloidal Stability *83*
3.2.2 Polymeric Stabilization by the Polyion Complexation Process *86*
3.3 EXPERIMENTAL PROCEDURES 93
3.3.1 Materials *93*
3.3.2 Synthesis of Poly(tert-butyl acrylate) Macroinitiator *94*
3.3.3 Silylation of 2-Hydroxyethyl Acrylate *95*
3.3.4 Synthesis of Poly(tert-butyl acrylate)-b-Poly(2-trimethylsilyloxyethyl acrylate) *96*
3.3.5 Hydrolysis of PtBA-b-PHEATMS *97*
3.3.6 Polyion Complexation Process *99*
3.3.7 Characterization *99*
3.4 RESULTS AND DISCUSSION 102
3.4.1 Synthesis of the Double-Hydrophilic Block Copolymers *102*
3.4.2 PIC Micelles in Water *108*
3.5 CONCLUSIONS 135

CHAPTER 4 TEMPLATING AND STABILIZING MAGNETIC NANOPARTICLES 137

4.1 OVERVIEW 138
4.2 INTRODUCTION 139
4.2.1 Coprecipitation Method *139*
4.2.2 Surface Modification of Templated MNPs for Improved Biocompatibility *144*

4.2.3 Advantages of Using Arborescent Copolymers as Templates for MNPs 148
4.3 Experimental Procedures 151
4.3.1 Templating 151
4.3.2 Stabilization 153
4.3.3 Characterization 154
4.4 Results and Discussion 156
4.4.1 Using PIC Micelles as Templates for MNPs 156
4.4.2 Templating – In Situ Coprecipitation 157
4.4.3 Stabilization of Magnetic Nanoparticles by the Polyion Complexation Technique 166
4.5 Conclusions 171
CHAPTER 5 MAGNETIC, RELAXOMETRIC AND HYPERTHERMIC PROPERTIES MEASUREMENTS 173
5.1 Overview 174
5.2 Introduction 175
5.2.1 Single Domain Theory and Superparamagnetism 175
5.2.2 Vibrating Sample Magnetometry – Magnetization Curve[9-11] 180
5.2.3 Magnetic Resonance Imaging - How Iron Oxides Affect Proton Relaxivity 184
5.2.4 Magnetic Field Hyperthermia 192
5.3 Experimental Procedures 200
5.3.1 Magnetic Polyion Complex Micelle Preparation 200
5.3.2 Characterization 201
5.4 Results and Discussion 204
5.4.1 Vibrating Sample Magnetometry 205
5.4.2 Relaxation Properties 210
5.4.3 Hyperthermia 223
5.5 Conclusions 229
CHAPTER 6 BIOCOMPATIBILITY ASSESSMENT AND *IN VITRO* CELL HYPERTHERMIA 231
6.1 Overview 232
6.2 Introduction 233
6.3 Experimental Procedures 236
6.3.1 Block Copolymer Synthesis 236
6.3.2 Polyion Complex Micelle Preparation 237

6.3.3 Magnetic Polyion Complex Micelle Preparation *238*
6.3.4 Biocompatibility Assessment *239*
6.3.5 In Vitro Magnetic Field Hyperthermia *244*
6.4 RESULTS AND DISCUSSION 246
6.4.1 Fluorescent Labeling of Block Copolymer *246*
6.4.2 Cytotoxicity Assessment *248*
6.4.3 Cell Internalization Studies *255*
6.4.4 In Vitro Cellular Radiofrequency Magnetic Field Hyperthermia *264*
6.5 CONCLUSIONS 272
CHAPTER 7 CONCLUSIONS 274
7.1 SUMMARY AND ORIGINAL CONTRIBUTIONS TO KNOWLEDGE 275
7.1.1 Study and Optimization of the Polyion Complexation Process to Produce Unimolecular Micelles *275*
7.1.2 Control over Fe_3O_4 Crystallite Size Using an Arborescent Copolymer *276*
7.1.3 Application of the Polyion Complexation Process to Produce Magnetic Micelles Stable Under Physiological Conditions *278*
7.1.4 Magnetic, Relaxometric and Hyperthermic Properties Measurements *278*
7.1.5 Biocompatibility Assessment *280*
7.1.6 In Vitro MFH Assessment *281*
7.2 PROPOSED FUTURE WORK 282
7.2.1 Fully Biocompatible Polymer Template *282*
7.2.2 Next Generation MNPS *283*
7.2.3 Cell Internalization *284*
7.2.4 Active Targeting by the MNPs *284*
7.2.5 Theranostics MNPs: Controlled Drug Release *285*
APPENDICES 287
REFERENCES 294

List of Figures

Figure 2-1. TEM images clearly showing: (a) lattice fringes; and (b) facetted shapes for nanoparticles coated with oleic acid, using 10 equivalents of reducing agent ($NaBH_4$) at room temperature. Reprinted with permission from Reference 4. Copyright 2011 WILEY-VCH Verlag GmbH & Co. KGaA, Weinheim.....11

Figure 2-2. Representation of two 1,4-linked α-L-guluronic acid (G)-blocks forming an "egg box" structure with ferrous ions. Reprinted with permission from Reference 13. Copyright 2000 Elsevier Science B.V. 17

Figure 2-3. TEM image for magnetite nanowires synthesized with poly(ethylene glycol) (PEG)/H_2O (1:2 by volume) at 150 °C for 24 h in an autoclave. The selected area electron diffraction (SAED) pattern is shown in the inset. Reprinted with permission from Reference 20. Copyright 2008 Elsevier B.V. 21

Figure 2-4. Suggested bond formation between COO^- and the Fe^{3+} ions at the ultra-small superparamagnetic iron oxide (USPIO) surface. Reprinted with permission from Reference 22. Copyright 2008 IOP Publishing Ltd. 24

Figure 2-5. Schematic structure of mPEG-*b*-PMAA-*b*-PGMA-Fe_3O_4 NPs loaded with adriamycin at neutral pH, designed to release the anticancer drug in the acidic environment of a tumor. mPEG: poly(ethylene glycol) monomethyl; PMAA: poly(methacrylic acid); PGMA: poly(glycerol methacrylate); and ADR: antitumor drug adriamycin. Reprinted with permission from Reference 27. Copyright 2008 The Royal Society of Chemistry. 28

Figure 2-6. Transmission electron micrographs for magnetic iron oxide precipitated in: (a) water alone; (b) the presence of poly(ethylene oxide) (PEO) homopolymer; and (c) the presence of PEO-*b*-poly(methacrylic acid) (PMAA) block copolymer. Note that Figure 2-6c is at somewhat higher magnification than the others; (d) magnetization curves for the PEO-*b*-PMAA coated NPs and for P(HEMA-*co*-MMA)

magnetic latexes obtained by inverse emulsion polymerization. Reprinted with permission from Reference 29. Copyright 2001 Elsevier. 31

Figure 2-7. EFTEM zero-loss images of: (a) β-FeOOH NPs; and (b) poly(ethylene glycol) (PEG)-*b*-poly(aspartic acid)-coated β-FeOOH NPs. Reprinted with permission from Reference 30. Copyright Elsevier B.V. 32

Figure 2-8. Size distribution by dynamic light scattering (DLS) (a, b, c, d) and from TEM images (a', b', c', d') of: (a, a') the initial suspension after coprecipitation in presence of PEO-*b*-PAA; (b, b') the non-captured particles; (c, c') the bleed-off samples; and (d, d') the captured clusters. Reprinted with permission from Reference 31. Copyright Elsevier B.V. 33

Figure 2-9. Morphology of poly(norbornene-*block*-deuterated norbornene dicarboxylic acid) loaded with iron oxide NPs (IONPs) at: (a) $\Phi_{PNOR/PNORCOOH}$ = 0.64/0.36 (disordered spheres); and (b) $\Phi_{PNOR/PNORCOOH}$ = 0.40/0.60 (interconnected spheres). Reprinted with permission from Reference 32. Copyright 2005 Elsevier Ltd. 34

Figure 2-10. Electron micrographs for poly(norbornene methanol)-*block*-poly(norbornene dicarboxylic acid) (PNORMEOH/PNORCOOH) diblock copolymer: (a) stained with I_2 vapor; and (b) doped with iron oxide by submerging a thin film in $FeCl_3$ solution. Reprinted with permission from Reference 33. Copyright 2006 Elsevier Ltd. 35

Figure 2-11. (a) *In situ* coprecipitation of iron oxide NPs (IONPs) at different polymer-to-Fe ratios; (b) polymer content measured by thermogravimetric analysis (TGA) for IONPs coated with different anchoring groups at a 1:2 [Polymer]:[Fe] weight concentration ratio. Reprinted with permission from Reference 37. Copyright 2014 Royal Society of Chemistry. 38

Figure 2-12. Strategy for the preparation of stabilized magnetic IONPs in aqueous media (top): (a) micelle formation by $PEGMA_x$-*b*-$AEMA_y$ diblock copolymer in water; (b) addition of the Fe^{3+}/Fe^{2+} mixture to the micellar solution, leading to complexation of the iron salts by the β-ketoester units inside the micellar core; and (c) transformation of the iron salt

"precursor" into IONPs inside the micellar core upon addition of NH_4OH solution; atomic force microscopy (AFM) images for the block copolymer micelles loaded with IONPs (bottom): (d) height image; (e) amplitude image; and (f) phase image. Reprinted with permission from Reference 38. Copyright 2009 American Chemical Society.....40

Figure 2-13. TEM of magnetic NPs (MNPs) obtained with: (a) molecular weight (MW) = 5.0×10^5 $g\cdot mol^{-1}$ non cross-linked chitosan; (b) cross-linked; (c) $\bar{M}_w$ = 1.0×10^5 $g\cdot mol^{-1}$ non cross-linked chitosan; (d) cross-linked. Reprinted with permission from Reference 40. Copyright 2006 Elsevier B.V. 42

Figure 2-14. Scanning electron microscope (SEM) images for: (a) as-synthesized $CoFe_2(C_2O_4)_3$ suspension after coprecipitation in a microemulsion; and (b) $CoFe_2O_4$ rods annealed at 720 °C. Reprinted with permission from Reference 41. Copyright 2005 Wiley-VCH.....44

Figure 2-15. (a) TEM image for an individual $CoFe_2O_4$ nanorod annealed at 720 °C; the insets illustrate SAED patterns acquired from two individual nanocrystals of size about 80 nm. The inset (a) shows the indexed diffraction pattern for the *fcc* crystals in the [011] beam direction, and inset (b) in the [001] beam direction; (b) high resolution transmission electron microscopy (HRTEM) image showing a grain boundary between two $CoFe_2O_4$ nanocrystals; and (c) HRTEM image for a $CoFe_2O_4$ nanocrystal. Reprinted with permission from Reference 41. Copyright 2005 Wiley-VCH. 44

Figure 2-16. Polyisoprene-*block*-poly(2-cinnamoylethyl methacrylate)-*block*-poly(*tert*-butyl acrylate) (PI-*b*-PCEMA-*b*-P*t*BA) as template: Photolysis cross-links the PCEMA shell (gray to black); the PI corona chains are made water-soluble by hydroxylating the double bonds (wavy lines to free-hand lines); the core is made inorganic-compatible by removing the *tert*-butyl groups (light gray to gridded pattern). Soaking the nanospheres in aqueous $FeCl_2$ leads to proton exchange (slanted to vertical grids) and the Fe^{2+} ions are precipitated (NaOH) and oxidized (H_2O_2) to yield cubic γ-Fe_2O_3 magnetic particles (last

step). Adapted with permission from Reference 42. Copyright 2000 American Chemical Society. 46

Figure 2-17. TEM images for PI-*b*-PCEMA-*b*-PtBA nanospheres at each step of the synthesis: (a) after PCEMA cross-linking and PI hydroxylation (stained with OsO_4); (b) after removal of the *tert*-butyl groups (stained with OsO_4); (c) after Fe_2O_3 loading (no staining); and (d) attraction by a magnet. Adapted with permission from Reference 42. Copyright 2000 American Chemical Society. 47

Figure 2-18. (a) Chemical structure of PEG-*b*-poly(4-vinylbenzylphosphonate) (PEG-*b*-PVBP) and schematic illustration of the proposed morphology of the pegylated IONPs (PIONs); and (b) TEM image for the PIONs and their size distribution as inset. Adapted with permission from Reference 43. Copyright 2011 Elsevier B.V. 48

Figure 2-19. (a) Representative TEM images for Fe_3O_4 NPs synthesized with star-like PAA-*b*-PS templates, $D(Fe_3O_4) = 10.1 \pm 0.5$ nm; (b) TEM; and (c) HRTEM images for Fe_3O_4-$PbTiO_3$ core–shell NPs formed with the star-like triblock copolymers nanoreactors. Reprinted with permission from Reference 44. Copyright 2013 Macmillan Publishers Limited.....50

Figure 2-20. TEM, HRTEM and digital camera images for core/shell Fe_3O_4/Au NPs: (a) Fe_3O_4 core ($D = 6.1 \pm 0.3$ nm); and (b) Fe_3O_4/Au core/shell NPs at different magnifications (Au shell thickness is 2.9 ± 0.2 nm). Fe_3O_4 appears dark in the center. The magnetic properties of Fe_3O_4 were retained, as evidenced by the response of the NP dispersion in toluene to a magnet (right panel in (b)). Reprinted with permission from Reference 44. Copyright 2013 Macmillan Publishers Limited.....50

Figure 2-21. TEM images for samples prepared in alcohol/water mixtures with various volume ratios of alcohol to water: (a) 0:1; (b) 1:1; and (c) 5:1. Reprinted with permission from Reference 45. Copyright Springer Science Business Media, LLC 2008. 51

Figure 2-22. (a) AFM height image for the polychelate of a poly(acrylic acid)-*graft*-poly(*n*-butyl acrylate) brush and $FeCl_3$ after dialysis; and (b) TEM image for the

unimolecular polymer brush polychelate of $FeCl_3$ (after dialysis). Adapted with permission from Reference 46. Copyright 2004 Springer-Verlag. 52

Figure 2-23. Synthesis of Fe_3O_4/polymer nanocomposite in the presence of poly(ethylene glycol) methyl ether acrylate (PPEGMEA)-*g*-PMAA densely grafted double-hydrophilic copolymer. Reprinted with permission from Reference 3. Copyright The Royal Society of Chemistry 2008. 53

Figure 2-24. (a) TEM micrograph for a lamellar PS-*b*-P2VP copolymer containing 1.2 meq of iron/g P2VP; sample heated to 195 °C for 24 h, scale bar = 50 nm; (b) TEM micrograph for the same copolymer containing a total of 1.2 meq of Fe and Co/g P2VP, with an atomic ratio of Fe to Co of 80:20; sample heated to 161 °C for 24 h, scale bar = 100 nm; and (c) scanning transmission electron microscopy micrograph for the copolymer containing a total of 1.2 meq of Fe and Co/g P2VP, atomic ratio of Fe to Co = 50:50; sample heated to 161 °C for 24 h; the atomic ratio of Fe:Co at the center of the large particles was 48.9:51.1 from energy dispersive X-ray spectroscopy (EDX); scale bar = 50 nm. Reprinted with permission from Reference 49. Copyright 2003 Elsevier B.V. 56

Figure 2-25. (a) TEM image for a self-assembled pattern of IONPs with hexagonal packing. The inset is a SAED pattern typical for γ-Fe_2O_3; (b) AFM image for the hexagonal pattern of IONPs on a silicon wafer; and (c) field emission-scanning electron microscopy (FE-SEM) image in tilt view. The molar ratio of $FeCl_3$ precursor to 4-vinylpyridine was 0.5 in all cases. Reprinted with permission from Reference 50. Copyright 2005 American Chemical Society. 57

Figure 2-26. Schematic illustration of the fabrication of oxide nanodots: (A) highly ordered PS-*b*-PEO thin film prepared by a solvent annealing process; (B) nanoporous template produced by activation of the PEO cylinders upon exposure to ethanol at 40 °C for 15 h; (C) the metal oxide precursor diffuses into the cylinders after spin coating of the metal nitrate solution; and (D) oxide dots remaining after the ultraviolet (UV)/ozone treatment. (a) TEM cross-sectional image for iron oxide nanodots; the inset shows a higher

magnification image; (b) cross-sectional HRTEM image for a single nanodot; and (c) HRTEM image for the nanodots after the UV/ozone treatment; the inset shows crystalline fringes corresponding to Fe_3O_4. Reprinted with permission from Reference 51. Copyright 2012 The Royal Society of Chemistry. 59

Figure 2-27. (a) AFM; and (b) SEM images for hexagonally ordered iron oxide nanodots after UV/ozone treatment. The inset of (b) shows the iron oxide nanodots after annealing at 800 °C for 1 h. Reprinted with permission from Reference 51. Copyright 2012 The Royal Society of Chemistry. 60

Figure 2-28. TEM images for unsupported Fe_3O_4 NPs synthesized by: (a, b) the hydrothermal method; (c, d) the *in situ* formation of Fe_3O_4 NPs on the CF composite; and (e) schematic representation of the *in situ* formation of Fe_3O_4 nanocrystals in the confined pores of carbon foam. Reprinted with permission from Reference 54. Copyright 2011 The Royal Society of Chemistry. 62

Figure 2-29. TEM images for sample sections: (a) 3.5 wt% Fe-loaded polystyrene–polyacrylate gel prior to reaction with NaOH (scale bar = 500 nm); (b) after reaction with NaOH, showing the distribution and uniformity of the magnetite nanocrystallites (scale bar = 500 nm); and (c) synthesis of the magnetic sponge-like copolymer gel. Comparison between an unloaded polymer gel (c, left), after exposure to a 0.2 M Fe^{2+} solution (c, middle), and after reaction with NaOH (c, right). The gels imaged with a digital camera in (c) were in the swollen state. Reprinted with permission from Reference 55. Copyright 1998 WILEY-VCH Verlag GmbH. 64

Figure 2-30. (a) Schematic representation and (b) appearance of a magnetic hybrid hydrogel obtained by photopolymerization and *in situ* coprecipitation; (c) in the second step, the ferrogel was exposed to NaOH to hydrolyze the cross-link points and induce the release of water-dispersible IONPs. Adapted with permission from Reference 58. Copyright 2011 Elsevier B.V. 66

Figure 2-31. (a) TEM image and (b) SAED pattern for magnetic Fe_3O_4 NPs synthesized by the coprecipitation of iron salts within a polymer disk; (c) typical HRTEM image for a single Fe_3O_4 NP, and size distribution of the Fe_3O_4 NPs for samples containing the cross-linker at: (d) 0.46 mol% and (e) 6.14 mol%. Reprinted with permission from Reference 58. Copyright 2011 Elsevier B.V. 67

Figure 2-32. Schematic views and pictures of polyacrylamide (PAAm) hydrogel networks at three steps of loading with magnetite NPs: (a) swollen hydrogel; (b) iron ion-loaded hydrogel; and (c) magnetite NPs in the hydrogel matrix, inset: TEM image showing well-dispersed MNPs of uniform size. Reprinted with permission from Reference 61. Copyright 2009 Elsevier B.V.....68

Figure 2-33. (a) TEM image for hybrid poly(*N*-isopropylacrylamide-*co*-acrylic acid-*co*-2-hydroxyethyl acrylate) (poly(NIPAM-*co*-AA-*co*-HEA)) microgels loaded with 0.618 g Fe_3O_4/g polymer; the scale bar is 150 nm; and (b) magnetization curve at 300 K. Reprinted with permission from Reference 62. Copyright 2004 American Chemical Society. 70

Figure 2-34. (a) Chemical structure of a poly(*N*-vinylcaprolactam/acetoacetoxyethyl methacrylate) copolymer; and SEM images for: (b) empty cross-linked microgels; (c) magnetite NPs; (d) composite microgels with 4% magnetite; (e) SEM; and (f) AFM images for microgels with 9.4% magnetite (the height scale of the AFM image in the height mode is 0–100 nm.) Reprinted with permission from Reference 63. Copyright 2004 American Chemical Society.....71

Figure 2-35. Optical images for various magnetic microparticles: (a) homogenous magnetic disks; (b) homogenous triangular particles; (c) Janus disks; and (d) gradient particles. Reprinted with permission from Reference 65. Copyright 2012 American Chemical Society. 73

Figure 2-36. Coprecipitation process in photopolymerized microgels with ~ 20 μm diameter prepared in a microfluidic channel. After deprotonation in 0.5 M NaOH and rinsing with 0.5% Tween 20 to reach pH 7, 0.2 M $FeCl_3$ and 1 M $FeCl_2$ solutions were mixed with

the microgels at a Fe^{3+}:Fe^{2+} ratio of 1:75. After diffusion of the iron ions in the polymer particles, excess salts were removed. After the addition of NH_4OH at 60 °C, the MNPs were nucleated and grown *in situ* before a final rinse with Tween 20. All these steps were repeated several times for successive growth cycles. Reprinted with permission from Reference 65. Copyright 2012 American Chemical Society. 74

Figure 2-37. TEM images for microgels with different magnetite contents: (a, b) no magnetite; (c, d) 8.4 wt%; (e, f) 15.4 wt%. Inset: EDX iron-mapping image. Reprinted with permission from Reference 66. Copyright 2007 Wiley-VCH Verlag GmbH & Co., Weinheim. 75

Figure 2-38. (a) Schematic representation of the preparation of Fe_3O_4 NPs embedded in PS microspheres by thermal decomposition of $Fe(oleate)_3$ at 300 °C; SEM images for: (b) the polymer seed microspheres prepared by dispersion polymerization; (c) the magnetic polymer microspheres prepared by swelling and thermolysis; (d) the outer surface of magnetic polymer microspheres; and (e) TEM image for the ultramicrotomed magnetic polymer microspheres, showing the location of the IONPs in the microspheres. Reprinted with permission from Reference 67. Copyright 2009 American Chemical Society. 77

Figure 3-1. Schematic representation of the approach of two sterically stabilized particles. The parameter δ represents the thickness of the solvophilic protective polymer layer forming the shell. Reprinted with permission from Reference 1. Copyright 1983 Academic Press. 84

Figure 3-2. Schematic illustration of the formation of a polyion complex micelle by PAA-*b*-PHEA and G0PS-*g*-P2VP in water. 92

Figure 3-3. ^1H NMR (400 MHz) spectra for (a) P*t*BA, (b) P*t*BA-*b*-P(HEATMS) in $CDCl_3$, and (c) PAA-*b*-PHEA in DMSO-d_6. 106

Figure 3-4. SEC chromatograms for P*t*BA homopolymers and P*t*BA-*b*-PHEATMS copolymers. 107

Figure 3-5. Ionization levels of CO_2H and N functional groups at different pH. 109

Figure 3-6. Hydrogen bonding between a P2VP unit and a PAA unit. 110

Figure 3-7. Intensity-weighted size distributions for G1 (pH 4) and G1@PAA-*b*-PHEA PIC micelles (pH 7) obtained at various *f* ratios at 25 °C.....112

Figure 3-8. Number-weighted size distributions for G1 (pH 4) and G1@PAA-*b*-PHEA PIC micelles (pH 7) obtained at various *f* ratios at 25 °C.....113

Figure 3-9. Intensity- or number-weighted hydrodynamic diameter and zeta potential of PIC micelles. The last points are not connected with the lines as they were off-scale. 115

Figure 3-10. Measured d*n*/d*c* of the PIC micelles as a function of composition. 121

Figure 3-11. Zimm plots for PIC micelles G1@PAA_{27}-*b*-$PHEA_{56}$ and G1@PAA_{13}-*b*-$PHEA_{50}$ for $f = 9$.....121

Figure 3-12. Zimm plots for PIC micelles G1@PAA_{13}-*b*-$PHEA_{150}$ for different *f* ratios. 122

Figure 3-13. Zimm plots for PIC micelles G1@PAA_{27}-*b*-$PHEA_{260}$ for different *f* ratios. 123

Figure 3-14. Dependence of A_2 on the number of –OH groups/PIC micelle. 130

Figure 3-15. Zeta potential and hydrodynamic diameter of PIC micelles G1@PAA_{27}-*b*-$PHEA_{260}$ for $f = 0.5$ at different pH.....131

Figure 3-16. 3D model, height and phase AFM images (from left to right) for the G1 substrate. 132

Figure 3-17. 3D models (row 1), height (row 2) and phase AFM images (row 3) for G1@PAA_{27}-*b*-$PHEA_{260}$ with $f = 0.5$ at set-points ratios of 0.96 (column 1), 0.92 (column 2), and 0.86 (column 3).....133

Figure 4-1. The different phases of iron oxyhydroxides formed in a bidimensional diagram *versus* the molar OH^-/Fe_{Total} hydroxylation ratio and the ferrous-ferric composition

in the system. Reprinted with permission from Reference 21. Copyright 2006 Académie des Sciences. 142

Figure 4-2. Size distributions for G0-G2 graft copolymers in HCl solutions (pH 4) at 25 °C. 150

Figure 4-3. (Left) Weak magnetization of the MNPs produced by coprecipitation of iron salts in the PIC micelle templates. (Right) Hydrodynamic size distribution by DLS at 25 °C for PIC micelles G1@ PAA_{27}-*b*-$PHEA_{260}$ *f* = 0.5 (pH 7), PIC micelles mixed with the iron salt solution (pH 2.6), and the product obtained after adding the NH_4OH solution (pH 9). .157

Figure 4-4. (Left) Hydrodynamic size distribution by DLS for G1 (pH 4) at 25 °C. (Right) TEM image for G1 prepared by depositing a THF solution, and staining with iodine. 158

Figure 4-5. Improved colloidal stability of templated G1@Fe_3O_4 ferrofluid as compared with non-templated Fe_3O_4 ferrofluid. 159

Figure 4-6. Crystallite size of Fe_3O_4 NPs synthesized in the presence of: linear P4VP at 50 °C, G1 at 50 °C, and G1 at 80 °C. Inset: Selected area diffraction pattern for templated G1@Fe_3O_4. 161

Figure 4-7. Top: TGA curves for pure G1 template (green, dotted), a mixture of dry G1 and Fe_3O_4 (blue, long dash), and G1@Fe_3O_4 (red, solid). Bottom: Temperature ramp (green, broken dash), weight loss (red, solid), and differential of the weight loss curve (blue, short dash) for G1@Fe_3O_4. 163

Figure 4-8. (a) Absorbance spectra for 5 M HCl without iron (top panel) and with 10 μg/mL iron (bottom panel). (b) Calibration curve in 5 M HCl generated for iron concentrations ranging from 0 to10 μg/mL. Preprinted with permission from Reference 96. Copyright 2007 BioTechniques. (c) Calibration curve generated in 5 M HCl at λ = 350 nm (path length *l* = 2 mm). 166

Figure 4-9. Size distributions for magnetic micelles G1@Fe_3O_4@PAA_{13}-*b*-$PHEA_{150}$ at different *f* ratios obtained at 25 °C and pH 7. 167

Figure 4-10. Size distributions for magnetic micelles G1@Fe_3O_4@ PAA_{27}-*b*-$PHEA_{260}$ at different *f* ratios obtained at 25 °C and pH 7. 168

Figure 4-11. TEM images for Fe_3O_4 crystallites in G1@Fe_3O_4@PAA_{27}-*b*-$PHEA_{260}$ *f* = 0.5. 169

Figure 4-12. AFM images for magnetic micelles G1@Fe_3O_4@PAA_{27}-*b*-$PHEA_{260}$ *f* = 0.5. 169

Figure 4-13. Magnetic micelles at various amplitude set points (the lower the value in mV, the higher the average deflection of the cantilever and thus the exerted force). 170

Figure 4-14. Zeta potential and intensity-weighted hydrodynamic diameter D_h of MPIC micelles G1@Fe_3O_4@PAA_{27}-*b*-$PHEA_{260}$ at *f* = 0.5 as a function of pH. 171

Figure 5-1. Switching of the magnetization in a particle across the anisotropy barrier under a) no external magnetic field; b) external magnetic field pointing downward; and c) external magnetic field pointing upward. 177

Figure 5-2. a) Main parameters of interest extracted from a generic hysteresis loop; b) Room temperature magnetization curve for superparamagnetic particles. 182

Figure 5-3. Nuclei spin oriented along B_0, with a slight excess in its direction producing a net longitudinal magnetization, M_0. Reprinted with permission from Reference 15. Copyright 2006 Humana Press Inc. 185

Figure 5-4. 180^o Refocusing pulse and the formation of a spin echo. Reprinted with permission from Reference 15. Copyright 2006 Humana Press Inc. 188

Figure 5-5. Outer-sphere relaxation of water protons in the vicinity of a superparamagnetic CA. Reprinted with permission from Reference 19. Copyright 2009 John Wiley & Sons, Inc. 190

Figure 5-6. (Left) Custom setup for single frequency (755 kHz) hyperthermia measurements in Bordeaux. (Right) Field lines calculated using cylindrical axi-symmetry with the finite element simulation freeware FEMM (http://www.femm.info), showing calculated *B* field values close to the experimentally measured ones (*B* = 1 mT corresponds to $H \sim 800\ A \cdot m^{-1}$). 203

Figure 5-7. Commercial DM3 device from nanoScale Biomagnetics (Zaragoza, Spain) designed for *in vivo* hyperthermia measurements with quad frequency capability. The simulation shows that the coil was specially designed with an observation window. 204

Figure 5-8. Magnetization curves (at 300 K) for the Fe_3O_4 samples. Sample nomenclature is explained in the text, and the iron oxide concentrations $\boldsymbol{C_{Fe3O4}}$(mg/mL) are listed in Table 5-1. 206

Figure 5-9. (Top) Correlation between the normalized transverse relaxivity and the particle diameter at high field (≥ 1 T) and 37 °C. (Bottom) Correlation between the transverse relaxivity and the normalized diameter at high field (≥ 1 T) and 37 °C. The transverse relaxivity $r_2 = 335\ s^{-1} \cdot mM^{-1}$ measured for sample 0.7-80-BC locates it in the high range of the spectrum. Adapted with permission from Reference 88. Copyright 2012 WILEY-VCH Verlag GmbH & Co. KGaA, Weinheim. 214

Figure 5-10. NMRD profiles for the various synthesized Fe_3O_4 samples. The sample nomenclature is described in the text. 216

Figure 5-11. Fits to the NMRD curves for the uncoated magnetic G1@Fe_3O_4 micelles. 218

Figure 5-12. Fits to the NMRD curves for the coated magnetic G1@Fe_3O_4 micelles. 219

Figure 5-13. Specific absorption rate (SAR) of magnetic G1 micelles as a function of magnetic field amplitude H_{max} at various fixed frequencies *f*.....225

Figure 5-14. Specific absorption rate (SAR) of magnetic G1 micelles as a function of magnetic field frequency for various fixed values of magnetic field amplitude H_{max}. 227

Figure 5-15. Specific absorption rate (SAR) of the magnetic micelles as a function of the product of squared magnetic field amplitude H_{max}^2 and frequency *f*.....228

Figure 6-1. (Left) 48-well plate where L929 and U87 cells were seeded and incubated with the MPIC micelles at 3 concentrations (1250, 700, and 140 µg Fe_3O_4 /mL) in DMEM before being rinsed, trypsinized and transferred to NMR tubes for magnetic field exposure in a 37°C thermostated bath (Right). The image also shows the two optical fibres linked to the signal conditioner (Opsens) recording the temperature profiles. 245

Figure 6-2. (Left) Fluorescence spectra for PAA-*b*-PHEA, free fluoresceinamine and fluorescently labeled PAA*-*b*-PHEA; (Right) Linear correlation of fluoresceinamine (*Ex*: 488 *Em*: 530) emission intensity vs. concentration in PBS buffer. 247

Figure 6-3. (Left) Fluorescence spectra for PIC and PIC* micelles in water; (Right) Fluorescence spectra for MPIC and MPIC* micelles in PBS buffer. 248

Figure 6-4. Cytotoxicity profiles for the PIC micelles G1@PAA-*b*-PHEA at various complexing ratios *f* with the fibroblast-like L929 cells determined via MTS assay at different concentrations after 48 h of incubation. The cell viability values are expressed as the mean values and the standard deviations from three independent experiments, each with four replicates per condition, relatively to untreated cells (100% control). 250

Figure 6-5. Cytotoxicity profiles for uncoated MNPs G1@Fe_3O_4 (*f* = 0) and MPIC micelles G1@Fe_3O_4@PAA-*b*-PHEA at various complexing ratios *f* towards fibroblast-like L929 cells determined via MTS assay at different concentrations after 48 h of incubation. Cell viability values are expressed as the mean values and standard deviations from three independent experiments with four replicates, relatively to the untreated cells (100% control). 251

Figure 6-6. Cellular toxicity induced by SPION (Reprinted with permission from Reference 61. Copyright 2010 Neenu Singh et al.).....253

Figure 6-7. CLSM images for the L929 cells treated with the PIC* micelles G1@PAA*$_{27}$-*b*-PHEA$_{260}$ *f* = 0.5; 2 mg/mL, 24 h incubation. 256

Figure 6-8. CLSM images for L929 cells treated with the MPIC* micelles G1@Fe_3O_4@PAA*$_{27}$-*b*-PHEA$_{260}$ *f* = 0.5; 140 µg Fe_3O_4/mL, 24 h incubation. 257

Figure 6-9. 3D construction and xz, yz sections for L929 cells internalized with MPIC* micelles G1@Fe_3O_4@PAA*$_{27}$-*b*-PHEA$_{260}$ *f* = 0.5; 140 µg Fe_3O_4/mL, 24 h incubation.....258

Figure 6-10. TEM images for L929 cells treated with an MPIC micelle solution (100 µg/mL, 24 h incubation), inset showing iron oxide NPs internalized in L929 cell. 260

Figure 6-11. Proposed mechanism of clathrin-mediated endocytosis of MPIC micelles into the L929 cells. 261

Figure 6-12. Dependence of the mean fluorescence intensity (MFI) for L929 cells treated with 100 µg/mL solution) of the MPIC* micelles G1@Fe_3O_4@PAA*$_{27}$-*b*-PHEA$_{260}$ *f* = 0.5 on the concentration (after 24 h incubation) and on the incubation time (*$p < 0.002$, **$0.002 < p < 0.01$ by the two-tailed Student's *t*-test, degrees of freedom = 4). 263

Figure 6-13. Linear regressions for the MFI and % positive L929 cells vs. incubation time. 264

Figure 6-14. Temperature variation of suspensions of control cells and cells incubated with MPIC micelles during exposure to an alternating magnetic field (755 kHz, 10.2 kA/m, 1.5 or 3 h).....268

Figure 6-15. Viability of L929 (left) and U87 (right) cells determined by the MTS assay after 24 h of incubation with MPIC micelles G1@Fe_3O_4@PAA$_{27}$-*b*-PHEA$_{260}$ *f* = 0.5, followed by or without exposure to the high frequency alternating magnetic field. Cell viability values were expressed as the mean values relative to the untreated cells (control 100%; statistical analysis was done by the two-tailed Student's *t*-test). 269

List of Tables

Table 2-1. Influence of the PEG:H_2O volume ratio on the identified phases and crystallite size collected from X-ray diffraction (XRD) data. All samples are prepared at 150 °C for 24 h. Reprinted with permission from Reference 20. Copyright 2008 Elsevier B.V…22

Table 2-2. Influence of reaction temperature and time on the phases of nanostructured iron oxides and crystallite sizes. All samples are prepared using PEG:H_2O = 1:2 in volume. Reprinted with permission from Reference 20. Copyright 2008 Elsevier B.V. 22

Table 2-3. Zeta potential and average hydrodynamic diameters of poly(acrylic acid) (PAA) or poly(styrene sulfonate-*alt*-maleic acid) (PSS-*alt*-MA)-coated IONPs with different cross-linking densities for an iron oxide concentration of 0.14 wt% at pH 8. Adapted with permission from Reference 34. Copyright 2011 American Chemical Society.....36

Table 2-4. Summary of TGA weight loss results and particle size (d_{TEM} and d_{XRD}) of polymer-coated IONPs at different polymer-to-iron ratios. PAEA: phosphonic acid ethyl acrylate. Reprinted with permission from Reference 37. Copyright 2014 Royal Society of Chemistry.....39

Table 2-5. Summary of the different organic templates used as host matrices for the synthesis of MNPs. In this review, the examples gathered from the literature were sorted according to their chemical nature and structural properties (e.g., geometry, dimensionality, size). DEX: dextran; Alg: alginate; PNIPAM: poly(*N*-isopropylacrylamide); PVA: poly(vinyl alcohol); PVP: polyvinylpyrrolidone; P4VP: poly(4-vinylpyridine); PMGI: poly(methyl glutarimide); DHBC: double-hydrophilic block copolymer; PGA: poly(glycerol acrylate); PAsp: poly(aspartic acid); PAEMA: poly[2-(acetoacetoxy) ethyl] methacrylate; PGMA: poly(glycerol methacrylate); PDMAEMA: poly[(*N*,*N*-dimethylamino)ethyl methacrylate] PNOR: polynorbornene; PAMPS: poly(2-acrylamido-2-methyl-1-propansulfonic acid).....79

Table 3-1. Theoretical estimates of van der Waals attraction between sterically stabilized particles (conditions leading to dispersion instability are bolded). Adapted with permission from Reference 1. Copyright 1983 Academic Press. 85

Table 3-2. Hydrodynamic diameter and PDI of G1@PAA-*b*-PHEA PIC micelles (in water at pH 7) obtained for various *f* ratios at 25 °C. The optimal *f* values for each DHBC are bolded. 114

Table 3-3. Measured (top) and calculated (bottom) refractive index increments of selected PIC micelles. 120

Table 3-4. Data derived from the SLS and DLS measurements on PIC micelles. 124

Table 4-1. Characterization data for G1-G3 arborescent copolymer templates. Adapted with permission from Reference 77. Copyright The Royal Society of Chemistry 2012. 149

Table 5-1. Magnetic properties of the Fe_3O_4 samples synthesized. 207

Table 5-2. Longitudinal and transverse relaxivities of the samples at 20 and 60 MHz. 211

Table 5-3. Relaxivities of 0.7-80-BC SPIONs and commercial contrast agents.....212

Table 5-4. Magnetic properties of Fe_3O_4 samples from NMRD analysis. 221

List of Schemes

Scheme 3-1. Synthesis of P*t*BA via ATRP. 103

Scheme 3-2. Silylation of HEA. 103

Scheme 3-3. ATRP synthesis of P*t*BA-*b*-PHEATMS and deprotection reaction to produce PAA-*b*-PHEA. 105

Scheme 4-1. Alkaline coprecipitation and oxidation reactions. 140

Scheme 4-2. Synthesis of an arborescent copolymer (G0PS-*g*-P2VP) by successive grafting reactions. Reprinted with permission from Reference 77. Copyright 2012 The Royal Society of Chemistry 2012. 148

List of Abbreviations and Symbols

2VP	2-vinylpyridine
A	exchange energy density (in critical radius equation)
*A**	Hamaker constant (for colloidal stability)
A_2	second virial coefficient
AAEM	acetoacetoxyethyl methacrylate
acac	acetylacetonate
ADR	antitumor drug adriamycin
AFM	atomic force microscopy
Alg	alginate
AMF	alternating magnetic field
AO	acridine orange
ATRP	atom transfer radical polymerization
AuNR	gold nanorods
B_0	strength of the magnetic field
BC	block copolymer
BIS	*N*,*N*'-methylene bisacrylamide
BSA	bovine serum albumin
C	specific heat capacity
CA	contrast agent or citric acid
CBMi	*N*-4-carboxybutylmaleimide
CD	cyclodextrin
CF	carbon foam
CHP	continuous hydrothermal processing
CLSM	confocal laser scanning microscopy
CNT	carbon nanotube
CRP	controlled radical polymerization

CTAB	cetyltrimethylammonium bromide
D_0	median diameter
DAPI	4',6'-diamidino-2-phenylindole
DEX	dextran
$D_{\mathrm{h}}^{\mathrm{I}}$ or D_{h}	intensity-weighted hydrodynamic diameter
$D_{\mathrm{h}}^{\mathrm{n}}$	number-weighted hydrodynamic diameter
DHBC	double-hydrophilic block copolymer
DLS	dynamic light scattering
D_{max}	maximum calculated diameter
DMEM	Dulbecco modified Eagle medium
DMF	*N*,*N*-dimethylformamide
DMSO	dimethyl sulfoxide
D_n	number-average diameter
d*n*/d*c*	refractive index increment
D_{v}	volume-average diameter
Đ	dispersity, molar-mass dispersity
E_{a}	anisotropy energy
EDC	1-ethyl-3-(3-dimethylaminopropyl) carbodiimide hydrochloride
EDS	energy-dispersive X-ray spectroscopy
EFTEM	energy filtering transmission electron microscopy
EG	ethylene glycol
EGFR	epithelial growth factor receptor
EPR	enhanced permeation and retention
f	complexation ratio CO_2H/N or magnetic field frequency
FA	fluoresceinamine
FACS	fluorescence-activated cell sorting
FBS	fetal bovine serum
FC	field cooled
FE-SEM	field emission-scanning electron microscopy

FID	free induction decay
FITC	fluorescein isothiocyanate
FT-IR	Fourier transform infrared spectroscopy
g	graft
G	1,4-linked α-l-guluronic acid
G1	G0 polystyrene-*graft*-poly(2-vinylpyridine)
$g^{(2)}(t)$	second-order autocorrelation function
Gly	glycidyl
H	magnetic field amplitude
H_c	coercive field
HEA	2-hydroxyethyl acrylate
HEATMS	2-trimethylsilyloxyethyl acrylate
HGMS	high-gradient magnetic separator
HRTEM	high resolution transmission electron microscopy
HSQC	heteronuclear single quantum coherence
ILP	intrinsic loss power
IONP	iron oxide nanoparticle
k_B or *k*	Boltzmann constant
K	magnetocrystalline anisotropy constant
LCST	lower critical solution temperature
l_{exch}	exchange length
LMP	lysosomal membrane permeabilization
l_{PHEA}	chain length of poly(2-hydroxyethyl acrylate) block
LRT	linear relaxation theory
m	concentration (g/L)
M	1,4-linked β-d-mannuronic acid
MA	maleic acid
MALLS	multiangle laser light scattering
M_d	mass specific magnetization

MFH	magnetic field hyperthermia
MFI	mean fluorescence intensity
M_{nr}	nonrelaxing magnetization
MNP	magnetic nanoparticle
mol%	mole percent
mPEG	poly(ethylene glycol) monomethyl ether
MPIC	magnetic polyion complex
MPIC*	fluorescently labeled magnetic polyion complex
MR	magnetic resonance
M_r	remanence magnetization
MRI	magnetic resonance imaging
M_s	volume specific magnetization
M_{sat}	saturation magnetization
MTS	3-(4,5-dimethylthiazol-2-yl)-5-(3-carboxymethoxyphenyl)-2-(4-sulfophenyl)-2H-tetrazolium
$\bar{M}_w$	mass-average molar mass
MWCO	molecular weight cutoff
NaDBS	sodium dodecylbenzenesulfonate
NIR	near infrared radiation
NMR	nuclear magnetic resonance
NMRD	nuclear magnetic relaxation dispersion
NP	nanoparticle
OE	octyl ether
P	heat dissipation
P(HEATMS)	poly(2-trimethylsilyloxyethyl acrylate)
P(PEO_nMA)	poly(ethylene oxide) methyl ether methacrylate
P2VP	poly(2-vinylpyridine)
P4VP	poly(4-vinylpyridine)
P4VP·EtBr	poly(*N*-ethyl-4-vinylpyridinium bromide)

PAA	poly(acrylic acid)
PAAm	polyacrylamide
PAEA	phosphonic acid ethyl acrylate
PAEMA	poly[2-(acetoacetoxy) ethyl] methacrylate
PAMPEO	poly(acrylate methoxy poly(ethylene oxide))
PAMPS	poly(2-acrylamido-2-methyl-1-propansulfonic acid)
PAsp	poly(aspartic acid)
PBO	poly(ethylene-*co*-butylene)
PCEMA	poly(2-cinnamoylethyl methacrylate)
PCL	poly(3-caprolactone)
PDI	polydispersity index
PDMAEMA	poly[(*N*,*N*-dimethylamino)ethyl methacrylate]
PEG	poly(ethylene glycol)
PEGDA	poly(ethylene glycol) diacrylate
PEGMA	poly (ethylene glycol methyl ether methacrylate)
PEO	poly(ethylene oxide)
PGA	poly(glycerol acrylate)
PGMA	poly(glycerol methacrylate)
PHEA	poly(2-hydroxyethyl acrylate)
PHEMA	poly(2-hydroxyethyl methacrylate)
PI	polyisoprene
PIB	polyisobutylene
PIC	polyion complex
PIC*	fluorescently labeled polyion complex
PION	pegylated iron oxide nanoparticle
PMAA	poly(methacrylic acid)
PMAA-PTTM	trithiol-terminated poly(methacrylic acid)
PMAO	poly(maleic anhydride-*alt*-1-octadecene)
PMDETA	*N*,*N*,*N′*,*N″*,*N‴*-pentamethyldiethylenetriamine

PMGI	poly(methyl glutarimide)
PnBA	poly(*n*-butyl acrylate)
PNIPAM	poly(*N*-isopropylacrylamide)
PNOR	polynorbornene
PNORCOOH	poly(norbornene dicarboxylic acid)
PNORMEOH	poly(norbornene methanol)
POEGA	poly(oligoethylene glycol acrylate)
POEGMA	poly(oligo(ethylene glycol) methacrylate)
PP	polymer precursor
PPEGMEA	poly(ethylene glycol) methyl ether acrylate
PPO	poly(propylene oxide)
PS	polystyrene
PSS	poly(styrene sulfonate)
PtBA	poly(*tert*-butyl acrylate)
PVA	poly(vinyl alcohol)
PVBP	poly(4-vinylbenzylphosphonate)
PVP	polyvinylpyrrolidone
PXRD	powder X-ray diffraction
R_1	longitudinal relaxation rate
r_1	longitudinal relaxivity
R_2	transverse relaxation rate
r_2	transverse relaxivity
RAFT/MADIX	xanthate reversible addition-fragmentation chain-transfer
RC	critical radius
RES	reticuloendothelial system
RF	radio frequency
R_g	radius of gyration
R_h	hydrodynamic radius
r_{NMR}	average crystal radius

ROMP	ring-opening metathesis polymerization
ROS	reactive oxygen species
SAED	selected area electron diffraction
SANS	small-angle neutron scattering
SAR	specific absorption rate
SAXS	small-angle X-ray scattering
SDS	sodium dodecyl sulfate
SEC	size-exclusion chromatography
SEM	scanning electron microscope
semi-IPN	semi-interpenetrating
SFL	stop-flow lithography
SLP	specific loss power
SLS	static light scattering
SPION	superparamagnetic iron oxide nanoparticle
SQUID	superconducting quantum interference device
STEM	scanning transmission electron microscopy
T_1	longitudinal or spin-lattice relaxation time
T_2	transverse or spin-spin relaxation time
T_B	blocking temperature
*t*BA	*tert*-butyl acrylate
TE	echo time
TEM	transmission electron microscopy
TFA	trifluoroacetic acid
THF	tetrahydrofuran
TGA	thermogravimetric analysis
THBC	triple-hydrophilic block copolymer
TMS-Cl	trimethylsilyl chloride
TMSMA	(trimethoxysilyl)propyl methacrylate
TR	repetition time

triEG	triethylene glycol
UC	uncoated
U_E	electrophoretic mobility
USPIO	ultra-small superparamagnetic iron oxide
UV-Vis	ultraviolet visible spectroscopy
V	crystal volume
VCL	*N*-vinylcaprolactam
VDW	van der Waals
VIm	vinylimidazole
vol%	volume percent
VSM	vibrating sample magnetometer
WAXS	wide-angle X-ray scattering
$\bar{X}_{\mathrm{n}}$	number-average degree of polymerization
wt%	weight percent
XPS	X-ray photoelectron spectroscopy
XRD	X-ray diffraction
ZFC	zero field cooled
ZP	zeta potential
γ_{e}	gyromagnetic ratio of the electron
δ	shell thickness
η_{f}	dimensionless constant in pre-exponential factor of the Néel relaxation time expression
ϑ	scattering angle or bond angle
λ	wavelength
μ_0	decay moment or permeability of free space
ρ	$R_{\mathrm{g}}/R_{\mathrm{h}}$ (rho parameter)
σ	standard deviation or steric factor (chain flexibility)
τ	effective relaxation time of magnetic moments
τ_0	pre-exponential factor of the Néel relaxation time expression

τ_{B}	Brownian relaxation time
τ_{C}	global relaxation time
τ_{N}	Néel relaxation time
τ_{D}	translation correlation time
φ	solid volume fraction
φ_{intra}	intra-aggregate volume fraction
χ''	alterating current magnetic susceptibility (imaginary part)
ω_{L}	Larmor frequency
ω_{I}	angular frequency of proton precession
Φ	magnetic flux

Chapter 1 Introduction

Chapter 1

1.1 Overview

Due to their small size and large surface-to-volume ratio as compared to their bulk counterparts, nanoparticles (NPs) display distinct physical and chemical properties making them attractive for applications in various fields including electronics, energy and optics, chemistry, and biology.[1-2] Among the broad spectrum of nanomaterials being investigated for biomedical uses, magnetic nanoparticles (MNPs) have received significant attention for applications in targeted drug delivery, as magnetic resonance imaging (MRI) contrast agents, and as heat mediators in the magnetic hyperthermia treatment of tumors.[3-5] Besides metallic and bimetallic MNPs, superparamagnetic iron oxide nanoparticles (SPIONs) have been favored because of their low cytotoxicity profile[6-7] and the possibility of surface modification with biocompatible coatings.[3,8-9]

SPIONs serve as contrast agents for MRI, a modern three-dimensional non-invasive diagnostic method based on the magnetic properties of body tissues, by effectively changing the relaxivity of water, thus enhancing the image contrast and improving its diagnostic value. Since the first time they were used for liver imaging 20 years ago, SPIONs (60 nm < D_h < 150 nm) serve as negative contrast agents,[10] most commonly by intravenous injection, while others designed for gastrointestinal imaging are administered orally.[11] Beside commercial SPIONs such as AMI-25 Ferumoxide (Endorem)[12], IOs (Resovist),[13] etc., numerous other types of particles were also suggested as potential MRI contrast agents such as silica-coated γ–Fe_2O_3,[14-16] as well as iron oxide encapsulated in a hydrogel,[17] in electrostatic complexes,[18] coated with amphiphilic block copolymers,[13] or enclosed in polymeric vesicles.[19] Controlling the size, shape and dispersity of the iron oxide crystals via the synthetic protocol, to allow tailoring of their properties, has been an ongoing research interest.

The therapeutic potential of SPIONs was further emphasized when hyperthermia was recognized as a promising form of cancer therapy. The heat generated by SPIONs when subjected to an alternating magnetic field (AMF) increases the local temperature and destroys temperature-sensitive cancer cells. Intracellular magnetic hyperthermia,[20-21] where heat is exclusively generated by internalized SPIONs during AMF exposure, must be differentiated

from magnetic fluid hyperthermia, where cells are dispersed in a magnetic medium.[22-23] In contrast to the belief that cancer cells can only be killed when the temperature is raised over 43 °C (defining the cumulative effective thermal dose at 43°C or CEM43), the induction of significant cell death by internalized SPIONs without a macroscopic temperature increase during AMF exposure (called "intra-lysosomal" or "cold" hyperthermia) has also been described.[24-25] Numerous studies have focused on tuning the magnetic properties of the materials used for that purpose by controlling the size, shape and dispersity of the iron oxide crystals.

1.2 Research Objectives and Thesis Outline

The main goal of this Ph.D. dissertation was to achieve the synthesis of SPIONs *in situ* within arborescent copolymers bearing a stabilizing hydrophilic shell. Control over the iron oxide nanoparticle synthesis and the stabilization process were demonstrated to provide a product with good potential as magnetic resonance imaging (MRI) contrast agent and for heat generation in cellular radiofrequency magnetic field hyperthermia (MFH) treatment. It is well-known that the magnetic properties of iron oxide NPs are strongly dependent on their average size and size distribution, as stated in many reviews[4,9,26-36] on the optimal design of magnetic NPs for MRI and MFH. This is particularly true for the specific magnetization M_s, defined as the weight concentration of magnetic moments at saturation (in a strong magnetic field), which is expressed in $Am^2 \cdot kg^{-1}$ (SI) or $emu \cdot g^{-1}$ (CGS). An arborescent copolymer of overall generation G1, namely a comb-branched (G0) polystyrene substrate grafted with poly(2-vinylpyridine) side chains, was used as a templating medium to encapsulate iron salt precursors and disperse them in discrete compartments, enabling tuning of the nucleation process and improved control over the average size and size distribution of the particles. These SPIONs adopt the shape and size distribution of the polymer template, which allows regulation of their hydrodynamic size and polydispersity. To enable the clinical applications ultimately targeted for these NPs, the SPIONs are shielded with a hydrophilic shell of poly(2-hydroxyethyl acrylate) to provide good colloidal stability, enhance their biocompatibility,

and achieve a sufficiently long blood circulation time to allow their accumulation in tumor tissues.

This dissertation is organized into seven main chapters. Following this Foreword, a detailed review on size and morphology control of MNPs using organic templates is presented in Chapter 2. This literature review highlights, among others, the impact of well-defined polymer structures on size and shape control of MNPs as compared to linear homopolymers and small molecules, differentiating studies with efficient templating effects from *in situ* syntheses whose results are often not signicantly improved over bulk syntheses. Another point showcased in Chapter 2 is the extensive use of vinylpyridine-based polymers as templates for iron oxide MNPs, the evidence for templating effects being more pronounced as the complexity of the polymeric structure increases. Furthermore, polymer templates are usually preferred that also combine stabilizing, biocompatible materials enhancing cellular uptake, reducing cytotoxicity and increasing biocompatibility, once the MNPs are exposed to physiological conditions.

Chapter 3 describes the preparation of a polymeric substrate combining both templating and stabilizing effects for the MNP synthesis, which is a polyion complex (PIC) micelle composed of a G1 arborescent copolymer, namely G0 polystyrene-*graft*-poly(2-vinylpyridine) or G0PS-*g*-P2VP, and a hydrophilic shell of the block copolymer poly(acrylic acid)-*b*-poly(2-hydroxyethyl acrylate), PAA-*b*-PHEA. The size and the core–shell morphology of the PIC micelles were investigated by different techniques including atomic force microscopy (AFM), dynamic light scattering (DLS), and multiangle laser light scattering (MALLS). Varying the length of the PAA and PHEA chain segments and the stoichiometric ratio of the arborescent and block copolymer components provided a means to tune the size and the shell density of the PIC micelles.

As it turns out, the direct *in situ* application of these PIC micelles as templates in MNP synthesis was of limited usefulness, since the PAA-*b*-PHEA added in the shell to improve the colloidal stability and the biocompatibility of the MNPs interfered with loading of the iron precursors. Chapter 4 therefore presents an alternative approach to this, which is

first to use the G1 copolymer as a template for Fe_3O_4 NP synthesis, and then bind the PAA-*b*-PHEA copolymer to enhance the colloidal stability and biocompatibility. The high density of 2-vinylpyridine units in the very compact structure of arborescent copolymers assisted the formation of G1@Fe_3O_4 MNPs by increasing the Fe_3O_4 crystallite size. The subsequent complexation of G1@Fe_3O_4 MNPs with PAA-*b*-PHEA created magnetic polyion complex (MPIC) micelles with improved colloidal stability at pH 7. The Fe_3O_4 crystallites of the MPIC micelles were characterized by transmission electron microscopy (TEM) and selected area electron diffraction (SAED), while the dimensions of the micelles were determined by DLS and AFM measurements.

The superparamagnetic and magnetic properties of the uncoated MNPs (G1@Fe_3O_4) and the MPIC micelles were investigated in Chapter 5 using vibrating sample magnetometry. Measurements of the r_1 and r_2 relaxivities and the ratio r_2/r_1 for MPIC micelles demonstrated their potential as negative contrast agents for T_2-weighted magnetic resonance imaging. Their use in inducing cell hyperthermia was also evaluated with specific absorption rate (SAR) measurements for radiofrequencies. The dependence of the SAR values on the magnetic field amplitude H and the frequency f was examined.

To be useful for biomedical applications NPs need to have good colloidal stability, but also good biocompatibility to achieve a sufficiently long blood circulation time and to allow their accumulation in tumor tissues.[37-38] In Chapter 6, the cytotoxicity and cell internalization of the PIC and MPIC micelles were evaluated *in vitro*. Cell internalization was visualized by confocal laser scanning microscopy (CLSM) and TEM, and quantified by fluorescence-activated cell sorting (FACS). Cell internalization by an endocytosis pathway was hypothesized. The usefulness of MPIC micelles for cellular radiofrequency magnetic field hyperthermia was also confirmed, as the MPIC micelles had a dual dose-dependent effect (concentration and duration of magnetic field exposure) on cell viability.

The overarching conclusions drawn from the Thesis work are presented in Chapter 7, which provides an overall summary of the body of research, the original contributions to knowledge, and suggestions for future work.

Chapter 1

In agreement with University of Waterloo Thesis Regulations, the format of each chapter is organized as a manuscript for publication in scientific journals. Each chapter therefore includes a summary, an introductory section providing relevant background information on the subject matter, experimental methods, results and discussion, and conclusions. Additionally, an overall extended abstract for the whole Thesis is provided in the preliminary pages of this dissertation together with its French translation which is a requirement of the Université de Bordeaux, and a single list of references at the very end of the document is organized and numbered according to each individual chapter.

Chapter 2 Templated Synthesis of Magnetic Nanoparticles Through the Self-Assembly of Polymers and Surfactants

Chapter 2

2.1 Overview

The synthesis of superparamagnetic nanoparticles (NPs) for various technological applications continues to be an interesting research topic. The successful application of superparamagnetic NPs to each specific area typically depends on the achievement of a high magnetization for the nanocrystals obtained, which is determined by their average size and size distribution. The size dispersity of magnetic NPs (MNPs) is markedly improved when, during the synthesis, the nucleation and growth steps of the reaction are well-separated. Tuning the nucleation process with the assistance of a hosting medium that encapsulates the precursors (such as self-assembled micelles), dispersing them in discrete compartments, improves control over particle formation. These inorganic-organic hybrids inherit properties from both the organic and the inorganic materials, while the organic component can also bring a specific functionality to the particles or prevent their aggregation in water. The general concept of interest in this review is that the shape and size of the synthesized MNPs can be controlled to some extent by the geometry and the size of the organic templates used, which thus can be considered as molds at the nanometer scale, for both porous continuous matrices and suspensions.

Chapter 2

2.2 Introduction

The synthesis of superparamagnetic iron oxide nanoparticles (SPIONs) and other transition metal (e.g., cobalt) ferrite nanoparticles (NPs) targeting various technological applications such as magnetic storage media, magnetic actuators or biosensors is a topic of ongoing interest for many researchers. In the biological and medical fields, magnetic NPs (MNPs) with a large specific surface area provide innovative potential in targeted drug delivery, in magnetic resonance imaging (MRI) as both positive and negative contrast agents, and in the magnetic hyperthermia treatment of tumors. The successful application of SPIONs in each specific area depends on the attainment of high magnetization values for the nanocrystals obtained, which is necessarily determined by their average size, size distribution, and crystallinity (absence of defects in the magnetic order). Additionally, to facilitate their biomedical applications, the nontoxicity, biocompatibility and stability of the coated magnetic particles in biological media have also been the topics of numerous studies.

MNPs can be synthesized by numerous chemical techniques such as the alkaline coprecipitation of aqueous salts, hydrothermal reactions, microemulsion and sol–gel syntheses, sonochemical reactions, the hydrolysis and thermolysis of precursors, flow injection and electrospray syntheses, etc. Irrespectively of the method used, the formation of superparamagnetic NPs always involves nucleation and growth steps. Their separation is extremely difficult in the aqueous coprecipitation route, involving complicated pathways through oxo-hydroxide phases and eventually to magnetic iron oxide nanocrystals.[1] The size dispersity of the NPs prepared is markedly improved when these two steps are well-separated, which is unfortunately hard to achieve without relying upon kinetic parameters, for example the temperature or mixing conditions.[2] These barriers have been investigated and might be overcome by tuning the nucleation process with the assistance of a hosting medium, that encapsulates the precursors and disperses them in discrete compartments (such as small molecule or polymeric micelles), thereby providing control over particle formation. These inorganic–organic hybrids are particularly interesting since they inherit the properties of both the polymer and the inorganic material. In addition, coating by polymer chains can efficiently

hinder aggregation of the particles.[3] The focus of this review is on methods providing some degree of control over the shape and the size of the synthesized NPs through variations in the geometry and size of the organic templates. Two classes of molds at the nanometer scale can be considered, consisting of either pores contained within a continuous matrix, or of individual objects suspended in a reaction medium. The organic component can also bring other advantages in addition to colloidal stability in aqueous media, such as the presence of specific functionalities.

2.3 *In Situ* Synthesis in Non-Polymeric Templates

Complexing groups such as the carboxylate, phosphate, sulfonate, and sulfate functionalities are known to bind strongly to the surface of magnetite. Furthermore, surfactants containing such head-groups can be tailored for stabilization in oil or hydrocarbon carrier fluids, as well as with charged ligands (citrate, oxalate, etc.) for aqueous media. The same type of moieties can be used to complex the divalent or trivalent iron precursors selected for the reactions leading to the MNPs, for example by the coprecipitation of Fe^{2+} and Fe^{3+} salts in water or in a polyol medium, or the oxidation, reduction, or thermal decomposition of $Fe^{2+/3+}$–ligand complexes in a high boiling point solvent.

2.3.1 Carboxylates

2.3.1.1 Oleic Acid Coating in Combination with Reduction

The templating ability of organic compounds bearing carboxylic functional groups, for example oleic acid and L-glutamic acid, was investigated in the aqueous phase reduction/hydrolysis of iron(III) acetylacetonate (acac) using $NaBH_4$.[4] The ratio of reducing agent to iron precursor required to produce the largest diameter bare NPs (8.08 ± 0.93 nm by transmission electron microscopy (TEM) and 8.95 nm by X-ray diffraction (XRD) was first determined and then applied to the *in situ* coating method. Both the uncoated and the coated NPs displayed clear lattice fringes in high resolution transmission electron microscopy (HRTEM) images (Figure 2-1a) with spacings of 2.9 Å and 2.5 Å, consistent

with a cubic spinel iron oxide structure and confirming the highly crystalline character of the NPs. It is noteworthy that some of the NPs coated with hydrophobic oleic acid had a facetted particle shape on the HRTEM images (inset on Figure 2-1b) rather than the spherical morphologies observed in most other cases, indicating that monolayer formation by the hydrophobic tail of oleic acid molecules brings a different templating effect as compared to several hydrophilic carboxylic compounds tested in the literature,[5] most often leading to a mere reduction in the final size of the MNPs due to capping of the crystallites.

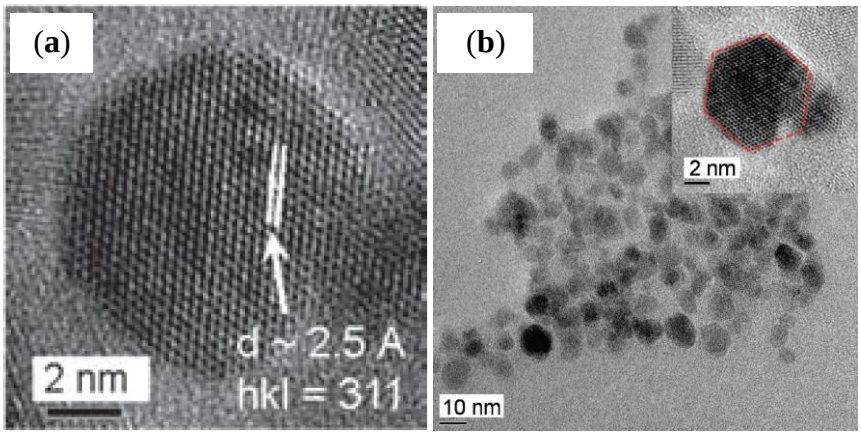

Figure 2-1. TEM images clearly showing: (a) lattice fringes; and (b) facetted shapes for nanoparticles coated with oleic acid, using 10 equivalents of reducing agent ($NaBH_4$) at room temperature. Reprinted with permission from Reference 4. Copyright 2011 WILEY-VCH Verlag GmbH & Co. KGaA, Weinheim.

2.3.2 Sulfonates and Sulfates

2.3.2.1 Sodium Dodecyl Sulfate (SDS) Microemulsions

The use of non-polymeric templates in MNP synthesis was actually investigated earlier by the group of Liu,[6] who performed $CoFe_2O_4$ NP synthesis by a microemulsion process with SDS as a surfactant. The size of the $CoFe_2O_4$ NPs was successfully controlled in a range from less than 4 nm to approximately 10 nm, by varying the concentration of metallic

precursors and the methylamine base added.[6] Interestingly, the influences of NP size and temperature on the magnetic properties were systematically studied. For example, a decline in the remnant magnetization of 8.5 nm $CoFe_2O_4$ NPs with increasing temperature, and its disappearance leading to the demagnetization of the NPs at 290 K were noted. Using field cooled (FC)/zero field cooled (ZFC) superconducting quantum interference device (SQUID) magnetometry, the magnetic susceptibility of NPs of different sizes was shown to exhibit the usual temperature dependence: initially increasing as the temperature was lowered, it reached a maximum at the point referred to as the blocking temperature (T_B), and eventually decreased. A correlation between higher T_B and increasing NPs diameters was convincingly pointed out. The superparamagnetism of the NPs above their T_B was confirmed by neutron diffraction measurements yielding the magnetic mesh size from the magnetic reflections (as opposed to atomic reflections, giving the crystallographic mesh size by more common X-ray diffraction), while the increases in the T_B, coercivity (H_c) and saturation magnetization (M_s) with the size of the particles were in agreement with the Stoner-Wohlfarth theory on single domain particles. Such a study could not have been completed without the exceptionally good control achieved over the size and size dispersity by the microemulsion templating process.

2.3.2.2 Sodium Dodecylbenzenesulfonate (NaDBS) Microemulsions

The same technique to control the size of MNPs by varying the relative concentrations of iron salts, surfactant, and solvent in a water-in-oil microemulsion system was demonstrated by Lee et al.[7] This efficient approach, using NaDBS microemulsions as nanoreactors and hydrazine as precipitating agent, allowed the size of the NPs to be tuned in the range of 2–10 nm with narrow size distributions and high levels of crystallinity. The lattice fringes appearing in HRTEM imaging again hinted at the highly crystalline structure of the MNPs obtained. The matching XRD patterns obtained for the MNPS and for a magnetite standard further confirmed the structure of the Fe_3O_4 phase, while the peak widths calculated from the Debye-Scherrer equation were consistent with the observed TEM sizes. The magnetization vs. temperature curves followed a pattern similar to the one previously

described, in which the T_B and M_s for larger particles had higher values. These results were in good agreement with the Stoner-Wohlfarth theory in terms of the increase in activation energy for larger particles, although determining the origin of the smaller H_c values observed as compared to related studies would require further investigation. More importantly, the procedure was taken a step further by producing several mixed metal ferrites in a size range of 4–8 nm, with uniform particle size distributions and an inverse spinel structure.

2.4 *In Situ* Synthesis with Polymers in Solution or in the Bulk State

The preparation of aqueous magnetic fluids was been achieved more recently using polymers as steric stabilizers in solution and polymer templates in the bulk state. These studies will be presented according to the different types of polymers used for that purpose.

2.4.1 Dextran (DEX) and Polysaccharide Derivatives

The term dextran refers to a class of branched polysaccharides composed from a majority of α-1,6- and a minority of α-1,3- or α-1,4-glycosidic linked glucose units, which are non-toxic, biocompatible and biodegradable hydrophilic polymers extensively used in biomedical applications and in NP preparation procedures. The general role of dextran in enhancing the biocompatibility of metal oxides, using green coprecipitation and gel template strategies, was previously discussed in a review by Patrinoiu et al.[8] For the purpose of this discussion, we are primarily interested in the efficiency of dextran in templating and controlling the shape and size of MNPs.

2.4.1.1 Influence of Dextran End-Group Reduction

In an attempt to optimize the nucleation of ultra-small superparamagnetic iron oxide (USPIO) particles in the presence of dextran, the effects of chemical functionalities and the molecular weight (MW) on the formation, stability, size, and magnetic properties of the hybrid particles obtained were investigated by Paul et al.[9] Reduced dextran, generated by sodium borohydride treatment of native dextrans with different MW, has many hydroxyl groups existing in the native structure but only one additional hydroxyl group converted from

the aldehyde (hemi-acetal) terminus. Despite this minor change in structure, reduced dextran was reported to successfully produce USPIOs with a volume-average diameter of less than 30 nm, while the size of native DEX-coated particles synthesized in the same conditions was larger than 700 nm in most cases and even reached 2.7 μm for 1 kDa dextran. Samples prepared with low MW reduced DEX (1 kDa and 5 kDa) possessed a magnetic susceptibility 5–25 times larger than their native counterparts. However, the influence of the reduced terminal unit on the size and the magnetic susceptibility of the USPIOs was diminished for dextrans of higher MW.

The minor change at the terminal sugar unit of 10 kDa MW dextran resulting from the reduction reaction also led to more efficient utilization of the templating material, as more stable autoclaved USPIOs with much smaller diameters (23 nm vs. 587 nm) were formed, with a higher percentage of metal-bound dextran (0.96 g DEX/g Fe vs. 0.59 g DEX/g Fe).

The size effect of reduced 10 kDa dextran was emphasized through similar experiments performed with 2.5–50 wt% addition of the simple sugar glucose vs. the amount of dextran used. The samples derived from reduced dextran with added glucose had radii similar to those prepared without sugar added, thus convincingly demonstrating binding enhancement arising from the additional OH groups in the linear polyol termini as compared to the aldehyde functionality present in the monosaccharide. It is worth mentioning that the size of the USPIO particles increased with the MW of dextran (20 nm for 1 kDa vs. 41 nm for 70 kDa dextran). However, stable colloids could only be created using reduced polysaccharides having a MW larger than 10 kDa as compared to 70 kDa for native dextran. This shows the dominant role of the MW of the chains in the growth of larger colloids from an initially unstable magnetic sol.

2.4.1.2 Dextran (DEX) Sulfate

Beyond the encapsulation enhancement brought by reduced DEX as compared to the native material, further modifications of this type of material may provide additional options

leading to improved physicochemical properties. In addition to being considered a ligand for macrophage scavenger receptors, DEX sulfate was also proposed as an advanced coating material as compared to reduced DEX: A mixture of only 5 wt% DEX sulfate with reduced DEX yielded particles with a hydrodynamic diameter of over 30 nm and insignificantly larger core sizes (7.9 ± 2.0 nm vs. 7.0 ± 1.9 nm for reduced DEX).[10] Experimental parameters including the reaction time and the pH were varied to create DEX sulfate-coated NPs with good magnetic resonance properties. The delayed addition of Fe^{2+} was mentioned as a technique to avoid overgrowth and cross-linking of the particles caused by interactions between excess Fe^{3+} and the polysaccharide coating. While an increase in the polysaccharide/Fe^{3+} ratio decreased the core size and thus the relaxivity of the particles, failure of particle formation was also reported at very low polysaccharide concentrations.

2.4.1.3 DEX-*b*-Poly(methacrylic acid)(Fe_3O_4)-*b*-Poly(*N*-isopropylacrylamide) with Thiol End Groups

The synthesis of quadruple-responsive nanocomposites was achieved in solutions of the copolymer DEX-*b*-poly(methacrylic acid)-*b*-poly(*N*-isopropylacrylamide) (DEX-PMAA-PNIPAM) where complexation was achieved by the poly(methacrylic acid) (PMAA) block, the PNIPAM units provided thermosensitivity, the iron oxide NPs (IONPs) offered the magnetic response, and nucleated gold nanorods (AuNR) induced near infrared radiation (NIR) response.[11] The diameter of the SPIONs before the AuNR encapsulation was 10 ± 3.5 nm (based on TEM analysis) with a narrow size distribution, while the aqueous hydrodynamic radius (R_h) measured by dynamic light scattering (DLS) was 66–69 nm, suggesting that a thick copolymer shell covered the SPIONs. The dependence of the lower critical solution temperature (LCST) on pH (29 °C at pH 4.5 vs. 35 °C at pH 12) was explained by changes in the hydrophobic/hydrophilic balance caused by protonation of the PMMA block. Vibrating sample magnetometer (VSM) measurements at room temperature revealed superparamagnetic properties with neither remanence nor H_c. At room temperature, SPIONs 10 ± 3.5 nm in size had limited stability in a 300 mT magnetic field, displaying slow aggregation under these conditions. The magnetic interactions were strongly enhanced

above the LCST, however, (e.g., at 50 °C), due to the phase transition of the hybrids that induced aggregation via hydrophobic as well as magnetic dipolar interactions. Owing to the presence of the PNIPAM block the phase transition was reversible, providing water solubility to the recovered SPIONs when the temperature was brought back below the LCST, due to the hydrophilic DEX units.

2.4.1.4 Alginate (Alg) Beads

As a naturally occurring, biocompatible and inexpensive polysaccharide widely used in encapsulation processes, alginate is constituted of 1,4-linked α-L-guluronic acid (G) and 1,4-linked β-D-mannuronic acid (M) units (Figure 2-2), either segregated into homopolymer blocks or combined in copolymer structures. Commercially available alginates extracted from the cell wall of either brown algae or bacteria have different M/G compositions, MW, sequences, and physicochemical properties which strongly affect their efficiency in encapsulation applications.[12]

The loading capacity of alginates with different M/G ratios was investigated in the *in situ* alkaline oxidation of ferrous ions to produce maghemite MNPs.[13] More precisely, this synthesis relied upon the alkaline coprecipitation of Fe^{2+} and Fe^{3+}, but with the particularity of the *in situ* production of Fe^{3+} ions by the oxidation of Fe^{2+} in air. After a first oxidation cycle, a higher iron content (ca. 31%) was recorded in a sample for which the M/G ratio was 0.6, as compared to ca. 14% for the alginate with M/G = 1.6. This result highlights the superior binding ability of guluronic vs. mannuronic acid units resulting from the "egg box" conformation of the guluronic acid segments that trap the Fe^{2+} ions more efficiently. Larger M_s values were recorded for the M/G = 0.6 samples, obviously due to their higher total iron content. As the total iron content in two samples reached the same maximum value after three oxidation cycles (approximately 47.1% vs. 48.3%), these two samples displayed similar magnetization curves. The superparamagnetic character of these fully oxidized samples at room temperature was confirmed by their large values of M_s, zero hysteresis, and from the paramagnetic Mössbauer spectra obtained. Although no further data were provided about the

size and the morphology of the maghemite NPs obtained, the hosting ability of alginate compounds was clearly demonstrated.

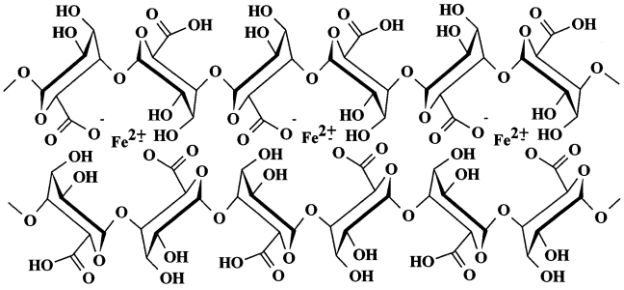

Figure 2-2. Representation of two 1,4-linked α-L-guluronic acid (G)-blocks forming an "egg box" structure with ferrous ions. Reprinted with permission from Reference 13. Copyright 2000 Elsevier Science B.V.

2.4.1.5 Precipitation in Aqueous Alginate Networks

Recently, questions related to the size and morphology of MNPs encapsulated in alginate networks were convincingly answered by the team of Srivastava et al.[12] who took the above approach one step further with the use of sodium alginate from *Laminaria hyperborea* (MW = 60,000–80,000 $g \cdot mol^{-1}$, M/G = 32/68) to synthesize Fe_3O_4/Alg nanocomposites with a core–shell structure in a controlled low-temperature oxidation/precipitation process at pH 4, 10 and 14. The Fe loading, the size and, more interestingly, the magnetic properties of the core–shell composites were efficiently controlled through the final pH used in the precipitation process. It was indeed reported that higher Fe loading could be achieved at low pH (4–5) than at high pH (14). The Fe_3O_4 content of the alginate composites synthesized at pH 4–5 was confirmed by XRD analysis. Calculation of the crystallite size from the XRD patterns gave a mean value of ca. 14 nm for Fe_3O_4/alginate, while the values determined for bare Fe_3O_4 using the Scherrer equation and from TEM micrographs were ca. 10 and 15 nm, respectively. As compared to bare Fe_3O_4 NPs, the alginate composites exhibited better dispersibility due to the alginate shell, essentially reducing the interactions between the MNPs. While neither H_c nor remnant magnetization were detected

in the *M-H* curves for the magnetite alginate composites, confirming their superparamagnetic behavior, the saturated magnetization values exhibited by the hybrids were much lower (below 6 emu/g) than for pure Fe_3O_4 NPs prepared by the same process (above 31 emu/g). This was assigned to differences in morphology among these two sample series: The Fe_3O_4 synthesized at pH 4 was better dispersed than the sample produced at pH 10, which was agglomerated to some extent. The M_s values for the composites were larger for the NPs synthesized at a higher pH, which is obviously in agreement with the Fe loading efficiency reported above.

2.4.2 Synthetic Linear Homopolymers

To maximize the *in situ* templating effect as well as to enhance the stability of the ferrofluids obtained, numerous attempts have been made in terms of: (i) changing the chemical nature of the template material; and (ii) varying the method employed to produce the NPs. The first approach is more convenient experimentally for synthetic linear homopolymer templates than for natural polysaccharide derivatives, due to the fact that the former materials can possess controlled chemical structures, MWs, and MW distributions, which facilitates magnetic property improvement and particle surface tailoring in terms of enhanced colloidal stability and biocompatibility.

2.4.2.1 Thermal Decomposition of Poly(vinyl alcohol)–$Fe(OH)_3$

One of the first synthetic homopolymers investigated as template for the preparation of MNPs was poly(vinyl alcohol) (PVA), containing a large number of hydroxyl functional groups available to interact with Fe^{3+} ions and leading to water-soluble complexes. In their pioneering work, Yokoi and Kantoh[14] successfully combined different amounts of PVA to $Fe(OH)_3$ and obtained Fe_3O_4 precipitates by thermal decomposition. Although agglomerates of sintered magnetite particles were obtained instead of uniform products, the diameter of the Fe_3O_4 crystals in the composites evaluated from the line width of the (311) diffraction peak linearly increased with the heating temperature, indicating that the growth of Fe_3O_4 crystals

at higher temperatures, under the reducing effect of PVA, converted one third of the Fe^{3+} into Fe^{2+}, as required by the stoichiometry of the coprecipitation reaction.

2.4.2.2 Fe^{2+}/Fe^{3+} Coprecipitation in PVA Membranes

In continuation of the earlier work using PVA solutions as *in situ* templates, Sairam et al.[15] performed the alkaline coprecipitation of various amounts of Fe^{2+} and Fe^{3+} previously impregnated in PVA membranes. The free-standing composite membranes prepared were expected to be useful as pervaporation separation systems to dehydrate organic solvents. The encapsulation of IONPs in PVA increased the mechanical strength of the membranes but also enhanced their water affinity, as shown by the improvement in solvent drying performance with increasing iron oxide content.

2.4.2.3 Conversion of Fe^{3+} in PVA into Hematite in Supercritical H_2O

Another study dealing with antiferromagnetic iron oxide (α-Fe_2O_3 or hematite)–PVA composites was conducted by Xu and Teja[16] using continuous hydrothermal processing (CHP) in supercritical H_2O, a process allegedly providing size and morphology control for metal oxide NPs. Although the influence of the experimental variables on the particle characteristics was not convincingly determined, a higher ferric nitrate concentration, longer residence time, or elevated temperature did result in increased average particle radii and crystallinity, as confirmed by narrowing of the peaks in XRD patterns. A larger average particle size (27.4 nm vs. 15.6 nm) and morphological transformations from spherical to rhombic (elongated) shapes were also reported as a consequence of a higher precursor concentration (0.06 vs. 0.03 M). More importantly, the particle size and size distribution (standard deviation) both decreased as the PVA concentration increased, as demonstrated in three experiments with a reaction time of 2.6 s (controlled by the residence time in the high pressure conducts). As the molar ratio of vinyl alcohol units to Fe^{3+} in the starting mixture was increased from 0:1 to 1:1 and 2:1, the average particle size of the samples decreased from 15.6 to 10.1 and 7.2 nm, respectively. This led the authors to conclude that a minimum amount of PVA was needed to coat all the particles, resulting in a polymeric layer with a thickness of approximately 10 nm that hindered further growth of the particles.

2.4.2.4 $Fe(acac)_3$ Decomposition/Diol Reduction in Octyl Ether (OE) with Polyvinylpyrrolidone (PVP)

It is widely accepted that the main limitation of the thermal decomposition of $Fe(CO)_5$ to prepare monodisperse Fe_3O_4 NPs is the high toxicity of the carbonyl precursor. In an attempt to solve this issue, Fe^{3+} acac was used in an one-pot polyol reduction process in OE and in the presence of a water-soluble polymer, PVP, playing the role of polymeric stabilizer.[17] The PVP-coated, monodisperse Fe_3O_4 NPs obtained had diameters < 5 nm and displayed well-defined superparamagnetic behavior at room temperature with zero H_c.

2.4.2.5 Controlled Precipitation in the Presence of Poly(4-vinylpyridine) (P4VP)

The role of polymers containing nitrogen-based functional groups in the synthesis of MNPs was furthered investigated in the *in situ* controlled precipitation of Fe^{3+} ions in Fe^{3+}–P4VP coordination complexes prepared beforehand in water/acetone mixtures and dried at 60 °C.[18] In this approach, the iron–P4VP solid matrix played the role of a growth-restricted medium, where ion diffusion was efficiently slowed down and the growing iron NPs were effectively "trapped" due to Fe–N interactions with the pyridine groups. More importantly, the hydrophilicity of protonated P4VP before precipitation, that facilitated N–Fe coordination, was described as an important factor controlling particle growth. At the onset of precipitation the protonated pyridine groups became hydrophobic, inducing the collapse of the homogeneous iron–polymer gel and the creation of a non-uniform microstructure consisting of hydrophilic and hydrophobic regions. The subsequent growth process was restricted by the amount of Fe ions available only in the hydrophilic regions, which led to small particles. The hybrid polymer nanocomposites obtained after washing and heating to 150 °C yielded rod-like NPs in TEM images. These nanorods, with lengths ranging from 15 to 75 nm and antiferromagnetic properties affected by the Cl/Fe atomic ratio, consisted of the antiferromagnetic chlorinated iron oxy-hydroxide "akaganeite" ($Fe_8O_8OH_8Cl_{1.35}$, also noted β-FeOOH). It was speculated that incomplete filling of the Cl^- sites affected the perfect compensation of antiferromagnetic sublattices, resulting in the appearance of a magnetic moment. Perfect sublattice alignment is indeed only achieved in a Cl^--saturated crystal

lattice (i.e., in a highly acidic P4VP environment). In that particular case, the templating effect of the polymer on the NPs can be partially ascribed to the chlorine counterions of this weak polyelectrolyte.

2.4.2.6 Poly(ethylene oxide) PEO in the "One-Pot" Synthesis of Pegylated Oxide NPs

Being known for its excellent solvating characteristics, good complexing ability for several transition metal cations, exceptional resistance to oxidation, reduction, and decomposition (by acids and bases at moderately high temperatures, hydrogen peroxide, and sodium borohydride), and the possibility of end-functionalization, poly(ethylene glycol) (PEG) or PEO has naturally become a good candidate to orient the synthesis of magnetic particles. Its stealth characteristics, that is, the ability to avoid non-specific interactions with proteins and uptake by the reticulo-endothelial system, provides to NPs pegylated on their surface a simple route for further medical applications.[19]

2.4.2.7 PEO in Alkaline Hydrothermal Treatment

While conventional templating methods often result in the formation of polycrystalline nanowires or nanorods, monocrystalline 25 nm × 1.5 μm magnetite nanowires (Figure 2-3) were successfully produced in a PEG-assisted hydrothermal process.[20]

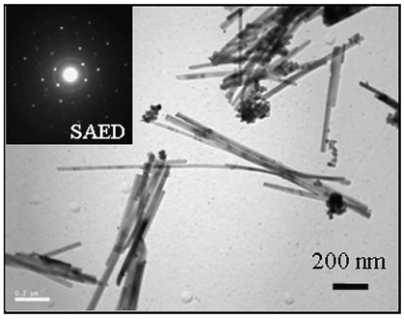

Figure 2-3. TEM image for magnetite nanowires synthesized with poly(ethylene glycol) (PEG)/H_2O (1:2 by volume) at 150 °C for 24 h in an autoclave. The selected area electron diffraction (SAED) pattern is shown in the inset. Reprinted with permission from Reference 20. Copyright 2008 Elsevier B.V.

Chapter 2

There are numerous challenges in controlling the size, morphology, and crystallinity of Fe_3O_4 nanowires due to their complex inverse spinel structure. Full control over the iron oxide nanostructure phase through careful variations in the PEG and H_2O concentrations and the reaction temperature was claimed (see Table 2-1 and Table 2-2). A maximum M_s value of ~91 emu/g, as obtained from vibrating magnetometer measurements, was achieved under the optimal conditions, confirming the crystalline perfection and extremely high purity of the sample (without γ-Fe_2O_3, having an M_s value in the bulk of 80 emu/g). The nanowire formation mechanism proposed involved PEG in a critical role as a stabilizer, mild reducing agent, and growth-orienting agent for the newborn Fe_3O_4 NPs into nanowires.

Table 2-1. Influence of the PEG:H_2O volume ratio on the identified phases and crystallite size collected from X-ray diffraction (XRD) data. All samples are prepared at 150 °C for 24 h. Reprinted with permission from Reference 20. Copyright 2008 Elsevier B.V.

PEG:H_2O (in volume)	Phases	Crystallite size (nm)
1:3	Fe_3O_4, α-Fe_2O_3	21.8
1:1	Fe_3O_4, α-Fe_2O_3, γ-Fe_2O_3	24.7
3:1	Fe_3O_4, α-Fe_2O_3, γ-Fe_2O_3	31.6
0:4	Fe_3O_4, α-Fe_2O_3, γ-Fe_2O_3	42.2
4:0	$NaFeO_2$	64.5

Table 2-2. Influence of reaction temperature and time on the phases of nanostructured iron oxides and crystallite sizes. All samples are prepared using PEG:H_2O = 1:2 in volume. Reprinted with permission from Reference 20. Copyright 2008 Elsevier B.V.

Conditions: temp. (°C)/time (h)	Phases	Crystallite size (nm)
100/24	Fe_3O_4 + $NaFeS_2(H_2O)_2$	10.6
125/24	Fe_3O_4 + α-Fe_2O_3 + $NaFeS_2(H_2O)_2$	13.8
150/24	Fe_3O_4	30.3
150/48	Fe_3O_4 + α-Fe_2O_3	24.1
150/72	Fe_3O_4 + α-Fe_2O_3 + γ-Fe_2O_3	28.4

2.4.2.8 Poly(acrylic acid) (PAA) Chains for Fe_3O_4 Growth Inhibition

Up to this point, the majority of synthetic polymeric stabilizers discussed did not contain functional groups able not only to bind efficiently to the surface of Fe_3O_4 particles, but also to add strong enough repulsions (electrostatic and/or steric) between the MNPs and lead to enhanced colloidal stability desirable for true "ferrofluids". In a search for different homopolymers with suitable functional groups, Lin et al.[21] investigated PAA with MW~2000 $g \cdot mol^{-1}$, whose carboxylic acid groups can theoretically form strong ionic bonds with Fe_3O_4, and thus act as template for iron oxide nucleation. Furthermore, the presence of excess COOH groups at the surface of the coated particles should provide both electrostatic and electrosteric stabilization enhancing the stability of aqueous magnetite suspensions.

The negative zeta potential obtained from laser light scattering velocimetry measurements demonstrated that the polymer molecules could bind to the surface of Fe_3O_4 NPs (particularly at alkaline pH), providing both electrostatic and steric stabilization against particle aggregation. This repulsion (especially at high concentrations of stabilizing polymer) sterically hindered the growth of the particles, producing much smaller products with narrow size distributions as compared with traditional methods.

Pseudo-aggregates of NPs, with a size of about 150–450 nm, were also observed several weeks after the ferrofluids were synthesized. The explanations suggested for this were hydrogen bonding between the COOH groups, or the entanglement of the PAA chains when the polymer was present at a high concentration in the synthesis. The fact that these large, broadly distributed aggregates were destroyed by sonication before light scattering measurements was confirmed by the appearance of 10–40 nm ferrofluid species with a much lower size dispersity. The M_s for the PAA-coated ferrofluid was about 35 emu/g, as compared with 50 emu/g for pure Fe_3O_4 NPs. The reduced value of M_s was explained by the presence in the particles of γ-Fe_2O_3 (which is ~20% less magnetized than pure Fe_3O_4), and by the significant reduction in M_s expected for particle sizes below 10 nm.

2.4.2.9 $FeCl_3$ Thermal Decomposition with PEG in Triethylene Glycol (Polyol)

In another study, PEG with carboxylic acid functionalities at both chain ends (PEG diacid, M_n ~ 600) was employed in a one-pot synthesis in a polar organic solvent, triethylene glycol (triEG), to yield surface-modified ultra-small SPIONs (USPIOs) with an average particle diameter (from TEM) of 1.7 nm.[22] These particles were nearly monodisperse and were highly water-dispersible, yielding a hydrodynamic diameter of about 5.4 nm, significantly larger than the diameter determined by TEM analysis (1.7 nm), due to the thickness of the hydrated PEG coating. The composition of USPIOs in the PEG-modified USPIOs, estimated from thermogravimetric analysis (TGA), was 30.7% and was used to correct the net magnetization values to yield 23.5 emu/g and 6.6 emu/g at T = 5 K and 300 K, respectively. Additional data obtained from the *M–H* curve indicated that the USPIOs were ferromagnetic at 5 K and superparamagnetic at 300 K. Fourier transform-infrared spectroscopy (FT-IR) spectra for PEG and the PEG-modified USPIOs exhibited a C–H stretch at 2890 cm^{-1}, and a C–O stretch at 1110 cm^{-1} in both cases, confirming the presence of PEG in the composites. More importantly, in the spectrum for the PEG-USPIO composites, the C=O stretch at 1745 cm^{-1} in PEG was not prominent and was shifted to 1645 cm^{-1} region, which suggests bonding between COO^- (rather than –O– of the polyether) and Fe ions on the surface of the particles, as shown on Figure 2-4.

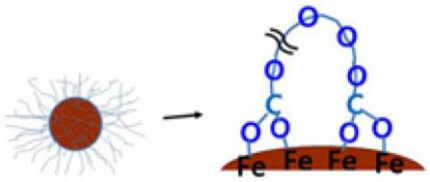

Figure 2-4. Suggested bond formation between COO^- and the Fe^{3+} ions at the ultra-small superparamagnetic iron oxide (USPIO) surface. Reprinted with permission from Reference 22. Copyright 2008 IOP Publishing Ltd.

Relaxivity measurements and magnetic resonance images obtained highlighted the potential usefulness of these particles as both T_1 and T_2 MRI contrast agents, due to their ultra-small size, and the possibility of achieving target-specificity and a long blood half-life.

2.4.2.10 Coprecipitation in the Presence of Trithiol-Terminated Poly(methacrylic acid) (PMAA-PTTM)

Another homopolymer containing multiple carboxylic acid groups is PMAA. A dual-functionality PMAA with trithiol chain ends (PMAA-PTTM) was used in a single-step aqueous coprecipitation procedure leading to narrowly distributed Fe_3O_4 nanocrystals.[23] Interestingly, an increase in the molar ratio of COOH to the Fe^{2+} and Fe^{3+} ions (from 0.7 to 3.4) clearly led to a decrease in size (from 6.1 to 4.5 nm), as well as narrowing of the size distribution of the particles (standard deviation decreasing from 1.1 to 0.4 nm), thus indicating the dominant role of the COOH groups vs. trithiol termini of the polymer in controlling the nucleating process. The less influential role of the trithiol chain ends in the impregnation step offers a facile post-synthesis functionalization path to the introduction of more reactive groups with further conjugation capacity, without causing large changes in size, size distribution or water-solubility of the NPs. The coated Fe_3O_4 nanocrystals had a size of 4.5 nm, clearly exhibited superparamagnetic characteristics on the *M-H* isotherms measured at 300 K, and possessed a calculated M_s of 48 emu/g Fe_3O_4, which is surprisingly high as compared with conventional magnetite particles of the same size (M_s < 15 emu/g). This low magnetization is usually attributed to several factors such as crystallinity defects including non-stoichiometry of the spinel structure, surface spin-canting, surface disorder caused by interactions with surface ligands, cation site distribution, etc. In a study by another team,[24] PMAA was also used to produce coated agglomerates by an aqueous coprecipitation method, having magnetic core sizes around 8 nm by TEM analysis and hydrodynamic mean sizes ranging from 1.5 to 3 μm. The PMAA-encapsulated magnetite particles did not exhibit superparamagnetic behavior however, but rather a small remnant magnetization and H_c, probably due to the aggregation of the magnetite NPs, although the individual 8 nm magnetite NPs displayed superparamagnetic properties. A low magnetization of 40 emu/g

determined at 7 T, as compared to the magnetization values for bulk magnetic iron oxides (92 emu/g for Fe_3O_4, magnetite, and 80 emu/g for γ-Fe_2O_3, maghemite), was assigned to the particle surface spin disorder effects listed above [24].

2.4.2.11 Poly(methyl glutarimide) (PMGI) Templated Iron NPs by Spin-Coating

While investigating a novel method to generate high-density and uniformly distributed carbon nanotube (CNT) mats, Lu et al.[25] employed spin-coating to prepare a film of PMGI loaded with various iron precursors (Fe^{3+} chloride, nitrate or acac, and the organometallic complex ferrocene) for the templated formation of IONPs, subsequently exploited as catalysts for CNT growth. Following the trend of using polymeric templates with specific characteristics, PMGI, a polymer widely used in the bilayer lift-off process, was expected to form complexes with Fe^{3+} ions by multidentate coordination.

The particle size, distribution, and overall yield in the spin-coating process were strongly influenced by the complexation tendency of the iron precursors used with the PMGI templates. The particles derived from strongly coordinated compounds like ferrocene and iron acac had a low density of iron oxide and broad size distributions, since the Fe^{3+} ions in these materials were unable to complex with the PMGI chains due to steric hindrance caused by the bulky counterions. Iron nitrate and iron chloride produced the highest and second highest density of IONPs, respectively, with small mean diameters, since both monodentate anions were less bulky and more loosely bound to iron.

2.4.3 Synthetic Linear Copolymers

Block copolymers exhibiting microphase separation into ordered morphologies such as lamellar, cylindrical and spherical microdomains provide a convenient self-assembled template for the synthesis of nanocomposites. These microdomains represent nanoreactors within which a variety of NP clusters can be synthesized.

2.4.3.1 Aqueous Coprecipitation with Double-Hydrophilic Block Copolymers (DHBCs)

To investigate the templating effects of DHBCs as well as tailored functional groups on the surfaces, Wan et al.[26] prepared stable aqueous ferrofluids using copolymers with poly(glycerol monoacrylate) (PGA) or poly(glycerol methacrylate) (PGMA) as one block, and either PAA, poly[(*N*,*N*-dimethylamino)ethyl methacrylate] (PDMAEMA) or poly(ethylene glycol) monomethyl (mPEG) ether as the other block.

When coated with PAA-*b*-PGA the surface of SPIONs carries negative charges, while the surface of particles obtained from PDMAEMA-*b*-PGMA, of which the PDMAEMA chains are protonated at neutral pH, possesses positive charges.

Multidentate coordination arising from the formation of five-membered rings between the 1,2-diol groups of the PGA or PGMA blocks and Fe^{2+} or Fe^{3+} cations at the surface of the magnetic particles was proposed to be more stable than the four-membered rings formed by the COOH groups in PAA. The disappearance of the COO^{-} adsorption band at 1592 cm^{-1} in the FT-IR spectra of PAA-*b*-PGA-coated IONPs indicated that the carboxylic groups of PAA-*b*-PGA were not coordinated with the $Fe^{2+/3+}$ cations. Additionally, magnetic fluids obtained with PGA or mPEG-*b*-PGA were stable over a wider pH range as compared to those prepared from PAA or mPEG-*b*-PAA. PGA was considered to be a better stabilizer than PAA for the dispersions, such that the PGA block of the copolymer was coordinated to the surface of the magnetite NPs, while the PAA block was extended into water.

The same conclusion was drawn in the cases of PDMAEMA-*b*-PGMA and mPEG-*b*-PGA block copolymers, of which the PGMA or PGA blocks were chemisorbed onto the surface of the IONPs, thus playing a decisive role in orienting particle synthesis while the PDMAEMA or mPEG blocks, with a swollen conformation in water, contributed to post-synthesis stability.

2.4.3.2 Aqueous Coprecipitation with Triple-Hydrophilic Block Copolymers (THBCs)

Following this research trend, triblock copolymers constituted from the monomers listed above, but particularly mPEG-*b*-PMAA-*b*-PGMA, were used in the alkaline coprecipitation of $Fe^{2+/3+}$.[27] PGMA influenced the nucleation step by tightly binding to the magnetite cores, while PMMA created an intermediate layer with a double function of bearing the mPEG corona and encapsulating the antibiotic and antitumor drug adriamycin (ADR), also called doxorubicin. The drug encapsulation was driven by both electrostatic interactions at pH 7.4 between anionic COO^- of PMMA and the protonated glycosidic amine of ADR (pK_a = 8.2), and by hydrophobic interactions between the PMAA main chain and the hydrophobic anthracycline ring of ADR (Figure 2-5). The size of the Fe_3O_4 core was estimated to be about 7–8 nm from TEM micrographs, whereas a narrow size distribution and an average R_h of 23 nm were determined for the coated particles by DLS analysis. Superparamagnetic behavior at 300 K without magnetic hysteresis was observed for the MNPs obtained.

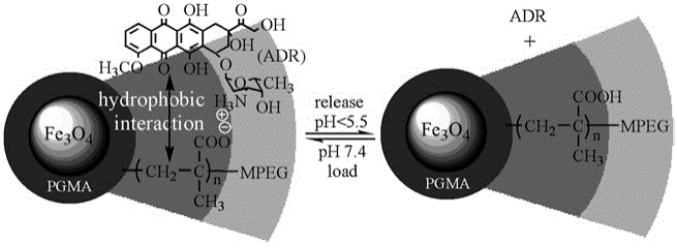

Figure 2-5. Schematic structure of mPEG-*b*-PMAA-*b*-PGMA-Fe_3O_4 NPs loaded with adriamycin at neutral pH, designed to release the anticancer drug in the acidic environment of a tumor. mPEG: poly(ethylene glycol) monomethyl; PMAA: poly(methacrylic acid); PGMA: poly(glycerol methacrylate); and ADR: antitumor drug adriamycin. Reprinted with permission from Reference 27. Copyright 2008 The Royal Society of Chemistry.

2.4.3.3 Fe^{2+}/Fe^{3+} Coprecipitation with Silicon-Containing Random Copolymers

The effectiveness of an amphiphilic random block copolymer of 3-(trimethoxysilyl)propyl methacrylate and ethylene glycol methyl ether methacrylate, denoted as poly(TMSMA-*r*-PEGMA), as stabilizer for MNPs was assessed by Lee et al.[28] In particular, the *in situ* synthesis of Fe_3O_4 was compared to the stepwise addition of the same copolymer to preformed iron oxide colloids. In both cases, covalent binding was achieved between the magnetite surface and the siloxane functionalities of the polymer hydrolyzing to silanol groups, while PEG more likely remained on the outside of the SPIONs. The cross-linking reaction of the silanol groups by self-condensation, promoted by heating, resulted in more stable coating layers. The hydrodynamic radii of SPIONs prepared with and without copolymer in the NP synthesis step were 16.0 ± 2.2 nm and 12.3 ± 1.2 nm, respectively, with narrow size distributions and core sizes in the range of 4–8 nm in both cases, consistent with a thicker layer of coating by the *in situ* preparation as compared to sequential addition. However, the SPIONs synthesized *in situ* had an M_s value of 65 emu/g Fe (equivalent to 45.5 emu/g Fe_3O_4), significantly lower than the 80 emu/g Fe (56 emu/g Fe_3O_4) value obtained for the post-synthesis coated SPIONs. This effect can be interpreted as reflecting the influence on crystallinity or magnetic order of the NPs of surface complexation by the silanol groups of the copolymer during the synthesis. However, unlike ligands such as carboxylic acids and polyethers, that can enter the "inner coordination sphere" of Fe^{2+} and Fe^{3+} cations, silanols mainly interact with the Fe-OH hydroxyls at the surface of the iron oxide nuclei already formed in the sol–gel process, i.e., the "outer-sphere" of the metal centers. The risk of magnetic properties decreases trough surface ligand or spin-canting effects is therefore lower than for strong ligands introduced during the synthesis. Furthermore, the SPIONs synthesized were found to allow the detection of tumors in T_2-weighted MR images within 1 h, as a result of the accumulation of the nanomagnets at the tumor site. Protein uptake by the surface of these coated SPIONs was reported to be significantly lower than by Feridex™ I.V., a popular contrast agent, thereby confirming the stealth effect in blood plasma of the PEG component of the copolymer.

2.4.3.4 Coprecipitation in Water in the Presence of Poly(ethylene oxide)-*block*-Poly(methacrylic acid) (PEO-*b*-PMAA) Double-Hydrophilic Block Copolymers (DHBCs)

In an attempt to confirm the roles of a PEO-*b*-PMAA double-hydrophilic diblock copolymer (DHBC) in directing the nucleation, controlling the growth, and sterically stabilizing the dispersions, a comparison was made among three cases: precipitation without polymer present, in the presence of "non-interacting" PEO, and in the presence of PEO-*b*-PMAA.[29] TEM images (Figure 2-6c) revealed that the particles coated with PEO-*b*-PMAA were much smaller (5 ± 4 nm) and more uniformly dispersed than those created using either PEO homopolymer or without polymer, highlighting the decisive role of the carboxylic acid groups in the PMAA block in promoting nucleation and inhibiting growth of the magnetic iron oxide particles. Although crystallinity was confirmed by powder XRD (PXRD) analysis, the magnetite and maghemite phases could not be distinguished by that technique because these two phases have the same spinel structure and their XRD peaks positions are quite close to each other. The PEO-*b*-PMAA-coated oxide exhibited substantial magnetism, as seen on Figure 2-6d, with a magnetization of 50 emu/g at a field strength H = 275 kA/m or B = 0.34 T), from which we can infer a saturation level around 53 emu/g (so the value of 60 emu/g given by the authors appears a little overestimated). The hydrophilic layer covering the particles facilitated their redispersion in hydrophilic mixtures of hydroxyethyl methacrylate and methacrylic acid monomers, before evaporation of the water. The waxy solid obtained was redispersed in an oil phase (decane) via sonication with poly(ethylene-*co*-butylene)-*block*-poly(ethylene oxide) (PBO-*b*-PEO) as emulsifier. Inverse emulsion polymerization of this sol yielded magnetic poly(hydroxyethyl methacrylate-*co*-methacrylic acid) P(HEMA-*co*-MMA) latexes with sizes broadly distributed from 35 nm to 250 nm, with the same superparamagnetic properties as the initial magnetic core–shell NPs, but also with a lower overall magnetization (10 emu/g latex) corresponding to 18 wt% of iron oxide in the polymer matrix.

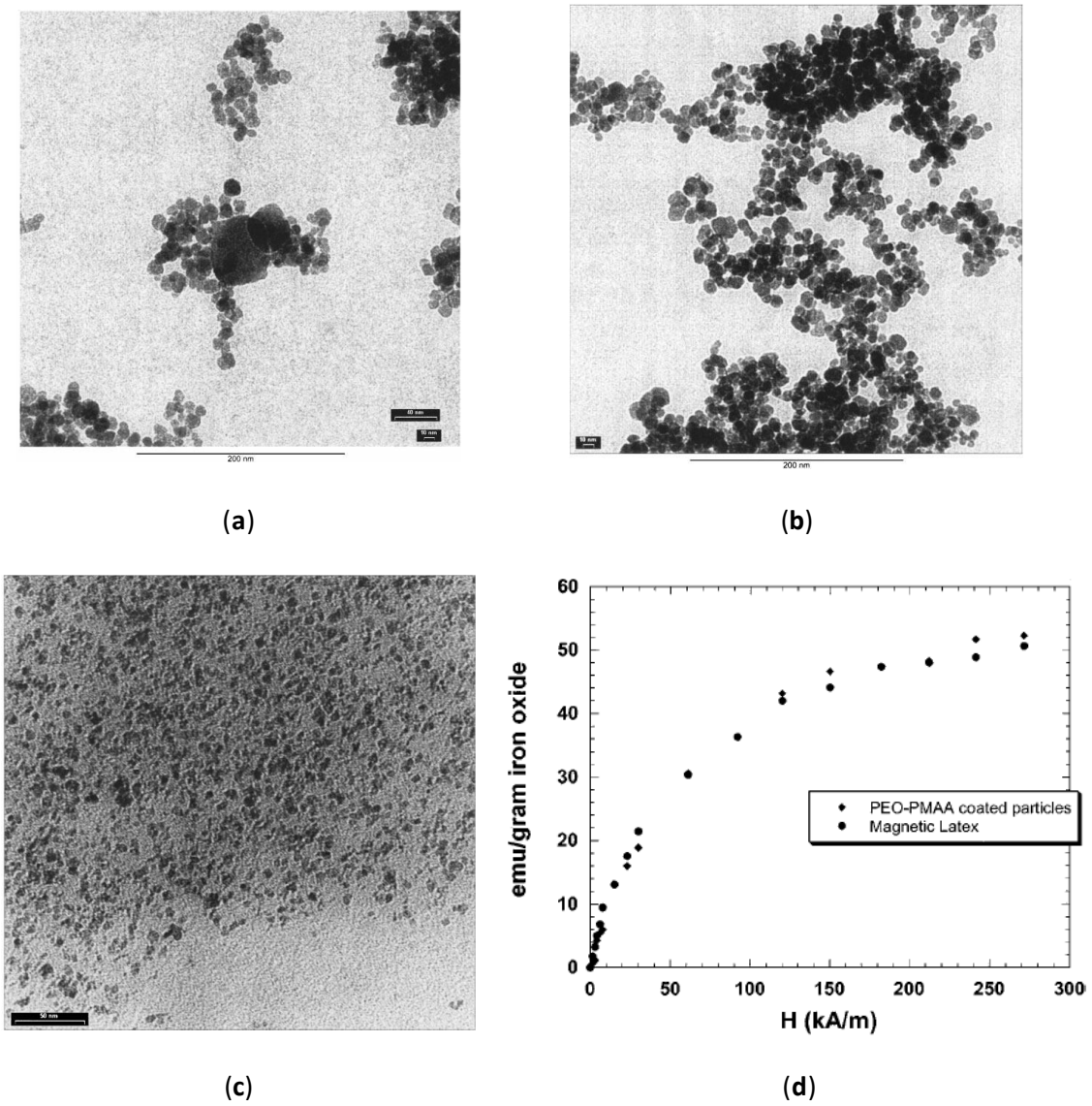

Figure 2-6. Transmission electron micrographs for magnetic iron oxide precipitated in: (a) water alone; (b) the presence of poly(ethylene oxide) (PEO) homopolymer; and (c) the presence of PEO-*b*-poly(methacrylic acid) (PMAA) block copolymer. Note that Figure 2-6c is at somewhat higher magnification than the others; (d) magnetization curves for the PEO-*b*-PMAA coated NPs and for P(HEMA-*co*-MMA) magnetic latexes obtained by inverse emulsion polymerization. Reprinted with permission from Reference 29. Copyright 2001 Elsevier.

2.4.3.5 Poly(ethylene glycol)-*block*-Poly(aspartic acid) (PEG-*b*-PAsp) Leading to Akaganeite Rods

In an effort to vary the chemical nature of the anchoring block as a polypeptide, while retaining PEG as a stabilizing moiety, Kumagai[30] prepared coordination complexes between $FeCl_3$ and PEG-*b*-PAsp in distilled water. Incubation of the mixture at 50 °C resulted in substantially homogeneous needle-shaped alkaganeite β-FeOOH particles, approximately 60 nm in length and 10 nm in width. Energy filtering transmission electron microscopy (EFTEM) zero-loss images revealed that the thickness of the PEG layer on the IONPs was 10–15 nm approximately (Figure 2-7). The anchoring interactions of the carboxylic groups with the β-FeOOH particles were confirmed using FT-IR spectroscopy, with the successful resolution of simultaneous hydrogen and coordination bonding (complexation) interactions. However, a control experiment without polymer also led to needle-like oxo-hydroxides. The formation of the needles may thus be more likely ascribed to the physical conditions used (e.g., pH, salts, etc.) rather than to a templating effect of the polymer.

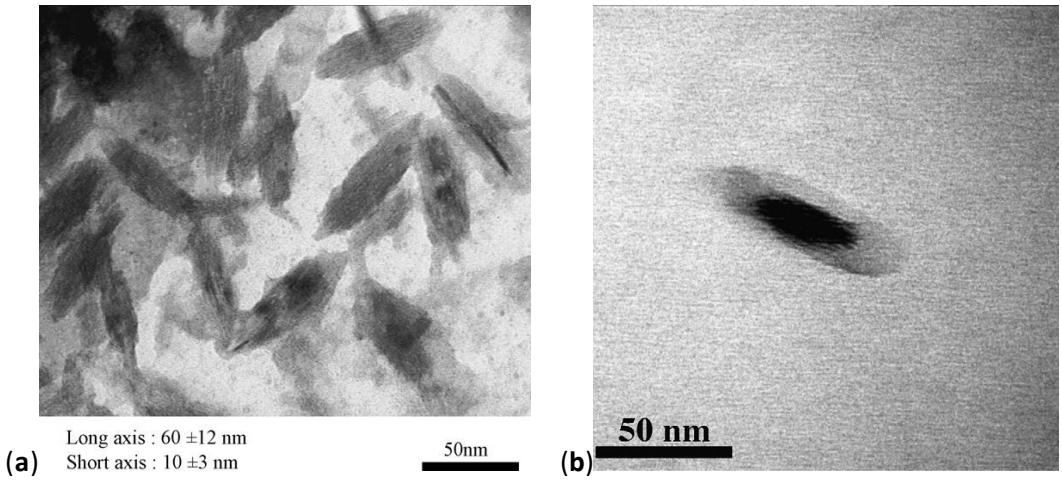

Figure 2-7. EFTEM zero-loss images of: (a) β-FeOOH NPs; and (b) poly(ethylene glycol) (PEG)-*b*-poly(aspartic acid)-coated β-FeOOH NPs. Reprinted with permission from Reference 30. Copyright Elsevier B.V.

2.4.3.6 Coprecipitation in Water with Poly(ethylene oxide)-*block*-Poly(acrylic acid) (PEO-*b*-PAA)

In a study by Hatton et al.,[31] the use of PEO-*b*-PAA in an aqueous coprecipitation route followed a size sorting step using a high-gradient magnetic separator (HGMS) yielded MNP clusters with sizes larger than 100 nm, containing several particles with average core sizes of 9.5 nm. Both the bleed-off and the captured clusters in the magnetic separator were superparamagnetic (M_s = 62.9 emu/g for the latter sample), thus indicating a single domain structure for the particles. The iron-to-polymer loading ratio (expressed as the molar ratio of the Fe^{3+}/Fe^{2+} cations to the polymer carboxylates) was varied, thus changing the polymer coverage of the MNPs. These results suggested that the formation of large clusters was induced by the limited amount of polymer added. Indeed, when a large excess of copolymer was used, the MNP clusters obtained became small enough to pass though the magnetic separator without being arrested. This HGMS method is thus very interesting to separate constituents such as free DHBC and individually dispersed MNPs from clusters with a relatively well-controlled spherical morphology and a finite size, as seen on Figure 2-8.

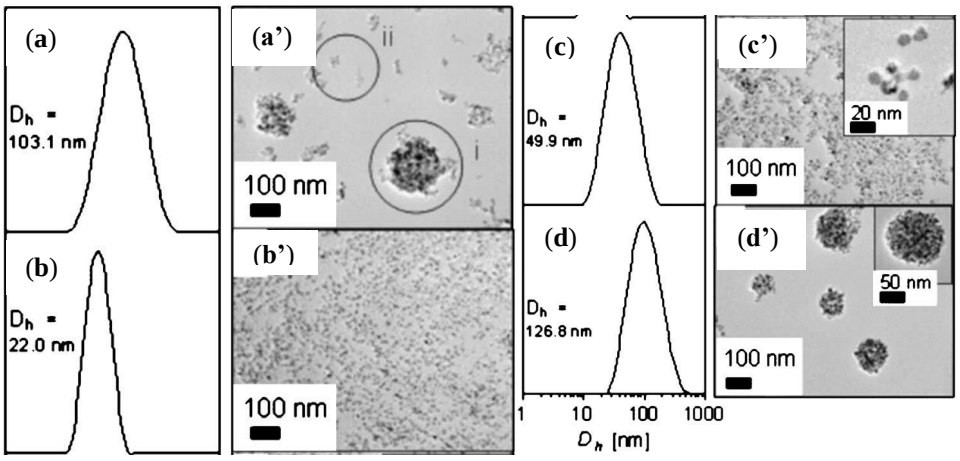

Figure 2-8. Size distribution by dynamic light scattering (DLS) (a, b, c, d) and from TEM images (a', b', c', d') of: (a, a') the initial suspension after coprecipitation in presence of PEO-*b*-PAA; (b, b') the non-captured particles; (c, c') the bleed-off samples; and (d, d') the captured clusters. Reprinted with permission from Reference 31. Copyright Elsevier B.V.

2.4.3.7 Deuterated Poly(norbornene) Block Copolymers

Poly(norbornene) (PNOR) is a rubbery material with interesting properties, such as the ability to absorb up to 10 times its own weight of hydrocarbons while still retaining its high tear strength and vibration damping ability. Amphiphilic block copolymers of this material, suitable as templates for the loading and coprecipitating iron salts, were obtained by the sequential ring-opening metathesis polymerization (ROMP) of norbornene and deuterated norbornene dicarboxylic acid (to provide better contrast between the two blocks in small-angle neutron scattering (SANS) experiments). The sodium salt form of the NOR-*b*-NORCOOH copolymer was dissolved in a THF solution, to achieve ion exchange between Fe^{3+} and the Na^{+} ions of the carboxylate block. Thin films prepared from this solution were then soaked in NaOH solutions to produce γ-Fe_2O_3 particles.[32] Variations in the constituent block volume fraction ratio ($\Phi_{NOR/NORCOOH}$), while ensuring a constant 1:1 ratio of $COOH/Fe^{3+}$, led to changes in the morphology (Figure 2-9) and characteristic distances for the microphase-separated block copolymer that were correlated with the size and the mean interparticle distance between the MNPs (as assessed by both SANS and the T_B measured by magnetometry).

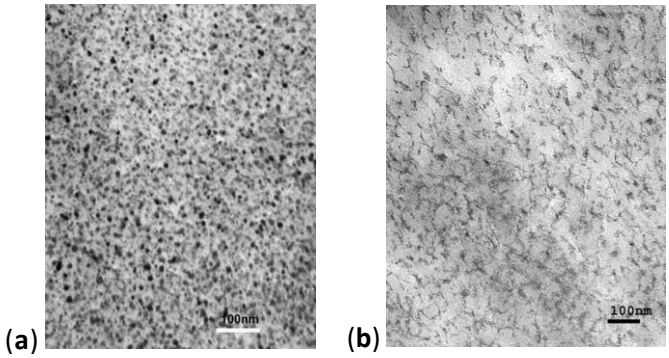

Figure 2-9. Morphology of poly(norbornene-*block*-deuterated norbornene dicarboxylic acid) loaded with iron oxide NPs (IONPs) at: (a) $\Phi_{PNOR/PNORCOOH}$ = 0.64/0.36 (disordered spheres); and (b) $\Phi_{PNOR/PNORCOOH}$ = 0.40/0.60 (interconnected spheres). Reprinted with permission from Reference 32. Copyright 2005 Elsevier Ltd.

Starting from 10.4 nm diameter disordered spherical particles at $\Phi_{NOR/NORCOOH}$ = 0.64/0.36 (Figure 2-9a), the samples changed to interconnected particles with 16 nm diameter at $\Phi_{NOR/NORCOOH}$ = 0.50/0.50 and 0.40/0.60 (Figure 2-9b), thus suggesting the possibility of controlling the nucleating process through the separation of the iron-doped hydrophilic blocks by the hydrophobic walls between the domains. The *d*-spacing between the metal oxide NPs measured by TEM (e.g., 62 nm for 0.64/0.36) was consistent with the correlation distance obtained from SANS analysis (e.g., 53 nm for 0.64/0.36), which proved the success of using microphase-separated domains as templates for the synthesis of IONPs. The ratio $d/(2R)$, where d is the average distance between the particles given by SANS and $2R$ is the individual particle diameter from TEM, was found to be inversely related to the T_B of interconnected NPs. The sample at $\Phi_{NOR/NORCOOH}$ = 0.40/0.60, with the largest hydrophilic block, led to the lowest $d/(2R)$ ratio, and thus the highest T_B (115 K) and the highest M_s (76 emu/g at 300 K), in agreement with the largest magnetic moments and magnetic dipolar interactions between them. The same *in situ* synthesis strategy was applied to a DHBC template of poly(norbornene methanol)-*b*-poly(norbornene dicarboxylic acid) (PNORMEOH-*b*-PNORCOOH),[33] resulting in a lamellar geometry with IONPs confined within the lamellar domains (Figure 2-10).

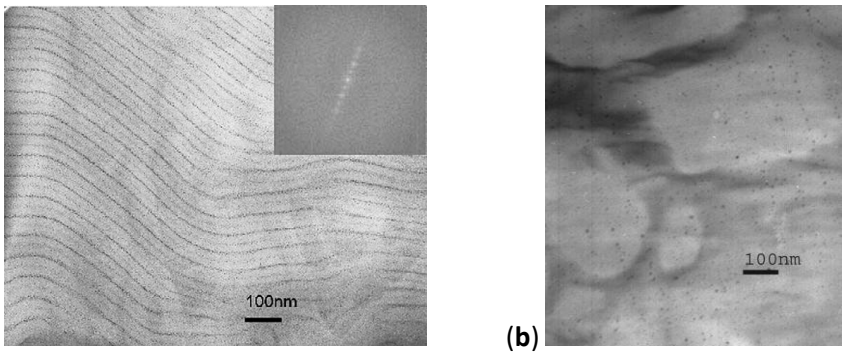

Figure 2-10. Electron micrographs for poly(norbornene methanol)-*block*-poly(norbornene dicarboxylic acid) (PNORMEOH/PNORCOOH) diblock copolymer: (a) stained with I_2 vapor; and (b) doped with iron oxide by submerging a thin film in $FeCl_3$ solution. Reprinted with permission from Reference 33. Copyright 2006 Elsevier Ltd.

Electron micrographs (with iodine staining) revealed that 6 nm average diameter γ-Fe_2O_3 particles decorated the lamellar structure of the copolymer in thin film samples, appearing in the images as thin lines of NPs, the spacing between the lines being 80 ± 10 nm.

2.4.3.8 Poly(styrene sulfonate-*alt*-maleic acid) (PSS-*alt*-MA) Shell with Subsequent Cross-Linking

The nucleating effects for the *in situ* coprecipitation of amphiphilic PSS-*alt*-MA and of hydrophilic PAA were nicely demonstrated by Yoon et al.[34] The coprecipitation was followed by cross-linking of the polymers with 1,6-hexanediamine, to prevent subsequent desorption of the polymer shell from the surface of the as-synthesized IONPs and to reach a good colloidal state through electrosteric stabilization. The zeta potential remained highly negative after cross-linking (Table 2-3), even at high salt concentrations (e.g., 8%) added to reduce the thickness of the electric double layer, thus weakening the electrostatic repulsions.

Table 2-3. Zeta potential and average hydrodynamic diameters of poly(acrylic acid) (PAA) or poly(styrene sulfonate-*alt*-maleic acid) (PSS-*alt*-MA)-coated IONPs with different cross-linking densities for an iron oxide concentration of 0.14 wt% at pH 8. Adapted with permission from Reference 34. Copyright 2011 American Chemical Society.

Cross-linking (%)	Hydrodynamic diameter (DLS) (nm)	Zeta potential (mV)
PSS-*alt*-MA before cross-linking	44 ± 9	−48.6 ± 4.7
PAA before cross-linking	83 ± 2	−39.7 ± 1.5
PAA, 12.5% cross-linking	69 ± 17	−48.6 ± 1.1
PAA, 50% cross-linking	126 ± 9	−44.3 ± 2.2
PAA, 12.5% cross-linking	77 ± 16	−47.1 ± 2.2
PAA, 100% cross-linking	91 ± 2	−38.3 ± 3.0

The sub-100-nm IONP clusters obtained were therefore stabilized by a balance of van der Waals and electrostatic interactions. The primary, highly crystalline IONPs exhibited superparamagnetism without hysteresis and an excellent M_s of ca. 90 emu/g_{Fe}, approaching

the theoretical magnetization value for bulk magnetite (92–100 emu/g Fe_3O_4,[35] equivalent to 127–138 emu/g_{Fe}), suggesting that the stabilizer did not lower the magnetization. These results confirmed good stabilizing effects for PAA and PSS-*alt*-MA, while not demonstrating a true template effect since the MNPs were still polydisperse.

2.4.3.9 Brush Linear Poly(oligo(ethylene glycol) methacrylate-*co*-methacrylic acid) P(OEGMA-*co*-MAA) as Nucleating and Stabilizing Ligand

Rather than relying upon the same copolymer block for both nucleation control and stabilization of the MNPs, Lutz et al.[36] developed in 2006 the idea of using a double-hydrophilic brush-linear block copolymer in which each block played a different, specific task. The coordinating ability of methacrylic acid units and the stabilizing capability of oligo(ethylene glycol) segments were examined in a coprecipitation process of iron ions using hydrophilic P(OEGMA-*co*-MAA). The hydrodynamic diameter of the MNPs obtained was readily tuned in the range of 10–24 nm (z-average values, polydispersity indices around 0.2) by variation of the initial polymer amount used as compared to the iron salts (from 1:1 to 0.42:1 wt:wt), thus also tuning their zeta potential from −14 mV to −7 mV. The 10 nm hydrodynamic diameter NPs were revealed as nearly monodisperse 7 nm particles in the TEM micrographs. As evidenced by TEM, the NPs had a quasi-spherical topology, in contrast to the "rock-like" shapes often obtained in coprecipitation methods. The stabilizing chain density was estimated as being relatively constantly in the range of 0.2–0.3 chains/nm^2 in all cases, which could explain the correlation found between the size of the NPs and the polymer amount used in the reaction. Moreover, the colloidal stability of the ferrofluids in physiological media, enhanced by the POEGMA block, allowed their *in vivo* use as MRI contrast agents.

2.4.3.10 Coprecipitation with DHBCs of Poly(oligoethylene glycol acrylate) (POEGA) and Different Binding Blocks

The groups of Boyer and Davis described the synthesis by the xanthate reversible addition-fragmentation chain-transfer (RAFT/MADIX) technique of DHBCs composed of the same repelling POEGA block and anchoring blocks with either phosphonic acid ethyl

acrylate (PAEA), carboxylic acid (PAA), or glycerol acrylate moieties in different copolymers.[37] These DHBCs were used for the *in situ* synthesis of IONPs by alkaline coprecipitation. The expected binding strength PAEA > PAA > PGA correlated nicely with the iron oxide loading, that also increased linearly with the feed-weight ratio of the iron salts (Figure 2-11b).

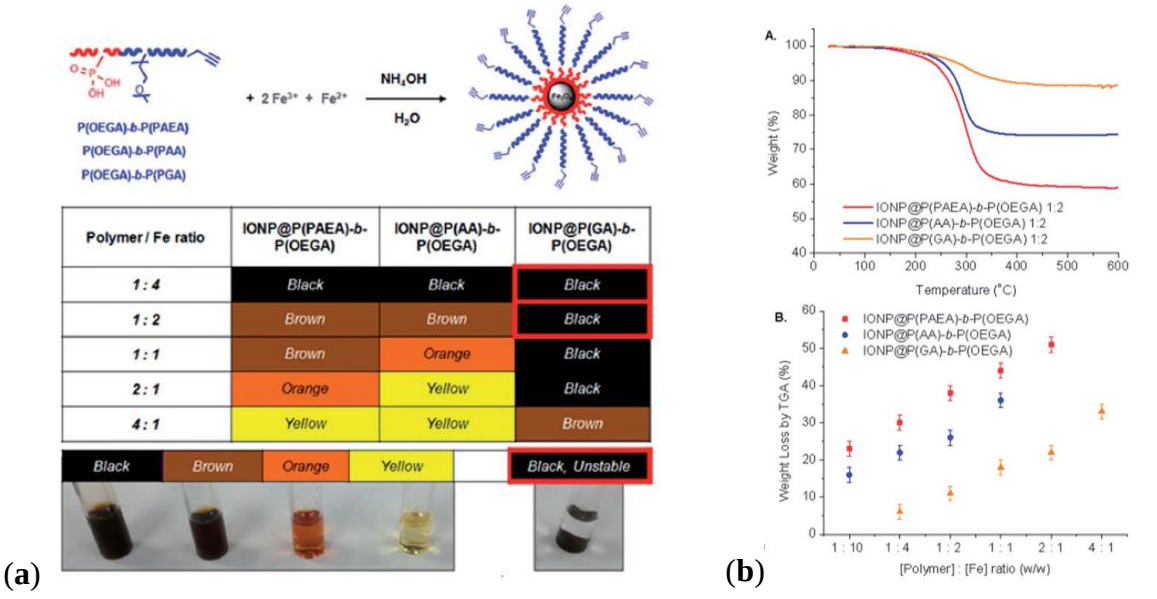

Figure 2-11. (a) *In situ* coprecipitation of iron oxide NPs (IONPs) at different polymer-to-Fe ratios; (b) polymer content measured by thermogravimetric analysis (TGA) for IONPs coated with different anchoring groups at a 1:2 [Polymer]:[Fe] weight concentration ratio. Reprinted with permission from Reference 37. Copyright 2014 Royal Society of Chemistry.

The size of the MNPs measured both by TEM and XRD followed the reverse order (PAEA < PAA < PGA) for a given polymer–iron feed ratio, i.e., the stronger the affinity for iron of the ligand, the smaller the magnetic core size. The size also decreased for increasing polymer contents (Table 2-4). All these observations confirmed a high degree of control over the nucleation and growth of the IONPs achieved with the copolymer template. The final products consisted in hybrid magnetic multi-core clusters (as seen on the TEM

images) exhibiting good colloidal stability in biological buffers and high T_2 relaxivity, which had the authors envision their use for *in vivo* MRI.

Table 2-4. Summary of TGA weight loss results and particle size (d_{TEM} and d_{XRD}) of polymer-coated IONPs at different polymer-to-iron ratios. PAEA: phosphonic acid ethyl acrylate. Reprinted with permission from Reference 37. Copyright 2014 Royal Society of Chemistry.

Hybrid magnetic core–shell	[Polymer]:[Fe] weight ratio	Wt loss TGA	d_{TEM} (nm)	d_{XRD} (nm)	Grafting density (nm^{-2})
IONP@P(PAEA)-*b*-P(OEGA)	1:10	23%	10.45	9.83	0.083 ± 0.005
	1:4	30%	9.80	9.10	0.124 ±0.003
	1:2	38%	9.40	8.52	0.168 ± 0.008
	1:1	44%	8.64	7.32	0.192 ± 0.01
	2:1	51%	-	-	-
IONP@P(AA)-*b*-P(OEGA)	1:10	16%	10.25	10.09	0.065 ± 0.001
	1:4	22%	8.91	8.75	0.084 ± 0.003
	1:2	26%	7.83	7.44	0.091 ± 0.003
	1:1	36%	-	-	-
IONP@P(GA)-*b*-P(OEGA)	1:4	6%	12.39	11.47	0.023 ± 0.001
	1:2	11%	10.24	10.62	0.039 ± 0.001
	1:1	18%	9.14	9.78	0.063 ± 0.002
	2:1	22%	8.65	8.41	0.073 ± 0.001
	4:1	33%	-	-	-

2.4.3.11 Spherical Micelles Loaded with IONPs

In the same context, amphiphilic block copolymers were also used as templates by introducing bidentate moieties, such as in poly[2-(acetoacetoxy) ethyl] methacrylate (PAEMA), to promote the nucleation of iron oxide. Papaphilippou et al.[38] investigated the use of this hydrophobic polymer in a copolymer with PEGMA as a hydrophilic and biocompatible second block, but also having a LCST near 60 °C. Highly stable hybrid micelles, visualized by atomic force microscopy (AFM) as spherical micelles loaded with IONPs (Figure 2-12), were obtained at various precursor salt concentrations. The maximum

amount of iron that could be encapsulated without precipitation was unfortunately not determined. A plateau magnetization M_s = 300 A/m was reached for the PEGMA$_{70}$-*b*-AEMA$_{16}$-coated MNPs at a 3:1 [Fe^{3+}]/[AEMA] molar ratio, but the specific magnetization cannot be calculated for this system since the corresponding iron concentration used was not specified. *In vitro* biocompatibility and macrophage uptake tests were also conducted and were encouraging in terms of toxicity and the minimization of recognition and phagocytosis.

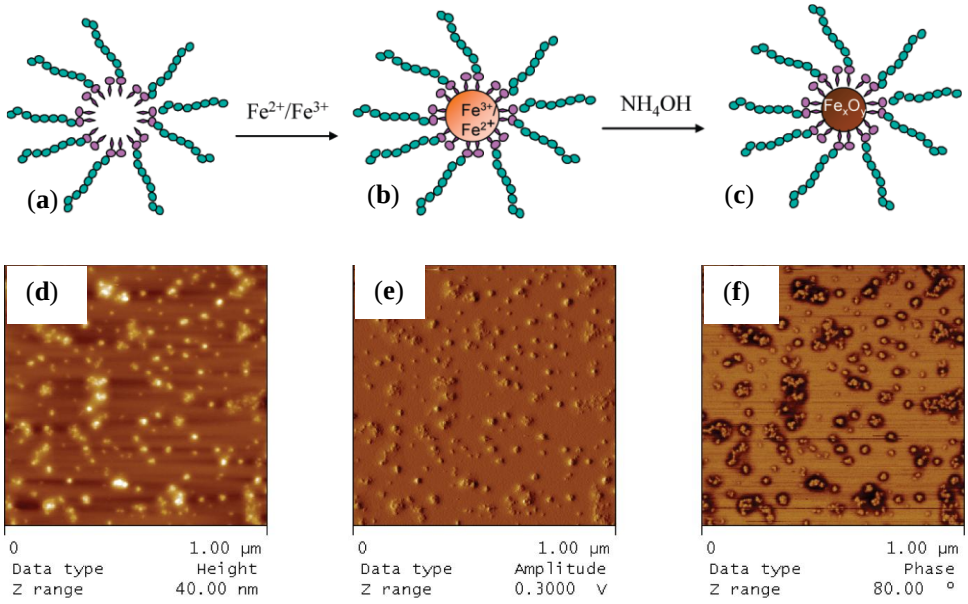

Figure 2-12. Strategy for the preparation of stabilized magnetic IONPs in aqueous media (top): (a) micelle formation by PEGMA$_x$-*b*-AEMA$_y$ diblock copolymer in water; (b) addition of the Fe^{3+}/Fe^{2+} mixture to the micellar solution, leading to complexation of the iron salts by the β-ketoester units inside the micellar core; and (c) transformation of the iron salt "precursor" into IONPs inside the micellar core upon addition of NH_4OH solution; atomic force microscopy (AFM) images for the block copolymer micelles loaded with IONPs (bottom): (d) height image; (e) amplitude image; and (f) phase image. Reprinted with permission from Reference 38. Copyright 2009 American Chemical Society.

As an intermediate case between (fully hydrophilic) DHBCs and amphiphilic block copolymers, graft polymers of composition PAA-*g*-PEO/PPO (PPO: poly(propylene oxide)) were studied by the group of Hatton.[39] In analogy with the commercial Pluronics® systems (PEO-*b*-PPO-*b*-PEO), the idea was to vary the hydration level of the micelles by tuning their PEO/PPO content while using the PAA backbone to complex with Fe^{2+}/Fe^{3+} ions. After alkaline coprecipitation, the water-based magnetic fluids obtained consisted of ca. 7.3 nm (TEM) magnetite NPs decorating the amphiphilic graft copolymer micelles. The magnetic core radii obtained by TEM and neutron scattering analyses had broad size distributions and irregular particle shapes however. Therefore the self-assembly of such copolymers with iron oxide precursors does not appear to provide a sufficient template effect for the synthesis of well-calibrated MNPs, and better controlled nanostructures need to be explored as reactors.

2.5 Synthesis Templated by Preformed Structures

Rather than using individual polymer chains and inducing their self-assembly in the presence of metallic salts, loading can be achieved by exposing preformed self-assembled structures to these precursors. This strategy is expected to minimize changes in morphology or size dispersity, but the ability of the metallic precursors to reach the anchoring moieties might be affected. Consequently, several studies aimed at optimizing the conditions for the *in situ* synthesis of MNPs in individual nanosized, well-defined objects.

2.5.1 Microemulsions in an Organic Solvent

The size, shape, morphology and physical properties of *in situ* synthesized MNPs are not only strongly influenced by the nature of the templates, but also by the methods used to load the precursors and create the MNPs. Among the emulsion methods, the nanosized droplets of water-in-oil microemulsions appear ideal as reactors inside which NPs can be synthesized, with a monodisperse distribution of diameters below 20 nm. The results obtained in this approach depend on the type of amphiphilic species used to stabilize the microemulsion.

2.5.1.1 Chitosan Shells in Fe^{2+} Microemulsions with Triton®-X

Due to the presence of numerous amine and hydroxyl groups, chitosan, a derivative of chitin with an acetylation level below 60%, has been considered as a template for loading metallic ions. Combined with other useful properties such as being non-toxic, hydrophilic, biocompatible, biodegradable and anti-bacterial, chitosan can be useful to shorten the gap between the synthesis of the MNPs and their biomedical applications. In research combining the advantages of microemulsion systems with the benefits of chitosan templates, Zhi et al.[40] proposed a route in which NaOH solution was quickly added to a microemulsion system of cyclohexane, *n*-hexanol, HCl, chitosan, and a ferrous salt stabilized by the Triton®-X 100 surfactant, with controlled exposure to oxygen. The type of iron oxide obtained in the NPs was efficiently controlled by the amount of oxygen in the N_2 gas added during the synthesis, with 0.05% of oxygen yielding 60–80 nm spherical chitosan particles encapsulating cubic-shaped Fe_3O_4 cores (Figure 2-13).

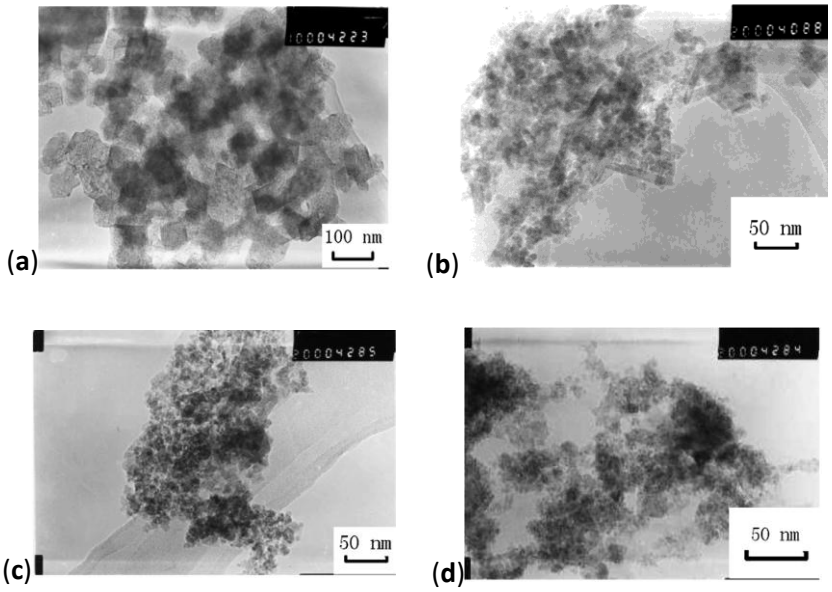

Figure 2-13. TEM of magnetic NPs (MNPs) obtained with: (a) molecular weight (MW) = 5.0×10^5 g·mol^{-1} non cross-linked chitosan; (b) cross-linked; (c) $\bar{M}_w$ = 1.0×10^5 g·mol^{-1} non cross-linked chitosan; (d) cross-linked. Reprinted with permission from Reference 40. Copyright 2006 Elsevier B.V.

Glutaraldehyde cross-linking of the magnetic chitosan NPs was suggested as a method to reduce the diameter of the obtained particles in the range of 10–50 nm without affecting the Fe_3O_4 cores. M_s values of 11.15 emu/g were reported for the composite NPs, in accordance with their iron oxide content.

2.5.1.2 Quaternary Microemulsions to Produce Aligned Spinel $CoFe_2O_4$ Nanorods

Quaternary microemulsions of cetyltrimethylammonium bromide (CTAB), water, cyclohexane and pentanol were used as microreactors for the coprecipitation of Co^{2+}, Fe^{2+} and oxalate anions, followed by the decomposition at high temperature of $CoFe_2(C_2O_4)_3$ (as "sacrificial template") and oxidation of Fe^{2+} into Fe^{3+} to produce spinel $CoFe_2O_4$ nanorods.[41] The calcination treatment was indispensable to convert the amorphous nanorods into crystalline nanorods while maintaining control over their dimensions (50–100 nm in diameter, several micrometers in length), by stimulating internal nucleation and crystallization, in analogy to the natural petrification process which requires centuries to complete. Scanning electron microscope (SEM) images highlighted the overall rod-like shape of the particles (Figure 2-14), and TEM images revealed the morphological transformation and the ripening of the rod-like particles upon heating, leading to the final state with individual $CoFe_2O_4$ crystals linearly arranged along the annealed nanorods (Figure 2-15a). The crystallographic alignment of the $FeCo_2O_4$ nanocrystals became visible after calcination in the high resolution TEM images as atomic planes (Figure 2-15c) and grain boundaries between the interconnected nanocrystals (Figure 2-15b). After annealing, the nanorods also exhibited magnetic H_c with a Curie temperature well above room temperature. Regarding their formation mechanism, the authors noted that the direct calcination of a coprecipitated $CoFe_2(C_2O_4)_3$ suspension in the absence of the microemulsion template did not lead to long crystalline anisotropic magnetic structures. Therefore an "oriented attachment" mechanism between the inorganic nuclei growing through the organic template was proposed. The ionic nature of the CTAB surfactant may also have played a role at the beginning of the calcination process, by forming a molten salt also favoring oriented nucleation.

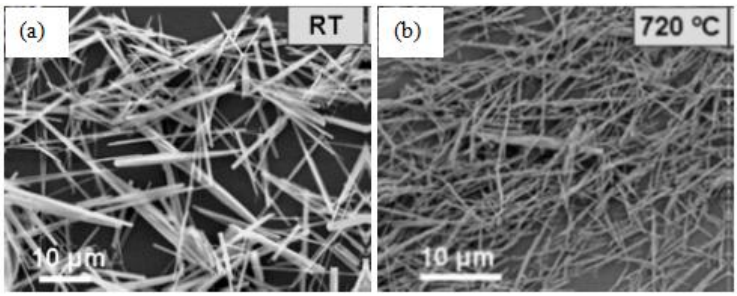

Figure 2-14. Scanning electron microscope (SEM) images for: (a) as-synthesized $CoFe_2(C_2O_4)_3$ suspension after coprecipitation in a microemulsion; and (b) $CoFe_2O_4$ rods annealed at 720 °C. Reprinted with permission from Reference 41. Copyright 2005 Wiley-VCH.

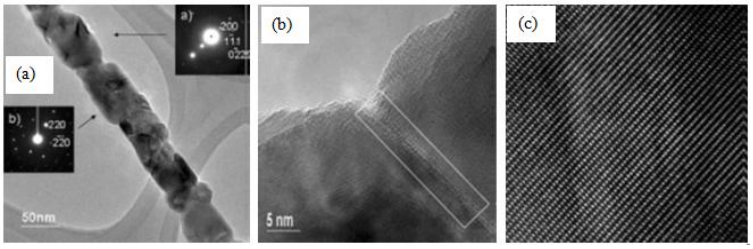

Figure 2-15. (a) TEM image for an individual $CoFe_2O_4$ nanorod annealed at 720 °C; the insets illustrate SAED patterns acquired from two individual nanocrystals of size about 80 nm. The inset (a) shows the indexed diffraction pattern for the *fcc* crystals in the [011] beam direction, and inset (b) in the [001] beam direction; (b) high resolution transmission electron microscopy (HRTEM) image showing a grain boundary between two $CoFe_2O_4$ nanocrystals; and (c) HRTEM image for a $CoFe_2O_4$ nanocrystal. Reprinted with permission from Reference 41. Copyright 2005 Wiley-VCH.

2.5.2 Spherical Micelles in Water

Templates with predetermined sizes and structures are good candidates to orient the nucleation process, as they can be designed with an appropriate anchoring block, carry highly stabilizing units, and optionally a cross-linkable segment providing additional versatility.

2.5.2.1 Triblock Polyisoprene-*block*-Poly(2-cinnamoylethyl methacrylate)-*block*-Poly(*tert*-butyl acrylate) (PI-*b*-PCEMA-*b*-PtBA) Copolymer Hollow Nanospheres

At first, spherical micelles with a structure locked by photo-cross-linking were prepared using a triblock copolymer PI-*b*-PCEMA-*b*-P*t*BA, in which PI forms the corona, PCEMA a solvent-insoluble shell, and P*t*BA a hydrolysable core.[42] Hydroxylation of the PI corona and cleavage of the *tert*-butyl groups to convert PtBA to PAA enabled the coordination of Fe^{2+} ions in the template. Finally, alkaline oxidation with NaOH and H_2O_2 yielded water-soluble Fe_2O_3-impregnated nanospheres. This multi-step pathway is represented schematically on Figure 2-16.

The diameter of the polymeric template (90 nm) did not change after the *tert*-butyl removal step (as seen by comparison of Figure 2-17b with Figure 2-17a), indicating the benefits of using templates with a predetermined size, shape and morphology. Inorganic cores with diameters ranging from 4 to 16 nm were visible on the TEM images (Figure 2-17c). The Bragg peaks detected in selected area electron diffraction (SAED) experiments were matched with the Miller indices of the maghemite (γ-Fe_2O_3) phase. Therefore such templates with a cross-linked polymer shell surrounding a porous polymer core coordinating ferrous precursors were efficient as templates for the preparation of IONPs, although further studies were suggested to control the size distribution of the magnetic cores.

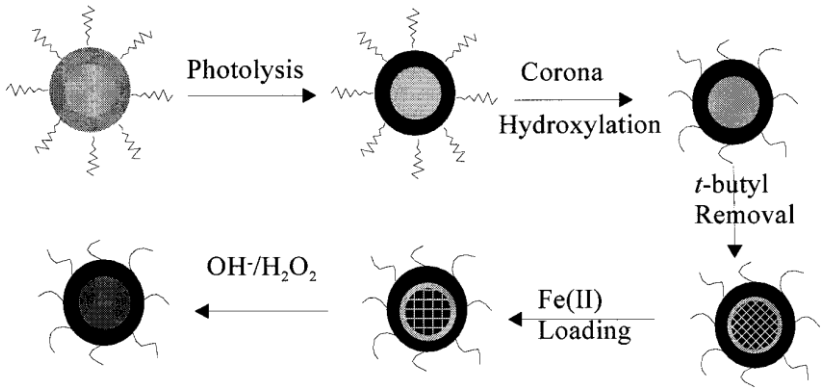

Figure 2-16. Polyisoprene-*block*-poly(2-cinnamoylethyl methacrylate)-*block*-poly(*tert*-butyl acrylate) (PI-*b*-PCEMA-*b*-P*t*BA) as template: Photolysis cross-links the PCEMA shell (gray to black); the PI corona chains are made water-soluble by hydroxylating the double bonds (wavy lines to free-hand lines); the core is made inorganic-compatible by removing the *tert*-butyl groups (light gray to gridded pattern). Soaking the nanospheres in aqueous $FeCl_2$ leads to proton exchange (slanted to vertical grids) and the Fe^{2+} ions are precipitated (NaOH) and oxidized (H_2O_2) to yield cubic γ-Fe_2O_3 magnetic particles (last step). Adapted with permission from Reference 42. Copyright 2000 American Chemical Society.

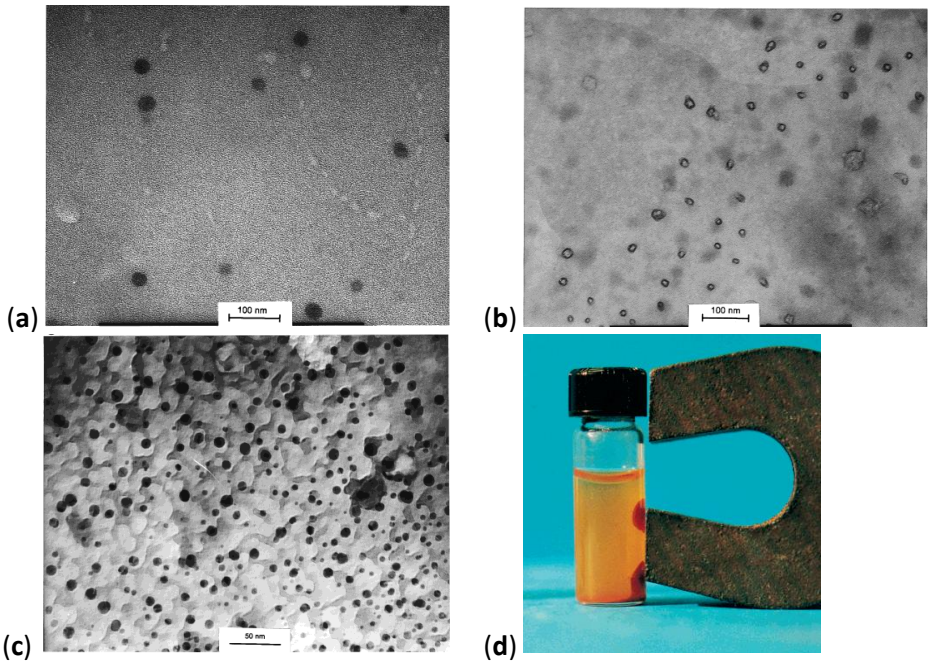

Figure 2-17. TEM images for PI-*b*-PCEMA-*b*-PtBA nanospheres at each step of the synthesis: (a) after PCEMA cross-linking and PI hydroxylation (stained with OsO_4); (b) after removal of the *tert*-butyl groups (stained with OsO_4); (c) after Fe_2O_3 loading (no staining); and (d) attraction by a magnet. Adapted with permission from Reference 42. Copyright 2000 American Chemical Society.

2.5.2.2 PEG-*b*-poly(4-vinylbenzylphosphonate) (PEG-*b*-PVBP) Micelles

Among the papers collected for this review, a small number concerned the surface coating density of pegylated IONPs (PIONs) for *in vivo* applications such as MRI. A recent study by Ujiie et al.[43] utilized PEG-*b*-PVBP block copolymers for *in situ* alkaline coprecipitation (Figure 2-18). A correlation between the (PEG-*b*-PVBP)/(iron salt) feed ratio and the surface density of PEG chains in the PEG-PIONs was revealed, suggesting an optimal ratio to obtain sufficiently small particles with a high PEG chain density. Interestingly, while the core sizes measured by TEM (≈ 7.7 nm) were typical for the aqueous

coprecipitation route, they were unrelated to the feed ratios used. Thus although a "template effect with micelle-like aggregates" was invoked, the main interest of this method is for the preparation of individually dispersed MNPs stable in biological buffers rather than achieving precise control over the size of the magnetic cores.

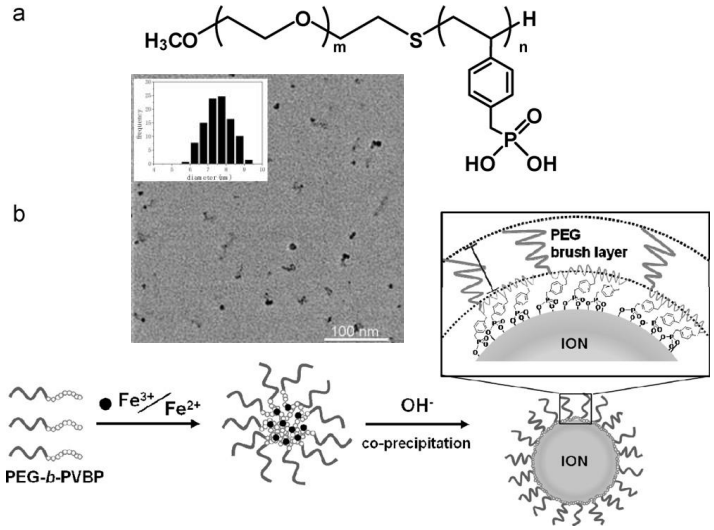

Figure 2-18. (a) Chemical structure of PEG-*b*-poly(4-vinylbenzylphosphonate) (PEG-*b*-PVBP) and schematic illustration of the proposed morphology of the pegylated IONPs (PIONs); and (b) TEM image for the PIONs and their size distribution as inset. Adapted with permission from Reference 43. Copyright 2011 Elsevier B.V.

It is worth noting that the phosphonate groups significantly contributed to the incorporation efficiency of the block copolymer, due to its well-known binding ability for various metal oxides. The $R_h \approx 30$ nm observed for the micelle-like aggregates before the ammonia addition was considered as reflecting a "templating effect" for metallic nucleation. This is the main reason why this study is reported in the preformed structures section instead of the block-copolymer section.

2.5.2.3 Multiarm Star-Like Amphiphilic or Double-hydrophilic Block Copolymers (DHBCs)

For linear block copolymer templates the size, shape, and the colloidal stability of the nanocrystals are greatly influenced by the experimental conditions used (e.g., concentration, solvent, temperature, and pH). Multi-arm star-like unimolecular micelles derived from either amphiphilic or double-hydrophilic block copolymers were successfully employed to achieve better control over the size and shape of the MNPs. Starting from a multi-arm ATRP initiator (suitably functionalized β-cyclodextrin (CD)), the polymeric blocks (P*t*BA or P4VP) serving to bind the inorganic precursor were synthesized first. These star-like homopolymers were then coupled by "click" chemistry with either hydrophobic (PS) or hydrophilic (PEO) polymeric segments, which imparted solubility to the micelles in either organic or aqueous environments.[44] The $FeCl_2$ and $FeCl_3$ precursors were loaded in the hosts in appropriate solvents. After ammonium hydroxide addition, Fe_3O_4 NPs were produced with different sizes (6, 10 and 16 nm, e.g., Figure 2-19a and Figure 2-20a), depending on the MW of the PAA block derived from P*t*BA (4.5, 8.4 and 16.8 kDa). These exhibited superparamagnetic properties at 300 K without hysteresis, and M_s increasing with the NP size. The advantages of triblock structures (β-CD-P4VP-P*t*BA-PS) and (β-CD-P4VP-P*t*BA-PEO) were also highlighted by producing NPs with Fe_3O_4 cores and $PbTiO_3$ (Figure 2-19b and Figure 2-19c) or Au shells (Figure 2-20b).

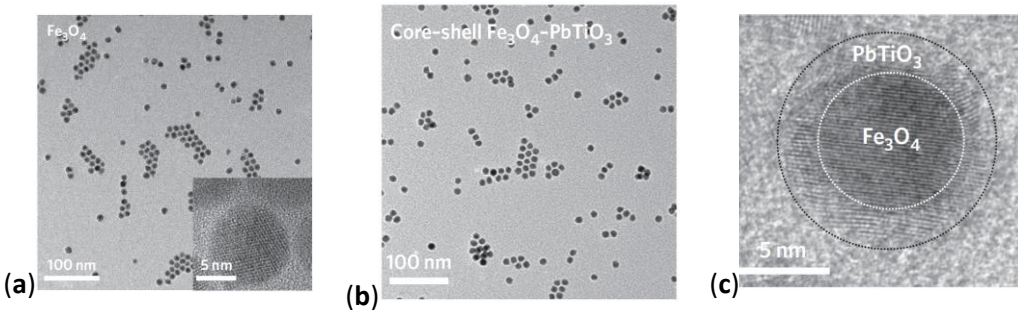

Figure 2-19. (a) Representative TEM images for Fe_3O_4 NPs synthesized with star-like PAA-*b*-PS templates, $D(Fe_3O_4)$ = 10.1 ± 0.5 nm; (b) TEM; and (c) HRTEM images for Fe_3O_4-$PbTiO_3$ core–shell NPs formed with the star-like triblock copolymers nanoreactors. Reprinted with permission from Reference 44. Copyright 2013 Macmillan Publishers Limited.

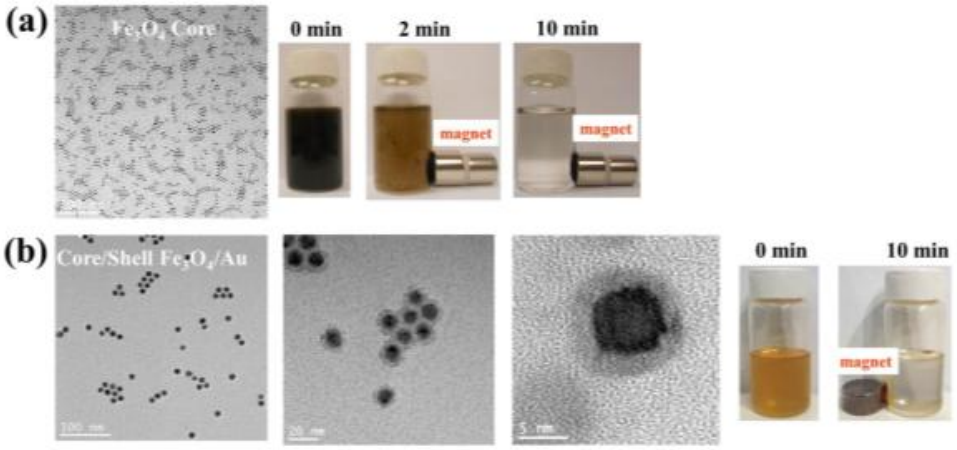

Figure 2-20. TEM, HRTEM and digital camera images for core/shell Fe_3O_4/Au NPs: (a) Fe_3O_4 core (D = 6.1 ± 0.3 nm); and (b) Fe_3O_4/Au core/shell NPs at different magnifications (Au shell thickness is 2.9 ± 0.2 nm). Fe_3O_4 appears dark in the center. The magnetic properties of Fe_3O_4 were retained, as evidenced by the response of the NP dispersion in toluene to a magnet (right panel in (b)). Reprinted with permission from Reference 44. Copyright 2013 Macmillan Publishers Limited.

More accurately, the magnetite NPs were encapsulated within the P4VP core, and the $PbTiO_3$ or Au layers were grown within the PAA shell (derived from the P*t*BA block after the first encapsulation step), thus retaining the magnetic properties of the NPs. TEM imaging revealed a uniform size and narrow size distribution for the NPs, while the crystalline lattices were characterized by HRTEM, XRD and energy-dispersive X-ray spectroscopy (EDS) measurements. Hollow gold NPs were also reported, aside from the magnetic-gold core–shell systems. This work undoubtedly evidences a strong templating effect in the *in situ* synthesis of inorganic NPs, in particular magnetic ones, using unimolecular star-like PAA-PEO micelles.

2.5.3 Cylindrical Multimolecular Micelles

Different morphologies were obtained by the self-assembly of commercial Pluronic® F127 PEO-*b*-PPO-*b*-PEO triblock copolymers in water/alcohol mixtures, to serve as templates for iron ion loading by coprecipitation.[45] Surprisingly, as the alcohol content in the solvent mixture increased, a gradual phase transformation from 15 nm Fe_3O_4 NPs (Figure 2-21a) to uniform (ca. 20 nm diameter, 200–300 nm length) α-FeOOH (goethite) nanorods (Figure 2-21b) was observed.

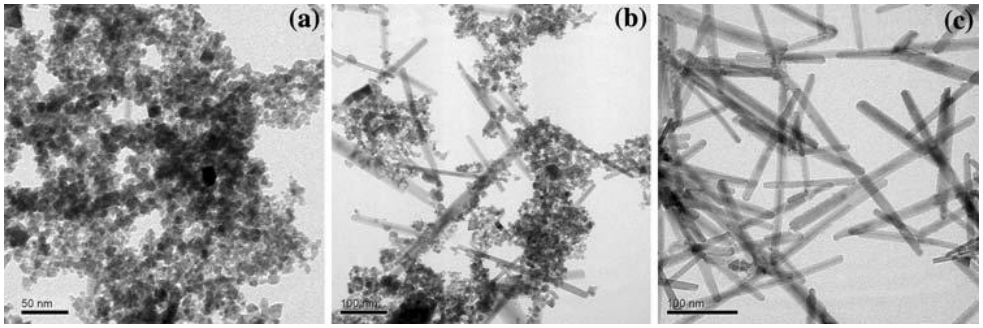

Figure 2-21. TEM images for samples prepared in alcohol/water mixtures with various volume ratios of alcohol to water: (a) 0:1; (b) 1:1; and (c) 5:1. Reprinted with permission from Reference 45. Copyright Springer Science Business Media, LLC 2008.

This shows that Pluronics® can serve as structure-directing agents that control both the metal oxide mesoscale size and the crystalline structure. The decrease in M_s of the samples observed was in agreement with this phase transformation from the superparamagnetic (maghemite) to the anti-ferromagnetic state (goethite).

2.5.3.1 Fe^{3+} Loading in Poly(acrylic acid)-*graft*-Poly(*n*-butyl acrylate) Brush

In an attempt to prepare hybrid magnetic unimolecular comb-like polymer micelles, Zhang and Müller reported a procedure employing amphiphilic core–shell cylindrical polymer brushes with poly(acrylic acid)-*block*-poly(*n*-butyl acrylate) (PAA-*b*-PnBA) side chains to impregnate Fe^{3+}.[46] It is worth noting that in order to increase the rate and extent of iron ion uptake, the COOH groups in the PAA blocks were deprotonated with NaOH before the encapsulating step was performed with an excess amount of $FeCl_3$. The polychelate effect was confirmed by FT-IR and ultraviolet visible spectroscopy (UV-VIS) measurements, while the TEM and atomic force microscopy images revealed the core of the unimolecular wormlike cylinder hybrids that had been mineralized by the ferric cations (Figure 2-22). However the authors did not go further than precursor loading, i.e., they did not describe the *in situ* alkaline coprecipitation.

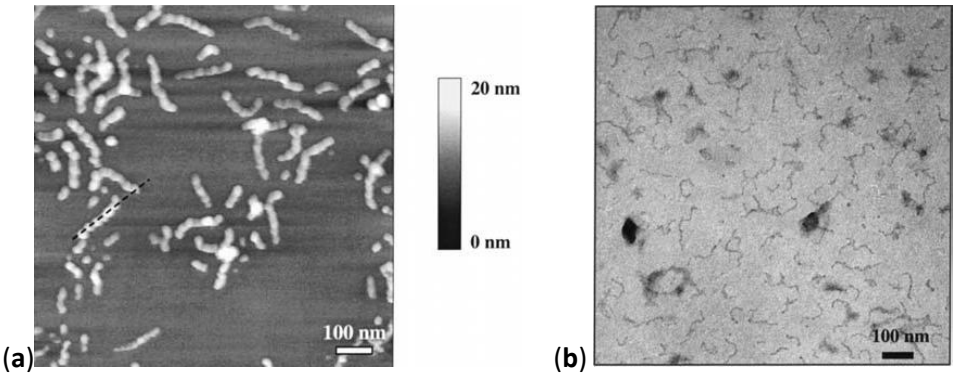

Figure 2-22. (a) AFM height image for the polychelate of a poly(acrylic acid)-*graft*-poly(*n*-butyl acrylate) brush and $FeCl_3$ after dialysis; and (b) TEM image for the unimolecular polymer brush polychelate of $FeCl_3$ (after dialysis). Adapted with permission from Reference 46. Copyright 2004 Springer-Verlag.

2.5.3.2 Fe^{3+}/Fe^{2+} Loading and Precipitation in Poly[poly(ethylene glycol) methyl ether acrylate]-*graft*-poly(methacrylic acid) (PPEGMEA-*g*-PMAA) Brush

Both nucleating and stabilizing abilities were introduced into a densely grafted bottle-brush double-hydrophilic copolymer constituted of two different types of hydrophilic segments, respectively a PMAA backbone providing COOH groups for the nucleation of Fe_3O_4 particles, and poly[poly(ethylene glycol) methyl ether acrylate] (PPEGMEA) side chains (Figure 2-23), introducing a shielding effect to prevent aggregation. Such a template was investigated for an *in situ* coprecipitation process.[3] Fe_3O_4/polymer clusters of uniform size and hydrodynamic sizes from 50–210 nm, carrying 7–15 nm diameter Fe_3O_4 crystals, were thus obtained. The magnetic core sizes were efficiently tuned by varying the polymer/Fe_3O_4 feed ratio and the length of the PMAA side chains. For example, the diameter of the MNPs increased from 8.5 to 9.5 and 10.4 nm when this ratio was varied from 1/1 to 1/2 and 1/3, respectively. Measurements on a VSM setup revealed the superparamagnetism of the hybrids at room temperature, with a concomitant increase of the M_s value from 48 to 49 and 50 emu/g. Such dense polymeric combs were thus considered to be influent templates to orient the distribution of sizes and to improve the magnetization properties of Fe_3O_4 NPs.

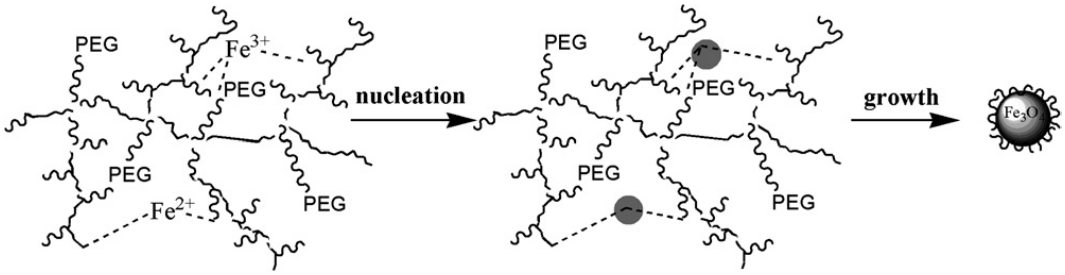

Figure 2-23. Synthesis of Fe_3O_4/polymer nanocomposite in the presence of poly(ethylene glycol) methyl ether acrylate (PPEGMEA)-*g*-PMAA densely grafted double-hydrophilic copolymer. Reprinted with permission from Reference 3. Copyright The Royal Society of Chemistry 2008.

2.5.3.3 Poly(glycerol monoacrylate)-*graft*-Poly(PEG methyl ether acrylate) (PGA-*g*-PEG) Copolymers

In a detailed study[47] aimed at investigating the influence of the graft density and the MW of the graft copolymer poly(glycerol monoacrylate)-*g*-poly(PEG methyl ether acrylate) (PGA-*g*-PEG) on the average size and the magnetic properties of MNPs, the possibility of changing the diameter of particles in the 4–18 nm range by employing polymers with different grafting densities was suggested. It is understandable that since the hydroxyl groups in the PGA block were the anchoring functionalities, the decreased feed ratio of the monomeric precursors of glycerol monoacrylate to the PEG methyl ether acrylate side chains in graft copolymerization resulted in the increased graft density *g*, reducing the coordinating capability of each individual graft polymer micelle and thus leading to ascending particle sizes. This observation was confirmed by the data obtained from XRD measurement were the Bragg peak widths were analyzed by the Scherrer equation: The average particle sizes were 4, 7, 9 and 18 nm, respectively, for g = 0.14, 0.23, 0.30 and 0.42. Interestingly, graft copolymers with different MW (from 4.2 kD to 7.6 kD and 15 kD) having the same graft density g = 0.24 produced particles of similar size. The particles were superparamagnetic at room temperature, with normalized M_s decreasing within the range of 30–42 emu/g for decreasing particle sizes, due to the smaller crystalline domains.

2.5.3.4 Poly(ethylene oxide)-*graft*-Poly(acrylic acid) (PEO-*g*-PAA) Graft Copolymer

The four-arm graft copolymers PEO-*co*-ethoxyethyl glycidyl ether-*graft*-PAA [PEO_x-*co*-Gly_y-*g*-PAA_z]$_4$ were employed in the same coprecipitation process reported above, leading to composite particles with narrow size distributions encapsulating 10–20 nm iron oxide single crystals inside the polymer capsules.[48] The TEM results were in good agreement with those from XRD analysis, with the exception that peak broadening was assigned to matrix constraints for the nanosized particles. The superparamagnetic properties were confirmed, and the calculated M_s was 56 emu/g Fe_3O_4. The size and the size distribution of the hybrid NPs could be tuned by changing the mass ratio of polymer to Fe_3O_4 and by varying the ratio of PAA/PEO segments in the graft copolymer (better template effects, with smaller particles and

narrower size distributions, were reported for larger proportions of PEO segments). More importantly, star-shaped polymers with a more confined structure exhibited a clearer template effect as compared to graft copolymers with similar components.

From the three preceding examples, which originate from different teams, one can conclude that despite changes in the chemical nature of the polymer segments, the graft polymer structures always induce more reproducible trends in the variation of the average size of the magnetite NPs synthesized by *in situ* coprecipitation. However these studies may have overestimated the template effect, in the sense that the size distributions observed on TEM images were always broad and did not correspond to true uniform samples.

2.5.4 Lamellar Films

2.5.4.1 Polystyrene-*block*-Poly(2-vinylpyridine) (PS-*b*-P2VP) Lamellae Hosting Pristine Iron Nanoparticles

The complexation ability of vinylpyridine moieties was investigated by the groups of Cohen and Ross[49] not only in the form of linear homo- and copolymers as discussed above, but also in bulk films of PS-*b*-P2VP. Nucleation was induced by the thermal decomposition of $Fe(CO)_5$ or $Co_2(CO)_8$. The impregnation of the organometallic complexes $Fe(CO)_5$ and nickelocene in vacuum-dried films produced monodispersed iron, iron–cobalt, and cobalt–nickel metallic NPs residing within the P2VP domains, that were superparamagnetic at room temperature. The lamellar structure of these composites was visible in TEM micrographs as a “cluster of grapes” morphology of pristine metal particles that were uniform in size when the metallic feed ratio of Fe to Co was 100:0 (Figure 2-24a) or 80:20 (Figure 2-24b), and bimodal when increasing the Co content to 50:50 (Figure 2-24c) or 20:80.

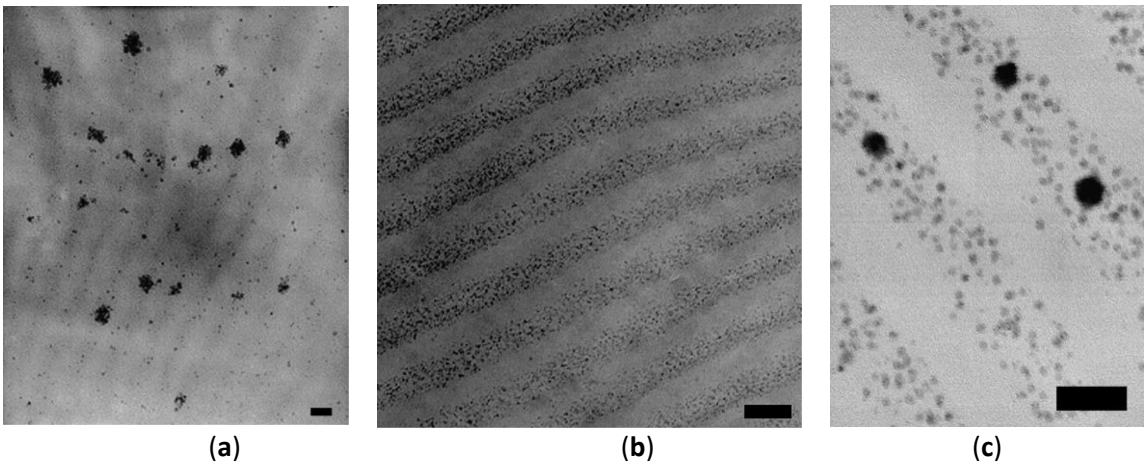

Figure 2-24. (a) TEM micrograph for a lamellar PS-*b*-P2VP copolymer containing 1.2 meq of iron/g P2VP; sample heated to 195 °C for 24 h, scale bar = 50 nm; (b) TEM micrograph for the same copolymer containing a total of 1.2 meq of Fe and Co/g P2VP, with an atomic ratio of Fe to Co of 80:20; sample heated to 161 °C for 24 h, scale bar = 100 nm; and (c) scanning transmission electron microscopy micrograph for the copolymer containing a total of 1.2 meq of Fe and Co/g P2VP, atomic ratio of Fe to Co = 50:50; sample heated to 161 °C for 24 h; the atomic ratio of Fe:Co at the center of the large particles was 48.9:51.1 from energy dispersive X-ray spectroscopy (EDX); scale bar = 50 nm. Reprinted with permission from Reference 49. Copyright 2003 Elsevier B.V.

The magnetization values of the samples varied from 1.1 emu/g P2VP in the first two cases, to 8.4 emu/g P2VP and 10.9 emu/g P2VP for the higher Co contents. The increase in M_s observed for higher Co contents was explained by the preference of cobalt atoms remaining at the surface of the particles to minimize their surface energy, which led to thinner layers and more walls (as shown by scanning transmission electron microscopy (STEM)) separating smaller particles with a larger surface-to-volume ratio. The smaller particles nucleated on the film were considered the dominant factor explaining the non-zero H_c observed at room temperature for some samples.

2.5.5 Hexagonal Ordered Films

2.5.5.1 Monolayer Films of Polystyrene-*block*-Poly(4-vinylpyridine) (PS-*b*-P4VP) Copolymer Micelles

To create monolayer films where the particles were arranged in a hexagonal array, PS-*b*-P4VP micelles (formed by self-assembly in toluene) encapsulating $FeCl_3$ within their P4VP core were spread onto cleaned silicon wafers by spin coating.[50] Oxygen plasma treatment was needed to convert the Fe^{3+} precursor into iron oxide and to remove the polymer template. The γ-Fe_2O_3 crystals formed at 1.0, 0.5, and 0.2 $FeCl_3$/P4VP molar ratios appeared on the TEM images (Figure 2-25a) as 25.0, 18.0, and 6.0 nm sized particles, respectively, arranged in a hexagonal self-assembled pattern. The wide range of IONP diameters obtained and the constant spacing of the IONP pattern in all three cases demonstrated that PS-*b*-P4VP is a powerful template that effectively controls the nucleation and the growth of the particles. AFM (Figure 2-25b) and field emission-scanning electron microscopy (FE-SEM) imaging (Figure 2-25c) revealed the hemispherical topology of the IONPs.

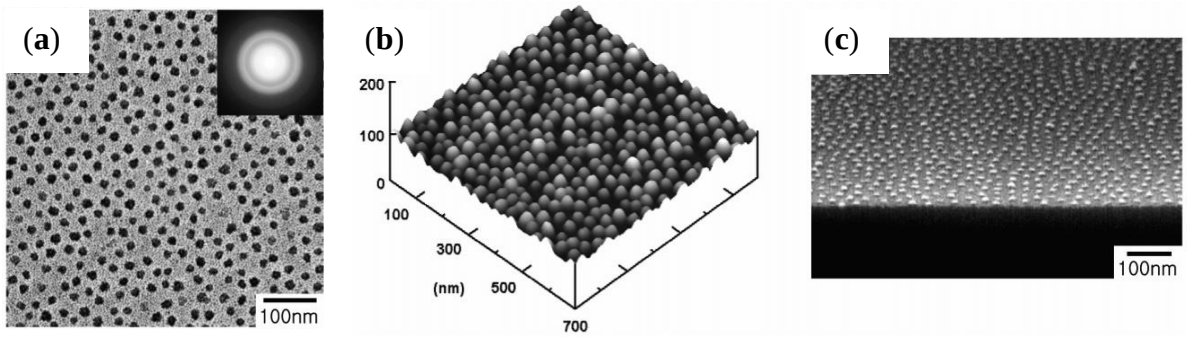

Figure 2-25. (a) TEM image for a self-assembled pattern of IONPs with hexagonal packing. The inset is a SAED pattern typical for γ-Fe_2O_3; (b) AFM image for the hexagonal pattern of IONPs on a silicon wafer; and (c) field emission-scanning electron microscopy (FE-SEM) image in tilt view. The molar ratio of $FeCl_3$ precursor to 4-vinylpyridine was 0.5 in all cases. Reprinted with permission from Reference 50. Copyright 2005 American Chemical Society.

Contrary to what was expected, the annealing process aiming to improve the crystallinity of the particles did not cause irregular shapes but slightly reduced the average diameter and height of the particles for all the samples with different $FeCl_3$/P4VP ratios, as shown in the tilt-view image of Figure 2-25c. The 25.0 nm-sized particles exhibited ferrimagnetism with normalized magnetization M_s = 100 emu/g and H_c = 50 Oe, while the 6.0 nm crystals possessed 30 emu/g saturated magnetization and zero hysteresis, corresponding to superparamagnetic properties. The impressive variations in the magnetic properties of the particles obtained was achieved by only changing the $FeCl_3$/P4VP feed ratio in the mixture.

2.5.5.2 Monolayer Films of Polystyrene-*block*-Poly(ethylene oxide) (PS-*b*-PEO) Copolymers

Also targeting the preparation of hexagonal arrays of NPs, the *in situ* synthesis of metal oxide NPs through a gas phase oxidation pathway in oriented cylinder structures was investigated by Ghoshal et al.[51] The ordered thin films were prepared using a commercial diblock copolymer of polystyrene (PS), with PEO as the metal-anchoring block. The block weight ratio was selected to yield cylindrical PEO domains 20 nm in diameter and 28 nm in height, regularly distributed within the PS matrix. One of the strategic details differentiating this research from the methods reported earlier was the microphase separation induced by a solvent mixture after spin coating of a toluene solution of the PS-*b*-PEO block copolymer onto cleaned silicon wafers. Annealing with a water/toluene mixture efficiently weakened the preferential interactions between PEO and the substrate, thus allowing vertical alignment of the PEO cylinders (Figure 2-26A). A subsequent treatment with an ethanol solution at 40 °C for 15 h (Figure 2-26B) appeared necessary as an “activation step” for the PEO cylinders to create a functional chemical pattern for nanodot development, which was interpreted by the authors as being due to the crystallization of the PEO blocks induced by ethanol. The affinity of $Fe(NO_3)_3$ for PEO as compared to PS allowed selective inclusion of the metallic salt by spin-coating of the 0.4 wt% precursor solution (Figure 2-26C). Finally, ultraviolet (UV)/ozone treatment (Figure 2-26D) produced highly ordered Fe_3O_4 particles (or

CeO_2 or CuO, depending on the precursor). This treatment not only produced the oxides from the precursors but also removed the polymer template. The Fe_3O_4 particles appeared in HRTEM images as nanodots 24 nm in diameter and 9 nm in height, with a regular spacing of 42 nm between their centers.

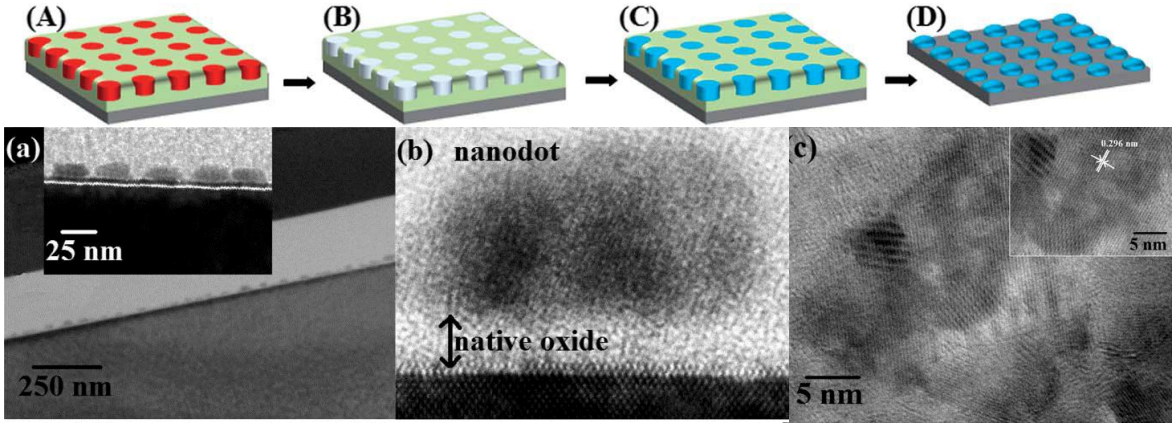

Figure 2-26. Schematic illustration of the fabrication of oxide nanodots: (A) highly ordered PS-*b*-PEO thin film prepared by a solvent annealing process; (B) nanoporous template produced by activation of the PEO cylinders upon exposure to ethanol at 40 °C for 15 h; (C) the metal oxide precursor diffuses into the cylinders after spin coating of the metal nitrate solution; and (D) oxide dots remaining after the ultraviolet (UV)/ozone treatment. (a) TEM cross-sectional image for iron oxide nanodots; the inset shows a higher magnification image; (b) cross-sectional HRTEM image for a single nanodot; and (c) HRTEM image for the nanodots after the UV/ozone treatment; the inset shows crystalline fringes corresponding to Fe_3O_4. Reprinted with permission from Reference 51. Copyright 2012 The Royal Society of Chemistry.

Control over the diameter and the height of the oxide nanodots was attained by varying the precursor concentration, which changed the height and the diameter of the nanodots without affecting their spacing. Precursor solution concentrations exceeding 1%

led to saturation of the PEO cylinder template, however. This method nevertheless offers great potential to easily tune the NP size for iron oxide and several other inorganic materials. In addition, the nanodots could be sintered without losing their structural order, as seen on Figure 2-27. For example at 800 °C in air, the IONPs shrunk in diameter by 3 nm and in height by 2 nm, which was ascribed to oxide densification.

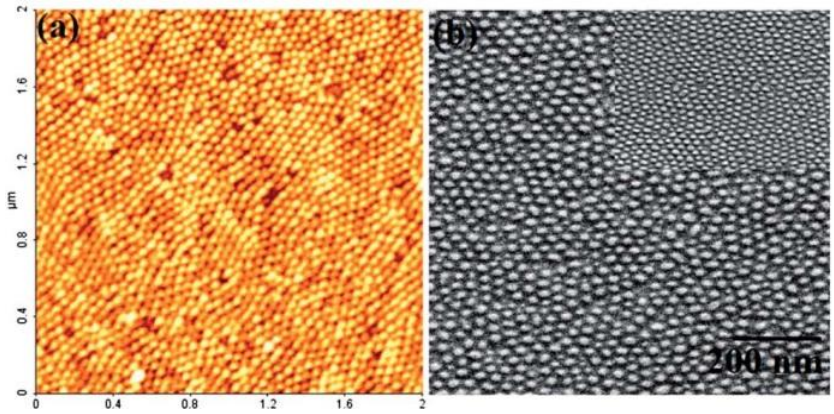

Figure 2-27. (a) AFM; and (b) SEM images for hexagonally ordered iron oxide nanodots after UV/ozone treatment. The inset of (b) shows the iron oxide nanodots after annealing at 800 °C for 1 h. Reprinted with permission from Reference 51. Copyright 2012 The Royal Society of Chemistry.

2.5.6 Holey Membranes

2.5.6.1 Poly(vinyl alcohol) (PVA)–Fe^{3+}/Citric Acid (CA)/Ethylene Glycol (EG) Calcination

Poly(vinyl alcohol) (PVA), containing a high density of hydroxyl functional groups available to complex ferric ions, was employed in a so-called "polymer precursor" (PP) method to produce porous iron oxide films.[52] The first step in the PVA-PP method involved the preparation of a viscous solution of Fe^{3+} ions complexed with PVA and the polyether produced *in situ* by the reaction of CA and EG. The solution was then spin-coated on a Pyrex® glass substrate before repeated calcination to decompose the PVA and yield a uniform

porous iron oxide film consisting of sintered 100 nm diameter ellipsoidal particles, with a micro-porosity volume (assessed by the N_2 adsorption isotherm method) increasing with the PVA/CA weight ratio. A change in crystal structure from α-Fe_2O_3 to γ-Fe_2O_3 was detected by PXRD and X-ray photoelectron spectroscopy (XPS) measurements when the PVA/CA ratio exceeded 1, which was interpreted as being due to the surface reduction of α-Fe_2O_3 into Fe_3O_4 crystals. The kinetic constant for this transformation was enhanced by a decrease in Gibbs energy for the reduction due to improved elimination of O_2 from the higher porosity films.

2.5.6.2 Loading of the Pores of a Nafion® Membrane Followed by Reduction

In comparison with commonly used methods like coprecipitation or thermal decomposition, fewer studies relied upon a reduction reaction. This route was selected by Yoon et al.[53] using a polymeric ion-exchange membrane to produce nanosized magnetic pristine iron particles. The method basically consisted in the diffusion of Fe^{3+} ions into a commercial porous perfluorinated sulfonate ionomer membrane, and the *in situ* reduction with $NaBH_4$ into magnetic Fe NPs. This led to the disappearance of the hysteresis loop at 120 K, corresponding to the T_B for very tiny Fe NPs, as well as ferromagnetism at 10 K and superparamagnetism at 200 K. The observation of 1.5–2.5 nm diameter spherical particles dispersed in a clear polymer background in the TEM images, combined with crystalline lattices revealed by EDS measurements, confirmed the single-domain structure of the iron NPs obtained.

2.5.7 Tridimensional Scaffolds (Macroscopic Samples)

In an encapsulation process, the strength of interactions between the anchoring moieties in a polymer matrix and the NPs is considered the most important criterion preventing the diffusion of the NPs out of the template and leading to successful directed nucleation and growth. One approach suggested to realize this condition was to rely on the large surface area and the complicated inner structure of polymer gel networks to perform the

in situ synthesis of MNPs. Tridimensional polymeric scaffolds containing further structural hierarchical microstructures offer great potential for size, shape, crystalline structure, and orientation control, and have consequently motivated a large number of studies.

2.5.7.1 Porous Preformed Carbon Foams (CF)

In an innovative study by Yoon et al.,[54] mesoporous CF produced by the resorcinol-formaldehyde method, with a very large pore volume (0.87 $cm^3 \cdot g^{-1}$) and specific surface area (834 $m^2 \cdot g^{-1}$) were loaded with a $Fe(NO_3)_3$ solution by repeated impregnation. After *in situ* thermal decomposition of the precursor at 450 °C under argon, Fe_3O_4 nanocrystals were obtained in the confined pores of the carbon template (Figure 2-28).

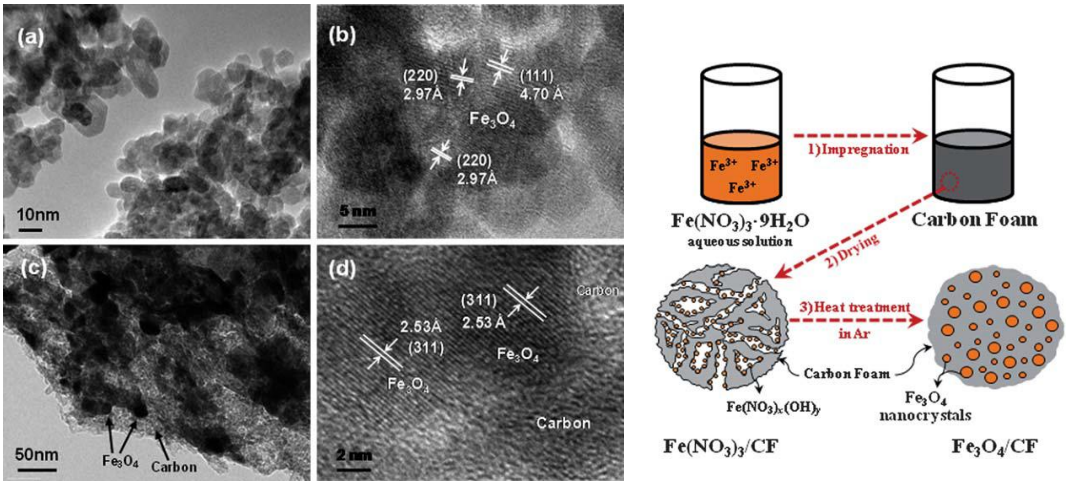

Figure 2-28. TEM images for unsupported Fe_3O_4 NPs synthesized by: (a, b) the hydrothermal method; (c, d) the *in situ* formation of Fe_3O_4 NPs on the CF composite; and (e) schematic representation of the *in situ* formation of Fe_3O_4 nanocrystals in the confined pores of carbon foam. Reprinted with permission from Reference 54. Copyright 2011 The Royal Society of Chemistry.

HRTEM images and XRD patterns confirmed the Fe_3O_4 composition of the crystals, which had a non-uniform size and shape distribution in the 5–50 nm range, i.e., larger and broader than the 7–15 mm particles obtained by the conventional (non-templated) polyol synthesis (same precursor but at 180 °C in EG). The width of the XRD peaks also yielded a significantly larger average crystallite size of 21.7 nm (as compared to 10.1 nm for the polyol pathway). Although physical adsorption was invoked rather than chemical interactions, due to the absence of coordinating functional groups, the roles of the carbon foam in orientating the growth of the iron oxide nanocrystals and preventing their agglomeration were clearly shown. When used as anode material for lithium-ion batteries, the as-prepared CF/Fe_3O_4 composites exhibited superior charge/discharge capacities as compared to the unsupported materials.

2.5.7.2 Sponge-Like Polystyrene/Polyacrylate Copolymer Gel

In their early work, the teams of Antonietti and Mann[55] successfully developed magnetic iron oxide nanocolloids using elastic sponge-like polystyrene–polyacrylate copolymer gels providing a mesoporous open-cell structure with carboxylic groups readily coordinating the metallic ions. The hierarchical structures of the microspherical pores, whose size could be further adjusted during the synthesis, offered enormous surface areas that effectively facilitated the templating and nucleation processes (allowing up to 20 wt% iron loading). It is worth noting that the gel structure was not changed after the loading step (Figure 2-29a). There were no crystalline structures in the air-dried composites, but rather amorphous hydrated Fe^{3+} oxide which gradually converted to 24 nm magnetic Fe_3O_4 crystals (based on wide-angle X-ray scattering (WAXS) line width analysis). These results were in agreement with the TEM analysis of gel sections showing homogeneous spherical and cubic particles with a mean size of 16.3 ± 9.4 nm trapped in the wall of the gels (Figure 2-29b). No hysteresis was reported in room temperature measurements, indicating superparamagnetism of the particles. This pioneering research using an easily tailored material was followed by many other studies on gel templates.

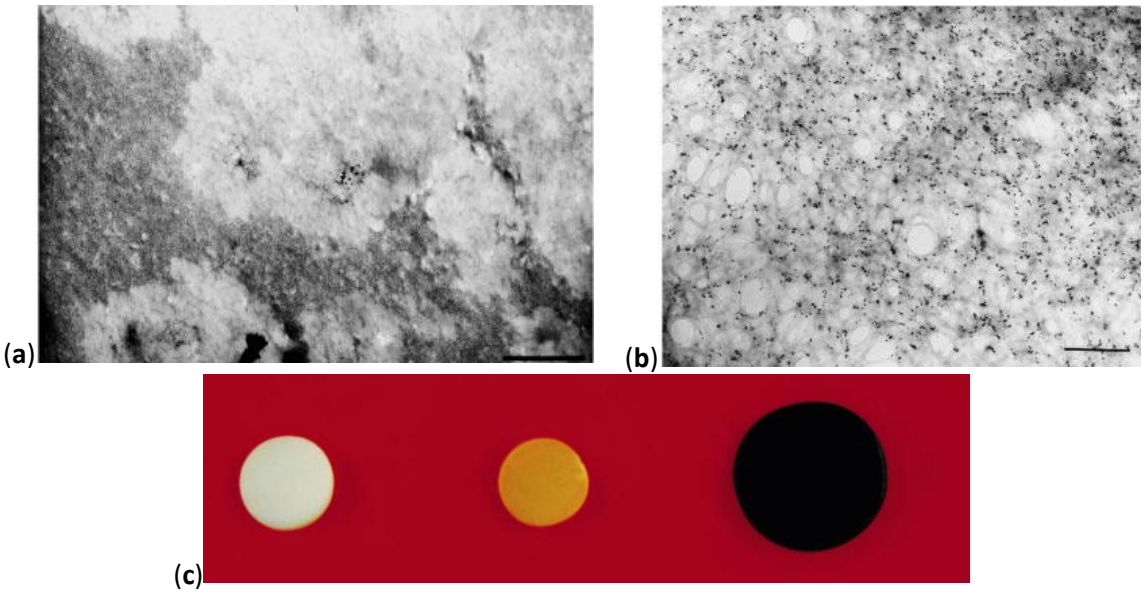

Figure 2-29. TEM images for sample sections: (a) 3.5 wt% Fe-loaded polystyrene–polyacrylate gel prior to reaction with NaOH (scale bar = 500 nm); (b) after reaction with NaOH, showing the distribution and uniformity of the magnetite nanocrystallites (scale bar = 500 nm); and (c) synthesis of the magnetic sponge-like copolymer gel. Comparison between an unloaded polymer gel (c, left), after exposure to a 0.2 M Fe^{2+} solution (c, middle), and after reaction with NaOH (c, right). The gels imaged with a digital camera in (c) were in the swollen state. Reprinted with permission from Reference 55. Copyright 1998 WILEY-VCH Verlag GmbH.

2.5.7.3 Cross-Linked Poly[styrene-*co*-(*N*-4-carboxybutylmaleimide)] Copolymer

Taking advantage of the facile polymerization of styrene and maleimide-based monomers, cross-linked networks were created from poly[styrene-*co*-(*N*-4-carboxybutylmaleimide)] copolymers poly(St-*co*-CBMi) in which CBMi acts as a metal-anchoring moiety. This copolymer was successfully prepared and used for the *in situ* synthesis of IONPs by deposition of Fe^{2+} and multi-step NaOH treatment.[56] The data

obtained from XRD analysis after two particle deposition cycles revealed the initial existence of maghemite (γ-Fe_2O_3) NPs, which were gradually transformed to goethite (α-FeOOH). This was likely not due to oxidation as ascribed by the authors, but rather a result of the unavoidable pH increase in such a multi-step NaOH treatment. The constant value of mean particle size (14 nm) calculated from the Scherrer equation and XRD diffractograms after several deposition cycles indicates that growth of the particles was inhibited by the constrained architecture of the polymer network. The maghemite content increased after each loading cycle, but the fourth cycle led to agglomeration. The magnetization of the hybrids also increased after each loading cycle but was maximized after the third one (8.04 emu/g). There was no subsequent change in M_s due to the appearance of the goethite crystals, that are known to be antiferromagnetic. The non-zero H_c values observed for the hybrids, even at room temperature, were assigned to the same reason, i.e., mixing of the two phases giving rise to spontaneous ferrimagnetism.

2.5.7.4 Semi-Interpenetrating (Semi-IPN) Polymer Networks of Alginate (Alg) and Poly(*N*-isopropylacrylamide) (PNIPAM)

In an attempt to synthesize IONPs within networks of mixed polymer hydrogels, Hernández et al.[57] initially prepared semi-IPN polymer networks from alginate bringing chelating carboxylate groups, and PNIPAM providing thermosensitivity to these materials. Cylindrical samples cut from the semi-IPN were submerged into a 1:2 solution of Fe^{2+} and Fe^{3+} ions, and then into a NH_3 solution for the *in situ* preparation of semi-IPN ferrogels. For samples with different numbers of alkaline bath treatments, the phase type of the IONPs within the gels was determined to be a combination of magnetite and maghemite, based on the diffraction patterns in wide angle X-ray analysis and characteristic peaks in Raman spectroscopy. The diameters calculated from the Debye-Scherrer equation for the (311) Bragg peak suggested larger sizes for the NPs seeded in the polymer networks (respectively D_{311} = 10.1 ± 2.5 nm and D_{311} = 11.2 ± 2.8 nm for one and two alkaline treatments) as compared to D_{311} = 6.7 ± 1.6 nm for NPs created in an alginate solution.

2.5.7.5 Cross-Linked Polyacrylamide (PAAm) Hydrogels

To prepare water-dispersible magnetite NPs, Xiong and Sun applied an *in situ* synthesis approach involving cross-linked PAAm hydrogels and NaOH solution treatments. As shown in Figure 2-30a, the PAAm hydrogel was photopolymerized with pentaerythritol triacrylate (PE-3A) as a hydrolysable cross-linker, and BDMBP as photoinitiator.[58] The polymer network was expected to act as a template possessing both sufficient capacity for ion impregnation and a restrained mesh structure limiting the growth of MNPs and preventing their aggregation.

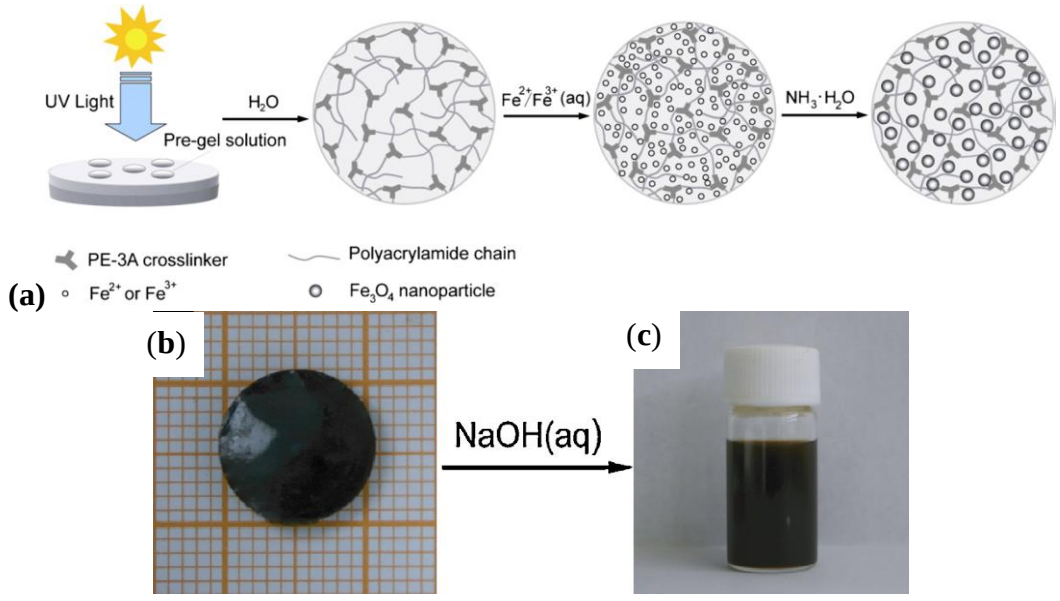

Figure 2-30. (a) Schematic representation and (b) appearance of a magnetic hybrid hydrogel obtained by photopolymerization and *in situ* coprecipitation; (c) in the second step, the ferrogel was exposed to NaOH to hydrolyze the cross-link points and induce the release of water-dispersible IONPs. Adapted with permission from Reference 58. Copyright 2011 Elsevier B.V.

Magnetite NPs with narrow size distributions were obtained by this method, as seen on Figure 2-31, with a size inversely related to the cross-linker density (8.3 nm for 0.46 mol% PE-3A, 6.3 nm for 6.14 mol%). In a second step, the hydrolysis of the acrylic ester cross-linker PE-3A in alkaline water liberated well-dispersed hydrophilic MNPs (Figure 2-30c). Interestingly, XPS results showed the existence of a thin layer of polymer chains bearing carboxylate and acrylamide groups covering the surface of these NPs, which explains their long term stability in water. Hysteresis and H_c were observed at 5 K, indicating ferromagnetism, but the particles were superparamagnetic at 300 K with negligible H_c. The saturated magnetization was 44.6 emu/g at 300K.

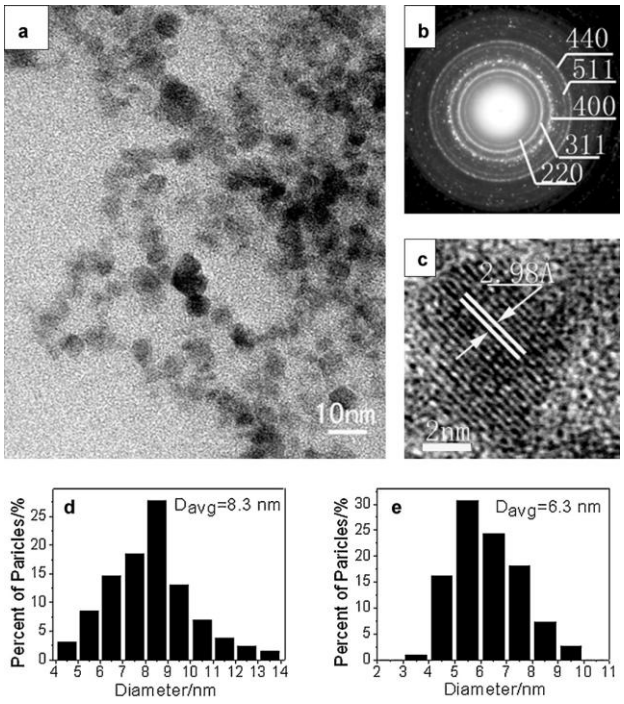

Figure 2-31. (a) TEM image and (b) SAED pattern for magnetic Fe_3O_4 NPs synthesized by the coprecipitation of iron salts within a polymer disk; (c) typical HRTEM image for a single Fe_3O_4 NP, and size distribution of the Fe_3O_4 NPs for samples containing the cross-linker at: (d) 0.46 mol% and (e) 6.14 mol%. Reprinted with permission from Reference 58. Copyright 2011 Elsevier B.V.

2.5.7.6 Poly(2-Acrylamido-2-methyl-1-propansulfonic Acid) (PAMPS) and P4VP-Based Hydrogels

Hydrogels prepared by radical copolymerization, either with a photoinitiator for PAMPS,[59] or a redox (persulfate) initiator for poly(4-vinyl pyridine) (P4VP) and poly(4-vinyl pyridine-*co*-2-hydroxyethyl metacrylate) (P4VP-*co*-HEMA),[60] were impregnated with $FeSO_4$ and $FeCl_3$ and employed in a coprecipitation reaction to create magnetic composite hydrogels. These hydrogels, designed for water remediation, absorbed toxic heavy metal ions efficiently in aqueous media. Unfortunately, no information was provided on the size and the morphology of the magnetic particles obtained.

2.5.7.7 Polyacrylamide (PAAm) Hydrogels

Polyacrylamide (PAAm) hydrogels were employed as templates for the coprecipitation of Fe^{2+} and Fe^{3+} to create pH-responsive magnetic hydrogels.[61] The magnetite particles obtained were 3–5 nm in size and homogeneously distributed inside the hydrogel network (Figure 2-32).

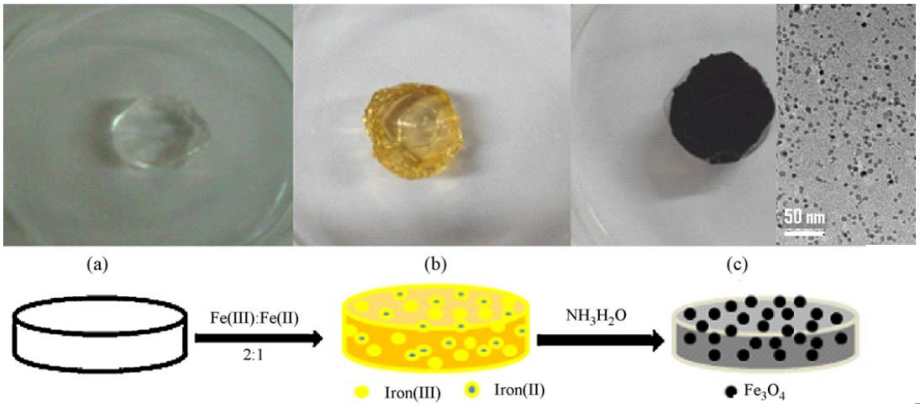

Figure 2-32. Schematic views and pictures of polyacrylamide (PAAm) hydrogel networks at three steps of loading with magnetite NPs: (a) swollen hydrogel; (b) iron ion-loaded hydrogel; and (c) magnetite NPs in the hydrogel matrix, inset: TEM image showing well-dispersed MNPs of uniform size. Reprinted with permission from Reference 61. Copyright 2009 Elsevier B.V.

The density of Fe_3O_4 particles increased for higher iron ion feeds (from 25 wt% to 100 wt% relatively to PAAm), indicating the good loading capacity of the template. Despite a low M_s value of 4 emu/g, ascribed to the small size of the MNPs and the large weight fraction of polymer matrix, the composite exhibited superparamagnetism with a small H_c of 14.8 Oe.

2.5.8 Dispersed Colloids (Microscopic)

2.5.8.1 Poly(*N*-isopropylacrylamide-*co*-acrylic acid-*co*-2-hydroxyethyl acrylate) (Poly(NIPAM-*co*-AA-*co*-HEA)) Microgels Cross-Linked with *N,N′*-Methylenebis(acrylamide) (BIS)

Sub-micrometer gels of poly(NIPAM-*co*-AA-*co*-HEA), prepared by suspension polymerization and cross-linked with BIS, were loaded with ferrous iron ions in an ion exchange process (with the ions in the interior of microgels).[62] A post-loading oxidation step with H_2O_2 was used to produce the IONPs (Figure 2-33a). The size of these microgels was successfully controlled by the polymerization conditions: A rise in pH from 2.3 to 9.2 transformed the PAA blocks from a highly compact and weakly hydrophobic conformation to a highly hydrophilic and expanded coil, and greatly increased the repulsive forces between COO^- groups, leading to larger particle sizes (from 200 to 600 nm). Not surprisingly, the concentration of COOH functionalities in the copolymer was the dominant parameter affecting the size and the loading capacity of the microgels. However the Fe^{2+} precursor concentration and the pH value range useable for the reactions were limited by the solubility product of $Fe(OH)_2$ ($K_s = 4.87 \times 10^{-17}$): For instance, the maximum allowable pH value was 7.1 for $[Fe^{2+}] = 1.5$ mM. Interestingly, the size distribution of the NPs obtained was relatively narrow (e.g., 8.5 ± 1.0 nm diameter by TEM). These Fe_3O_4 NPs trapped in the 500 nm diameter microgels exhibited superparamagnetic properties at 300 K (both the remnant field and the H_c were zero) with a specific M_s of 32.4 emu/g (Figure 2-33b).

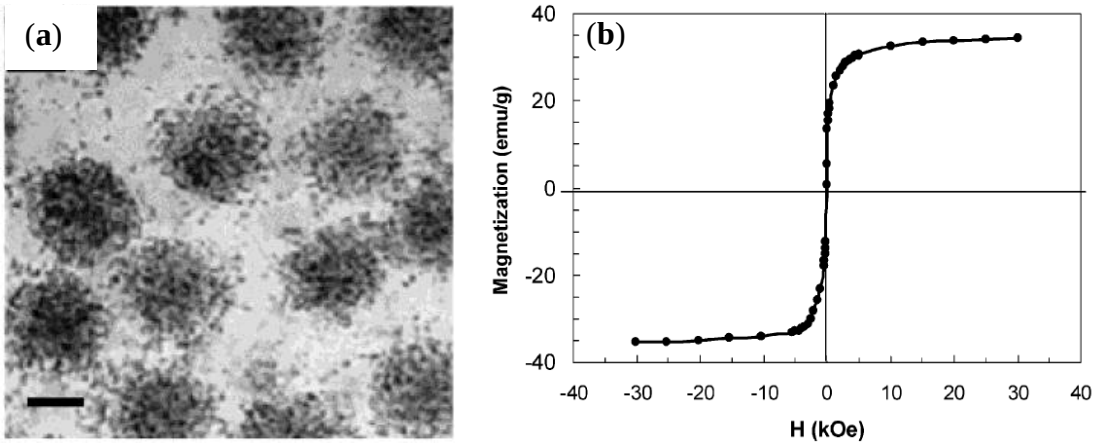

Figure 2-33. (a) TEM image for hybrid poly(*N*-isopropylacrylamide-*co*-acrylic acid-*co*-2-hydroxyethyl acrylate) (poly(NIPAM-*co*-AA-*co*-HEA)) microgels loaded with 0.618 g Fe_3O_4/g polymer; the scale bar is 150 nm; and (b) magnetization curve at 300 K. Reprinted with permission from Reference 62. Copyright 2004 American Chemical Society.

2.5.8.2 Poly(*N*-vinylcaprolactam-*co*-acetoacetoxyethyl methacrylate) P(VCL-*co*-AAEM) Microgels

An interesting characteristic of this system is that the chemical composition of the microgels could be adjusted to provide additional properties to the MNPs. One example of this is the work of Pich et al.,[63] who successfully employed microgels obtained by the copolymerization of AAEM and VCL to synthesize thermosensitive magnetic hybrids (Figure 2-34). It is common knowledge that thermoresponsive polymers such as PVCL can extensively and reversibly swell in appropriate solvents at temperatures below the LCST, but shrink rapidly above the LCST. The PVCL-rich shell of the microgels, exhibiting an LCST, offers the possibility to control their size through temperature changes, while the AAEM-rich portions provide a high iron-loading capacity via bidendate coordination.

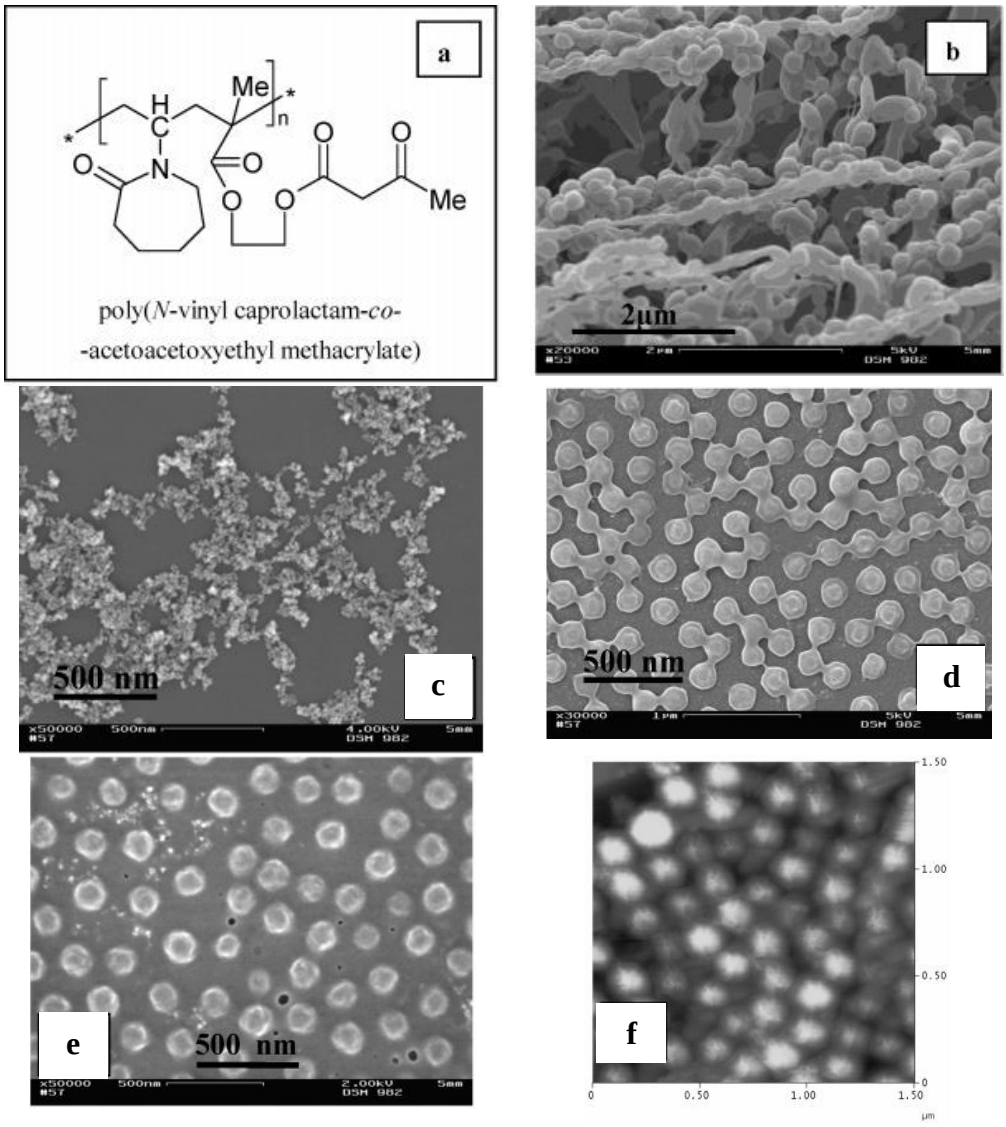

Figure 2-34. (a) Chemical structure of a poly(*N*-vinylcaprolactam/acetoacetoxyethyl methacrylate) copolymer; and SEM images for: (b) empty cross-linked microgels; (c) magnetite NPs; (d) composite microgels with 4% magnetite; (e) SEM; and (f) AFM images for microgels with 9.4% magnetite (the height scale of the AFM image in the height mode is 0–100 nm.) Reprinted with permission from Reference 63. Copyright 2004 American Chemical Society.

The observed non-monotonic increase in R_h of the microgels for increasing magnetite loadings was explained in terms of the chemical interactions formed. The slight decrease in R_h observed when increasing the Fe_3O_4 loading from 0 to 7 wt% was attributed to multivalent complexation between the β-diketone groups of AAEM and the $Fe^{2+/3+}$ ions linking simultaneously several AAEM units, thus leading to additional cross-linking and shrinkage of the microgels. When the loading level surpassed 7 wt%, repulsive forces among the crowded Fe_3O_4 particles led to swelling of the microgels (increase in hydrodynamic size). An increase in magnetite content (e.g., from 4 to 9.4%), leading to larger magnetite-filled microgel cores, also affected the colloidal stability of the microgels in suspension as measured by their sedimentation velocity. Superparamagnetism was reported, with plateau values of the magnetization curve corresponding to 75 emu/g Fe_3O_4. The variation in the magnetic core size vs. magnetite-to-polymer content in the hybrid microgels was not investigated in this study.

2.5.8.3 Sulfonated Copolymer Beads

Polymer beads produced by the suspension copolymerization of styrene and a small amount of divinylbenzene were sulfonated to add complexing moieties to the polymer chains and facilitate the encapsulation of Fe^{3+} and Co^{2+} cations for the synthesis of MNPs *in situ*.[64] The presence of a $CoFe_2O_4$ spinel phase was confirmed from its characteristic XRD peaks. TEM images obtained from ground powder displayed 7 nm, nearly spherical particles well-distributed within the polymer matrix. The absence of hysteresis, remanence and H_c demonstrated the superparamagnetic character of these hybrids, the saturated magnetization being also low (0.818 emu/g) due to the low content of magnetic material in the beads.

2.5.8.4 Poly[poly(ethylene glycol diacrylate-*co*-acrylic acid) (PEGDA-co-PAA) Copolymer Hydrogels Prepared by Microfluidics

Janus particles, combining two distinct materials on the opposite sides of the NP, were designed in the groups of Doyle and Hatton to work as selective nanoreactors for the *in situ* synthesis of magnetic species.[65] Figure 2-35 shows the Janus-like and other non-spherical hydrogel magnetic particles prepared by stop-flow lithography (SFL), with one part

of PEG diacrylate (PEGDA) non-interacting with iron salts, and another part constituted of a copolymer of PEGDA and acrylic acid (AA) to coordinate the iron ions. Since the polymerization was initiated by a photosensitive radical initiator, the shape of the hydrogels could be varied at will (e.g., disks, triangles, etc.) by an appropriate mask shaping the UV beam illuminating the reactants in a Y-shaped laminar flow chamber (Figure 2-36). Then the transfer of the gels into an alkaline solution converted the COOH groups into COO^- and induced swelling due to electrostatic repulsion between the anionic carboxylate groups. Interestingly, the Fe^{3+}/Fe^{2+} feed ratio used (1:75) was much lower than the required 2:1 stoichiometric ratio, due to the different adsorption affinities of these two ions toward COO^-. The iron content of the particles was increased by repetition of the loading process, which allowed the adsorption of more ions at unoccupied nucleation sites and/or the surface of the magnetic particles, leading to larger, visibly darker and more magnetic particles.

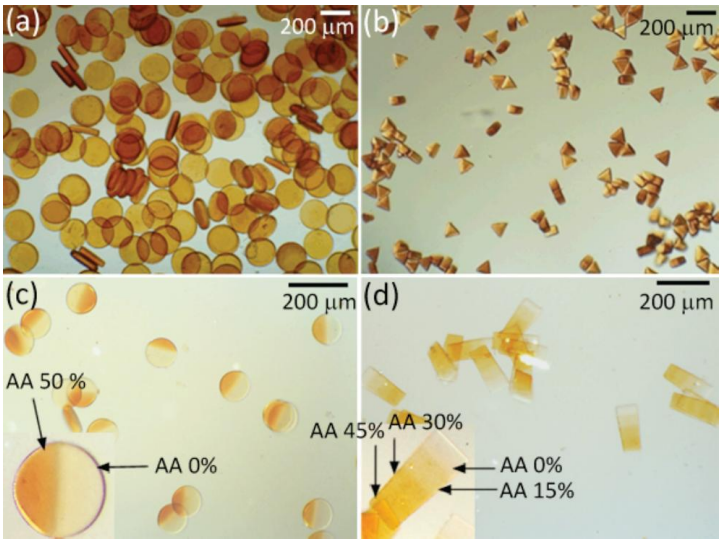

Figure 2-35. Optical images for various magnetic microparticles: (a) homogenous magnetic disks; (b) homogenous triangular particles; (c) Janus disks; and (d) gradient particles. Reprinted with permission from Reference 65. Copyright 2012 American Chemical Society.

The hydrogel particles obtained after eight loading cycles reached a M_s value of 42 emu/g. It is worth noting that the maximum magnetic domain diameter reported was 5.7 nm (but with a high σ of 0.3–0.4), which was considered to be limited by the swollen mesh size of the polymer network. This suggests partial size control for the MNPs synthesized *in situ* in such a hydrogel scaffold.

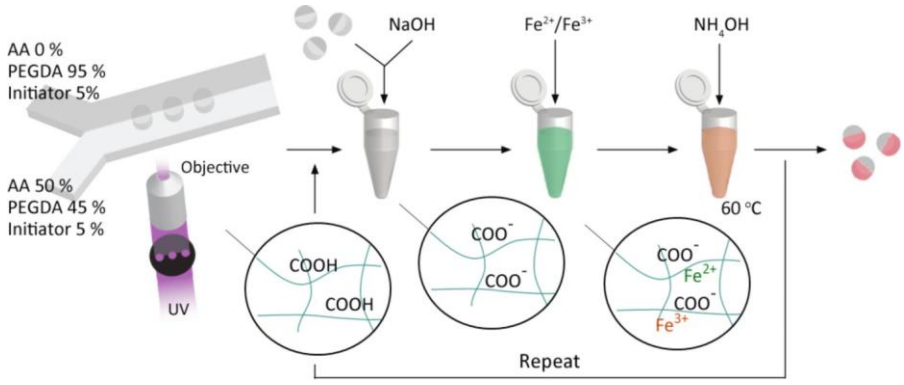

Figure 2-36. Coprecipitation process in photopolymerized microgels with ~ 20 µm diameter prepared in a microfluidic channel. After deprotonation in 0.5 M NaOH and rinsing with 0.5% Tween 20 to reach pH 7, 0.2 M $FeCl_3$ and 1 M $FeCl_2$ solutions were mixed with the microgels at a Fe^{3+}:Fe^{2+} ratio of 1:75. After diffusion of the iron ions in the polymer particles, excess salts were removed. After the addition of NH_4OH at 60 °C, the MNPs were nucleated and grown *in situ* before a final rinse with Tween 20. All these steps were repeated several times for successive growth cycles. Reprinted with permission from Reference 65. Copyright 2012 American Chemical Society.

2.5.8.5 Multi-Responsive Microgels Made from Copolymers of *N*-Vinylcaprolactam (VCL), Acetoacetoxyethyl Methacrylate (AAEM) and Vinylimidazole (VIm)

The wide range of polymeric materials available in terms of number and structural variety, but also in terms of physical and chemical characteristics, have inspired many researchers to look for novel materials combining different properties. To prepare "multi-

stimuli-responsive" magnetic hybrid microgel particles, Bhattacharya et al. thus performed coprecipitation reactions of iron ions in the presence of microgels obtained by the batch copolymerization of *N*-vinylcaprolactam (VCL), acetoacetoxyethyl (AAEM), and vinylimidazole (VIm) cross-linked with *N*,*N*′-methylene bisacrylamide (BIS) (Figure 2-37).[66]

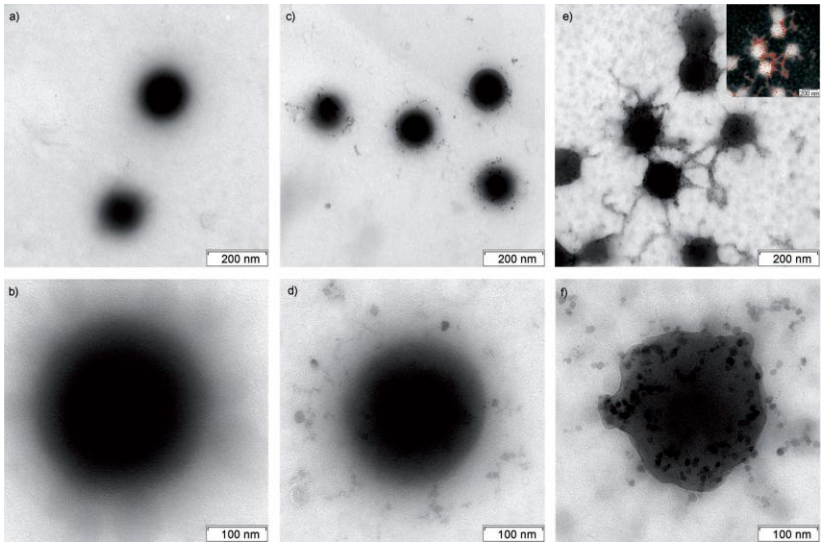

Figure 2-37. TEM images for microgels with different magnetite contents: (a, b) no magnetite; (c, d) 8.4 wt%; (e, f) 15.4 wt%. Inset: EDX iron-mapping image. Reprinted with permission from Reference 66. Copyright 2007 Wiley-VCH Verlag GmbH & Co., Weinheim.

The poly(VCL-*co*-AAEM-*co*-VIm) hybrid microgels were expected to exhibit thermosensitivity brought by the VCL units, pH responsiveness ascribed to the AAEM-rich core, and magnetic switchable properties owning to the encapsulated iron oxide particles. Unfortunately, the concentration of VIm units in the copolymer was found to strongly influence the swelling behavior and the transition temperature of the hydrogels. Shrinkage of the hybrid particles was also observed at higher magnetite contents (which led to partial collapse of the network in some cases), in agreement with a previous study.[63] The magnetite

particles had a diameter of ca. 10 nm determined from the TEM images (Figure 2-37). The highest M_s measured was 30 emu/g for the highest loading obtained of 15.4 wt% magnetite. Evidence for pH responsiveness and temperature-sensitive properties was shown for the hybrids, indicating the success of monomer blending to obtain copolymer microgels with combined characteristics and the creation of multifunctional materials.

2.5.9 Preformed Microspheres in Organic Solvents

2.5.9.1 Polystyrene (PS) Microspheres Swollen in $CHCl_3$

Interestingly, even water-insoluble cross-linked polystyrene (PS) microspheres were found to be capable of serving as hosts for the thermal decomposition of encapsulated ferric trioleate, after swelling of the microspheres in an organic solvent ($CHCl_3$) to facilitate the impregnation.[67] The magnetic character of the NPs thus obtained strongly depended on the decomposition temperature used, since the dissociation of the $Fe(oleate)_3$ complex only started around 200–240 °C but was completed at 300 °C, while crystal growth only took place above 310 °C and led to strong magnetism. TGA results showed that decomposition of the polymer matrix occurred between 380 and 450 °C, yielding an inorganic content of 15.9 wt% for the composite spheres. SEM and TEM images (Figure 2-38) revealed nearly spherical IONPs with a mean diameter of 11 nm and a low size dispersity (21% standard deviation), distributed uniformly within the network serving as template, by allowing nucleation but inhibiting the overgrowth of NPs. XRD analysis confirmed the Fe_3O_4 composition of the iron oxide. The particles exhibited superparamagnetic characteristics at room temperature (M_s = 12.6 emu/g and T_B = 171 K), with excellent magnetic responsiveness but readily redispersing after removal of the magnetic field.

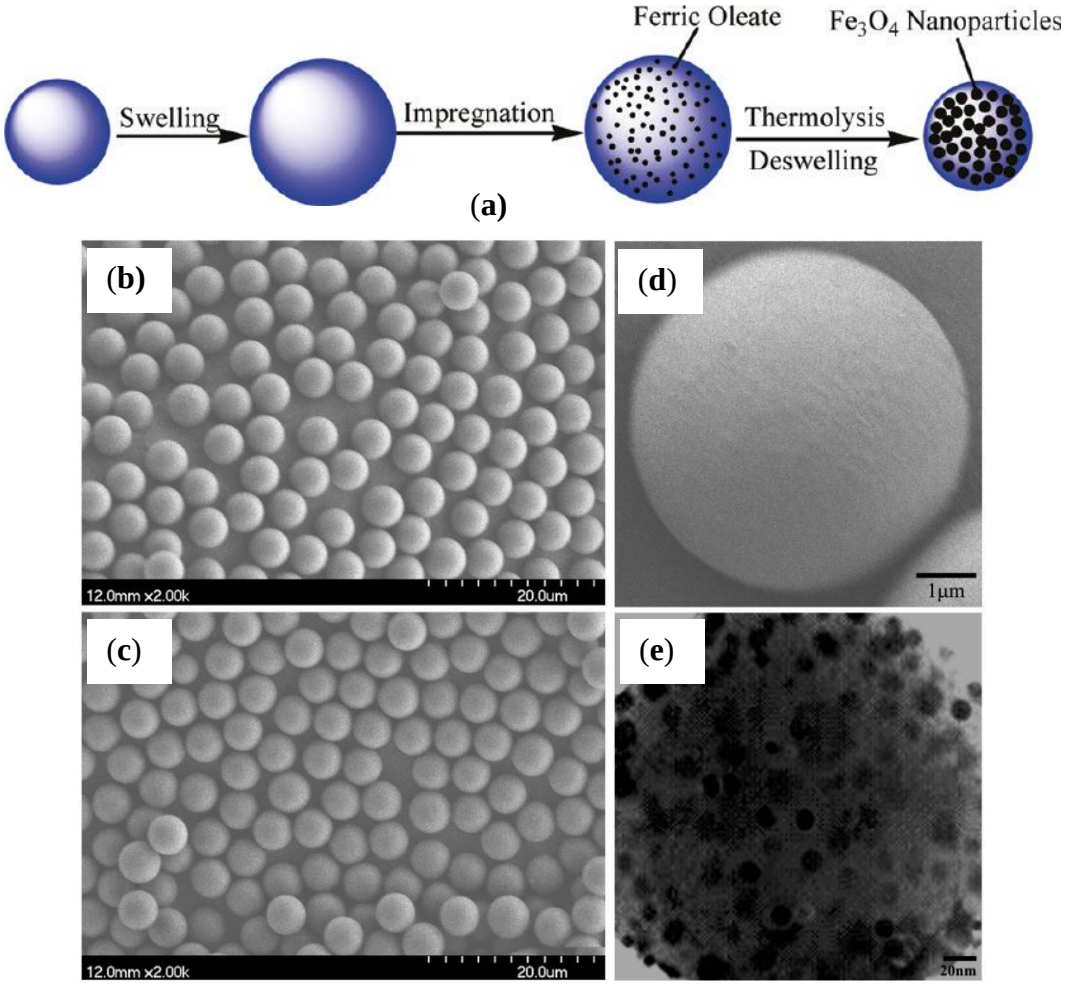

Figure 2-38. (a) Schematic representation of the preparation of Fe_3O_4 NPs embedded in PS microspheres by thermal decomposition of $Fe(oleate)_3$ at 300 °C; SEM images for: (b) the polymer seed microspheres prepared by dispersion polymerization; (c) the magnetic polymer microspheres prepared by swelling and thermolysis; (d) the outer surface of magnetic polymer microspheres; and (e) TEM image for the ultramicrotomed magnetic polymer microspheres, showing the location of the IONPs in the microspheres. Reprinted with permission from Reference 67. Copyright 2009 American Chemical Society.

2.6 Conclusions

In recent years, multiple routes have been explored for the synthesis of IONPs. This includes the alkaline coprecipitation of ferric and ferrous salts, the oxidation of $FeSO_4$, the thermal decomposition of iron complexes, the polyol route, and hydrothermal processes in various organic templates, as summarized in Table 2-5. One feature common to all the systems explored so far is the ability of one of the components used to interact with the iron oxide precursor, most often through coordination with the iron ions. A number of the *in situ* syntheses did not give results significantly different from bulk synthesis methods, as these were realized under similar physicochemical conditions (pH, temperature, etc.). For instance, syntheses by alkaline coprecipitation leading to IONPs with rock-like shapes and a broad diameter distribution around 7 nm do not make a strong case for a true templating effect by the organic matrix. In contrast, several investigation listed in this review (in particular those using well-defined polymer structures) highlighted a significant influence of the polymer/precursor ratio on the outcome of the synthesis. This is the case, for instance, for tridimensional networks such as hydrogels, for which the importance of mesh size was recognized as a parameter limiting the diameter of the MNPs grown *in situ*. It was also demonstrated on several occasions that strong ligands (such as phosphate groups) directed the synthesis towards smaller particle sizes, which seems to be a general well-known trend in coordination chemistry that can be ascribed to hampering of ion diffusion through the ligand shell during the growth of nanocrystals. On the contrary, other studies reported MNP diameters that increased from 10 to 20 nm with the template. This is the case for chemical reactions performed at high temperatures, were an important property required from the organic template is to prevent the aggregation of the growing nanocrystals. This protecting effect was observed in particular in the last study reported, where a polystyrene matrix could withstand temperatures as high as 310 °C necessary for the thermal decomposition of iron oleate.

Table 2-5. Summary of the different organic templates used as host matrices for the synthesis of MNPs. In this review, the examples gathered from the literature were sorted according to their chemical nature and structural properties (e.g., geometry, dimensionality, size). DEX: dextran; Alg: alginate; PNIPAM: poly(*N*-isopropylacrylamide); PVA: poly(vinyl alcohol); PVP: polyvinylpyrrolidone; P4VP: poly(4-vinylpyridine); PMGI: poly(methyl glutarimide); DHBC: double-hydrophilic block copolymer; PGA: poly(glycerol acrylate); PAsp: poly(aspartic acid); PAEMA: poly[2-(acetoacetoxy) ethyl] methacrylate; PGMA: poly(glycerol methacrylate); PDMAEMA: poly[(*N*,*N*-dimethylamino)ethyl methacrylate] PNOR: polynorbornene; PAMPS: poly(2-acrylamido-2-methyl-1-propansulfonic acid).

Surfactants: $–COO^-$, $–SO_3^-$, $–SO_4^-$ **Natural polysaccharides**: DEX, DEX sulfate, Alg, DEX-*b*-PMAA-*b*- PNIPAM	**Synthetic linear polymers**: PVA, PVP, P4VP, PEO, PAA, PMAA, PMGI **Linear DHBC or amphiphilic copolymers**	**Hydrophilic blocks**: iron-complexing (PGMA, PGA, P(norbornene-methanol or di-carboxy), PMAA, PAA, PAsp, PAEA, PAEMA) or repulsive block (PEO, PEOGMA, PDMAEMA)	**Hydrophobic blocks**: PMMA, PNOR, PVBP **Tri-blocks**: Pluronics®, PI-*b*-PCEMA-*b*-PtBA
Three-dimensional scaffold macroscopic matrices: Carbon foam, sponge-like PS-*co*-PAA, P(S-*co*-CBMi) networks, Alg/PNIPAM semi-IPN, PAAm, PAMPS, P(4VP-*co*-HEMA) hydrogels	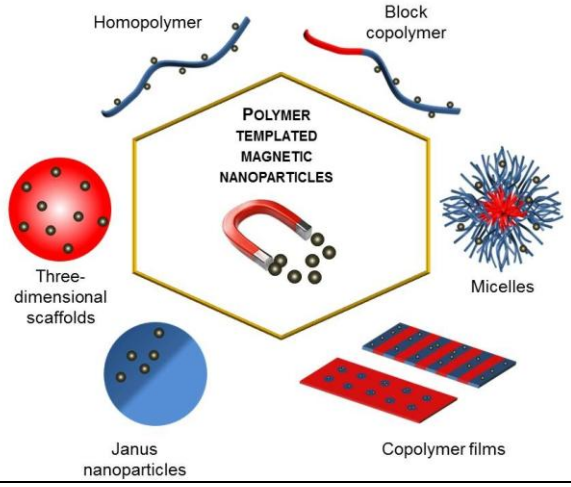		**Star-like** (PPO-*b*-PAA, PEO-*b*-PS) **Comb-like** (PPEGMEA-*g*-PMAA, PEO-*g*-PAA) **Spherical micelles** (PS-*b*-P2VP) **Cylindrical multimolecular/ unimolecular micelles**
Dispersed colloids: microgels, hydrophobic PS microbeads	**Janus, gradient or triangle**: PEGDA, PVCL-*co*-AAEM core-VIm shell microgels	**Lamellar** or **hexagonally ordered cylinders** (PS-*b*-P2VP, PS-*b*-PEO) **Membranes** (PVA, Nafion®)	**Microemulsions**: hexane/Triton®-X/Chitosan, CTAB

Regarding shape control, several studies claimed success of the organic templating method to orient the synthesis towards rod-like NPs. However, caution should be used in that the physicochemical conditions used may themselves favor the precipitation of antiferromagnetic ferrihydrite phases such as goethite or akaganeite. A more convincing case of needle-like cobalt ferrite microparticle formation was reported for a microemulsion process, based on the oriented aggregation of nanocrystals. One interesting aspect that can be brought by polymer-templated synthesis is the ability to prepare NPs with highly magnetic properties (useful for MRI contrast or magnetic hyperthermia) directly covered by a polymer shell, providing colloidal stability and stealth properties in biological media. This was achieved in several investigations by employing either double-hydrophilic or amphiphilic copolymers, in particular those forming micelles with a dense core strongly binding to the precursor species and a shell with multiple hydrophilic arms providing steric repulsion.

In all these studies, both with macroscopic matrices and individually dispersed objects, loading of the inorganic precursor into the adsorption sites was critical and needed to be optimized (by an iterative process or by the careful removal of excess $Fe^{2+/3+}$ ions) to achieve a true templating effect.

Chapter 3 Polyion Complex Micelles Synthesis from Arborescent Polymers

Chapter 3

3.1 Overview

This Chapter focuses on the preparation of water-dispersible polyion complex micelles from a G1 arborescent copolymer, G0 polystyrene-*graft*-poly(2-vinylpyridine) or G0PS-*g*-P2VP. Poly(acrylic acid)-*block*-poly(2-hydroxyethyl acrylate) (PAA-*b*-PHEA) double-hydrophilic block copolymers (DHBCs) were employed as polymeric stabilizers in this process, whereby electrostatic interactions between the PAA and P2VP segments were used to couple the block copolymer chains with the arborescent substrate while the PHEA tails provided a stabilizing shell. Four PAA-*b*-PHEA copolymers with tailored chain lengths were prepared by atom transfer radical polymerization (ATRP), by producing successively a poly(*tert*-butyl acrylate) macroinitiator and the corresponding poly(2-trimethylsilyloxyethyl acrylate) block copolymer, followed by deprotection of both blocks. The hydrodynamic radius, size distribution and zeta potential of the micelles obtained by the polyion complex (PIC) process were monitored by the dynamic light scattering (DLS) technique, whilst the absolute molar mass, radius of gyration and second virial coefficient of the micelles were extracted from multi-angle laser light scattering (MALLS) data. Tuning the length of the copolymer blocks and varying the amount used with respect to the arborescent substrate provided control over the size and the structure of the PIC micelles obtained, from large flocculated species to stable unimolecular PIC micelles with diameters ranging from 42 to 67 nm. Higher stability was observed when decreasing the length of the PAA block from 27 to 13 units at a constant PHEA block length of ca. 50 units, presumably due to increased packing density of the block copolymers at the surface of the PIC micelles. However stabilization was most effective when the PHEA chain length reached 150 and 260 units, even when using lesser amounts of stabilizer in comparison to the copolymers with shorter PHEA blocks. Changes in morphology of the arborescent copolymer before and after complexation were observed by atomic force microscopy (AFM), especially when varying the force applied with the AFM tip on the samples.

Chapter 3

3.2 Introduction

Colloidal dispersions are ubiquitous in our everyday lives, from polymer latexes in paints and plastics, through agricultural emulsions and dispersions, to blood and other biological fluids.[1] In biomedical applications, colloidal stability is of critical importance to ensure the safety and efficacy of nanoscale products,[2] since particles larger than 5 μm can cause capillary blockage and embolism.[3] Modification of the surface of nanoparticles by self-assembly or complexation with a copolymer is a technique commonly applied to the delivery of DNA (gene therapy)[4-7] and oligonucleotides (anti-sense therapy),[4,6] dendrimer porphyrins (photodynamic therapy),[8-11] drugs[12-13] and other types of hydrophobic nanomaterials,[14-16] by protecting (shielding) specific functions within the micellar core. Recently reported approaches to bind copolymers onto the surface of particles and improve the stability of colloidal dispersions will be first considered. This will be followed by a discussion of the polyion complexation process, particularly for materials incorporating polyvinylpyridine (PVP), in both organic solvents and aqueous dispersions. Finally, the types of interactions imparting stability in the complexation process, and control over the complexation parameters in relation to the structure of the PIC micelles obtained will be addressed.

3.2.1 Colloidal Stability

Van der Waals (VDW) interactions are considered the main driving force inducing instability in particle dispersions.[1,17-18] The magnitude of the attraction force (V_A) between two core–shell particles approaching each other (Figure 3-1) is given by[1,19]

$$V_A = -\frac{A^* \alpha}{12\, H_\circ}$$

where A^* is the effective Hamaker constant, α the radius of the core, and H_o is the minimum distance of approach between the surface of the cores.

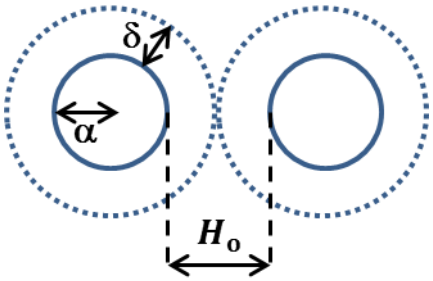

Figure 3-1. Schematic representation of the approach of two sterically stabilized particles. The parameter δ represents the thickness of the solvophilic protective polymer layer forming the shell. Reprinted with permission from Reference 1. Copyright 1983 Academic Press.

Taking two sterically stabilized polystyrene (PS) latex particles ($A^* = 5\times10^{-21}$ J or 1.2 *kT*) as an example, the magnitude of the VDW forces calculated when the particles just touch ($H_o = 2\delta$) reflects the stability of the dispersion. If V_A is larger than *kT* flocculation occurs despite the existence of the polymer coating, as seen for large cores stabilized by a low $\bar{M}_w$ polymer (Table 3-1). Increasing the $\bar{M}_w$ of the stabilizing polymer efficiently reduces the magnitude of the VDW forces relatively to *kT* and thus imparts stability to the dispersed phase. In our work, the particle core is an arborescent PS substrate grafted with P2VP chains (likewise mostly hydrophobic in their neutral state). Given the small diameter of the G1 substrate (below 50 nm), this calculation suggests that even a polymer with $\bar{M}_w = 2500$ g/mol may suffice to stabilize this system (V_A is just 0.5 *kT* and the layer thickness is slightly larger than the VDW effective radius of 5 nm). However a minimum value of $\bar{M}_w$ for stabilizers of 10,000 g/mol was suggested to ensure good colloidal stability.[1]

There are limited options available to stabilize colloidal dispersions, which are mainly electrostatic stabilization and polymer (steric) stabilization. Electrostatic stabilization tends to be problematic since the thickness of the electrical double layers is very sensitive to the ionic strength and the dielectric constant of the dispersion medium. The thickness of the double layer typically exceeds the effective range of VDW attraction (5–10 nm) in water at low ionic strengths ($I < 1$ mM), but it shrinks to less than 1 nm in a 0.1 M ionic strength environment.[1]

Electrostatic repulsions thus become insufficient to outweigh VDW attractions under these conditions. For that reason, polymeric stabilization (also referred to as steric stabilization), or a combination of steric and electrostatic (electrosteric) stabilization, have been more frequently employed to achieve the colloidal stability of dispersions in the literature and will be thus preferred in this work.

Table 3-1. Theoretical estimates of van der Waals attraction between sterically stabilized particles (conditions leading to dispersion instability are bolded). Adapted with permission from Reference 1. Copyright 1983 Academic Press.

$\bar{M}_w$ **of stabilizer (g/mol)**	**Layer thickness* (nm)**	$\lvert V_A \rvert$ **(*kT*) between particles with**	
		Core radius = 50 nm	Core radius = 200 nm
600	2.5	1	**4**
2500	5	0.5	**2**
10000	10	0.25	1
63000	25	0.1	0.4

* The steric layer thickness was calculated based on the molar mass of the polymer as $\delta \sim \alpha f l \left(\frac{2\overline{M_w}}{M_o} C_\infty\right)^{1/2} \sim 0.1 \times \overline{M_w}^{1/2}$ with the intramolecular expansion factor α = 1.3; the expansion factor for chains normal to the interface f = 1.3; bond length l = 0.15 nm; polymer limiting characteristic ratio C_∞ = 7, and molar mass of the repeating unit M_o = 100.

Different strategies have been suggested to attach polymeric stabilizers to the surface of particles, namely physical adsorption, ionic bonding and covalent grafting.[14] Considering the composition of the arborescent PS-*g*-P2VP copolymer used in this investigation, whose 2VP units can be easily protonated, a polymer stabilizing shell bound through ionic

interactions appears promising, as it offers stronger interactions than physical adsorption and is much more versatile than covalent bonding.

3.2.2 Polymeric Stabilization by the Polyion Complexation Process

Electrostatic interactions between two linear and oppositely charged polymers to form polyion complex micelles, first reported in the mid-1990s by Harada and Kataoka,[20] Kabanov et al.,[21] and Cohen Stuart et al.,[22] immediately drew considerable attention. The main driving force for polyion complexation comprises two contributions: Coulombic attractions, and an entropy gain through the release of counterions.[20-26] More precisely, complex formation is ascribed to a decrease in total electrostatic free energy, due to a change in translational entropy for the microions and the total electrostatic field energy.[25] Hydrophobic interactions and hydrogen bonding are sometimes considered as additional contributions to the PIC formation process. Steric constraints oppose complexation of the polyelectrolytes however, resulting in a lower degree of effective charge neutralization.[25]

The complexation process has been investigated for different polymeric materials including PVP homopolymers and PVP-containing block copolymers.

3.2.2.1 PVP Homopolymers

Poly(2-vinylpyridine) (P2VP) and poly(4-vinylpyridine) (P4VP) homopolymers were complexed with poly(acrylic acid) (PAA) and poly(methacrylic acid) (PMAA) in ethanol/water (1:1) solutions.[27] The presence of hydrogen bonds between the PMAA and P2VP or P4VP chains was confirmed by Fourier transform-infrared (FT-IR) spectroscopy, based on the absence of pyridinium ions (protonated form) in the spectrum and the shift in the pyridine ring band. The acidic PAA formed complexes with both P2VP and P4VP through ionic interactions, as evidenced by the appearance of a ring stretching band for pyridinium ions at 1632 cm^{-1} in FT-IR spectroscopy, and also confirmed in X-ray photoelectron spectroscopy (XPS). When the PAA content in the complex was increased, a higher intensity of the pyridinium ion band and a shift in the pyridine ring band at 1595 cm^{-1}

toward higher wavenumbers were reported. Since the complexes were dried and ground to fine powders, no information was reported on their hydrodynamic size. Hydrogen bonding was also cited as the driving force for the self-assembly of P4VP homopolymer with polystyrene-*block*-poly(acrylic acid) (PS-*b*-PAA) to micelles in ethanol.[28] It is interesting to note the influence of the complexation solvent on the nature of the driving force for the complexation between PAA and P4VP segments: Weak hydrogen bonding was observed in ethanol, while strong polyionic interactions were reported in ethanol/water (1:1) solutions.

Pergushov et al.[29] published an informative study on water-dispersible micelles produced by the complexation in water of a strong cationic polyelectrolyte, poly(*N*-ethyl-4-vinylpyridinium bromide) (P4VP·EtBr), and poly(methacrylic acid)-*b*-polyisobutylene (PMAA-*b*-PIB). It is noteworthy that at pH 9, PIC formation and micellization of the amphiphilic PMAA-*b*-PIB block copolymer occurred simultaneously. The structure of the self-assembled PMAA-*b*-PIB micelles allowed the complexation of P4VP·EtBr with the PMAA shell through a polyion exchange reaction. This hypothesis was verified by DLS measurements, revealing the smaller size of the PIC micelles for $[N^+]/[CO_2^-]$ = 0.4 as compared to the self-assembled species (19 nm vs. 22.5 nm, due to the collapse of some segments of the formerly stretched PMAA blocks interacting with PVP·EtBr). An onion-like structure consisting of a PIB core, a shell of polyion-complexed P4VP·EtBr and PMAA, and a corona of excess PMAA fragments not involved in polyion complexation was concluded on the basis of *i)* fluorescence spectroscopy measurements using pyrene as a polarity probe, and *ii)* small-angle neutron scattering (SANS) data showing an increase in size for the micellar nucleus, attributed to the penetration P4VP·EtBr into the core (R_{core} increased from 3.4 nm to 6.3 nm, yielding a much higher scattering intensity and a larger slope at intermediate *q*-values). The penetration of P4VP·EtBr into the core was explained by their preference to be localized in the vicinity of the PIB cores. “Dynamic” micelles were formed under these conditions rather than “frozen” micelles, the latter being usually obtained by micellization in organic solvents, followed by transfer to aqueous media either by heating or stepwise dialysis.

Polyion complexation in an aqueous environment was not as straightforward for the weak base P2VP as for quaternized P4VP·EtBr as described above, due to their difference in base strengths. Warnant et al.[30] thus investigated the physicochemical properties of pH-sensitive PIC micelles derived from a P2VP homopolymer and a double-hydrophilic block copolymer (DHBC) of poly(acrylic acid)-*b*-poly(acrylate methoxy poly(ethylene oxide)) PAA-*b*-PAMPEO. It was suggested that the pH used for complexation was a crucial parameter influencing the micellization process, as it was necessary to ionize both weak polyelectrolytes before complexation. The selection of a hydrophilic block (PAMPEO) rather than a hydrophobic block (PIB) as described above[29] eliminated the complication of concurrent self-assembly of the amphiphilic copolymer before complexation. A core–corona morphology for the PIC micelles was suggested on the basis of *i)* fluorescence spectroscopy measurements using Auramine O as probe, and *ii)* variable density contrast experiments between the core and the corona in small-angle X-ray scattering experiments (SAXS). The hydrodynamic diameter of the PIC micelle was reported to be 36 nm, with a narrow size distribution (PDI = 0.28). The PIC micelles were unstable above pH 5 as the P2VP became insoluble, collapsed and dehydrated, leading to macroscopic precipitation.

3.2.2.2 PVP-Containing Block Copolymers

Unusual rod-like and buckle-like micelles were produced by the complexation of poly(2-vinylpyridine)-*b*-poly(ethylene oxide) (P2VP-*b*-PEO) with sodium poly(4-styrenesulfonate) (PSS) homopolymer in water acidified to pH 5.[31] The formation of these different morphologies was assigned to stretching of the core-forming blocks (the P2VP and PSS segments in this case), the surface tension between the micelle core and the solvent outside the core, and to the corona–chain segment interactions.[32] The dissociation of the PIC micelles observed at elevated pH and their reassembly upon decreasing the pH was highlighted as an interesting feature of this system, for biomedical applications requiring pH responsiveness over a narrow range, *e.g.* from pH 5 to 7–8.

Attempts at using PAA homopolymers to complex with amphiphilic block copolymers including PS-*b*-P4VP in DMF[33] and poly(3-caprolactone)-*block*-poly(2-vinyl

pyridine) (PCL-*b*-P2VP) in THF/ethanol[34] were also reported. Reasonably, in both cases micelle formation was ascribed to intermolecular hydrogen bonding between the PAA units and the P2VP segment of the block copolymers, as shown by FT-IR analysis. The size of the PIC micelles formed in DMF depended more on the length of the P4VP segment than the PAA segment. Small variations in hydrodynamic diameter were observed for the PIC micelles produced from PCL-*b*-P2VP in organic solutions when the amount of PAA was varied, suggesting that the complexes were saturated.[34] By changing the solvent, tuning the chain length and adjusting the stoichiometry ratio of the complex, the extent of hydrogen bonding could be controlled. Likewise using DMF as the complexing medium, Jérôme and Gohy observed nanophase separation within the corona of the spherical PIC micelles obtained by mixing a polystyrene-*b*-poly(2-vinylpyridine)-*b*-poly(ethylene oxide) (PS-*b*-P2VP-*b*-PEO) triblock copolymer with a tapered triblock of poly(ethylene oxide) methyl ether methacrylate and acrylic acid, $P(PEO_{11}MA)_{63}$-*b*-PAA_{657}-*b*-$P(PEO_{11}MA)_{63}$.[35] Hydrogen bonding between PAA and P2VP stabilized the micellar core, while the outer corona contained both PS and PEO chains. Since the hydrophilic PEO chains were relatively insoluble in DMF, they tended to cluster to avoid interactions with the hydrophobic PS blocks, which resulted in nanophase separation within the corona.

Layered core–shell–corona micellar complexes were formed by the complexation of preformed polystyrene-*b*-poly(acrylic acid) (PS-*b*-PAA) micelles and poly(ethylene glycol)-*block*-poly(4-vinyl pyridine) (PEG-*b*-P4VP) in ethanol.[36] The complexation of PEG-*b*-P4VP preformed micelles having a P4VP corona resulted in shrinking of the micellar structures from 75.8 nm to 57.6 nm for a weight mixing ratio of 0.25. Assuming that there was no change in the size of the PS core (R_c = 15.1 nm), which was kinetically frozen in ethanol at 25 °C, the shell thickness of the PIC micelles obtained ranged from 10.5 to 14.5 nm, depending on the weight ratio of the two complexing components.

Efforts were also made to control the PIC process in water by changing the complexation parameters. The formation of PIC micelles by mixing protonated poly(2-vinylpyridine)-*block*-poly(ethylene oxide) (P2VP-*b*-PEO) with neutralized poly(methacrylic

acid)-*block*-poly(ethylene oxide) (PMAA-*b*-PEO) was thus achieved within a limited pH range (2 < pH < 6.1). This pH range was employed to avoid both the self-assembly of PMAA-*b*-PEO at acidic pH and of P2VP-*b*-PEO at pH > 6.[37] The fact that the PIC micelles dissociated at NaCl concentrations above 0.35 M due to electrostatic screening highlights the sensitivity of PIC micelles to ionic strength and, more importantly, it confirms the role of electrostatic interactions in the micellar structures.

Interesting phase behavior and micellization phenomena were also observed at various pH in the self-complexation of a poly(2-vinylpyridine)-*b*-poly(methyl methacrylate)-*b*-poly(acrylic acid) block terpolymer (P2VP-*b*-PMMA-*b*-PAA) in aqueous dilute solutions.[38] At low pH (1–2) heteroarm star-like micelles were formed via interactions of the P2VP and PAA arms in the corona, wrapping the hydrophobic PMMA core. As the pH was increased from 2 to 3, electrostatic intermicellar attraction forces led to the formation of irregular aggregates. An insoluble two-phase region was observed between pH 3.2 and 5.8, i.e., around the isoelectric point of the ampholytic chains. Finally, under alkaline conditions, aggregated amphiphilic heteroarm star-like micelles were observed after deposition on mica substrates.

The penetration of poly(*N*-isopropylacrylamide-*co*-4-vinylpyridine) statistical copolymers (PNIPAM-*co*-P4VP) into rigid preformed core–shell microspheres of poly(styrene-*co*-methacrylic acid) (PS-*co*-PMAA), synthesized by a one-step surfactant-free emulsion polymerization technique, was also reported by Wang et al.[39] The complexation was performed in water, with PNIPAM-*co*-P4VP dissolved in an HCl solution, thus allowing electrostatic interactions to dominate as the driving force for self-assembly. The diameter of the resulting composite microspheres formed was slightly larger than that of the core–shell PS-*co*-PMAA microspheres, indicating the insertion of the copolymer of PNIPAM-*co*-P4VP into the PMAA shell layer of the core–shell microspheres.

A similar approach was used by Xiong et al.[40] to obtain a core–shell structure starting with the self-assembly of a PS-*b*-PAA block copolymer in ethanol, a good solvent for the PAA block but a non-solvent for the PS segment. Complexation of the preformed micelles

with a poly(4-vinyl pyridine)-*b*-poly(*N*-isopropylacrylamide) (P4VP-*b*-PNIPAM) block copolymer was then achieved in DMF/ethanol. Dialysis of the PIC micelles against water at pH 4 and heating to 45 °C led to the collapse of the thermosensitive PNIPAM corona onto the interacting PAA/P4VP sites, thus leaving an excess of P4VP segments as the corona. It was argued that the reversible response of PNIPAM upon temperature and pH variations provided the flexibility needed for applications in drug delivery, as catalyst carriers, templates, and so on.

3.2.2.3 Summary Remarks and Approach for the Current Work

Most of the studies discussed above were performed with PVP homopolymers or block copolymers, using PAA or PMAA as the block interacting with the PVP segments. Until now, to the best of our knowledge, no studies have been performed on the complexation of complex polymer architectures containing PVP segments. Organic solvents would allow the two components to be combined by hydrogen bonding, while aqueous environments at a suitable pH should give rise to electrostatic interactions. It is noteworthy that micelles formed in organic solvents remain frozen when transferred to aqueous environments, while direct complexation in aqueous solution tends to yield dynamic micelle structures, with additional electrostatic repulsions from excess ionic groups increasing the stability of the system.[28,38]

Using an arborescent copolymer G0PS-*g*-P2VP as a platform for the complexation reaction, we expect the PAA block of the complexing copolymer to penetrate into the arborescent structure and interact with the 2VP units. Water was used as the solvent for complexation, since we wanted to create dynamic PIC micelle systems and to characterize them in their dispersed form before examining their structure in the dry state, as it was done in most investigations mentioned above. The purpose of the PIC process was to stabilize the G1 hydrophobic arborescent copolymer with the double-hydrophilic copolymer PAA-*b*-PHEA, to obtain micellar structures colloidally stable in water at pH 7, and most importantly biocompatible due to PHEA, a highly biocompatible material.[41-45] The PIC formation process relies upon the presence of electrostatic interactions between the PAA and P2VP segments in

water after suitable adjustment of the pH (Figure 3-2). These interactions are assumed to anchor the block copolymer chains onto the surface of the arborescent copolymer, while the PHEA tails provide a swollen shell increasing the separation distance between the particles to the extent that van der Waals attractions become negligible (> 5 nm, as observed for many colloidal systems).[1] Moreover, electrostatic stabilization due to repulsion between the negatively charged PIC micelles at neutral pH would also be expected to impart colloidal stability to the dispersion, at least at low ionic strengths.

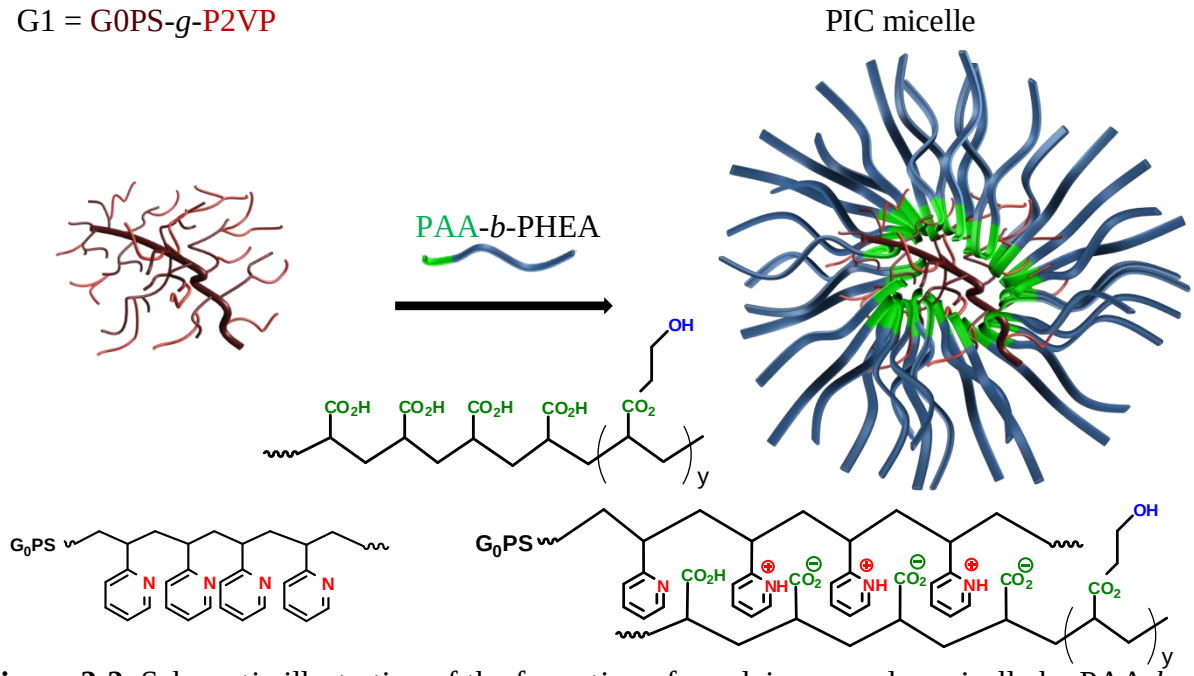

Figure 3-2. Schematic illustration of the formation of a polyion complex micelle by PAA-*b*-PHEA and G0PS-*g*-P2VP in water.

The ability of PAA-*b*-PHEA copolymers (synthesized with different block lengths) to stabilize the hydrophobic arborescent G1 copolymer was monitored by the DLS and laser Doppler velocimetry techniques to determine the hydrodynamic diameter, size distribution and zeta potential of the micelles obtained. The absolute molar mass, radius of gyration and second virial coefficient of the PIC micelles in aqueous solutions were also extracted from

multi-angle laser light scattering (MALLS) data, to obtain information on their structure. Changes in morphology of the arborescent polymer before and after complexation were furthermore revealed by atomic force microscopy (AFM), by varying the force applied with the AFM tip on the samples.

3.3 Experimental Procedures

3.3.1 Materials

Acetone (Sigma-Aldrich, > 99.7%), dichloromethane (Sigma-Aldrich, > 99.5%), ethyl acetate (Sigma-Aldrich, > 99.8%), tetrahydrofuran (THF, Sigma-Aldrich anhydrous, ≥ 99.9%, inhibitor-free), ethanol (Sigma-Aldrich, ACS reagent, 99.8%), triethylamine (Et_3N, Fisher, ≥ 99.0 %), anisole (Alfa Aesar, 99.0%), trifluoroacetic acid (TFA, Sigma-Aldrich, > 99.0%), methyl 2-bromopropionate (Sigma-Aldrich, 98%), and trimethylsilyl chloride (TMS-Cl, Alfa, ≥ 98.0%) were used as received from the suppliers. Milli-Q water (18.2 MΩ·cm) was obtained from a Milli-Q deionized water purification system (PURELAB Classic, ELGA LabWater).

N,*N*,*N*′,*N*″,*N*″-Pentamethyldiethylenetriamine (PMDETA, Sigma-Aldrich, 99%) was purified by distillation under reduced pressure and stored under N_2 at 4°C. Copper(I) bromide (CuBr, Sigma-Aldrich, 98%) was purified by washing twice (4 h and 24 h) with glacial acetic acid (Sigma-Aldrich, 99.75%), three times with absolute ethanol (Sigma-Aldrich, ≥ 99.8%), and finally with diethyl ether (Sigma-Aldrich, anhydrous, ≥ 99.0%). The white powder was dried under vacuum overnight and stored under N_2.

tert-Butyl acrylate (*t*BA, Sigma-Aldrich, 98%) was stirred overnight with freshly crushed calcium hydride (CaH_2, Sigma-Aldrich, lumps, reagent grade, 95%), distilled under reduced pressure and stored under N_2 at 4 °C. 2-Hydroxyethyl acrylate (HEA, Sigma-Aldrich, 96%, with 200–650 ppm hydroquinone monomethyl ether as inhibitor) was purified by liquid-liquid extraction to remove diacrylates and acrylic acid impurities before

distillation.[42] An aqueous solution of HEA (81 mL, 0.65 mol) in deionized water (27 mL, 25% v/v) was washed 10 times with *n*-hexanes (Sigma-Aldrich, ACS reagent, ≥ 98.5%) and saturated with sodium chloride. The HEA in the aqueous phase was then extracted with diethyl ether (Sigma-Aldrich, ACS reagent, ≥ 99.0%, 3 × 75 mL). This monomer solution was dried over anhydrous $MgSO_4$ powder (Fisher, Certified) before concentration by rotary evaporation. Hydroquinone (Alfa Aesar, 99.0%, 75 mg, 0.1% w/w) was added as an inhibitor and the purified monomer was stored at –15 °C until distillation under reduced pressure immediately before use.

The G1 arborescent graft copolymer used in this study was synthesized earlier by anionic polymerization and grafting.[58] It consists of a G0 or comb-branched polystyrene substrate ($\bar{M}_n$ = 9.7×10^4 g/mol; $\bar{M}_w/\bar{M}_n$ = 1.03; branching functionality f_n = 17) grafted with poly(2-vinylpyridine) chains ($\bar{M}_n$ = 5.5×10^3 g/mol; $\bar{M}_w/\bar{M}_n$ = 1.15). Purification of the copolymer from linear polymer contaminants was performed with 3 cycles of precipitation/fractionation from 5 g·L^{-1} solutions in THF/methanol (4/1 v/v) mixtures with *n*-hexane. The graft copolymer G0PS-*g*-P2VP ($\bar{M}_n$ = 1.1×10^6 g/mol; $\bar{M}_w/\bar{M}_n$ = 1.08; branching functionality f_n = 182) had a 2VP units content of 91 mol%.[46]

3.3.2 Synthesis of Poly(*tert*-butyl acrylate) Macroinitiator

Low molar mass macroinitiators P*t*BA-Br were synthesized via atom-transfer radical-polymerization (ATRP), by adapting a procedure reported by Davis and Matyjaszewski[47] as illustrated in Scheme 3-1. Briefly, methyl 2-bromopropionate (0.37 mL, 3.3 mmol, 1 equiv), CuBr (0.252 g, 1.75 mmol, 0.53 equiv), PMDETA (0.36 mL, 1.74 mmol, 0.52 equiv), degased acetone (5 mL), and *t*BA (20 mL, 140 mmol, 42.4 equiv) were added to an oven-dried round-bottomed flask (rbf) and the reagent mixture was degased with 3 freeze–pump–thaw cycles. The green-colored reaction mixture (ascribed to the Cu^I-PMDETA complex) was then placed in an oil bath at 60 °C for 2 h 40 min to reach $\bar{X}_n$ = 13, and 5 h 20 min to reach $\bar{X}_n$ = 27. The reactions were stopped by cooling the flask in liquid nitrogen and non-

degased acetone (ca. 10 mL) was added. The solution was passed through a column (10 cm height × 1 cm diameter) of activated neutral alumina (Sigma-Aldrich, Brockmann I grade, 150-mesh size) using ca. 50 mL acetone as eluent. After removal of the organic solvent by rotary evaporation, the polymer was dissolved in a minimum amount of methanol (ca. 10 mL) and further purified by dialysis in a 1,000 MWCO Spectra/Por® 7 regenerated cellulose bag against 1 L of methanol. The solvent was changed thrice within 24 h, and the polymer was collected by removal of the solvent under vacuum.

P*t*BA$_{13}$ ^{1}H NMR ($CDCl_3$, 400 MHz): $\bar{M}_n$ (NMR) = 1660, DP = 13, δ (ppm): 1.06–1.13 (m, 3H), 1.14–1.65 (b, 140H), 1.65–2.02 (b, 6H), 2.01–2.34 (b, 14H), 2.34–2.62 (b, 2H), 3.55–3.65 (s, 3H), 3.98–4.15 (m, 1H); $\bar{M}_n$ (SEC–PS) = 1724, $Đ_{(SEC)} = \bar{M}_n/\bar{M}_w$ = 1.05.

P*t*BA$_{27}$ ^{1}H NMR ($CDCl_3$, 400 MHz): $\bar{M}_n$ (NMR) = 3460, DP = 27, δ (ppm): 1.06–1.13 (m, 3H), 1.14–1.65 (b, 283H), 1.65–2.02 (b, 11H), 2.01–2.34 (b, 28H), 2.34–2.62 (b, 2H), 3.55–3.65 (s, 3H), 3.98–4.15 (m, 1H); $\bar{M}_n$ (SEC–PS) = 3524, $Đ_{(SEC)}$ = 1.06.

P*t*BA$_{13}$ and P*t*BA$_{27}$ ^{13}C NMR ($CDCl_3$, 100 MHz) δ (ppm): 27.68 ($\underline{C}H_2$), 28.08 (C-($\underline{C}H_3)_3$), 41.88 ($\underline{C}H_2$-CH-Br), 42.34 ($\underline{C}$H-CH_3), 80.33 ($\underline{C}$-$(CH_3)_3$), 174.18 ($\underline{C}$O).

3.3.3 Silylation of 2-Hydroxyethyl Acrylate

Protection of the hydroxyl functionality of HEA was carried out according to a procedure reported by Mühlebach et al.,[42] illustrated in Scheme 3-2. The monomer HEA (75 mL, 0.652 mol, 1.0 equiv), purified as described in Section 3.3.1, dichloromethane (750 mL) and triethylamine (109.5 mL, 0.79 mol, 1.21 equiv) were added in a 2–L rbf and the solution was cooled to 0 °C in an ice bath. Trimethylsilyl chloride (91.5 mL, 0.72 mol, 1.1 equiv) was then added drop-wise, resulting in the formation of a white precipitate ($Et_3N{\cdot}HCl$). The solution was stirred in the ice bath overnight and allowed to reach room temperature gradually. Suction filtration (Whatman® filter paper, grade 4) was employed to remove the precipitate, the solvent was removed by rotary evaporation, and the liquid residue was filtered once more. The protected monomer, 2-trimethylsilyloxyethyl acrylate (HEATMS),

was purified by dissolution in ethyl acetate (300 mL) and washing with water (300 mL) three times. Anhydrous $MgSO_4$ (ca. 5 g) was then added to the solution which was decanted after 15 min, and the solvent was removed under vacuum.

^{1}H NMR ($CDCl_3$, 400 MHz) δ (ppm): 0.07 (s, 9H), 3.69 (t, J = 4.8 Hz, 2H), 4.10 (t, J = 4.8 Hz, 2H), 5.70 (dd, $^3J_{cis}$ = 10.41 Hz, ^2J = 1.21 Hz, 1H), 6.02 (dd, $^3J_{trans}$ = 17.33 Hz, $^3J_{cis}$ = 10.42 Hz, 1H), 6.30 (dd, $^3J_{trans}$ = 17.33 Hz, ^2J = 1.21 Hz, 1H).

^{13}C NMR ($CDCl_3$, 100 MHz) δ (ppm): –0.62 (Si-($\underline{C}H_3$)$_3$), 60.55 ($\underline{C}H_2$-O-SiMe$_3$), 65.60 ($\underline{C}H_2$-O-CO), 128.24 ($\underline{C}$H), 130.72 ($\underline{C}H_2$-CH), 166.01 ($\underline{C}$O).

3.3.4 Synthesis of Poly(*tert*-butyl acrylate)-*b*-Poly(2-trimethylsilyloxyethyl acrylate)

Poly(*tert*-butyl acrylate)-*b*-poly(2-trimethylsilyloxyethyl acrylate) or P*t*BA-*b*-P(HEATMS) was synthesized by ATRP using either P(*t*BA)$_{13}$-Br ($\overline{M}_n$ = 1660 g/mol) or P(*t*BA)$_{27}$-Br ($\overline{M}_n$ = 3460 g/mol) as macroinitiator. The procedure reported here used the macroinitator with $\overline{M}_n$ = 3460 g/mol. In a 100–mL Schlenk flask were added CuBr (65 mg, 450 µmol, 1 equiv), anisole (10 mL), PMDETA (93 µL, 44.5 mmol, 0.99 equiv), and freshly distilled HEATMS (31.6 mL, 157 mmol, 350 equiv). The reaction mixture was stirred for 5 min before the addition of P*t*BA-Br (1.555 mg, 450 µmol, 1.0 equiv). The solution was then degased by three successive freeze–pump–thaw cycles, the flask was filled with N_2, and heated to 85 °C for 4 h 20 min to reach $\bar{X}_n$ = 60, and 19 h to reach $\bar{X}_n$ = 260. The reactions were stopped by submerging the flask in liquid nitrogen, before the addition of acetone (50 mL). The solution was passed through a column (15 cm height × 2 cm diameter) of activated neutral alumina (Aldrich-Sigma, Brockmann I grade, 150 mesh size) using acetone (100 mL) as eluent. After removal of the organic solvent by rotary evaporation, the polymer was dissolved in a minimum amount of methanol (ca. 30 mL) and further purified by dialysis in a 1,000 MWCO Spectra/Por® 7 regenerated cellulose bag against 1 L of methanol. The solvent was changed thrice within 24 h, and the polymer was collected after removal of the solvent under vacuum.

P*t*BA$_{13}$-*b*-PHEATMS$_{50}$ ^{1}H NMR ($CDCl_3$, 400 MHz): $\bar{M}_n$(NMR) = 11060, $\bar{X}_{n,PHEATMS}$ = 50, δ (ppm): 0.14 (s, 450H), 1.06–1.13 (m, 3H), 1.14–1.47 (b, 145H), 1.47–1.74 (b, 70H) 1.74–2.02 (s, 32H), 2.16–2.24 (b, 65H), 3.55–3.72 (b, 103H), 3.88–4.28 (b, 100H); $\bar{M}_n$ (SEC–PS) = 11850, $\bar{M}_n \cdot \bar{M}_w^{-1}$ = 1.15.

P*t*BA$_{13}$-*b*-PHEATMS$_{150}$ ^{1}H NMR ($CDCl_3$, 400 MHz): $\bar{M}_n$(NMR) = 29860, $\bar{X}_{n,PHEATMS}$ = 150, δ (ppm): 0.14 (s, 1356H), 1.06–1.13 (m, 3H), 1.14–1.47 (b, 145H), 1.47–1.74 (b, 216H) 1.74–2.02 (s, 86H), 2.16–2.24 (b, 167H), 3.55–3.72 (b, 307H), 3.88–4.28 (b, 318H); $\bar{M}_n$ (SEC–PS) = 37620, $\bar{M}_n \cdot \bar{M}_w^{-1}$ = 1.23.

P*t*BA$_{27}$-*b*-PHEATMS$_{56}$ ^{1}H NMR ($CDCl_3$, 400 MHz): $\bar{M}_n$(NMR) = 14730, $\bar{X}_{n,PHEATMS}$ = 56, δ (ppm): 0.14 (s, 506H), 1.06–1.13 (m, 3H), 1.14–1.47 (b, 283H), 1.47–1.74 (b, 93H) 1.74–2.02 (s, 46H), 2.16–2.24 (b, 83H), 3.55–3.72 (b, 115H), 3.88–4.28 (b, 114H); $\bar{M}_n$ (SEC–PS) = 14350, $\bar{M}_n \cdot \bar{M}_w^{-1}$ = 1.08.

P*t*BA$_{27}$-*b*-PHEATMS$_{260}$ ^{1}H NMR ($CDCl_3$, 400 MHz): $\bar{M}_n$(NMR) = 50450, $\bar{X}_{n,PHEATMS}$ = 260, δ (ppm): 0.14 (s, 2306H), 1.06–1.13 (m, 3H), 1.14–1.47 (b, 283H), 1.47–1.74 (b, 348H) 1.74–2.02 (s, 180H), 2.16–2.24 (b, 286H), 3.55–3.72 (b, 552H), 3.88–4.28 (b, 520H$\bar{M}_n$ (SEC–PS) = 65780, $\bar{M}_n \cdot \bar{M}_w^{-1}$ = 1.16.

P*t*BA-*b*-PHEATMS ^{13}C NMR ($CDCl_3$, 100 MHz), δ (ppm): –0.01 (Si-($\underline{C}H_3$)$_3$), 23.67($\underline{C}H_3$-CH), 26.10 (C-($\underline{C}H_3$)$_3$, 39.43 ($\underline{C}H_2$ backbone), 58.49 ($\underline{C}$H backbone), 64.60 ($\underline{C}H_2$-O), 66.03 ($\underline{C}H_2$-O-SiMe$_3$), 78.38 ($\underline{C}H_2$-O-CO), 173.07 ($\underline{C}$O).

3.3.5 Hydrolysis of P*t*BA-*b*-PHEATMS

The hydrolysis of the protecting groups on the four P*t*BA-*b*-PHEATMS block copolymer samples was performed to produce the corresponding PAA-*b*-PHEA derivatives. The procedure reported here was applied to P(*t*BA)$_{27}$-*b*-P(HEATMS)$_{260}$. To a mixture of THF (83 mL) and CH_2Cl_2 (83 mL) was added P(*t*BA)$_{27}$-*b*-P(HEATMS)$_{260}$ (16.5 g, 81.9

mmol HEATMS units, 8.5 mmol *t*BA units, ca. 10% v/v). The flask was cooled in an ice–water bath with vigorous stirring and when the polymer was dissolved, H_2O (5 mL) was added to the solution followed by trifluoroacetic acid (TFA, 277 mL, 3.62 mol, 40 equiv) drop-wise. The solution was left to react for 24 h. The solvent was then removed under vacuum and the deprotected polymer was redissolved in ethanol (EtOH, 30 mL). Solvent exchange was performed by dialysis in a 1,000 MWCO Spectra/Por® 7 regenerated cellulose bag against EtOH (2 L) for 24 h, followed by EtOH/H_2O (50/50 v/v, 2 L) for 24 h, and finally against 6 changes of H_2O (5 L) for 72 h. To accelerate dialysis, the pH of the H_2O used in the last step was maintained at pH 7 by the addition of NaOH solution. The clear solution obtained was collected and stored at 4°C.

PAA_{13}-*b*-$PHEA_{50}$ ^{1}H NMR (DMSO-d_6, 400 MHz) δ (ppm): 1.01–1.11 (b, 3H), 1.37–1.70 (b, 99 H), 1.70–1.89 (b, 32H), 2.01–2.47 (b, 65), 3.49–3.65 (b, 103H), 3.82–4.24 (b, 100H), 4.58–4.88 (b, 131H).

PAA_{13}-*b*-$PHEA_{150}$ ^{1}H NMR (DMSO-d_6, 400 MHz) δ (ppm): 1.00–1.11 (b, 3H), 1.35–1.70 (b, 177H), 1.74–1.91 (b, 68H), 2.01–2.47 (b, 165), 3.49–3.7 (b, 303H), 3.82–4.24 (b, 300 H), 4.58–4.88 (b, 121H).

PAA_{27}-*b*-$PHEA_{56}$ ^{1}H NMR (DMSO-d_6, 400 MHz) δ (ppm): 1.00–1.11 (b, 3H), 1.35–1.70 (b, 134H), 1.74–1.91 (b, 41H), 2.01–2.47 (b, 81H), 3.49–3.7 (b, 116H), 3.82–4.24 (b, 113 H), 4.58–4.88 (b, 46H).

PAA_{27}-*b*-$PHEA_{260}$ ^{1}H NMR (DMSO-d_6, 400 MHz) δ (ppm): 1.00–1.11 (b, 3H), 1.35–1.70 (b, 379H), 1.74–1.91 (b, 104H), 2.01–2.47 (b, 283H), 3.49–3.7 (b, 523H), 3.82–4.24 (b, 521H), 4.58–4.88 (b, 241H).

PAA-*b*-PHEA ^{13}C NMR (DMSO-d_6, 100 MHz), δ (ppm): 34.35 (*C*H), 40.08 (*C*H_2), 58.79 (*C*H_2-O), 65.63 (*C*H_2-OH), 174.07 (*C*O).

3.3.6 Polyion Complexation Process

Complexation of the G1 arborescent copolymer with various amounts of different PAA-*b*-PHEA block copolymers was carried out in aqueous solutions. Hereafter the parameter f = CO_2H/N will be used to quantify the molar ratio between the CO_2H groups (from PAA chains of the block copolymer) and N moieties (2VP units of the arborescent copolymer):

$$f = \frac{\text{number of moles of } CO_2H \text{ groups from PAA chains}}{\text{number of moles of N groups from P2VP chains}}$$

The following procedure describes the complexation of the G1 copolymer with PAA_{27}-*b*-$PHEA_{260}$ for f = 0.5. In a 10–mL vial, G1 (1.7 mg, 14.7 µmol of N) was completely dissolved in 300 µL of aqueous HCl solution at pH 1.4 by sonication (37 kHz, 30 min, Ultrasonic Cleaner Elmasonic SH075EL). A pH 7 aqueous solution of PAA_{27}-*b*-$PHEA_{260}$ (8.5 mg, 5 mg/mL, 7.35 µmol of CO_2H) was quickly added. The mixture was stirred for 1 h before the pH was adjusted to 4.7 with a 1 M NaOH solution, and stirring was continued for 1 h. The pH was further adjusted to 7 with 0.1 M NaOH and the solution was stirred for 30 min. The solution was then dialyzed (50,000 MWCO Spectra/Por® 7 regenerated cellulose bag) against Milli-Q water (5 L) for 24 h before it was collected and stored at 4 °C.

3.3.7 Characterization

3.3.7.1 Nuclear Magnetic Resonance Spectroscopy

The number-average degree of polymerization, the silylation of HEA, the composition of the polymers, and the deprotection reaction were monitored by nuclear magnetic resonance ^{1}H, ^{13}C and heteronuclear single quantum coherence (HSQC) spectroscopy analysis on a 400 MHz (100 MHz for the ^{13}C experiments) Bruker Avance I NMR spectrometer with a 5 mm BBFO probe. The concentration of the samples for the analysis ranged from 10–30 mg/mL.

3.3.7.2 Size-Exclusion Chromatography

The apparent molar mass dispersity $Đ_{SEC} = \bar{M}_w / \bar{M}_n$ of the polymers was determined by size-exclusion chromatography (SEC) analysis on a PL-GPC 50 Plus (Agilent Technologies) instrument with RI and UV detectors and TOSOH TSK gel columns (G40000HXL, G3000HXL, G2000HXL). The instrument was calibrated with low dispersity polystyrene standards, and THF (with toluene as a flow rate marker) served as eluent at a flow rate of 1.0 mL/min at 40 ºC.

3.3.7.3 Dynamic Light Scattering

The measurements were performed on a Zetasizer Nano ZS90 (Malvern Instruments) equipped with a 4 mW He–Ne laser operating at 633 nm and 25.0 °C, at a scattering angle of 90°. Each sample was measured in triplicate using disposable PS cuvettes or quartz cuvettes. The samples were prepared at concentrations of 3–5 mg/mL in Milli-Q water (at 25 °C, refractive index 1.330, viscosity 0.8872 cP), and filtered through a nylon membrane with 0.45 μm nominal pore size. The light scattering data were analyzed with the Zetasizer 7.11 Software (Malvern Instruments). The intensity-weighted autocorrelation function $g^{(2)}(\tau)$ produced by the digital correlator was used to extract the particle size distributions. The second order cumulants analysis algorithm was applied for relatively monodisperse particles, while the non-negatively constrained least-squares method (NNLS) or CONTIN analysis were employed for polydisperse samples. The hydrodynamic radius of the particles was determined from the Stokes–Einstein equation $R_h = \frac{k_B T}{6\pi\eta D_T}$ with the diffusion coefficient (D_T) obtained from the decay rate (Γ) and the instrumental component $q^2 = \frac{4\pi n_o}{\lambda} \sin\frac{\theta}{2}$.

3.3.7.4 Static Light Scattering

The static light scattering (SLS) measurements to determine the absolute weight-average molar mass $\bar{M}_w$, the second virial coefficient (A_2) and radius of gyration (R_g) were performed using an ALV/CGS-3 platform-based goniometer system equipped with a He–Ne

laser (λ = 632.8 nm, 22 mW output power), a proprietary ALV optical fiber-based detector, an APD-based single photon detector, ALV/LSE-5003 Electronics, and an ALV-5000/EPP correlator. The measurements were carried out with 5 samples at 0.2–1 mg/mL in aqueous solutions at 25 °C, at angles ranging from 30 to 150°. The intensity of scattered light was measured with the photomultiplier detector, and the data were analyzed by the Zimm extrapolation technique to zero concentration and angle.

For selected PIC systems, the refractive index increment (d*n*/d*c*) needed for the calculations was determined using a differential refractometer (Wyatt Technology) at 658 nm, by injecting a series of 5 micellar solutions at 0.2–1 mg/mL. The data were processed with the ASTRA 6 software. The linear correlation found between d*n*/d*c* vs. composition was used to interpolate the d*n*/d*c* values for the other PIC systems.

3.3.7.5 Zeta Potential Measurements

The electrical double layer surrounding a particle is composed of an inner region (called the Stern layer**,** where the ions are strongly bound) and an outer, diffuse region (where the ions are less firmly attached). A slipping plane is a notional boundary within the diffuse layer, inside which the ions move with the particle as it moves. The potential existing at this boundary is known as the Zeta potential.[48]

Zeta potential (ZP) measurements were performed on a Zetasizer Nano ZS90 instrument (Malvern) equipped with a 4 mW He–Ne laser (633 nm) and at 25.0 °C. In this instrument the laser beam is split into a reference beam and an incident beam, before passing through the sample placed in a capillary cell. The scattered light detected at 17° is then combined with the reference beam to provide the rate of fluctuation, which is proportional to the velocity of the particles (electrophoretic mobility U_E). The zeta potential (ζ) is calculated from the electrophoretic mobility U_E using the Henry equation[49]

$$U_{\mathrm{E}} = \frac{2\varepsilon\zeta f(Ka)}{3\eta}$$

where ε is the dielectric constant, η the viscosity, and $f(Ka)$ is Henry's function. This function was set at 1.5, as the system was fitted to the Smoluchowski model.[50]

3.3.7.6 Atomic Force Microscopy

Freshly cleaved mica was used as sample substrate. The polymer solutions were prepared in Milli-Q water at concentrations ranging from 0.05 to 0.1 mg/mL. A 20 µL aliquot of PIC dispersion was deposited on the mica substrate and spin-coated at 3000 rpm for 180 s under ambient conditions. Atomic force microscopy (AFM) images were recorded in the tapping mode in air on a Veeco Dimension Icon System equipped with a Nanoscope V controller belonging to the NsySA group at ENSCBP headed by Pr Neso Sojic. The probes used were Olympus® AC160TS-R3 micro cantilevers with a spring constant of 26 – 56 N/m, a resonance frequency of 300 – 399 kHz and a curvature radius of 8 – 10 nm. The scan rate was typically between 0.7 and 1.2 Hz, at a scan angle of 0°, acquiring 512 samples/line. Image analysis was done using the Nanoscope Analysis V1.20 software from Bruker.

3.4 Results and Discussion

3.4.1 Synthesis of the Double-Hydrophilic Block Copolymers

The synthesis of the double-hydrophilic block copolymers (DHBC) PAA-*b*-PHEA was carried out in a multistep process involving monomer protection, atom transfer radical polymerization (ATRP), and deprotection steps. ATRP is a well-known controlled radical polymerization (CRP) technique allowing the synthesis of homopolymers and copolymers with narrow size distributions, in particular for polyacrylates.[47,51-53] Low molar mass P*t*BA samples were first prepared in acetone at 60 °C, using methyl 2-bromopropropionate as initiator, CuBr as catalyst, and PMDETA as ligand as shown in Scheme 3-1.[47]

The ^{1}H NMR spectrum of P*t*BA (Figure 3-3a) is dominated by the *tert*-butyl protons at δ 1.14 – 1.65 ppm (*d*). The $\bar{M}_n$ value of the two homopolymers P(*t*BA)$_{13}$ and P(*t*BA)$_{27}$ was determined by integrating the methine protons in the repeat units (δ 2.01–2.34 ppm, *a2*) and

in the terminal unit (next to the bromine atom) at 4.00–4.19 ppm (*a1*). The peak area ratios for the methoxy proton (*b*) to (*a1*), and for the methyl group (*e*) to (*a1*) are both in a 3:1 ratio, which confirms the presence of a single *ω*–bromine group on every polymer chain and allows this material to work as macroinitiator in the next ATRP reaction to synthesize the desired block copolymers. In our work, the protected form of HEA was used as the monomer to increase the monomer conversion (otherwise limited to < 50 %)[54] and to achieve fast kinetics, while obtaining well-defined block copolymers with a low dispersity.[41,54] The protection of HEA with a trimethylsilyl group is depicted in Scheme 3-2, whilst the structure of the protected monomer was confirmed by ^{1}H NMR analysis (Section 3.3.3).

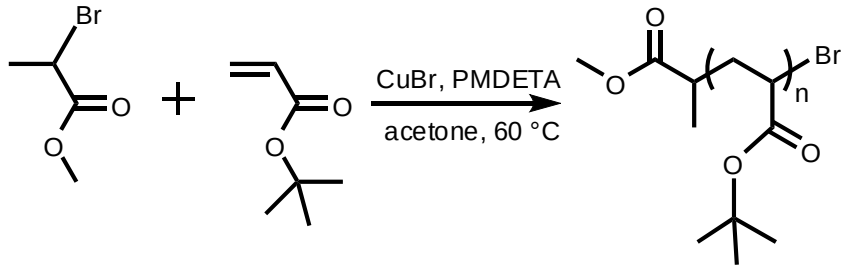

Scheme 3-1. Synthesis of P*t*BA via ATRP.

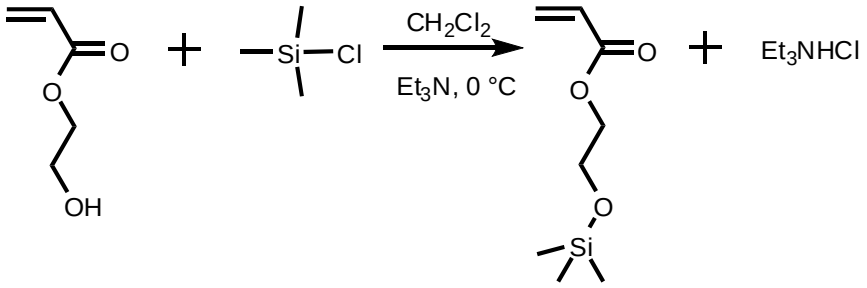

Scheme 3-2. Silylation of HEA.

The ATRP of P*t*BA-*b*-(PHEATMS) using a macroinitiator and the protected monomer (Scheme 3-3) was performed in anisole to facilitate the formation of the CuBr/PMDETA complex.[47] The ^{1}H NMR spectrum for the P*t*BA-*b*-(PHEATMS) copolymer in Figure 3-3b is dominated by the trimethylsilyl protons at δ 0.14 ppm (*f*) and the two strong methylene resonances at 3.5–4.5 ppm (*g* and *h*), which confirms the presence of the HEATMS units in the copolymer. The number-average degree of polymerization of the copolymers was determined from the area of the trimethylsilyl protons at δ 0.14 ppm (*f*) and the methyl groups at δ 1.06–1.13 (*e*). Similar calculations using either the methylene group (*g* or *h*) to (*e*) gave the same $\bar{X}_{\mathrm{n}}$ values, despite the overlap of peaks (*b*) and (*h*). The SEC chromatograms for the two homopolymers and four block copolymers, compared in Figure 3-4, confirm the low dispersity of the polymers obtained and the molar mass growth in the second polymerization step.

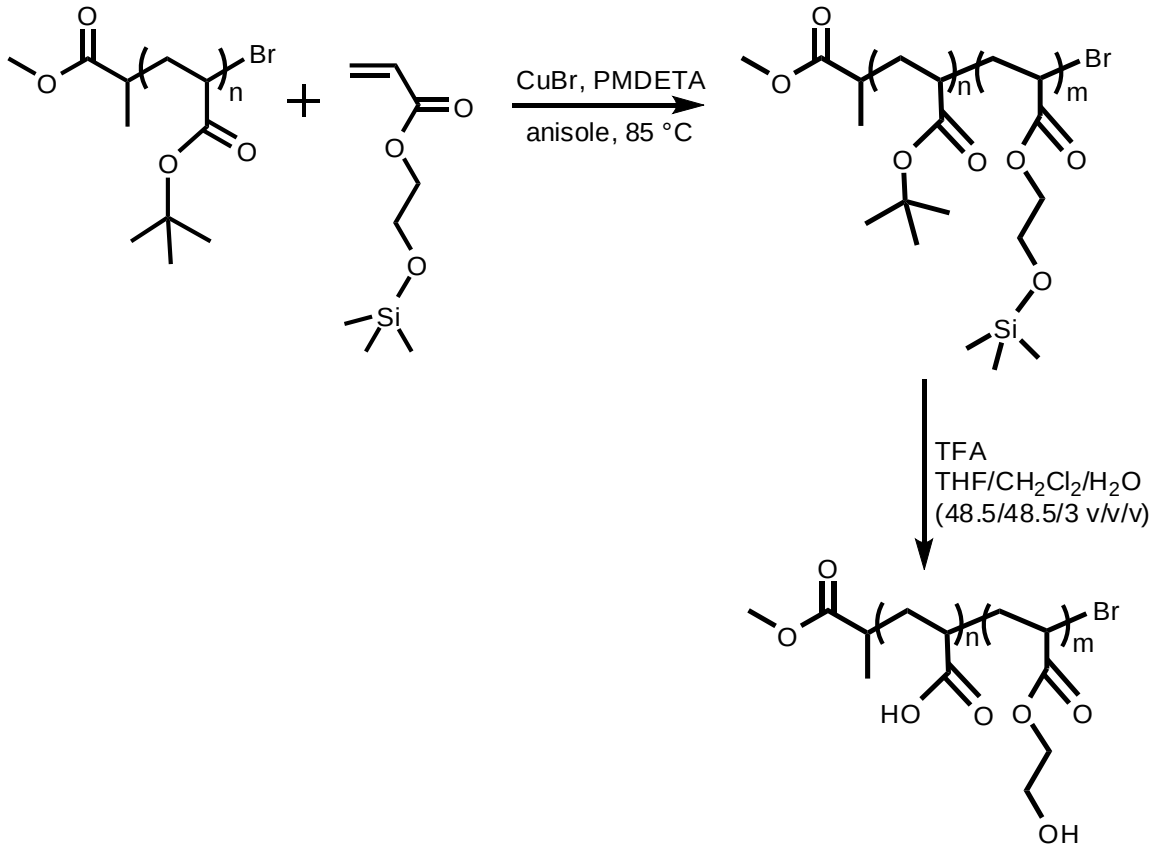

Scheme 3-3. ATRP synthesis of P*t*BA-*b*-PHEATMS and deprotection reaction to produce PAA-*b*-PHEA.

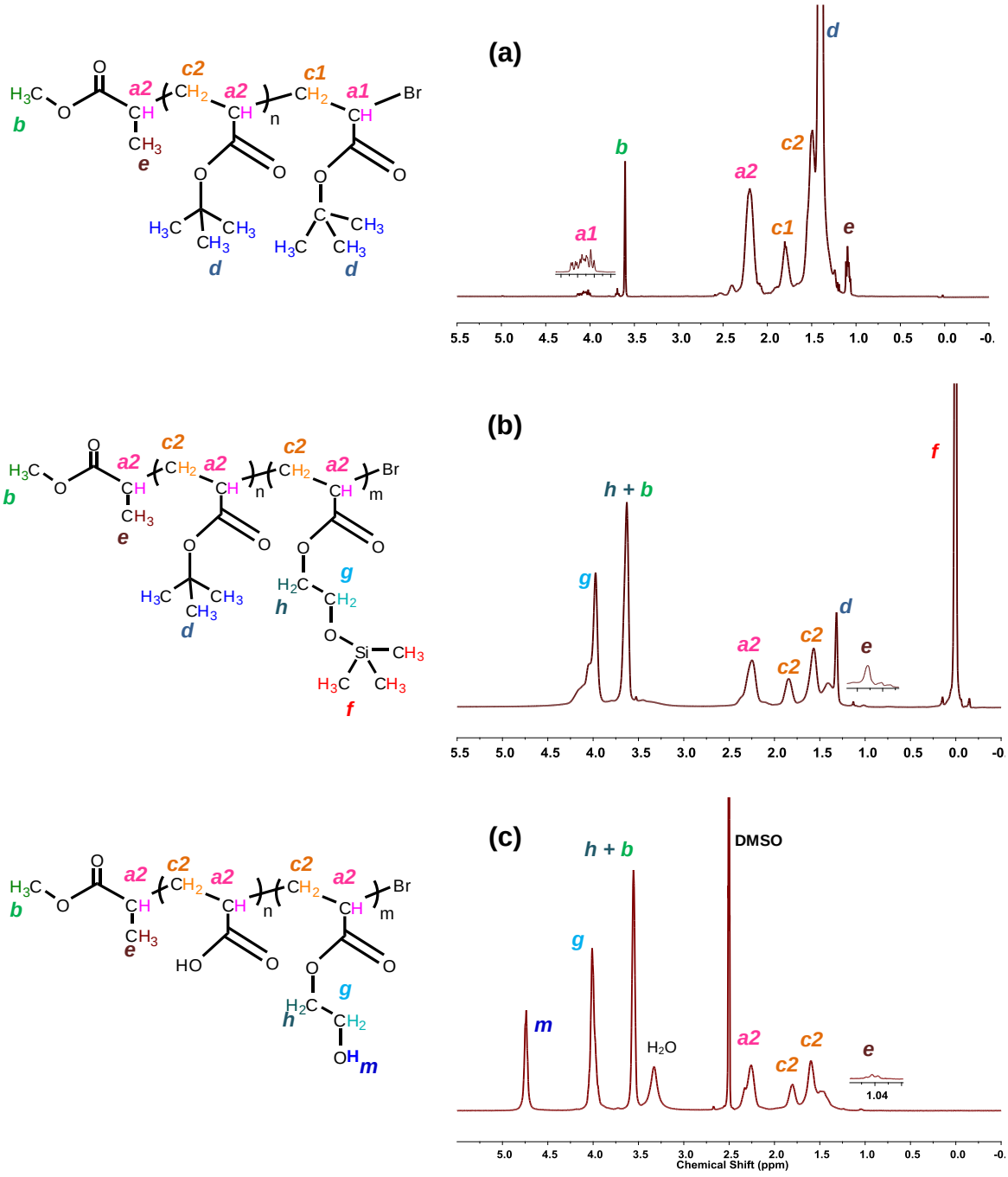

Figure 3-3. ^{1}H NMR (400 MHz) spectra for (a) P*t*BA, (b) P*t*BA-*b*-P(HEATMS) in $CDCl_3$, and (c) PAA-*b*-PHEA in DMSO-d_6.

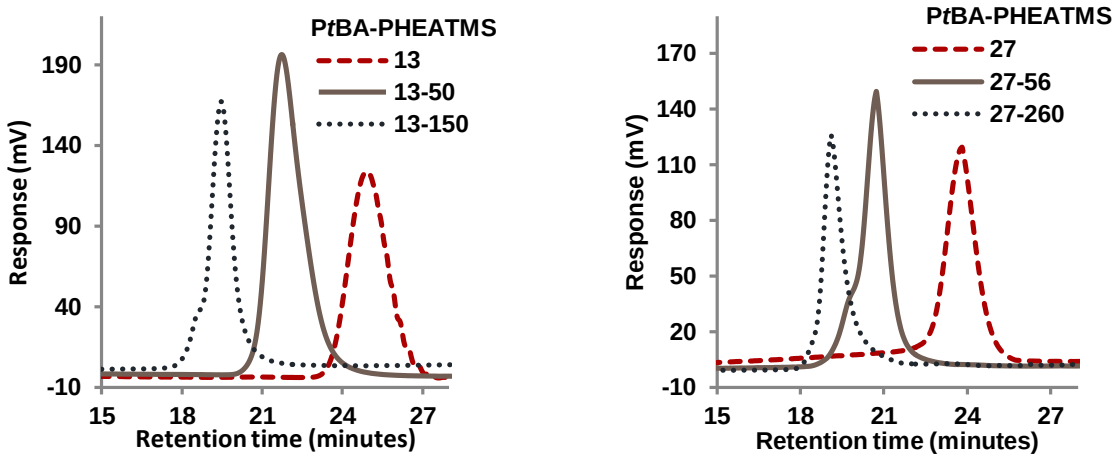

Figure 3-4. SEC chromatograms for P*t*BA homopolymers and P*t*BA-*b*-PHEATMS copolymers.

Simultaneous hydrolysis of both the *t*BA and TMS protecting groups was accomplished with an excess of TFA in a THF/CH_2Cl_2/H_2O (48.5/48.5/3 v/v/v) mixture for 24 h. Complete removal of the *tert*-butyl groups was confirmed by *i)* the absence of the peak at δ 1.42 ppm (*d*) in the ^{1}H NMR spectrum (Figure 3-3c), *ii)* the disappearance of the carbon peak at δ 26.10 ppm (*d*) in the ^{13}C NMR spectrum (Sections 3.3.4 and 3.3.5), and *iii)* the disappearance of the these two resonance signals and their cross-peak in the HSQC NMR spectrum (Figure S3-1). Similarly, complete hydrolysis of the TMS groups was evidenced by *i)* the absence of the resonance at δ 0.14 ppm (*f*), *ii)* the appearance of a hydroxyl proton (*m*) at δ 4.58–4.88 in the ^{1}H NMR spectrum in DMSO-d_6 (Figure 3-3), *iii)* the disappearance of the carbon peak at δ –0.01 ppm (*f*) in the ^{13}C NMR spectrum (Sections 3.3.4 and 3.3.5), and *iv)* the disappearance of these two resonance signals and their cross-peaks in the HSQC spectrum (Figure S3-1). The $\bar{X}_n$ for the PHEA segments, calculated by integrating the signals for the methylene group (*g*) and the methyl group (*e*), or for (*h*+*b*) and (*e*), gave the same values. However the $\bar{X}_n$ of the PAA segment could be only calculated by subtraction of the methine signal for PHEA from the total values for the methine groups (*a2*) of the block copolymer.

3.4.2 PIC Micelles in Water

The arborescent G0PS-*g*-P2VP copolymer is insoluble in aqueous media at neutral pH, while PAA-*b*-PHEA is soluble, but no micelles or aggregates are formed despite the fact that PAA is a weak polyelectrolyte.[55] At pH values below the pK_a of PAA, more than 50% of the carboxyl functionalities of PAA exist in their hydrophobic form (COOH),[56] which may turn the double-hydrophilic block copolymer into amphiphilic species but also reduce the complexation efficiency. The pK_a of PAA-based polyelectrolytes in solution in the absence of added salts was reported to fall within a narrow range from 5.7 to 6.5.[56-59] Based on the similarities in the polymer structures tested and our double-hydrophilic block copolymer, pK_a = 6.5[56,59] was used in the theoretical calculations for this work. Such a decrease in acidity is usually noted for polyelectrolytes as compared to small molecule carboxylic acids. Water is a non-solvent for the PS segments, while P2VP is also a weak polyelectrolyte (pK_a = 5)[30] with a lower basicity than its monomer (pK_a = 5.6).[60]

As previously mentioned, the presence of electrostatic interactions between the PAA and P2VP segments is expected to be vital to couple the BC chains with the G1 substrate. To maximize polyelectrolyte interactions, it is crucial to ionize of these components before the complexation,[30] by protonating the amine groups of P2VP (pK_a = 5) to NH^+ in an acidic environment, and ionizing the COOH moieties of PAA (pK_a = 6.5) to CO_2^-. Ideally, a pH range where both components can be mostly present in their ionic form is required to form stable electrostatic interactions between polycations and polyanions,[30,61] but this was not possible for the system investigated here (Figure 3-5). Complexation is unfavorable at extreme pH values, but pH 4.7 was selected such that ca. 67% of the 2VP moieties remained protonated, and 1.6% of the carboxylic groups stayed in their anionic form. To compensate for the low level of COOH ionization, a larger amount of COOH (from PAA-*b*-PHEA) was used as compared to N, i.e., a higher *f* ratio. The effective $f^* = CO_2^-/NH^+$ ratios for various *f* at pH 4.7 are listed as supporting information (Table S3-1).

pH	CO_2^- / total CO_2H[a]	NH^+ /total N[b]
1.4	0.00%	99.9%
4.7	1.6%	67%
7	76%	1%

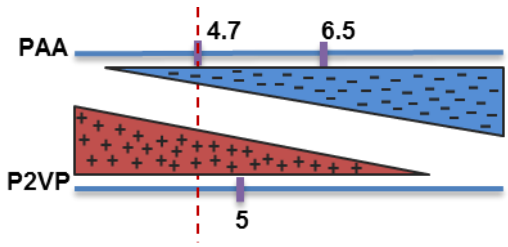

[a] Based on the Henderson–Hasselbalch equation for poly(acrylic acid), pK_a = 6.5

$$\mathrm{pH} = \mathrm{p}K_\mathrm{a} + \log\frac{[\mathrm{CO_2^-}]}{[\mathrm{CO_2H}]}$$

[b] Based on the Henderson–Hasselbalch equation for protonated poly(2-vinyl pyridine), pK_a = 5

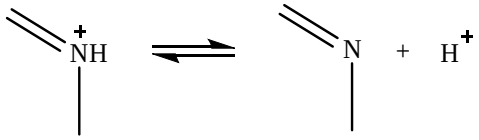

$$\mathrm{pH} = \mathrm{p}K_\mathrm{a} + \log\frac{[\mathrm{N}]}{[\mathrm{NH^+}]}$$

Figure 3-5. Ionization levels of CO_2H and N functional groups at different pH.

It should be mentioned that intermolecular hydrogen bonding between neutral COOH groups in the PAA segments and neutral N groups in P2VP, as illustrated in Figure 3-6, has been suggested by many authors.[34,40] This interaction is claimed to be the main driving force for complexations performed in organic solvents.[33-35,40,62] In aqueous environments at pH 4.7, the presence of multiple intermolecular hydrogen bonding interactions may also have assisted electrostatic interactions in the complexation process. However at pH 7 these hydrogen bonds should be perturbed due to increased ionization of the COOH groups, allowing electrostatic interactions to play a dominant role in the polyion complexation process.[61]

It is noteworthy that complexation at pH 4.7 was carried out for 1 h before the addition of NaOH to increase the pH to 7, at which point ca. 76% of the COOH functionalities should exist in their ionic form while much less (< 1%) of the N moieties stay protonated, which results in the negatively charged PIC micelles obtained at every *f*

investigated (Figure 3-5). Electrostatic repulsion between these negatively charged PIC micelles, as indicated by their zeta potential values (Figure 3-9), may have contributed significantly to colloidal stabilization of the particles, in addition to steric stabilization by the PHEA chains bearing multiple OH groups.

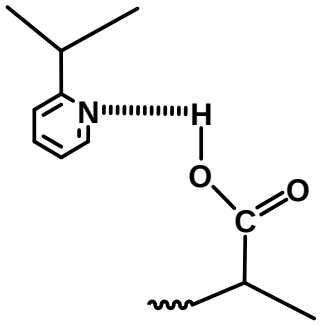

Figure 3-6. Hydrogen bonding between a P2VP unit and a PAA unit.

3.4.2.1 Dynamic Light Scattering Measurements

Nanoparticles with a diameter below 200 nm are preferable for *in vivo* biomedical applications in terms of systemic circulation.[63-67] The PIC process was therefore optimized in terms of its ability to yield exclusively unimolecular micellar structures, with only one G1 arborescent copolymer forming the core. The intensity-weighted hydrodynamic diameter D_h^I of the G1 copolymer at pH 4 was measured to be 29 ± 4 nm (PDI = 0.04), much larger than the hypothetical hard-core diameter (D_{G1} = 14.6 nm calculated from the density of PS and P2VP and the molar mass of the G1 polymer) for a collapsed PS-P2VP hydrophobic sphere as expected at pH 7. This D_{G1} = 14.6 nm value is however in good agreement with *i*) a diameter of 15 nm derived from a similar calculation by Sheiko et al.[68] for an arborescent grafted polystyrene G0PS-*g*-PS with the same $\bar{M}_w$; *ii*) R_g = 7.5 nm obtained from small-angle neutron scattering (SANS) measurements on G0PS-*g*-PS in *d*-cyclohexane and *d*-toluene,[69] and *iii*) R_g = 7.3 nm estimated by fitting a core–shell model to the SANS data for an arborescent G0PS-*g*-P2VP copolymer in *d*-methanol.[70] The coiled dimensions of the PHEA

segment in the different block copolymers, ranging from 7.1 to 12.2 nm, suggests that the absolute maximum diameter of *unimolecular* PIC micelles (derived from a single G1 molecule) D_{max} should be in a range of ca. 29–40 nm. These should also have a narrow, unimodal size distribution, in analogy to the G1 copolymer substrate.

The efficacy of each DHBC as colloidal stabilizer was screened using dynamic light scattering (DLS) measurements. The intensity-weighted hydrodynamic diameters D_h^I and the size dispersity, defined in the cumulant analysis of DLS data by the polydispersity index (PDI, defined in Section 3.3.6) vs. the f ratio were used to compare the results, which are summarized in Figure 3-7, Figure 3-8, Figure 3-9, and Table 3-2. In all cases where an intensity-weighted unimodal size distribution was observed, similar results were also obtained for number- and volume-weighted distribution curves, but at slightly different peak positions. Since the intensity-weighted z-average D_h^I is obtained by cumulants analysis of the autocorrelation function of the scattered intensity and is proportional to the sixth power of the particle size, it is biased toward larger particle sizes, particularly in the case of bimodal distributions or aggregation. However when unimodal distributions are obtained, the number-weighted distribution mean diameter D_h^n is customarily used to describe the size of NPs with no bias toward larger sizes. The number-weighed diameters are reported here in parallel with the intensity-weighed values, and are used to provide more realistic dimensions of the NPs for comparison with other measurements providing number-weighted results (e.g., AFM analysis).

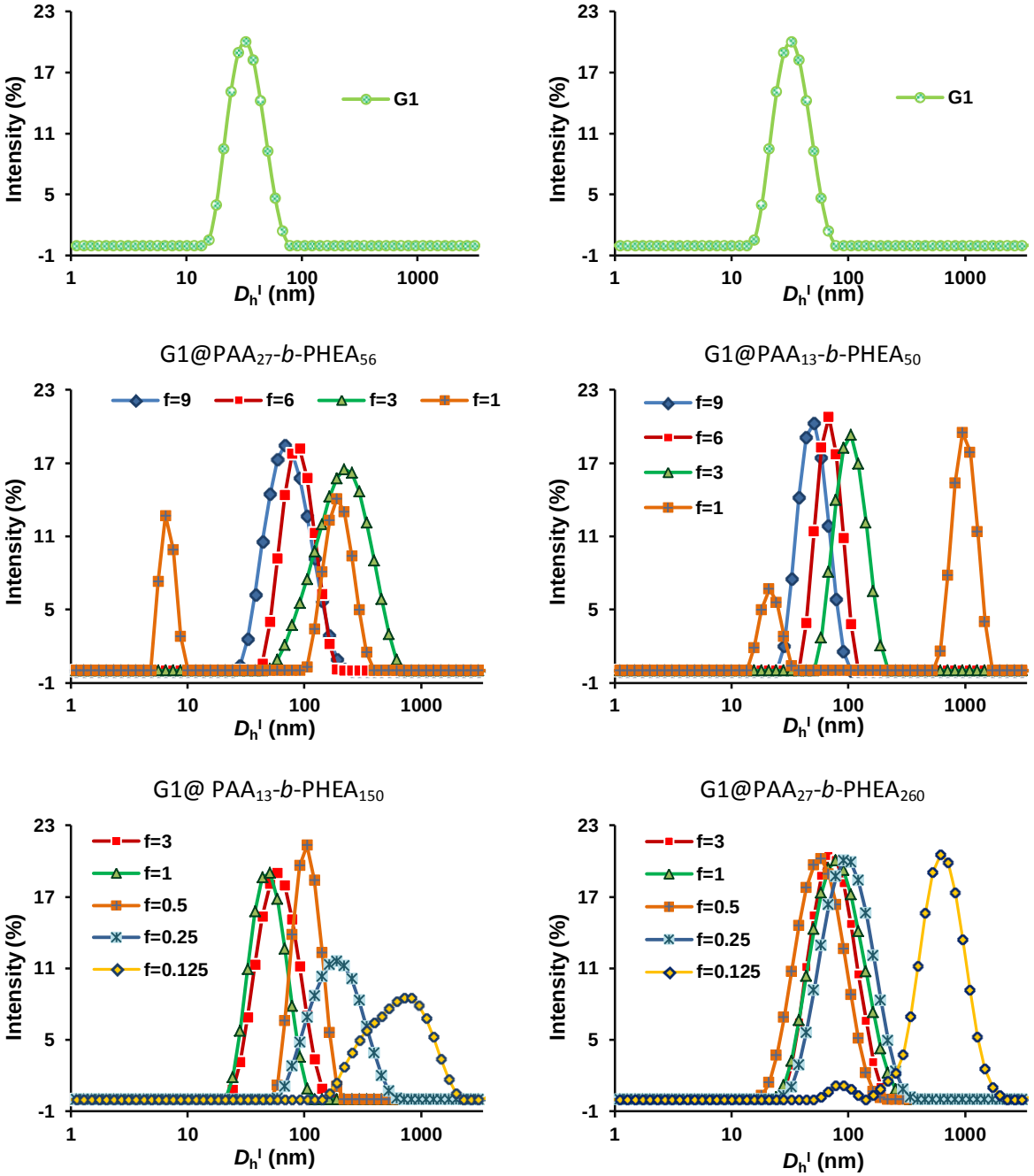

Figure 3-7. Intensity-weighted size distributions for G1 (pH 4) and G1@PAA-*b*-PHEA PIC micelles (pH 7) obtained at various *f* ratios at 25 °C**.**

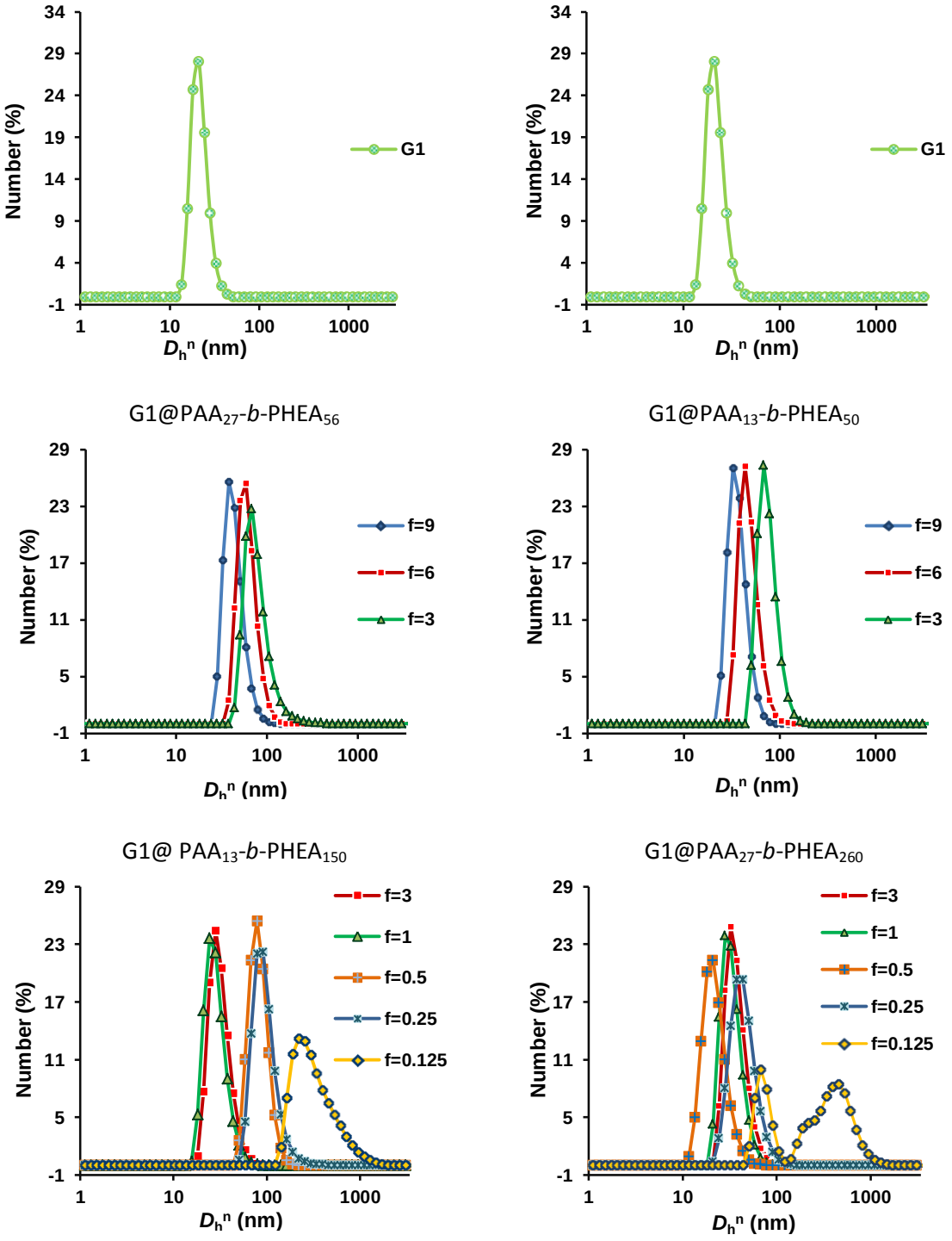

Figure 3-8. Number-weighted size distributions for G1 (pH 4) and G1@PAA-*b*-PHEA PIC micelles (pH 7) obtained at various *f* ratios at 25 °C**.**

Table 3-2. Hydrodynamic diameter and PDI of G1@PAA-*b*-PHEA PIC micelles (in water at pH 7) obtained for various *f* ratios at 25 °C. The optimal *f* values for each DHBC are **bolded**.

	f	**9**	**6**	**3**	**1**	**0.5**	**0.25**	**0.125**
G1@PAA$_{27}$-*b*-PHEA$_{56}$ (l_{PHEA} ≈ 7.3 nm, D_{max} ≈ 29 nm)	D_h^I/D_h^n (nm)[a]	**67/44**	84/61	184/80	1600	-	-	-
	PDI	**0.16**	0.10	0.20	~1	-	-	-
	δ^n (nm)[b]	**15**	-	-	-	-	-	-
	ZP (mV)	**-29**	-30	-28	-29			
G1@PAA$_{13}$-*b*-PHEA$_{50}$ (l_{PHEA} ≈ 7.1 nm, D_{max} ≈ 29 nm)	D_h^I/D_h^n (nm)[a]	**48/36**	66/45	100/75	1290	-	-	-
	PDI	**0.07**	0.10	0.07	~1	-	-	-
	δ^n (nm)[b]	**11**	-	-	-	-	-	-
	ZP (mV)	**-26**	-23	-13	-34			
G1@PAA$_{13}$-*b*-PHEA$_{150}$ (l_{PHEA} ≈ 10.1 nm, D_{max} ≈ 35 nm)	D_h^I/D_h^n (nm)[a]	-	-	50/32	**46/29**	104/83	169/98	660
	PDI	-	-	0.18	**0.14**	0.04	0.16	0.47
	δ^n (nm)[b]	-	-	9	**7**	-	-	-
	ZP (mV)			-13	**-15**	-14	-18	-31
G1@PAA$_{27}$-*b*-PHEA$_{260}$ (l_{PHEA} ≈ 12.2 nm, D_{max} ≈ 39 nm)	D_h^I/D_h^n (nm)[a]	-	-	63/37	51/34	**42/26**	87/53	642
	PDI	-	-	0.18	0.13	**0.08**	0.18	0.44
	δ^n (nm)[b]	-	-	11	10	**6**	-	-
	ZP (mV)			-19	-17	**-15**	-18	-34

[a] D_h^I and D_h^n: intensity-weighted and number-weighted hydrodynamic diameters

[b] Thickness of protecting layer $\delta^n = \frac{1}{2}[D_{h(PIC)}^n - D_{G1}]$ of assumed unimolecular micelle, where D_{G1} ≈ 14.6 nm for a collapsed spherical PS-*g*-P2VP core

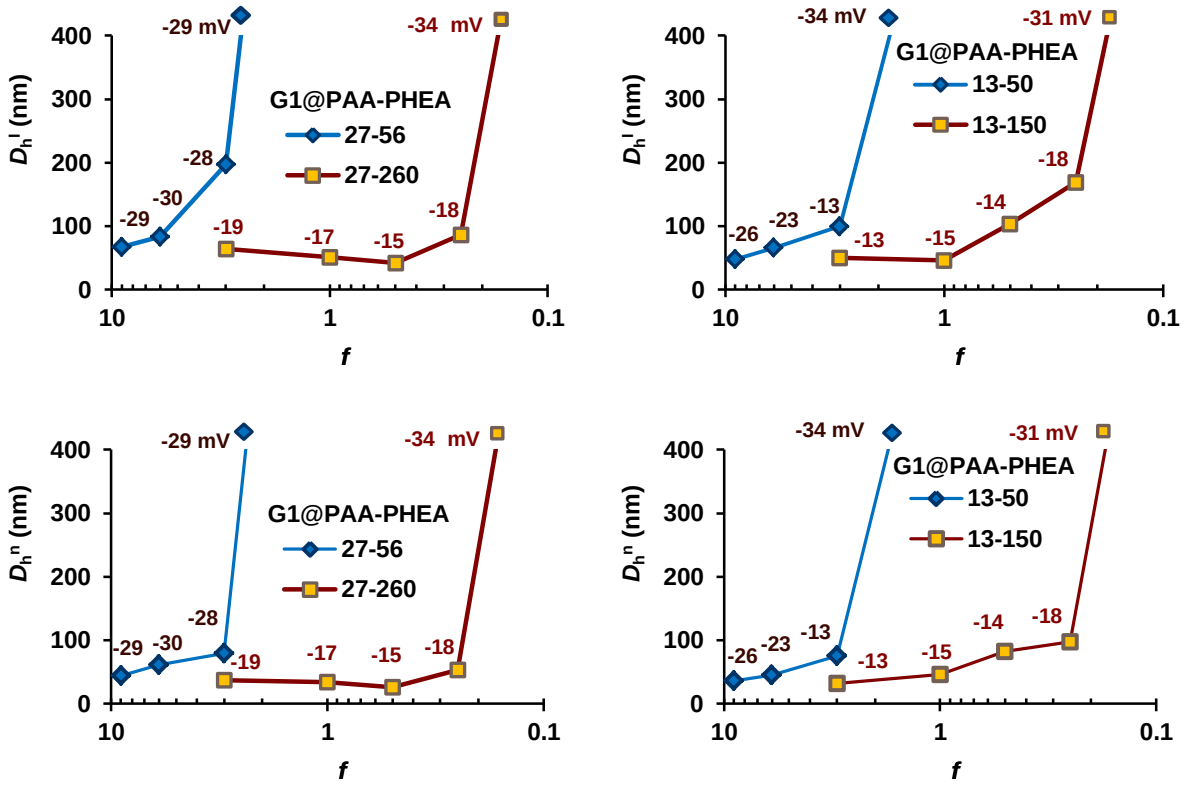

Figure 3-9. Intensity- or number-weighted hydrodynamic diameter and zeta potential of PIC micelles. The last points are not connected with the lines as they were off-scale.

3.4.2.1.1 G1@PAA_{27}-*b*-$PHEA_{56}$

The first polymeric stabilizer investigated had $\bar{M}_n$ = 8,090 g/mol, close to $\bar{M}_n \approx$ 10,000 g/mol suggested to achieve good colloidal stability (Section 3.2.1). That polymer may thus impart sufficient steric stabilization to the system even without the additional contribution from electrostatic repulsion. The coiled dimensions of the PHEA block l_{PHEA} was calculated to be 7.3 nm, which suggests a maximum diameter for unimolecular PIC micelles of ca. 29 nm. As shown by the charge equivalence calculation provided in Table S3-1, this DHBC may stabilize the G1 copolymer, but only for $f > 1$. It should be mentioned that for $f = 1$, the G1 and BC molecules agglomerated to form 1.6 µm diameter particles, confirming the inability of the BC chains to form a dense-enough polymeric shell to stabilize the G1 molecules. The

very negative zeta potential of the aggregates (–29 mV) also confirms the excess of CO_2^- at pH 7 in the aggregates, as predicted previously. At this ratio, even a combination of electrostatic and steric stabilization was insufficient to prevent flocculation of the G1 substrate. The arborescent polymers assembled into larger particles to reduce their surface area, until the protecting shell composed of the limited amount of BC chains and the negative charge from CO_2^- groups sufficed to stabilize the system.

For f = 3, 6 and 9, stable PIC micelle dispersions were obtained with D_h^n values of 80, 61 and 44 nm, respectively, closer to the size of the collapsed G1 core. Increasing the f ratio provided more BC chains to the stabilizing shell and increased the CO_2^- density surrounding the G1 molecules, leading to larger electrosteric repulsions, as well as smaller and more stable particles due to their enhanced colloidal stability. However even for the highest ratio (f = 9), the micelles do not seem to be unimolecular since the D_h^n = 44 nm is much larger than the maximum calculated diameter $D_{max} \approx$ 29 nm. This multimolecular hypothesis is confirmed by the larger thickness $\delta^n \approx$ 15 nm as compared to $l_{PHEA} \approx$ 7.3 nm. Due to its lowest diameter observed among the PIC micelles tested, f = 9 was selected as the optimal ratio for this system.

3.4.2.1.2 G1@*PAA$_{13}$-b-PHEA$_{50}$*

This DHBC, designed with a PAA chain length half as large as the previous one whilst maintaining a comparable length for the PHEA block, would be expected to provide better stabilization for the G1 substrate. Indeed when PAA$_{27}$-*b*-PHEA$_{56}$ and PAA$_{13}$-*b*-PHEA$_{50}$ are used at the same f ratio, the latter corresponds to twice as many BC chains for the same number of COOH functionalities. Although this polymer has $\bar{M}_n$ = 5,580 g/mol, lower than PAA$_{27}$-*b*-PHEA$_{56}$ and the 10,000 g/mol limit (Section 3.2.1), it could perform comparably to the previous polymer. The coiled dimensions of the PHEA$_{50}$ block was calculated to be $l_{PHEA} \approx$ 7.1 nm, which suggests that the maximum diameter of unimolecular PIC micelles would be ca. 29 nm.

For f = 3 the D_h^n of the PIC micelles was 75 nm, i.e., as large as for PIC micelles with PAA_{27}-*b*-$PHEA_{56}$ at the same f, whilst the size distribution was much narrower (PDI = 0.07). A decrease in number-weighted PIC micelle diameter (to 45 and 36 nm) was also observed for f = 6 and f = 9, respectively, lower than for PIC micelles derived from PAA_{27}-*b*-$PHEA_{56}$**.** This indicates that the particles are better shielded by a higher density of stabilizing segments. The contribution from electrostatic repulsion to PIC micelle stability may also be more important in this case, due to reduced steric repulsion caused by shortening of the BC chains.

The optimal composition of this system was determined to be for f = 9, at which point 36 nm diameter PIC micelles with a very narrow size distribution (PDI = 0.07) were obtained. This is still larger than the maximum diameter $D_{max} \approx 29$ nm and the thickness $\delta^n > l_{PHEA}$, which suggests that these micelles are not unimolecular. In spite of the lower molar mass of PAA_{13}-*b*-$PHEA_{50}$ as compared to PAA_{27}-*b*-$PHEA_{56}$, the DHBC with a shorter PAA segment produced smaller but still stable PIC micelles. The optimal f = 9 noted is still relatively high however. To provide better protection, a DHBC with the same PAA chain length but a longer PHEA block, PAA_{13}-*b*-$PHEA_{150}$, was designed and tested as stabilizer.

3.4.2.1.3 G1@PAA_{13}-*b*-$PHEA_{150}$

This block copolymer, with $\bar{M}_n$ = 18,300 g/mol and a PHEA chain three times larger than PAA_{13}-*b*-$PHEA_{50}$ ($l_{PHEA} \approx 10.1$ nm), should provide unimolecular PIC micelles with $D_{max} \approx 35$ nm. Better stabilization was observed for a ratio f = 3, yielding PIC micelles with D_h^n = 32 nm (smaller than $D_{max} \approx 35$ nm) and a relatively narrow size distribution (PDI = 0.18). The seemingly unimolecular character of these micelles highlights the advantages of this third polymer. The thicker PHEA shell (shell thickness $\delta^n \approx 9$ nm, exceeding the 5 nm effective distance of the van der Waals forces) provides enhanced steric stability for the PIC micelles, which favors the formation of unimolecular species even though the contribution from electrostatic stabilization is fairly small (ZP = –13 mV).

Stabilization was also investigated for f =1, yielding PIC micelles with D_h^n = 29 nm, PDI = 0.14 and ZP = –15 mV. These PIC micelles are still considered unimolecular, with a shell thickness $\delta^n \approx 7$ nm. Reducing the f ratio from 3 to 1 decreased the density of BC in the micelles 3-fold, such that steric stabilization due to the long polymer chains likely dominated colloidal stability. These results show that by introducing more HEA units into the polymeric stabilizer, the colloidal stability of the PIC micelles changed from electrosteric (a combination of electrostatic repulsion and steric stabilization, when using short PHEA chains) to predominantly steric stabilization (when employing longer PHEA blocks).

Upon reducing the f ratio further to 0.5, 0.25 and 0.125, the decreased density of BC chains in the PIC assemblies led to flocculation. The fact that the optimal f for this DHBC is f = 1 stills confirms the benefits of using longer PHEA chains as stabilizer.

3.4.2.1.4 G1@*PAA$_{27}$-b-PHEA$_{260}$*

While the goal of determining the characteristics required for a DHBC to stabilize a G1 arborescent copolymer and form unimolecular structures was already achieved to some extent, understanding and controlling the size of PIC micelles by tuning the BC chain segment lengths was also an interesting challenge. Polymer PAA$_{27}$-*b*-PHEA$_{260}$ ($l_{PHEA} \approx 12.2$ nm) was designed to roughly double the size of the most effective BC tested up to this point (PAA$_{13}$-*b*-PHEA$_{150}$). The D_h^n of the PIC micelles obtained for f = 3 and f = 1 was comparable with micelles formed by PAA$_{13}$-*b*-PHEA$_{150}$, but interestingly the layer thickness increased by ca. 2–3 nm, in agreement with the larger dimensions of the PHEA chains. When comparing PAA$_{27}$-*b*-PHEA$_{260}$ with PAA$_{27}$-*b*-PHEA$_{56}$ at the same f, for example, the G1@PAA$_{27}$-*b*-PHEA$_{260}$ f = 1 PIC micelles were efficiently stabilized by the long chain BC, whilst G1@PAA$_{27}$-*b*-PHEA$_{56}$ f = 1 aggregated due to insufficient steric stabilization by the short BC chains.

The influence of steric stabilization imparted by longer BC chains is also evident for f = 0.5. Indeed, the PIC micelles G1@PAA$_{27}$-*b*-PHEA$_{260}$ f = 0.5 had D_h^n = 26 nm, fairly close to the size of the collapsed G1 core ($D_{G1} \approx 14.6$ nm, $\delta^n \approx 6$ nm), and a narrow size

distribution (PDI = 0.08) confirms their unimolecular structure. The G1@PAA_{27}-*b*-$PHEA_{260}$ *f* = 0.5 PIC micelles are the smallest colloidally stable micelles obtained. The ca. 6 nm shell thickness gives a closest distance of approach between two cores of 12 nm, still exceeding the 5 nm minimum effective distance[1] and further confirming the superior stabilization ability of this BC. Further reductions in the *f* ratio led to fewer BC chains per micelle. For *f* = 0.25 and 0.125, the BC content was insufficient for stabilization of the G1 copolymer in its unimolecular form, which led to the formation of larger, multimolecular species.

The most efficient BC tested for the preparation of unimolecular micelles was therefore PAA_{27}-*b*-$PHEA_{260}$, as it maintained a sufficient thickness for the protecting shell while allowing a sufficient density of BC chains to cover the G1 substrate. For these polymers, the optimal *f* was about 0.5–1.

3.4.2.2 Determination of Refractive Index Increment

Further investigations using static light scattering measurements were performed to confirm the unimolecular character of the PIC structures. To determine the molar mass of polymers accurately by light scattering, the refractive index increment (d*n*/d*c*) of the samples must be determined. The refractive index increment of three of the PIC micelle dispersions was thus determined at 25 °C and λ = 658 nm, i.e., the same conditions used in the static light scattering measurements. Among the PIC micelles obtained, the ones incorporating the long chain BC were of particular interest due to their good stability and uniform size. We also selected these three systems due to their smaller size, to minimize intraparticle scattering effects and to avoid sedimentation of the particles. Moreover, the concentration of the dispersions was maintained in a low range (0.2–1.0 mg/mL) for the analysis. The refractive index increment of the three selected PIC micelle dispersions was determined by plotting the refractive index of each dispersion vs. concentration. The d*n*/d*c* values, corresponding to the slope of the graphs, are listed in Table 3-3.(top).

Table 3-3. Measured (top) and calculated (bottom) refractive index increments of selected PIC micelles.

Samples	**G1@PAA$_{13}$-*b*-PHEA$_{150}$**	**G1@PAA$_{27}$-*b*-PHEA$_{260}$**	
f	3	1	0.5
%wt G1	3.3	10.5	16.5
d*n*/d*c* (mL/g)	0.1294 ± 0.0005	0.1367 ± 0.0002	0.1389 ± 0.0004
R^2	0.99993	0.99999	0.99996

Samples	**G1@PAA$_{13}$-*b*-PHEA$_{150}$**			**G1@PAA$_{27}$-*b*-PHEA$_{260}$**		**G1@PAA$_{13}$-*b*-PHEA$_{50}$**	**G1@PAA$_{27}$-*b*-PHEA$_{56}$**
f	1	0.5	0.25	3	0.25	9	9
%wt G1	7.9	15.3	31.1	3.4	36.8	3.4	5.9
Cal. d*n*/d*c* (mL/g)	0.1334	0.1388	0.1503	0.1301	0.1545	0.1301	0.1319

The d*n*/d*c* values for the PIC micelles display consistent trends, with a magnitude increasing with the weight fraction of the higher refractive index components (PS and P2VP) as expected. The correlation coefficients were higher than 0.9999 in all cases. The linear correlation found between d*n*/d*c* vs. composition (Figure 3-10) was used to interpolate the d*n*/d*c* values for the other PIC systems (Table 3-3. bottom).

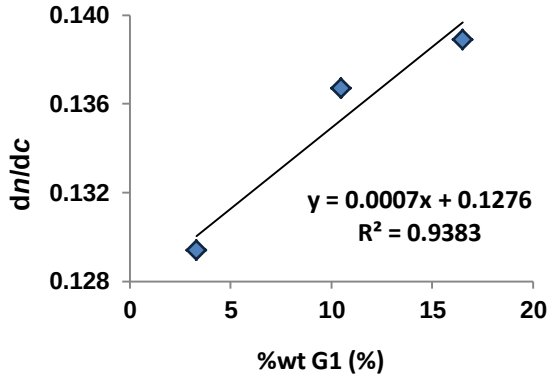

Figure 3-10. Measured d*n*/d*c* of the PIC micelles as a function of composition.

3.4.2.3 Multi-Angle Laser Light Scattering

The data from multi-angle laser light scattering (MALLS) measurements were extrapolated to zero concentration and angle by the Zimm technique (Figure 3-11 to Figure 3-13) to determine the mass-average absolute molar mass ($\bar{M}_w$) of the PIC micelles, their radius of gyration (R_g), and second virial coefficient (A_2) as summarized in Table 3-4.

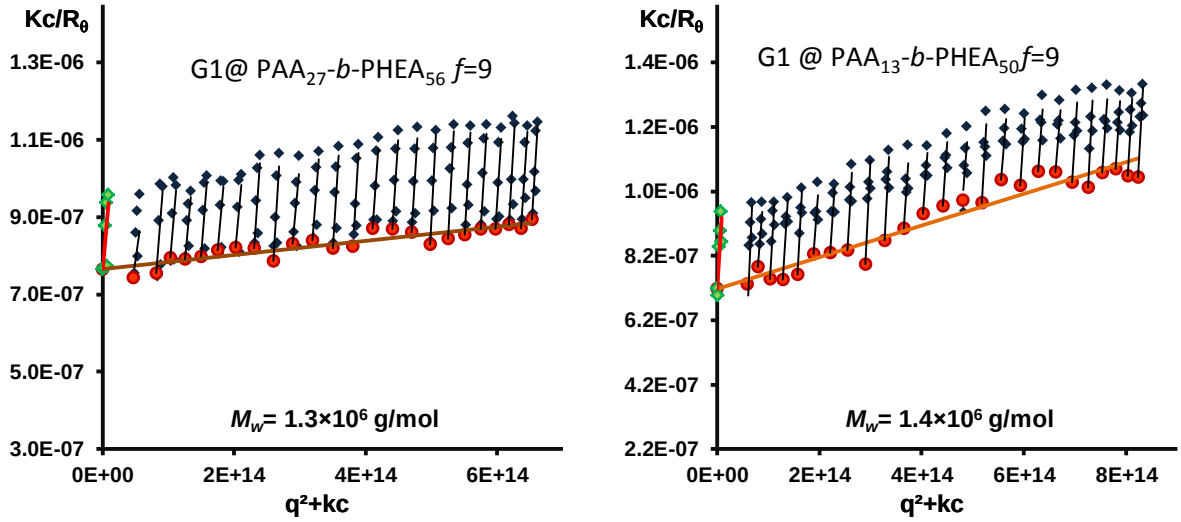

Figure 3-11. Zimm plots for PIC micelles G1@PAA$_{27}$-*b*-PHEA$_{56}$ and G1@PAA$_{13}$-*b*-PHEA$_{50}$ for f = 9.

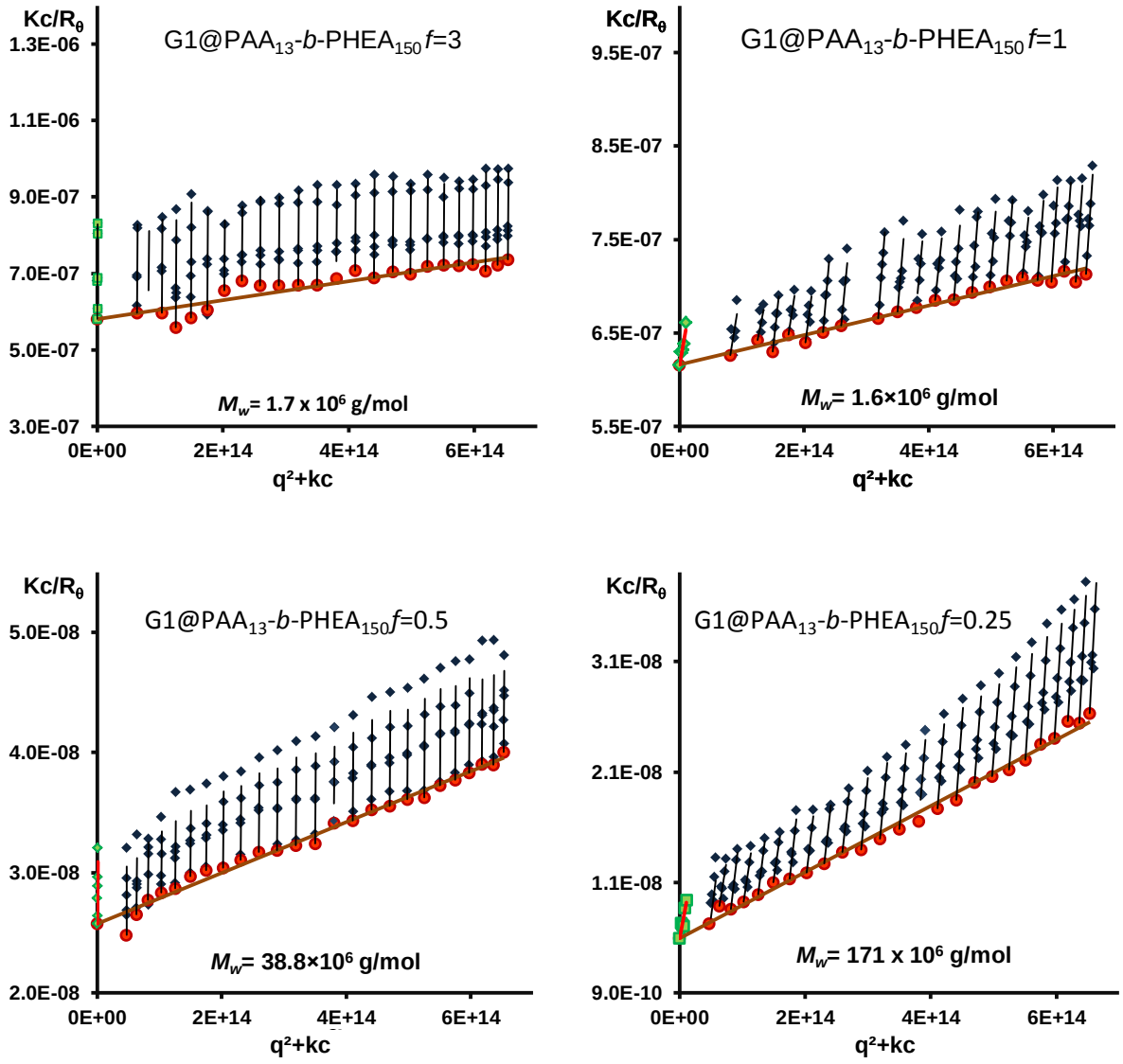

Figure 3-12. Zimm plots for PIC micelles G1@PAA$_{13}$-*b*-PHEA$_{150}$ for different *f* ratios.

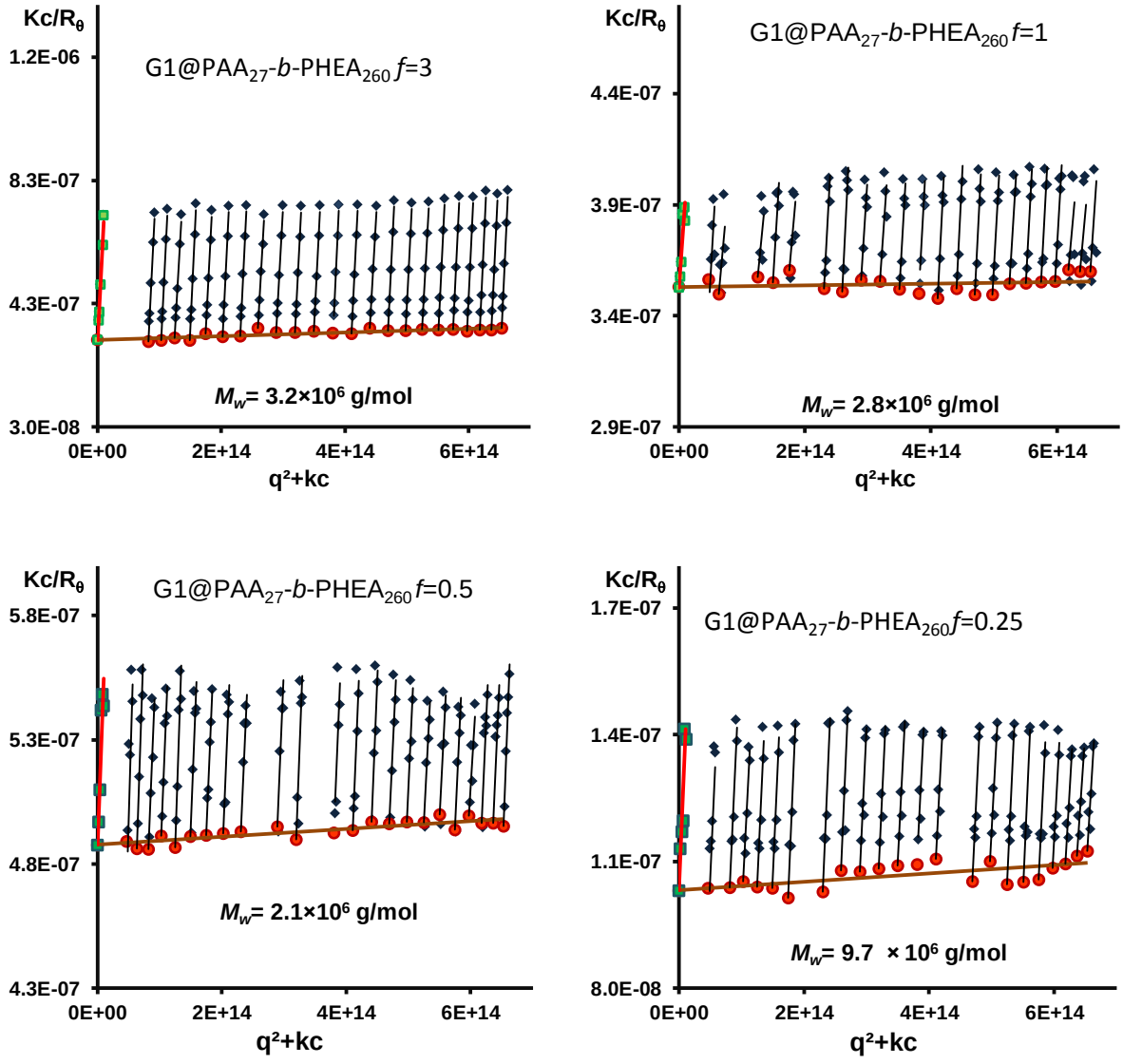

Figure 3-13. Zimm plots for PIC micelles G1@PAA_{27}-*b*-$PHEA_{260}$ for different *f* ratios.

The uni- vs. multimolecular character of the PIC micelles may be evaluated by comparison of the experimental mass-average molar mass $\bar{M}_{w(Exp)}$ obtained from SLS data analysis with the molar mass of the arborescent substrate ($\bar{M}_{w(G1)}$ = 1.1×10^6 g/mol) and the theoretical molar mass based on the amounts of each component used in the complex formation, $\bar{M}_{w(Theor)} = \bar{M}_{w(G1)}\times wt_{(G1+BC)}/wt_{(G1)}$ where $wt_{(G1+BC)}$ is the total weight of PIC

micelles recovered after dialysis. The formation of unimolecular micelles can be confirmed if $\bar{M}_{w(Exp)}$ is in a range comparable to $\bar{M}_{w(G1)}$, while for $\bar{M}_{w(Exp)} > \bar{M}_{w(Theor)}$ the formation of aggregates is unambiguously demonstrated. The radius of gyration, when combined with the hydrodynamic radius (from the DLS measurements) provides further hints about the structure of the PIC micelles, whilst the magnitude of the second virial coefficient A_2 characterizes the interactions between the PIC micelles and the solvent.

Table 3-4. Data derived from the SLS and DLS measurements on PIC micelles.

G1@ PAA_x-*b*-$PHEA_y$	f	$\bar{M}_w$ (10^6 g/mol) Theor.	Exp.	#BC /PIC	R_g (nm)	R_h (nm)	ρ	A_2 (10^{-5} $cm^3 \cdot mol \cdot g^{-2}$)
27-56	9	18.7	1.3	22	26.7	33.5	0.80	9.5
13-50	9	32.5	1.4	54	45.3	24	1.89	12.1
13-150	3	33.2	1.7	33	35.8	25	1.43	12.3
	1	14.0	1.6	27	27.7	23	1.20	1.8
	0.5	7.2	39	-	49.6	52	0.95	0.3
	0.25	3.5	170	-	124	84.5	1.47	0.2
27-260	3	32.8	3.2	68	23.9	32	0.76	19.3
	1	10.5	2.8	51	12.2	25.5	0.48	1.9
	0.5	6.6	2.1	32	9.9	21	0.47	3.3
	0.25	2.9	9.7	-	17.4	43.5	0.40	1.7

3.4.2.3.1 Uni- vs. *Multimolecular Micelles*

The unimolecular character of PIC micelles prepared from the BC with long PHEA segments, G1@PAA_{13}-*b*-$PHEA_{150}$ with f = 3 and 1, and G1@PAA_{27}-*b*-$PHEA_{260}$ with f = 0.5 was previously concluded from the DLS measurements. This is also confirmed by the SLS data since $\bar{M}_{w(Exp)} < 2\times\bar{M}_{w(G1)}$ with $\bar{M}_{w(G1)} = 1.1\times10^6$ g/mol. This is probably also true for G1@PAA_{27}-*b*-$PHEA_{260}$ f = 3 and f = 1, for which $\bar{M}_{w(Exp)} < 3\times\bar{M}_{w(G1)}$ and unimolecular character was likewise concluded from the DLS measurements when comparing the D_h^n of the arborescent substrate and the PIC micelles. This assumption allows the calculation of the

average number of BC chains shielding a G1 core in the micelles. For the five samples deemed to be unimolecular in nature the number of BC chains per micelle varies from 27 PAA_{13}-*b*-$PHEA_{150}$ surrounding one G1 core for f = 1, to 68 molecules for G1@PAA_{27}-*b*-$PHEA_{260}$ with f = 3. The number of BC molecules per micelle increased as the amount of BC (f ratio) used in their preparation increased, which seems reasonable. It is also larger for the PAA_{27}-*b*-$PHEA_{260}$ sample series in comparison to the PAA_{13}-*b*-$PHEA_{150}$ samples, in spite of the longer $PHEA_{260}$ segment increasing BC bulkiness. This highlights the dominating influence of the anchoring PAA segment length in determining the number of BC chains incorporated in the PIC micelles.

The $\bar{M}_{w(Exp)}$ reported for PIC micelles G1@PAA_{13}-*b*-$PHEA_{150}$ with f = 0.5 and 0.25, and G1@PAA_{27}-*b*-$PHEA_{260}$ with f = 0.25 being larger than $\bar{M}_{w(Theor.)}$, the G1 cores clearly flocculated due to the lack of stabilizer within the PIC shell. Contrary to our expectations, the G1@PAA_{13}-*b*-$PHEA_{50}$ and G1@PAA_{27}-*b*-$PHEA_{56}$ systems with f = 9, thought to be multimolecular on the basis of the DLS measurements, were found to have $\bar{M}_{w(Exp)} < 2\times\bar{M}_{w(G1)}$. The expected structure of these two assemblies will be further discussed on the basis of their ρ-parameter below.

3.4.2.3.2 ρ-Parameter

The ratio R_g/R_h, also known as the ρ-parameter, is structure-sensitive and may provide information on the morphology of PIC micelles. For example, ρ = 0.775 is expected for spheres of uniform density[71] (also called rigid spheres), while ρ = 1.7–2.0 is typically observed for randomly coiled polymer chains.[72-73] The situation can be more complicated when the density of the molecules or particles is highly heterogeneous however, e.g., for particles combining a dense core and partly coiled, less dense chain segments forming a shell. Due to the small radius of gyration of these systems resulting from concentration of the mass within their core, ρ values below the rigid sphere "limit" are often observed. Furthermore, values close to 0.775 do not necessarily reveal a rigid sphere morphology for inhomogeneous systems (as is customarily assumed for homogenous materials), but it more

likely reflects a core–shell structure with non-homogenous density. The ρ-parameter remains a useful tool to obtain information on particle morphology, but it must be used with caution and one must also consider the composition of the material and its behavior under the conditions used for its characterization, as illustrated in the following examples.

1. ρ Below the Rigid Sphere Limit

Spherical PS microgels synthesized by microemulsion polymerization with cross-linking within the restricted micellar volume were reported to have $0.58 < \rho < 0.68$.[74] The solvent used for the measurements was toluene, a good solvent for linear and lightly cross-linked PS, but a bad solvent for a rigid, highly cross-linked PS. The low ρ-parameter values found for both lightly ($0.58 < \rho < 0.61$) and moderately cross-linked microgels ($0.61 < \rho < 0.68$) were attributed to the different swelling behaviors of the outer shell and the core. This phenomenon decreased the mass concentration of material in the shell relatively to the core. The result $\rho = 0.741$ was also obtained for highly cross-linked microgels, that acted essentially like spheres of homogenous density ($R_g = 58$, $R_h = 78$ nm).

Micelles formed by the self-assembly of polystyrene-*block*-poly(methacrylic acid) PS-*b*-PMAA and of triblock PMAA-*b*-PS-*b*-PMAA copolymers were reported to have ρ values ranging from 0.37 to 1.23, when characterized in a dioxane : water 80:20 v/v solvent mixture.[75] Values between 0.37 and 0.6 were assigned for structures with polystyrene segregated within the micellar core, surrounded by less dense PMAA segments. More interestingly, $\rho \sim 0.9$ was explained by the presence of micellar clusters corresponding to two micelles touching each other to form a dumbbell. Similar values were obtained for other small clusters, while longer linear (pearl necklace-like) clusters yielded much larger values.[75]

2. ρ Above the Rigid Sphere Limit

It is also possible for a core–shell structure to have $\rho > 0.775$, as reported for CdS@PS-*b*-PMMA nanoparticles with $\rho = 1.1–1.3$.[76] In toluene, the quantum dots were covered by a shell of both swollen PMMA and PS chain segments ($R_g = 41$ nm, $R_h = 31$ nm,

ρ = 1.3). Collapse of the PS chains onto the particles was observed when replacing toluene with acetone however, which gave rise to a dense core and partly coiled PMMA chain segments yielding a smaller ρ-value (R_g = 24 nm, R_h = 21 nm, ρ = 1.1). The shift in mass concentration to the core was concluded to be the main factor responsible for the smaller ρ-parameter.

3. ρ-Parameter for the PIC Micelles

A collapsed core–loose BC stabilizing shell morphology was postulated earlier for the arborescent PIC micelles, so these assemblies may fall in the second category above, depending on the relative masses of the G1 core and the BC shell components. For that reason, the trends in ρ observed among the different samples will be discussed separately below.

For the PIC micelles G1@PAA_{27}-*b*-$PHEA_{56}$ with f = 9, the value ρ = 0.80 obtained could suggest a structure behaving similarly to a rigid sphere. However the unexpectedly large average hydrodynamic diameter (D_h^n = 44 nm) as compared to the calculated maximum diameter for *unimolecular* PIC micelles ($D_{max} = D_{G1} + 2l_{PHEA} \approx 29$ nm) suggests an aggregation pattern corresponding to a mixture of unimolecular and multimolecular species. The average $\bar{M}_{w(Exp)}$ of these species being larger than $\bar{M}_{w(G1)}$ but less than $2\times\bar{M}_{w(G1)}$, this most likely results from a dominant population of unimolecular species in comparison to the other species. The situation could be similar for G1@PAA_{13}-*b*-$PHEA_{50}$ with f = 9, with ρ = 1.89 and a slightly larger $\bar{M}_{w(Exp)} = 1.4\times10^6$ g/mol (as compared to $\bar{M}_{w(Exp)} = 1.3\times10^6$ g/mol in the previous case) corresponding to more extensive aggregation.

It was previously concluded that PIC micelles G1@PAA_{13}-*b*-$PHEA_{150}$ with f = 3 and 1 were unimolecular. These micelles have ρ = 1.43 and 1.20, respectively, consistent with a core–shell structure (below the 1.7–2.0 range expected for randomly coiled chains). These values are still well above the rigid sphere value however, which evidences the large contribution from the mass of swollen BC chains in the shell surrounding the collapsed arborescent core. Among these two samples, the protecting shell was likely less dense for the

G1@PAA_{13}-*b*-$PHEA_{150}$ micelles with f = 1 than for f = 3, as evidenced by their somewhat lower $\bar{M}_{w(Exp)}$. This also led to smaller R_g (27.7 vs. 35.8 nm) and ρ (1.20 vs. 1.43) for f = 1, in agreement with our interpretation of the results.

The aggregates produced by PIC micelles G1@PAA_{13}-*b*-$PHEA_{150}$ with f = 0.5 had R_g = 49.6 nm and ρ = 0.95, suggesting the formation of a dense core from multiple G1 molecules, as indicated by the large $\bar{M}_{w(Exp)} = 3.9\times10^7$ g/mol obtained, surrounded by a loose shell of BC chains. This seems a normal consequence of decreasing the "feed" amount of BC in the self-assembly process. However this lower ρ-parameter value could also be due to the presence of small clusters composed of many PIC micelles, as shown in the work of Qin et al.[75] On the other hand, the ρ = 1.47 value obtained for the large aggregates of G1@PAA_{13}-*b*-$PHEA_{150}$ micelles with f = 0.25, apart from incorporating an even larger number of G1 molecules, more likely correspond to linear cluster structures, given that ρ is significantly larger than in the previous case.

Among the R_g values obtained for the G1@PAA_{27}-*b*-$PHEA_{260}$ system, only the values for f = 3 and 0.25 are considered reliable since the other two samples had $R_g < \lambda/20 \approx 15$ nm, i.e., dimensions in a range leading to large errors. On that basis, ρ = 0.76 obtained for the PIC micelles with f = 3 is considered consistent with a core–shell morphology. It is tempting to come to the same conclusion for f = 1 and 0.5, in spite of the large errors expected on the R_g values. Furthermore, the unimolecular PIC micelles in the G1@PAA_{27}-*b*-$PHEA_{260}$ series with f = 3, 1 and 0.5 exhibit a larger ρ-value for f = 3. This could be due to a more extended conformation for the BC chains in the shell of the f = 3 sample, resulting from increased steric crowding in this sample which has the highest molar mass among all the unimolecular samples ($\bar{M}_{w(Exp)} = 3.2\times10^6$ g/mol).

The aggregates produced by the PIC micelles G1@PAA_{27}-*b*-$PHEA_{260}$ with f = 0.25 were characterized by ρ = 0.40, indicating the formation of a dense collapsed core with a relatively small number of G1 molecules ($\bar{M}_{w(Exp)} = 9.7\times10^6$ g/mol). This is presumably due to the low colloidal stability achieved for f = 0.25.

3.4.2.3.3 Second Virial Coefficient A_2

The second virial coefficient (A_2) of polymers in solution obtained from SLS data is a measure of solvent quality. Its magnitude depends on the solvent-polymer interactions, as well as the molar mass of the polymer and its architecture through scaling relationships of the type $A_2 \propto \bar{M}_w^{a}$.[72] The second virial coefficient is thus a weakly decreasing function of the polymer molar mass as $A_2 \propto \bar{M}_w^{-0.2}$ for linear polymers,[77] but this molar mass dependence is more pronounced for star-branched structures.[72] For highly branched polymers displaying rigid sphere behavior such as the arborescent polymers, the scaling relationship reaches $A_2 \propto \bar{M}_w^{-1}$.[78]

Since structural variations are fairly small among the different PIC micelles obtained, the A_2 values should reflect mainly solvent–polymer interactions. All the measured A_2 values are positive, reflecting favorable interactions between the –OH groups on the PHEA segments of the PIC micelles with the solvent (water). However, the range of values observed (from 0.2×10^{-5} to 19.3×10^{-5} $cm^3\cdot mol\cdot g^{-2}$) is indicative of variations in the quality of these solvent–polymer interactions as follows:

1. Values in the high end were observed mostly for systems with $f > 1$, regardless of the specific BC used, thus reflecting the importance of interactions between the -OH groups on the PHEA chains and water.
2. A decrease in A_2 values was observed for lower f ratios among the series of PIC micelles derived from the same BC type. This is also consistent with the first statement.
3. Comparisons among the PIC micelles G1@PAA_{13}-*b*-$PHEA_{150}$ and G1@PAA_{27}-*b*-$PHEA_{260}$ at the same f ratio produce the same result: The A_2 values for the former are smaller than for the latter. This is again related to differences in the number of –OH groups per PIC micelle. Taking $f = 3$ as an example, the G1@PAA_{13}-*b*-$PHEA_{150}$ micelle had ca. 5,000 –OH groups provided by 33 BC side chains; G1@PAA_{27}-*b*-$PHEA_{260}$ carried ca. 17,500 –OH groups on 68 BC side chains.

The lowest A_2 values are observed for the aggregated systems as expected: The largest PIC micelle G1@PAA_{13}-*b*-$PHEA_{150}$ with $f = 0.25$ ($\bar{M}_w = 170\times10^6$ g/mol) had $A_2 = 0.2\times10^{-5}$

and so on. There is no obvious correlation between A_2 and the $\overline{M}_w$ of the PIC micelles for the aggregated systems however, possibly because the PIC micelles have a heterogeneous chemical composition: the hydrophobic G1 and the hydrophilic PAA-PHEA components. Considering the dominating contribution from –OH/water interactions to A_2, a correlation was found between the number of –OH groups in the molecules and the A_2 values for non-aggregated systems with $f > 1$ (Figure 3-14).

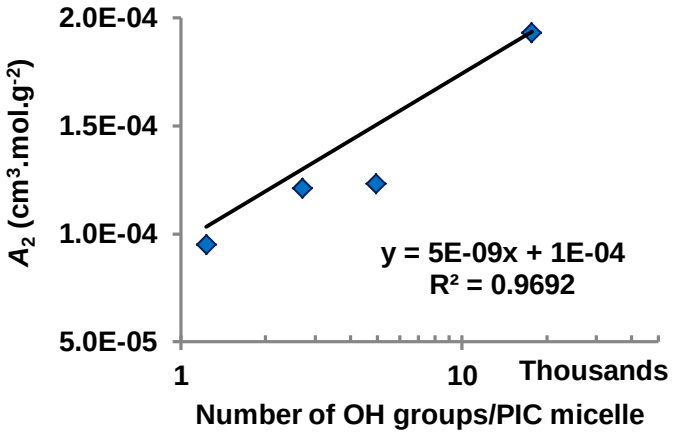

Figure 3-14. Dependence of A_2 on the number of –OH groups/PIC micelle.

3.4.2.4 pH Responsiveness of PIC Micelles

The zeta potential of the PIC micelles G1@PAA_{27}-*b*-$PHEA_{260}$ for f = 0.5 was investigated and found to be pH-dependent. A large negative potential (ca. –27 mV) was measured at pH ≥ 7 (Figure 3-15), due to the presence of CO_2^- functionalities. The potential of the PIC micelles remained fairly constant under basic conditions, indicating complete ionization of the COOH groups beyond pH 7. The increase in zeta potential in the acidic pH range is assigned to protonation of the carboxylate groups, yielding the more hydrophobic COOH derivatives, and of the amine groups in the G1 core to yield hydrophilic NH^+ derivatives. The isoelectric point of the PIC micelles was around pH 4.

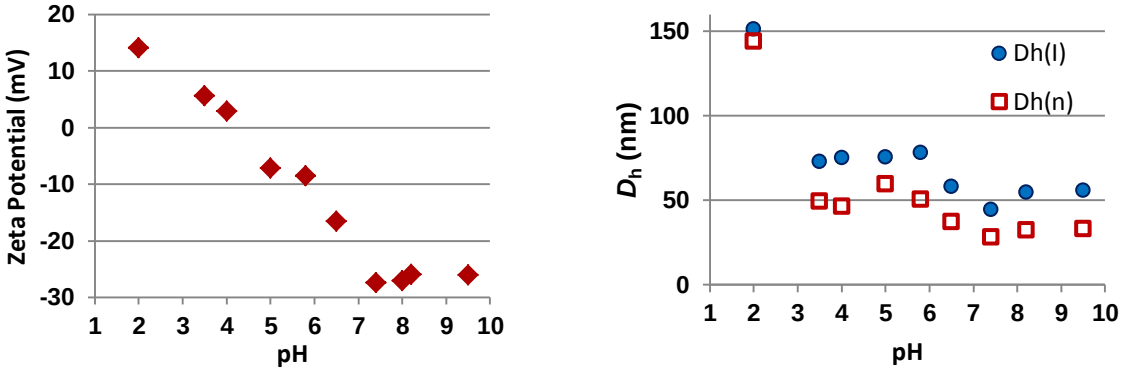

Figure 3-15. Zeta potential and hydrodynamic diameter of PIC micelles G1@PAA_{27}-*b*-$PHEA_{260}$ for f = 0.5 at different pH.

The corresponding pH-dependent variations in D_h^I and D_h^n of the PIC micelles were similar (Figure 3-15), thus the discussion of variations in D_h^n mirrors the trends seen in D_h^I. At pH 7.4 the number-weighted hydrodynamic diameter is 28.5 nm. Slight swelling of the PIC micelles to ca. 33 nm at pH 8–9.5 is probably caused by electrostatic repulsion among adjacent CO_2^- groups, even at higher ionic strengths due to the addition of 0.1 M NaOH. The hydrodynamic diameter of the micelles almost doubled when the pH was decreased from 7.4 to 5.8, and tripled at pH 2, indicating the formation of multimolecular PIC micelles. At the isoelectric point (pH 4) the PIC micelles formed small clusters, but no PIC micelle dissociation was observed within the pH range tested. The changes in zeta potential and size were reversible over the range of pH ≥ 7 (unimolecular structures), while between 3.5 ≤ pH ≤ 6.5 small clusters formed that persisted even if the pH was brought back up to 7. The response of PIC micelles to pH variations could be useful for applications such as the preparation of metallic nanoparticles.

3.4.2.5 Atomic Force Microscopy

The size, size distribution, morphology and morphology of the G1 substrate and the PIC micelles were investigated by atomic force microscopy (AFM) imaging in the tapping mode. The samples were prepared by spin coating deposition of the materials onto freshly

cleaved mica surfaces. The G1 substrate, deposited from acidic solutions (pH 4), exhibited ill-defined morphologies because the arborescent graft copolymer flattened extensively on mica (visible more clearly on the phase image of Figure 3-16), presumably due to strong electrostatic interactions between the protonated G1 and negatively charged mica. Both the molecular diameter (ca. 43 nm, larger than the D_h^I= 29 nm in acidic solutions) and the height (ca. 1.9 nm) obtained by section analysis of the height image confirm strong flattening of the molecules.

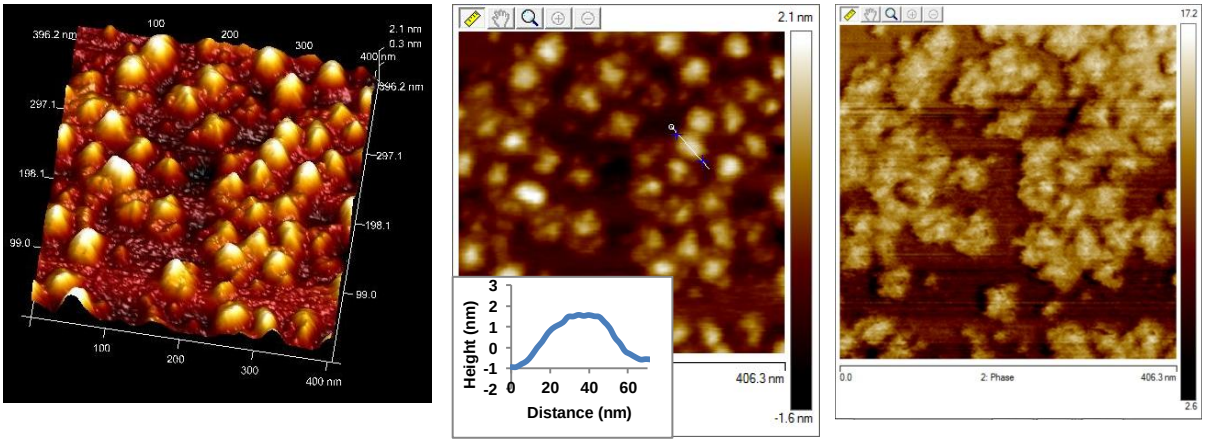

Figure 3-16. 3D model, height and phase AFM images (from left to right) for the G1 substrate.

It is noteworthy that the PIC micelles obtained after complexation appeared as uniformly distributed, almost spherical particles with a narrow size distribution on the mica surface. The spherical morphology of the PIC micelles, shown in the 3D images and in section analysis of the images (Figure 3-17, column 1), are attributed in part to electrostatic repulsions between the PIC micelles and mica, both negatively charged. In this case the particle diameter of the solid PIC micelles determined from section analysis was 27 nm, which was smaller than the D_h^I = 42 nm measured in the aqueous dispersions, and the height of particles was ca. 2.3 nm.

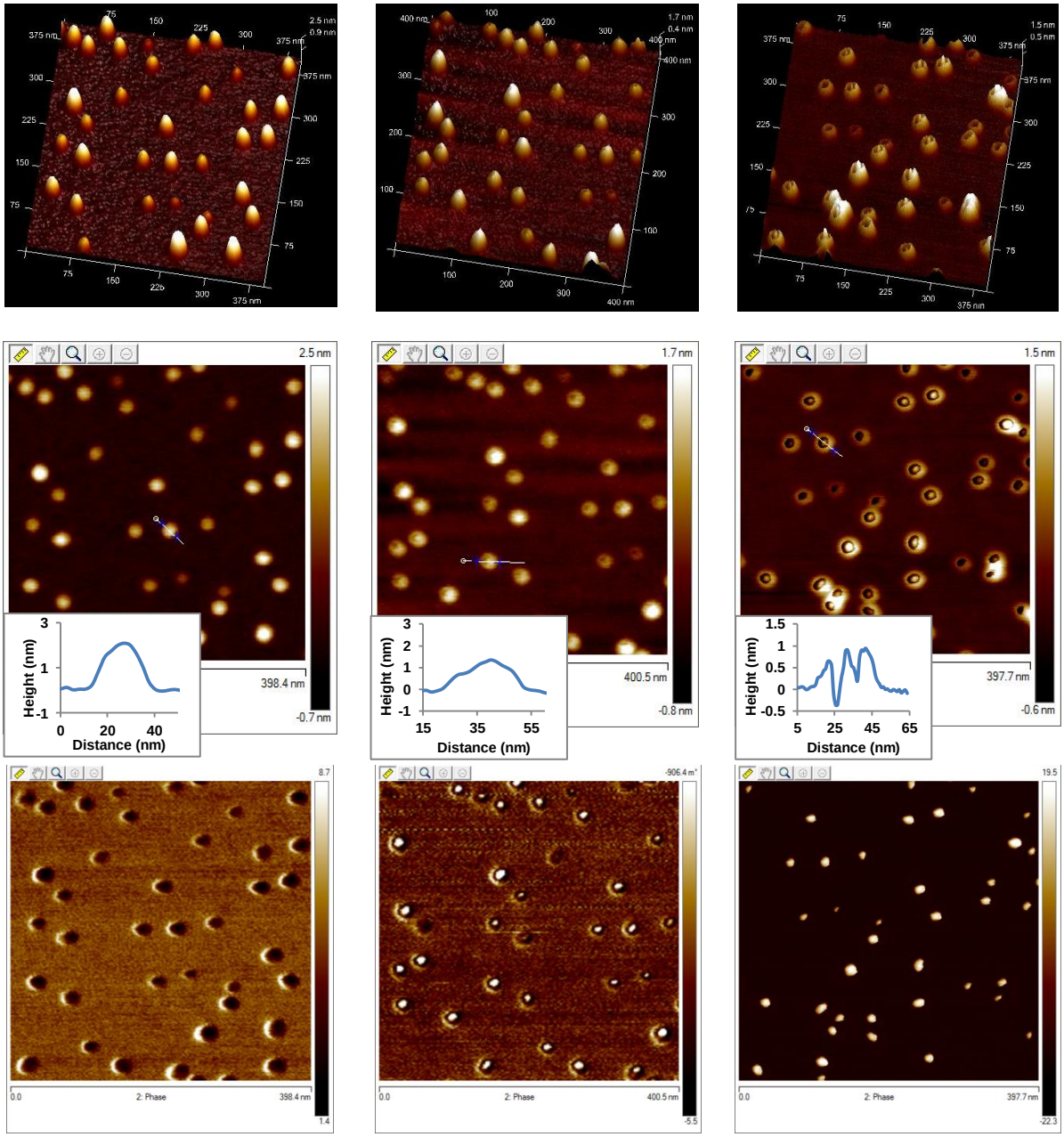

Figure 3-17. 3D models (row 1), height (row 2) and phase AFM images (row 3) for G1@PAA_{27}-*b*-$PHEA_{260}$ with f = 0.5 at set-points ratios of 0.96 (column 1), 0.92 (column 2), and 0.86 (column 3).

Phase imaging in the tapping mode can reveal nanometer-scale information on surface structure and properties often not detected by other microscopy techniques.[79-81] The phase lag (or phase shift) of the cantilever oscillations with respect to the applied force is sensitive to variations in composition, adhesion, friction, viscoelasticity, as well as other factors.[82-85] The dark domains of phase images have been assigned to "soft" materials in several reports,[83,86-87] whilst the bright regions were ascribed to stiffer phases. The surface of PIC micelles changed dramatically in comparison to the G1 substrate, from a "stiff" G0PS-*g*-P2VP matrix appearing in bright yellow color to a "soft" coating layer. This could be due to plasticization by water absorbed in the hydrophilic PHEA phase (indicated by black particles on the phase images). The size, size distribution and uniformity of the PIC particles provides strong evidence for the success of the polyion complexation process using DHBC PAA_{27}-*b*-$PHEA_{260}$**,** providing PIC micelles with good hydrophilicity and colloidal stability.

In the tapping mode, the cantilever is excited by the piezoelectric driver to lightly tap the surface. Feedback from the oscillation amplitude is used to both measure topographic variations in the sample, and to monitor and minimize amplitude variations.[80] The tapping force applied during scanning is related to the ratio of the set-point amplitude to the free-oscillation amplitude, usually defined as the set-point ratio.[80] For set-point ratios close to but less than 1, a low force is applied on the surface and the tip just lightly taps the surface whilst at smaller set-point ratios, the AFM tip interacts more strongly with the sample.[83] By tuning the amplitude set-point and thus varying the interaction forces between the AFM tip and the particles, the morphology of PIC micelle can be probed.

The G1@PAA_{27}-*b*-$PHEA_{260}$ PIC micelles (Figure 3-17) appear as spherical particles surrounded by a layer of "soft" PHEA (in dark color) at a set-point ratio 0.96 (column 1). A stronger force applied at a set-point ratio of 0.92 (column 2) reveals the "hard" PS core (bright color) inside each PIC micelle, with a surrounding softer ring (dark color), thus confirming the core–shell morphology of the micelles. This structure was further confirmed by the "mountain-like" morphology of PIC micelles (shown in the 3D models and in the section analyses) when the set-point ratio was further decreased to 0.86 (column 3), at which

point the PIC micelles appeared in a "sunny side up" egg-like morphology on the height AFM images. Only the rigid PS component could be detected in these phase images. The morphology of aggregates of G1@PAA_{27}-*b*-$PHEA_{260}$ for f = 0.25, and of G1@PAA_{13}-*b*-$PHEA_{150}$ for f = 0.5 and 0.25 is also shown in Figure S3-2 in the supporting information. It may thus be concluded beyond any doubt that AFM analysis confirmed the formation of a DHBC stabilizing layer on the G1 arborescent substrate, and of unimolecular micellar species as deduced from the DLS and MALLS measurements.

3.5 Conclusions

The synthesis of four PAA-*b*-PHEA block copolymers was achieved by ATRP, followed by hydrolysis of the protecting groups on both blocks. These copolymers were employed as polymeric stabilizers for a G1 (G0PS-*g*-P2VP) arborescent copolymer through the formation of polyion complexes in water. This is the first report on the complexation of PAA-*b*-PHEA segments with preformed P2VP-containing nanostructures in water to produce unimolecular PIC micelle species. The electrostatic interactions between PAA and P2VP segments enabled coupling of the block copolymer chains on the surface of the arborescent polymer, while the PHEA tails provided a stabilizing shell. Control over the size and structure of the PIC micelles, from large flocculated species to stable unimolecular entities with sizes ranging from 42 to 67 nm, was accomplished by controlling the density of the polymer stabilizing layer around the G1 core, either by varying the BC stoichiometry or the length of the PAA anchoring block, and most notably by varying the length of the nonionic PHEA block. Short PHEA tails were insufficiently bulky to impart good colloidal stability to the PIC micelles, and stable dispersions with low degrees of aggregation were only achieved at high BC contents (f ratios) in the complexation process. Slightly better stability was achieved by decreasing the PAA block length from 27 to 13 units at constant length of the PHEA block, which led to increased coverage by the block copolymers on the surface of the micelles. However most effective stabilization was achieved when the length of the nonionic segments was increased to 260 units, imparting good colloidal stability to the PIC micelles

even when a complexation ratio f = 0.5 was used. The hydrodynamic diameter of the micelles, when compared with the dimensions calculated for the collapsed core, provided evidence for uni- vs. multimolecular structure formation.

The MALLS measurements provided additional information on the structure of PIC micelles: The $\bar{M}_w$ and ρ-parameter values hinted at uni- vs. multimolecular structures formation, while the second virial coefficient A_2 highlighted the dominating role of –OH/water interactions. The soft shell of PHEA surrounding the stiff G1 core was observed in AFM images, confirming the success of the complexation process in producing unimolecular micelles. Most notably, the core–shell morphology of PIC micelles was confirmed through variations in the AFM amplitude set-point. The PIC process using double-hydrophilic block copolymer to stabilize hydrophobic G1 was thus optimized, to be applied to the templated preparation of iron oxide nanoparticles, which will be discussed in detail in Chapter 4.

Chapter 4 Templating and Stabilizing Magnetic Nanoparticles

Chapter 4

4.1 Overview

Vinylpyridine-containing polymers have been employed extensively as templates in the preparation of iron oxide magnetic nanoparticles (MNPs). Polymer templates may also be combined with stabilizing and biocompatible materials to enhance cellular uptake, while reducing cytotoxicity, once the MNPs are exposed to physiological conditions. We prepared a substrate combining templating and stabilizing effects for the MNP synthesis, which is a polyion complex (PIC) micelle derived from a G1 arborescent copolymer, G0 polystyrene-*graft*-poly(2-vinylpyridine), and a poly(acrylic acid)-*block*-poly(2-hydroxyethyl acrylate) copolymer, PAA-*b*-PHEA, forming a hydrophilic shell. As it turns out, the direct *in situ* application of these PIC micelles as templates in MNP synthesis was of limited usefulness since the MNPs formed had weak magnetization and large sizes unsuitable for biomedical applications. An alternative approach to this was to first use the G1 copolymer as a template for the synthesis of Fe_3O_4 NPs, before binding the PAA-*b*-PHEA copolymer for PIC formation to enhance their colloidal stability and biocompatibility. It is the first time that a dendritic graft (arborescent) copolymer is used to assist in MNP synthesis. Magnetic suspensions with improved colloidal stability in aqueous environments over a wide pH range were obtained by that method, as confirmed by dynamic light scattering (DLS) measurements. The magnetic micelles had a hydrodynamic diameter $D_h \approx 130$ nm (polydispersity index PDI = 0.136) from DLS analysis, and a core–shell morphology was observed by atomic force microscopy imaging. The Fe_3O_4 content of the micelles was quantified by thermogravimetric analysis, and large Fe_3O_4 crystallites were visualized by transmission electron microscopy. The biocompatible poly(2-hydroxyethyl acrylate) shell coating these MNPs should facilitate their clinical applications as MRI contrast agents and hyperthermia mediators.

Chapter 4

4.2 Introduction

Due to their small size and large surface-to-volume ratio, nanoparticles (NPs) display different physical and chemical properties as compared to their bulk counterparts since a significant fraction of their atoms are located at the surface.[1-2] Some NPs combine optical, catalytic, electronic and magnetic properties making them attractive for applications in various fields from optics, energy and electronics, to chemistry and biology.[1-2] Among the broad spectrum of nanomaterials being investigated for biomedical uses, magnetic nanoparticles (MNPs) have received significant attention for uses in targeted drug delivery, as magnetic resonance imaging (MRI) contrast agents, and as heat mediators in the magnetic hyperthermia treatment of tumors.[3-5] Besides metallic and bimetallic MNPs, superparamagnetic iron oxide nanoparticles (SPIONs) have been favored because of their low cytotoxicity profile[6-7] and the possibility of surface modification with biocompatible coatings.[3,8-9] Among numerous chemical techniques by which SPIONs can be synthesized, the ferric/ferrous ions alkaline coprecipitation method has been preferred as the simplest and most efficient route.[9]

4.2.1 Coprecipitation Method

Introduced in 1981 by Massart[10] in Europe and by Molday and Mackenzie[11] in the USA, the coprecipitation method is probably the most efficient and reproducible, yet simplest route to prepare magnetic particles, and is still the method of choice in the industry to produce large quantities of superparamagnetic MRI contrast agents.[12] A stoichiometric mixture of ferric and ferrous salts (Fe^{3+}/Fe^{2+} 2:1) in aqueous media precipitates upon addition of a strong base (NH_4OH or NaOH) in a non-oxidizing environment to yield a finely dispersed magnetic iron oxide solid phase[13] (Scheme 4-1a). Complete precipitation is expected for a molar base-to-total-iron ratio greater than the stoichiometric value $R = 8/3 \approx 2.67$, leading to a final pH between 9 and 14 depending on the excess of base present. Magnetite NPs produced by the coprecipitation route typically have magnetic saturation

values in the range of 30–60 emu·g^{-1}, lower than the value for bulk magnetite (92 emu·g^{-1}). Oxidation of the air-sensitive Fe_3O_4 to γ-Fe_2O_3 occurs easily in the presence of oxygen under acidic conditions, through desorption of Fe^{2+} ions from the surface into solution as $[Fe(H_2O)_6]^{2+}$ (Scheme 4-1b), or by direct oxidation of superficial ferrous ions under basic condition.[9] In the magnetite crystal structure (called "inverse spinel"), the iron ions are distributed within the octahedral (Oh) and tetrahedral (Td) sites of a face-centered cubic (fcc) stacked oxygen mesh according to $([Fe^{3+}]_{Td}[Fe^{3+}Fe^{2+}]_{Oh}O_4)$[14] (Figure 4-1). Fast electron hopping between Fe^{2+} and Fe^{3+} in the octahedral sublattice, evidenced by Mossbauer spectroscopy, plays an important role in the crystallization of the spinel structure and facilitates the transformation of this inverse spinel structure to a non-stoichiometric spinel γ-Fe_2O_3, $[Fe^{3+}]_{Td}[Fe^{3+}{}_{5/3}V_{1/3}]_{Oh}O_4$, where V stands for a cationic vacancy[14] (Figure 4-1).

$$2\,Fe^{3+} + Fe^{2+} + 8OH^- \longrightarrow Fe_3O_4 + H_2O \qquad (a)$$

$$Fe_3O_4 + 2H^+ \longrightarrow \gamma\text{–}Fe_2O_3 + Fe^{2+} + H_2O \qquad (b)$$

Scheme 4-1. Alkaline coprecipitation and oxidation reactions.

The main disadvantage of alkaline coprecipitation is the lack of control over the particle size distribution since the size of the crystals is mainly determined by nucleation, followed by rapid crystal growth. In the nucleation step, the collision of iron ions or molecules in solution leads to the formation of stable "embryonic" nuclei. These nuclei are involved in a breakup and reforming process until their size exceeds a critical limit at which the particles start to grow.[15] Crystal growth occurs either through the diffusion and adsorption of the solute on the surface of the crystals, or by the oriented aggregation of nuclei.[16-19] The growth kinetics is determined by the lowest rate between mass transport and surface equilibration. The driving force for dissolution increases as the size decreases, thus facilitating the dissolution of small particles and their re-deposition onto larger particles (Ostwald ripening).[19]

Since nucleation and crystal growth occur simultaneously, particles obtained by the coprecipitation route are polydisperse in sizes. Decoupling of the nucleation process from crystal growth is mandatory for the formation of iron oxide nanoparticles of uniform size.[20] Ideally, if the nucleation process can be controlled in a way such that all the nuclei are created at the same time, subsequent slow crystal growth from these nuclei is expected to produce particles with a very narrow size distribution. Jolivet et al.[21] suggested room temperature quasi-instantaneous electron transfer between Fe^{2+} and Fe^{3+} as a processes leading to the crystallization of spinel. The incorporation of a small proportion (ca. 10 mol%) of Fe^{2+} into the precipitate formed initially (a poorly crystalline Fe^{3+}-ferrihydrite FeOOH weakly diffracting X-rays or electrons, and thus called 2-line ferrihydrite) can induce the crystallization of all the iron into spinel via fast electron hopping, causing local structure rearrangements and driving spinel ordering. The crystallization of spinel can occur by a dissolution–crystallization mechanism forming two types of non-stoichiometric spinel particles with very different mean sizes. The Fe^{2+} content in the system determines which pathway dominates: only for $0.60 \leq \frac{[Fe^{3+}]}{[Fe^{3+}]+[Fe^{2+}]} \leq 0.66$ is a single Fe_3O_4 phase produced in the coprecipitation process.[21]

The first superparamagnetic iron oxide particles (with an average diameter of 8 nm, as measured by XRD) were produced by the alkaline coprecipitation of $FeCl_3$ and $FeCl_2$ by Massart.[13] Tailoring the size, size distribution, and thus the magnetic characteristics of the iron oxide NPs has been attempted in multiple investigations by adjusting the pH, temperature and ionic strength of the reaction medium, or by changing the Fe^{2+}/Fe^{3+} ratio, the medium composition, the order of addition of the reactants, the rate of mixing, or the nature of the base used. Higher pH values (facilitating the dissolution-crystallization process) and low ionic strengths (corresponding to low Cl^- concentrations) resulted in smaller NPs with narrower size distributions.[14,22] Elevated temperatures led to the formation of more ordered crystals but a decrease in magnetite content.[23] The ferrous-to-ferric ratio had a strong impact on the mean size, and thus on the properties of iron oxide NPs: higher Fe^{2+}/Fe^{3+} ratios yielded larger NPs,[23-24] but only particles formed in the ratios range from 0.4 to 0.6 were

capable of enhancing the contrast in magnetic resonance imaging (MRI).[23,25] Interestingly, maghemite (γ-Fe_2O_3) obtained for a Fe^{2+}/Fe^{3+} ratio of 0.118 in the preparation step (with dextran coating) exhibited higher genotoxicity than magnetite (Fe_3O_4) prepared for a ratio of 0.435 (also dextran-coated), indicating that Fe^{3+} ions are more potent at inducing DNA damage.[26] However, adjusting the reaction conditions as discussed above is not likely to provide significant improvements in size dispersity as compared to the unmodified coprecipitation method. A solution to this issue must be searched elsewhere.

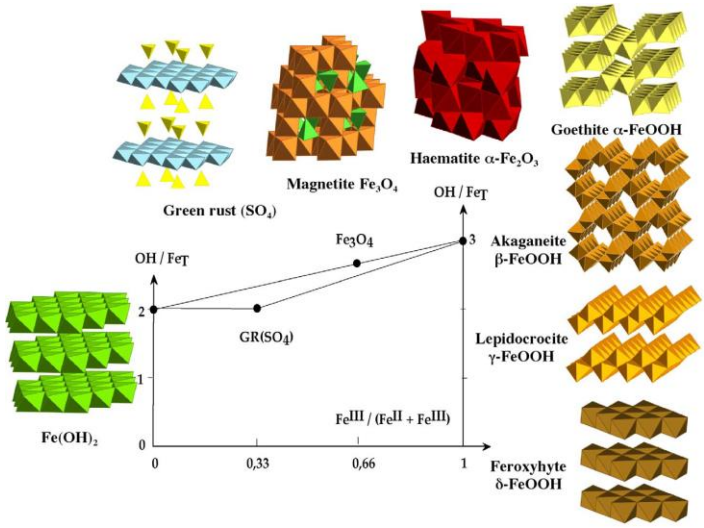

Figure 4-1. The different phases of iron oxyhydroxides formed in a bidimensional diagram *versus* the molar OH^-/Fe_{Total} hydroxylation ratio and the ferrous-ferric composition in the system. Reprinted with permission from Reference 21. Copyright 2006 Académie des Sciences.

The addition of organic complexing agents during coprecipitation can assist in the synthesis of more uniform NPs. The chelation of metal ions by organic agents can hinder nucleation, thus limiting the number of nuclei formed and leading to fewer but larger particles since the system is dominated by crystal growth. However if the chelation of metal

ions by organic agents inhibits crystal growth, the formation of small NPs is favored. For example, the presence of citrate anions in various molar ratios resulted in 2–8 nm diameter γ-Fe_2O_3 NPs.[27]

Among numerous methods developed to improve the uniformity of iron oxide NPs, creating nanoreactors with surfactants to provide a constrained environment that prevents further nucleation or inhibits crystal growth has been reported. The water-in-oil microemulsion system reported by Pillai et al.[28] is an excellent example of this approach to produce iron oxide nanoparticles with a narrow size distribution. This was achieved by adding tetraethylammonium hydroxide to a water-in-oil microemulsion of ferrous sulfate in a CTAB/*n*-butanol/*n*-octane mixture to induce the hydrolysis of Fe^{2+} ions. A second microemulsion with sodium nitrite as the dispersed aqueous phase was then added. Frequent collisions and coalescence of the droplets allowed the reaction of the Fe^{2+} ions and sodium nitrite, resulting in the formation of Fe^{3+} species, and then of iron oxide, within the aqueous core of the droplets. The surfactant concentration played an important role in controlling the droplet size, thus restricting the growth of the iron oxide NPs. The advantages of using microemulsions to control the size of iron oxide NPs were further enhanced by adding chitosan, a biocompatible hydrophilic stabilizing agent, into the system.[29] The size of the hybrid nanoparticles (10 to 80 nm) could be controlled with chitosan having different molar masses, while the weight ratio of chitosan to Fe_3O_4 greatly impacted the magnetization properties of the composites.

The separation of nucleation and growth may be achieved by tuning the nucleation process through a hosting medium such as small amphiphilic molecules or polymeric micelles, able to encapsulate the iron precursors and disperse them in discrete compartments, thereby providing control over particle formation. These inorganic-organic hybrids inherit the properties of both the inorganic material and the organic component. In the case of polymers, compartmentalization provides confinement for the reactants and steric stabilization, thus improving the colloidal stability and in some cases, introducing new functional groups. Control over the size and the morphology of MNPs achieved through

adjustment of the geometry and the size of the organic templates has been considered in our review,[30] whereby well-defined polymer structures exerted stronger impact on the outcome of size- and shape-controlled MNPs than simple homopolymer chains. Although the accessibility of metallic precursors complexed by anchoring moieties might be affected, well-defined polymer templates offer predetermined structures with minimal changes in morphology and size dispersity.

4.2.2 Surface Modification of Templated MNPs for Improved Biocompatibility

Uncoated iron oxide NPs can easily precipitate under the influence of gravitational forces (sedimentation), agglomerate under physiological (high salinity) conditions, or when submitted to a magnetic field (dipolar interactions) due to their insufficiently repulsive interactions. In a clinical setting for example, precipitation and agglomeration of the iron oxide NPs can lead to clotting in blood vessels.[31] There are theoretically four types of interactions contributing to the overall equilibrium state of a colloidal magnetic suspension:

- forces originating from electric dipoles in matter, either permanent, induced or dispersive componly refered to as “van der Waals forces”, that create strong short-range isotropic attractions;

- electrostatic repulsive forces, which are long-range, but according to the Debye-Hückel, theory, they can be partially or totally screened out as the ionic strength (defined as the sum of all the concentrations of ionic species, weighted by the square of their elementary charge) of the dispersion medium is increased;

- magnetic dipolar forces between the magnetic particles, which are basically anisotropic attractions that can be attractive or repulsive, depending on the field orientation;

- steric repulsion forces observed for coated particles, that are related to the entropy loss when macromolecular chains highly swollen by a solvent are brought into contact.

The stabilization of magnetic suspensions can be achieved most conveniently using electrostatic and/or steric repulsions.[32]

Electrostatic repulsion appears when the NPs carry charges on their surface, which may originate from the adsorption of charged ions or molecules, or from the ionization of pre-existing functional groups on their surface. Charged particles have a double-layered structure: the inner (Stern) layer, consisting of highly organized solvated H_2O molecules and chemically adsorbed ions, and a diffuse layer composed of counterions balancing the charge at the surface, called the Debye layer. The iron atoms at the surface of iron oxide NPs act as a Lewis acid capable of coordination with electron-donating ligands. In aqueous solutions, the Fe^{3+} and Fe^{2+} cations form octahedral coordination complexes with water that dissociate into hydroxyl groups. These hydroxyl groups may react with acids or bases, or exchange with other functional groups such as carboxylates (citrate,[33-34] gluconic acid,[35] dimercaptosuccinic acid[36]), sulfates,[37] or phosphates (alkyl phosphonates,[37] poly(vinyl alcohol phosphate)[38]). Phosphonate and phosphate ligands, due to their biocompatibility,[39] enable the use of magnetic nanoparticles for biomedical applications. The coordination complexes between iron cations and small molecule stabilizers are reversible, the stability of the magnetic suspension depending strongly upon the pH and the concentration of non-adsorbed molecules.[40-44] The sensitivity of electrostatic forces to ionic strength of the dispersion environment is well-documented. Increased ionic strength drastically decreases the thickness of the electrical double layer: An ionic strength above 100 mM typically reduces the thickness of a double layer to less than 1 nm, which is insufficient to prevent aggregation driven by van der Waals forces.[45] At physiological salt concentrations (around 150 mM), electrostatic repulsion is thus unable to impart sufficient stability to hinder the precipitation of NPs.

The limited usefulness of electrostatic repulsion leaves steric stabilization as the preferred option to enhance the colloidal stability of magnetic NP suspensions. Steric stabilization arises upon coating the NPs with a corona of macromolecular stabilizer chains, that effectively increase the distance between NPs and outweighs the van der Waals

attraction. A surfactant layer with a thickness of 2 nm yields steric repulsion sufficient to compensate for the attractive forces between magnetic particles, thereby preventing their agglomeration.[46] These steric stabilizers can be adsorbed or grafted onto the NP surface during or after their synthesis. If the macromolecules can interact strongly with the NP surface and efficiently prevent clustering, they have the potential to serve as steric stabilizers. However, the chemical nature of the coating on NPs has strong if not vital impact on their cellular uptake efficiency, cytotoxicity, biocompatibility, and biodegradability once they are exposed to physiological conditions.[47-48] To enable any clinical application, the coating should consist of biocompatible materials or biological molecules such as antibodies, peptides, polysaccharides, etc. to enhance their biocompatibility[49] and to maintain a sufficiently long blood circulation half-life time that permits accumulation of the MNPs in tumor tissues through the so-called "enhanced permeation and retention effect" (EPR).[50]

Biocompatible materials such as dextran,[51] citrate[33-34] and PEGylated starch[7] have been used to coat MNPs. Fe_3O_4 NPs coated with poly(ethylene glycol) (PEG),[52] pullulan[53] or poly(maleic anhydride-*alt*-1-octadecene)-*g*-poly(ethylene glycol) PMAO-*g*-PEG[54] displayed no apparent cytotoxicity in *in vitro* assays when exposed to cells at various concentrations (1–2 mg/mL), owing to the biocompatible coating preventing the iron oxide core from interacting with cells. The anti-biofouling property (resistance to protein adsorption) of PEG[50,55-56] makes this polymer a very useful coating material. Methoxypoly(ethylene glycol)-oligo(aspartic acid) MPEG-Asp_3-NH_2-coated iron oxide nanoparticles thus had no cytotoxicity on OCTY mouse cells at a concentration of 400 µg/mL, but methoxypoly(ethylene glycol)-*block*-poly(acrylic acid) MPEG-*b*-PAA-coated and PAA-coated nanoparticles killed 84% of the cells.[57] The relation between cellular uptake and the repulsive properties of the polymer shell on MNPs was recently studied by Berret et al.[58] in the case of PEO chains with phosphonic acid side chains, that are much more efficient than a PAA coating. Apart from these polymer coatings, silica-coated iron oxide nanoparticles,[49,59-63] Ferumoxsil (AMI-121), has also been proposed and tested in clinical trials by oral administration.[64-65] Other inorganic materials such as gold[66-70] or gadolinium(III)[71-72] have

also been used not only to stabilize the nanoparticles in solution, but also to help in binding various biological ligands to the nanoparticle surface.

The stability of the coatings and their biodegradation characteristics also affect the biocompatibility of MNPs. Commercially available contrast agents such as Ferridex®, Resovist®, Supravist® and Sinerem® are coated with dextran or carboxy-dextran.[7,73] These materials are not ideal for coating due to their weak binding to iron oxide NPs however, which makes them more prone to detachment and aggregation.[73-74] Dextran-magnetite NPs thus caused cell death and reduced cell proliferation as strongly as uncoated iron oxide particles,[51] because the dextran coating can collapse and expose iron oxide NP aggregates to the cellular components, leading to lipid membrane disruption by often invoked intracellular production of reactive oxygen species (ROS). However, only limited information is known on the effects of these coatings on DNA damage and oxidative stress.[31]

The molar mass ($\bar{M}_w$) of the stabilizer is another criterion determining its usefulness for *in vivo* applications. Magnetic nanoparticles (MNPs) with hydrodynamic diameters < 50 nm can be distributed to both lymph nodes and the reticuloendothelial system (RES, comprising in particular the spleen and liver), while MNPs with diameters > 50 nm are located only in the reticuloendothelial system.[48] Large-sized magnetic NPs are also cleared by the reticuloendothelial system from the bloodstream faster than smaller-sized particles.[75] Very high $\bar{M}_w$ stabilizers, while imparting good colloidal stabilization to the coated NPs, also yield hybrid NPs with a large hydrodynamic size, leading to different biodistribution and clearance pathways and thereby limiting the potential applications of these NPs.

Two approaches for the preparation of stable MNPs with a hydrophilic shell are presented in this Chapter. The first method is to use PIC micelles incorporating a well-defined branched poly(2-vinylpyridine) (P2VP) polymer structure and a hydrophilic shell of poly(2-hydroxyethyl acrylate) (PHEA) as templates for MNPs. The second pathway is to first use the G1 copolymer as a template for the Fe_3O_4 NP synthesis, and to then bind the PAA-*b*-PHEA copolymer to enhance the colloidal stability and biocompatibility. The high density of 2-vinylpyridine units in the very compact structure of arborescent copolymers was expected

to assist the templating Fe_3O_4 NPs. The polyion complexation process of G1@Fe_3O_4 MNPs with PAA-*b*-PHEA was designed to produce magnetic polyion complex (MPIC) micelles with improved colloidal stability at pH 7.

4.2.3 Advantages of Using Arborescent Copolymers as Templates for MNPs

The preparation, structure and properties of dendritic graft – also called arborescent or dendrigraft – copolymers will be briefly reviewed to highlight the expected advantages of this kind of polymer as a template for MNP synthesis. These polymers are synthesized by successive grafting reactions of well-defined polymeric building blocks. The arborescent copolymer G0PS-*g*-P2VP or G1 used in the current investigation was prepared by Munam and Gauthier[76] via cycles of acetylation of linear PS substrate to introduce coupling sites, grafting living PS chains onto the linear substrate, and further acetylation and grafting with living poly(2-vinylpyridine) chains to obtain the G1 copolymer (Scheme 5-2).

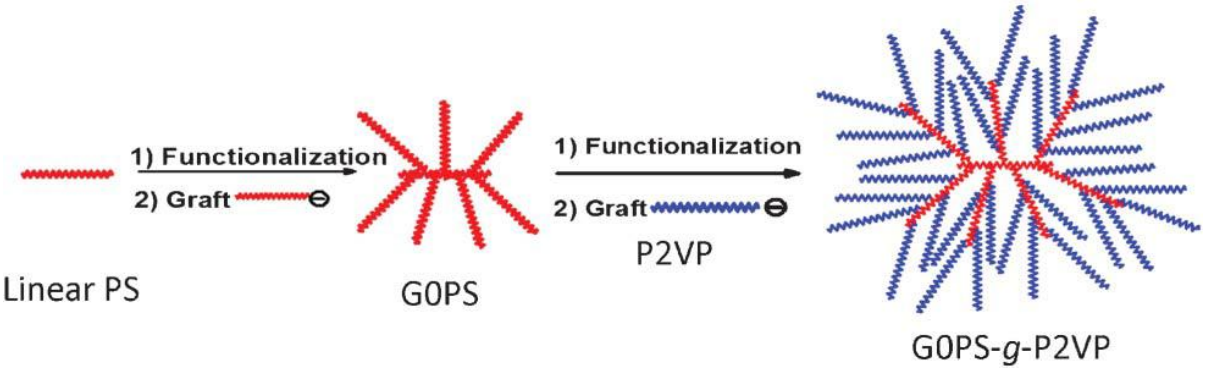

Scheme 4-2. Synthesis of an arborescent copolymer (G0PS-*g*-P2VP) by successive grafting reactions. Reprinted with permission from Reference 77. Copyright 2012 The Royal Society of Chemistry 2012.

The linear PS substrate, with $\bar{M}_n$ = 5200 g·mol^{-1} and $\bar{M}_w/\bar{M}_n$ = 1.06, was acetylated and grafted with $\bar{M}_n$ = 5500 g·mol^{-1} living polystyryllithium chains to obtain a G0PS substrate with $\bar{M}_n$ = 9.7×10^4 g·mol^{-1}, $\bar{M}_w/\bar{M}_n$ = 1.03, and 17 PS side chains. The G0PS product, after

purification by precipitation fractionation (to remove the linear PS contaminant) and acetylation, was grafted with living P2VP having $\bar{M}_n$ = 5500 g·mol^{-1} and $\bar{M}_w/\bar{M}_n$ = 1.15. The resulting G0PS-*g*-P2VP or G1 arborescent copolymer, purified by fractionation, had $\bar{M}_n$ = 1.1×10^6 g·mol^{-1}, $\bar{M}_w/\bar{M}_n$ = 1.08, and 182 P2VP side chains (corresponding to 9500 2VP units). Arborescent graft copolymers PS-*g*-P2VP (G0) and G1PS-*g*-P2VP (G2), also briefly examined as templates, were prepared by the same procedure.

Table 4-1. Characterization data for G1-G3 arborescent copolymer templates. Adapted with permission from Reference 77. Copyright The Royal Society of Chemistry 2012.

	G(n-1)PS substrate		P2VP side chains		Graft copolymer Gn = G(n-1)PS-*g*-P2VP				
G	$\bar{M}_n$ (g·mol^{-1})[a]	$\bar{M}_w/\bar{M}_n$	$\bar{M}_n$ (g·mol^{-1})[a]	$\bar{M}_w/\bar{M}_n$	$\bar{M}_n$ (g·mol^{-1})[b]	$\bar{M}_w/\bar{M}_n$	f_n[c]	2VP (mol%)[d]	2VP groups[e]
0	5.2×10^3	1.06	5.1×10^3	1.15	7.4×10^4	1.08	13	93	625
1	9.7×10^4	1.03	5.5×10^3	1.15	1.1×10^6	1.08	182	91	9500
2	1.1×10^6	1.03	6.2×10^3	1.10	8.4×10^6	1.09	1180	87	6.9×10^5

[a] Absolute values from SEC-MALLS. [b] Values estimated by combining the absolute M_n of the substrate with the copolymer composition from ^{1}H NMR analysis. [c] Branching functionality: Number of branches grafted in the last cycle. [d] From ^{1}H NMR analysis. [e] From $\bar{M}_n$ and f_n.

The P2VP arborescent copolymers are soluble in polar solvents (DMF, methanol), and in water upon protonation by a strong acid (e.g., HCl or trifluoroacetic acid). The apparent pK_a of such a polymer depends on the degree of protonation of the chains, the electrolyte concentration and particularly on steric hindrance, which is difficult to define precisely.[78] The hydrodynamic diameter of G0-G2 arborescent copolymers measured in HCl-acidified aqueous solution are shown in Figure 4-2. Clustering was observed when dissolving the G0 copolymer, probably due to its smaller number of P2VP chains (f_n = 13) leading to insufficient electrostatic repulsion between the molecules. Based on this observation, the G0 copolymer was not explored as a magnetic nanoparticle template. Both the G1 and G2 copolymers exhibited narrow size distributions and no agglomeration (PDI = 0.04 and 0.05,

respectively) when dissolved in HCl solutions (pH 4). The bulkier and more rigid structure of the G1 and G2 molecules could be useful in templating MNPs, but potentially also induce colloidal instability. The smaller G0 hydrophobic PS core of the G1 molecules may lessen these disadvantages. Last but not least, our goal was to generate hybrid magnetic polymeric nanoparticle structures ideally in a range of 10–100 nm, considered optimal for intravenous administration, since particles > 200 nm are sequestered by the spleen and those < 10 nm are removed by renal clearance.[79] The smaller size of the G1 copolymer (D_h = 29 nm) as compared to G2 (D_h = 58 nm) is thus considered another advantage. The high content of the copolymers in 2VP, a ligand that coordinates with iron ions, combined with the very compact structure of the G1 arborescent copolymer, should make it a very good platform for the complexation of iron and templating of the MNPs.

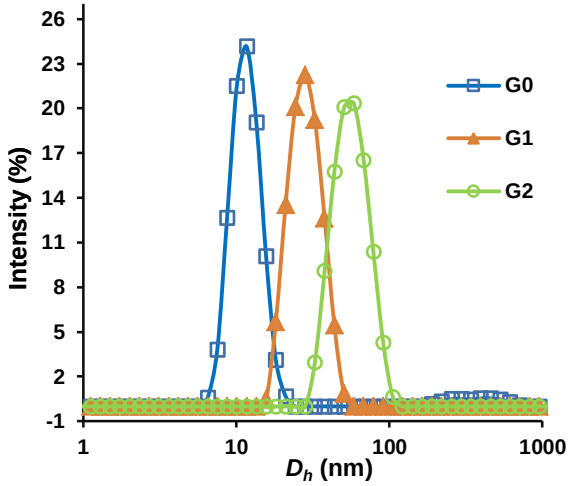

Figure 4-2. Size distributions for G0-G2 graft copolymers in HCl solutions (pH 4) at 25 °C.

4.3 Experimental Procedures

4.3.1 Templating

4.3.1.1 Materials

Iron(III) chloride ($FeCl_3$, Sigma-Aldrich, anhydrous, powder, ≥ 99.99% trace metals basis), iron(II) sulfate heptahydrate ($FeSO_4 \cdot 7H_2O$, Sigma-Aldrich, ACS reagent, ≥ 99.0%), hydrochloric acid (HCl, Sigma-Aldrich, ACS reagent, 37%), ammonia (NH_4OH Sigma-Aldrich, 28-30% solution), and sodium hydroxide (NaOH, Sigma-Aldrich, pellets, semiconductor grade, 99.99% based on trace metals basis) were used as received. Milli-Q water (18.2 MΩ·cm) was obtained from a Milli-Q water purification system (Purelab Classic, Elga Lab Water).

The G1 arborescent graft copolymer used in this study was synthesized by anionic polymerization and grafting.[58] The graft copolymer *G*0PS-*g*-P2VP ($\bar{M}_n$ = 1.1×10^6 g·mol^{-1}; $\bar{M}_w/\bar{M}_n$ = 1.08; branching functionality f_n = 182) consisted of 9500 2VP units, corresponding to 91 mol% of 2VP (Table 4-1).[77]

4.3.1.2 Polyion Complex Micelle Preparation The polyion complex (PIC) micelles used as templates for MNP synthesis in this work were prepared from a G1 arborescent graft copolymer (G0PS-*g*-P2VP) and a DHBC according to the procedures described in Section 3.3.6. The complexation of G1 with the PAA_{27}-*b*-$PHEA_{260}$ block copolymer was carried out in aqueous solution. The parameter $f = CO_2H/N$ was used to quantify the molar ratio of CO_2H groups (from the PAA segment of the block copolymer) and the amine moieties (from the 2VP units of the arborescent copolymer):

$$f = \frac{\text{number of moles of } CO_2H \text{ groups from PAA chains}}{\text{number of moles of N groups from P2VP chains}}$$

The following procedure describes the complexation of the G1 copolymer with PAA_{27}-*b*-$PHEA_{260}$ for f = 0.5. Briefly, in a 10-mL vial, G1 (1.9 mg, 16.7 µmol of N) was completely dissolved in 300 µL of aqueous HCl solution at pH 1.4. A pH 7 aqueous solution of PAA_{27}-*b*-$PHEA_{260}$ (9.6 mg, 5 mg/mL, 8.3 µmol of CO_2H) was quickly added. The mixture

was left to react for 1 h before the pH was adjusted to 4.7 with a 1 M NaOH solution, and stirring (400 rpm) was continued for 1 h. The pH was further adjusted to 7 with a 0.1 M NaOH solution and the solution was stirred for 30 min. The solution was dialyzed against Milli-Q water for 48 h before it was collected and stored at 4 °C.

4.3.1.3 Templating Procedure Using PIC micelles

A stock solution of $FeCl_3$ (24 mg, 0.148 mmol) and $FeSO_4{\cdot}7H_2O$ (24.2 mg, 0.087 mmol) in 2 mL of Milli-Q water acidified with HCl (pH 1.4) was prepared before use. The sulfate salt was preferred for the production of Fe^{3+} ions in situ by the oxidation of Fe^{2+} with H_2O_2, since the chloride salt will generate Cl_2 gas. In a 15 × 150 mm^2 test tube, a water solution (pH 7) of PIC micelles G1@PAA_{27}-*b*-$PHEA_{260}$ (11.2 mg, 33.3 μmol of 2VP units) in 600 μL was prepared. The PIC micelle solution was stirred vigorously in an oil bath at 80 °C and 200 μL of the iron stock solution was quickly added (Fe/2VP molar ratio = 0.7), followed by 17 μL of concentrated NH_4OH to trigger the coprecipitation. The solution color changed from yellow to brown, probably corresponding to different precipitated phases of iron oxyhydroxides rather than magnetite (black). Sedimentation of the magnetic nanoparticles (MNPs) in the magnetic field of a NdFeB permanent magnet (Calamit magnets, Milan, Italy) and decantation allowed complete removal of the excess reagents. The MNPs were rinsed water (2 × 5 mL) and redispersed in 2 mL of H_2O to produce an orange coloured ferrofluid.

4.3.1.4 Templating Procedure Using the G1 Arborescent Polymer

A stock solution of $FeCl_3$ (24 mg, 0.148 mmol) and $FeSO_4{\cdot}7H_2O$ (24.2 mg, 0.087 mmol) in 2 mL of Milli-Q water acidified with HCl (pH 1.4) was prepared before use. In a 15 × 150 mm^2 test tube, G1 (3.9 mg, 33.3 μmol of 2VP units) was completely dissolved in 600 μL of HCl solution (pH 1.4) by sonication at 37 kHz for 30 min (Ultrasonic Cleaner Elmasonic SH075EL). The G1 solution was then stirred vigorously with a mechanical rotor (> 800 rpm) in an oil bath at either 50, 80 or 100 °C and 200 μL of the iron stock solution

was quickly added (Fe/2VP molar ratio = 0.7), followed by 17 µL of concentrated NH_4OH to trigger the coprecipitation. The solution color quickly changed from yellow to black. Sedimentation of the magnetic nanoparticles (MNPs) in the magnetic field of an NdFeB permanent magnet allowed complete removal of the excess reagents. The MNPs were rinsed with water (2 × 5 mL), acetone (2 × 5 mL), and diethyl ether (2 × 5 mL) before being redispersed in 2 mL of dilute HNO_3 (pH 1.4) to produce a black homogenous ferrofluid that was a relatively stable colloidal dispersion of MNPs.

4.3.2 Stabilization

The procedures and the characterization techniques for the synthesis of the double-hydrophilic block copolymers (DHBC) poly(acrylic acid)-*b*-poly(2-hydroxyethyl acrylate) by atom-transfer radical polymerization (ATRP) were previously described (Section 3.3). Among the four block copolymers obtained, PAA_{13}-*b*-$PHEA_{150}$ ($\overline{M}_n$ = 18340 g/mol, $Đ_M = \overline{M}_n \cdot \overline{M}_w^{-1}$ = 1.23) and PAA_{27}-*b*-$PHEA_{260}$ ($\overline{M}_n$ = 30940 g/mol, $Đ_M = \overline{M}_n \cdot \overline{M}_w^{-1}$ = 1.16) were selected for the present investigation.

Complexation of the G1-templated MNPs with various amounts of the two PAA-*b*-PHEA block copolymers was carried out in aqueous solutions. The parameter $f = CO_2H/N$ (defined above) was used to quantify the molar ratio of CO_2H groups and 2VP units. The following procedure describes the complexation of the G1-templated MNPs G1@Fe_3O_4 with PAA_{27}-*b*-$PHEA_{260}$ for f = 0.5. In a 10-mL vial, G1@Fe_3O_4 (0.99 mg Fe_3O_4, 1.9 mg of G1, 16.7 µmol of N functional groups) was dispersed in 1 mL of HNO_3 solution (pH 1.4). A pH 7 aqueous solution of PAA_{27}-*b*-$PHEA_{260}$ (9.6 mg, 5 mg/mL, 8.3 µmol of CO_2H functional groups, $f = CO_2H/N$ = 0.5) was quickly added, the mixture was stirred for 1 h before the pH was adjusted to 4.7 with a 1 M NaOH solution, and stirring was continued for 1 h. The pH was further adjusted to 7 with 0.1 M NaOH and the solution was stirred for 30 min. The solution was then dialyzed (50,000 MWCO Spectra/Por® 7 regenerated cellulose bag) against Milli-Q water (5 L) for 24 h before it was collected and stored at 4 °C.

4.3.3 Characterization

4.3.3.1 Dynamic Light Scattering

The measurements were performed on a Zetasizer Nano ZS90 (Malvern Instruments) equipped with a 4 mW He-Ne laser operating at 633 nm and 25.0 °C, at a scattering angle θ = 90°. Each sample was measured in triplicate using disposable PS cuvettes or quartz cuvettes. The samples were prepared at concentrations of 3–5 mg/mL in Milli-Q water (at 25 °C, refractive index n_o = 1.330, viscosity η = 0.8872 cP), and filtered through a nylon membrane with 0.45 µm nominal pore size. The light scattering data were analyzed with the Zetasizer™ 7.11 Software (Malvern Instruments). The intensity-weighted autocorrelation function $g^{(2)}(\tau)$ produced by the digital correlator was used to extract the particle size distributions. The second order cumulants analysis algorithm was applied for relatively monodisperse particles, while the non-negatively constrained least-squares method (NNLS) or CONTIN analysis were employed for polydispersed samples. The hydrodynamic radius R_h of the particles was determined from the Stokes-Einstein equation $R_h = \frac{k_B T}{6\pi\eta D_T}$ with the diffusion coefficient (D_T) obtained from the decay rate ($\Gamma = D_T \times q^2$) of the amplitude autocorrelation function $g^{(1)}(\tau)$ and the instrumental scattering wave vector defined as $q = \frac{4\pi n_o}{\lambda}\sin(\theta/2)$.

In this Chapter, for simplicity, we will use D_h (rather than D_h^I) for the intensity-weighted hydrodynamic diameter, and D_h^n for the number-weighted hydrodynamic diameter.

4.3.3.2 Transmission Electron Microscopy

Transmission Electron Microscopy (TEM) images were obtained at the Bordeaux Imaging center (BIC) on a Hitachi H7650 microscope working at 80 kV. Samples were prepared by depositing 0.7 µL of the MNPs aqueous solution onto a copper grid (200-mesh coated with holey carbon film) and removing the excess after 5 min. The grids were dried overnight in a fume hood. The metal-free samples were stained by exposing the grids to iodine vapors for 60 min.

4.3.3.3 Thermogravimetric analysis

Thermogravimetric analysis (TGA) was carried out on a Q500 (Q Series™ TA Instrument) using the following program:

1: Select gas 1 (N_2)

2: Equilibrate at 30 °C

3: Ramp at 10 °C/min to 140 °C

4: Isothermal for 25 min

5: Ramp at 10 °C/min to 470 °C

6: Isothermal for 20 min

7: Select gas 2 (O_2)

8: Ramp at 10 °C/min to 800 °C

9: Isothermal for 2 min

10: Equilibrate at 200 °C

4.3.3.4 Atomic Force Microscopy

Freshly cleaved mica was used as sample substrate. The polymer solutions were prepared in Milli-Q water at concentrations ranging from 0.05 to 0.1 mg/mL. A 20 μL aliquot of MPIC micelle dispersion was deposited on the mica substrate and spin-coated at 3000 rpm for 180 s under ambient conditions. Atomic force microscopy (AFM) images were recorded in the tapping mode in air on a Veeco Dimension Icon System equipped with a Nanoscope V controller. The probes used were Olympus® AC160TS-R3 micro cantilevers with a spring constant of 26–56 N/m, a resonance frequency of 300–399 kHz, and a curvature radius of 8–10 nm. The scan rate was typically set between 0.7 and 1.2 Hz, at a scan angle of 0°, acquiring 512 samples/line. Image analysis was done with the Nanoscope Analysis V1.20 software from Bruker.

4.4 Results and Discussion

In this Chapter the term magnetic nanoparticles (MNPs) will be used for G1@Fe_3O_4 NPs, while the magnetic polyion complex (MPIC) micelles will be identified as G1@Fe_3O_4@PAA-*b*-PHEA NPs. The superparamagnetic properties of the MNPs and MPIC micelles will be confirmed in Chapter 5, but the term superparamagnetic iron oxide nanoparticles (SPIONs) will not be used until then. The number-weighted hydrodynamic diameter, D_h^n, will not be discussed frequently, thus for simplicity we will use D_h (rather than D_h^I) to represent the intensity-weighted hydrodynamic diameter.

4.4.1 Using PIC Micelles as Templates for MNPs

The PIC micelles have an arborescent polymer structure with 2-vinylpyridine units (2VP, a ligand that strongly coordinates with iron ions) and a hydrophilic shell of poly(2-hydroxyethyl acrylate) PHEA. Unfortunately, the direct *in situ* application of PIC micelles to the Fe_3O_4 alkaline coprecipitation reaction resulted in weak magnetization for the products, causing difficulty in MNP sedimentation with a permanent magnet (Figure 4-3). The orange-brown color and the weak magnetization of the products were probably due to the formation of different phases of iron oxyhydroxides rather than magnetite (Figure 4-1). We hypothesize that mixing of the PIC micelle solution at pH 7 with an aliquot of Fe^{2+} and Fe^{3+} salts at pH 1.4 yielded a solution with pH 2.6, insufficiently low to prevent the precipitation of ferric hydroxide (with a very low solubility product $K_s = [Fe^{3+}][OH]^3 = 10^{-44}$)[80] and ferrous hydroxide ($K_s = [Fe^{2+}][OH]^2 = 10^{-34}$).[80] Another reason for the failure of templating may be the presence of the PAA-*b*-PHEA block copolymer in the shell, designed to improve the colloidal stability and biocompatibility of the end product, interfering with the accessibility of the iron precursors to the 2-vinylpyridine moieties, since PAA is also a complexing ligand for ferrous and ferric cations.

As shown on Figure 4-3 (right), contact of the PIC micelles (stabilized at pH 7, D_h = 42 nm, PDI = 0.08) with the acidified iron solution (pH 1.4) yielded a pH 2.6 solution, inducing a low level of aggregation (D_h = 180 nm, PDI = 0.282), similarly to the pH response

of PIC micelles discussed in Section 3.4.2.4. The addition of NH_4OH solution to induce alkaline coprecipitation resulted in very large particles at pH 9 (bimodal, $D_h \approx 470$ nm, PDI ≈ 0.456, Figure 4-3, right), unsuitable for biomedical applications. Nanoparticles with diameters below 200 nm and homogeneous in size are indeed desired for systemic circulation, i.e., long blood half-lives, especially if they are coated with a neutral polymer sheath to achieve steric repulsion towards proteins.[81]

Due to the poor performance of this approach both in terms of templating and stability, the direct *in situ* employment of PIC micelles for Fe_3O_4 alkaline coprecipitation was abandoned. The second preparation pathway, separating the templating and stabilization steps, was rather investigated.

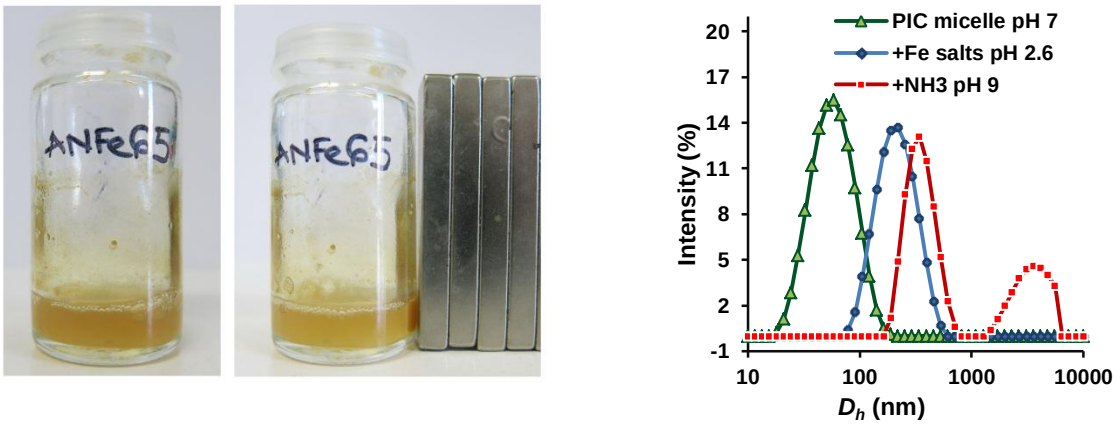

Figure 4-3. (Left) Weak magnetization of the MNPs produced by coprecipitation of iron salts in the PIC micelle templates. (Right) Hydrodynamic size distribution by DLS at 25 °C for PIC micelles G1@ PAA_{27}-*b*-$PHEA_{260}$ f = 0.5 (pH 7), PIC micelles mixed with the iron salt solution (pH 2.6), and the product obtained after adding the NH_4OH solution (pH 9).

4.4.2 Templating – *In Situ* Coprecipitation

Due to its high content (91 mol%) of 2VP units (a strong iron-coordinating ligand) grafted in a very compact structure with small dimension (D_h = 29 ± 4 nm, PDI = 0.04,

D_{TEM} = 22 ± 3 nm), the G1 arborescent polymer should be a useful platform in itself for templating iron oxide NP formation (Figure 4-4).

After redispersion in HNO_3 solution (pH 1.4), the MNPs prepared by *in situ* coprecipitation in the template, G1@Fe_3O_4, had better colloidal stability than bare Fe_3O_4 NPs prepared as a control sample produced under the same conditions without G1 arborescent copolymer. The bare Fe_3O_4 NPs clustered and aggregated after a short time period (10 min), or immediately when subjected to a weak magnetic field, while the G1@Fe_3O_4 ferrofluid was stable in both cases (Figure 4-5).

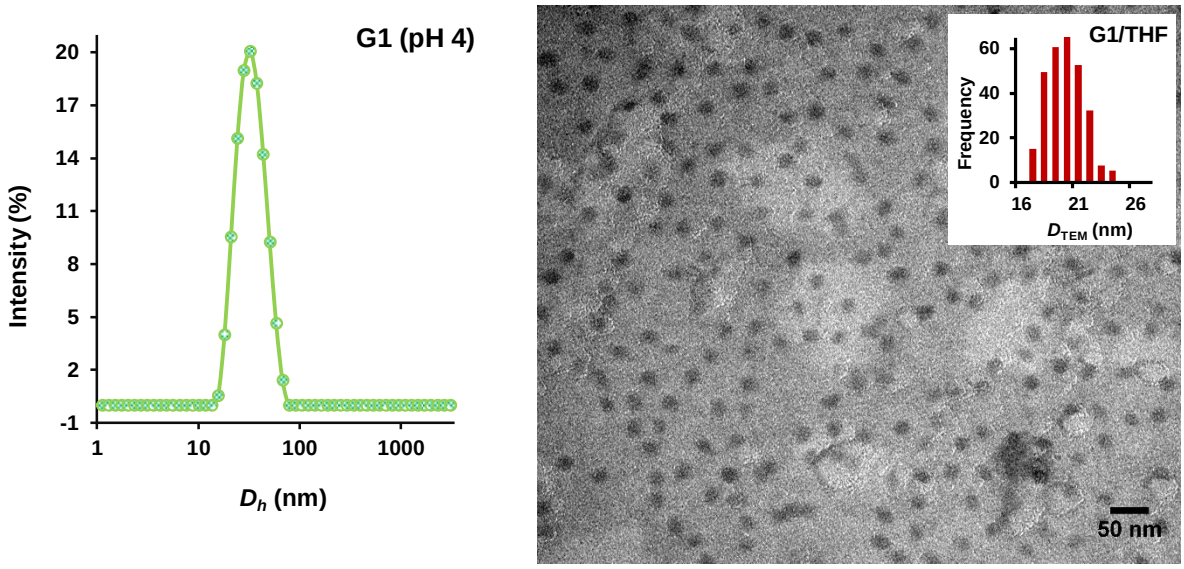

Figure 4-4. (Left) Hydrodynamic size distribution by DLS for G1 (pH 4) at 25 °C. (Right) TEM image for G1 prepared by depositing a THF solution, and staining with iodine.

The hydrodynamic diameter of the bare Fe_3O_4 NPs determined by DLS analysis in HNO_3 at pH 1.4, $D_h \approx 1$ µm, PDI = 0.8, was much larger and much less uniform than for G1@Fe_3O_4, with D_h = 131 nm, PDI = 0.286 (Figure 4-5). In a diluted acidic environment (e.g. a few tens mM HNO_3), the Fe-OH moieties at the surface of the iron oxide NPs become

protonated to Fe-OH_2^+, inducing electrostatic repulsions between the particles. These electrostatic repulsions were insufficient to stabilize the system however, resulting in clustering and aggregation. For G1@Fe_3O_4, better stability is attributed to the additional repulsive forces originating from the protonated 2VP units, together with steric repulsion. The G1 copolymer acted as a template that encapsulated the Fe_3O_4 precursors and stabilized the MNPs to some extent after their *in situ* synthesis. The discrepancy between the intensity-weighted D_h = 131 nm and number-weighted D_h^n = 92 nm, combined with a broad size distribution, nonetheless indicate a low level of aggregation.

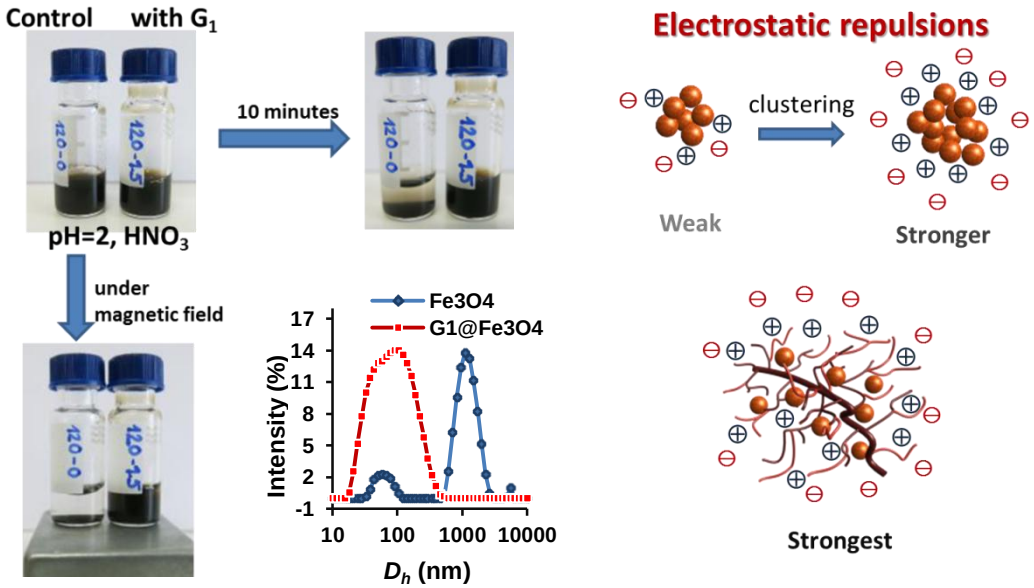

Figure 4-5. Improved colloidal stability of templated G1@Fe_3O_4 ferrofluid as compared with non-templated Fe_3O_4 ferrofluid.

The size and size distribution of the MNPs strongly influence their magnetization properties. Among iron oxide NPs with a size of 5–14 nm, the 14 nm NPs were indeed found to have the highest Specific Absorption Rate (SAR) value of 447 $W \cdot g^{-1}$ when submitted to a 400 kHz, 24.5 kA/m alternating magnetic field.[82] De la Presa et al.[83] reported a four-fold

increase in the SAR value (from 10 to 40 $W \cdot g^{-1}$) when increasing the size of maghemite NPs from 8 to 11 nm, and 1.3-fold (from 40 to 55 $W \cdot g^{-1}$) from 11 to 13 nm. In general, higher SAR values are also obtained for samples with lower polydispersity values, regardless of the NP size.[84]

To emphasize the advantages of the G1 arborescent copolymer as a template, coprecipitation in the presence of linear poly(4-vinylpyridine) P4VP ($\bar{M}_n$ = 65,000 $g \cdot mol^{-1}$) was also carried out, and Transmission Electron Microscopy (TEM) served to determine the crystallite size of the Fe_3O_4 NPs (composed of both crystalline and amorphous components). The size measured by TEM is a number-weighted value, and we performed size analysis based on greater than 100 particles to obtain meaningful statistical results. The crystallite size of P4VP@Fe_3O_4 determined by TEM analysis was 7.0 ± 1.4 nm, which is typical for samples prepared by non-templated coprecipitation.[13] The crystallite size of the Fe_3O_4 NPs increased to 9.1 ± 1.7 nm in the presence of G1 template (Figure 4-6). The encapsulation of $Fe^{2+/3+}$ ions within the G1 template presumably distributed the ions into a smaller volume, which allowed a short burst in the nucleation rate as compared to homogeneous nucleation. In comparison to homogenous nucleation, heterogeneous nucleation within the P2VP phase of the G1 micelles forces the Fe^{2+} and Fe^{3+} cations closer to each other, since complexation partly overcomes electrostatic repulsion. In so doing, the nucleation and growth steps are more likely to be separated.

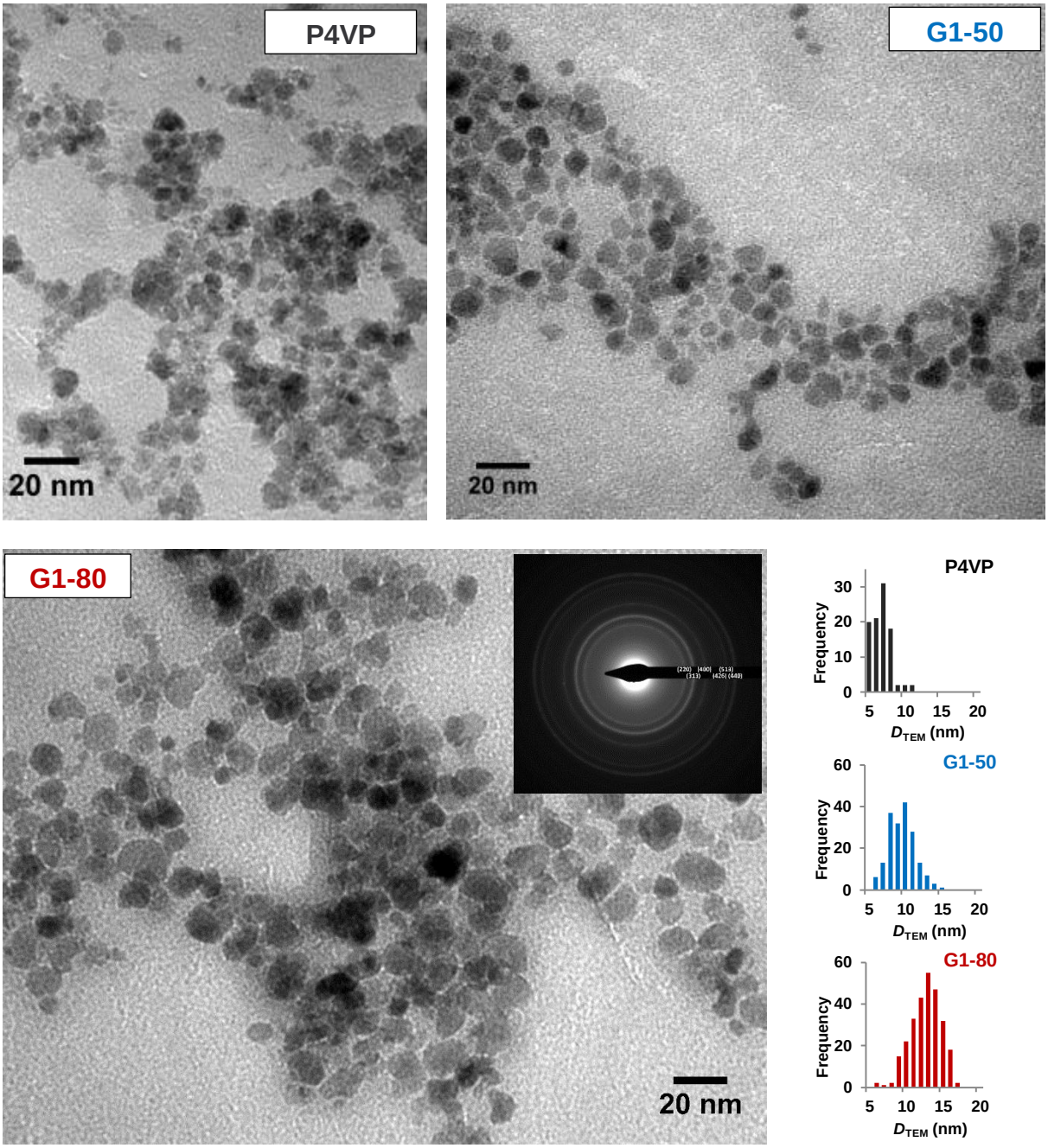

Figure 4-6. Crystallite size of Fe_3O_4 NPs synthesized in the presence of: linear P4VP at 50 °C, G1 at 50 °C, and G1 at 80 °C. Inset: Selected area diffraction pattern for templated G1@Fe_3O_4.

Growth of the Fe_3O_4 crystallites to 12.1 ± 2.0 nm was achieved when the G1-templated coprecipitation was performed at 80 °C (Figure 4-6). The elevated temperature probably accelerated both the nucleation and growth steps, resulting in a larger crystallite size. An attempt at 100 °C led to a higher oxidation level: the ferrofluid had a brownish color. We therefore decided to produce subsequent G1@Fe_3O_4 samples at 80 °C. The coprecipitation method can produce MNPs in a size range of 2–25 nm, but with a broad size distribution (usually greater than ± 25% from the mean).[85] The microemulsion technique can narrow the size distribution to within ± 5% from the mean, at the expense of a more challenging purification procedure and a much smaller quantity of product.[85] In our work a slight improvement in size distribution from ± 20% to ± 16.5% from the mean was observed, and the crystallites appeared separated by an organic layer (bright stripe around the dark cores), which is consistent with their better dispersibility (bare inorganic grains in close contact experience strong van der Waals attraction and usually cannot be separated).

Selected area electron diffraction (SAED) was employed to reveal and characterize the phases present in the oxide. The Bragg diffraction pattern confirmed a spinel structure of either magnetite Fe_3O_4 or maghemite γ–Fe_2O_3 (Figure 4-6). Unfortunately, the SAED patterns cannot distinguish magnetite from maghemite due to their isostructural character: both are cubic, with similar unit cell parameters. A few peaks are different for these two phases, but they usually appear with a low intensity and are easily blurred by background noise or crystallite size effects.[86]

Thermogravimetric analysis (TGA) served to determine the relative amounts of iron oxide and polymer template in the nanocomposites. Decomposition of the G1 polymer started at ca. 350 °C and ended at ca. 450 °C (dotted curve, Figure 4-7). The thermogravimetric trace for a physically blended mixture of dry G1 powder and Fe_3O_4 paste was similar to that of the pure G1 sample except for a weight loss after 140 °C, much sooner than for G1 alone. This is attributed to the loss of physically adsorbed water (on the surface of the nanoparticles) and surface hydroxyl groups (forming H_2O molecules by elimination

from adjacent hydroxyl groups).[87-91] This step differs from the evaporation of unbound water ending earlier, at ca. 130 °C.

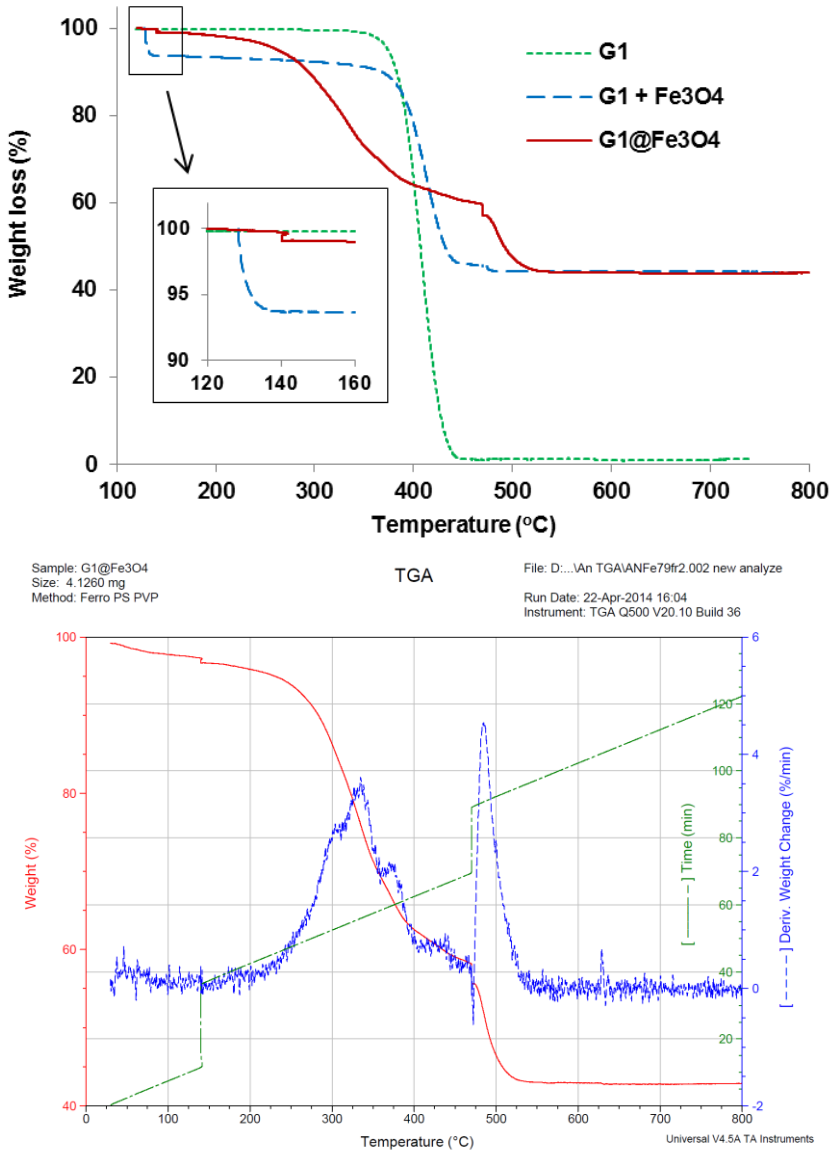

Figure 4-7. Top: TGA curves for pure G1 template (green, dotted), a mixture of dry G1 and Fe_3O_4 (blue, long dash), and G1@Fe_3O_4 (red, solid). Bottom: Temperature ramp (green, broken dash), weight loss (red, solid), and differential of the weight loss curve (blue, short dash) for G1@Fe_3O_4.

The thermal decomposition (in N_2) or combustion (in oxygen) of the templated NPs G1@Fe_3O_4 was characterized by a three-stage weight loss profile, more clearly visible in the differential of the weight loss curve for G1@Fe_3O_4 (Figure 4-7 bottom):

- A small weight loss at 140 °C, attributed to the elimination of physically adsorbed water and surface hydroxyl groups,[87-91] as observed for the mixture of dry G1 powder and Fe_3O_4 paste. The slightly larger weight loss at 140 °C (solid trace, inset of Figure 4-7 top) evidences the abundance of physically adsorbed water molecules and of surface hydroxyl groups, since the G1 template was protonated. An almost flat plateau was observed after the 140 °C isothermal step, as shown by the derivative of the weight change curve (Figure 4-7. bottom), which is consistent with the continuous evaporation of a small amount of physically adsorbed water and the elimination of surface hydroxyl groups.

- A massive weight loss in the 300–470 °C range, attributed to decomposition of PS and P2VP in the G1 template not coordinated with Fe_3O_4. The rate of weight loss decreased before reaching 470 °C. This weight loss is similar to what was observed for the two other samples, where the G1 template had no chemical interactions with Fe_3O_4.

- A weight loss that accelerated rapidly with the introduction of O_2 (at 470 °C), indicating burning of the P2VP phase coordinated with the Fe cations.

The stepwise thermal degradation of polymers in magnetic hybrids has been previously reported by different groups.[87-89,92] Zhang et al.[92] observed a two-step weight loss when characterizing folate-tetra(ethylene glycol)-terminated polyglycerol monoacrylate (FA-TEG-PGA) Fe_3O_4 nanoparticles. PGA, with 1,2-diols groups, was assumed to be chemisorbed onto the Fe_3O_4 NPs. The first weight loss was attributed to decomposition of the FA-TEG blocks and the second one, occurring at a higher temperature, was assigned to the degradation of PGA bound to Fe_3O_4. This phenomenon also occurred with dopamine L-glutamic acid linear and dendritic ligands used to functionalize Fe_3O_4 NPs.[88] At 460 °C a portion of the ligands immobilized at the surface of MNPs decomposed, while more energy (a higher temperature) was needed to break the bonds formed between dopamine and Fe_3O_4.

The stepwise thermal degradation of the G1 template likewise evidences strong interactions between P2VP and Fe_3O_4, thus confirming the success of templating.

Beyond the initial 3.1 wt% loss due to the elimination of water ($T \leq 140$ °C), a 54.9 wt% loss of organic material was observed for the G1 template for $T \leq 470$ °C, and a residual mass of ca. 42.0 wt% was found at the end of the TGA experiment. If this the composition of the residue were pure γ–Fe_2O_3, this would correspond to 43.3 wt% γ–Fe_2O_3 after correction for the initial water loss. This is higher than the theoretical composition of 35.1 wt% Fe_2O_3 calculated for a Fe/2VP molar ratio = 0.7 (Section 4.3.1.4). The γ–Fe_2O_3 content overestimation is attributed to incomplete degradation/combustion of the organic material in TGA analysis, leaving some carbonaceous material in the residue. This phenomenon has been observed before, for example by Huang et al.[93] who used TGA to determine the iron content in cross-linked poly(methacrylic acid)/iron oxide magnetic microspheres, and reported 25.8 % residual weight (measured by TGA), higher than the Fe_3O_4 content of 19.8 wt% determined by spectrophotometry analysis, indicating the presence of organic components in the residue even after a temperature of 750 °C was reached. The thermogravimetric analysis of paramagnetic microparticles functionalized with poly(ethylene glycol) (PEG) and carboxyl groups also resulted in a slightly larger mass fraction of residue at the end of the TGA experiment as compared to the Fe_3O_4 content measured by atomic absorption spectroscopy.[91] Wang et al.[94] likewise expected a theoretical value for the Fe_3O_4 content of 62.4 wt% for nanoparticles capped with oleic acid, but obtained a residual mass fraction of 68 wt% after TGA. The small discrepancy was attributed to the surface oxidation of Fe_3O_4 to γ–Fe_2O_3 in the presence of oxygen in the TGA experiment in that case, which slightly increased the inorganic component weight.[94]

The actual mass of Fe_2O_3 in the residue was determined by UV-VIS analysis in 5 M HCl. The residue (ca. 1.73 mg) was not completely soluble in 5 M HCl, leaving some black particles clearly evidencing the presence of organic material. The Fe content was determined from a linear calibration curve relating the iron concentration to the optical density at $\lambda = 350$ nm (OD_{350}) as suggested by Arosio et al.,[95] and inspired from the literature[96] (Figure 4-8).

The absorbance peak at this wavelength is ascribed to the hexachloride complex $[FeCl_6]^{3-}$ in 5 M HCl medium. An OD_{350} = 0.3695 was obtained for sample, corresponding to 1.29 mg Fe_2O_3. The total sample weight loaded for the TGA analysis was 4.126 mg, of which 3.1 wt% was water, leaving 3.998 mg of nanocomposite. The Fe_2O_3 content based on UV-VIS analysis of the residue is therefore 1.29/3.998 = 32.2 wt%, reasonably close to the theoretical composition of 35.1 wt% Fe_2O_3. As compared to TGA, the UV-VIS analysis method was therefore more reliable to determine the Fe (and Fe_3O_4) content of the MNPs.

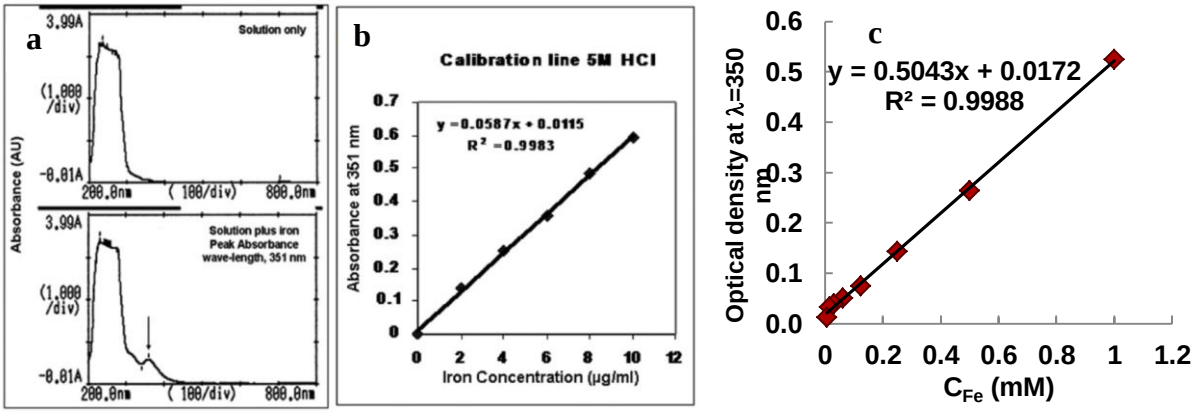

Figure 4-8. (a) Absorbance spectra for 5 M HCl without iron (top panel) and with 10 µg/mL iron (bottom panel). (b) Calibration curve in 5 M HCl generated for iron concentrations ranging from 0 to10 µg/mL. Preprinted with permission from Reference 96. Copyright 2007 BioTechniques. (c) Calibration curve generated in 5 M HCl at λ = 350 nm (path length l = 2 mm).

4.4.3 Stabilization of Magnetic Nanoparticles by the Polyion Complexation Technique

Block copolymers (BC) with a long PHEA segment, PAA_{13}-*b*-$PHEA_{150}$ and PAA_{27}-*b*-$PHEA_{260}$, proved to be the most efficient stabilizers among the BC series tested as they could form stable unimolecular micelles with the G1 arborescent copolymer, even at low f = CO_2H/N ratios. These BCs were therefore tested to form micelles with G1@Fe_3O_4 by the

same procedure applied to G1 alone. As expected, stable magnetic polyion complex (MPIC) micelles were formed for the same *f* ratios as the bare copolymers. PAA_{13}-*b*-$PHEA_{150}$ assembled with G1@Fe_3O_4 *f* = 1 to form MPIC micelles with an intensity-weighted D_h = 124 nm and a number-weighted D_h^n = 66 nm (to handle with caution, since the Malvern software does not handle the Mie-scattering model for hybrid particles made from two materials with different refractive indices and optical absorption coefficients), PDI = 0.172 (Figure 4-9). Increasing the BC amount further yielded MPIC micelles in the same size range PDI = 0.175. A lack of BC stabilizer at *f* = 0.5 almost led to doubling the size of the MPIC micelles (D_h = 181 nm, D_h^n = 118 nm, PDI = 0.150). Therefore *f* = 1 was the optimal ratio for the complexation of G1@Fe_3O_4 with PAA_{13}-*b*-$PHEA_{150}$. The MPIC micelles formed for *f* = 1 and 0.5 were nevertheless both prepared to be tested for biocompatibility (Chapter 6).

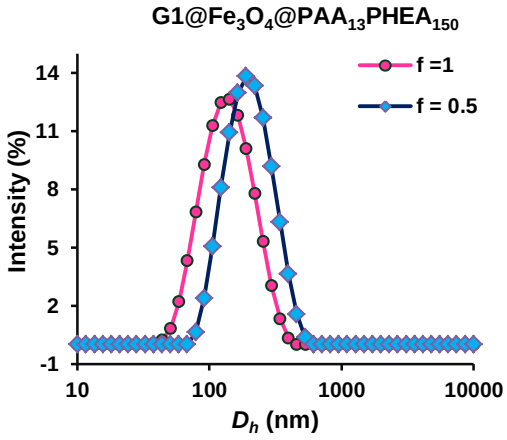

Figure 4-9. Size distributions for magnetic micelles G1@Fe_3O_4@PAA_{13}-*b*-$PHEA_{150}$ at different *f* ratios obtained at 25 °C and pH 7.

PAA_{27}-*b*-$PHEA_{260}$ also assembled with G1@Fe_3O_4 to form stable MPIC micelles (Figure 4-10). The intensity-weighted D_h = 126 nm and number-weighted D_h^n = 83 nm, PDI = 0.136 were obtained for *f* = 0.5, the optimal ratio observed for complexation with the G1

substrate. While a ratio f = 0.25 failed to prevent aggregation in complexation with G1 alone, it was able to stabilize G1@Fe_3O_4 and formed MPIC micelles in the same size range (D_h^I = 128 nm, D_h^n = 62 nm, and PDI 0.166) as for f = 0.5. The presence of Fe_3O_4 in the G1@Fe_3O_4 structure likely increased the volume of the G1 template, exposing more coordination sites and thus resulting in more efficient complexation even at the lower f ratio. The lower stability limit for PAA_{27}-*b*-$PHEA_{260}$ BC was determined to be f = 0.25, since the MPIC micelles obtained for f = 0.125 aggregated further (D_h = 235 nm and PDI = 0.322). The samples obtained for f = 0.5 and 0.25 were tested for biocompatibility (Chapter 6).

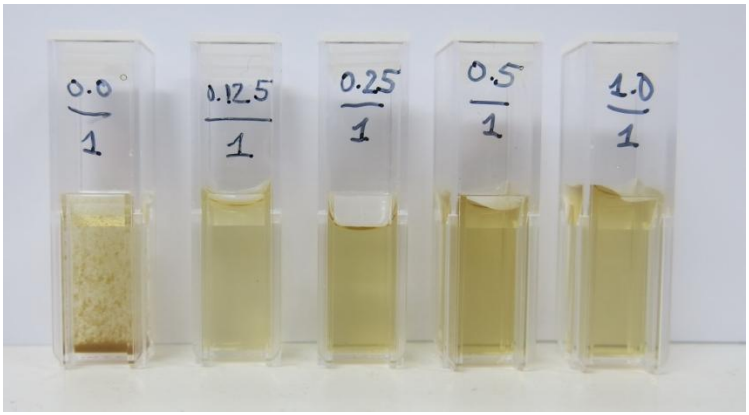

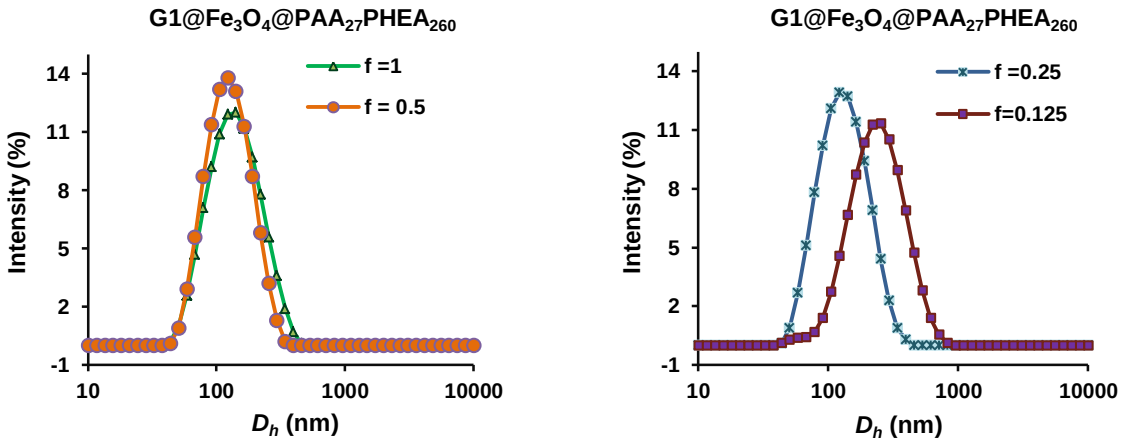

Figure 4-10. Size distributions for magnetic micelles G1@Fe_3O_4@ PAA_{27}-*b*-$PHEA_{260}$ at different f ratios obtained at 25 °C and pH 7.

MPIC micelles at f = 0.5 appeared as aggregates of Fe_3O_4 NPs in the TEM images, with D_{TEM} = 11.6 ± 2.0 nm for the Fe_3O_4 crystallites (Figure 4-11). When observed by AFM, the MPIC micelles appeared as spheres (D_{AFM} = 58 ± 15 nm) with a rather broad size distribution on the mica surface. A soft hydrophilic shell surrounding each MPIC micelle was visualized around a harder core on the phase image, confirming the presence of a PHEA layer (Figure 4-12). A larger phase lag in tapping mode AFM is indeed associated with a softer material.[97-98] The inner core–shell morphology of the MPIC micelles was probed using different amplitude set points (Figure 4-13), i.e., different forces exerted by the cantilever on the surface.

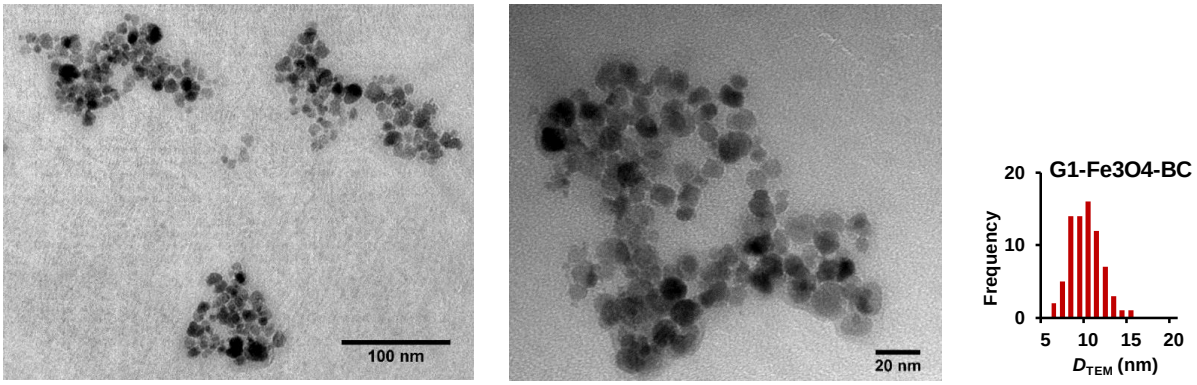

Figure 4-11. TEM images for Fe_3O_4 crystallites in G1@Fe_3O_4@PAA_{27}-*b*-$PHEA_{260}$ f = 0.5.

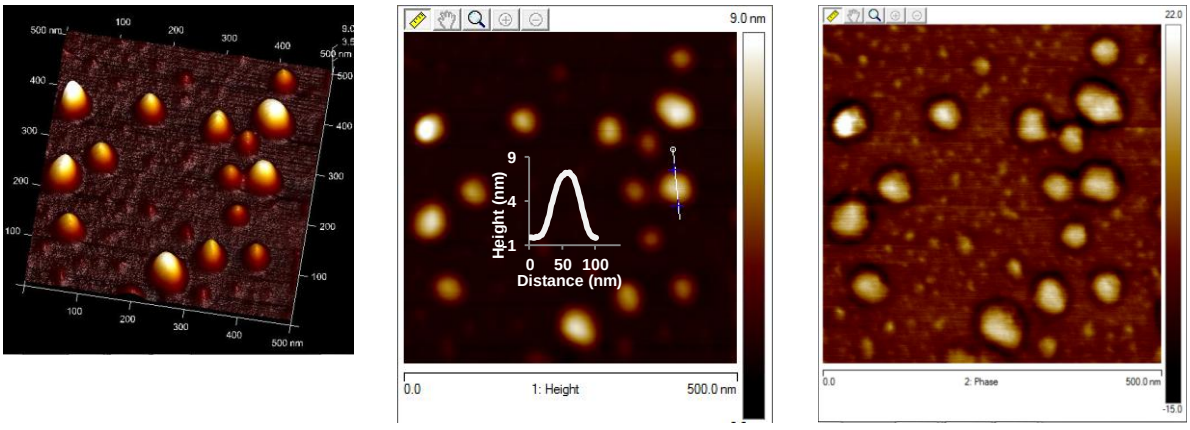

Figure 4-12. AFM images for magnetic micelles G1@Fe_3O_4@PAA_{27}-*b*-$PHEA_{260}$ f = 0.5.

The zeta potential of the MPIC micelles G1@Fe_3O_4@PAA_{27}-*b*-$PHEA_{260}$ f = 0.5 was found to be pH-dependent, similarly to the metal-free PIC complexes discussed in Chapter 3. Highly negative charges (ca. –20 mV) were found at pH ≥ 7 (Figure 4-14) due to the presence of CO_2^- functionalities. In the highly basic range, a plateau in the zeta potential of the MPIC micelles indicates complete ionization of the CO_2H groups. The increase in zeta potential in the acidic pH range is assigned to protonation of the carboxylate groups to produce a hydrophobic CO_2H derivatives, while the 2VP units of the G1 substrate yield NH^+ moieties. The point of zero charge (isoelectric point) of the MPIC micelles was around pH 3.

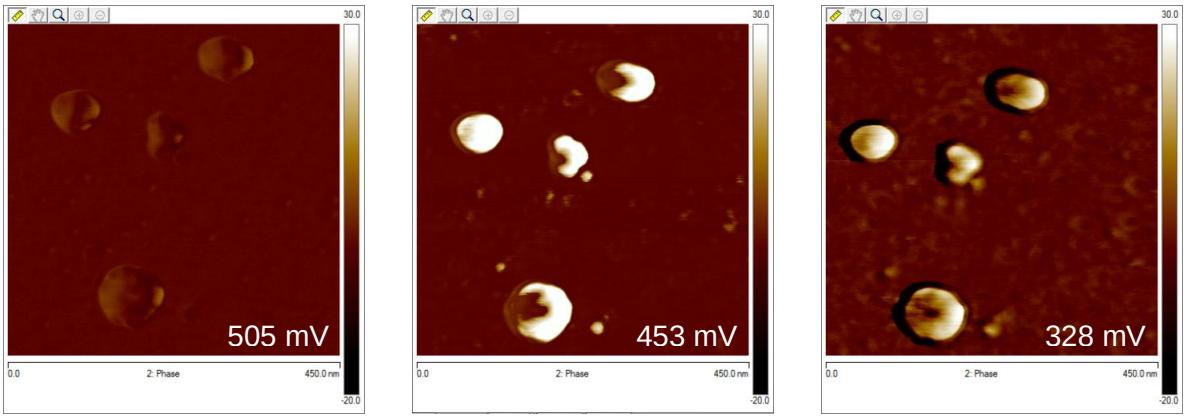

Figure 4-13. Magnetic micelles at various amplitude set points (the lower the value in mV, the higher the average deflection of the cantilever and thus the exerted force).

At pH 7.4 the intensity-weighted hydrodynamic diameter was 130 nm, almost identical with D_h = 126 nm at pH 7, the small change being possibly due to slightly higher ionization of the CO_2H groups leading to stronger electrostatic repulsion among adjacent CO_2^- groups. Slight shrinking in the high pH range (8–9.5) is assigned to the increased ionic strength. Adjusting the pH to acidic also reduced the hydrodynamic size of the MPIC micelles, this time due to protonation of CO_2^- groups to produce CO_2H derivatives. Neither clustering nor destabilization was observed over the whole pH range, indicating good colloidal stability of the MPIC micelles. At the isoelectric point (point of zero charge, pH ~

3) the MPIC micelles were also stable with D_h = 104 nm. Disassembly of the MPIC micelles into their individual components (polymers and MNPs) was not observed at any pH tested. The changes in zeta potential and size were reversible over the whole pH range. The presence of Fe_3O_4 in the MPIC micelles apparently improved the colloidal stability of the hybrid NPs as compared to the PIC micelles obtained at the same *f* ratio. This suggests that the PAA block of the DHBC forms a complex not only with the P2VP segments, but also with the Fe_3O_4 phase.

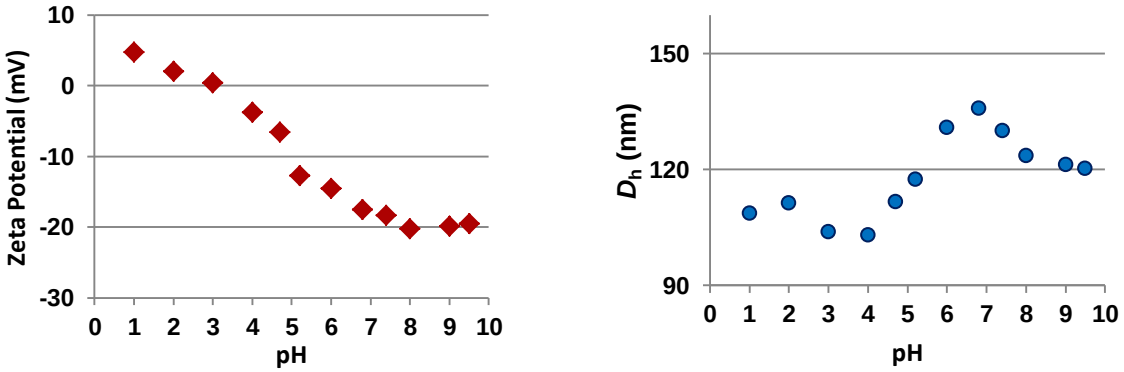

Figure 4-14. Zeta potential and intensity-weighted hydrodynamic diameter D_h of MPIC micelles G1@Fe_3O_4@PAA_{27}-*b*-$PHEA_{260}$ at *f* = 0.5 as a function of pH.

4.5 Conclusions

We observed poor performance for preformed PIC micelles as templates for the synthesis of MNPs: The product formed displayed weak magnetization and a large size. Neither templating nor stabilization were efficient by this approach, presumably because: *i)* the Fe^{2+}/Fe^{3+} salts and the PIC micelles required different pH (1.4 and 7, respectively), and an intermediate pH led to the undesirable precipitation of Fe^{2+}/Fe^{3+} hydroxides and the aggregation of PIC micelles; and *ii)* the presence of the PAA-*b*-PHEA block copolymer as a potentially competing ligand in the shell, interfering with the accessibility of the iron precursors to the 2-vinylpyridine moieties.

Chapter 4

For the first time, an arborescent copolymer (G0PS-*g*-P2VP) was used as a polymeric template to control the size and improve the size distribution of iron oxide NPs. The presence of the G1 component led to larger Fe_3O_4 crystallites ($D_{TEM} \approx 12 \pm 2$ nm) and enhanced colloidal stability due to electrostatic repulsion by the protonated NH^+ groups of the P2VP chains. A slight improvement in size distribution from ± 20% to ± 16.5% from the mean was observed, i.e. lower than the ± 25% variation usually reported for non-templated NPs.[85] When using thermogravimetric analysis (TGA) to determine the amount of iron oxide in the nanocomposites, we observed a three-stage weight loss profile for the thermal decomposition/combustion of the templated NPs G1@Fe_3O_4. The overestimation of the γ–Fe_2O_3 content by that method was ascribed to the incomplete degradation (in N_2) or combustion (in O_2) of the organic phase in the TGA experiment, which is in good agreement with literature reports.[91,93-94] The presence of carbonaceous material in the residue was confirmed by UV-VIS analysis in 5 M HCl. UV-VIS analysis therefore proved to be more reliable to determine the Fe (and corresponding Fe_3O_4) content of the MNPs, so UV-VIS analysis was preferred to TGA.

The G1@Fe_3O_4 MNPs were then complexed with a PAA-*b*-PHEA block copolymer to produce stable magnetic micelles whose core–shell morphology was revealed by tapping mode AFM height and phase imaging. We observed the stabilization of G1@Fe_3O_4 to yield MPIC micelles even for smaller amounts of block copolymer that were insufficient to prevent aggregation of the corresponding metal-free PIC micelles. The presence of Fe_3O_4 in G1@Fe_3O_4 likely increased the volume of the G1 template, exposing more coordination sites and resulting in more efficient complexation even at lower *f* ratios. The MPIC micelles obtained, with suitable hydrodynamic diameters $D_h \approx 130$ nm and good colloidal stability, not only under physiological conditions (pH 7) but also over a wide pH range, hold great promise for the biomedical applications targeted in this work.

Chapter 5 Magnetic, Relaxometric and Hyperthermic Properties Measurements

Chapter 5

5.1 Overview

The properties of magnetic nanoparticles (MNPs) obtained using a G1 arborescent copolymer as template, both in their bare and block copolymer-coated forms, were investigated by vibrating sample magnetometry, relaxometry, and alternating magnetic field hyperthermia efficiency measurements probed by calorimetry. The materials prepared displayed properties typical of superparamagnetic iron oxide nanoparticles (SPIONs). The influence of the Fe/N ratio, the coprecipitation temperature, and the Fe_3O_4 NP coating on the magnetization properties was examined. Discrepancies among the NP radii determined by relaxometry, TEM and magnetometry were explained by the different nature of these characterization methods. The magnetization value obtained by relaxometry was lower than by magnetometry, due to the larger relaxometric size englobing the non-magnetic polymer coating. The relaxivities of all the uncoated and block copolymer-coated magnetic nanoparticles were measured. The coated SPIONs had better colloidal stability but displayed limited clustering (due to their multicore nature), and thus had higher transverse relaxivity r_2 = 335 (s^{-1} mM^{-1}) and r_2/r_1 = 31.4 values (1.47 T, 37 °C) than the uncoated SPIONs. Our MNPs fare well when compared with contrast agents commercially available and in the literature, and could be useful as negative agents for T_2-weighted magnetic resonance imaging. The nuclear magnetic resonance dispersion (NMRD) curves for the MNPs exhibited no low-field dispersion. The divergence observed between the experimental NMRD curves and the theoretical fits was ascribed to the complicated internal structure of the MNPs in comparison to the common "Outer-Sphere" model developed for individually dispersed ultrasmall superparamagnetic iron oxide particles. The uncoated samples had low relaxation rates and flat NMRD profiles, indicating strong agglomeration and confirming the essential role of the block copolymer coating. A good specific absorption rate (SAR = 55.6 $W \cdot g^{-1}$) was obtained by alternating magnetic field calorimetry (755 kHz, 10.2 $kA \cdot m^{-1}$). The dependence of the SAR values on the magnetic field amplitude H and frequency f was also investigated.

Chapter 5

5.2 Introduction

Superparamagnetic iron oxide nanoparticles (SPIONs) can be used for numerous biomedical applications including magnetic resonance imaging contrast agents and heat mediators in magnetic field hyperthermia (MFH). To begin with, single domain theory and superparamagnetism will be briefly reviewed and followed by an introduction on vibrating sample magnetometry, a method commonly used to measure the magnetization curve vs. applied magnetic field strength. The contrast enhancement effect by iron oxide nanoparticles in magnetic resonance imaging will also be presented. Finally, heat dissipation mechanisms will be discussed and followed by a literature review on optimizing the specific absorption rate (SAR) values of SPIONs.

5.2.1 Single Domain Theory and Superparamagnetism

The internal structure of a bulk ferromagnet (iron, cobalt, nickel…) is split into *magnetic domains* to minimize the internal energy. Inside a magnetic domain all the magnetic moments are coupled in the same direction, thus allowing the representation of that domain by a single magnetization vector accounting for all of the magnetic moments per volume unit. Magnetic domains are separated from each other by *domain walls*, a transition region between two domains where a gradual reorientation of the magnetic moments (usually by 90° or 180°) occurs. The domain wall thickness depends on several energetic, crystallographic and geometric factors, but usually spans across ca. 100–150 atoms.[1] Domain walls can be moved across the sample by a small magnetic field. A larger ferromagnet has more possibilities of forming domain walls, due to its higher need for energy minimization and greater ease to anneal structure defects. Decreasing the sample size leads to lower energy minimization, fewer structural defects to anneal, and thus reduced wall formation. The sample size or volume may be decreased until a critical value is reached, at which point the system prefers one *single domain* configuration called a “Weiss domain”; below this threshold size, multidomain configurations are energetically unfavorable since the energy cost for domain wall formation becomes greater than the energy reduction obtained by

splitting domains. The critical radius R_C is estimated by the following formula given in the texbook on solid state physics by Kittle:[2]

$$R_C = \frac{36\sqrt{KA}}{\mu_0 {M_s}^2}$$

where M_s is the spontaneous magnetization, K is the anisotropy constant (in J/m^3), and A is the exchange energy density or constant (energy per unit length). One can define also the lengthscale below which the attractive exchange energy dominates the repulsive dipolar energy between neighboring magnetic moments:

$$l_{exch} = \sqrt{\frac{2A}{\mu_0 {M_s}^2}}$$

A sample with dimensions below R_C acquires the single domain configuration; Its magnetization can be represented by one single vector. In the absence of an external field, the magnetization of the sample is dictated to spontaneously point in a particular crystallographic direction, called the *easy magnetization axis*. The energy that prevents the magnetization from changing freely between all possible orientations is called the *anisotropy energy*, which depends upon the angle between the magnetization vector and the crystallographic direction. The direction minimizing the anisotropy energy is called the anisotropy direction or *easy axis*. The anisotropy energy increases very rapidly as the crystal radius increases, because it is proportional to the crystal volume (the proportionality constant being K). The assumption that the anisotropy has uniaxial symmetry is usually applied to systems of higher symmetry based on cubic models, since the calculations for more complicated symmetries are time-consuming without producing a complete solution.[3] Stoner-Wohlfarth[4-5] proposed the magnetic anisotropy energy of a noninteracting single-domain spherical particle with uniaxial anisotropy in zero magnetic field as

$$E(\theta) = KV\sin^2\theta$$

where K is the magnetocrystalline anisotropy constant, V is the sample volume, and θ is the angle formed between the magnetic moment and the easy axis.

The dependence of the anisotropy energy on θ is depicted schematically in Figure 5-1. Both orientation states with minimum energy (θ = 0 or π) are equally probable and are separated by an anisotropy energy barrier E_a=KV. An external magnetic field H applied along the easy axis reduces the magnetic anisotropy energy barrier, facilitating switching of the magnetization from an energy-unfavorable state (opposite to the field) to an energy-favorable state (along the field and oriented in the same direction), thus the interaction energy between the moment and the external field appears as a negative correction to the previous equation,

$$E(\theta) = KV\sin^2\theta - M_S H M_{nr}\cos\theta$$

where M_{nr} is the nonrelaxing magnetization.

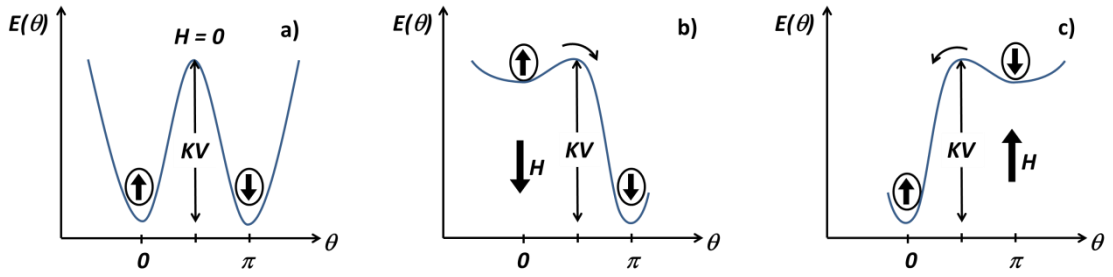

Figure 5-1. Switching of the magnetization in a particle across the anisotropy barrier under a) no external magnetic field; b) external magnetic field pointing downward; and c) external magnetic field pointing upward.

The anisotropy energy decreases when decreasing the volume of the MNPs, although the anisotropy energy constant K becomes larger for very low values of the sample diameter (d). More precisely, it was shown that the effective anisotropy constant is the sum of a volume term K_V and a surface term K_S according to the $K = K_V + K_S/d$ where K_V=10.4 kJ/m^3 and K_S=39 μJ/m^2 for Fe_3O_4 NPs.[6] Nevertheless, reductions in size can decrease the magnetic anisotropy energy barrier $E_a = KV$ down to a critical level where it becomes comparable to or

even lower than the thermal activation energy (k_BT, k_B being Boltzmann constant). The energy barrier for magnetization reversal is thermally overcome; the magnetic moments rapidly fluctuate from one orientation state to another, a behavior also found in paramagnetism, but with magnetic moments several orders of magnitude higher. The sample then enters the *superparamagnetic* regime. A system is commonly described as superparamagnetic when *i*) the M/M_s vs. H/T curves for a range of temperatures above the so-called "blocking temperature" T_B superimpose on each other; *ii*) neither coercive field H_c, remanence magnetization M_r, nor hysteresis exist (Section 5.2.2).

Another important magnetic parameter for single domain particles is the Néel relaxation time. This is the time that a magnetic moment needs to return to thermal equilibrium after a perturbation. When the anisotropy energy is sufficiently large, it keeps the magnetization locked along an easy axis. Once the Stoner-Wohlfarth energy of magnetization exceeds the anisotropy barrier, the Néel relaxation time is defined as the fluctuation time for a magnetic moment to flip between easy axes. The Néel relaxation time τ_N is defined as:

$$\tau_N = \tau_0 \exp \frac{E_a}{k_B T}$$

where E_a is the anisotropy energy, k_B is the Boltzman constant, T is the absolute temperature, and τ_0 is the pre-exponential factor of the Néel relaxation time expression also called "attempt time" because it is the repetition time between attempts for the magnetic moment to cross the barrier:[7]

$$\tau_0 = \frac{\sqrt{\pi}}{4} \frac{M_s(0)V}{E_a \gamma_e} \left[\frac{1}{\eta_f} + \eta_f \left(\frac{M_s(T)}{M_s(0)} \right)^2 \right] \sqrt{\frac{kT}{E_a} \left(1 + \frac{kT}{E_a} \right)}$$

where V is the crystal volume, $M_s(0)$ is the specific magnetization of the crystal extrapolated at 0 K, $M_s(T)$ is the specific magnetization at the experimental temperature, γ_e is the gyromagnetic ratio of the electron, and η_f is a dimensionless constant.

The parameter τ_0 depends on several factors: the temperature, magnetic field strength, magnetization, particle size, etc. but it is usually assumed to be a constant within a range of

10^{-9}–10^{-13} s. The Néel relaxation time varies with the temperature and the size of the magnetic nanoparticles. For small size particles with a small anisotropy energy at high temperatures, the anisotropy energy is easily exceeded by the thermal energy ($E_a << k_BT$), and therefore the exponential factor tends to 1. The Néel relaxation time is determined by the pre-exponential term τ_0, which decreases with increasing E_a. At a given temperature, if the measurement time is longer than the Néel relaxation time, the magnetization rapidly relaxes by thermal fluctuation. The system has an "unblocked" magnetization typical of the superparamagnetic state. When $E_a >> k_BT$, the Néel relaxation time is determined by the exponential factor, which rapidly rises as the anisotropy energy increases. If the measurement time is shorter than the Néel relaxation time, the magnetization relaxes slower – it seems to be "blocked". The specific temperature at which the relaxation time matches the measurement time is called the *blocking temperature*, usually noted T_B. External fields, interactions, and especially the particle size distribution were found to affect the blocking temperature. As most magnetization measurements (VSM or SQUID) have experimental times within one minute ($\tau_{meas} \approx 10^2$ s), the blocking temperature usually obeys to the phenomenological equation $\tau_{meas} = \tau_0 \exp(E_a(T_B)/k_BT_B)$, defining numerically $E_a(T_B) = 2.3 \times 11k_BT_B \approx 25k_BT_B$. Experimentally, blocking temperatures are determined qualitatively at the maximum of the "zero field cooled" curve (ZFC) representing the sample magnetization vs. temperature or, for polydispere samples, through a more quantitative fitting of the ZFC curve.[8]

For well-dispersed magnetic NPs in a magnetic fluid, the effective relaxation time of the magnetic moments τ is determined not only by the Néel relaxation time τ_N but also by the Brownian relaxation time τ_B, reflecting the rotation of the particles in a viscous medium:

$$\frac{1}{\tau} = \frac{1}{\tau_N} + \frac{1}{\tau_B}$$

$$\tau_B = \frac{3V\eta}{kT}$$

Large particles have short τ_B and long τ_N values, since τ_B is proportional to the crystal volume *V* but τ_N has *V* in its exponential function. The relaxation time is therefore determined by the shorter relaxation time, in this case τ_B, which explains why the relaxation time for a magnetic fluid is faster than when the solvent is frozen or for a dry powder, and why the magnetization curve is reversible: Even if their moment is blocked along an easy axis, the particles in a *superparamagnetic* regime can physically rotate when the magnetic field changes its polarity; thus the overall magnetization of the suspension can follow the field (some authors refer to this phenomenon as "extrinsinc superparamagnetism" as the magnetic suspension in a fluid carrier still exhibits superparamagnetism even in the case where the moments are blocked, corresponding to ferro- or ferrimagnetism behavior in the solid state).

5.2.2 Vibrating Sample Magnetometry – Magnetization Curve[9-11]

Vibrating sample magnetometry (VSM) is a method to measure the magnetic moment of a sample by its continuous vibrational motion parallel to a uniform magnetizing field, through the synchronous detection of the magnetic flux induced in a "pickup coil" at the same frequency as the mechanical oscillation of the sample.[10] The first instruments invented by Foner had a sensitivity of up to 10^{-5}–10^{-6} emu (the detectable range for a modern VSM instrument is as low as 10^{-6}–10^{-8} emu)[9] and a stability of 0.01%. VSM is simple, less expensive than a magnetometer with a superconducting quantum device (SQUID), and versatile. VSM indeed enables the minimization of many sources of error found in other methods and permits precision magnetic moment measurements in a uniform magnetizing field as a function of temperature, magnetizing field strength, and crystallographic orientation.[10]

In a VSM experiment, the sample is placed inside the uniform magnetic field created by an electromagnet to magnetize the sample before it is oscillated at fixed frequency (about 80 Hz), which creates an electromotive force in the pickup coil. The induced voltage is

proportional to the magnetic moment of the sample, but independent of the strength of the applied magnetic field (that is homogeneous and constant, thus also its flux through the coil): $V_{coil} = 2\pi f C m A \sin(2\pi f t)$; where C is a coupling constant, A is the oscillation amplitude, f is the oscillation frequency, and m is the DC magnetic moment of the sample. The induced voltage measured by the detection coil can be written, according to the Lenz law:

$$V_{coil} = \frac{d\Phi}{dt} = \left(\frac{d\Phi}{dz}\right)\left(\frac{dz}{dt}\right)$$

where Φ is the magnetic flux of the magnetic induction B lines enclosed by the pickup coil, z is the vertical position of the sample with respect to the coil, and t is time.

When applying cyclic positive and negative magnetic field values to a sample, a *hysteresis loop* indicating irreversible changes in magnetization M with respect to the applied field strength H_{applied} can be obtained (Figure 5-2a). Since the sample is initially unmagnetized, the initial path indicating the increase in M as H is increased is called a "*minor loop"*. The most useful parameters extracted from the hysteresis loop are the *saturation magnetization* M_{sat}, the *remanence magnetization* M_{r}, and the *coercive field* H_{c}. The *saturation magnetization* M_{sat} is the limiting value that the curve can reach within the high-magnetization-field region – when all the magnetic moments are aligned with the magnetic field. When the field is decreased the magnetization of the sample decreases, but it is unable to recover its unmagnetized state. The amount of magnetization retained in the sample at zero-field is called the the remanent magnetization M_{r} or simply *remanence*. The *coercive field* H_{c} is the field needed to demagnetize a sample exhibiting (irreversible) magnetic hysteresis. A system is commonly described as superparamagnetic when *i*) the M/M_{s} vs. H/T curves for a set of temperatures above T_{B} superimpose on each other; *ii*) neither coercivity H_{c}, remanence M_{r}, nor hysteresis exist (Figure 5-2b).

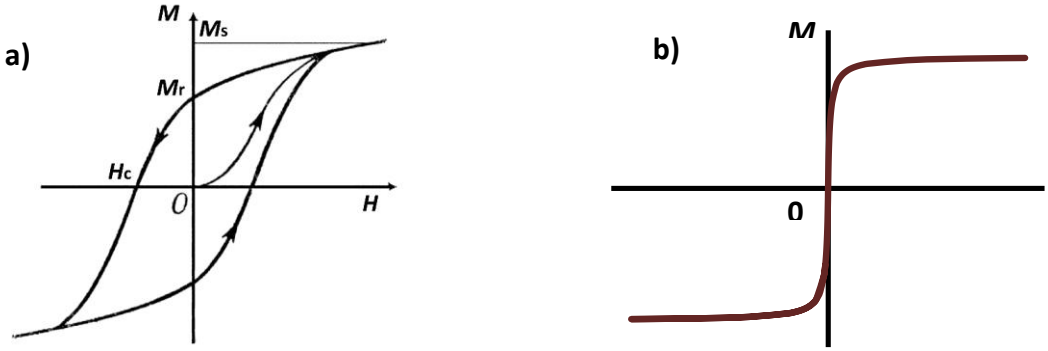

Figure 5-2. a) Main parameters of interest extracted from a generic hysteresis loop; b) Room temperature magnetization curve for superparamagnetic particles.

It is possible to extract parameters of interest from the room temperature magnetization curve of a ferrofluid if a log-normal particle size distribution is assumed to describe the size dispersity: the saturation magnetization M_{sat}; the specific magnetization M_s; the width of the size distribution expressed as Ln(D) (σ); and the median particle diameter of the distribution (D_0), which is defined as a value separating the particles into 50% of larger-than-D_0 particles and 50 % of smaller-than-D_0 particles. In work published in 1978, Chantrell et al.[12] reported discrepancies between the magnetic-size-distribution parameters (measured by VSM) and the physical-size-distribution parameters (measured by microscopy): $D_0 < D_{0phy}$ and $\sigma > \sigma_{phy}$, which was later confirmed by Popplewell et al.[13] Later on, Bacri et al.[14] suggested the treatment of superparamagnetic colloidal solutions (or suspensions) as an ensemble of polydisperse magnetic moments using the *Langevin's equation of superparamagnetism* convolved with a size distribution $P(D)$. Each ferromagnetic single domain particle carries a permanent magnetic moment μ that progressively aligns along the magnetic field H, starting from a random orientation at zero-field. The magnetization $M(D)$ of a monodisperse population of particles of diameter D in a magnetic field of strength H was given by Langevin:

$$M(D,H) = M_{\text{sat}}\,\mathrm{L}(D,H) = M_{\text{sat}}\left[\coth\left(\frac{\mu\,H}{k_{\mathrm{B}}T}\right) - \frac{k_{\mathrm{B}}T}{\mu\,H}\right]$$

$$\mu(D) = \mu_0 M_{\mathrm{s}} \pi D^3/6$$

$$M_{\text{sat}} = M_{\mathrm{s}}\varphi$$

where M_{sat} is the magnetic moment of the sample under saturation conditions, μ_0 is the vacuum magnetic permeability, M_{s} is the specific magnetization of the magnetic material in the suspension of nanometric grains (always smaller than in the bulk); φ is the solid volume fraction, related to the molar content through the molar volume (15.77 cm^3/mol for γ–Fe_2O_3); T is the temperature, and k_{B} is the Boltzmann constant. One salient feature of Langevin's law is its linear variation at low field, whose slope is called magnetic susceptibility and writes:

$$\chi(D) = \frac{\mu_0 \varphi M_s^2 \pi D^3}{18 k_B T}$$

showing the $1/T$ dependence characteristic of (super)paramagnetism (Curie's law).

In reality, ferrofluid samples are never monodisperse; a log-normal distribution $P(D)$ is usually assumed as probability law for quasi-spherical magnetic particles of diameter D:

$$P(D) = \frac{1}{D\sigma\sqrt{2\pi}} \exp\left(\frac{\ln^2(\frac{D}{D_0})}{2\sigma^2}\right)$$

where D_0 is the median particle diameter of the distribution and σ is the size distribution width, defined as the standard deviation for the $\mathrm{Ln}(D/D_0)$ distribution.

The mean-average and volume-average diameters may then be calculated from the equations:

$$\langle D \rangle_{\mathrm{n}} = D_0 \exp\left(\frac{\sigma^2}{2}\right)$$

$$\langle D \rangle_{\mathrm{v}} = \frac{\langle D^4 \rangle}{\langle D^3 \rangle} = D_0 \exp\left(\frac{7\sigma^2}{2}\right)$$

and the diameter-dispersity can be defined by analogy to the molar mass dispersity of polymers: $Đ = \exp(3\sigma^2)$.

Size dispersity introduces a distortion in the magnetization curve

$$M = \int_0^{+\infty} M(D)P(D)\mathrm{d}D$$

since M/M_{sat} becomes a function of $M_{\mathrm{s}}D_0^3 H/k_{\mathrm{B}}T$ and σ. From the shape of the magnetization M versus field intensity H curve, a computational fit of the experimental data to a log-normal probability law of median diameter D_0 yields M_{s}, σ and D_0. In this work, we used the fitting technique developed by Bacri et al. using the least mean-square solver of MS Excel.[14] The susceptibility is also shifted towards larger values by size dispersity according to

$$\chi(D_0, \sigma) = \frac{\mu_0 \varphi M_s^2 \pi D_0^3}{18 k_{\mathrm{B}} T} \exp\left(\frac{9\sigma^2}{2}\right)$$

5.2.3 Magnetic Resonance Imaging - How Iron Oxides Affect Proton Relaxivity

5.2.3.1 Magnetic Resonance Imaging

Among the nuclei commonly found in high abundance in the body hydrogen ^{1}H (but not ^{12}C nor ^{16}O), with an odd mass number (number of nucleons) is selected for magnetic resonance imaging (MRI) because it has a non-zero spin – a quantum mechanical property reflecting the rotation of the nucleus around its own axis. This rotation can be considered as a circulation of charge or a tiny current loop producing its own magnetic moment. Each magnetic moment undergoes a *precession* motion, and a population of hydrogen atoms has its magnetic moments pointing in random directions. When subjected to an external field B_0,

the magnetic moments precess, i.e. they are animated by a rotary motion with a tilt angle around the direction of B_0. In thermal equilibrium, according to the Boltzmann distribution, there are slightly more nuclei oriented along B_0 (zero tilt angle) than against it (tilt angle is π), inducing a small net longitudinal magnetization, M_0 (Figure 5-3). However all the magnetic moments precess with random phases; therefore they produce no net transverse magnetization. The frequency at which the nuclei precess around the magnetic field is called the Larmor frequency, ω_L, which is proportional to the strength of the magnetic field B_0:

$$\omega_L = \gamma B_0$$

where γ is the gyromagnetic ratio of the nucleus ($\gamma \approx 2.67 \times 10^8$ rad/s/T for the proton ^{1}H).

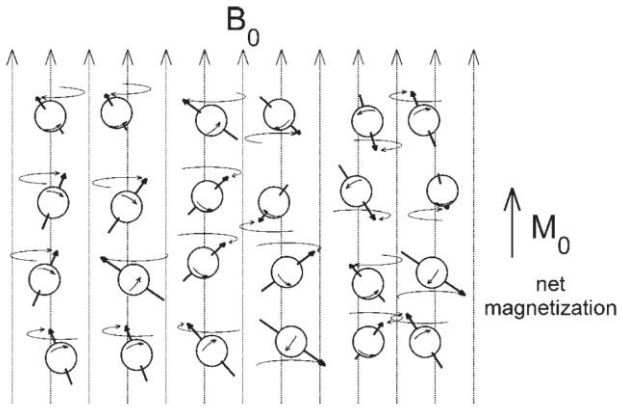

Figure 5-3. Nuclei spin oriented along B_0, with a slight excess in its direction producing a net longitudinal magnetization, M_0. Reprinted with permission from Reference 15. Copyright 2006 Humana Press Inc.

Applying a radio frequency (RF) magnetic pulse with pulsation $\omega_{RF} = \omega_L$ in the direction perpendicular (B_1) to the population of oriented nuclei induces two events:

1. The nuclear magnetizations are tipped away from the longitudinal axis with a flip angle, increasing the net energy of the nuclei above their equilibrium value. The nuclear magnetization continues to precess, but now around the B_1 axis.
2. The nuclei that had been oriented by B_0 now precess in phase/in synchrony, producing a transverse magnetization in the transverse plane, called M_{xy}.

These induced magnetizations can be detected with an RF coil, also called a "detection antenna". When the RF pulse is turned off, there are two relaxation regimes occuring:

1. The nuclei gradually lose the additional energy through interactions with neighboring nuclei and the environment, bringing the system back to its equilibrium state and producing an oscillating magnetic field that can be detected with a radio frequency coil. The recovery of the longitudinal (M_z) magnetization toward its equilibrium value M_0 occurs during a time interval T_1, termed *longitudinal or spin-lattice relaxation*.
2. Nuclei undergo *transverse or spin-spin relaxation*: They stop precessing in phase, losing their phase coherence. The transverse magnetization (M_{xy}) gradually decays back to zero with a characteristic decay time T_2.

Despite the variety and complexity of RF pulse sequences used in MRI to manipulate the population of spins and create MR images, the simpliest one is the spin-echo sequence, represented in Figure 5-4. According to the solutions of Bloch equations describing longitudinal and transverse relaxations, the MRI signal detected by the antenna along M_{xy} is proportional to the density of protons and to the product $\left(1 - e^{-\mathrm{TR}/T_1}\right) \cdot e^{-\mathrm{TE}/T_2}$, where TR and TE are respectively the repetition time and the echo time. Sequences with short TR and short TE are considered as "T_1-weighted" sequences, while those with long TR and long TE are "T_2-weighted", and sequences with long TR and short TE are considered "density-weighted" (i.e. their contrast depends only on the local concentration of protons).

The value of T_1 varies according to the host molecule (e.g. in body tissues, it differs for water and lipids in fat, and in brain for grey matter, i.e., the cellular body of neurons vs. white matter) and its immediate surroundings. The T_1 for water in body fluids (blood and

cerebrospinal fluid) is longer than 1 s at 1.5 T, much longer than in fat (250 ms at 1.5 T) and much longer than in solid tissues, where motions are more restricted. The T_1 variations among tissues produce signal contrast on the MR images: Fat and solid tissues relax quickly, producing a signal with a high intensity appearing bright on a T_1-weighted image while water, with much slower longitudinal relaxation, induces a lower signal and appears dark. T_1-weighted sequences are used to create T_1-weighted images, demonstrating differences in T_1 relaxation times of the tissues. The production of T_1-weighted images with good contrast requires the repetition of excitation and signal acquisition. The repetition time between successive excitations TR needs to be sufficiently long to allow the longitudinal magnetization of tissues of interest to fully recover their equilibrium state before the next excitation, but it also needs to be sufficiently short to create tissue contrast within a reasonable time frame.

Transverse relaxation happens more rapidly than longitudinal relaxation, because it involves both microscopic and mesoscopic processes. The transverse relaxation caused by microscopic processes (due to intrinsic factors, namely the molecular size and tissue type) is denoted as T_2. Mesoscopic factors such as the magnetic field inhomogeneity and magnetic susceptibility differences among the tissues in fact decrease the transverse magnetization relaxation time to a T_2* value. Free water in body fluids, due to its constant rotation, relaxes relatively slowly in ca. 3–4 s, more slowly than immobilized fat tissues ($T_2 \approx 100$ ms), which explains why water appears bright while fat tissues appear dark when sufficiently long repeat time TR and echo time TE are used. T_2 and T_2* differences between the tissues can be used to produce contrast on T_2- and T_2*-weighted images.

The dephasing caused by mesoscopic factors follows a free induction decay (FID) regime and can be reversed by applying a 180° RF pulse of B_1 (a refocusing pulse). This pulse creates inverse field inhomogeneities that gradually attenuate the phase differences among faster and slower spins, until they precess in phase again, producing a brief signal called “spin echo”. The time for the spins to rephase equals the time for which they were allowed to dephase, and the total is known as the echo time, TE.

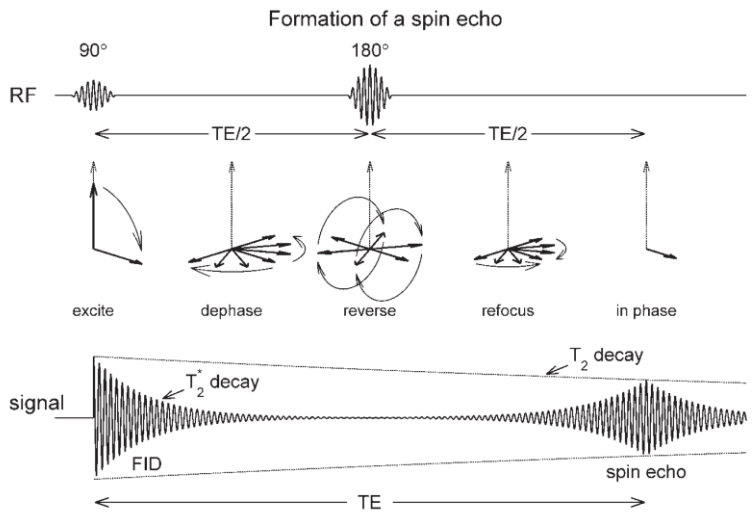

Figure 5-4. 180° Refocusing pulse and the formation of a spin echo. Reprinted with permission from Reference 15. Copyright 2006 Humana Press Inc.

Microscopic interactions, varying as the molecules under thermal agitation rotate and diffuse, cannot be compensated by the refocusing procedure. Therefore FID acquisitions provide T_2* weighting contrast, whereas spin-echo acquisitions offer T_2 weighting contrast. A longer delay between the RF excitation and the signal acquisition allows more time for transverse relaxation, so that tissues with short T_2 or T_2* will appear darker than those with longer relaxation times.

To obtain good tissue contrast for T_1-weighted images, short TR and TE are usually selected to record the signal differences between the tissues. Setting TR to a long value allows the T_1 effect on tissue contrast to disappear and for a sufficient long TE, the differences in signals induced by the transverse relaxation will emphasize the tissue T_2-contrast, defining the sequence parameters for T_2-weighted images (long TR and long TE).

Individual nuclei obey the laws of quantum mechanics. It is therefore possible to apply the rules of quantization and the quantum mechanical description of RF excitation and signal emission to describe MR physics.[15] However since the number of nuclei in a

macroscopic sample is extremely large, a discussion of MR in terms of classical physics is more adequate to explain many aspects of their collective behavior and to understand the imaging techniques.[15]

5.2.3.2 Magnetic Resonance Contrast Agent – How SPIONs Affect Proton Relaxation

Magnetic resonance contrast agents (MR CAs) reduce the T_1 and T_2 relaxation times of proton nuclei in the target tissue. Depending on whether the relative reduction in relaxation times is greater for T_1 or T_2, the MR CAs are categorized as either 'T_1 agents' or 'T_2 agents'. The efficiency of SPION as MRI contrast agents is determined by their relaxivities r_1 and r_2: the enhancement of the longitudinal or transverse relaxation rates induced by an aqueous solution containing 1 mmol of iron per L:

$$R_{\mathrm{i(obs)}} = \frac{1}{T_{\mathrm{i(obs)}}} = \frac{1}{T_{\mathrm{i(diam)}}} + r_{\mathrm{i}}C\ ;\ \ \mathrm{i} = 1 \text{ or } 2$$

where $R_{\mathrm{i(obs)}}$ is the total relaxation rate of the aqueous system (s^{-1}), $T_{\mathrm{i(diam)}}$ is the relaxation time of the system without addition of the contrast agent, C is the concentration of the paramagnetic center ($mmol \cdot L^{-1}$), and r_{i} is the relaxivity ($s^{-1} \cdot mmol^{-1}L$).

The origin of contrast enhancement lies in the different properties of healthy and diseased tissues. Diseased tissues are metabolically different from healthy tissues: Due to an anarchic and leaky vasculature, they have a much higher CA uptake, resulting in enhanced contrast in the MRI images. T_1 agents produce positive image contrast due to the increased image signal intensity at the tissue site where the T_1 shortening effect dominates, through the contribution $\left(1 - e^{-\mathrm{TR}/T_1}\right)$ that makes the signal larger than without the CA. The negative image contrast induced by T_2 agents is ascribed to the predominant effect of T_2 shortening, lowering the term $e^{-\mathrm{TE}/T_2}$.[16] Iron oxide NPs could thus be designed either as positive CAs to detect metastatic lymph nodes, or negative CAs for liver tumor imaging.[17]

The influence of MR CAs on the proton relaxation of a system stems from two contributions: the inner- and outer-sphere relaxations. Inner-sphere relaxation is assigned to the direct exchange of energy between protons and electrons located in the first hydration

sphere of the paramagnetic metallic cation or superparamagnetic particle surface. For SPIONs, the inner-sphere relaxation is minor because most of the Fe^{3+} cations are located inside the crystals, and thus their coordination sphere is already full. It is thus negligible as compared to the outer-sphere relaxation, which is related to the behavior of water protons in the magnetic field gradients created by the SPIONs in their vicinity (Figure 5-5). A SPION behaves differently from a paramagnetic complex: While each individual atom of a paramagnetic molecule is influenced independently by an external magnetic field, the magnetic moments of the entire SPION particle are all aligned together and re-orient cooperatively with the magnetic field. The magnetic moments of the individual ions do not cancel out but are collectively aligned, providing the SPION with a permanent magnetic moment that is much larger than that of a single molecule of paramagnetic Gd chelate (typically by a factor of 1000) in the presence of a magnetic field.[3,18]

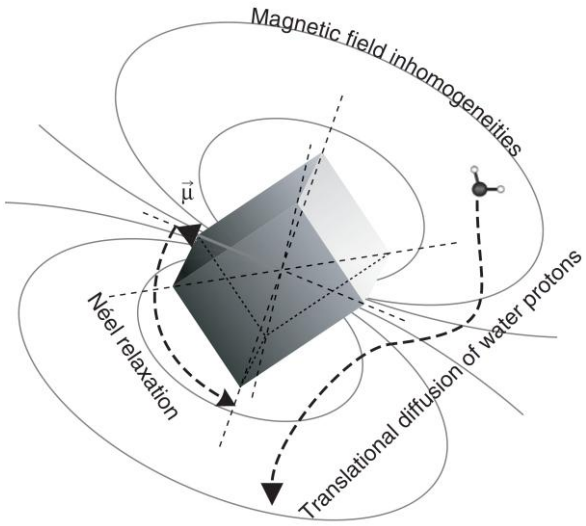

Figure 5-5. Outer-sphere relaxation of water protons in the vicinity of a superparamagnetic CA. Reprinted with permission from Reference 19. Copyright 2009 John Wiley & Sons, Inc.

The fluctuations in dipolar magnetic coupling between the water proton spins and the magnetic moments of the SPIONs are influenced by the translational diffusion of water

protons and by the Néel relaxation (flip of the particle magnetic moment between easy axes). The relaxation rate increases with the fluctuation correlation time and with the magnitude of this fluctuation. The translational diffusion of water protons varies with the minimal approach distance between the surface of a SPION and the water molecules. The translation correlation time τ_D, defined as the time for a water molecule to diffuse within a radius *r*, is given by $\tau_D = r^2/D$, where D is the water diffusion coefficient and r is the outer-sphere radius, that is either the crystal radius for a bare SPIO particle, or the total radius including the shell thickness in the case of a SPIO particle or multi-core cluster coated by a non-magnetic layer impermeable to water. The correlation time of the Néel relaxation is called the Néel relaxation time (τ_N), which depends on crystal anisotropy. The combination of these two relaxation processes results in a global relaxation time τ_C with $1/\tau_C = 1/\tau_D + 1/\tau_N$.

If τ_C is longer than the precession period of the spin within the external magnetic field B_0, i.e. $\tau_C > 1/\omega_I$ or $\omega_I\tau_C > 1$ (where ω_I is the angular frequency of the proton precession), the fluctuation is averaged by the precession and thus inefficient to relax the proton spins. Rapid fluctuations in the interactions between the magnetic moment of the particle and the proton spins of water is expected to efficiently relax the proton spin magnetization, i.e. when τ_C is shorter than the precession period of the proton spin: $\tau_C < 1/\omega_I$ or $\omega_I\tau_C < 1$. The correlation between proton relaxation and the applied magnetic field B_0 or frequency is discussed in details in Section 5.4.2

In small crystals on the contrary, the anisotropy energy is comparable to the thermal energy and the particle magnetization is no longer locked onto the anisotropy directions, allowing some electron spin precession around the direction of the B_0 field. Under these conditions the assumption of rigorous locking of the magnetization along the easy axes becomes less valid, which leads to the requirement of a new theory that introduces anisotropy energy as a quantitative parameter in the problem. However this model does not provide an analytical solution for the NMRD profile, and the fitting of experimental NMRD curves by a

heuristic method, which in theory can lead to the determination of the anisotropy energy E_a, is in practice time-consuming in numerical computing.[3,19]

SPIONs are therefore mostly used with T_2 or T_2*- weighted MR pulse sequences, introducing a "negative contrast" on images, i.e. they produce darker regions where they accumulate in comparison to pure buffer or tissues. The classification of MR CAs as either 'T_1 agents' or 'T_2 agents' is not always accurate, since any CA that shortens T_1 also shortens T_2. However, any agent that reduces T_2 does not necessarily reduce T_1, at least at the high magnetic field strengths used in clinical MRI scanners. Whether the CA functions as a 'T_1 agent' or 'T_2 agent' depends on the imaging sequence used, the magnetic field strength, the size of the CA, and how the CA is compartmentalized in the tissue.[16] Nevertheless, a good performance criterion for these materials is the ratio of relaxivities r_2/r_1 at a given field/frequency value: One can expect positive contrast enhavement only for $r_2/r_1 < 4$ at most (since the signal is measured by the antenna in the M_{xy} plane, it is cancelled by any too large T_2 effect).

5.2.4 Magnetic Field Hyperthermia

5.2.4.1 Heat Dissipation Mechanism

Both ferri/ferromagnetic materials and superparamagnetic NPs dissipate heat when subjected to an alternating magnetic field (AMF) due to several mechanisms. While ferri/ferromagnetic materials produce heat as a result of hysteresis losses, which can be measured by integrating the area of the static hysteresis loop of magnetization vs. DC field strength, superparamagnetic NPs dissipate heat through relaxation losses, categorized as Néel relaxation and Brownian relaxation.[20] The equations for the Néel and Brownian relaxation times were given earlier. The size of the superparamagnetic NPs determines the predominance of one relaxation type over the other – losses by Néel relaxation are prevalent for small NPs, while Brownian relaxation dominates for larger NPs.[21-23] The anisotropy energy of a magnetic material also assigns the primary mode of relaxation since the Néel

relaxation time varies exponentially with the anisotropy energy, while the Brownian relaxation time depends on both the suspension viscosity and the hydrodynamic volume of the particles.[24] For hyperthermia applications, relaxation through the Néel mechanism is preferable since a change in the medium viscosity is unavoidable once the particles are internalized in the cells, which hampers the free rotation of particles.

The combination of the two magnetic relaxation rates gives the overall effective relaxation rate of the particles: $1/\tau_{\text{eff}} = 1/\tau_{\text{B}} + 1/\tau_{\text{N}}$. The reorientation of the magnetic moment between easy axes in a Néel relaxation regime with each oscillation of the external magnetic field creates an internal 'friction', while the rotation of the entire particle in the Brownian relaxation regime induces solvent velocity gradients and an external viscous friction.[23] Under exposure to an AMF oscillating faster than the relaxation time of the MNPs, both internal and external frictions lead to a phase lag between the magnetic moment of the particles and the external magnetic field. The delay in the relaxation of the magnetization response is described by a complex magnetic susceptibility $\tilde{\chi}(f)$, the thermal losses being related to the imaginary part $\chi''(f)$ of the susceptibility.[18,20]

The dissipated heat power (P) is given by[25]:

$$P = \mu_0 \pi \chi'' f H_{\text{max}}^2$$

where P is the heat dissipation value, μ_0 is the permeability of free space, χ'' is the AC magnetic susceptibility (imaginary part), f is the frequency of the applied AC magnetic field, and H_{max} is the amplitude of the applied AC magnetic field.

The heat dissipation ability of magnetic nanoparticles in an AMF is usually quantified through the specific absorption rate (SAR) expressed in $W \cdot g^{-1}$ (also referred to as the specific loss power – SLP):[21]

$$SAR = \frac{P}{m} = \frac{C}{m}\frac{\Delta T}{\Delta t}$$

where C is the specific heat capacity of the sample (usually assimilated to the value of the solvent, C=4.18 J/°C/g for water), m is the mass concentration of magnetic material in suspension (g of Fe_3O_4/ g of water) and $\Delta T/\Delta t$ is the initial slope of the time-dependent heating curve (°C/s).

5.2.4.2 Tuning the SAR Values

A suspension of MNPs with a high SAR is highly desirable for clinical magnetic field hyperthermia (MFH), because a smaller amount of MNPs would then be required for *in vivo* injection. The SAR value of a magnetic fluid depends on the frequency and the amplitude of the alternating magnetic field,[26-27] and on instrinsic properties of the particles: their chemical composition,[27-28] size,[26,29-30] size distribution,[30] shape,[29] saturation magnetization, and on their surface modification.[31] Maximizing the hysteresis loop area of ferri- or ferromagnetic materials requires a high magnetic field to overcome the coercive field H_c, which is not clinically practical due to technical and physiological restrictions. The frequency for biomedical purpose has to be higher than 50 kHz to avoid neuromuscular electrostimulation, and lower than 10 MHz to achieve an appropriate penetration depth for the RF field.[32] In general, to avoid any detrimental effects on healthy tissues due to electromagnetic radiation exposure, the product of H_{max} by f should not exceed an experimentally estimated threshold of 5×10^9 $Am^{-1}s^{-1}$, which is already less strict than the usually called "Brezovich criterion" $H_{max}\cdot f < 4.85\times10^8$ $Am^{-1}s^{-1}$.[26,33] Multi-domain hysteretic NPs exhibit high SAR values at lower radiofrequencies (e.g. 100 kHz) but can require magnetic field strengths outside the allowed range (e.g., H_{max} > 50 kA/m). On the contrary, superparamagnetic NPs can produce much more heat at lower field amplitudes (e.g., H_{max} = 10 kA/m), characterized by high SAR values (up to hundreds of W/g),but they require radiofrequencies of few hundreds of kHz.[30]

The chemical composition of particles is the most commonly cited parameter affecting magnetization, and thus the magnetic energy loss power and heating rate. Although they have the highest saturation magnetization values, pure transition metals are not ideal for biomedical applications as they are prone to oxidation, liberating toxic reactive oxygen

species, and exhibit poor chemical stability.[20] The good magnetic properties and chemical stability of various pure and mixed metal ferrites have drawn the attention of many research groups. For example, mixed Co–Zn ferrite $Co_{1-x}Zn_xFe_2O_4$ nanoparticles exhibit higher saturation magnetization than the corresponding mixed Mn–Zn ferrite $Mn_{1-x}Zn_xFe_2O_4$ nanoparticles, and thus exhibit higher SAR values.[34] The magnetization and SAR values of mixed Fe–Mn ferrite nanoparticles $Fe_{1-x}Mn_xFe_2O_4$ was found to vary with the Mn concentration: The values initially increased with x up to x = 0.4 before decreasing.[28] The dependence of the SAR on H_{max} varied from linear to quadratic relations, which was attributed by the authors to "changes in ferrofluid composition", which may mean a transition from a superparamagnetic to a ferromagnetic state depending on the value of x.[28] The presence of both Zn and Mn in the ferrite structure $(Zn_{0.4}Mn_{0.6})Fe_2O_4$ increased the SAR value to 432 $W \cdot g^{-1}$, 4 times higher than 115 $W \cdot g^{-1}$ reported for commercial Ferridex® iron oxide nanoparticles under identical magnetic field conditions (500 kHz, 3.7 $kA \cdot m^{-1}$).[35] Changing the composition is also a good method to modulate the Curie temperature of the particles (T_C: the temperature above which MNPs exhibit zero magnetization, in the range of 500–600 °C for iron oxides), which allows the preparation of low Curie temperature MNPs that can perform "self-controlled" hyperthermia and prevent overheating.[36-37] The T_C value of $Y_3Fe_{5-x}Al_xO_{12}$ ($0 \leq x \leq 2$) garnet sub-micron MNPs ranged from 280 to −40 °C, and their saturation magnetization decreased for increasing x, avoiding overheating at a desired temperature close to T_C.[38] Replacing partially magnetic Fe^{3+} ions by half of the same number of non-magnetic Ti^{4+} ions in $Mn_{1+x}Ti_xFe_{2-2x}O_4$ structure decreased T_C from 300 °C at x = 0 to 46 °C at x = 0.55, restricting heating to below 46 °C.[39] Similar substituted ferrite structures $ZnGd_xFe_{2-x}O_4$ x = 0.02 (T_C = 45 °C)[40] and $Mg_{1+x}Fe_{2-2x}Ti_xO_4$ x = 0.37 (T_C = 46 °C)[41] were reported as potential heat mediators for self-controlled hyperthermia avoiding overheating of the surrounding healthy tissues. However due to their ease of synthesis and surface modification, combined with low toxicity and good biocompatibility, iron oxide NPs are still the most intensely studied materials for hyperthermia applications.[20]

Since magnetic behavior is strongly size-dependent, varying the size can readily tune the magnetization, coercivity, blocking temperature, and thus the SAR values. The particle size *d* is a determining parameter of the SAR value, since it dictates the heating mechanisms that arise from either hysteresis losses or Néel and Brownian relaxation processes when the particles are placed in an alternating magnetic field. Hysteresis losses are responsible for the heating of large ferro- or ferrimagnetic nanoparticles while Néel relaxation dominates for NPs with $d < 20$ nm, and Brownian relaxation for NPs with $d > 20$ nm.[42] A threshold size of ca. 9.8 nm was established by Jeun et al. below which the SAR of particles was insufficient for hyperthermia applications, while particles in a size range of 11.8 to 22.5 nm had SAR values ca. one order of magnitude larger.[43] According to Lartigue et al. the threshold should be 10 nm, since no significant heating was generated below this particle size, while 35 nm rhamnose-coated Fe_3O_4 MNPs had a SAR ~ 76 $W \cdot g^{-1}$ at 168 kHz and 21 $kA \cdot m^{-1}$.[44] Some 14 nm diameter Fe_3O_4 MNPs yielded a SAR of 447 $W \cdot g^{-1}$ at 400 kHz and 24.5 $kA \cdot m^{-1}$, larger than for 5, 10, and 12.8 nm diameter particles.[45] A 4-fold increase in SAR values (from ~10 to 40 $W \cdot g^{-1}$) was reported when the particle size increased from 8 to 11 nm, whereas only 40% increase in SAR values (from ~ 40 to 55 $W \cdot g^{-1}$) was observed for an increase from 11 to 13 nm.[46] Additional values of SAR vs. particle size can be found in a recent review by Kolhatkar et al.,[37] although comparisons among literature values are not straightforward since many authors quote different magnetic field intensities and frequencies (most of the time without stating how they were measured), and the experiments suffer from different sources of uncertainties and the lack of standardization of the setups and methods.

In an attempt to rationalize the design of MNPs for magnetic hyperthermia, the optimal volume of MNPs with random orientation of the moments was suggested by Carrey et al. to achieve the highest SAR value as:[47]

$$V_{\text{optimal}} = \frac{-k_{\text{B}} T \ln(\pi f \tau_0)}{K_{\text{eff}} \left(1 - \frac{1.69 \mu_0 H_{\max} M_{\text{s}}}{2K_{\text{eff}}}\right)^{4/3}}$$

where k_B is the Boltzmann constant, T is the absolute temperature, f is the applied field frequency, τ_0 is the attempt time, K_{eff} is the anisotropy constant, H_{max} is the field amplitude, μ_0 is the magnetic permability of vacuum, and M_s is the saturation magnetization. Along the same line, according to Krishnan et al., for an AMF at f = 373 kHz with H_{max} = 14 kA·m^{-1}, depending on the anisotropy constant K_{eff} of magnetite (which varies from below 10 to above 20 kJ/m^3, depending on the samples and authors), the optimal diameter can range from 13 to 17 nm.[48] One parameter that is often not taken into account in the literature is the direct effect of temperature on the SAR, even for iron oxide NPs far below T_C. For example, Garaio et al.[49] observed a 40% decrease in SAR between 10 and 60 °C in a multi-parametric study of dynamic hysteresis losses with size-graded maghemite NPs by AC magnetometry.

Size control alone may be insufficient to ensure the desired results since the size, shape and structure of particles have a complex influence on the SAR.[29] The optimal size to achieve the highest possible SAR value was suggested to be near the transition from superparamagnetic to ferromagnetic behavior.[30] Hergt et al. used magnetic separation to investigate the influence of the size distribution on the SAR values, and found that the imaginary magnetic susceptibility spectra $\chi''(f)$ and the SAR both varied remarkably with the mean particle core diameter.[29,50] A narrow size distribution and an optimal mean core size (near the transition from superparamagnetic to ferromagnetic behavior) resulted in high SAR values.[29-30] Later on Garaio et al.[49] showed that passing the theoretical size maximizing the SAR also resulted in a transition from a negative thermal behavior (SAR decreasing with temperature) to a positive one (SAR increasing with temperature), as predicted by the so-called "linear relaxation theory" (LRT) introduced by Rosensweig.[26] Negative influence of the size dispersity of magnetite particles on the SAR values is also expected from the LRT model, indicating the advantages of more uniform samples.[50] Fractionation of a ferrofluid to improve the size distribution of the particles thus increased the SAR values from 60 to 332 W·g^{-1} (at f = 400 kHz, H_{max} = 10 kA·m^{-1}).[51] Pegylated Fe_3O_4@PEG_{6000} with a smaller magnetically active core with diameter d = 10 nm, a broader size distribution (standard deviation 3 nm), and a lower anisotropy constant yielded a significantly lower SAR of 60

$W \cdot g^{-1}$ in comparison to Fe_3O_4@PEG200 reaching 195 $W \cdot g^{-1}$ for d = 12 nm, a standard deviation of 2 nm, and a higher anisotropy constant.[52]

Even though this has been the scope of intensive research, there are still no clear conclusions on the effects of particle shape on the SAR, based on the limited studies currently available. A maximum SAR of 2450 $W \cdot g^{-1}$ was measured for cubic Fe_3O_4 with an edge length of 19 ± 3 nm (at f = 520 kHz, H_{max} = 29 $kA \cdot m^{-1}$),[53] while larger-sized $Zn_{0.4}Fe_{2.6}O_4$ nanocubes (edge length 40 nm) exhibited a maximum SAR of 4060 $W \cdot g^{-1}$, but at even higher field strength (at f = 500 kHz, H_{max} = 37.4 $kA \cdot m^{-1}$).[54] Highly uniform quasi-cubical (9.6 nm) MNPs synthesized by thermal decomposition exhibited a higher SAR value than spherical ones with an equivalent size.[55] As another significant example, a SAR of 1990 $W \cdot g^{-1}$ under an AMF at f = 700 kHz of moderate intensity, H_{max} = 21.5 $kA \cdot m^{-1}$, was obtained for nanoparticles qualified as 24 nm flower-like assemblies composed of multiple smaller grains of maghemite (11 nm as determined by TEM and X-rays diffraction). Such a high value was ascribed to the cooperative combination of moments (these nanoflowers behaving like large magnetic monodomains).[56] Another possibility to obtain high SAR values is to play on an exchange-bias mechanism between a superparamagnetic shell built around an antiferromagnetic core. This was achieved for FeO@Fe_3O_4 nanospheres of 19 nm ± 15% diameter, exibiting SAR values at 700 kHz (484 W/g for 2 mM [Fe]) analogous to $Fe_{3-x}O_4$ nanocubes with an edge of 16 nm ± 12% (450 W/g for 2 mM [Fe].[57]

According to the heat dissipation equations from the linear rexation theory (LRT), the SAR values increase with an increase in frequency f or applied field amplitude H_{max}, thereby reducing the therapeutically needed concentration of MNPs.[30] However, this strategy also unavoidably increases the power dissipated by the electric field via Joule effect in healthy tissues surrounding the tumor ("eddy currents" heating) and reduces the selectivity of the treatment.[58] To minimize unwanted and non-selective heating generated in healthy tissues, the product $H_{max} \cdot f$ should not exceed an experimentally estimated threshold of 5×10^9 $Am^{-1}s^{-1}$.[26] Various studies focused on selecting an optimal set of $H_{max} \cdot f$ and d to be used in

hyperthermia.[30,47] The SAR heating characteristics of MNPs are often studied at various applied fields, to reveal its dependence on magnetic field amplitude and frequency.

In order to be useful for biomedical applications, MNPs are usually coated with a shell that prevents them from aggregating (which can also change their magnetic properties) and increases their biocompatibility by excluding them from reticulo-endothelial clearance, thus extending their circulation time in the bloodstream. The nature of the protecting material determines how it interacts with the crystal core and modifies the magnetic properties of the whole system. Silica coating was thus found to increase the surface spin disorder of Fe_3O_4@SiO_2 nanoparticles, inhibiting a fraction of $Fe^{2+/3+}$ cations from being magnetically active at room temperature and resulting in low SAR values.[59] Negative effects for surface coating by phosphorylated methoxy poly(ethylene glycol) (mPEG) on the SAR values of magnetite NPs were also reported.[60] Short mPEG chains ($\bar{M}_w$ = 2,000 g/mol) provided Fe_3O_4 cores with $d(Fe_3O_4)$ = 9 and 19 nm with good colloidal stability, and maintained good magnetization properties. Lower SAR values were observed when the $\bar{M}_w$ of mPEG was increased to 5,000 and 20,000 g/mol, but larger cores $d(Fe_3O_4)$ = 31 nm needed mPEG $\bar{M}_w$ = 5,000 g/mol to be stable since shorter chains (2,000 g/mol) were insufficient to prevent aggregation, while longer chains (20,000 g/mol) formed a layer too thick for efficient heating.[60] A surface coating with optimal thickness can maintain and sometimes improve the magnetization properties by hindering agglomeration of the MNPs, which otherwise leads to strong dipolar intearactions hampering Néel relaxation. Chitosan coating also improved the SAR value of Fe_3O_4@chitosan to 119 $W \cdot g^{-1}$, as compared to 79 $W \cdot g^{-1}$ for bare NPs (f = 265 kHz, H_{max} = 26.7 $kA \cdot m^{-1}$).[61] A similar influence on the heating efficiency of ferromagnetic $La_{0.7}Sr_{0.3}MnO_3$ particles was observed with a dextran coating.[62] Similarly, a bilayer of oleic acid improved the hyperthermia properties of $La_{0.7}Sr_{0.3}MnO_3$ NPs from 25 to 40 $W \cdot g^{-1}$ (f = 267 kHz, H_{max} = 26.7 $kA \cdot m^{-1}$) by enhancing the colloidal stability of the suspension.[63]

The physicochemical properties of a magnetic suspension such as the ionic strength, medium viscosity, and temperature also influence its heating efficiency. A decrease in the chitosan coating thickness of $La_{0.7}Sr_{0.3}MnO_3$@chitosan, induced by increased ionic strength,

also resulted in agglomeration and a decreased SAR value.[63] A viscous medium slows down particle rotation, therefore limiting heat generation by Brownian relaxation.[20] A systematic drop in heating efficiency for various MNPs was reported when Brownian relaxation was inhibited, either in the cellular environment or when the nanoparticles were attached to the cell membrane.[64] The SAR values of NPs with several volume-average sizes (12, 14, and 15 nm) decreased with the temperature of the measurements, whereas the opposite trend was observed for the largest size sample (D_v = 16 nm).[49] The extent of SAR variations with temperature was also reported as being frequency-dependent for maghemite NPs, as interepreted within the frame of the LRT model for these size-graded samples.[49]

In order to compare the SAR values obtained by different research groups, measured at different frequencies and applied field amplitudes, the intrinsic loss power[65] parameter defined as $\mathrm{ILP} = {}^{\mathrm{SAR}}/_{[H_{\max}^2 f]}$ was introduced. Since the ILP is obtained by normalization of the SAR values through the frequency and the square of the field amplitude, it is theoretically independent of the magnetic field parameters. However the linear dependency of the SAR on frequency and the quadratic dependency on the field strength can be questioned in practice, so the usefulness of the ILP is not universally recognized among researchers.

5.3 Experimental Procedures

5.3.1 Magnetic Polyion Complex Micelle Preparation

The uncoated (UC) magnetic nanoparticles G1@Fe_3O_4 used for the magnetization measurements were prepared by alkaline coprecipitation in the presence of the G1 arborescent copolymer template (Section 3.3.6). The Fe^{2+} and Fe^{3+} iron oxide precursors were loaded in the template by mixing the iron salts stock solution with G1 in HCl solution at pH 1.4. Concentrated NH_4OH was then added to trigger the formation of colloidal Fe_3O_4.

The magnetic nanoparticles (MNPs) were washed and redispersed in HNO_3 solution at pH 1.4 to produce a black homogeneous ferrofluid.

The magnetic polyion complexation (MPIC) micelles used for the magnetization measurements were prepared from the G1 templated magnetic nanoparticles G1@Fe_3O_4 and the PAA_{27}-*b*-$PHEA_{260}$ block copolymer with f = CO_2H/N = 0.5. Briefly, the G1@Fe_3O_4 ferrofluid prepared in HNO_3 solution at pH 1.4 (0.99 mg Fe_3O_4, 1.9 mg of G1, 16.7 µmol of N functional groups) was loaded in a 10 mL vial. An aqueous solution of PAA_{27}-*b*-$PHEA_{260}$ at pH 7 (9.6 mg, 5 mg/mL, 8.3 µmol of CO_2H functional groups) was quickly added, the mixture was left to react for 1 h with stirring before adjusting the pH to 4.7, and stirring for 1 h with a magnetic stirring bar at 400 rpm. The pH was adjusted further to 7 and the solution was stirred for 30 min. The solution was dialyzed against Milli-Q water (5 L) for 48 h before it was collected and stored at 10 °C.

5.3.2 Characterization

5.3.2.1 Vibrating Sample Magnetometry

Magnetometry curves for the Fe_3O_4 NPs (for field strengths up to 5 T) were recorded using a Quantum Design™ Physical Property Measurement System (PPMS®) with the vibrating sample magnetometer (VSM) device. At room temperature, a sufficiently concentrated (ca. 1 mg/mL) aqueous suspension of Fe_3O_4 NPs was moved periodically (at fixed frequency) in a magnetic field varying in strength from 0 to 5 T. In this experiment the voltage induced in the detection coils, which is proportional to the magnetic moment, is recorded vs. field strength or temperature. The diamagnetic contribution from water and the container are subtracted from the data obtained.

5.3.2.2 Relaxometry

These measurements were performed in the NMR and Molecular Imaging Laboratory of Professors Sophie Laurent and Luce Vander Elst, and the Biomedical Physics Unit of Professor Yves Gossuin at UMONS, Belgium.

The longitudinal (R_1) and transverse (R_2) relaxation rates were measured at 0.47 and 1.41 T on Minispec mq20 and mq60 relaxometers (Bruker, Karlsruhe, Germany). Nuclear magnetic relaxation dispersion (NMRD) profiles were measured using a Stelar Spinmaster fast-field-cycling (FFC) NMR relaxometer (Stelar, Mede PV, Italy) over a magnetic field strength range of 0.24 mT to 0.7 T. A Bruker AMX 300 (7 T) spectrometer was also used for the high-field measurements. The measurements were performed on 0.6 mL samples contained in 10 mm (outside diameter) Pyrex tubes at 37 °C.

The saturation magnetization M_{sat} and the size of the superparamagnetic crystals, r_{NMR}, were determined by fitting the NMRD curves with the MINUIT minimization program using the outer-sphere model and a standard phenomenological approximation.[66-67] In most of the plots shown in this work, the magnetic field is expressed in terms of the proton Larmor frequency: A field of 1 T corresponds to a Larmor frequency of 42.6 MHz. The results are represented in terms of longitudinal and transverse relaxivities r_1 and r_2, respectively.

The iron concentration was determined from the longitudinal relaxation rate (R_1) measurements at 0.47 T and 37 °C after microwave digestion (MLS-1200 MEGA, Milestone) into ferric ions with a mixture of nitric acid and hydrogen peroxide.[68] The iron content of the sample was also verified by UV-VIS analysis.[69]

5.3.2.3 Specific Absorption Rate Measurements

To minimize the effects of magnetic field inhomogeneities, a small NMR plastic tube was totally filled with the sample. The diameter (5 mm external) was not so small as to cause large thermal losses, and the volume (0.35–0.4 mL) was as reported in the literature for MFH experiments on cells.[24] The well-defined sample geometry (cylindrical shape and large aspect

ratio), and the sample was oriented parallel to the coil axis to allow minimization of the so-called "demagnetization effect", similarly to a VSM experiment.[14]

The setup for hyperthermia measurements in Bordeaux (Figure 5-6) was used to create a high frequency alternating magnetic field (f = 755 kHz, H_{max} = 10.2 kA·m^{-1}). The tubes were placed in a double-walled jacketed vessel, maintained at a temperature of 20 °C during the treatment by a thermostated circulating bath (Huber Polystat CC). The whole system was inserted in an induction coil (4 turns with 1 cm spacing, 55 mm diameter, cooled by internal water circulation at 18 °C). The coil was fed with a current of 234 A at full power of the generator (3 kW MOSFET solid state resonant circuit, Seit Electronica Junior™, Treviso, Italy) producing a high frequency alternating magnetic field (f = 755 kHz, H_{max} = 2.8 kA·m^{-1} at minimum power, H_{max} = 10.2 kA·m^{-1} at full power according to a calibration by Dr Eneko Garaio with RF current measurement techniques). The temperature of the sample was monitored with a fiber optic thermometer (OTG-M420, Opsens, Québec, QC, Canada).

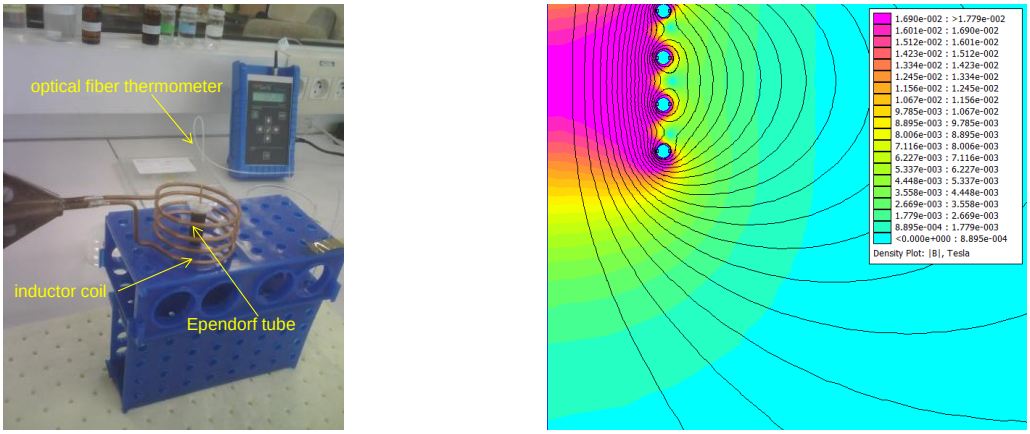

Figure 5-6. (Left) Custom setup for single frequency (755 kHz) hyperthermia measurements in Bordeaux. (Right) Field lines calculated using cylindrical axi-symmetry with the finite element simulation freeware FEMM (http://www.femm.info), showing calculated B field values close to the experimentally measured ones (B = 1 mT corresponds to H ~ 800 A·m^{-1}).

Chapter 5

SAR measurements with medium and lower range radiofrequency alternating magnetic fields (f = 473.5 kHz, H_{max} = 4.0–13.4 kA·m^{-1}; f = 344.5 kHz, H_{max} = 4.0–16.2 kA·m^{-1}; f = 217 kHz, H_{max} = 4.0–20.7 kA·m^{-1}; and f = 146 kHz, H_{max} = 4.0–22 kA·m^{-1}) were performed on a DM3 commercial device (DM100 Series) from nanoScale Biomagnetics (Zaragoza, Spain) specially designed for accurate application of the alternating magnetic field, local sensing, and experimental monitoring on mice and rats by well-calibrated hyperthermia procedures (Figure 5-7).

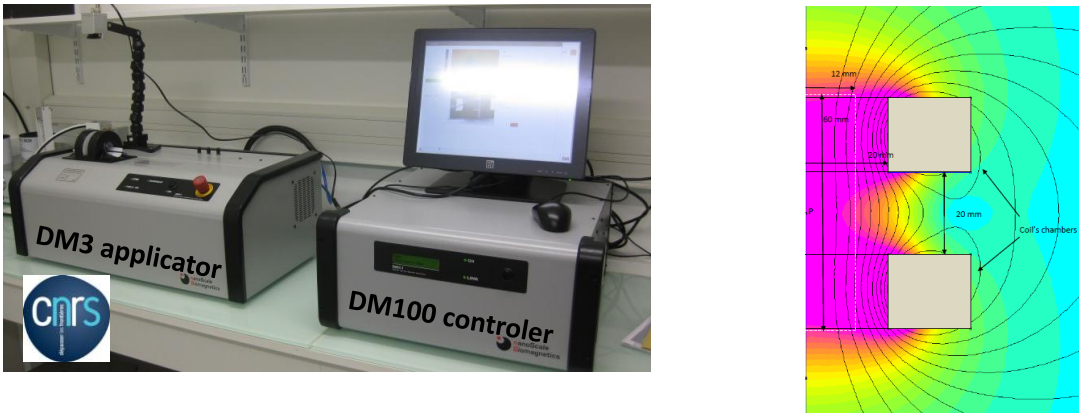

Figure 5-7. Commercial DM3 device from nanoScale Biomagnetics (Zaragoza, Spain) designed for *in vivo* hyperthermia measurements with quad frequency capability. The simulation shows that the coil was specially designed with an observation window.

5.4 Results and Discussion

The terminology G1@Fe_3O_4 used to refer to the magnetic nanoparticles (MNPs), and G1@Fe_3O_4@PAA-*b*-PHEA for the magnetic polyion complex (MPIC) micelles in Chapter 4, does not fit well within the scope of this Chapter, since we deal with MNPs and MPIC micelles synthesized under different conditions. Consequently, we will hereafter use a three-component nomenclature system to describe the samples: first figure (0.7 or 1.0) is the molar ratio of Fe/N used in coprecipitation reaction, the second figure (80 or 100) is the

temperature (°C) of coprecipitation reaction, and the third figure (UC or BC) refers to particles that are either bare (uncoated) or coated with block copolymer PAA_{27}-*b*-$PHEA_{260}$. Therefore a sample labeled as 0.7-80-BC corresponds to a Fe/N ratio of 0.7, a reaction temperature of 80 °C, and particles coated with the block copolymer.

Since the superparamagnetic character of the MNPs and MPIC micelles will be confirmed by vibrating sample magnetometry in Section 5.4.1, the term superparamagnetic iron oxide nanoparticles (SPIONs) will also be used to refer to them.

5.4.1 Vibrating Sample Magnetometry

The magnetic properties of the Fe_3O_4 nanoparticles were characterized with a vibrating sample magnetometer (VSM) at 300 K. The magnetization curves of *M* versus the applied field strength *H* (between −4000 $kA \cdot m^{-1}$ and +4000 $kA \cdot m^{-1}$) obtained for the various samples are shown in Figure 5-8. All the curves exhibit no hysteresis loop, zero coercivity and zero remanence, thus indicating superparamagnetic behavior for the Fe_3O_4 nanoparticles. As the applied field was increased from 0 to 1000 $kA \cdot m^{-1}$, the magnetization *M* rose sharply and gradually reached saturation around 2000 $kA \cdot m^{-1}$. Since only 1 or 2 experiments were used to obtain these results, their statistical significance is unfortunately limited and they should be viewed with caution. However, the Fe/N ratio in the template, the temperature, and the coating material all influenced the magnetization properties of the NPs to some extent (Table 5-1).

At both temperatures tested (80 and 100 °C), the G1@Fe_3O_4@BC samples prepared with a molar ratio Fe/N = 0.7 had a higher magnetization than those produced with Fe/N = 1, due to the formation of magnetite NPs with a larger median diameter and a narrower size distribution. Figure 5-8a depicts the higher saturation value of magnetization for 0.7-80-BC as compared to 1.0-80-BC. The former sample, with less $Fe^{2+/3+}$ ions involved in the coprecipitation reaction, also had a larger median diameter D_0 (6.26 vs. 6.08 nm), a more

uniform size (σ = 0.385 vs. 0.492), and a smaller volume-average diameter D_v (11.1 vs. 14.2 nm) (Table 5-1).

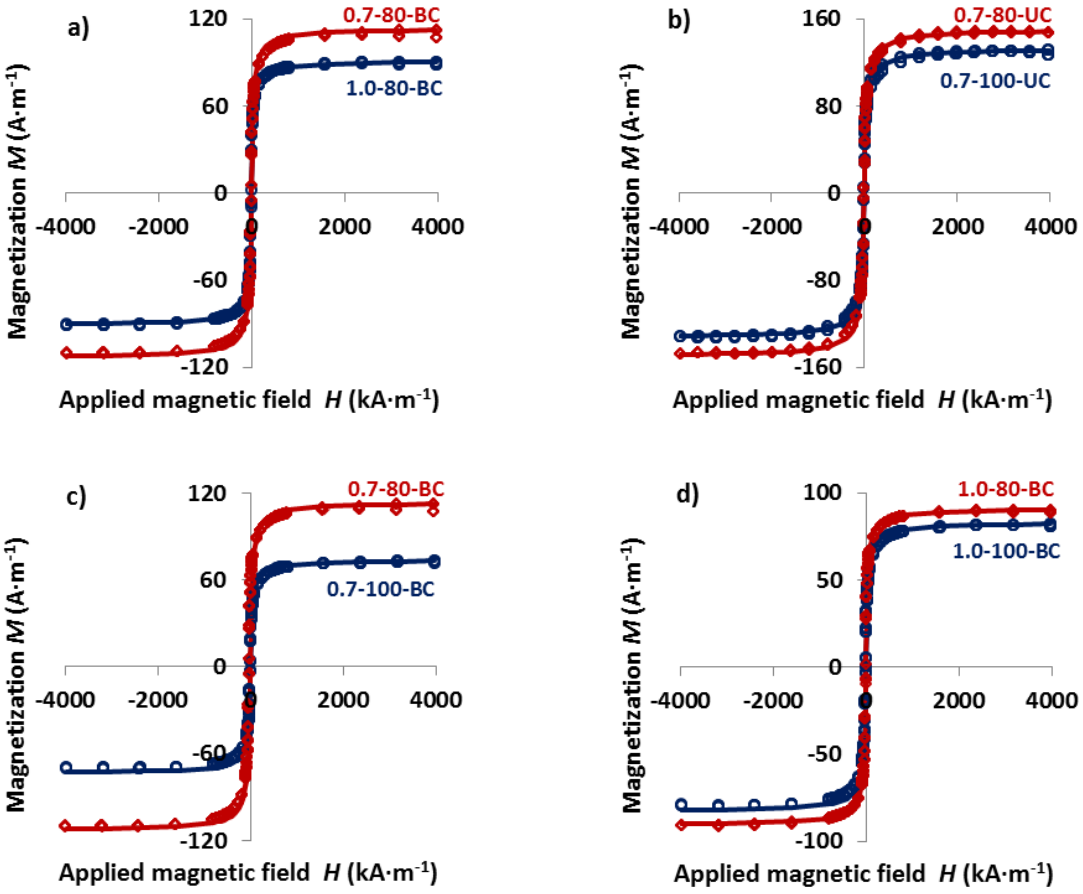

Figure 5-8. Magnetization curves (at 300 K) for the Fe_3O_4 samples. Sample nomenclature is explained in the text, and the iron oxide concentrations $C_{Fe_3O_4}$(mg/mL) are listed in Table 5-1.

These results can be explained as follows:

1. An increased number of nuclei formed in the nucleation step of the akaline coprecipitation reaction when the Fe^{2+}/Fe^{3+} ions were present at a higher concentration (for Fe/N = 1.0 as compared to 0.7), leading to a decrease in the radius of the MNPs. As stated in the LaMer

model of nucleation-growth,[70] a minimum concentration of monomer (in our case: Fe_3O_4) is needed to overcome the energy barrier of the nucleation process: burst nucleation occurs at that point, and stable nuclei are formed. A higher monomer concentration results in a larger number of nuclei and thus of final NPs, but with a smaller median diameter (e.g. D_0 = 6.08 nm for 1.0-80-BC), while a lower monomer concentration leads to a smaller number of nuclei and NPs, but with a larger median diameter (e.g. D_0 = 6.26 nm for 0.7-80-BC).

Table 5-1. Magnetic properties of the Fe_3O_4 samples synthesized.

Sample*	$C_{Fe_3O_4}$ **(mg/mL)**	M_s **(10^5 A/m)**	M_d **(emu/g Fe_3O_4)**	D_0 **(nm)**	σ	D_n **(nm)**	D_v **(nm)**
0.7-80-UC	3.4	2.28	44.7	6.66	0.386	7.2	11.2
1.0-80-UC	2.9	2.70	52.9	6.20	0.457	6.9	12.9
0.7-100-UC	2.9	2.65	51.9	6.26	0.389	6.75	10.6
1.0-100-UC	2.9	2.36	46.3	5.96	0.447	6.6	12.0
0.7-80-BC	1.9	3.04	59.6	6.26	0.385	6.8	11.3
1.0-80-BC	1.9	2.49	48.7	6.08	0.492	6.9	14.2
0.7-100-BC	1.3	2.85	55.9	6.34	0.409	6.9	11.4
1.0-100-BC	1.6	2.64	51.8	6.01	0.458	6.7	12.5

M_S and M_d: volume- and mass-average specific magnetization; D_0: median diameter; D_n and D_v: number- and volume-average diameter; σ: polydispersity; the sample nomenclature is described in the text.

2. Less efficient templated nucleation at higher $Fe^{2+/3+}$ concentrations (for Fe/N = 1.0 as compared to 0.7), due to limited accessibility of the $Fe^{2+/3+}$ ionic precursors to the anchoring moieties (N). Due to the compact structure of the G1 template, it is very unlikely that 100% of the N moieties can be targeted (especially for Fe/N = 1.0), which gives rise to partial non-templated nucleation. The broad size distribution (σ = 0.492) observed is actually analogous to what is normally achieved for non-templated alkaline coprecipitation. The narrower size distributions for 0.7-80-BC (σ = 0.385) and 0.7-80-UC (σ = 0.386) are evidence for

templating effects achieved with a proper Fe/N ratio. The templating effect for a material with limited accessibility such as the G1 copolymer may be complex, especially since the influence of simple ligands like oleic acid and citric acid on NP size still is unclear.[71-76] The ratio of metal cations to organic agents can either lead to the hindrance of nucleation (resulting in larger particles) or the inhibition of crystal growth (resulting in smaller particles).

3. Uneven/non-homogeneous crystal growth of the embryonic nuclei due to limited accessibility of the G1 template. The diffusion and adsorption of the solute on the surface of the crystals were presumably facilitated for particles located near the G1 template surface as compared to those buried inside, leading to the formation of both small and large particles. The volume-weighted diameter D_v – which emphasizes the contribution from larger particles – was much larger than the number-weighted D_n, and the ratio of these two values $Đ = \exp(3\sigma^2)$ can be calculated from the width of the log-normal size distribution whose standard deviation of Ln(D), σ, is used to compute the number- and volume-average diameters (see Section 5.2.2). For example, sample 0.7-80-BC had D_v = 11.3 nm, close to D_n = 6.81 nm ($Đ = 1.66$), while sample 1.0-80-BC had D_v = 14.2 nm, much more different from D_n = 6.86 nm ($Đ = 2.07$). A narrower size distribution (σ = 0.385) was indeed found for 0.7-80-BC than for 1.0-80-BC (σ = 0.492). The reactions with a sub-stoichiometric amount of $Fe^{2+/3+}$ precursors (i.e. Fe/N = 0.7 rather than 1.0), designed to attenuate non-homogeneous crystal growth, resulted in narrowing of the size distribution, as apparent by a decrease in the gap between D_v and D_n under every condition tested.

The BC-coated samples prepared at 80 °C were found to have higher magnetization values (Figure 5-8 b, c, d) as compared to samples prepared at 100 °C, while no significant change in size distribution was observed. A higher reaction temperature facilitated the oxidation reaction, converting magnetite Fe_3O_4 (with a higher M_s value) to maghemite γ-Fe_2O_3 (with an M_s value lower by ~20%). Coprecipitation reactions performed at 100 °C usually formed larger particles (D_h = 206 nm, PDI = 0.2), which would be expected to

hamper internalization of the particles by the cells, so we chose to carry out the coprecipitation reactions at 80 °C.

Samples coated with block copolymer (BC) PAA_{27}-*b*-$PHEA_{260}$ had a higher magnetization, a larger median diameter and a narrower size distribution than the UC (uncoated) samples (Table 5-1). The magnetization of the "optimal" G1@Fe_3O_4@PAA_{27}-*b*-$PHEA_{260}$ nanoparticles (denoted as 0.7-80-BC) was 59.6 emu/g at 300K, which is 65% of the magnetization of bulk magnetite (~92 emu/g). The good magnetic properties are attributed to the morphology of these G1@Fe_3O_4@PAA_{27}-*b*-$PHEA_{260}$ nanoparticles, where the Fe_3O_4 crystallites are distributed within the G1 template and protected by block copolymer chains functioning as surface-active agents. The uncoated samples were stored and characterized in HNO_3 solution at pH 1.4, which facilitated the oxidation reaction converting magnetite Fe_3O_4 (with a higher M_s value) to maghemite Fe_2O_3 (with a 20% lower M_s value). The BC thus acts as a protecting layer minimizing the oxidation of the Fe_3O_4 NPs.

Attempts to oxidize G1@Fe_3O_4 to G1@γ–Fe_2O_3 with $Fe(NO_3)_3$, followed by a size grading step using a concentrated HNO_3 solution, led to destruction of the templating effect: The G1@γ–Fe_2O_3@PAA_{27}-*b*-$PHEA_{260}$ NPs had a large $D_h^I \approx 300$ nm, which is less useful for *in vitro* applications.

For samples 0.7-80-UC and 0.7-80-BC, we observed a discrepancy between the diameters calculated from the VSM analysis (D_n = 6.8–7.2 nm) and measured by TEM (D_{TEM} = 12.1 ± 2.00 nm), which has often been ascribed to spin canting occurring at the surface or within the particles.[71,77] The spin canting effect at the surface of nanoparticles has been described as misaligned spins or non-colinear arrangement, and related to local changes in magnetic anisotropy induced by breaking of the quantic exchange bonds between adjacent metal centers.[77-79] Spin canting within the volume of the particles occurs because of Fe^{3+} vacancies, which are more frequent in maghemite.[77,79] Baaziz et al.[71] suggested size-dependent oxidation defects and surface or volume spin canting to explain the lower saturation magnetization observed for MNPs as compared to the bulk materials. Smaller NPs

(< 8 nm) were indeed almost completely oxidized to maghemite, with mainly surface spin canting. NPs of intermediate sizes (8–12 nm) exhibited surface, but particularly also volume spin canting as a result of a disordered structure induced by the perturbed oxidation state of these NPs. Larger NPs displayed a core–shell morphology of magnetite and maghemite, which explained why their magnetization depended on the oxidized shell thickness, defects and surface spin canting.

5.4.2 Relaxation Properties

5.4.2.1 Relaxivity Measurements at 0.41 and 1.47 T

Relaxivity measurements were performed for all the uncoated (UC) and block copolymer-coated (BC) magnetic nanoparticles at 0.41 T (20 MHz) and 1.47 T (60 MHz) field strengths, that closely match the magnetic field strengths of most clinical MRI systems (0.5 T and 1.5 T, although human 3 T MRI is also frequent in hospitals). The longitudinal r_1 and transverse r_2 relaxivities acquired at 0.41 and 1.47 T displayed similar trends (Table 5-2). Since only 1 or 2 experiments were used to obtain these results, their statistical significance is unfortunately limited and they should be viewed with caution.

A good T_2 contrast agent has a high r_2 and r_2/r_1 ratio. The transverse relaxivity r_2, the most important parameter for negative CAs, expresses the increase in the T_2-relaxation per millimolar concentration of magnetic centers. The ratio r_2/r_1 provides a precise picture of the availability of nuclear longitudinal magnetization after each subsequent acquisition for signal averaging.[80] This ratio increases with the particle volume, and the threshold value for an effective negative contrast is above 3–4.[80] Ultrasmall superparamagnetic iron oxide particles (USPIOs, D_h < 40 nm) composed of a monocrystalline core can produce a low r_2/r_1 < 3–4 (at 20 MHz) allowing them to perform as "positive contrast agents" (producing brighter regions where they are delivered) as long as they remain individually dispersed in the suspension.[81-83] Superparamagnetic iron oxide particles (SPIOs, 60 nm < D_h < 150 nm) containing polycrystalline clusters are often reported to have high r_2/r_1 ratios, making them "negative contrast agents", i.e. producing dark zones associated with a high local accumulation of

CA.[80] Values of r_2/r_1 reaching several hundreds can be obtained, depending on the magnetic field strength of the MRI scanner.[83]

Table 5-2. Longitudinal and transverse relaxivities of the samples at 20 and 60 MHz.

	20 MHz			60 MHz		
Sample	r_1 ($s^{-1}\cdot mM^{-1}$)	r_2 ($s^{-1}\cdot mM^{-1}$)	r_2/r_1	r_1 ($s^{-1}\cdot mM^{-1}$)	r_2 ($s^{-1}\cdot mM^{-1}$)	r_2/r_1
0.7-80-UC	11.1	89.3	8.1	7.3	99.2	13.6
1.0-80-UC	11.6	60.1	5.2	6.5	38.9	6.0
0.7-100-UC	9.6	45.8	4.8	6.5	36.3	5.6
1.0.100-UC	11.2	69.5	6.2	6.8	68.6	10.1
0.7-80-BC	27.3	269.0	9.9	10.7	335.8	31.4
1.0-80-BC	23.5	200.7	8.6	8.4	239.8	28.4
0.7-100-BC	21.1	195.1	9.3	8.4	213.9	25.5
1.0-100-BC	22.7	205.4	9.1	9.0	263.1	29.4

Sample nomenclature is described in the text.

Block copolymer-coated SPIONs display higher r_2 and r_2/r_1 values than uncoated SPIONs. The transverse relaxivity of SPIONs is significantly greater than their longitudinal relaxivity, which explains their effectiveness as negative contrast agents for T_2-weighted imaging. The lack of block copolymer coating favors the agglomeration of uncoated samples, leading to decreased relaxivities due to exchange between the water molecules inside the agglomerates (which relax rapidly) and the bulk water (relaxing more slowly), as previously reported by Roch et al.[84] By preventing agglomeration, a block copolymer coating is thus essential to maintain good MRI contrast properties.

Sample 0.7-80-BC (with Fe/N = 0.7) displayed larger r_2 and r_2/r_1 values than 1.0-80-BC, suggesting that 0.7-80-BC would be a better contrast agent. Increasing the coprecipitation temperature to 100 °C led to some agglomeration, as can be interpreted from

the decreases in both r_1 and r_2 observed at both frequencies. The most promising sample, 0.7-80-BC, has r_2 reaching 269 $s^{-1}\cdot mM^{-1}$ with r_2/r_1 = 9.9 at 20 MHz, and r_2 = 336 $s^{-1}\cdot mM^{-1}$ with r_2/r_1 = 31.4 at 60 MHz.

In comparison with different commercial materials, sample 0.7-80-BC can be viewed as an efficient negative contrast agent characterized by comparably high relaxivities, which allows smaller injection amounts for the patients. Sample 0.7-80-BC is more efficient than AMI-25 Ferumoxide (Endorem)[85] and IOs (Resovist)[86], but less effective than IO-loaded PLGA-mPEG.[86] The relaxivities of commercial USPIOs, used as positive contrast agents, are also listed in Table 5-3.

Table 5-3. Relaxivities of 0.7-80-BC SPIONs and commercial contrast agents.

		r_1 ($s^{-1}\cdot mM^{-1}$)	r_2 ($s^{-1}\cdot mM^{-1}$)	r_2/r_1
SPIOs				
0.7-80-BC (this study)	0.41 T, 37 °C	27.3	269.0	9.9
	1.47 T, 37 °C	10.7	335.8	31.4
AMI-25 Ferumoxide® (Endorem®)[85]	0.4 T, 37 °C	25.0	147.0	5.9
	0.47 T, 39 °C	23.7	107.0	4.5
IOs (Resovist®)[86]	1.5 T, 37 °C	11.4	282.4	24.8
IO-loaded PLGA-mPEG[86]	1.5 T, 37 °C	7.5	532.7	71.0
USPIOs				
AMI-227 (Sinerem®)[85]	0.47 T, 39 °C	22.7	53.1	2.3
MION46L (Clariscan®)[87]	0.47 T, 35 °C	22.2	43.7	2.0
	1.5 T, 37 °C	3.95	19.6	4.9

The relaxivities and magnetization properties of superparamagnetic iron oxide, both commercialized and in the literature, were compiled in a paper published by Vuong et al.[19] These authors suggested a universal scaling law to compare the efficiency of magnetic

nanoparticles as MRI T_2-contrast agents (Figure 5-9), using data from their own samples and from the literature, provided that these follow the outer-sphere theory or the so-called Redfield condition $\Delta\omega \cdot \tau_D < 1$, where $\Delta\omega = \gamma\mu_0 M_v/3$ is the angular frequency shift experienced by a proton at the equator of a particle, $\gamma = 2.67513\times10^8$ rad·s^{-1}·T^{-1} is the gyromagnetic factor of the proton, and $\mu_0 = 4\pi10^{-7}$ T·m·A^{-1} is the magnetic permeability of vacuum. The square of the specific magnetization M_v (denoted as M_s in this work) was used as a normalization parameter. The intra-aggregate volume fraction of magnetic material φ_{intra} was used for clusters and hybrids to correct the relaxivity as $r_2' = r_2 \times \varphi_{intra}$.

A good correlation[88] was found, as shown in Figure 5-9:

$$r_2 \times \varphi_{\text{intra}}/M_v^2 = a_{\text{exp}}\, d^2 = 11.6 \times 10^{-12}\, d^2\,;\; R^2 = 0.94$$

We applied this correlation to evaluate the intra-aggregate volume fraction φ_{intra} for sample 0.7-80-BC, using r_2 = 335.8 s^{-1}·mM^{-1} (measured at 1.41 T), $d = D_{(\text{NMR})} = 2 \times r_{NMR} = 2 \times 8.1 = 16.2$ nm, and $a_{\text{exp}} = 11.6 \times 10^{-12}$. The specific mass-magnetization of the MPIC micelle extracted from the NMRD profile $M_{s(\text{NMR})} = 31.1$ emu/g (Table 5-4) was also converted, using the respective densities ~ 1 g·cm^{-3} for the polymer and ~ 5 g·cm^{-3} for iron oxide, into the specific volume-magnetization $M_V = 3.2 \times 10^4$ A·m^{-1}. Then a volume fraction $\varphi_{\text{intra}} = 9.4 \times 10^{-3}$ obtained for sample 0.7-80-BC from the scaling law was subsequently used to calculate the number of Fe_3O_4 NPs in one MPIC micelle:

$$N_{Fe_3O_4/\text{MPIC}} = \varphi_{\text{intra}} \left(\frac{D_{\text{MPIC}}}{D_{Fe_3O_4}}\right)^3$$

where $D_{Fe_3O_4} = D_{\text{TEM}} = 12$ nm and $D_{\text{MPIC}} = D_h^I = 130\, nm$. The value obtained $N_{Fe_3O_4/\text{MPIC}} = 12.6$ corresponds to around 13 spherical Fe_3O_4 NPs of 12 nm diameter coexisting in a polymer-stabilized sphere with ca. 130 nm hydrodynamic diameter, which is consistent with the TEM and AFM images obtained for the magnetic PIC micelles.

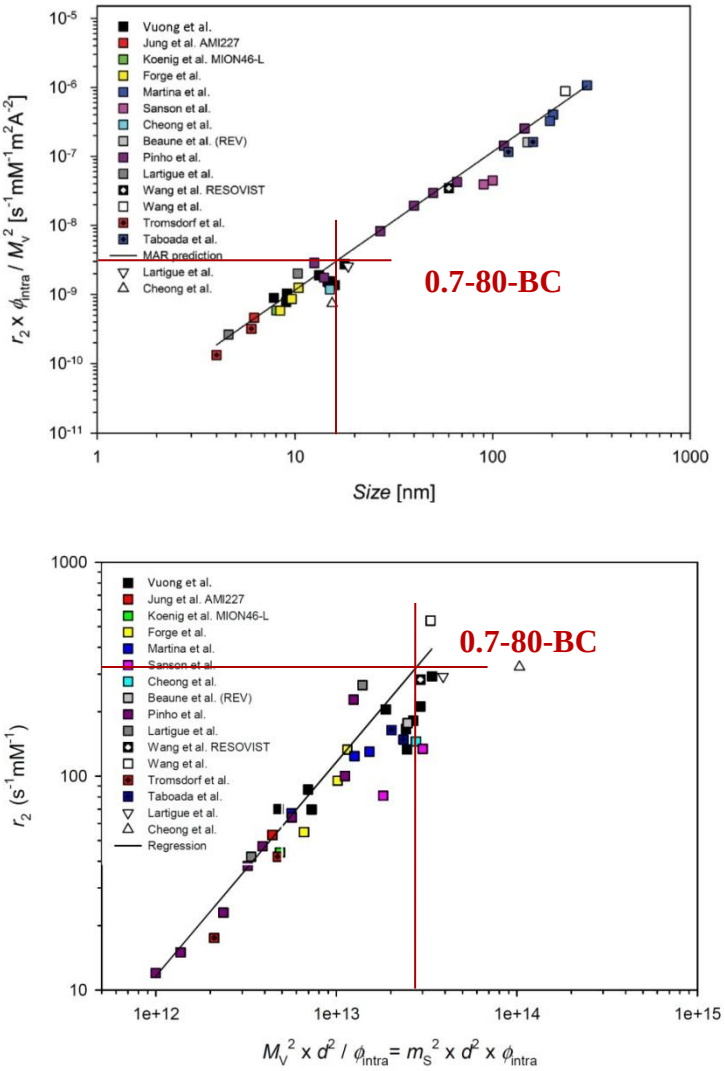

Figure 5-9. (Top) Correlation between the normalized transverse relaxivity and the particle diameter at high field (≥ 1 T) and 37 °C. (Bottom) Correlation between the transverse relaxivity and the normalized diameter at high field (≥ 1 T) and 37 °C. The transverse relaxivity r_2 = 335 $s^{-1}{\cdot}mM^{-1}$ measured for sample 0.7-80-BC locates it in the high range of the spectrum. Adapted with permission from Reference 88. Copyright 2012 WILEY-VCH Verlag GmbH & Co. KGaA, Weinheim.

Finally, the transverse relaxivity r_2 = 335.8 $s^{-1}\cdot mM^{-1}$ is located in the high end of the overall spectrum, which suggests good potential of this suspension as a T_2 MRI contrast agent.

5.4.2.2 NMRD Profiles

The relaxivities of the uncoated (UC) and block copolymer-coated (BC) magnetic nanoparticles prepared by alkaline coprecipitation at various Fe/N templating ratios and temperatures were studied. The nuclear magnetic relaxation properties of a compound can be further explored through its nuclear magnetic resonance dispersion (NMRD) profile, a curve of relaxivity change vs. the external magnetic field strength, providing a tool to estimate the spectral density $j(\omega\tau_D)$. The NMRD profiles of longitudinal relaxivity r_1 vs. frequency (Figure 5-10) were obtained from measurements on a fast field cycling (FFC) relaxometer. Since only 1 or 2 experiments were used to obtain these results, their statistical significance is unfortunately limited and they should be viewed with caution.

These curves (Figure 5-10) exhibit no low-field dispersion (the left part of curve is flat), which is typical of large superparamagnetic iron oxide nanoparticles for which the anisotropy energy E_a is sufficiently large in comparison with the thermal energy for the direction of the crystal magnetic moment to be locked to the anisotropy axes, precession of the electronic magnetization being thus forbidden.[89] This plateau observed at low magnetic fields is ascribed to the magnetic fluctuations arising from jumps of the moment between different easy axes (Néel relaxation). The precession limitation is introduced in the "outer-sphere" model equations by setting the electron Larmor precession frequency to zero. The longitudidal relaxation dispersion profile $r_1(\nu)$ is generally governed by the so-called Freed equations and originates from the modulation of dipolar interaction by the characteristic times of Néel relaxation (τ_N) and water diffusion (τ_D), respectively.[18,89]

At high fields the magnetic moment is locked onto the magnetic field direction, following the Curie law of paramagnetism (SPIONs rather follow the equivalent Langevin

law for superparamagnetism, but the "outer-sphere" model was originally designed for paramagnetic contrast agents like gadolinium complexes). Therefore Néel relaxation is restricted and the so-called Curie relaxation dominates. Curie relaxation refers to the relaxation of water protons in a locally fluctuating inhomogeneous dipolar magnetic field induced by motions of the water molecules relatively to the SPIONs. Here the translational diffusion correlation time is much shorter than the Néel relaxation time ($\tau_N \rightarrow \infty$), thus τ_C is dominated by water diffusion ($\omega_I \tau_D \sim 1$) and the Freed equations are reduced to the Ayant equations. In particular, the drop of $r_1(\nu)$ to zero for high fields / frequencies is explained by the absence of a "secular term" in the right-hand part of one of these equations (too long to be reproduced here).[18,90]

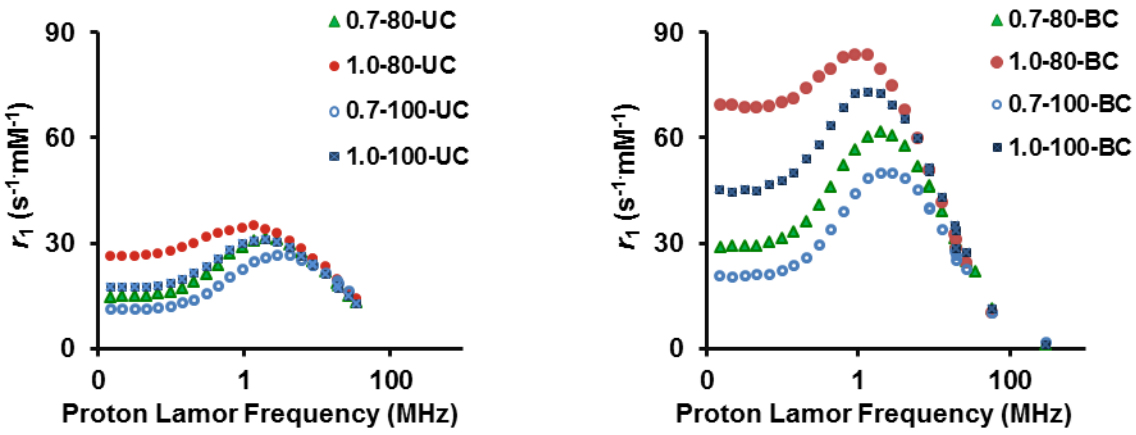

Figure 5-10. NMRD profiles for the various synthesized Fe_3O_4 samples. The sample nomenclature is described in the text.

At intermediate magnetic fields / frequencies, both the local magnetic field (Curie relaxation) and the fluctuating magnetic moments (Néel relaxation) contribute to the relaxation of water protons spins.[3,18] The degree of orientation of the magnetic moment depends on B_0, and therefore the relaxation rate is dominated by the terms proportional to the

squared Langevin function.[89] This gives a maximum in the curve of $r_1(\nu)$ proportional to the square of the saturation magnetization M_s of the sample, which is caused by the increased magnetization and the successive alignment of the particle magnetic moments under the influence of the increased magnetic field.[66,91]

Numerical fits were done using the MINUIT minimization program within the framework of the "outer-sphere" model and a standard phenomenological approximation[66-67] assuming that each profile corresponds to a log-normal size distribution. The divergence between the NMRD curves for the uncoated G1@Fe_3O_4 magnetic micelles (UC samples) and the fits (Figure 5-11) is most likely due to the multimodal size distribution and the significant contribution from the hydrophobic polymeric G0PS-P2VP core to the NMRD profiles, that may not simply lead to reduced magnetization but also to other effects such as reduced water diffusivity in the vicinity of the micelles. Storage of the uncoated G1@Fe_3O_4 magnetic micelles in dilute HNO_3 (pH 1.4) may also have caused partial oxidation and/or agglomeration, thus resulting in a multimodal size distribution. The interference of non-magnetic materials partially impermeable to water (for example SiO_2) with the relaxivity of SPIONs was reported earlier: A good fits was observed for bare Fe_3O_4 SPIONs, but not for the SiO_2-coated NPs.[92] Subtraction of the diamagnetic contribution from silica was suggested to obtain better fits.[92] This solution is not applicable to our magnetic micelles however, due to their inhomogeneous morphology with Fe_3O_4 NPs encapsulated within the porous G0PS-*g*-P2VP micelles, with their internal polar P2VP surface that *i)* disturbs dipolar coupling between neighboring crystals, decreasing the anisotropy energy, and *ii)* partially inhibits the exchange of water molecule in both directions (from the outside in, and from the inside out), thus interfering with the translational diffusion of water molecules.

The fits to the NMRD curves for the block copolymer-coated (BC) samples G1@Fe_3O_4@PAA-PHEA obtained by the same protocol suffers from less interference (Figure 5-12), presumably because the Fe_3O_4 crystals are covered by a layer of double-hydrophilic copolymer, which prevents their aggregation. For every pair of analogous BC and UC samples, the BC sample exhibits a higher relaxivity (suggesting lower anisotropy

energy E_a) than the UC sample at very low magnetic fields. The presence of a hydrophilic layer such as PHEA should increase the inter-crystal distance, reducing the dipolar coupling energy between neighboring crystals. Large dipolar interactions are known to increase the anisotropy energy, slowing down Néel relaxation, and thus decreasing the proton relaxivity at very low magnetic fields (and also the SAR, which is likewise related to τ_N). Therefore the repulsive effect of the PHEA shell is favorable. Similar phenomena were observed by Laurent et al.[93] for dextran-coated SPIONs, and by Sharifi et al.[94] for carboxyethylsilanetriol-coated SPIONs.

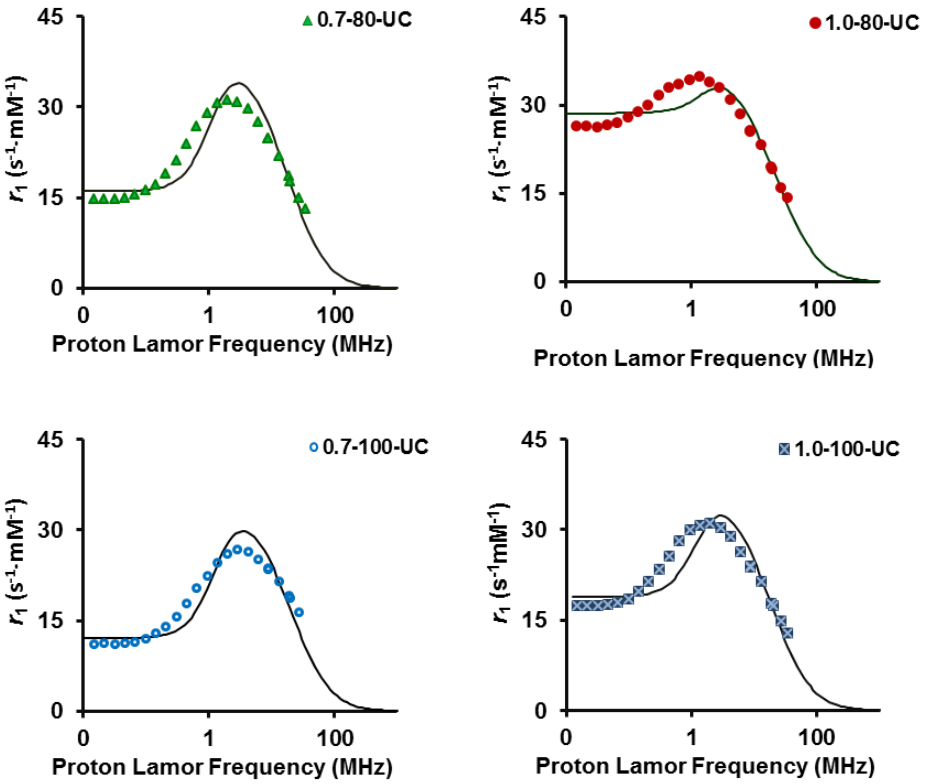

Figure 5-11. Fits to the NMRD curves for the uncoated magnetic G1@Fe_3O_4 micelles.

The UC samples are characterized by a low relaxation rate and flat NMRD profiles indicating agglomeration. Similar observations were reported by Roch et al., who claimed that the agglomeration of SPIONs induced by progressive removal of their dextran coating flattened the NMRD profiles.[84] This effect was ascribed to exchange between the "rapidly-relaxing-water-inside-the-agglomerates" and the "slowly-relaxing-water-in-the-bulk". The essential role of the block copolymer coating in preventing the agglomeration is thus demonstrated for the magnetic G1@Fe_3O_4 arborescent copolymer micelles.

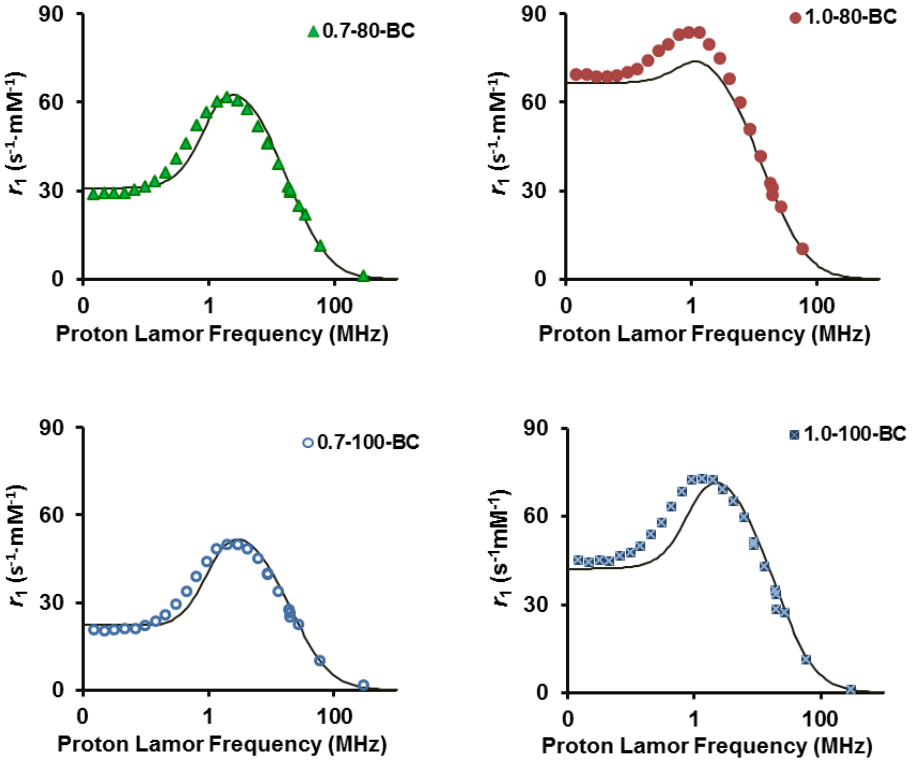

Figure 5-12. Fits to the NMRD curves for the coated magnetic G1@Fe_3O_4 micelles.

Due to the complexity of the G1@Fe_3O_4 magnetic copolymer micelle structure, we attempted subtracting the diamagnetic contribution of water before fitting the NMRD profiles and obtained the following information of interest:

(1) Average crystal radius (r_{NMR}). At high magnetic fields, the relaxation rate only depends upon the translational correlation time τ_D, which can be extracted from the inflection point where $\omega_{\mathrm{I}} \cdot \tau_{\mathrm{D}} \sim 1$. An equivalent crystal / outer-sphere radius r_{NMR} can be calculated from the equation $\tau_D = r_{\mathrm{NMR}}^2/D$, where D is the translational diffusion coefficient of water at the measurement temperature.[66,80,95]

(2) Specific magnetization (M_{s}). At high fields, M_{s} can be obtained from the equation $M_{\mathrm{S}} \sim \sqrt{R_{\mathrm{max}}/C \cdot \tau_{\mathrm{D}}}$, where C is a constant and R_{max} is the maximum relaxation rate.[66,80,95]

Significant divergence was observed when fitting the data for all the samples synthesized with Fe/N = 1.0, probabely due to clustering of non-templated Fe_3O_4 when the Fe precursors exceeded the encapsulating capability of the G1 template, resulting in a broad size distribution of Fe_3O_4 crystals, as determined earlier from the large standard deviation (σ > 0.45) measured by VSM. This confirms that Fe/N = 1.0 is larger than the optimal ratio. The parameters extracted from these fits (M_{S} and r_{NMR}) cannot have physical significance because of the existence of such a broad size distribution.

Fits for the samples with Fe/N = 0.7 gave much better results, which is consistent with a narrower size distribution (as confirmed by a lower standard deviation $\sigma \approx 0.38$ from VSM); The parameters obtained are thus useful to interpret the results. The larger NMRD radius values for the BC set as compared to the UC set (Table 5-4) are interpreted as being due to the desirable presence of hydrophilic block copolymers around the crystals. At very high fields, when Curie relaxation dominates over Néel relaxation, the presence of a hydrophilic layer like PHEA increases the translational diffusion correlation time τ_{D}, which is the predominant component contributing to the total correlation time τ_{C}. Sharifi found a very small (0.06 nm) increase when comparing the apparent crystal radii (from NMRD) for the bare Fe_3O_4 NPs and Fe_3O_4 NPs coated with carboxyethylsilanetriol,[94] which is analogous to our results ($r_{\mathrm{NMR(BC)}} - r_{\mathrm{NMR(UC)}} = 0.1$ nm). Laurent et al. reported a larger increase from 40 to 55 nm, definitely related to the increase in the $\bar{M}_{\mathrm{w}}$ of dextran coating the particles from 35,000 to 200,000 g/mol.[93] Hannecart et al. also reported an increase in outer-sphere radius

between MNPs coated with small molecules (silanes) vs. NPs grafted with a thermosensitive polymer shell: The gap increased from 0.5 nm when the chains were swollen by water at low temperature, to 1.8 nm when the shell became impermeable to water above the lower critical solution temperature (LCST), a plausible value based on the radius of gyration estimated under poor solvency conditions for PPO-*co*-PEO (2,000 g/mol).[83]

The UC samples stored in diluted HNO_3 suffered from partial oxidation that converted Fe_3O_4 to γ–Fe_2O_3 and led to a reduction in M_s values by ~ 21–26% as compared to BC samples, as expected from the respective bulk magnetization values. The complexation with BC to create a stabilizing, protecting layer for the SPIONs is thus essential to maintain high magnetization values with good potential as MRI contrast agents. A 6 % reduction in M_s values was reported by Sharifi et al. when comparing magnetization values for carboxyethylsilanetriol-coated SPIONs to bare SPIONs.[94] On the other hand, the temperature of the coprecipitation reaction did not show a significant influence on the M_s and r_{NMR} values.

Table 5-4. Magnetic properties of Fe_3O_4 samples from NMRD analysis.

Sample	r_{NMR} (nm)	$M_{s(NMR)}$ (emu/g Fe_3O_4)	r_{NMR}/r_{VSM} *	$M_{s(NMR)}/M_{d(VSM)}$
0.7-80-UC	8.0	22.9	1.4	0.51
0.7-80-BC	8.1	31.1	1.4	0.52
0.7-100-UC	7.9	23.0	1.5	0.44
0.7-100-BC	8.0	29.2	1.4	0.52

The sample nomenclature is explained in the text. *The VSM radius is defined as half of the volume-average diameter obtained from a log-normal law: $r_{VSM} = D_v/2$; D_v values listed in Table 5-1.

The radius obtained by relaxometry is 33% larger than from TEM, and 43% larger than from magnetometry (assuming a log-normal distribution of sizes when calculating the

volume-average diameters), which can be explained by the fact that fitting of the NMRD profiles leads to the distance of closest approach (also called the outer sphere diameter) of water molecules to the superparamagnetic surface, thus comprising the hydrophobic polymer part (excluding water penetration), whereas the TEM and VSM data give the radius of the crystallites and the magnetic core, respectively. The ratios of crystal radii $r_{\mathrm{NMR}}/r_{\mathrm{VSM}}$ found were in the range of 1.4–1.5, likely due to the presence of the hydrophobic PS-P2VP core. Bare SPIONs and SPIONs with a thin dextran coating were reported to have $r_{\mathrm{NMR}}/r_{\mathrm{VSM}} \approx$ 1.1–1.4,[92-93,96] while this ratio rose to 1.5–3.9 for SiO_2-coated SPIONs as the SiO_2 coating thickness was increased, even though it was partially permeable to water, since silica synthesized by a sol-gel process has a mesoporous struture.[92]

The magnetization obtained from NMRD is lower than by magnetometry, as a result of a larger sample size probed by relaxometry. The magnetization value for individual Fe_3O_4 crystals is not changed, but rather diluted in a larger volume: The particles behaves as though they have a larger size, but are less magnetized.[92] We found ratios $M_{\mathrm{s(NMR)}}/M_{\mathrm{d(VSM)}} \approx$ 0.4–0.5, close to values reported by other groups ($M_{\mathrm{s(NMR)}}/M_{\mathrm{d(VSM)}} \approx$ 0.5–0.8).[91,96] Increasing the thickness of the diamagnetic SiO_2 coating reduced this ratio to 0.1.[92]

In conclusion, the transverse relaxivity r_2 and r_2/r_1 ratio measured for magnetic micelles 0.7-80-BC are relatively large when compared to commercial products, indicating good potential of these materials for T_2-contrast enhancement. The minimal proton approach size and relaxivity of this magnetic micelle are well-fitted by the "outer-sphere" (OS) model extensively described previously in the literature. The NMRD profiles for the uncoated and coated magnetic micelles revealed: *i)* the determining effect of size dispersity on the quality of the fits; *ii*) the contribution of the hydrophobic polymer template to the dipolar coupling energy between neighboring crystals, affecting the anisotropy energy through its shape and demagnetization-effect component; *iii)* the limited accessibility of water near the superparamagnetic surface, hampering the translational diffusion of water; and *iv)* the agglomeration of uncoated samples due to the lack of a protecting layer, flattening the curves and resulting in poor fits. The role of a hydrophilic stabilizing shell in preventing

agglomeration is therefore essential. The NMRD curves for samples synthesized with the optimal ratio Fe/N = 0.7 can be fitted quite well with the OS model, suggesting that these samples contain a narrow size distribution. The presence of the double-hydrophilic diblock copolymer led to a larger equivalent OS radius and was found crucial to maintain a high magnetization for the SPIONs. The discrepancy observed when comparing parameters obtained by relaxometry and magnetometry was explained by the different nature of these methods: the equivalent OS radius derived from relaxometry is larger than from magnetometry, due to the diamagnetism and the partial impermeability of the polymer shell to water. The magnetization obtained from NMRD was lower than by magnetometry due to dilution of the magnetic moment in the micelle volume (since the magnetization M_s is, by definition, the concentration of moments per unit micelle volume). The specific magnetization and Néel relaxation phenomenon will be of utmost importance when dealing with the last property for which the magnetic micelles were designed, namely magnetic field hyperthermia intended for anticancer therapy (cytotoxicity).

5.4.3 Hyperthermia

The specific absorption rate (SAR) of the magnetic micelles was determined by AMF calorimetry. The SAR values were calculated from $\Delta T/\Delta t$, the initial rate of temperature rise measured in water when the magnetic micelles suspension was placed in the AMF generated by a solenoid coil fed by the power generator. The SAR values were corrected for thermal losses of the calorimeter and parasitic heating of the coil by the Joule effect (in spite of being refrigerated by internal cold water circulation) using pure water as a reference blank, and were normalized by the iron oxide content. The specific absorption rate of the magnetic micelle suspensions increased with the magnetic field amplitude H_{max} and frequency f, and was found to be independent of the concentration of magnetic material.[50] A maximum SAR value of 55.6 $W \cdot g^{-1}$ was measured at f = 755 kHz and H_{max} = 10.2 $kA \cdot m^{-1}$. Recently, some authors[97] suggested subtracting from the positive slope of the T versus time curve when the

AMF is ON, the negative slope when the AMF is OFF (for reach instantaneous temperature) to correct for non-adiabatic conditions, a procedure which we have also used.

The heating characteristics of SPIONs are a complex function of the individual crystal properties, and of the structure and state of the crystals in the particles and in suspension.[98] Therefore, the SAR heating characteristics need to be evaluated at various field amplitudes and frequencies. According to the heat dissipation equations of the linear relaxation theory (LRT) introduced by several authors (Rosensweig, Hergt, Pankhurst…), the SAR values increase with the frequency f and the applied field amplitude H_{max}. We determined the SAR values as a function of magnetic field amplitude H_{max} for five fixed frequencies f available on the two experimental setups used (Figure 5-13). In the literature, it is described that the field amplitude dependency of SAR follows power laws of nearly second order for superparamagnetic samples, and higher order (e.g. three to four) for ferromagnetic samples above a threshold field strength identified as the anisotropy field H_K, as observed for various ferrofluids.[30-31,50,53,99-101] For the magnetic micelles studied here, the SAR vs. H_{max} power trend lines at high and medium frequencies were below, but nevertheless close to second order (slopes on double-logarithmic plots of 1.73 at 755 kHz, 1.68 at 473 kHz, and 1.56 at 344.5 kHz), which is consistent with the superparamagnetic character of the magnetic micelles, and with Néel relaxation being the main contribution to the heating process.

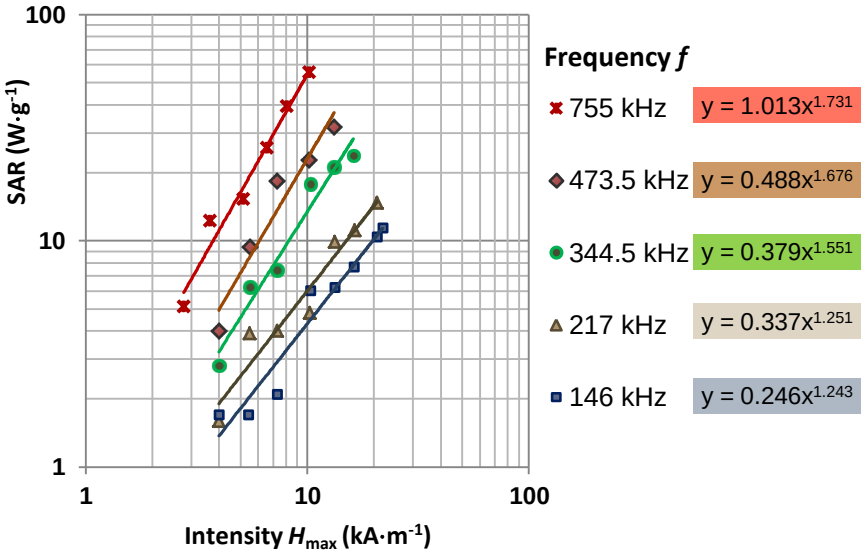

Figure 5-13. Specific absorption rate (SAR) of magnetic G1 micelles as a function of magnetic field amplitude H_{max} at various fixed frequencies f.

Smaller orders of 1.25 and 1.24 were obtained at the lower frequencies of 217 and 146 kHz, respectively. Reductions in the SAR values leading to a linear correlation with the field amplitude H_{max}, contradicting the quadratic increase predicted by the linear response theory, have been observed by various groups, in particular for multi-core nanoflower morphologies.[56-57,99,102-105] It is also noteworthy that the linear response theory (LRT) was proposed and used for non-interacting superparamagnetic nanoparticles in the limit of low magnetic field strengths and sample concentrations, but it failed to account for many aspects of colloidal MNP suspensions, such as interparticle interactions and particle motions.[57,98]

The reduction in the SAR values demonstrates the larger contribution of Brownian relaxation to the heating process at lower frequencies as compared to medium-range frequencies. Hergt et al. also observed smaller SAR values at very low frequencies (1–10 kHz) for gel suspensions (in which the MNPs were immobilized) as compared to the original aqueous suspensions.[99] This decrease in heating power was ascribed to the reduced

contribution of Brownian relaxation. This group also claimed the existence of a transition region of intermediate frequencies into a higher frequency zone, where the Néel regime predominates.[99] This hypothesis can be applied to our magnetic micelles to explain the close-to-first-order dependence observed at low frequencies, since the complex and bulky nanostructure of the micelles might hamper Brownian relaxation, reducing the SAR values and resulting in smaller than square dependence on H_{max}. In the high and medium frequency ranges, where Néel relaxation dominates, restricted Brownian relaxation has less influence on the SAR values, resulting in higher values that obey the square power law. Similar reasons leading to first order laws were also suggested by Yuan and Borca-Tasciuc[106] in the form of "cluster oscillation".

For our magnetic micelles, the encapsulation of multiple Fe_3O_4 crystals inside an uncoated G1 polymer template probably enhanced the dipole-dipole inter-crystal interactions, but this effect was counterbalanced by the hydrophilic shell in the micelles coated with PAA_{27}-*b*-$PHEA_{260}$. Walter et al.[57] claimed that aggregation and strong dipole-dipole interactions led to reduced SAR values at high concentrations. Lartigue et al.[102] proposed inter-core dipolar interactions occurring in dense three-dimensional multi-core clusters as the cause for the hysteresis area reduction, while Materia et al.[103] ascribed the SAR reduction to magnetic dipolar interactions between very close nanocubes within clusters. In general, many authors[107-108] agree that dipolar interactions have a negative effect on the SAR and use this argument to explain experimental findings where the measured SAR values increase as the overal iron oxide concentration decreases (less dipolar interactions).

The linear dependence of the SAR of magnetic micelle on the magnetic field frequency was tested for various fixed magnetic field amplitudes (Figure 5-14). Deviations from first order were also reported in the literature for cobalt ferrite (with Brownian relaxation), but not for γ–Fe_2O_3.[50]

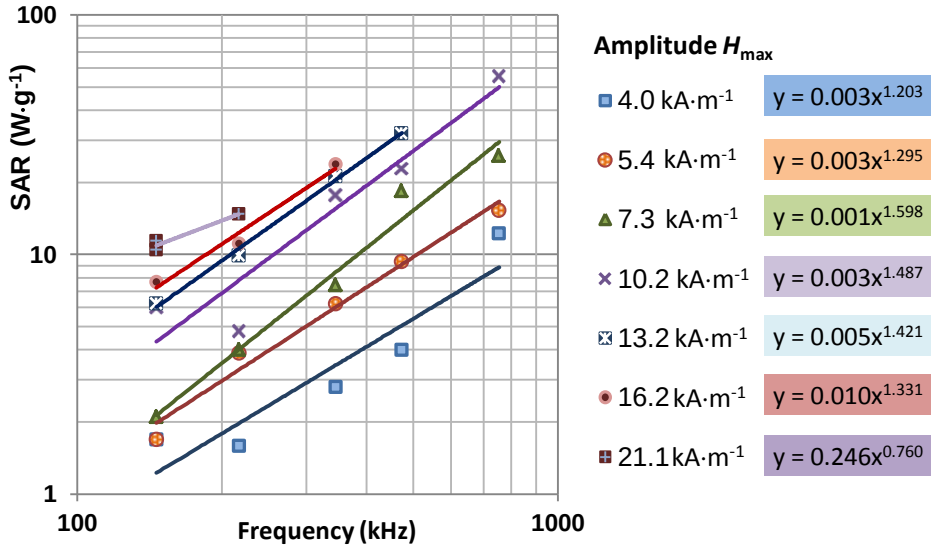

Figure 5-14. Specific absorption rate (SAR) of magnetic G1 micelles as a function of magnetic field frequency for various fixed values of magnetic field amplitude H_{max}.

Moreover, the size dispersity of samples was also suggested as a factor responsible for the deviations between experimental results and LRT predictions.[50] However, a closer look at the fundamental equation of LRT giving the dissipated power $P = \mu_0 \pi \chi'' f H_{max}^2$ shows that the SAR cannot be perfectly linear with frequency, since P is a linear function of f but also proportional to the imaginary part of magnetic susceptibility, $\chi''(f)$, which reaches a maximum near the characteristic relaxation rate $\tau_C^{-1} = \tau_N^{-1} + \tau_B^{-1}$ of the magnetic NPs. As a result of the near-to-square dependence of the SAR of magnetic micelles on the field magnitude and its near-to-linear dependence on the field frequency, the linear correlation of the SAR with the product $H_{max}^2 f$ is only valid at the highest frequency tested (755 kHz) but not for the lower ones, with much lower correlation coefficients R^2 (Figure 5-15). The parameter $H_{max}^2 f$ has actually been suggested as a normalization factor to yield the intrinsic loss power ILP $= {SAR}/{[H_{max}^2 \cdot f]}$ parameter,[65] with the idea to allow a more or less direct

comparison between experiments by different authors, but our results show that this normalization must be done with caution.

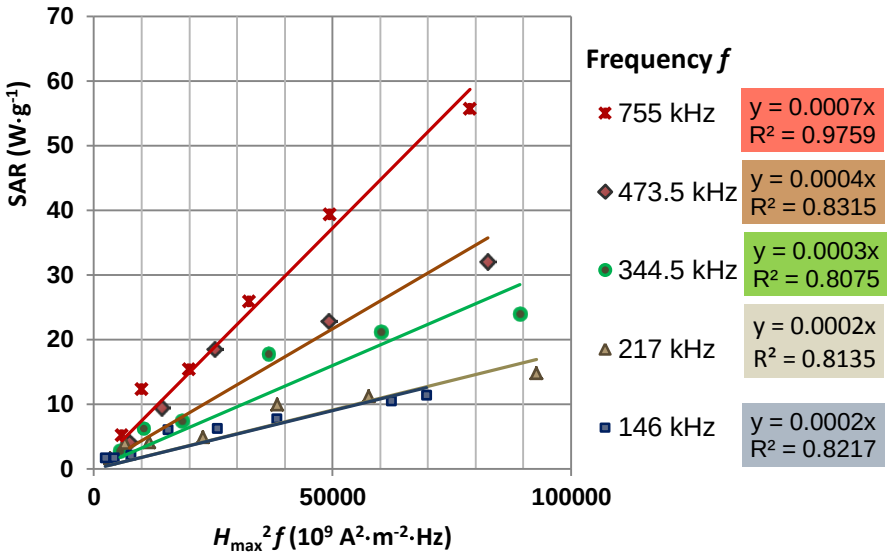

Figure 5-15. Specific absorption rate (SAR) of the magnetic micelles as a function of the product of squared magnetic field amplitude H_{max}^2 and frequency f.

In conclusion, double-hydrophilic BC-coated magnetic micelle suspensions exhibited good SAR values for different field conditions. Nearly square correlation between the SAR values and the magnetic field amplitude was observed for high- and medium-range frequencies, while a less pronounced dependence was obtained at lower frequencies. These variations in comparison to the LRT predictions are most likely related to *i)* the complex internal structure of our magnetic micelles leading to dipole-dipole interactions between neighboring crystals, moderated by complexation of the iron oxide surface with the double-hydrophilic block copolymer, and *ii)* restricted Brownian relaxation, particularly at lower radiofrequencies. Both of these characteristics conflict with the models routinely used to characterize the SAR as a function of H_{max} and f. Nevertheless, the good SAR values

determined for these coated magnetic micelle suspensions justify the next step of the work, which is *in vitro* hyperthermia-induced cytotoxicity assays on cancer and control cells.

5.5 Conclusions

The magnetic properties of Fe_3O_4 nanoparticles (bare and coated with a double-hydrophilic block copolymer) were characterized by vibrating sample magnetometry. All the Fe_3O_4 nanoparticles exhibited superparamagnetic behavior, i.e. no hysteresis loop, zero coercivity and zero remanence. The templating Fe/N ratio, temperature, and the presence of coating materials were found to influence the magnetization and relaxometric properties of the Fe_3O_4 NPs to different extents. G1@Fe_3O_4@BC samples prepared with a ratio Fe/N = 0.7 displayed higher magnetization than those produced with Fe/N = 1, due to the formation of larger median diameter magnetite NPs with narrower size distributions. Samples prepared at 80 °C exhibited higher saturation magnetization than samples prepared at 100 °C, while no significant change in size distribution was observed, since a higher temperature facilitated the oxidation reaction converting magnetite Fe_3O_4 to maghemite γ–Fe_2O_3. Higher magnetization was also found for samples coated with PAA_{27}-*b*-$PHEA_{260}$. The observed discrepancy between diameters determined by VSM and by TEM was ascribed to spin canting occurring at the surface or within the volume of the nanoparticles.

The relaxivities of all the uncoated (UC) and block copolymer-coated (BC) magnetic nanoparticles were measured. The coated SPION 0.7-80-BC had superior colloidal stability, which prevented their agglomeration and led to higher r_2 = 335 $s^{-1}\cdot mM^{-1}$ and r_2/r_1 = 31.4 values (1.47 T, 37 °C) than the uncoated SPIONs, suggesting that they could be efficient negative contrast agents for T_2-weighted imaging. Samples produced with Fe/N = 0.7 also displayed better relaxivity (larger r_2 and r_2/r_1 ratio) than for Fe/N = 1 ratio, and are thus considered better contrast agents. When compared with commercial products and from the literature, sample 0.7-80-BC fared well as an efficient negative contrast agent, characterized by comparably high relaxivities, allowing smaller injection doses for the patients.

The nuclear magnetic resonance dispersion (NMRD) curves for the MNPs exhibited no low-field dispersion. The divergence between the NMRD curves obtained for the uncoated magnetic micelles and fits using the equations from the outer-sphere theory was assigned to the broader size distribution and to significant interference from the hydrophobic PS core and P2VP surface on the water diffusivity and exchange rates probed in the NMRD profiles. Uncoated (UC) samples were characterized by low relaxation rates and flat NMRD profiles indicating agglomeration, thus confirming the essential role of the block copolymer coating. The radii obtained from NMRD analysis were larger than those from TEM (by ca. 33%) and from magnetometry (by ca. 43%), which can be explained by the different nature of these characterization methods, for which the polymer component of the micelles can be invisible (TEM), non-magnetic (VSM), and partially impermeable (NMRD). The magnetization values obtained from the fits to the NMRD profiles were smaller than those determined by magnetometry, as a result of a larger effective sample size for relaxometry and dilution of the iron oxide in the polymer (pushing further the limit of the outer-sphere).

The specific absorption rate (SAR) of the magnetic micelles was determined by AMF calorimetry. A maximum SAR value of 55.6 $W \cdot g^{-1}$ was measured at f = 755 kHz, H_{max}=10.2 $kA \cdot m^{-1}$. The SAR values obtained had a nearly square dependence on the magnetic field amplitude H_{max} at fixed frequency f in the high- and medium-frequency ranges, consistent with the superparamagnetic nature of the coated micelles and a main contribution from Néel relaxation to the heating process. Closer-to-one exponents of the SAR vs. H_{max} were observed at lower frequencies and were explained by the contribution of Brownian relaxation of the MNPs to the heating process, and the enhancement of dipole-dipole inter-crystal interactions, despite the positive effect of the hydrophilic polymer coating separating multiple magnetic cores within the same G1 micelle.

Chapter 6 Biocompatibility Assessment and *In Vitro* Cell Hyperthermia

Chapter 6

6.1 Overview

The properties of magnetic polyion complex (MPIC) micelles stabilized by a poly(2-hydroxyethyl acrylate) (PHEA) shell were shown to be promising for applications as magnetic resonance imaging (MRI) contrast agents and for heat generation in cellular radiofrequency magnetic field hyperthermia (MFH) treatment. In this Chapter, the cytotoxicity and cell internalization of polyion complex (PIC) micelles and MPIC micelles were evaluated *in vitro*. Good colloidal stability and non cytotoxicity of the micelles were observed and assigned to the good biocompatibility of the PHEA shell. Cells incubated for 48 h with MPIC micelles at the highest concentration (1250 μg of Fe_3O_4/mL) had a cell viability of 91%, as compared with 51% when they were incubated with bare (unprotected) magnetic nanoparticles. Cell internalization was visualized by confocal laser scanning microscopy (CLSM) and TEM, and quantified by fluorescence-activated cell sorting (FACS). In spite of bearing negative charges, fluorescently labeled PIC* and MPIC* micelles were both rapidly internalized by L929 cells. The presence of iron oxide crystallites inside intracellular lipid organelles called lysosomes, i.e. their wrapping by cellular membranes, suggests that the cells internalized the MPIC micelles by an endocytosis pathway (either calvaolae- or clathrin-dependent). The cellular uptake exhibited strong dependence on the NP concentration and incubation time. The linear correlations obtained between the mean fluorescence intensity and % positive cells vs. incubation time could serve as a predictive tool for the cellular uptake kinetics.

The usefulness of MPIC micelles for cellular radiofrequency magnetic field hyperthermia was also confirmed, as the MPIC micelles had a dual dose-dependent effect (concentration and duration of magnetic field exposure) on cell viability. The viability of L929 fibroblast cells incubated with MPIC micelles at 1250 μg Fe_3O_4/mL concentration decreased to 46% after 1.5 h and to 30% after 3 h of exposure to a high frequency magnetic field (755 kHz, 10.2 kA/m). Similar treatments on U87 human glioblastoma cells resulted in 57% and 35% cell viability after 1.5 and 3 h exposure, respectively, suggesting an effective and tunable treatment for various types of cells.

Chapter 6

6.2 Introduction

Nanomaterials have significantly different properties and reactivity as compared to their bulk material counterparts, in part due to their larger surface area which enables an exponential increase in the number of molecules exposed on the surface as the particle size decreases to < 100 nm.[1] These unique properties provide nanomaterials with immense potential for various applications. Nanomaterials offer innovations in biomedical imaging, sensing, diagnosis, and in designing novel approaches to the treatment of diseases. Translating an application from the laboratory to clinical settings requires the evaluation of the impact of nanomaterials on cellular and animal models under acute or chronic exposures, and of the fate of nanoparticles in biological systems (i.e., their clearance mechanisms).[2] Biocompatible nanoparticles must resist premature enzymatic degradation and aggregation, be able to target specific tissues, cross biological barriers such as epithelia (e.g., the blood brain barrier), extracellular matrix, and eventually the cell plasma membrane, and to perform their desired function without inducing toxicity or an immune response.[3-4] Potential toxicity and the response of cells upon exposure of nanomaterials must therefore be investigated.

Toxicity is a complex event *in vivo* since it is related to direct cellular damage, as well as physiological, inflammatory, and other systemic effects. Even for *in vitro* assays it is currently difficult to monitor systemic and physiological effects, so most assays investigate effects at the cellular level, or cytotoxicity.[5] Although cytotoxicity assays simplify the events that might occur, they are still useful as a first screening step before further investigations are performed because they are more economical, easily quantified, reproducible, and more ethically acceptable than animal testing. The evaluation method for cytotoxicity used herein was adapted from ISO 10993-5 (2009) guidelines, using the mouse fibroblast L929 line. The MTS assay was used to determine whether the NPs have effects on cell proliferation or have direct cytotoxic effects leading to cell death. In this assay, cells in the exponential phase of growth are exposed to the nanoparticles for a set duration for maximal damage to occur. Cell proliferation is allowed to occur for two to three population-doubling times. All the viable cells, those capable of proliferation as well as those that remain viable but cannot proliferate,

are distinguished from dead cells.[5] Cell viability in the cultures was monitored by the reduction of clear yellow tetrazolium salt (MTS) to its brown soluble formazan product upon exposure to NADH-dependent cellular oxidoreductase enzymes found in the mitochondria of metabolically active cells.[6-7] While negatively charged MTS does not readily penetrate cells and must be used with an intermediate electron acceptor to transfer electrons from the cytoplasm or plasma membrane and facilitate its reduction, the MTS assay is still preferable to MTT (3-(4,5-dimethylthiazol-2-yl)-2,5-diphenyltetrazolium bromide), because the formazan products generated by the reduction of MTS are soluble in the cell culture medium rather than in organic solvents such as DMSO, thus making the protocols more convenient.[8]

Understanding how nanoparticles interact with cells is a first step in assessing the biomedical functions and toxicity of nanomaterials, allowing the prediction of the toxicological consequences of nanoparticles *in vivo*. It is known that nanoparticles, due to their small size, readily penetrate through cell membranes and can translocate among targeted cells, tissues, and organs, as required for efficient diagnostic or therapeutic functions.[9] Study of the cell internalization mechanism of nanoparticles is thus necessary towards understanding their biological fate. It is noteworthy recalling the dynamic structure of the plasma membrane, composed of lipid bilayers and membrane proteins that segregate the cytoplasm from the external medium and regulate the transport of matter into the cells. Cell membranes are semi-permeable and allow only small molecules to pass through via diverse mechanisms that are either passive or active (consuming the biochemical fuel ATP molecules). The free diffusion of oxygen, carbon dioxide, water, and small hydrophobic molecules through the plasma membrane is driven by concentration gradients, while ions and amino acids penetrate the cell via the active transport system of integral membrane protein pumps or ion channels. Nanoscale hydrophilic biomacromolecules are usually transported by endocytosis.[8]

Endocytosis is a form of active transport in which cells uptake objects by invagination of the plasma membrane, enclosing them into vesicles called “endosomes”. These processes occur mainly via phagocytosis, pinocytosis, and caveolae-dependent or

clathrin-mediated endocytosis.[10-12] Particles with large diameters (> 750 nm) are uptaken via the phagocytosis pathway, through the formation of an internal phagosome usually observed in specialized mammalian cells (like monocytes, macrophages, and neutrophils).[13] Pinocytosis or macropinocytosis occurs in almost all cell types to uptake smaller particles ranging from a few to several hundred nanometers. Clathrin-mediated endocytosis is an energy-dependent pathway that allows cargo deposited in small endocytic vesicles (usual diameter < 100 nm) to fuse with early endosomes.[14-15] The relationship between NP size,[9,16-17] shape[17-18] or charge[14,17,19] and its uptake kinetics and mechanism have been extensively studied. It is well-known that nanoparticles of uniform size with diameters below 200 nm and homogeneous in composition are desirable for systemic circulation, i.e., long blood half-lives, especially if they coated with a neutral polymer sheath.[3-4] Spherical NPs with a diameter of 50 nm are taken up by mammalian cells at a faster rate and at higher concentrations than other sizes and shapes.[9,16] Positively charged particles are expected to be more efficiently endocytosed than negatively charged ones due to their effective binding to the negatively charged cell surface. This expectation was proven by a 2-fold higher uptake of positively charged particles into HeLa cells when compared with negatively charged nanoparticles of equal size (80 nm).[14] However the work of Zhang et al. depicted higher uptake for negatively charged quantum dots into HEK cells, which was explained by a lipid raft-mediated mechanism, different from the clathrin-dependent pathway reported for positively charged NPs.[19] Further investigation is therefore needed to determine the relationship between NP size, surface charge, and internalization pathways.

To target biomedical applications for MPIC micelles as MRI contrast agent or in hyperthermia treatment, the cytotoxicity and cell internalization of the MPIC micelles need to be evaluated *in vitro*. The same protocols were performed with PIC micelles, to provide an *in vitro* biocompatibility platform for their future biomedical use (e.g., biosensor, drug delivery, gene delivery, cancer therapy). The study of the interactions of nanoparticles with the cells is the first step to predict the toxicological consequences of nanoparticles *in vivo* and to reveal the fate of the NPs once they enter the organism. The cellular uptake, location of the

NPs and any biological consequences, such as cytotoxicity of the MPIC micelles were thus investigated herein. An *in vitro* study of magnetic field hyperthermia was also performed. In this case a colloidal suspension of MNPs (the MPIC micelles) was incubated with the cells, allowing the MNPs to be internalized through the cell membrane. The application of an external alternating magnetic field (AMF) induced heat in the MNPs to kill the cells, presumably by an oxidative pathway (ROS production) as described in recent literature.[20-22] In our work, the incubation concentration of MPIC micelles and the AMF exposure time strongly influenced the viability of murine L929 and human glioblastoma U87 cells.

6.3 Experimental Procedures

6.3.1 Block Copolymer Synthesis

The chemicals, procedures and characterization techniques for the synthesis of the double-hydrophilic block copolymers (DHBC) poly(acrylic acid)-*b*-poly(2-hydroxyethyl acrylate) by atom-transfer radical-polymerization (ATRP) were described in Section 3.3. Briefly, low molar mass poly(*tert*-butyl acrylate) P*t*BA-Br macroinitiators synthesized via ATRP were employed in a second ATRP reaction to create poly(*tert*-butyl acrylate)-*b*-poly(2-trimethylsilyloxyethyl acrylate) P*t*BA-*b*-P(HEATMS). These block copolymers were then hydrolyzed to produce the corresponding PAA-*b*-PHEA copolymers, which were purified by dialysis and stored in aqueous solutions at pH 7. Two block copolymers, PAA_{13}-*b*-$PHEA_{150}$ ($\bar{M}_n$ = 18,340 g/mol, $\bar{M}_n.\bar{M}_w^{-1}$ = 1.23) and PAA_{27}-*b*-$PHEA_{260}$ ($\bar{M}_n$ = 30,940 g/mol, $\bar{M}_n.\bar{M}_w^{-1}$ = 1.16), were used in the investigation.

One of the block copolymers was labeled with a fluorescent dye using 1-ethyl-3-(3-dimethylaminopropyl) carbodiimide hydrochloride (EDC, Sigma-Aldrich, ≥ 99.0%) and fluoresceinamine isomer I (FA, Sigma-Aldrich, 75%). The labeled PAA_{27}-*b*-$PHEA_{260}$ copolymer (hereinafter referred to as PAA_{27}^{*}-*b*-$PHEA_{260}$) was prepared via amidation of the carboxylic groups in the PAA block with fluoresceinamine as illustrated in Scheme S6-1. A water dispersion of PAA_{27}-*b*-$PHEA_{260}$ (50 mg, 0.162 µmol BC, 43.6 µmol of COOH groups)

was prepared while fluoresceinamine (FA, 3.35 mg, 9.65 µmol, FA/COOH = 6/27 mol/mol) was dissolved in DMF (2 mL). The two solutions were combined and vigorously stirred for 10 min before EDC (67.73 mg, 436 µmol, EDC/COOH = 270/27) was added to create the highly reactive O-acylisourea intermediate. The mixture was allowed to react for 24 h before the product was dialyzed against deionized water for 5 d with 15 changes of water. The PAA_{27}^{*}-*b*-$PHEA_{260}$ copolymer was collected and stored at 10 °C. The fluorescence emission of the block copolymer was monitored on a UV/Vis/Fluorescence SpectraMax® M2e Multimode Microplate Reader. The number of FA molecules conjugated to each PAA_{27}-*b*-$PHEA_{260}$ molecule (containing 27 CO_2H groups), determined by fluorometry, was 1.88 ± 0.15 (Section 6.4.1), corresponding to 7.0 mol%.

6.3.2 Polyion Complex Micelle Preparation

The polyion complex (PIC) micelles used for the biocompatibility tests in this Chapter were prepared from a G1 arborescent graft copolymer (G0PS-*g*-P2VP) and the DHBC by the procedure described in Section 3.3.6. The following procedure describes the complexation of the G1 copolymer with PAA_{27}-*b*-$PHEA_{260}$ for $f = CO_2H/N = 0.5$ (molar ratio of CO_2H groups on the PAA segment of the block copolymer and N moieties of the P2VP segments on the arborescent copolymer). Briefly, in a 10-mL vial, G1 (1.7 mg, 14.7 µmol of N) was completely dissolved in 300 µL of aqueous HCl solution at pH 1.4. A pH 7 aqueous solution of PAA_{27}-*b*-$PHEA_{260}$ (8.5 mg, 5 mg/mL, 7.35 µmol of CO_2H) was quickly added. The mixture was left to react for 1 h before the pH was adjusted to 4.7 with a 1 M NaOH solution and stirring was continued for 1 h. The pH was further adjusted to 7 with a 0.1 M NaOH solution and the solution was stirred for 30 min. The solution was dialyzed against Milli-Q water for 48 h before it was collected and stored at 10 °C.

The preparation of the fluorescently labeled PIC micelles (hereinafter referred to as PIC* micelles) was performed in the dark by the same procedure, but with a mixture of 5% PAA_{27}^{*}-*b*-$PHEA_{260}$ (7.0% labeled) and 95 mol% of (non-labeled) PAA_{27}-*b*-$PHEA_{260}$.

6.3.3 Magnetic Polyion Complex Micelle Preparation

The magnetic polyion complex (MPIC) micelles used for biocompatibility tests in this Chapter were prepared from the G1 templated magnetic nanoparticles G1@Fe_3O_4 and the DHBC obtained by the procedure of Section 3.3.6. Briefly, the magnetic nanoparticles G1@Fe_3O_4 were prepared by coprecipitation in the presence of the G1 copolymer as a template. The iron oxide precursors were loaded by mixing Fe^{2+} sulfate and Fe^{3+} chloride salts stock solutions (at 1:2 stoichiometric ratio) with the G1 template in HCl solution at pH 1.4. Concentrated NH_4OH was added to trigger the coprecipitation into colloidal Fe_3O_4. The magnetic nanoparticles (MNPs) were washed and redispersed in HNO_3 at pH 1.4 to produce a black homogeneous ferrofluid.

Complexation of the G1 templated MNPs with various amounts of PAA-*b*-PHEA block copolymers was carried out in aqueous solutions. The f = CO_2H/N ratio (defined previously) was varied within the range f = 0.25–1. Briefly, the G1@Fe_3O_4 ferrofluid in HNO_3 pH 1.4 (0.99 mg Fe_3O_4, 1.9 mg of G1, 16.7 µmol of N functional groups) was loaded in a 10-mL vial and an aqueous solution of PAA-*b*-PHEA at pH 7 (9.6 mg, 5 mg/mL, 8.3 µmol of CO_2H functional groups) was quickly added. The mixture was left to stir for 1 h before adjusting the pH to 4.7, and stirring further for 1 h. The pH was then adjusted to 7 and the solution was stirred for 30 min, dialyzed against Milli-Q water (5 L) for 48 h, collected and stored at 10 °C.

The preparation of the fluorescently labeled MPIC* micelles was performed in the dark by the same procedure, but with a mixture of 5% PAA_{27}^{*}-*b*-$PHEA_{260}$ (7.0% labeled) and 95% of non-labeled PAA_{27}-*b*-$PHEA_{260}$**.**

6.3.4 Biocompatibility Assessment

6.3.4.1 Materials

For cell culture, Dulbecco modified Eagle medium (DMEM, with 4.5 g/L glucose, sodium bicarbonate, without sodium pyruvate, sterile-filtered, suitable for cell culture), GlutaMAX fetal bovine serum (FBS), and 0.5% trypsin solution 10× were purchased from Gibco, Grand Island, NY. Sodium pyruvate was obtained from Biowhittaker (Walkersville, MD). PBS solution (with Ca^{2+} and Mg^{2+}), PBS solution (without Ca^{2+} and Mg^{2+}), penicillin and streptomycin were purchased from Lonza. The mouse fibroblast-like L929 cell line was purchased from LifeTechnologies. The U87 human glioblastoma was the line *ATCC*® HTB-14™ obtained from the American Tissue Culture Collection (Manassas, VA). 3-(4,5-dimethylthiazol-2-yl)-5-(3-carboxymethoxyphenyl)-2-(4-sulfophenyl)-2H-tetrazolium (MTS) was obtained from Promega (Madison, WI) for the cell viability tests. Paraformaldehyde (Sigma-Aldrich, powder 95%), Triton X-100 (Sigma-Aldrich, BioXtra, for molecular biology), bovine serum albumin (BSA), Alexa Fluor® 594 phalloidin (Life Technologies, 300 units), 4',6'-diamidino-2-phenylindole (DAPI, Sigma-Aldrich 98.0%), VECTASHIELD HardSet Mounting Medium (Vector laboratories) served for the cell internalization experiments.

6.3.4.2 Cell Cultures

The fibroblast-like L929 cells derived from normal subcutaneous areolar and adipose tissue of a 100-day old male C3H/An mouse[23] was purchased from LifeTechnologies. This murine fibroblast cell line is recommeneded for cytotoxic assays of nanomaterial in the ISO10993-1:2009 procedure "Biological evaluation of medical devices". Both cell types (U87 and L929) were cultured in DMEM supplemented with 10 vol% of heat-inactivated fetal bovine serum (FBS), 1 vol% of antibiotics (10,000 units of penicillin and 10,000 units of streptomycin/mL), 1 vol% sodium pyruvate and 1 vol% GlutaMAX. The cells were maintained at 37 °C in a 5% CO_2 humidified incubator. After rinsing with PBS (Ca^{2+}/Mg^{2+} free) solution to remove the serum, the cells were detached with trypsin solution 10× diluted 10-fold with PBS (Ca^{2+}/Mg^{2+} free) buffer solution.

6.3.4.3 Cytotoxicity Assessment

Cell viability was evaluated via the MTS assay. After detachment, the L929 or U87 cells were seeded in a 96-well plate at a density of 2×10^3 cells/well, and grown in DMEM complete medium in a humidified incubator (5 vol% CO_2) at 37 °C for 24 h prior to treatment. The PIC micelle solutions with different final concentrations in the culture medium (10, 2, 1, 0.4 and 0.2 mg of PIC micelles/mL) were prepared in a mixture of 10% PBS solution (pH 7.4, 154 mM NaCl, Ca^{2+}/Mg^{2+} free) and 90% DMEM complete medium before cell treatment. The solutions of MPIC micelles were also prepared in the same mixture consisting of 10 vol% PBS solution (pH 7.4, 154 mM NaCl, Ca^{2+}/Mg^{2+} free) and 90 vol% DMEM complete medium with 700, 140, 70, 28, and 14 μg of Fe_3O_4/mL final concentrations before use. The highest Fe_3O_4 concentration of 1250 μg/mL was tested only with the G1@Fe_3O_4@PAA_{27}-*b*-$PHEA_{260}$ f = 0.5 MPIC micelles. The cells were exposed to either the PIC or MPIC micelle solutions, incubated for 48 h, and rinsed with PBS (with Ca^{2+}/Mg^{2+}) solution (100 μL/well). A 120 μL aliquot of MTS solution (containing 20 μL of MTS solution and 100 μL of PBS with Ca^{2+}/Mg^{2+}) was then added into each well. The plates were incubated at 37 °C for 120 min. Cell viability in the cultures was monitored by the reduction of clear yellow trezolium salt (MTS) to the brown formazan product by NADH-dependent cellular oxidoreductase enzymes found in metabolically active cells.[6-7] The absorbance at 490 nm was measured on a PowerWave X (BioTek Instrument Inc.) micro-plate UV-VIS spectrometer. The positive controls were cells incubated with the complete media alone. The results were expressed as the percentage of metabolic activity of treated cells relatively to untreated cells (control, 100% viability). Independent experiments were performed 3 times with 4 replicates per condition. According to ISO 10993-5 (2009) guidelines, the cytotoxicity potential was considered less than 70% of the blank control.

6.3.4.4 Cell internalization Studies

6.3.4.4.1 Confocal Laser Scanning Microscopy

The mouse fibroblast-like L929 cells were seeded on the surface of a sterile glass coverslip placed in the well of a 12-well plate at a density of 5×10^4 cells/2 mL/well and

allowed to attach and to grow at 37 °C in a 5% CO_2 humidified incubator. The fluorescently labeled PIC micelle solution (2 mg of PIC micelles/mL) was prepared in a mixture of 10% PBS solution and 90% DMEM complete medium before cell treatment. The solutions of fluorescently labeled MPIC micelles were prepared in the same mixture consisting of 10 vol% PBS solution and 90 vol% DMEM complete medium at 140 µg of Fe_3O_4/mL. After 24 h of cell growth, the DMEM complete medium was replaced with 2 mL of either fluorescently labeled PIC or MPIC micelle suspensions. From this point the plate was protected from light exposure by wrapping in aluminum foil when it was not in use. After 24 h of exposure to the nanoparticles, the suspension was removed and the cells were rinsed twice with PBS (with Ca^{2+}/Mg^{2+}) solution to completely remove non-uptaken nanoparticles. The cells were then fixed with 2 mL of paraformaldehyde cross-linking agent (4 vol%) diluted in PBS (with Ca^{2+}/Mg^{2+}) solution at 4 °C for 20 min. The fixative solution was then removed and the cells were washed twice with PBS (with Ca^{2+}/Mg^{2+}) buffer solution. Permeabilization of cell membranes to provide access to intracellular or intraorganellar antigens[24] was performed by treating the cells with 2 mL of 0.5 vol% Triton X-100 in PBS (with Ca^{2+}/Mg^{2+}) solution for 20 min at 4 °C. The Triton X-100 surfactant solution was removed and the cells were rinsed twice with PBS (with Ca^{2+}/Mg^{2+}) buffer solution. The protein-binding sites on the membranes were blocked by incubating with 1 vol% BSA in PBS (with Ca^{2+}/Mg^{2+}) solution (2 mL) at 37 °C for 30 min. The blocking agents were removed and the cells were washed twice with PBS (with Ca^{2+}/Mg^{2+}) solution before 2 mL of 1.67 vol% of Alexa Fluor® 594 phalloidin in PBS (with Ca^{2+}/Mg^{2+}) solution was added to label the *F*-actin cytoskeleton of the fixated cells. The actin staining was allowed to occur for 1 h at 37 °C in the humidified incubator before the cells were washed twice with PBS (with Ca^{2+}/Mg^{2+}) buffer solution. The cell nuclei were then stained with 2 mL of 0.025 vol% of DAPI in PBS (with Ca^{2+}/Mg^{2+}) solution for 10 min at 4 °C. The staining solution was finally removed and the cells were rinsed twice and stored in 0.05 vol% of Tween-20 in PBS (with Ca^{2+}/Mg^{2+}) buffer solution, to improve the assay sensitivity by reducing background interference. The coverslips were picked up, allowed to dry for 2 h, turned over and

permanently mounted to the glass slide using one drop of VECTASHIELD HardSet Mounting Medium (refractive index 1.452).

Analysis of the treated L929 cells was performed using a Leica TCS SP5 confocal laser scanning microscope equipped with a 405 nm diode UV laser for blue fluorescent labeling (DAPI filter set, *Ex*: 405 nm, *Em*: 461 nm), an argon laser for green labeling (Green Fluorescent Protein filter set, *Ex*: 488 nm, *Em*: 525 nm) and a DPSS 561 laser for red fluorescent labeling (Alexa filter set, *Ex*: 581 nm, *Em*: 609 nm). The scan speed was 400 Hz. The used objective was a Leica HCX PL APO 63x magnification /1.3 numerical aperture objective lens embedded in 100% glycerol (refractive index 1.46). Images were taken at 1024 pixel × 1024 pixel resolution. Photomultiplicator gain and offset configurations were set up on control cells so as to correct the images for green auto-fluorescence. A *Z*-stack of 50 frames covering a depth of 10 µm was recorded for assessment of the NP distribution across the section.

6.3.4.4.2 Transmission Electron Microscopy

The mouse fibroblast-like L929 cells were seeded in a 6-well plate at a density of 2.5×10^5 cells/2 mL/well and allowed to grow at 37 °C in a 5% CO_2 humidified incubator. The MPIC micelle solution (140 µg of Fe_3O_4/mL) was prepared in a mixture of 10% PBS solution and 90% DMEM complete medium before cell treatment. After 24 h the DMEM complete medium was replaced with 2 mL of MPIC micelle suspension. After 24 h of exposure to the nanoparticles, the suspension was removed and the cells were rinsed twice with PBS (without Ca^{2+}/Mg^{2+}) solution to completely remove non-uptaken nanoparticles. After being detached with trypsin solution 10× diluted 10-fold in PBS (without Ca^{2+}/Mg^{2+} free) buffer solution, the cells were centrifuged at 200 rcf for 5 min. The trypsin solution was carefully removed and the cells were fixed with a 2.5% glutaraldehyde solution diluted in PBS solution at 20 °C for 30 min. The cells were then centrifuged at 200 rcf for 5 min, the fixative was removed, and the cells were washed and redispersed in H_2O.

For observation by transmission electron microscopy, the cells were first placed in vials where they were post-fixed for 30 min in 1% OsO_4, washed with water, and air-dried. Epoxy resin (Epon 812, AGAR 100) was directly cast and polymerized in the vial. To facilitate sectioning, the cell resin was isolated and cut in two halves before re-embedding in resin prepared in flat silicone rubber molds. Sections with a thickness estimated at approximately 200 nm were cut with a glass knife. Observation was made without further staining on a Philips 301 electron microscope at an accelerating voltage of 80 kV.

6.3.4.4.3 Fluorescence-Activated Cell Sorting

The mouse fibroblast-like L929 cells were seeded in a 24-well plate at a density of 4×10^5 cells/well and allowed to grow at 37 °C in a 5% CO_2 humidified incubator. For the kinetics experiments, the fluorescently labeled MPIC* micelle solution (140 µg of Fe_3O_4 content/mL) was prepared in a mixture of 10% PBS solution and 90% DMEM complete medium before cell treatment. For concentration effect experiments, the MPIC* micelle solutions were also prepared in a mixture of 10% PBS solution and 90% DMEM complete medium at various concentrations (1.4, 14, 28, 70 and 140 µg of Fe_3O_4/mL). After 24 h the DMEM complete medium was replaced with 1 mL of MPIC micelle suspension. The magnetic nanoparticle exposure time periods for cells in the kinetics experiments were 1, 4, 8, 12 and 24 h, while all the cells used in the concentration tests were exposed to the magnetic nanoparticles for 24 h. After desired exposure to the nanoparticles, the suspension was removed and the cells were rinsed twice with PBS (without Ca^{2+}/Mg^{2+}) solution to remove non-uptaken nanoparticles. After being detached with trypsin solution 10× diluted 10-fold in PBS (without Ca^{2+}/Mg^{2+}) solution, the cells were centrifuged at 200 rcf for 5 min. The trypsin solution was removed before the cells were fixed with a 4% solution of paraformaldehyde diluted in PBS solution at 20 °C for 30 min. The cells were then centrifuged at 200 rcf for 5 min, the fixative was removed, and the cells were washed and redispersed in PBS solution. The control cells were prepared using the same protocol but without being exposed to fluorescently labeled magnetic nanoparticles. Quantitative studies were performed using the fluorescence-activated cell sorting (FACS) technique on a

FACScan system (FACS, Becton-Dickinson). The mean fluorescence intensity (MFI) of 10,000 treated L929 cells was compared with that of 10,000 untreated cells. The percentage of fluorescence-positive cells per 10,000 cells was also reported. The mean values are reported with the standard deviations from three independent experiments.

6.3.5 *In Vitro* Magnetic Field Hyperthermia

The mouse fibroblast-like L929 cells and human glioblastoma U87 cells were seeded in a 48-well plate at a density of 2×10^4 cells/0.5 mL/well and allowed to grow at 37 °C in a 5% CO_2 humidified incubator. The MPIC micelles were prepared in DMEM complete medium at 1250, 700, and 140 μg of Fe_3O_4/mL before cell treatment. After 6 h the DMEM complete medium was replaced with 0.5 mL of magnetic PIC micelle suspension and the control cells were incubated in complete media alone. After overnight exposure (15 h) to the nanoparticles, the suspension was removed and the cells were rinsed twice with PBS (without Ca^{2+}/Mg^{2+}) solution to remove non-uptaken nanoparticles. After being detached with trypsin solution 10× diluted 10-fold in PBS (without Ca^{2+}/Mg^{2+} free) buffer solution, both control and treated cells were centrifuged at 200 rcf for 5 min. To minimize the effects of magnetic field inhomogeneities a small sample volume (0.35–0.4 mL) is recommended,[25] so the cells were suspended in small NMR plastic tubes. This choice was also made to control the local magnetic field experienced by the cells, through well defined sample geometry (cylindrical shape with a large aspect ratio), location in the solenoid (6 NMR tubes can be placed simultaneously near the center of the coil) and orientation (parallel to the coil axis). This minimizes the so-called "demagnetization effect". On the other hand, the diameter was not so small as to increase the effect of thermal losses. Each magnetic field treatment was applied on 6 tubes (3 samples, 3 controls). The trypsin solution was removed before the cells were redispersed in 0.35 mL of DMEM complete medium (containing 10 mM HEPES, to maintain the pH in the absence of a controlled CO_2 pressure) and transferred to sterile vials (0.4 mL, 3 mm diameter). These vials, containing cells with or without internalized MPIC micelles

(controls), were placed in a small bath of de-ionized water inside a double-walled jacket maintained at a temperature of 37 °C during the treatment. The whole system was inserted in an induction coil (4 turns with 1 cm spacing and 55 mm diameter, cooled by internal water circulation at 18 °C, as shown on Figure 6-1.

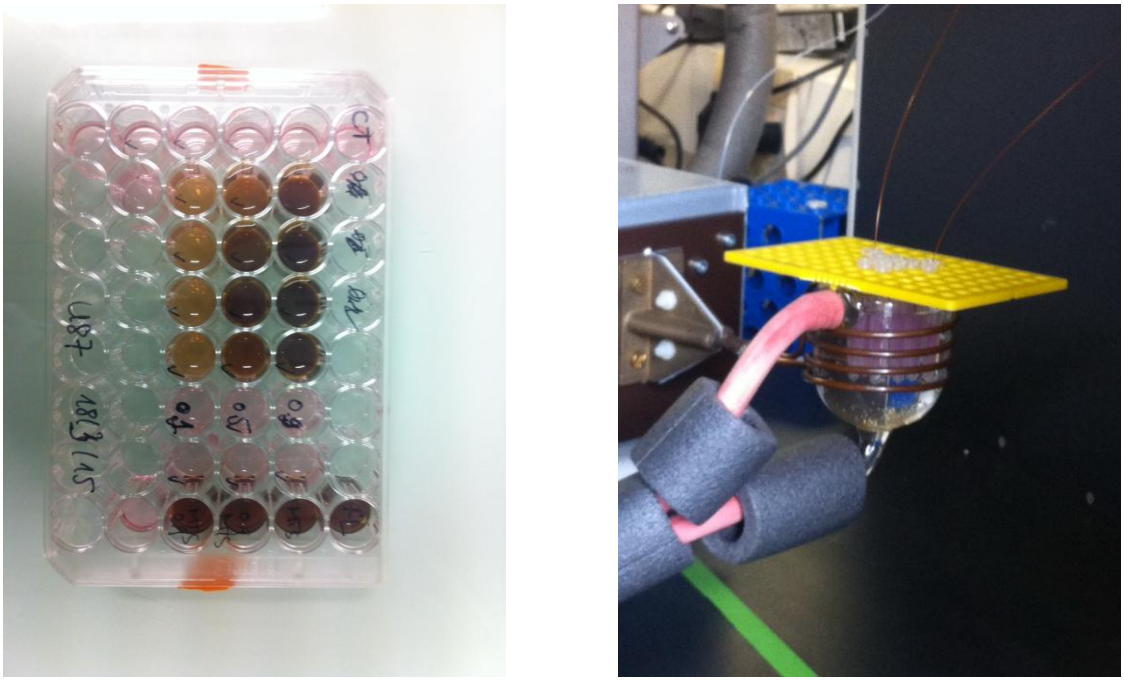

Figure 6-1. (Left) 48-well plate where L929 and U87 cells were seeded and incubated with the MPIC micelles at 3 concentrations (1250, 700, and 140 µg Fe_3O_4 /mL) in DMEM before being rinsed, trypsinized and transferred to NMR tubes for magnetic field exposure in a 37°C thermostated bath (Right). The image also shows the two optical fibres linked to the signal conditioner (Opsens) recording the temperature profiles.

The coil was driven by a current of 234 A at full power of the generator (3 kW MOSFET solide state resonant circuit, Seit Elettronica Junior™, Treviso, Italy) to produce a

high frequency alternating magnetic field (f = 755 kHz, H_{max} = 10.2 kA/m according to calibration by an electrical engineering method). Two field exposure times were tested: 1.5 and 3 h. The temperatures of the media in one control sample and in one treated sample were simultaneously monitored with two fibre optic thermometers (OTG-M420, Opsens, Québec, QC, Canada). After exposure to the RF magnetic field, the cells were reseeded in a 48-well plate and incubated at 37 °C in a 5% CO_2 humidified incubator. After 15 h of incubation the complete medium was removed and the cells were rinsed with PBS (with Ca^{2+}/Mg^{2+}) solution (0.5 µL/well) before the addition of 60 µL of MTS solution (prior dilution in 300 µL of PBS with Ca^{2+}/Mg^{2+}). The plates were incubated at 37 °C for 120 min before measurement of the absorbance at 490 nm. The results were expressed as the percentage of intracellular reductase activity for the treated cells relatively to the untreated cells (control, 100% viability). Independent experiments were performed twice.

6.4 Results and Discussion

6.4.1 Fluorescent Labeling of Block Copolymer

As discussed in the previous Chapters, among the four PAA-*b*-PHEA block copolymers synthesized, PAA_{27}-*b*-$PHEA_{260}$ exhibited the best stabilizing ability when complexed with the G1 arborescent copolymer and G1@Fe_3O_4 magnetic nanoparticles, and thus was selected to be labeled with the fluoresceinamine dye. Fluorescenly labeled PAA_{27}*-*b*-$PHEA_{260}$ was obtained via amidation of a fraction of the carboxylic groups in the PAA block with fluoresceinamine in the presence of EDC[26] as illustrated in Scheme S6-1. EDC reacted with the carboxylic acid groups to form a highly reactive but short-lived O-acylisourea intermediate, which reacted with the primary amine group on fluoresceinamine (FA) to form an amide bond.

An emission band, absent for the non-labeled block copolymer, appeared when PAA_{27}*-*b*-$PHEA_{260}$ was excited at 488 nm (Figure 6-2). A bathochromic shift in the emission peak from 530 nm (for free FA) to 543 nm (for FA conjugated with the block

copolymer) was observed, evidencing covalent linking of the dye to the block copolymer. This phenomenon has also been reported for fluorescein isothiocyanate (FITC) and is related to local changes in the environment of the dye (pH, temperature, ionic strength),[27-29] and in particular to polarity (dielectric constant) changes when conjugating FITC with bovine serum albumin (BSA).[30] Therefore the bathochromic shift in the emission peak observed for PIC* and MPIC* micelles (Figure 6-3) indicates the presence of conjugated FA molecules in the micellar structures. The presence of fluorescence emission for MPIC* also shows that the absorbance by iron oxide in the short wavelength region of the UV-VIS spectrum does not impede the fluorescence of the dye, at least within the iron oxide concenration range tested.

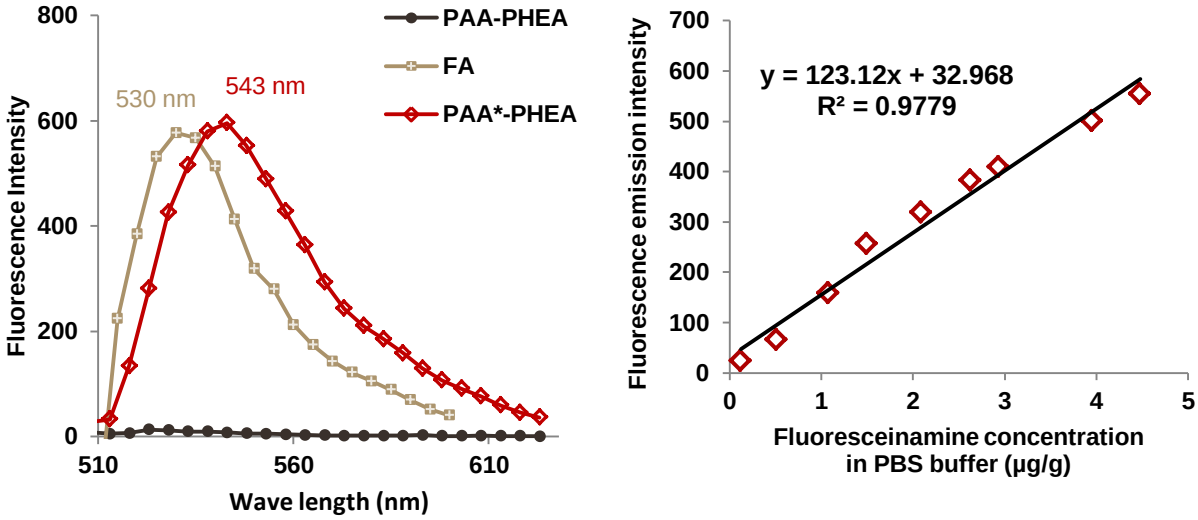

Figure 6-2. (Left) Fluorescence spectra for PAA-*b*-PHEA, free fluoresceinamine and fluorescently labeled PAA*-*b*-PHEA; (Right) Linear correlation of fluoresceinamine (*Ex*: 488 *Em*: 530) emission intensity vs. concentration in PBS buffer.

To avoid the effects of pH and ionic strength variations, all the samples were prepared in phosphate-buffered saline (PBS) 1× (137 mM NaCl, 10 mM K_2HPO_4/KH_2PO_4, 2.7 mM KCl, and pH 7.4) solution. A linear relation between the emission intensity and the

concentration of FA in the solution was observed in PBS solution. This correlation (Figure 6-2) was then applied to determine the concentration of FA grafted to the block copolymer. The fluorescence emission intensity was recorded at 530 nm for FA in its free form and at 543 nm for PAA*-PHEA. The number of FA molecules conjugated per PAA*$_{27}$-*b*-PHEA$_{260}$ molecule (containing 27 CO_2H groups) determined from the calibration curve was 1.88 ± 0.15, corresponding to 7.0 mol% labeling.

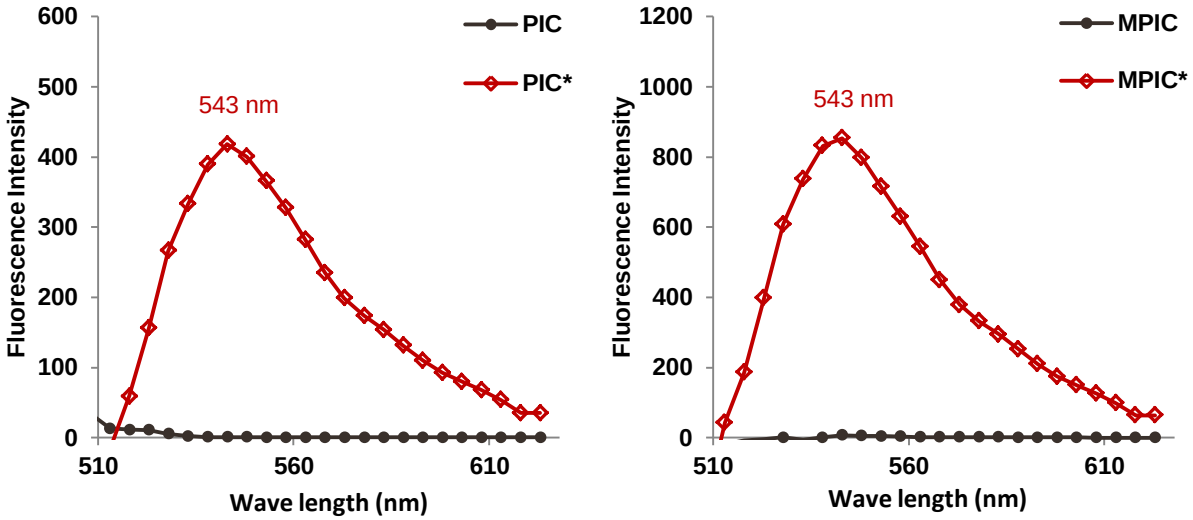

Figure 6-3. (Left) Fluorescence spectra for PIC and PIC* micelles in water; (Right) Fluorescence spectra for MPIC and MPIC* micelles in PBS buffer.

6.4.2 Cytotoxicity Assessment

6.4.2.1 PIC Micelles

The PIC micelles are composed of several polymers: polystyrene (PS), poly(2-vinylpyridine) P2VP, poly(acrylic acid) PAA, and poly(2-hydroxyethyl acrylate) PHEA. Previous studies have shown varying degrees of biocompatibility for these polymers. Commercial green fluorescent PS nanoparticles were found to be nontoxic at concentrations

of up to 40 mg/mL.[31] The cell toxicity of poly(2-vinylpyridine) has not been studied as much as for its quaternized derivatives, likely due to its hydrophobicity. For example, quaternized poly(4-vinylpyridine) is a microbicidal polymer that is effective to kill a wide range of bacteria; however this polymer is not biocompatible, with LD_{50} = 2330 mg/kg obtained in acute toxicity experiments.[32-34] Due to the hydrophobicity of PS and P2VP at physiological pH, these polymers would be most likely isolated within the core of the micellar system, thus shifting the need for biocompatibility to the protecting shell, in our case, PAA and PHEA. PAA has been used as an adhesive and surface-protective agent in dentistry[35-36] and for the slow release of drugs in eyedrops,[37-38] suppositories, capsules, wart creams,[39-41] and in ophthalmic gels.[42] PAA used as a coating polymer for superparamagnetic iron oxide NPs increased the colloidal stability and the biocompatibility of the magnetic particles.[43-46] PHEA has similar biocompatibility including low cytotoxicity and cell compatibility,[47-51] similarly to the more widespread poly(2-hydroxyethyl methacrylate) (PHEMA). PHEA-based materials have been used in controlled release drug delivery[52] and in cell culture media without significant cytotoxicity, indicating that PHEA-based materials are useful for *in vitro* applications.[50]

Cell viability after exposure to the PIC micelles was assessed using the MTS cell metabolic activity test. The fibroblast-like L929 cells were incubated for 48 h with micelle concentrations ranging from 0.2 to 10 mg/mL, to reveal toxicity exerted by the polymeric nanoparticles. Within the concentration range tested, none of the PIC micelles displayed any cytotoxicity on the L929 cells (Figure 6-4), despite their different sizes. In this Chapter, we will only refer to the intensity-weighted hydrodynamic diameter as D_h. The G1@PAA_{27}-*b*-$PHEA_{260}$ f = 0.5 and G1@PAA_{13}-*b*-$PHEA_{150}$ f = 1 PIC micelles had hydrodynamic diameters below 50 nm, while the G1@PAA_{27}-*b*-$PHEA_{260}$ f = 0.25 micelles had D_h = 87 nm (PDI = 0.18), and G1@PAA_{13}-*b*-$PHEA_{150}$ f = 0.5 had D_h = 104 nm (PDI = 0.04). Even after a long incubation period (48 h) the L929 cells were well spread in the wells and some of them were still undergoing mitosis, indicating the proliferation capability of the cells after their exposure to the nanoparticles. The good cell viability is attributed to the high hydrophilicity,

biocompatibility and electrostatic neutrality of the PHEA shell. The diffrences observed among the range of conditions used were found to be insignificant using Student's *t*-test.

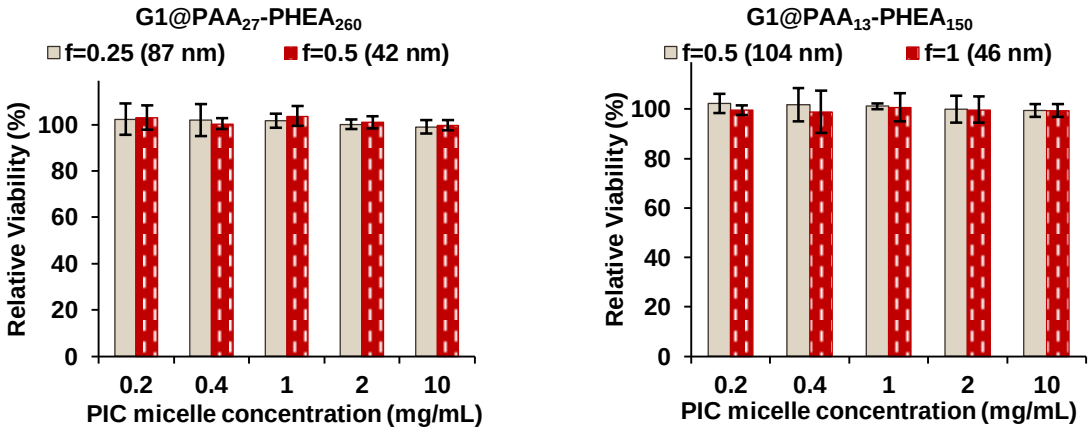

Figure 6-4. Cytotoxicity profiles for the PIC micelles G1@PAA-*b*-PHEA at various complexing ratios *f* with the fibroblast-like L929 cells determined via MTS assay at different concentrations after 48 h of incubation. The cell viability values are expressed as the mean values and the standard deviations from three independent experiments, each with four replicates per condition, relatively to untreated cells (100% control).

6.4.2.2 MPIC Micelles

The cytotoxicity of the MPIC micelles – if significant – could be due to their hybrid polymeric and iron oxide composition. The cytotoxicity of bare Fe_3O_4 nanoparticles has been reported to be dose-dependent based on MTT cell viability studies conducted with a short time exposure (24 h).[53-54] At the lowest concentration tested (50 µg of Fe_3O_4 SPION/mL), 20% loss of cell viability was reported as compared with the control. Cell viability further dropped to 40% at 2000 µg of Fe_3O_4 SPION/mL. Similar results were published by Hussain et al.,[55] reporting a 30% decrease in cell viability at a concentration of 250 µg Fe_3O_4

SPION/mL. Brief (4 h) exposure to a higher concentration of 23.05 mM of SPION (ca. 5347 µg Fe_3O_4 SPION/mL) was found to have no effect on cell viability.[56]

In our work, the bare G1@Fe_3O_4 particles were also found to have dose-dependent cytotoxicity. At the highest concentration tested (1250 µg Fe_3O_4 /mL) for a long exposure time of 48 h, L929 cell viability was 51 ± 8% (Figure 6-5, non-coated, f = 0). The relative viabilities were higher (57 ± 3% and 81 ± 4%) when treated with 700 and 140 µg of Fe_3O_4/mL solutions, respectively. These results are analogous to the toxicity of bare Fe_3O_4 NPs reported in the literature, indicating that the G1 template had no significant effect on L929 cell viability in itself.

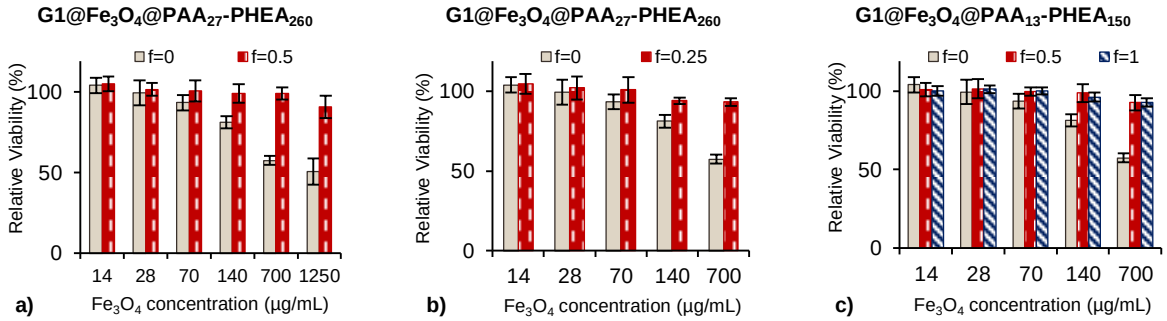

Figure 6-5. Cytotoxicity profiles for uncoated MNPs G1@Fe_3O_4 (f = 0) and MPIC micelles G1@Fe_3O_4@PAA-*b*-PHEA at various complexing ratios f towards fibroblast-like L929 cells determined via MTS assay at different concentrations after 48 h of incubation. Cell viability values are expressed as the mean values and standard deviations from three independent experiments with four replicates, relatively to the untreated cells (100% control).

Significant toxic effects such as plasma membrane damage leading to leakage of cytosolic lactate dehydrogenase, impaired mitochondrial function, inflammation, the formation of apoptotic bodies, chromosome condensation, the generation of reactive oxygen species (ROS), and DNA damage (Figure 6-6) have been associated with exposure to

SPIONs.[57-60] Among various mechanisms for iron oxide toxicity, one suggestion was the highly localised accumulation of NPs within the targeted tissue (necessary to maximize the therapeutic or diagnostic benefits), in combination with the degradation of Fe_3O_4 into dissolved Fe^{2+} and Fe^{3+} ions.[61] The iron overload can cause aberrant cellular responses including cytotoxicity, DNA damage, oxidative stress, epigenetic events and inflammatory processes.[57,62-64] Several mechanisms for iron-induced carcinogenesis have been suggested and associated to the damage of DNA and proteins, and to lipid peroxidation.[65-68] The generation of reactive oxygen species (ROS) was also suggested as a mechanism by which Fe_3O_4 NPs induce (geno)toxicity.[60] Dissolved Fe^{2+} ions can cross the mitochondrial membrane and react with hydrogen peroxide and oxygen (produced by the mitochondria), forming highly reactive $^{\bullet}OH$ and $O_2^{\bullet-}$ radicals which causes damage *in vivo* to DNA, proteins, polysaccharides and lipids.[69]

It is well-established that NPs without any coating designed to avoid this are rapidly covered by a layer of proteins and other biomolecules when they are in contact with a biological fluid such as serum.[10,70-73] This biomolecule corona confers a new identity to the NPs and is sufficiently stable to be retained when the NPs are internalized into the lysosomes. The degradation of this biomolecule corona inside lysosomes exposes the bare surface of the NPs, resulting in lysosomal damage, cytosolic release of the lysosomal content and apoptosis (assuming that the NPs have cytotoxicity).[74-76] However in more complicated physiological environments such as the bloodstream, surface opsonisation – interaction of the NPs with opsonins, i.e., blood-circulating proteins – leads to conformational rearangements of the opsonins, inducing biorecognition by phagocytes that triggers a protein complement activation and results in a phagocytic removal process.[77] Surface coatings using flexible and hydrophilic polymers provides a solution to prevent opsonisation, thus extending the circulation time of the NPs.[78-79] Various natural (dextran, hyaluronic acid, chitosan, etc.) and synthetic polymers (poly(vinyl pyrrolidone), poly(vinyl alcohol), polyacrylamide, poly(ethylene glycol) (PEG), PEG-based copolymers, etc.) have been used for that purpose.[77-82]

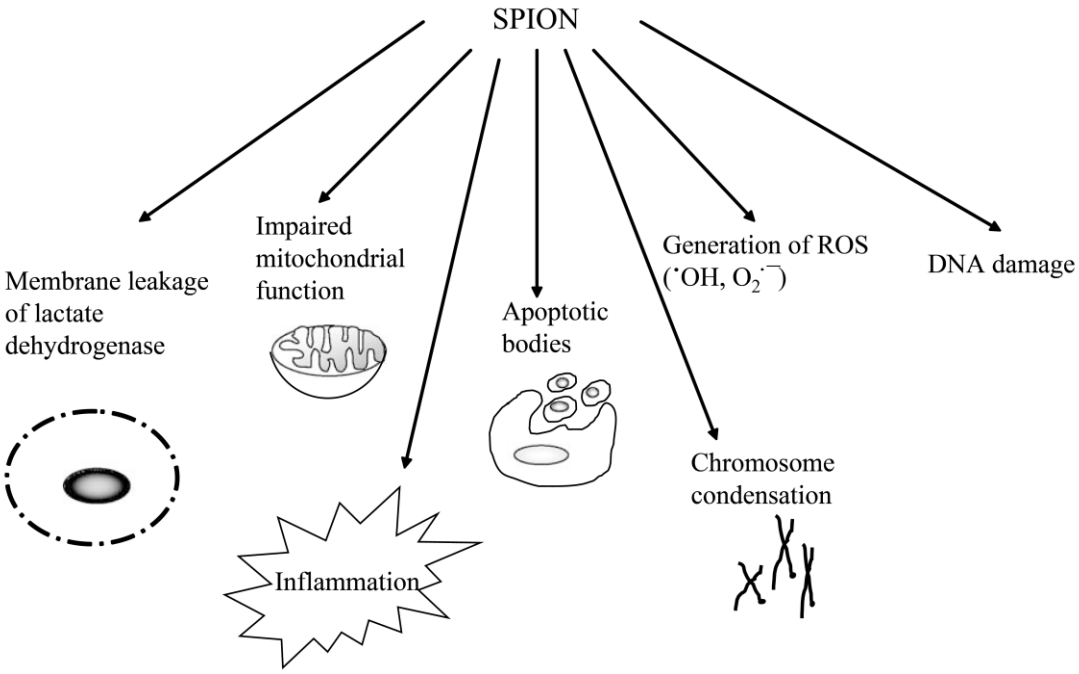

Figure 6-6. Cellular toxicity induced by SPION (Reprinted with permission from Reference 61. Copyright 2010 Neenu Singh et al.).

Coated Fe_3O_4 NPs were thus found to be relatively nontoxic, even at high concentrations. In one study, 99% of telomerase-immortalized primary human fibroblast cells remained viable relatively to the control after 24 h of exposure to PEG-coated nanoparticles at a concentration of 1 mg Fe_3O_4/mL.[53] Using the same cell type, only 8% cell loss was observed for incubation with pullulan-coated Fe_3O_4 NPs (2 mg of Fe_3O_4/ml) for 24 h, preventing the iron oxide core from interacting with the cells.[54] Solutions of 100 nM of poly(maleic anhydride-*alt*-1-octadecene)-*co*-poly(ethylene glycol) PMAO-PEG-coated Fe_3O_4 in water (0.023 μg Fe_3O_4/mL) led to less than 5% of SK-BR-3 human breast cancer cell death after 24 h of incubation.[83] However cell cytotoxicity strongly depends on the type of cell tested, the density and the chemical nature of the coating. Thus after 24 h of incubation with 170 μg of Fe_3O_4/mL solution of amino-SPIONs (polymer/Fe coating ratio 20), less than

40% of human melanoma metastasis Me237 cells were viable; the viability reported for Me275 cells was even lower, below 20%.[84] SPIONs coated with less polymer agglomerated and were no longer internalized by cells, thus showing no cytotoxicity.[84] Wan et al. attested that for an iron concentration of 400 μg/mL (ca. 550 μg of Fe_3O_4/mL), MPEG-Asp_3-NH_2-coated iron oxide nanoparticles had no cytotoxicity on OCTY mouse cells, while MPEG-PAA-coated and PAA-coated iron oxide nanoparticles significantly reduced cell viability, resulting in 84 % cell loss.[85]

In our work, we studied the cytotoxicity for four types of MPIC micelles. Two of them were the magnetic nanoparticles G1@Fe_3O_4 coated with the PAA_{13}-*b*-$PHEA_{150}$ block copolymer at two different ratios, f = 1 (optimal in term of colloidal stability) and f = 0.5, while the other two were for the same magnetic core complexed with PAA_{27}-*b*-$PHEA_{260}$ at f = 0.5 (optimal) and f = 0.25. We observed low cytotoxicity for the MPIC micelles up to the highest concentration tested (1250 μg Fe_3O_4/mL) after 48 h of incubation. Specifically, we observed over 91 ± 7% cell viability for the MPIC micelles as compared with 51 ± 8% cell viability for the bare MNPs. Even after a long incubation period (48 h), the L929 cells were well-spread in the wells and some were still undergoing mitosis, indicating their ongoing capability to proliferate after exposure to the nanoparticles. The cell loss ratios were negligible at reduced Fe_3O_4 concentrations (700, 140, 70, 28, and 14 μg of Fe_3O_4/mL). The MPIC micelles formed at optimal coating ratios caused no or negligible reductions in cell viability. The MPIC micelles coated with a less dense polymeric shell showed slightly higher reductions in cell viability, but only at the higher concentrations tested. These results show that PAA-*b*-PHEA successfully formed a protective, biocompatible shell around the Fe_3O_4 nanoparticles.

6.4.3 Cell Internalization Studies

Cell internalization of the PIC micelles was visualized by confocal laser scanning microscopy (CLSM). Cellular uptake of the MPIC micelles was evidenced by CLSM but also by transmission electron microscopy (TEM), since the Fe_3O_4 crystallites showed high contrast towards electrons, and was quantified by fluorescence-activated cell sorting (FACS).

6.4.3.1 Confocal Laser Scanning Microscopy

Preliminary qualitative cellular uptake studies were done with the same cell line used for the cytotoxicity assessment. The cytoskeleton *F*-actin was labeled with phalloidin (red), while the nuclei were labeled with DAPI (blue). The PIC and MPIC micelles (G1@PAA-*b*-PHEA and G1@Fe_3O_4@PAA-*b*-PHEA) labeled with the fluorescent probe fluoresceinamine (FA, *Ex*: 488 nm and *Em*: 525 nm) were visualized as green fluorescent species.

Even though they were negatively charged, the PIC* micelles G1@PAA*$_{27}$-*b*-PHEA$_{260}$ f = 0.5 were successfully internalized in the L929 cells, as evidenced by the green fluorescence found primarily in the cytoplasm at the periphery of the nuclear membrane, and probably in vesicles (Figure 6-7). This observation is in good agreement with the residence of nanoparticles in endosomes or lysosomes reported by other groups.[9,19,86] The ease of internalization of the NPs is attributed to the small size (D_h = 42 nm, PDI = 0.08) of the PIC micelles, which is close to the 50 nm range mentioned above. The spherical shape of individual PIC* micelles was clearly visualized, the PHEA shell possibly preventing degradation induced by proteases and other enzymes existing in the low pH environment of late endosomes and lysosomes. The cells contained variable numbers of PIC micelles.

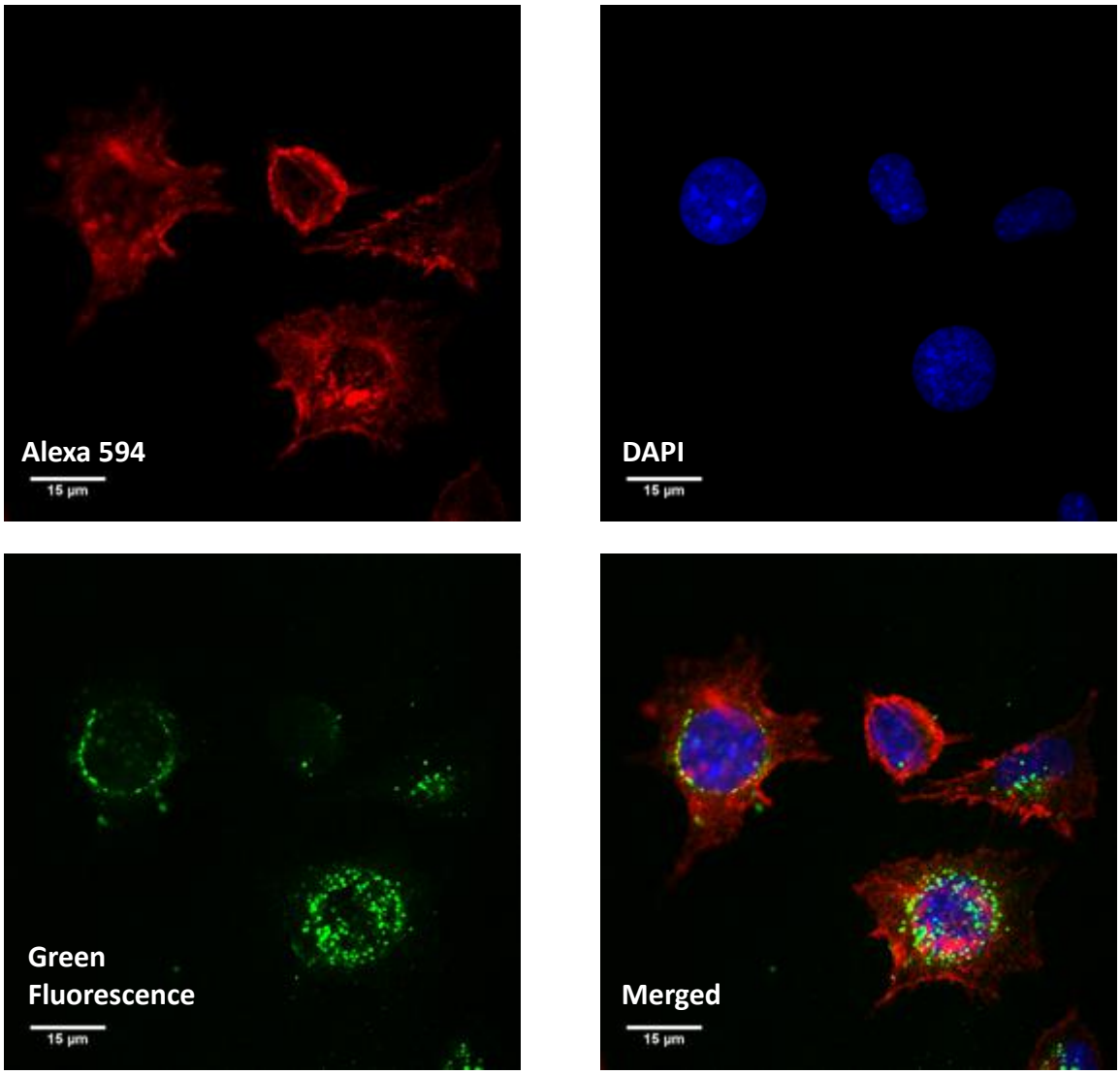

Figure 6-7. CLSM images for the L929 cells treated with the PIC* micelles G1@PAA*$_{27}$-*b*-PHEA$_{260}$ *f* = 0.5; 2 mg/mL, 24 h incubation.

Internalization of the MPIC* micelles G1@Fe_3O_4@PAA*$_{27}$-*b*-PHEA$_{260}$ *f* = 0.5 through the cell membrane was achieved in the same manner. The MNPs were mainly located at the periphery of the nuclear membrane and probably in cytoplasmic vesicles (Figure 6-8). From the literature, most nanoparticles internalized by cells are accumulated within endosome-like

vesicles.[87-92] The stability of the MPIC* micelles at low pH was demonstrated in Chapter 4. The appearance of spherical green fluorescence dots inside those compartments supports the stability of MPIC* micelles in a low pH environment in the presence of degrading enzymes.

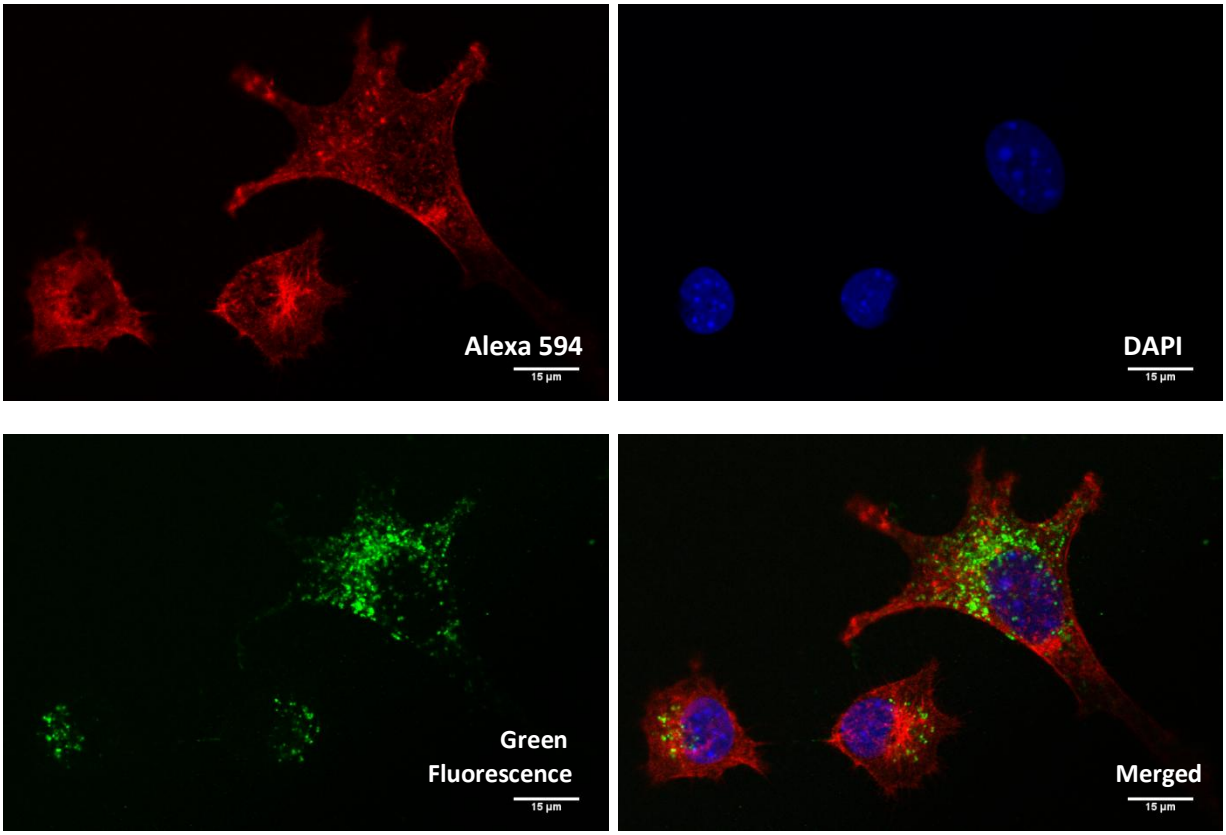

Figure 6-8. CLSM images for L929 cells treated with the MPIC* micelles G1@Fe_3O_4@PAA*$_{27}$-*b*-PHEA$_{260}$ f = 0.5; 140 µg Fe_3O_4/mL, 24 h incubation.

The cellular uptake of MPIC micelles appeared no different from PIC micelles even though the MPIC micelles had a larger diameter (D_h = 104 nm, PDI = 0.14) as compared to the PIC micelles (D_h = 42 nm, PDI=0.08). The 3D construction from 50 stacks (video clip provided in the CD-ROM attached) and in Figure 6-9 clearly show the location of the MPIC micelles inside the cytoplasm, although some also stayed at the periphery of the nuclear

membrane. Significant clustering after the endocytosis of iron oxide nanoparticles in the intracellular environment has been mentioned as a reason for the enhancement of magnetic properties and increased magnetic resonance imaging contrast.[90]

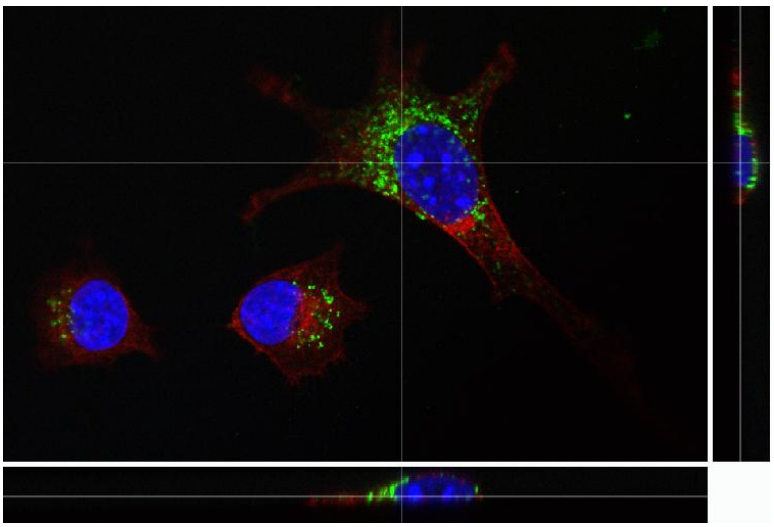

Figure 6-9. 3D construction and xz, yz sections for L929 cells internalized with MPIC* micelles G1@Fe_3O_4@PAA*$_{27}$-*b*-PHEA$_{260}$ *f* = 0.5; 140 µg Fe_3O_4/mL, 24 h incubation.

Our work was performed with fibroblast-like L929 cells derived from normal subcutaneous areolar and adipose tissue of a 100-day old male C3H/An mouse.[23] Diseased tissues such as tumors have a metabolism different from healthy tissues and a much higher NP uptake,[93] suggesting that the effectiveness of the NPs in their targeted biomedical applications (MRI contrast enhancement and hyperthermia) would be even greater in diseased tissues.

6.4.3.2 Transmission Electron Microscopy

The internalization mechanism of MNPs into cells has been the topic of different studies. Bertorelle et al. reported that rhodamine-grafted iron oxide nanoparticles were internalized into HeLa cells through small 100 nm vesicles, followed by tranfer into larger

600 nm endosomes.[88] Lu et al.[87] relied upon various pharmacological inhibitors to investigate the uptake mechanism. The uptake of SiO_2-coated superparamagnetic iron oxide nanoparticles labeled with FITC (SPIO@SiO_2-FITC) was impeded by clathrin and actin inhibitors but not by caveola or microtubule inhibitors, which strongly suggested that the internalization pathway was via clathrin- and actin-dependent endocytosis, with subsequent intracellular localization in late endosomes/lysosomes. The colocalization of the NPs inside the lysosomes was further confirmed by overlapping of the green fluorescence from the SPIO@SiO_2-FITC nanocomposites and the red fluorescence from the lysosome marker, which resulted in a merged yellow fluorescent signal.[87] Negatively charged SPIONs coated with poly(isobutylene-*alt*-maleic anhydride) were first found in endosomes and subsequently in lysosomes, while positively charged SPIONs coated with polyethylenimine were found exclusively inside lysosomes.[94] An energy-dependent clathrin-mediated endocytosis pathway was suggested by Soenen et al.[90] based on the localization of MNPs in lysosomes, and the fact that none of the MNPs tested were incorporated by endocytosis at 4 °C, the ATP hydrolysis-dependent mechanisms being impeded at this low temperarure.

In our work, TEM was used to confirm internalization of the MPIC micelles, and to determine the distribution of MNPs after the cellular uptake. Iron oxide crystallites appeared with high contrast inside large intracellular endosomes or lysosomes visible in a clearer area that could be differentiated from the grey background of the cytoplasm (Figure 6-10). This location of the iron oxide crystallites is in good agreement with the results reported in the literature, suggesting that MPIC micelles were also internalized through the cell membrane by clathrin-dependent endocytosis (Figure 6-11, although the formal proof of this internalization pathway would require complementary experiments with clathrin inhibitors).

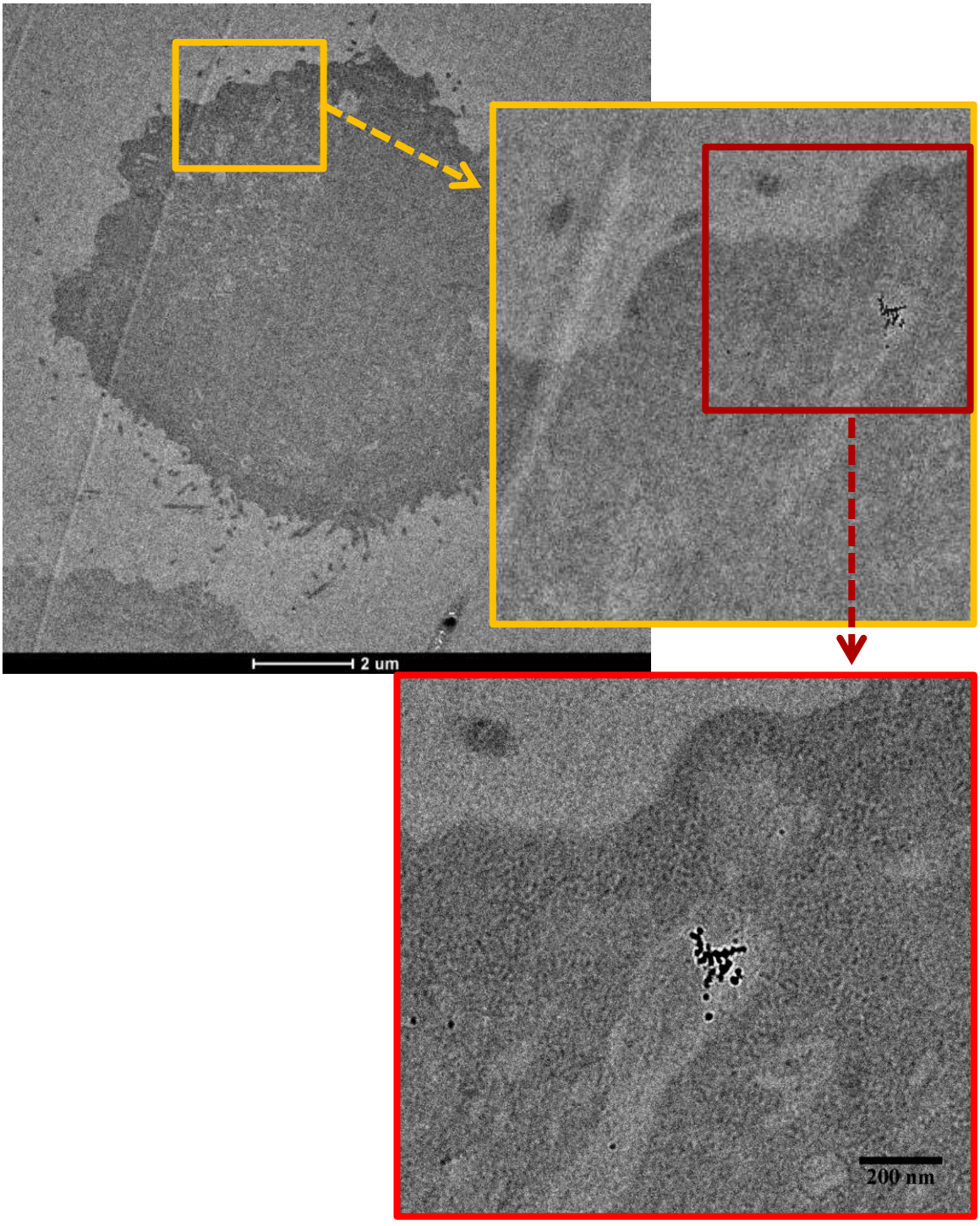

Figure 6-10. TEM images for L929 cells treated with an MPIC micelle solution (100 µg/mL, 24 h incubation), inset showing iron oxide NPs internalized in L929 cell.

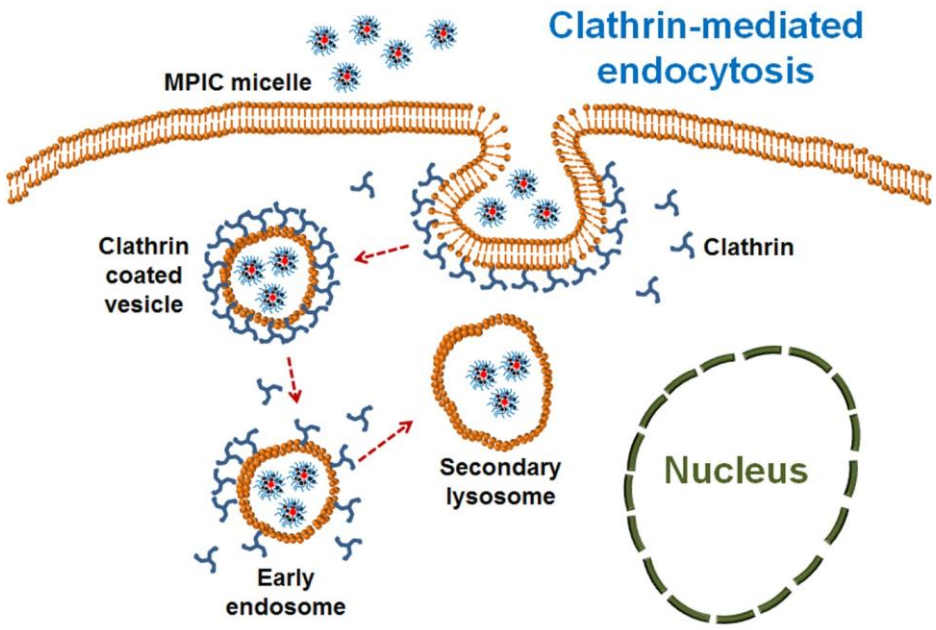

Figure 6-11. Proposed mechanism of clathrin-mediated endocytosis of MPIC micelles into the L929 cells.

6.4.3.3 Fluorescence-Activated Cell Sorting

Cell internalization was quantified by fluorescence-activated cell sorting (FACS). The number of fluorescence-positive cells counted per 10,000 cells, expressed as % positive cells, and the ratio of fluorescence intensity of 10,000 treated cells to that of 10,000 untreated cells, expressed as their mean fluorescence intensity (MFI), were extracted from the FACS data to evaluate the extent of cellular uptake.

The extent of cellular uptake exhibited a strong dependence on MNP concentration (Figure 6-12). Even at low MPIC micelle concentrations (1.4 µg Fe_3O_4/mL), 0.6% of the cells were reported as fluorescence-positive, emitting a low MFI signal (MFI = 69). The number of positive cells and their MFIs increased for increasing MNP incubation concentrations. Exposure to a low concentration (28 µg Fe_3O_4/mL) was sufficient for 42.5% of cells to uptake the fluorescently labeled MPIC micelles, emitting 373 MFI units.

Increasing the concentration to 70 µg Fe_3O_4/mL almost doubled the number of cells with MNPs internalized (80.5%) and the emitted MFI (624 units). Incubation with higher MNP concentrations therefore resulted in a larger number of positive cells and a larger amount of internalized MNPs. The small rise in % positive (fluorescein-containing) cells (from 80.5% to 98%), as compared with a ca. 40% increase of the MFI signal (from 624 to 1057) when doubling the Fe_3O_4 incubation concentration from 70 to 140 µg/mL, indicates that positive cells continued to uptake more MNPs, which led to a variable amount of MNPs among the cells. This is in good agreement with the uneven internalization observed by confocal imaging. A similar phenomenon was reported by Asín et al. who observed a slight change in the % positive cells accompanied by a large increase in the MFI values when incubating cells with a higher MNP concentration.[20]

The incubation time was an important parameter that also influenced cell internalization. Increased MFI signals from the cells only 1 h after treatment with 140 µg of Fe_3O_4/mL solution demonstrated the rapid uptake of MPIC micelles by L929 cells. Extending the incubation period further enhanced the cellular uptake. After 12 h of incubation, 45.6% of the cells fluoresced with an MFI = 444 units while after 24 h, these figures were 97.2% and 1067 MFI units. Linear regressions for the MFI and % positive cells vs. incubation time extracted from the data suggests a steady rate of MNP internalization (within the time interval tested), which could be used as a predictive tool for cellular uptake kinetics (Figure 6-13).

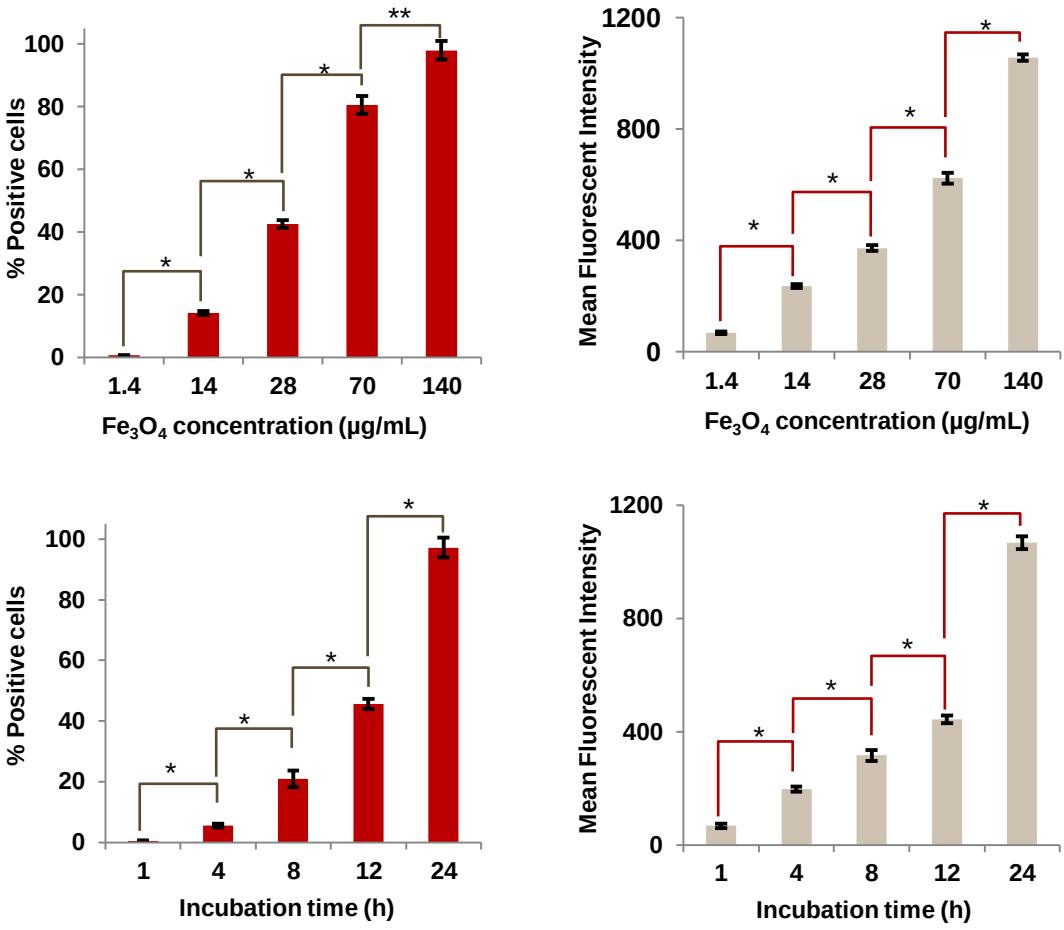

Figure 6-12. Dependence of the mean fluorescence intensity (MFI) for L929 cells treated with 100 μg/mL solution) of the MPIC* micelles G1@Fe_3O_4@PAA*$_{27}$-*b*-PHEA$_{260}$ *f* = 0.5 on the concentration (after 24 h incubation) and on the incubation time (*p < 0.002, **0.002 < p < 0.01 by the two-tailed Student's *t*-test, degrees of freedom = 4).

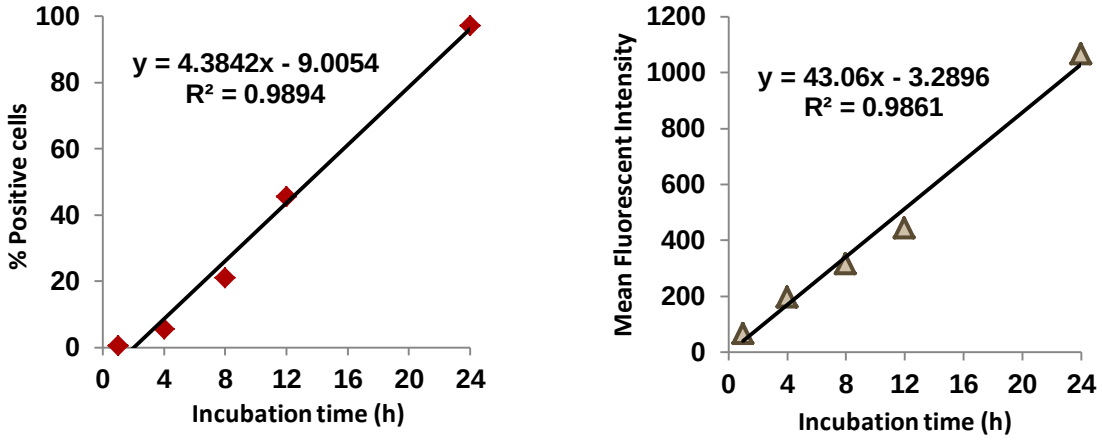

Figure 6-13. Linear regressions for the MFI and % positive L929 cells vs. incubation time.

6.4.4 *In Vitro* Cellular Radiofrequency Magnetic Field Hyperthermia

Hyperthermia is a medical treatment that brings body tissues to slightly higher temperatures than the highest tolerable physiological value (42 °C) for the purpose of making the cells more sensitive to radiotherapy or to specific drugs.[95-96] However this therapy has been used more widely to damage or kill cancer cells by provoking cell apoptosis[97-98] (also called programmed cell death[98] that occurs spontaneously in cells), thus retarding tumour growth. While the exact mechanism by which hyperthermia kills cells is still an open question, membrane alteration and cytoskeletal damage such as cell rounding and blebbing due to heat-induced protein denaturation are found to be the most apparent phenomena leading to cell death.[99-100] As compared to normal cells which can maintain physiological temperatures (i.e., up to 42 °C) during hyperthermia treatment, tumour cells were discovered to have a disorganized and abnormal vasculature architecture, resulting in poor heat dissipation capability and thus are more sensitive to heat-induced-apoptosis.[93,101] As compared to whole-body hyperthermia and regional hyperthermia, local hyperthermia is considered a safer and less invasive technique.[102] In hyperthermia treatments using MNPs as mediators of heat, a suspension of MNPs is injected directly into the tumor, allowing the MNPs to be internalized by the cancer cells or at least in the tumor microenvironment

(extracellular matrix).[103] The heat produced by the oscillating magnetic moments of the MNPs exposed to an external alternating magnetic field (AMF), usually at a frequency of several hundreds of kHz, will lead to cell death. It is believed that cancer cells can only be killed when the temperature is raised over 43 °C, defining the cumulative effective thermal dose at 43°C or CEM43. However work by Creixell et al. [104] and Asín et al.[20] demonstrated the possibility of causing significant cell death with internalized MNPs without increasing a macroscopic temperature increase during AMF exposure, an effect sometimes called "intra-lysosomal" or "cold hyperthermia".

It is important to categorize published *in vitro* magnetic hyperthermia research into magnetic fluid hyperthermia, where cells are dispersed in a magnetic fluid during AMF exposure, and intracellular magnetic hyperthermia, where heat is exclusively generated by internalized MNPs. In the first category, Ota et al.[105] reported cell viability reduced to 50% by exposing a suspension of cells dispersed in a magnetic fluid to an AMF (210 kHz, 250 Oe, 19.9 kA/m, 1 h) that brought the temperature to 46.2 °C. Cell viability was further reduced to 30 % by performing the same treatment using CH11 antibody-complexed MNPs. Higher cell death rates were also observed for a 5–15 min exposure to an AMF of 114 kHz, 89.9 kA/m using a $Mn_{0.6}Zn_{0.4}Fe_2O_4$-based magnetic fluid, with exceptional magnetic and heating properties (SAR 1102.4 W/g).[106] In the second category, intracellular magnetic hyperthermia was carried out by Fortin et al.[25] by heating a cell pellet in a volume of 0.35 mL, containing 20 million human prostatic adenocarcinoma cells incubated with MNPs (at a Fe_3O_4 concentration of 2.5 mg/mL, SAR = 203 $W.g^{-1}$), to 44.6 °C after applying an AMF of 700 kHz at B_0 = 31 mT (H_0 = 24.8 kA/m) for 10 min. The maximum temperature reached showed strong dependence on the concentration of the MNPs in the cell pellet: Cells incubated at 0.41 mg Fe_3O_4/mL only reached a plateau temperature below 39 °C. More importantly, the lower efficiency of heating induced by intracellular MNPs as compared to freely dispersed MNPs in water was likely due to confinement of the MNPs within the intracellular vesicles, implying that Néel relaxation was the sole mechanism of heat generation by intracellular MNPs. This conclusion was later confirmed by Di Corato et al.[107] who suggested the

complete inhibition of Brownian relaxation in cellular conditions on the basis of abruptly decreasing specific absorption rate (SAR) values, especially when the MNPs were attached to the cell membrane or internalized into intracellular vesicles.

Magnetic hyperthermia was also applied to enhance release of the drug doxorubicin encapsulated in alginate microbeads.[108] Only 5.7% of viable cells resulted when doxorubicin release was triggered by the hyperthermia of MNPs after 2 h of exposure to an AMF of 700 kHz and B_0 = 10 mT (H_0 = 8 kA/m) amplitude, which brought the cells to 45 °C. Using an AMF with doxorubicin and iron oxide dual-loaded hydrogels resulted in 60% of viable cells, although a temperature of 45 °C was also reached in that case, also contributing to cellular death. A similar approach using MNPs and doxorubicin-loaded polymersomes performed by Oliveira et al.[109] resulted in an 18 % increase in cell toxicity after 72 h of post-AMF exposure (750 kHz at B_0=14 mT (H_0=11.2 kA·m^{-1}) for 10 min, 3 times a day, without macroscopic variation of temperature due to the release of doxorubicin triggered by melting of the polymersome membranes. Using a sub-lethal dose of doxorubicin encapsulated in polymersomes (12 µg/mL), the authors evidenced that cell viability for HeLa cells decreased to 55% after field treatment, which was lower less than for the controls (95% for polymersomes loaded with MNPs but without drug, and 73% for cells incubated with the drug and MNP-loaded polymer vesicles, but without magnetic field application).

While reaching a lethal cell temperature is the most common goal in hyperthermia treatment, Creixell et al. reported a method that reduces cell viability without a perceptible temperature rise, by comparing the magnetic hyperthermia-induced toxicity of Fe_3O_4 MNPs and Fe_3O_4 MNPs grafted with antibodies against the epithelial growth factor receptor (EGFR), which is often overexpressed in tumoral vasculature.[104] Only 50% of the cells incubated with Fe_3O_4 MNPs were viable after AMF exposure (233 kHz, 37.5 kA/m, 2 h). In comparison, EGFR-targeted Fe_3O_4 MNPs resulted in 40% of cell viability even in absence of magnetic field. Exposing the cells incubated with EGFR-targeted Fe_3O_4 MNPs to the same AMF treatment reduced cell viability to 4–6%, evidencing the synergetic effect of specific targeting receptors with antibodies and magnetic hyperthermia. Asín et al. also demonstrated

the possibility of killing cells without perceptible temperature increase by exposing cells incubated with MNP-loaded dendritic cells to an AMF (260 kHz, 12.7 kA/m). [20] In that case, 100% cell death was reported based on a trypan blue staining after 15 min of AMF exposure.

Sanchez et al.[21] grafted iron oxide NPs with gastrin, a peptidic ligand that specifically binds to CCK2R, a G-protein coupled receptor overexpressed in several malignant cancers including endocrine pancreas cancer. Iron oxide NPs grafted with the ligand were internalized and found to accumulate in lysosomes. Exposure to an AMF (275 kHz, 52 mT, 2 h) reduced cell survival to 30%, even though the amount of internalized iron was low (2.2 pg Fe/cell). Using a confocal microscope simultaneously with AMF application, thanks to a miniaturized induction applicator, Connord et al.[22] discovered that cell damage seen exclusively in cells containing MNPs exposed to AMF was induced by lysosomal membrane permeabilization and ROS generation. The self-alignment of lysosomes with internalized MNPs into needles under the influence of the AMF was also observed.

In vivo magnetic hyperthermia following the direct injection of an iron oxide nanoparticle fluid has also proven successful in many animal models: rat glioma,[110-111] melanoma (in combination with immunotherapy),[112] prostate cancer[112-113] and liver tumors in rats (arterial embolization hyperthermia).[114] The promising results of the first clinical magnetic fluid hyperthermia conducted in 2003 on 14 patients suffering from glioblastoma multiform led to a phase II study involving 66 patients.[115] The magnetic hyperthermia method after intra-tumor injection of MNPs was authorized (in combination with conventional radiotherapy) to treat patients with this uncurable brain cancer in 2011, but this method only extended their life expectation by 2 months.[116]

Since our experiments showed that MPIC micelles could be easily internalized by L929 cells, we studied their use in intracellular magnetic hyperthermia on both L929 and U87 cells. Because the amount of internalized MPIC micelles showed strong dependence on the incubation concentration, the cells were incubated with MPIC micelle solutions at Fe_3O_4 concentrations of 1250, 700, and 140 µg/mL in complete DMEM culture medium for 15 h. The cells were then extensively rinsed with PBS to ensure that all the MPIC micelles not

taken up (e.g., simply adsorbed on cell membranes) were removed and that the hyperthermia effect, if present, was only due to intracellular nanoparticles. The cells were suspended in culture medium during AMF exposure (755 kHz at 10.2 kA/m, for 1.5 or 3 h) before they were seeded for the cell viability assay. The control cells were incubated in complete medium and exposed to the same AMF. Exposure to the AMF alone did not affect cell viability nor the propotion of cells at any cell cycle stage.[117]

The temperature of the control sample and the incubated sample was monitored during AMF exposure and, in both cases, no increase in temperature was observed (Figure 6-14), indicating that there was no macroscopic heating and that the amout of heat dissipated by the intracellular MNPs was insufficient to raise the temperature of the whole sample. This observation seems to confirm our hypothesis that AMF excitation of the intracellular MNPs was the main factor leading to programmed cell death (apotosis), without heating of the bulk medium.

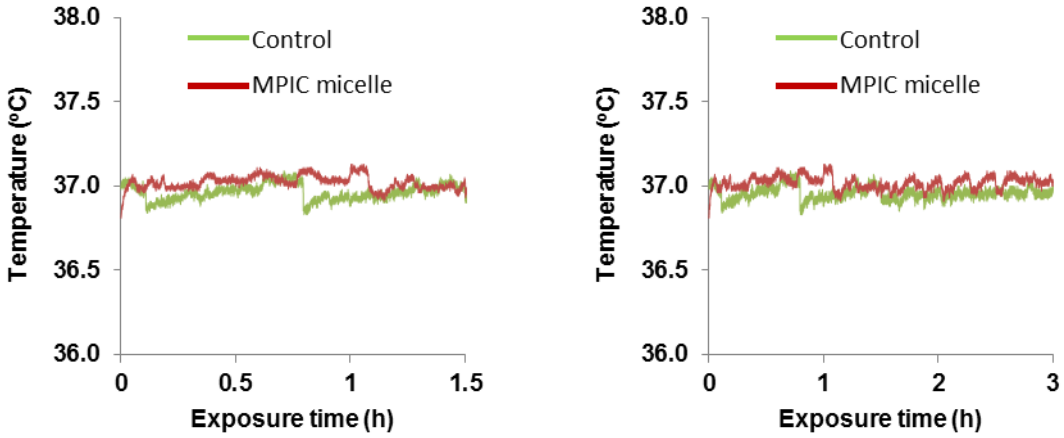

Figure 6-14. Temperature variation of suspensions of control cells and cells incubated with MPIC micelles during exposure to an alternating magnetic field (755 kHz, 10.2 kA/m, 1.5 or 3 h).

Cell viability had a strong dependence on both the incubation concentration and exposure time (Figure 6-15). For a concentration of 140 µg Fe_3O_4/mL, ca. 71–76% of the cells of both types survived after 3 h of AMF exposure. Increasing the incubation concentration to 700 µg/mL reduced cell viability to 72–77% after 1.5 h, and to 38–54% after 3 h of magnetic field application. At 1250 µg/mL (the highest concentration at which cell cytotoxicity without field application can be negleted), lower cell viabilities were observed: about 46–57% of cells remained after 1.5 h of treatment and 30–35% remained after 3 h. The drop in cell viability at higher incubation concentrations is ascribed to the larger number of internalized MNPs in the cells.

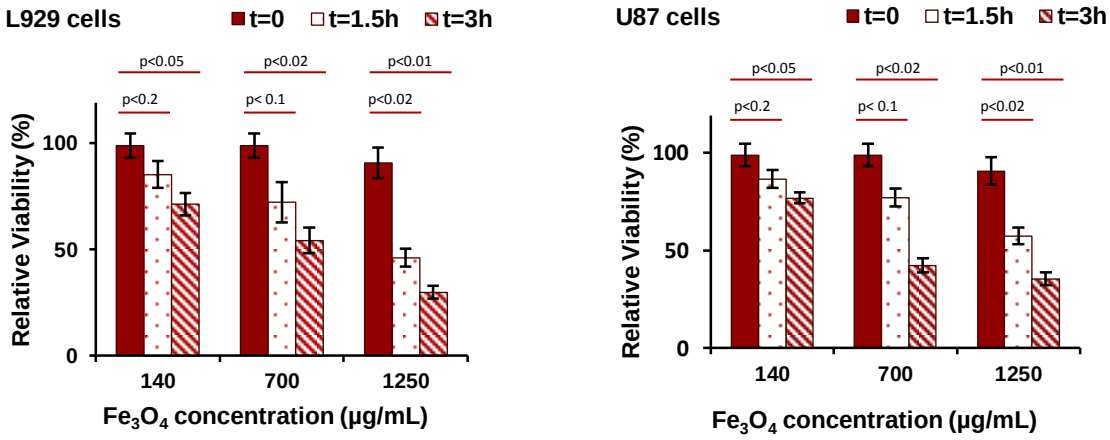

Figure 6-15. Viability of L929 (left) and U87 (right) cells determined by the MTS assay after 24 h of incubation with MPIC micelles G1@Fe_3O_4@PAA_{27}-*b*-$PHEA_{260}$ *f* = 0.5, followed by or without exposure to the high frequency alternating magnetic field. Cell viability values were expressed as the mean values relative to the untreated cells (control 100%; statistical analysis was done by the two-tailed Student's *t*-test).

Chapter 6

The search for a mechanism leading to cell death focused on answering two main questions:

1. What kind of and how is the energy generated?

Local heating produced by MNPs exposed to an AMF is generally assumed as the main source of energy inducing membrane alteration, cytoskeletal damage and apoptosis in cells. Riedinger designed molecular temperature probes consisting in a fluoresceinamine dye attached at different distances from the surface of the MNPs through a thermally sensitive azo linker, using PEG spacers of different $\bar{M}_w$.[118] Rapid local heating with a temperature rise of up to 45 °C was measured at distances below 0.5 nm from MNPs surface, based on thermally induced cleavage of the azo molecules and the subsequent realease of the dye. The temperature decayed exponentially with distance, thus explaining the significant difference between the local temperature at the nanoparticle surface and that of the bulk. The concept of local heating was further developed by Huang and co-workers[119] who employed DyLight549 red fluorescence as a thermometer to record the temperature increase distribution in cells. After 30–45 s of exposure to an AMF, a local temperature increase of more than 15 °C (determined from the change in DyLight549 fluorescence intensity) was measured at the plasma membrane where the MNPs were attached, but no temperature change was observed at the Golgi apparatus. The local temperature increase was sufficient to open the TRPV1 channels, leading to an influx of calcium ions. After 15 s of AMF exposure, the cytosolic calcium concentration increased 16-fold, confirming the successful thermal activation of the TRPV1 channels by the MNPs and AMF exposure. High-frequency motions of the NPs may also be an energy generation mechanism killing the cells in magnetic hyperthermia experiments without leading to a perceptible temperature rise. Carrey et al.[120] exposed MNPs to an inhomogeneous AMF and found that the MNPs could mechanically oscillate and generate ultrasound waves, due to the alternating gradient. The idea of generating ultrasounds by internalized MNPs was seen as a possibility to apply ultrasound therapy at the cellular level.

2. Why do cells die? What are the effects that the energy generated by the MNPs under AMF can bring to cells?

Apoptosis has been proposed as a main cause leading to cell death. Villanueva et al.[121] reported significant cellular damage that led to cell death by an apoptotic mechanism when applying a AMF to HeLa tumour cells incubated with MNPs. Hoechst-33258 stained apoptotic nuclei were visualized and counted by fluorescence microscopy. Approximately 20% of the cells were reported to have morphological characteristics typical of apoptosis (round shape, condensation, shrinkage, and chromatin fragmentation) accompanied with cell detachment, even though the cell culture temperature increased by less than 0.5 °C.

Lysosomal membrane permeabilization (LMP)[20-21,122] has been suggested more often as a mechanism causing cell death. Work by Domenect et al. thus showed that epidermal growth factor receptors (EGFR) targeting the MNPs after they were internalized into the cells could cause LMP when subjected to an AMF.[122] Lysosomal rupture was confirmed with acridine orange (AO), a lysosomal dye that emits red fluorescence inside intact lysosomes and a weak green fluorescence when bound to DNA or in the cytosol. The reduction in AO intensity revealed a 4-fold increase in cells with lysosomal rupture. The origin of the LMP was assigned to heat dissipation or to the rotation of MNPs adjacent to lysosomes, that increased the production of reactive oxygen species (ROS) and resulted in the massive peroxidation of membrane lipids.[122] A similar mechanism leading to cell death was proposed by Sanchez et al.[21] who used LysoTracker Red as a lysosome stain to detect a decrease in the number of lysosomes. Lysosome membrane permeabilization followed by leaking of their content (lower pH, metalloproteases…) was suspected to cause tumoral cell death under AMF.

Asín et al.[20] proposed a mechanism leading to cell death involving sudden disruption of the lysosomes containing the MNPs releasing toxic agents into the supernatant triggering the death of neighbouring cells. This mechanism was supported by the fact that 0% cell viability was achieved even though only 50–60% of the cells internalized NPs. Replacing the

medium after the AMF treatment with fresh medium resulted in about 15% cell viability. Zero cell viability was also reported when treating cells with the toxic medium removed after AMF, even though these cells were neither treated with MNPs nor subjected to AMF.

In our study, lysosomal membrane permeabilization due to local heating is deemed to be the most likely mechanism leading to cell death because *i)* macroscopic heating was absent; and *ii)* MNPs were found in vesicles, probably lysosomes, after they were internalized through the cell membranes. Extending the AMF exposure time resulted in killing more cells, probably due to the variable number of MNPs internalized observed by FACS. The cells uptaking a sufficiently large number of MNPs should be more sensitive to AMF exposure, while cells with a lower number of MNPs may be killed only for longer AMF exposure times. In order to confirm apoptosis and/or necrosis, a fluorescent labeling method can be used with the assistance of fluorescent microscopy and flow cytometry.

6.5 Conclusions

The cytotoxicity of PIC micelles and MPIC micelles was investigated. None of the PIC micelles incorporating a G1 arborescent core and a shell of PAA-*b*-PHEA (tested at concentrations of up to 10 mg/mL) showed any significant cytotoxicity for L929 cells, in spite of their different coating densities and sizes. The good colloidal stability and non-cytotoxicity of the PIC micelles are likely due to their high biocompatibility and hydrophilicity, and to the neutrality of the PHEA shell. Within the range of coating densities and polymeric stabilizer chain lengths tested, no significant differences in cell viability were observed. Similarly, the MPIC micelles were non-cytotoxic up to the highest concentration tested (1250 μg Fe_3O_4/mL) after 48 h of incubation, resulting in over 91% cell viability as compared to 53% for the bare MNPs. A slightly higher cell loss was reported for the MPIC micelles coated with a lower amount of polymeric shell material, but only at high concentrations. This confirms the efficiency of the PAA-*b*-PHEA copolymers as protecting agents preventing the interaction of the Fe_3O_4 cores with the cells.

Cell internalization of the MNPs was visualized by CLSM and TEM, and quantified by FACS. In spite of being negatively charged, both fluorescently labeled PIC* G1@PAA*$_{27}$-b-PHEA$_{260}$ f = 0.5 and MPIC* micelles G1@Fe_3O_4@PAA*$_{27}$-b-PHEA$_{260}$ f = 0.5 were successfully internalized through the L929 cell membrane, as evidenced by the green fluorescence found primarily at the periphery of the nuclear membrane and in intracytoplasmic vesicles. The fast cellular uptake kinetics of both PIC and MPIC micelles showed the influence of their small size on cell internalization. However clustering of the iron oxide nanoparticles after endocytosis was observed, and has been suggested in the literature to explain the enhancement of the magnetic properties and for increased magnetic resonance imaging contrast. Higher uptake of the NPs is expected for cancer cell lines, suggesting that the NPs will be even more effective in their targeted biomedical applications (MRI contrast enhancement and hyperthermia). The appearance of iron oxide crystallites with high contrast inside large intracellular endosomes or lysosomes suggests that the MPIC micelles were internalized by a clathrin-dependent endocytosis pathway. Cellular uptake exhibited strong dependence on the NP concentration and incubation time. Linear correlations between the intensity level (MFI) and the % of positive cells vs. incubation time obtained could serve as a predictive tool for cellular uptake kinetics.

An *in vitro* MFH assessment was conducted and exhibited strongly decreased cell viability as a function of both increased incubation concentration and exposure time. At 1250 µg/mL iron oxide the lowest cell viabilities were observed: about 46–57% after 1.5 h of treatment, and 30–35% after 3 h. The hypothesis that AMF-excitation of the intracellular MNPs was the main factor leading to cell death based on the fact that cell viability was decreased in a dose-dependent manner with the concentration of internalized MNPs in the cells, even in the absence of macroscopic heating.

Chapter 7 Conclusions

Chapter 7

7.1 Summary and Original Contributions to Knowledge

The major goal of this Ph.D. research work was to synthesize superparamagnetic iron oxide nanoparticles *in situ* within the core of arborescent copolymer micelles bearing a stabilizing hydrophilic shell. Control over the iron oxide nanoparticle synthesis and the subsequent stabilization process was achieved to obtain a product with good potential as magnetic resonance imaging (MRI) contrast agent and for heat generation in cellular (and eventually *in vivo*) radiofrequency magnetic field hyperthermia (MFH) treatment. Six main research areas were investigated as detailed below.

7.1.1 Study and Optimization of the Polyion Complexation Process to Produce Unimolecular Micelles

We reported the successful synthesis of poly(acrylic acid)-*block*-poly(2-hydroxyethyl acrylate) PAA-*b*-PHEA block copolymers by atom transfer radical polymerization (ATRP). To the best of our knowledge, this is also the first report on the complexation of PAA-*b*-PHEA with preformed P2VP-containing nanostructures in water to produce unimolecular polyion complex (PIC) micellar species. Water was used as the solvent for complexation, allowing the formation of dynamic PIC micelles (unlike other glassy copolymer micelles formed in organic solvents, remaining frozen when transferred to aqueous environments). Their structure was characterized in aqueous dispersions, and then in the dry state by atomic force microscopy (AFM) and transmission electron microscopy (TEM), as it was done in most PIC system investigations in the literature. We successfully performed the polyion complexation process in water by adjustment of the pH to a narrow range where both components (N and CO_2H) can be partially present in their ionic forms, which is a requirement to form strong electrostatic interactions between polycations and polyanions.[1-2] Once formed, these PIC micelles were found to be stable in neutral pH buffers such as cell growth media.

Control over the size and the structure of the PIC micelles, from large flocculated species to stable unimolecular entities with sizes ranging from 42 to 67 nm, was

accomplished by tuning the density of the stabilizing polymer layer around the G1 core, either by varying the block copolymer stoichiometry or the length of the PAA anchoring block, and most notably by varying the length of the nonionic PHEA block. Most effective stabilization was achieved when the length of the nonionic segments was increased to 260 units, producing stable unimolecular PIC micelles even when a complexation ratio f = CO_2H/N = 0.5 was used. This approach was later on applied to improve the colloidal stability of magnetic nanoparticles G1@Fe_3O_4 at pH 7, enabling their use in physiological environments. Evidence for uni- vs. multimolecular structure formation was provided by the difference between the hydrodynamic diameter of the PIC micelle to that of the collapsed core, as well as the $\bar{M}_w$ and ρ-parameter values obtained from static light scattering measurements. We used atomic force microscopy (AFM) phase images to distinguish the soft shell of PHEA surrounding the stiff G1 core, and used different AFM amplitude set-points to reveal the core–shell morphology of the PIC micelles.

7.1.2 Control over Fe_3O_4 Crystallite Size Using an Arborescent Copolymer

In a context where many reviews were published earlier with more general goals such as summarizing pathways for the synthesis of magnetic nanoparticles,[3-8] their surface modification,[3-4,6-7,9-10] their physicochemical characterization[3,5,8,11-12] and biological applications,[3-6,8-19] our literature review aimed at a more specific aspect: the possibility of controlling the shape and size of the synthesized magnetic nanoparticles (MNPs) through the size and geometry of the polymer templates, as well as the idea of using polymer templates, in the forms of both porous continuous matrices and polymer self-assembled suspensions, as nanometer-scale molds. Investigations demonstrating significant influence of the polymer/precursor ratio on the outcome of the synthesis (in particular those using well-defined polymer structures) were highlighted in comparison to other *in situ* syntheses not making a strong case for a true templating effect, and those affected by a high reaction temperature. Micelles formed by double-hydrophilic or amphiphilic copolymers, having a

dense core and a shell with multiple hydrophilic arms, emerged as efficient templates to prepare multi-functional NPs with highly desirable magnetic properties, and good colloidal stability and biocompatibility. The polymers used in this Ph.D. work not only represent a further development of this core–shell structure concept, but also take advantage of the good templating effect of a preformed arborescent structure (a well-defined structure that compacts a large number of vinylpyridine moieties into a small volume), allowing the targeting of lower hydrodynamic sizes and dispersities for the MNPs (in contrast to those synthesized without these self-assembled systems).

For the first time, a G1 arborescent copolymer (G0PS-*g*-P2VP) was used as a polymer template to control the size and improve the size distribution of iron oxide NPs. The templating effect of G1 was evidenced by: *i*) the formation of larger Fe_3O_4 crystallites with $D_{TEM} \approx 12 \pm 2$ nm, *ii*) enhanced colloidal stability due to electrostatic repulsion from protonated NH^+ groups of the P2VP chains, *iii*) a slight improvement in the size distribution as compared to non-templated magnetic NPs, and *iv*) separation of the crystallites appearing in the TEM images with an organic layer (bright stripe around the dark cores), lowering their dipolar interactions, which has many positive effects on the properties such as yielding a higher specific absorption rate (SAR) in magnetic hyperthermia, and a higher relaxivity, i.e. a higher MRI contrast, and better dispersability (inorganic grains at close contact usually experience strong van der Waals attraction and cannot be separated). The three-stage weight loss thermal decomposition and combustion profile observed for the templated MNPs G1@Fe_3O_4 was comparable to previously published results, evidencing strong interactions between P2VP and Fe_3O_4, and thus successful templating. The slight overestimation of the γ–Fe_2O_3 content by thermogravimetric analysis was ascribed to incomplete degradation (in N_2) or combustion (in air) of the organic material, in agreement with literature reports.[20-22] The presence of residual organic material was supported by UV-VIS analysis in 5 M HCl, a method that proved to be reliable to determine the equivalent Fe (and corresponding Fe_3O_4) content of MNPs.

7.1.3 Application of the Polyion Complexation Process to Produce Magnetic Micelles Stable Under Physiological Conditions

The experience gathered from the PIC process investigation reduced the time needed to optimize the complexation between G1@Fe_3O_4 MNPs and the PAA-*b*-PHEA block copolymer to produce magnetic micelles stable at pH 7. The presence of Fe_3O_4 in the G1@Fe_3O_4 structure probably swelled the G1 template to a larger volume, exposing more binding sites and thus resulting in more efficient complexation even at smaller f = CO_2H/N ratios. Tapping mode AFM height and phase imaging were again applied to reveal the core–shell morphology of the MNPs. The magnetic micelles obtained had $D_h \approx 130$ nm (PDI ≈ 0.136) and good colloidal stability not only under physiological conditions (at pH 7 with salts), but also over a wide pH range, which shows great promise in terms of the biocompatibility and biomedical applications being targeted.

7.1.4 Magnetic, Relaxometric and Hyperthermic Properties Measurements

The superparamagnetism of the Fe_3O_4 nanoparticles (bare and coated with the double-hydrophilic block copolymer) was revealed by the absence of a hysteresis loop, coercivity and remanence in the magnetization (*M* vs. *H*) curves. The Fe/N templating ratio, temperature, and the presence of the coating material were found to influence the magnetic and relaxometric properties of Fe_3O_4 NPs to different extents, confirming the possibility of tuning their magnetic and relaxometric properties via the synthetic procedure used.

Attempts to compare the results obtained by fitting the experimental data with literature, and among the different measurement techniques (relaxometric size vs. magnetic and TEM size) were made. On the basis of these results: 1) The divergence between the nuclear magnetic resonance dispersion (NMRD) curves for the uncoated/coated magnetic micelles and the outer-shell model fits was ascribed to the multimodal size distribution, and to significant interference from the hydrophobic PS-*g*-P2VP polymeric core. 2) The low relaxation rates and flat NMRD profiles observed for the bare G1@Fe_3O_4 samples were

indicative of agglomeration, thus confirming the essential role of the block copolymer coating. 3) The discrepancy between the magnetic domain diameters determined by VSM and by TEM was ascribed to spin canting occurring at the surface of or within the volume of the nanoparticles. 4) The radii obtained from NMRD analysis were larger than from TEM and magnetometry, which can be explained by the different nature of these characterization methods. The polymer component of the micelles is invisible in TEM, non-magnetic in VSM, and partially impermeable to water in NMRD. 3) The magnetization obtained from the fits to the NMRD profiles was lower than that determined by magnetometry, as a result of the larger relaxometry sample size and dilution of the iron oxide by the polymer (pushing further the limit of the Outer-Sphere). The scaling law introduced by Vuong et al.[23] to relate the transverse relaxivity of magnetic hybrid particles to their structure enabled the estimation of the intra-aggregate volume fraction of Fe_3O_4 in the polymer micelles to φ_{intra}~1%. This estimated volume fraction corresponds to roughly twelve magnetite crystallites per micelle, a number compatible with the AFM and TEM observations.

We successfully synthesized SPIONs with high values of transverse relaxivity r_2 = 335 (s^{-1} mM^{-1}) and transverse-over-longitudinal relaxivity ratios r_2/r_1 = 31.4 (1.47 T, 37 °C), comparable with or even larger than commercial products, suggesting their efficiency as negative contrast agents for T_2-weighted imaging. Moreover, a maximum SAR value of 55.6 $W \cdot g^{-1}$ was measured by AMF calorimetry at f = 755 kHz, H_{max}=10.2 $k \cdot Am^{-1}$. The SAR values were also evaluated under other AMF conditions, to compare them with predictions from the linear relaxation theory. It was determined that: 1) The SAR values varied nearly with the square of the magnetic field amplitude H_{max} for different fixed frequencies f in the high and medium ranges, consistently with the superparamagnetic nature of the MNPs and a dominant contribution from Néel relaxation to the heating process. 2) Closer-to-1 exponents for the SAR vs. H_{max} curves at lower frequencies, which were explained by a more significant contribution from Brownian relaxation of the MNPs to the heating process, and enhanced dipole-dipole inter-crystal interactions, despite the positive influence of the hydrophilic polymer coating in separating multiple magnetic cores within the same G1 micelle.

Regarding frequency variations, the exponent slightly larger than unity highlights the caution needed when using the intrinsic loss power concept (the definition of *ILP* indeed assumes a perfect quadratic variation of the SAR with the field strength, and a linear variation with the frequency).

7.1.5 Biocompatibility Assessment

Biocompatibility assessments for the MPIC micelles were completed within the recommended guidelines to evaluate the biological safety of manufactured nanoparticles: first with a cytotoxicity assay, followed by cell internalization, visualized by confocal laser scanning microscopy (CLSM) and TEM, and quantified by fluorescence-activated cell sorting (FACS). The MPIC micelles were non-cytotoxic up to the highest concentration tested (1250 μg Fe_3O_4/mL), evidencing the efficiency of the PAA-*b*-PHEA copolymers as protecting agents preventing the interaction of the Fe_3O_4 cores with the cells (potentially causing ROS production with Fe^{2+} leaking through the Fenton reaction). The role of the protecting shell was further confirmed by the slightly higher cell losses observed for MPIC micelles coated with a lower amount of polymeric shell material, but only at high concentrations. In spite of being negatively charged, labeled MPIC micelles were successfully internalized through the L929 cell membrane, as evidenced by CLSM revealing green fluorescence mainly at the periphery of the nuclear membrane and in intracytoplasmic vesicles. The TEM images confirmed the presence of iron oxide crystallites with a high contrast inside large intracellular endosomes or lysosomes. Clustering of the iron oxide nanoparticles after endocytosis was observed, which has been suggested in the literature to explain enhancement of the magnetic resonance imaging negative (T_2-weighted) contrast.

The fast cellular uptake kinetics of MPIC micelles was ascribed to their small size. Higher NP uptake is expected for cancer cell lines, suggesting that the NPs will be even more effective in their targeted biomedical applications (MRI contrast enhancement and hyperthermia). Cellular uptake exhibited strong dependence on the NP concentration and

incubation time. Linear correlations between the fluorescence intensity level (MFI) and the percentage of positive cells vs. incubation time obtained could serve as a predictive tool for the cellular uptake kinetics. A clathrin-dependent endocytosis pathway was suggested.

The PIC micelles were similarly tested for cytotoxicity, and their cell internalization was visualized by CLSM. None of the PIC micelles showed any significant cytotoxicity for L929 cells at concentrations of up to 10 mg/mL, in spite of their different coating densities and sizes. The good colloidal stability and non-cytotoxicity of the PIC micelles are likely due to their high biocompatibility and hydrophilicity, and to the neutrality of the PHEA shell. CLSM confirmed the successful internalization of the labeled, negatively charged PIC micelles through the L929 cell membrane, suggesting that this micellar system is a highly biocompatible platform with good potential for biomedical uses (e.g. as biosensorss, for drug delivery, gene delivery, or cancer therapy).

7.1.6 *In Vitro* MFH Assessment

An *in vitro* MFH assessment was conducted with fibroblast-like L929 cells and U87 human glioblastoma cells, using custom-built MFH equipment and a newly proposed cell treatment protocol, under prolonged treatment with an AMF at 37°C in a HEPES buffer to avoid the need for CO_2 pressure control. Cell viability strongly decreased as a function of both increased incubation concentration and increased exposure time to the AMF, evidencing a dual dose-effect. At the maximum incubation dose (1250 µg/mL iron oxide), the lowest cell viabilities with applied AFM were observed: about 46–57% after 1.5 h of treatment, and 30–35 % after 3 h for the L929 cell line. We verified the hypothesis that AMF excitation of the intracellular MNPs was the main factor leading to cell death, based on the fact that cell viability was decreased in a dose-dependent manner with the concentration of internalized MNPs in the cells, even in the absence of macroscopic heating.

7.2 Proposed Future Work

7.2.1 Fully Biocompatible Polymer Template

Our MNPs were composed of a biocompatible shell, and Fe_3O_4 NPs with a low toxicity profile, however the G0PS-*g*-P2VP core is not considered biocompatible. One possible extension of the work to improve the biocompatibility of the system would be to replace the PS-*g*-PVP template by an equivalent arborescent structure made, for example, of poly(L-lysine), a cationic polymer widely used as a nonviral carrier for gene delivery.[24-25] Poly(ethylene glycol)-*block*-poly(L-lysine) dendrimers[26] or hyperbranched polylysine[24-25,27] synthesized by the liquid-phase peptide synthesis method could also be good candidates due to their well-defined structure and large number of surface amino groups to coordinate the $Fe^{2+/3+}$ cations and form polyionic complexes with the PAA-*b*-PHEA block copolymer, as it is done with plasmid DNA under physiological conditions,[26-27] to form compact and water-soluble polyion complexes.

Hyperbranched poly(γ-benzyl L-glutamate) (PBLG)-based polymers could also be an interesting replacement since PBLG is a nontoxic, biocompatible and biodegradable material that has been used widely in drug and gene delivery.[28] Hyperbranched poly(ethylene glycol)-polyethylenimine-poly(γ-benzyl L-glutamate) (PEG-PEI-PBLG) block copolymers, synthesized by the ring-opening polymerization (ROP) of the *N*-carboxyanhydride of γ-benzyl-L-glutamate (BLG-NCA) with PEG-PEI as a macroinitiator, could likewise serve as template and stable, biocompatible carrier for the MNP synthesis.[29] One can also cite recently reported copolymers with blocks of respectively PBLG, PEO, poly(L-lysine) and poly(L-histidine), also synthesized by ROP, in that case from the *N*-carboxyanhydride of a protected version of L-histidine (Trt-HIS-NCA), which offers the unique combined properties of pH-sensitiveness (with possible intra-lysosomal drug delivery by the so-called "proton sponge effect"), thermo-sensitivity (through changes in secondary structure, i.e. thermally induced breaking of β-sheets), and a high complexing ability for most metallic cations

including iron, which has already enabled the templated synthesis of gold nanoparticles by reduction of the $HAuCl_4$ precursor.[30]

7.2.2 Next Generation MNPS

Due to their low cytotoxicity profile,[31-32] their ease of synthesis,[3-8] and the possibility of surface modification with biocompatible coatings,[3-4,6-7,9-10,33] superparamagnetic iron oxide nanoparticles (SPIONs) have been intensively studied, particularly for bioimaging applications such as magnetic resonance imaging (MRI) contrast agents, and for therapeutics by magnetic hyperthermia.[6,34-35] However the potential use of SPIONs for magnetically targeted drug delivery is limited by their relatively low saturation magnetization ($M_S \approx 300–400$ emu·cm^{-3}).[35-37] Thanh et al.[35] have published an interesting review on the 'Next Generation Magnetic Nanoparticles for Biomedical Applications', highlighting the importance of developing new superparamagnetic (metallic, bimetallic) materials that have a higher magnetocrystalline anisotropy energy and higher saturation magnetization (the M_S of metallic Fe is ca. 1,700 emu·cm^{-3},[38] and the M_s of bimetallic FePt, CoPt, FeCo and SmCo are in the range of 800–1,900 emu·cm^{-3}),[29,32-34] much larger than SPIOs, to overcome this limit. The aqueous reduction of metallic salts by reducing agents is a common method to produce uniform MNPs, in which the presence of suitable surfactants can assist in separating the nucleation and growth steps, and prevent MNP aggregation.[35] Since alkyl thioether end-functionalized poly(methacrylic acid) (PMAA-DDT) was reported as a capping ligand for Co MNP synthesis,[38] it would be interesting to test a similarly modified G0PS-*g*-P2VP arborescent copolymer for its ability to load metal precursors (although the hydrophobicity of this polymer in a basic environment could be a challenge in the reduction step). It is however noteworthy that most of these new materials are not biocompatible and, particularly, not suitable for *in vivo* applications, although their superior magnetic properties and enhanced hyperthermia performance allow their application at sufficiently low concentrations to reduce their toxicity.[35] Otherwise, a coating strategy is needed to mitigate their toxicity.

7.2.3 Cell Internalization

In our work, cell internalization of the NPs was visualized by CLSM and TEM, revealing their presence mainly at the periphery of the nuclear membrane and in intracytoplasmic vesicles. Possible work complementary to ours would be to study the internalization mechanism of the MNPs into cells. Specific pharmacological (clathrin/actin/caveolae/microtubule) inhibitors can be used to reveal the internalization pathway.[39] Another solution would be to label the lysosomes with a red fluorescence marker (e.g. LysoTraker™ Red), to visualize the colocalization of the NPs inside the lysosomes. Overlapping of the red fluorescence with the green fluorescence from the NPs would result in a merged yellow fluorescent signal, as shown for another system.[39]

The fate of the MNPs after they are internalized in the cells (isolated or aggregated) could be further investigated by TEM, by increasing the MNP incubation concentration to 1250 μg/mL (rather than 100 μg/mL). When the MNPs are internalized at a high incubation concentration, different phenomena such as transcytosis can be observed,[40] i.e. the transport of macromolecular cargo from one side of a cell to the other within a membrane-bound carrier, which causes leakage of the MNPs into the medium.

7.2.4 Active Targeting by the MNPs

A most significant development for our work would be to enable active targeting by attaching targeting molecules (e.g., antibodies that specifically bind to antigens overexpressed by tumor tissue, but have a low affinity for healthy tissue) to the surface of the MNPs. Antibody-conjugated MNPs were indeed shown to have higher accumulation at tumor sites,[41-43] and thus enhanced the effectiveness of magnetic hyperthermia.[44] However, monoclonal antibodies (mAbs) contain elements that may be recognized by the recipient as foreign and can activate immune and innate reactions.[45-46] Acute reactions following the

infusion of mAbs were reportedly caused by various mechanisms: acute anaphylactic and anaphylactoid reactions against the mAb, serum sickness, the tumor lysis syndrome, and the cytokine release syndrome.[46] The use of antibodies has been associated with various antibody-induced adverse effects including immunosuppression, immunostimulation and hypersensitivity (immunogenicity),[47] which can manifest themselves clinically as local skin reactions at the injection site, pyrexia and an influenza-like syndrome, or even acute anaphylaxis and a systemic inflammatory response syndrome, which could be fatal.[46] The attachment of antibodies on the surface of MNPs can therefore trigger active targeting and enhance the accumulation at tumor sites, but at the cost of increased potential for immunotoxicity. Antibody-conjugated Fe_3O_4 MNPs targeting the epithelial growth factor receptor (often overexpressed in tumoral vasculature) thus resulted in 40% of cell viability even in absence of magnetic field vs. results without targeting.[44]

The unique ability of MNPs to be guided by an external magnetic field[48] can also be used to enhance their accumulation in specific organs. However this option depends more upon the design and control of the magnet system to ensure that the nanoparticles can efficiently accumulate at specific sites such as deeper tissue tumors.[49]

7.2.5 Theranostics MNPs: Controlled Drug Release

There have been a number of studies demonstrating hyperthermia-based controlled drug delivery, in which the magnetic nanoparticles generate local heat triggering the release of drugs,[50] either by breaking bonds binding the drugs to the MNP or to a polymer,[51-52] or by enhancing permeability to release drugs encapsulated within a polymer matrix, or dispersed in magnetic polymer carriers.[53-60] This possible development for our magnetic polyion complex (MPIC) micelles is inspired by Carregal-Romero et al.,[60] who designed layer-by-layer assembled polyelectrolyte microcapsules of poly(allylamine hydrochloride) and poly(styrene sulfonate), incorporating 18 nm iron oxide nanocubes within their walls. The microcapsules were loaded with an organic fluorescent polymer (Cascade Blue-labeled

dextran), used as a model molecular cargo. The authors reported the successful use of AMF to destroy the microcapsule walls, leading to release of the embedded cargo to the surrounding solution.[60] Based on the structure of the MPIC micelles, a hydrophilic drug could be embedded into the arborescent P2VP matrix of the G1@Fe_3O_4 NPs just before polyion complexation with the PAA-*b*-PHEA block copolymer. Encapsulation of the drug could be enhanced if it is negatively charged. A negatively charged drug would consume some of the 2VP moieties subsequently serving for the polyion complexation; however this interference may be minor, since there should be enough 2VP moieties left to form strong electrostatic interactions with a negative polyelectrolyte like PAA. The heat generated by Fe_3O_4 MNPs sandwiched between the polyelectrolyte layers under AMF irradiation would be expected to weaken the electrostatic interactions and release the encapsulated drug, thus producing a new example of "magneto-chemotherapy".

Appendices

Appendices

1. Chapter 3 Supporting Information

Table S3-1. Effective $f^* = CO_2^-/NH^+$ ratios at pH 4.7 and 7.

f **pH 4.7**	**CO_2^-** equiv	**CO_2H** equiv	**NH^+** equiv	**N** equiv	***f*** =* **CO_2^- /NH^+**
9	0.14	8.86	0.67	0.33	0.21
6	0.09	5.91	0.67	0.33	0.14
3	0.05	2.95	0.67	0.33	0.07
1	0.02	0.98	0.67	0.33	0.02
0.5	0.01	0.49	0.67	0.33	0.01
0.25	0.00	0.25	0.67	0.33	0.01
0.125	0.00	0.12	0.67	0.33	0.00

f **pH 7**	**CO_2^-** equiv	**CO_2H** equiv	**NH^+** equiv	**N** equiv	***f*** =* **CO_2^- /NH^+**
9	6.84	2.16	0.01	0.99	684
6	4.56	1.44	0.01	0.99	456
3	2.28	0.72	0.01	0.99	228
1	0.76	0.24	0.01	0.99	76
0.5	0.38	0.12	0.01	0.99	38
0.25	0.19	0.06	0.01	0.99	19
0.125	0.09	0.03	0.01	0.99	9

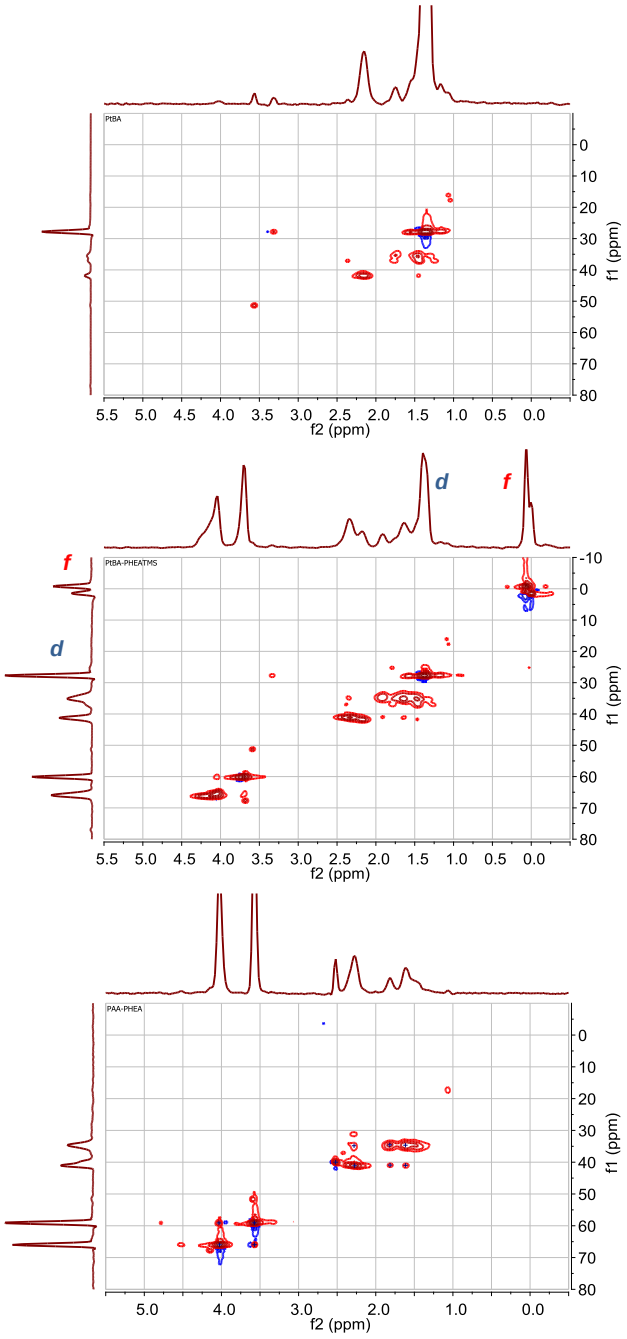

Figure S3-1. HSQC spectra for P*t*BA and P*t*BA-*b*-PHEATMS in $CDCl_3$, and for PAA-*b*-PHEA in DMSO-d_6 (from top to bottom).

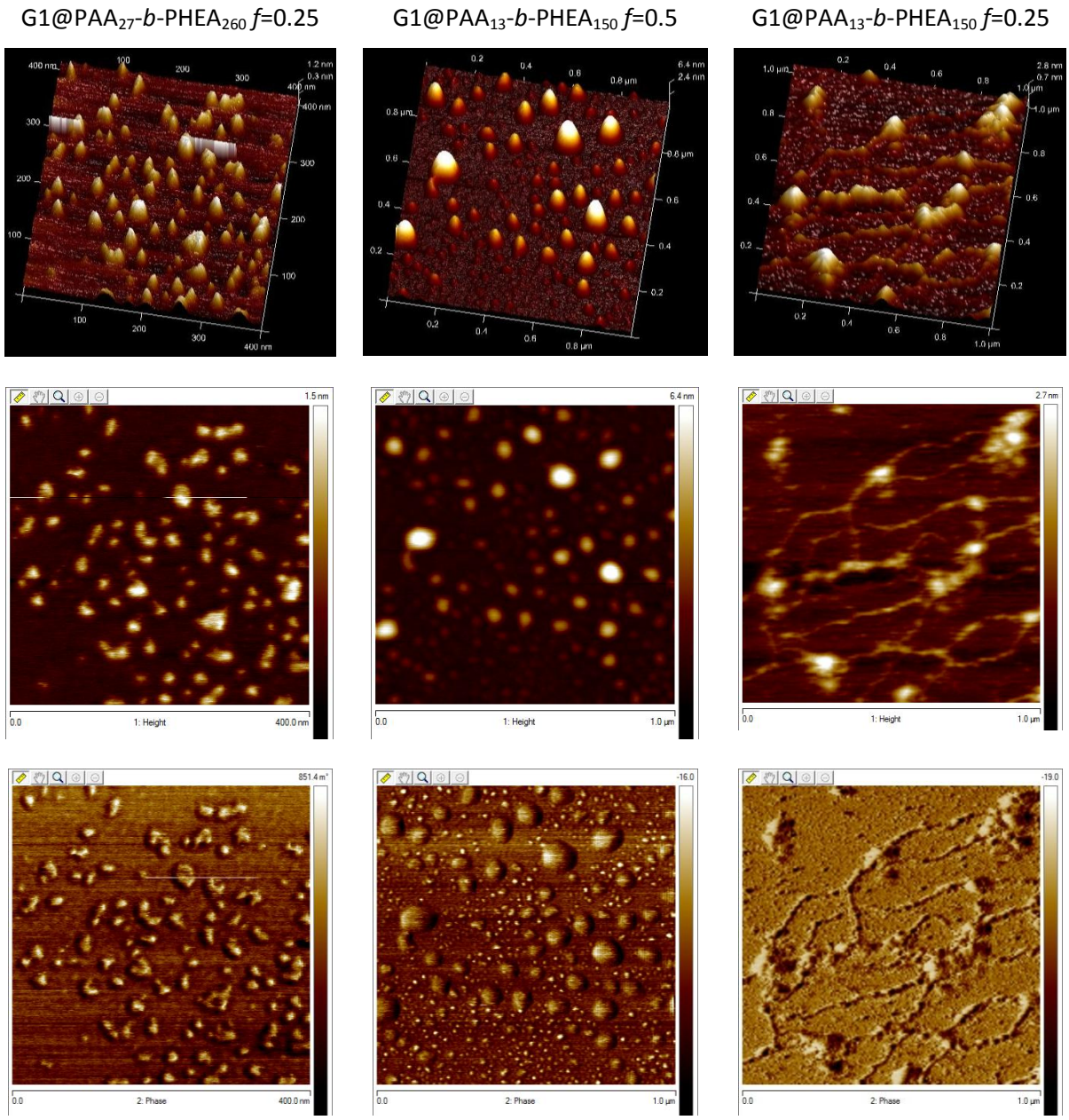

Figure S3-2. 3D models (row 1), height (row 2) and phase AFM images (row 3) for G1@PAA_{27}-*b*-$PHEA_{260}$ at f = 0.25 (column 1), G1@PAA_{13}-*b*-$PHEA_{150}$ at f = 0.5 (column 2) and G1@PAA_{13}-*b*-$PHEA_{150}$ at f = 0.25 (column 3).

2. Chapter 6 Supporting Information

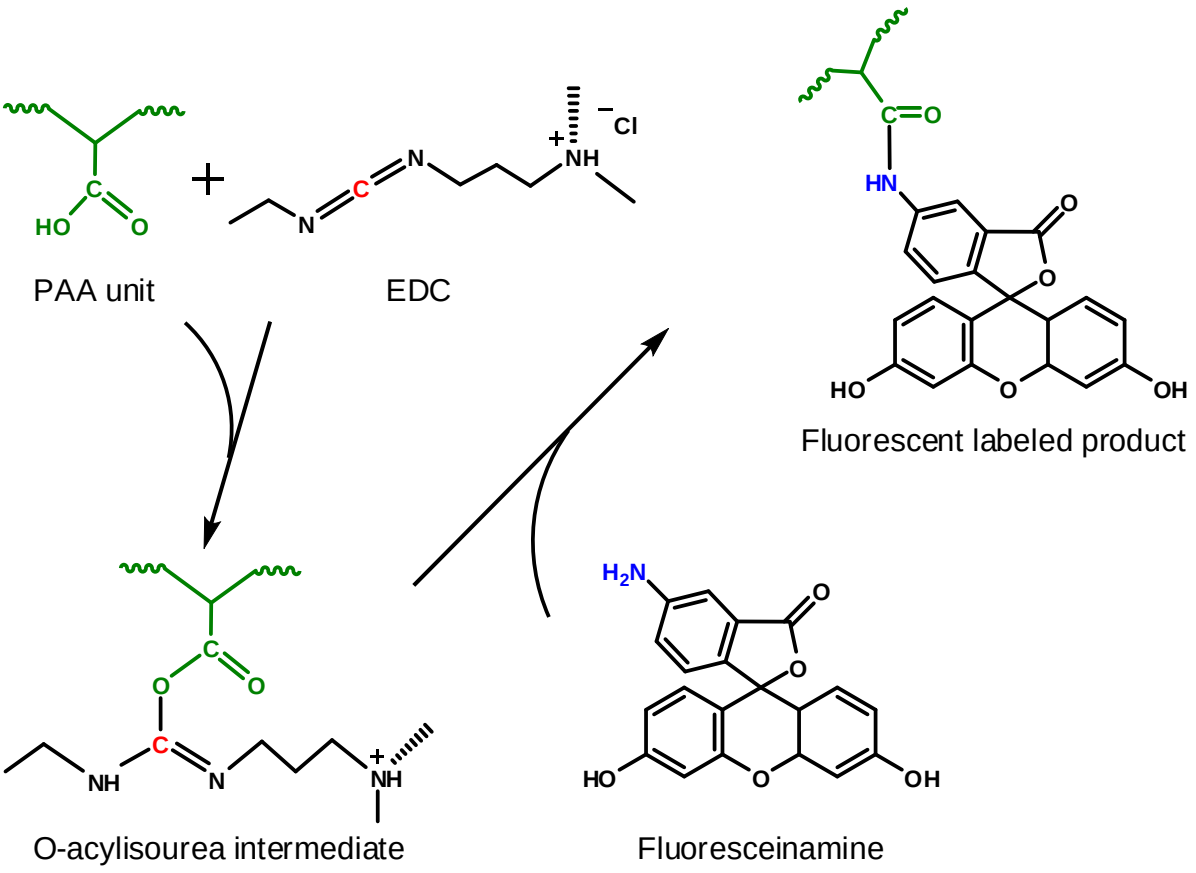

Scheme S6-1. Fluorescent labeling of PAA units of DHBC PAA-*b*-PHEA mediated by EDC.

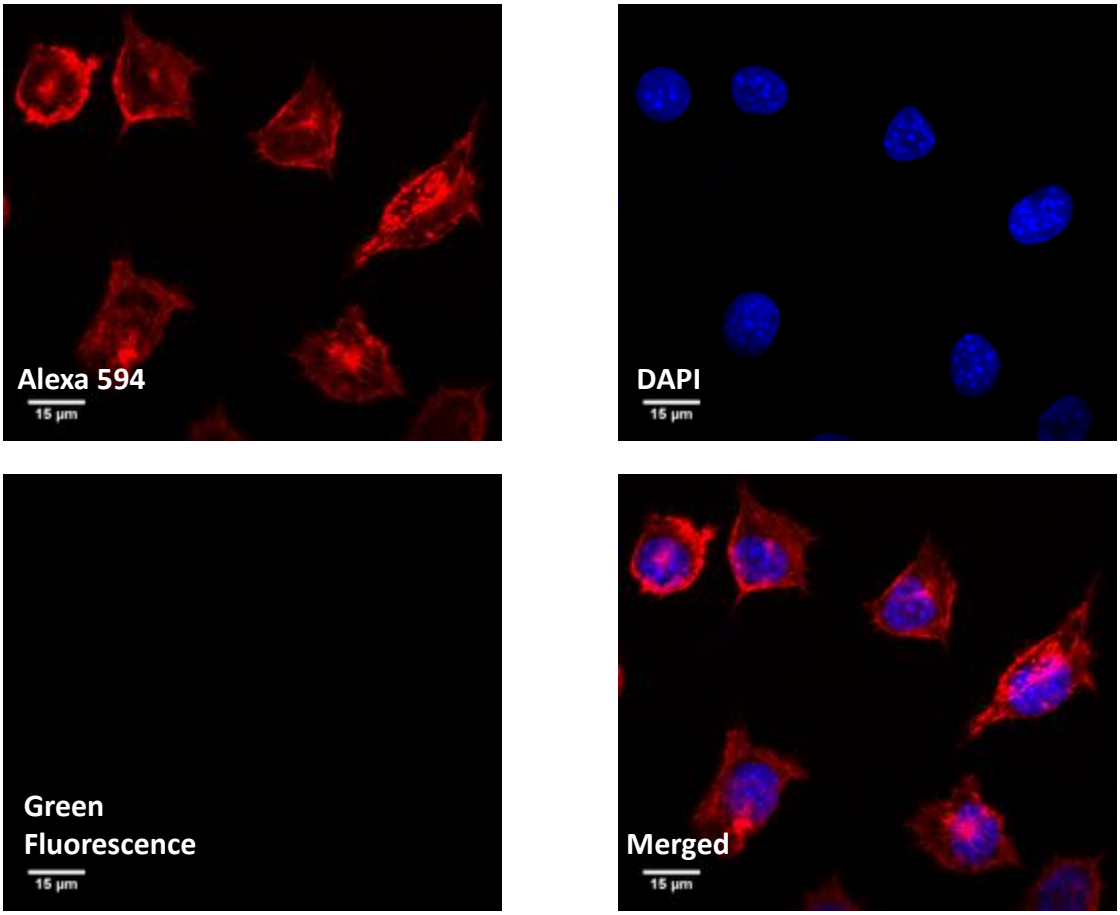

Figure S6-1. CLSM images for L929 cells untreated with either PIC micelles or MPIC micelles, after 24 h of incubation.

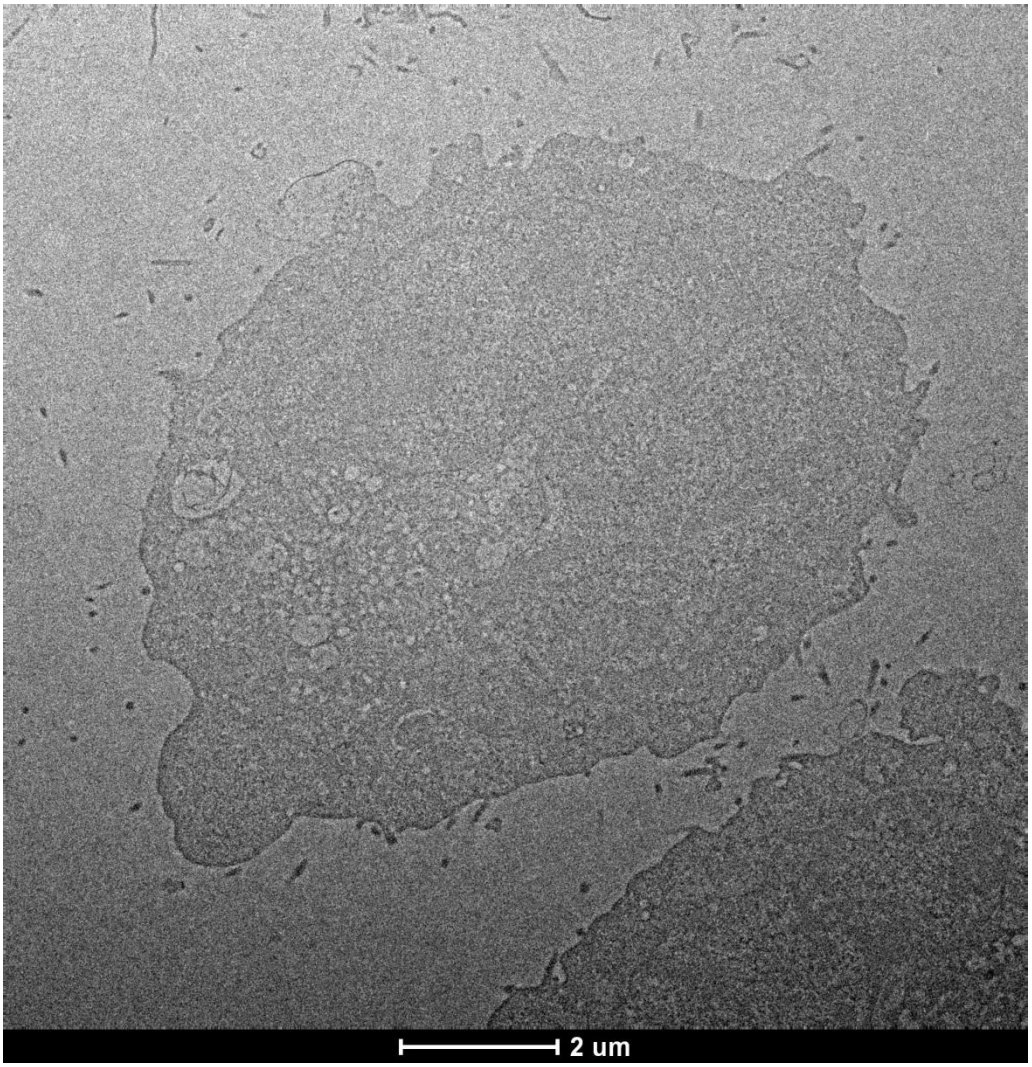

Figure S6-2. TEM image for the L929 cells untreated with MPIC micelles, after 24 h of incubation.

References

References

1. Chapter 1

1. Ferrari, M., Cancer Nanotechnology: Opportunities and Challenges. *Nat Rev Cancer* **2005,** *5* (3), 161-171.
2. Sanvicens, N.; Marco, M. P., Multifunctional Nanoparticles – Properties and Prospects for Their Use in Human Medicine. *Trends in Biotechnology* **2008,** *26* (8), 425-433.
3. Gupta, A. K.; Gupta, M., Synthesis and Surface Engineering of Iron Oxide Nanoparticles for Biomedical Applications. *Biomaterials* **2005,** *26* (18), 3995-4021.
4. Veiseh, O.; Gunn, J. W.; Zhang, M., Design and Fabrication of Magnetic Nanoparticles for Targeted Drug Delivery and Imaging. *Advanced Drug Delivery Reviews* **2010,** *62* (3), 284-304.
5. TrinhThang, T.; Shinya, M.; Nguyen Thi Kim, T., Next Generation Magnetic Nanoparticles for Biomedical Applications. In *Magnetic Nanoparticles*, CRC Press: 2012; pp 99-126.
6. Lewinski, N.; Colvin, V.; Drezek, R., Cytotoxicity of Nanoparticles. *Small* **2008,** *4* (1), 26-49.
7. Wang, Y.-X.; Hussain, S.; Krestin, G., Superparamagnetic Iron Oxide Contrast Agents: Physicochemical Characteristics and Applications in MR Imaging. *European Radiology* **2001,** *11* (11), 2319-2331.
8. Gupta, A. K.; Naregalkar, R. R.; Vaidya, V. D.; Gupta, M., Recent Advances on Surface Engineering of Magnetic Iron Oxide Nanoparticles and Their Biomedical Applications. *Nanomedicine* **2007,** *2* (1), 23-39.
9. Laurent, S.; Forge, D.; Port, M.; Roch, A.; Robic, C.; Vander Elst, L.; Muller, R. N., Magnetic Iron Oxide Nanoparticles: Synthesis, Stabilization, Vectorization, Physicochemical Characterizations, and Biological Applications. *Chemical Reviews* **2008,** *108* (6), 2064-2110.
10. Casula, M. F.; Floris, P.; Innocenti, C.; Lascialfari, A.; Marinone, M.; Corti, M.; Sperling, R. A.; Parak, W. J.; Sangregorio, C., Magnetic Resonance Imaging Contrast Agents Based on Iron Oxide Superparamagnetic Ferrofluids. *Chemistry of Materials* **2010,** *22* (5), 1739-1748.
11. Gossuin, Y.; Gillis, P.; Hocq, A.; Vuong, Q. L.; Roch, A., Magnetic Resonance Relaxation Properties of Superparamagnetic Particles. *Wiley Interdisciplinary Reviews: Nanomedicine and Nanobiotechnology* **2009,** *1* (3), 299-310.
12. Jung, C. W.; Jacobs, P., Physical and Chemical Properties of Superparamagnetic Iron Oxide MR Contrast Agents: Ferumoxides, Ferumoxtran, Ferumoxsil. *Magnetic Resonance Imaging* **1995,** *13* (5), 661-674.
13. Wang, Y.; Ng, Y. W.; Chen, Y.; Shuter, B.; Yi, J.; Ding, J.; Wang, S. c.; Feng, S. S., Formulation of Superparamagnetic Iron Oxides by Nanoparticles of Biodegradable Polymers for Magnetic Resonance Imaging. *Advanced Functional Materials* **2008,** *18* (2), 308-318.

14. Lartigue, L.; Innocenti, C.; Kalaivani, T.; Awwad, A.; Sanchez Duque, M. d. M.; Guari, Y.; Larionova, J.; Guérin, C.; Montero, J.-L. G.; Barragan-Montero, V.; Arosio, P.; Lascialfari, A.; Gatteschi, D.; Sangregorio, C., Water-Dispersible Sugar-Coated Iron Oxide Nanoparticles. An Evaluation of their Relaxometric and Magnetic Hyperthermia Properties. *Journal of the American Chemical Society* **2011,** *133* (27), 10459-10472.
15. Pinho, S. L. C.; Pereira, G. A.; Voisin, P.; Kassem, J.; Bouchaud, V.; Etienne, L.; Peters, J. A.; Carlos, L.; Mornet, S.; Geraldes, C. F. G. C.; Rocha, J.; Delville, M.-H., Fine Tuning of the Relaxometry of γ-Fe_2O_3@SiO_2 Nanoparticles by Tweaking the Silica Coating Thickness. *ACS Nano* **2010,** *4* (9), 5339-5349.
16. Pinho, S. L. C.; Laurent, S.; Rocha, J.; Roch, A.; Delville, M.-H.; Mornet, S.; Carlos, L. D.; Vander Elst, L.; Muller, R. N.; Geraldes, C. F. G. C., Relaxometric Studies of γ-Fe_2O_3@SiO_2 Core Shell Nanoparticles: When the Coating Matters. *The Journal of Physical Chemistry C* **2012,** *116* (3), 2285-2291.
17. Paquet, C.; de Haan, H. W.; Leek, D. M.; Lin, H.-Y.; Xiang, B.; Tian, G.; Kell, A.; Simard, B., Clusters of Superparamagnetic Iron Oxide Nanoparticles Encapsulated in a Hydrogel: A Particle Architecture Generating a Synergistic Enhancement of the T2 Relaxation. *ACS Nano* **2011,** *5* (4), 3104-3112.
18. Berret, J.-F.; Schonbeck, N.; Gazeau, F.; El Kharrat, D.; Sandre, O.; Vacher, A.; Airiau, M., Controlled Clustering of Superparamagnetic Nanoparticles Using Block Copolymers: Design of New Contrast Agents for Magnetic Resonance Imaging. *Journal of the American Chemical Society* **2006,** *128* (5), 1755-1761.
19. Sanson, C.; Diou, O.; Thévenot, J.; Ibarboure, E.; Soum, A.; Brûlet, A.; Miraux, S.; Thiaudière, E.; Tan, S.; Brisson, A.; Dupuis, V.; Sandre, O.; Lecommandoux, S., Doxorubicin Loaded Magnetic Polymersomes: Theranostic Nanocarriers for MR Imaging and Magneto-Chemotherapy. *ACS Nano* **2011,** *5* (2), 1122-1140.
20. Fortin, J.-P.; Gazeau, F.; Wilhelm, C., Intracellular Heating of Living Cells through Néel Relaxation of Magnetic Nanoparticles. *European Biophysics Journal* **2008,** *37* (2), 223-228.
21. Di Corato, R.; Espinosa, A.; Lartigue, L.; Tharaud, M.; Chat, S.; Pellegrino, T.; Ménager, C.; Gazeau, F.; Wilhelm, C., Magnetic Hyperthermia Efficiency in the Cellular Environment for Different Nanoparticle Designs. *Biomaterials* **2014,** *35* (24), 6400-6411.
22. Ota, S.; Yamazaki, N.; Tomitaka, A.; Yamada, T.; Takemura, Y., Hyperthermia Using Antibody-Conjugated Magnetic Nanoparticles and Its Enhanced Effect with Cryptotanshinone. *Nanomaterials* **2014,** *4* (2), 319-330.
23. Qu, Y.; Li, J.; Ren, J.; Leng, J.; Lin, C.; Shi, D., Enhanced Magnetic Fluid Hyperthermia by Micellar Magnetic Nanoclusters Composed of $Mn_xZn_{1-x}Fe_2O_4$ Nanoparticles for Induced Tumor Cell Apoptosis. *ACS Applied Materials & Interfaces* **2014,** *6* (19), 16867-16879.
24. Creixell, M.; Bohórquez, A. C.; Torres-Lugo, M.; Rinaldi, C., EGFR-Targeted Magnetic Nanoparticle Heaters Kill Cancer Cells without a Perceptible Temperature Rise. *ACS Nano* **2011,** *5* (9), 7124-7129.

References

25. Asin, L.; Goya, G. F.; Tres, A.; Ibarra, M. R., Induced Cell Toxicity Originates Dendritic Cell Death Following Magnetic Hyperthermia Treatment. *Cell Death Dis* **2013,** *4*, e596.
26. Pankhurst, Q. A.; Connolly, J.; Jones, S. K.; Dobson, J., Applications of Magnetic Nanoparticles in Biomedicine. *Journal of Physics D: Applied Physics* **2003,** *36* (13), R167.
27. Mornet, S.; Vasseur, S.; Grasset, F.; Duguet, E., Magnetic Nanoparticle Design for Medical Diagnosis and Therapy. *Journal of Materials Chemistry* **2004,** *14* (14), 2161-2175.
28. Lu, A.-H.; Salabas, E. L.; Schüth, F., Magnetic Nanoparticles: Synthesis, Protection, Functionalization, and Application. *Angewandte Chemie International Edition* **2007,** *46* (8), 1222-1244.
29. Jun, Y.-w.; Lee, J.-H.; Cheon, J., Chemical Design of Nanoparticle Probes for High-Performance Magnetic Resonance Imaging. *Angewandte Chemie International Edition* **2008,** *47* (28), 5122-5135.
30. Pankhurst, Q. A.; Thanh, N. T. K.; Jones, S. K.; Dobson, J., Progress in Applications of Magnetic Nanoparticles in Biomedicine. *Journal of Physics D: Applied Physics* **2009,** *42* (22), 224001.
31. Wang, Y.-X. J., Superparamagnetic Iron Oxide Based MRI Contrast Agents: Current Status of Clinical Application. *Quantitative Imaging in Medicine and Surgery* **2011,** *1* (1), 35-40.
32. Lee, N.; Hyeon, T., Designed Synthesis of Uniformly Sized Iron Oxide Nanoparticles for Efficient Magnetic Resonance Imaging Contrast Agents. *Chemical Society Reviews* **2012,** *41* (7), 2575-2589.
33. Rümenapp, C.; Gleich, B.; Haase, A., Magnetic Nanoparticles in Magnetic Resonance Imaging and Diagnostics. *Pharmaceutical Research* **2012,** *29* (5), 1165-1179.
34. Canfarotta, F.; Piletsky, S. A., Engineered Magnetic Nanoparticles for Biomedical Applications. *Advanced Healthcare Materials* **2014,** *3* (2), 160-175.
35. Dutz, S.; Hergt, R., Magnetic Particle Hyperthermia: a Promising Tumour Therapy? *Nanotechnology* **2014,** *25* (45), 452001.
36. Wei, W.; Zhaohui, W.; Taekyung, Y.; Changzhong, J.; Woo-Sik, K., Recent Progress on Magnetic Iron Oxide Nanoparticles: Synthesis, Surface Functional Strategies and Biomedical Applications. *Science and Technology of Advanced Materials* **2015,** *16* (2), 023501.
37. Pouton, C. W.; Seymour, L. W., Key Issues in Non-Viral Gene Delivery. *Advanced Drug Delivery Reviews* **2001,** *46* (1–3), 187-203.
38. Bally, M. B.; Harvie, P.; Wong, F. M. P.; Kong, S.; Wasan, E. K.; Reimer, D. L., Biological Barriers to Cellular Delivery of Lipid-Based DNA Carriers. *Advanced Drug Delivery Reviews* **1999,** *38* (3), 291-315.

References

2. Chapter 2

1. Ahn, T.; Kim, J. H.; Yang, H.-M.; Lee, J. W.; Kim, J.-D., Formation Pathways of Magnetite Nanoparticles by Coprecipitation Method. *The Journal of Physical Chemistry C* **2012,** *116* (10), 6069-6076.
2. Laurent, S.; Forge, D.; Port, M.; Roch, A.; Robic, C.; Vander Elst, L.; Muller, R. N., Magnetic Iron Oxide Nanoparticles: Synthesis, Stabilization, Vectorization, Physicochemical Characterizations, and Biological Applications. *Chemical Reviews* **2008,** *108* (6), 2064-2110.
3. Gu, L.; Shen, Z.; Feng, C.; Li, Y.; Lu, G.; Huang, X.; Wang, G.; Huang, J., Synthesis of PPEGMEA-*g*-PMAA Densely Grafted Double Hydrophilic Copolymer and Its Use as a Template for The Preparation of Size-Controlled Superparamagnetic Fe_3O_4/Polymer Nano-Composites. *Journal of Materials Chemistry* **2008,** *18* (36), 4332-4340.
4. Yathindranath, V.; Rebbouh, L.; Moore, D. F.; Miller, D. W.; van Lierop, J.; Hegmann, T., A Versatile Method for the Reductive, One-Pot Synthesis of Bare, Hydrophilic and Hydrophobic Magnetite Nanoparticles. *Advanced Functional Materials* **2011,** *21* (8), 1457-1464.
5. Bee, A.; Massart, R.; Neveu, S., Synthesis of Very Fine Maghemite Particles. *Journal of Magnetism and Magnetic Materials* **1995,** *149* (1–2), 6-9.
6. Chao Liu; Rondinone, A. J.; Zhang, Z. J., Synthesis of Magnetic Spinel Ferrite $CoFe_2O_4$ Nanoparticles from Ferric Salt and Characterization of The Size-Dependent Superparamagnetic Properties. *Pure and Applied Chemistry* **2000,** *72* (1-2), 37-45.
7. Lee, Y.; Lee, J.; Bae, C. J.; Park, J. G.; Noh, H. J.; Park, J. H.; Hyeon, T., Large-Scale Synthesis of Uniform and Crystalline Magnetite Nanoparticles Using Reverse Micelles as Nanoreactors under Reflux Conditions. *Advanced Functional Materials* **2005,** *15* (3), 503-509.
8. Patrinoiu, G.; Visinescu, D.; Tirsoaga, A.; Carp, O., Green Synthetic Strategy for Oxide Materials: Polysaccharides-Assisted Synthesis. Part III. Dextran-Assisted Synthesis of Nanosized Metal-Oxides. *Revue Roumaine de Chimie* **2011,** *56* (2), 6.
9. Paul, K. G.; Frigo, T. B.; Groman, J. Y.; Groman, E. V., Synthesis of Ultrasmall Superparamagnetic Iron Oxides Using Reduced Polysaccharides. *Bioconjugate Chemistry* **2004,** *15* (2), 394-401.
10. Benjamin, R. J.; Michele, F.; Jacob, V.; Angelique, Y. L., Size-Controlled Synthesis of Dextran Sulfate Coated Iron Oxide Nanoparticles for Magnetic Resonance Imaging. *Nanotechnology* **2007,** *18* (3), 035603.
11. Feng, W.; Lv, W.; Qi, J.; Zhang, G.; Zhang, F.; Fan, X., Quadruple-Responsive Nanocomposite Based on Dextran–PMAA–PNIPAM, Iron Oxide Nanoparticles, and Gold Nanorods. *Macromolecular Rapid Communications* **2012,** *33* (2), 133-139.
12. Srivastava, M.; Singh, J.; Yashpal, M.; Gupta, D. K.; Mishra, R. K.; Tripathi, S.; Ojha, A. K., Synthesis of Superparamagnetic Bare Fe_3O_4 Nanostructures and Core/Shell (Fe_3O_4/Alginate) Nanocomposites. *Carbohydrate Polymers* **2012,** *89* (3).

References

13. Llanes, F.; Ryan, D. H.; Marchessault, R. H., Magnetic Nanostructured Composites Using Alginates of Different M/G Ratios as Polymeric Matrix. *International Journal of Biological Macromolecules* **2000,** *27* (1), 35-40.
14. Yokoi, H.; Kantoh, T., Thermal Decomposition of the Iron(III) Hydroxide and Magnetite Composites of Poly(vinyl alcohol). Preparation of Magnetite and Metallic Iron Particles. *Bulletin of the Chemical Society of Japan* **1993,** *66* (5), 1536-1541.
15. Sairam, M.; Naidu, B. V. K.; Nataraj, S. K.; Sreedhar, B.; Aminabhavi, T. M., Poly(vinyl alcohol)-Iron Oxide Nanocomposite Membranes for Pervaporation Dehydration of Isopropanol, 1,4-Dioxane and Tetrahydrofuran. *Journal of Membrance Science* **2006,** *283* (1–2), 65-73.
16. Xu, C.; Teja, A. S., Continuous Hydrothermal Synthesis of Iron Oxide and PVA-Protected Iron Oxide Nanoparticles. *Journal of Supercritical Fluids* **2008,** *44* (1), 85-91.
17. Liu, H.-L.; Ko, S. P.; Wu, J.-H.; Jung, M.-H.; Min, J. H.; Lee, J. H.; An, B. H.; Kim, Y. K., One-Pot Polyol Synthesis of Monosize PVP-Coated Sub-5 nm Fe_3O_4 Nanoparticles for Biomedical Applications. *Journal of Magnetism and Magnetic Materials* **2007,** *310* (2, Part 3), e815-e817.
18. Millan, A.; Urtizberea, A.; Natividad, E.; Luis, F.; Silva, N. J. O.; Palacio, F.; Mayoral, I.; Ruiz-González, M. L.; González-Calbet, J. M.; Lecante, P.; Serin, V., Akaganeite Polymer Nanocomposites. *Polymer* **2009,** *50* (5), 1088-1094.
19. Karakoti, A. S.; Das, S.; Thevuthasan, S.; Seal, S., PEGylated Inorganic Nanoparticles. *Angewandte Chemie International Edition* **2011,** *50* (9), 1980-1994.
20. Harraz, F. A., Polyethylene Glycol-Assisted Hydrothermal Growth of Magnetite Nanowires: Synthesis and Magnetic Properties. *Physica E: Low-dimensional Systems and Nanostructures* **2008,** *40* (10), 3131-3136.
21. Lin, C.-L.; Lee, C.-F.; Chiu, W.-Y., Preparation and Properties of Poly(acrylic acid) Oligomer Stabilized Superparamagnetic Ferrofluid. *Journal of Colloid and Interface Science* **2005,** *291* (2), 411-420.
22. Ja Young, P.; Patel, D.; Gang Ho, L.; Seungtae, W.; Yongmin, C., Highly Water-Dispersible PEG Surface Modified Ultra Small Superparamagnetic Iron Oxide Nanoparticles Useful for Target-Specific Biomedical Applications. *Nanotechnology* **2008,** *19* (36), 365603.
23. Li, Z.; Tan, B.; Allix, M.; Cooper, A. I.; Rosseinsky, M. J., Direct Coprecipitation Route to Monodisperse Dual-Functionalized Magnetic Iron Oxide Nanocrystals Without Size Selection. *Small* **2008,** *4* (2), 231-239.
24. Tural, B.; Özkan, N.; Volkan, M., Preparation and Characterization of Polymer Coated Superparamagnetic Magnetite Nanoparticle Agglomerates. *Journal of Physics and Chemistry of Solids* **2009,** *70* (5), 860-866.
25. Lu, J. Q.; Moll, N.; Fu, Q.; Liu, J., Iron Nanoparticles Derived from Iron-Complexed Polymethylglutarimide to Produce High-Quality Lithographically Defined Single-Walled Carbon Nanotubes. *Chemistry of Materials* **2005,** *17* (9), 2237-2240.

26. Wan, S.; Zheng, Y.; Liu, Y.; Yan, H.; Liu, K., Fe_3O_4 Nanoparticles Coated with Homopolymers of Glycerol Mono(meth)acrylate and their Block Copolymers. *Journal of Materials Chemistry* **2005,** *15* (33), 3424-3430.
27. Guo, M.; Yan, Y.; Zhang, H.; Yan, H.; Cao, Y.; Liu, K.; Wan, S.; Huang, J.; Yue, W., Magnetic and pH-Responsive Nanocarriers with Multilayer Core-Shell Architecture for Anticancer Drug Delivery. *Journal of Materials Chemistry* **2008,** *18* (42), 5104-5112.
28. Lee, H.; Lee, E.; Kim, D. K.; Jang, N. K.; Jeong, Y. Y.; Jon, S., Antibiofouling Polymer-Coated Superparamagnetic Iron Oxide Nanoparticles as Potential Magnetic Resonance Contrast Agents for *In Vivo* Cancer Imaging. *Journal of the American Chemical Society* **2006,** *128* (22), 7383-7389.
29. Wormuth, K., Superparamagnetic Latex via Inverse Emulsion Polymerization. *Journal of Colloid and Interface Science* **2001,** *241* (2), 366-377.
30. Kumagai, M.; Imai, Y.; Nakamura, T.; Yamasaki, Y.; Sekino, M.; Ueno, S.; Hanaoka, K.; Kikuchi, K.; Nagano, T.; Kaneko, E.; Shimokado, K.; Kataoka, K., Iron Hydroxide Nanoparticles Coated with Poly(ethylene glycol)-Poly(aspartic acid) Block Copolymer as Novel Magnetic Resonance Contrast Agents for In Vivo Cancer Imaging. *Colloids and Surfaces B* **2007,** *56* (1–2), 174-181.
31. Sondjaja, R.; Alan Hatton, T.; Tam, M. K. C., Clustering of Magnetic Nanoparticles Using a Double Hydrophilic Block Copolymer, Poly(ethylene oxide)-*b*-Poly(acrylic acid). *Journal of Magnetism and Magnetic Materials* **2009,** *321* (16), 2393-2397.
32. Akcora, P.; Zhang, X.; Varughese, B.; Briber, R. M.; Kofinas, P., Structural and Magnetic Characterization of Norbornene–Deuterated Norbornene Dicarboxylic Acid Diblock Copolymers Doped With Iron Oxide Nanoparticles. *Polymer* **2005,** *46* (14), 5194-5201.
33. Akcora, P.; Briber, R. M.; Kofinas, P., TEM Characterization of Diblock Copolymer Templated Iron Oxide Nanoparticles: Bulk Solution and Thin Film Surface Doping Approach. *Polymer* **2006,** *47* (6), 2018-2022.
34. Yoon, K. Y.; Kotsmar, C.; Ingram, D. R.; Huh, C.; Bryant, S. L.; Milner, T. E.; Johnston, K. P., Stabilization of Superparamagnetic Iron Oxide Nanoclusters in Concentrated Brine with Cross-Linked Polymer Shells. *Langmuir* **2011,** *27* (17), 10962-10969.
35. Mehdaoui, B.; Meffre, A.; Lacroix, L. M.; Carrey, J.; Lachaize, S.; Gougeon, M.; Respaud, M.; Chaudret, B., Large Specific Absorption Rates in The Magnetic Hyperthermia Properties of Metallic Iron Nanocubes. *Journal of Magnetism and Magnetic Materials* **2010,** *322* (19), L49-L52.
36. Lutz, J.-F.; Stiller, S.; Hoth, A.; Kaufner, L.; Pison, U.; Cartier, R., One-Pot Synthesis of PEGylated Ultrasmall Iron-Oxide Nanoparticles and Their *In Vivo* Evaluation as Magnetic Resonance Imaging Contrast Agents. *Biomacromolecules* **2006,** *7* (11), 3132-3138.
37. Basuki, J. S.; Jacquemin, A.; Esser, L.; Li, Y.; Boyer, C.; Davis, T. P., A Block Copolymer-Stabilized Co-Precipitation Approach to Magnetic Iron Oxide Nanoparticles for Potential Use as MRI Contrast Agents. *Polymer Chemistry* **2014**.

References

38. Papaphilippou, P.; Loizou, L.; Popa, N. C.; Han, A.; Vekas, L.; Odysseos, A.; Krasia-Christoforou, T., Superparamagnetic Hybrid Micelles, Based on Iron Oxide Nanoparticles and Well-Defined Diblock Copolymers Possessing B-Ketoester Functionalities. *Biomacromolecules* **2009,** *10* (9), 2662-2671.
39. Moeser, G. D.; Green, W. H.; Laibinis, P. E.; Linse, P.; Hatton, T. A., Structure of Polymer-Stabilized Magnetic Fluids: Small-Angle Neutron Scattering and Mean-Field Lattice Modeling. *Langmuir* **2004,** *20* (13), 5223-5234.
40. Zhi, J.; Wang, Y.; Lu, Y.; Ma, J.; Luo, G., *In Situ* Preparation of Magnetic Chitosan/Fe_3O_4 Composite Nanoparticles in Tiny Pools of Water-in-Oil Microemulsion. *Reactive and Functional Polymers* **2006,** *66* (12), 1552-1558.
41. Zhang, Z.; Rondinone, A. J.; Ma, J. X.; Shen, J.; Dai, S., Morphologically Templated Growth of Aligned Spinel $CoFe_2O_4$ Nanorods. *Advanced Materials* **2005,** *17* (11), 1415-1419.
42. Underhill, R. S.; Liu, G., Triblock Nanospheres and Their Use as Templates for Inorganic Nanoparticle Preparation. *Chemistry of Materials* **2000,** *12* (8), 2082-2091.
43. Ujiie, K.; Kanayama, N.; Asai, K.; Kishimoto, M.; Ohara, Y.; Akashi, Y.; Yamada, K.; Hashimoto, S.; Oda, T.; Ohkohchi, N.; Yanagihara, H.; Kita, E.; Yamaguchi, M.; Fujii, H.; Nagasaki, Y., Preparation of Highly Dispersible and Tumor-Accumulative, Iron Oxide Nanoparticles: Multi-Point Anchoring of PEG-*b*-Poly(4-vinylbenzylphosphonate) Improves Performance Significantly. *Colloids and Surfaces B: Biointerfaces* **2011,** *88* (2), 771-778.
44. Pang, X.; Zhao, L.; Han, W.; Xin, X.; Lin, Z., A General and Robust Strategy for The Synthesis of Nearly Monodisperse Colloidal Nanocrystals. *Nature Nanotechnology* **2013,** *8* (6), 426-431.
45. Yang, Y.; Jiang, J.-S., Gradual Phase and Morphology Transformation of Fe_3O_4 Nanoparticles to α-FeOOH Nanorods in Alcohol/Water Media in the Presence of Surfactant F127. *Journal of Materials Science* **2008,** *43* (12), 4340-4343.
46. Zhang, M.; Müller, A. H. E.; Teissier, P.; Cabuil, V.; Krekhova, M., Polychelates of Amphiphilic Cylindrical Core–Shell Polymer Brushes with Iron Cations. *Prog. Coll. Polym. Sci.* **2004,** *126*, 35-39.
47. Wan, S.; Huang, J.; Yan, H.; Liu, K., Size-Controlled Preparation of Magnetite Nanoparticles in the Presence of Graft Copolymers. *Journal of Materials Chemistry* **2006,** *16* (3), 298-303.
48. Li, P.; Huang, J., Preparation of Poly (ethylene oxide)-*graft*-Poly (acrylic acid) Copolymer Stabilized Iron Oxide Nanoparticles via an *In Situ* Templated Process. *Journal of Applied Polymer Science* **2008,** *109* (1), 501-507.
49. Abes, J. I.; Cohen, R. E.; Ross, C. A., Block-Copolymer-Templated Synthesis of Iron, Iron-Cobalt, and Cobalt-Nickel Alloy Nanoparticles. *Materials Science and Engineering C* **2003,** *23*, 641-650.
50. Yun, S.-H.; Sohn, B.-H.; Jung, J. C.; Zin, W.-C.; Lee, J.-K.; Song, O., Tunable Magnetic Arrangement of Iron Oxide Nanoparticles In Situ Synthesized on the Solid Substrate from Diblock Copolymer Micelles. *Langmuir* **2005,** *21* (14), 6548-6552.

51. Ghoshal, T.; Shaw, M. T.; Bolger, C. T.; Holmes, J. D.; Morris, M. A., A General Method for Controlled Nanopatterning of Oxide Dots: A Microphase Separated Block Copolymer Platform. *Journal of Materials Chemistry* **2012**.
52. Uekawa, N.; Kaneko, K., Nonstoichiometric Properties of Nanoporous Iron Oxide Films. *Journal of Physical Chemistry B* **1998,** *102* (44), 8719-8724.
53. Yoon, M.; Kim, Y. M.; Kim, Y.; Volkov, V.; Song, H. J.; Park, Y. J.; Vasilyak, S. L.; Park, I. W., Magnetic Properties of Iron Nanoparticles in a Polymer Film. *Journal of Magnetism and Magnetic Materials* **2003,** *265* (3), 357-362.
54. Yoon, T.; Chae, C.; Sun, Y.-K.; Zhao, X.; Kung, H. H.; Lee, J. K., Bottom-up *In Situ* Formation of Fe_3O_4 Nanocrystals in a Porous Carbon Foam for Lithium-Ion Battery Anodes. *Journal of Materials Chemistry* **2011,** *21* (43), 17325-17330.
55. Breulmann, M.; Cölfen, H.; Hentze, H.-P.; Antonietti, M.; Walsh, D.; Mann, S., Elastic Magnets: Template-Controlled Mineralization of Iron Oxide Colloids in a Sponge-like Gel Matrix. *Advanced Materials* **1998,** *10* (3), 237-241.
56. Sepúlveda-Guzmán, S.; Lara, L.; Pérez-Camacho, O.; Rodríguez-Fernández, O.; Olivas, A.; Escudero, R., Synthesis and Characterization of an Iron Oxide Poly(styrene-*co*-carboxybutylmaleimide) Ferrimagnetic Composite. *Polymer* **2007,** *48* (3), 720-727.
57. Hernández, R.; Sacristán, J.; Nogales, A.; Ezquerra, T. A.; Mijangos, C., Structural Organization of Iron Oxide Nanoparticles Synthesized Inside Hybrid Polymer Gels Derived from Alginate Studied with Small-Angle X-ray Scattering. *Langmuir* **2009,** *25* (22), 13212-13218.
58. Xiong, Z.; Sun, Z.-B.; Zheng, M.-L.; Cao, Y.-Y.; Jin, F.; Chen, W.-Q.; Zhao, Z.-S.; Duan, X.-M., A Facile Method for the Room-Temperature Synthesis of Water-Soluble Magnetic Fe_3O_4 Nanoparticles: Combination of *In Situ* Synthesis and Decomposition of Polymer Hydrogel. *Materials Chemistry and Physics* **2011,** *130* (1–2), 72-78.
59. Ozay, O.; Ekici, S.; Baran, Y.; Aktas, N.; Sahiner, N., Removal of Toxic Metal Ions With Magnetic Hydrogels. *Water Research* **2009,** *43* (17), 4403-4411.
60. Ozay, O.; Ekici, S.; Aktas, N.; Sahiner, N., P(4-vinyl pyridine) Hydrogel Use for the Removal of and Th^{4+} from Aqueous Environments. *Journal of Environment Management* **2011,** *92* (12), 3121-3129.
61. Sivudu, K. S.; Rhee, K. Y., Preparation and Characterization of pH-Responsive Hydrogel Magnetite Nanocomposite. *Colloids and Surfaces A: Physicochemical and Engineering Aspects* **2009,** *349* (1–3), 29-34.
62. Zhang, J.; Xu, S.; Kumacheva, E., Polymer Microgels: Reactors for Semiconductor, Metal, and Magnetic Nanoparticles. *Journal of the American Chemical Society* **2004,** *126* (25), 7908-7914.
63. Pich, A.; Bhattacharya, S.; Lu, Y.; Boyko, V.; Adler, H.-J. P., Temperature-Sensitive Hybrid Microgels with Magnetic Properties. *Langmuir* **2004,** *20* (24), 10706-10711.
64. García-Cerda, L. A.; Chapa-Rodríguez, R.; Bonilla-Ríos, J., *In Situ* Synthesis of Iron Oxide Nanoparticles in a Styrene-Divinylbenzene Copolymer. *Polymer Bulletin* **2007,** *58* (5-6), 989-994.

65. Suh, S. K.; Yuet, K.; Hwang, D. K.; Bong, K. W.; Doyle, P. S.; Hatton, T. A., Synthesis of Nonspherical Superparamagnetic Particles: In Situ Coprecipitation of Magnetic Nanoparticles in Microgels Prepared by Stop-Flow Lithography. *Journal of the American Chemical Society* **2012**.
66. Bhattacharya, S.; Eckert, F.; Boyko, V.; Pich, A., Temperature-, pH-, and Magnetic-Field-Sensitive Hybrid Microgels. *Small* **2007,** *3* (4), 650-657.
67. Yang, C.; Shao, Q.; He, J.; Jiang, B., Preparation of Monodisperse Magnetic Polymer Microspheres by Swelling and Thermolysis Technique. *Langmuir* **2009,** *26* (7), 5179-5183.

3. Chapter 3

1. Napper, D. H., *Polymeric Stabilization of Colloidal Dispersions*. Academic Press London: 1983; Vol. 7.
2. Wu, L.; Zhang, J.; Watanabe, W., Physical and Chemical Stability of Drug Nanoparticles. *Advanced Drug Delivery Reviews* **2011,** *63* (6), 456-469.
3. Patravale, V. B.; Date, A. A.; Kulkarni, R. M., Nanosuspensions: A Promising Drug Delivery Strategy. *Journal of Pharmacy and Pharmacology* **2004,** *56* (7), 827-840.
4. Gebhart, C. L.; Kabanov, A. V., Perspectives on Polymeric Gene Delivery. *Journal of Bioactive and Compatible Polymers* **2003,** *18* (2), 147-166.
5. Kabanov, A. V.; Kabanov, V. A., DNA Complexes with Polycations for the Delivery of Genetic Material into Cells. *Bioconjugate Chemistry* **1995,** *6* (1), 7-20.
6. Boussif, O.; Lezoualc'h, F.; Zanta, M. A.; Mergny, M. D.; Scherman, D.; Demeneix, B.; Behr, J. P., A Versatile Vector for Gene and Oligonucleotide Transfer into Cells in Culture and *In Vivo*: Polyethylenimine. *Proceedings of the National Academy of Sciences of the United States of America* **1995,** *92* (16), 7297-7301.
7. Felgner, P. L.; Barenholz, Y.; Behr, J. P.; Cheng, S. H.; Cullis, P.; Huang, L.; Jessee, J. A.; Seymour, L.; Szoka, F.; Thierry, A. R.; Wagner, E.; Wu, G., Nomenclature for Synthetic Gene Delivery Systems. *Human Gene Therapy* **1997,** *8* (5), 511-512.
8. Stapert, H. R.; Nishiyama, N.; Jiang, D.-L.; Aida, T.; Kataoka, K., Polyion Complex Micelles Encapsulating Light-Harvesting Ionic Dendrimer Zinc Porphyrins. *Langmuir* **2000,** *16* (21), 8182-8188.
9. Jang, W.-D.; Nishiyama, N.; Zhang, G.-D.; Harada, A.; Jiang, D.-L.; Kawauchi, S.; Morimoto, Y.; Kikuchi, M.; Koyama, H.; Aida, T.; Kataoka, K., Supramolecular Nanocarrier of Anionic Dendrimer Porphyrins with Cationic Block Copolymers Modified with Polyethylene Glycol to Enhance Intracellular Photodynamic Efficacy. *Angewandte Chemie International Edition* **2005,** *44* (3), 419-423.
10. Li, Y.; Jang, W.-D.; Nishiyama, N.; Kishimura, A.; Kawauchi, S.; Morimoto, Y.; Miake, S.; Yamashita, T.; Kikuchi, M.; Aida, T.; Kataoka, K., Dendrimer Generation

Effects on Photodynamic Efficacy of Dendrimer Porphyrins and Dendrimer-Loaded Supramolecular Nanocarriers. *Chemistry of Materials* **2007,** *19* (23), 5557-5562.

11. Ideta, R.; Tasaka, F.; Jang, W.-D.; Nishiyama, N.; Zhang, G.-D.; Harada, A.; Yanagi, Y.; Tamaki, Y.; Aida, T.; Kataoka, K., Nanotechnology-Based Photodynamic Therapy for Neovascular Disease Using a Supramolecular Nanocarrier Loaded with a Dendritic Photosensitizer. *Nano Letters* **2005,** *5* (12), 2426-2431.
12. Bronich, T. K.; Keifer, P. A.; Shlyakhtenko, L. S.; Kabanov, A. V., Polymer Micelle with Cross-Linked Ionic Core. *Journal of the American Chemical Society* **2005,** *127* (23), 8236-8237.
13. Bronich, T. K.; Ouyang, M.; Kabanov, V. A.; Eisenberg, A.; Szoka, F. C.; Kabanov, A. V., Synthesis of Vesicles on Polymer Template. *Journal of the American Chemical Society* **2002,** *124* (40), 11872-11873.
14. Gambinossi, F.; Mylon, S. E.; Ferri, J. K., Aggregation Kinetics and Colloidal Stability of Functionalized Nanoparticles. *Advances in Colloid and Interface Science* **2014**.
15. Kizilay, E.; Kayitmazer, A. B.; Dubin, P. L., Complexation and Coacervation of Polyelectrolytes with Oppositely Charged Colloids. *Advances in Colloid and Interface Science* **2011,** *167* (1-2), 24-37.
16. Voets, I. K.; de Keizer, A.; Cohen Stuart, M. A., Complex Coacervate Core Micelles. *Advances in Colloid and Interface Science* **2009,** *147–148*, 300-318.
17. Ishikawa, Y.; Aoki, N.; Ohshima, H., Colloidal Stability of Aqueous Polymeric Dispersions: Effect of Water Insoluble Excipients. *Colloids and Surfaces B: Biointerfaces* **2005,** *45* (1), 35-41.
18. Ishikawa, Y.; Katoh, Y.; Ohshima, H., Colloidal Stability of Aqueous Polymeric Dispersions: Effect of pH and Salt Concentration. *Colloids and Surfaces B: Biointerfaces* **2005,** *42* (1), 53-58.
19. Evans, R.; Napper, D. H., On the Calculation of the van der Waals Attraction between Latex Particles. *Journal of Colloid and Interface Science* **1973,** *45* (1), 138-147.
20. Harada, A.; Kataoka, K., Formation of Polyion Complex Micelles in an Aqueous Milieu from a Pair of Oppositely-Charged Block Copolymers with Poly(ethylene glycol) Segments. *Macromolecules* **1995,** *28* (15), 5294-5299.
21. Kabanov, A. V.; Bronich, T. K.; Kabanov, V. A.; Yu, K.; Eisenberg, A., Soluble Stoichiometric Complexes from Poly(*N*-ethyl-4-vinylpyridinium) Cations and Poly(ethylene oxide)-*block*-Polymethacrylate Anions. *Macromolecules* **1996,** *29* (21), 6797-6802.
22. Cohen Stuart, M. A.; Besseling, N. A. M.; Fokkink, R. G., Formation of Micelles with Complex Coacervate Cores. *Langmuir* **1998,** *14* (24), 6846-6849.
23. Gohy, J.-F.; Varshney, S. K.; Antoun, S.; Jérôme, R., Water-Soluble Complexes Formed by Sodium Poly(4-styrenesulfonate) and a Poly(2-vinylpyridinium)-*block*-Poly(ethyleneoxide) Copolymer. *Macromolecules* **2000,** *33* (25), 9298-9305.
24. Hofs, B.; Voets, I. K.; de Keizer, A.; Cohen Stuart, M. A., Comparison of Complex Coacervate Core Micelles from Two Diblock Copolymers or a single Diblock

Copolymer with a Polyelectrolyte. *Physical Chemistry Chemical Physics* **2006,** *8* (36), 4242-4251.

25. de Vries, R.; Cohen Stuart, M., Theory and Simulations of Macroion Complexation. *Current Opinion in Colloid & Interface Science* **2006,** *11* (5), 295-301.
26. Kříž, J.; Dybal, J.; Dautzenberg, H., Cooperative Interactions of Unlike Macromolecules: 3. NMR and Theoretical Study of the Electrostatic Coupling of Sodium Polyphosphates with Diallyl(dimethyl)ammonium Chloride−Acrylamide Copolymers. *The Journal of Physical Chemistry A* **2001,** *105* (31), 7486-7493.
27. Zhou, X.; Goh, S. H.; Lee, S. Y.; Tan, K. L., XPS and FTi.r. Studies of Interactions in Poly(carboxylic acid)/Poly(vinylpyridine) Complexes. *Polymer* **1998,** *39* (16), 3631-3640.
28. Zhang, W.; Shi, L.; An, Y.; Wu, K.; Gao, L.; Liu, Z.; Ma, R.; Meng, Q.; Zhao, C.; He, B., Adsorption of Poly(4-vinyl pyridine) Unimers into Polystyrene-*block*-Poly(acrylic acid) Micelles in Ethanol Due to Hydrogen Bonding. *Macromolecules* **2004,** *37* (8), 2924-2929.
29. Pergushov, D. V.; Remizova, E. V.; Gradzielski, M.; Lindner, P.; Feldthusen, J.; Zezin, A. B.; Müller, A. H. E.; Kabanov, V. A., Micelles of Polyisobutylene-*block*-Poly(methacrylic acid) Diblock Copolymers and their Water-Soluble Interpolyelectrolyte Complexes Formed with Quaternized Poly(4-vinylpyridine). *Polymer* **2004,** *45* (2), 367-378.
30. Warnant, J.; Marcotte, N.; Reboul, J.; Layrac, G.; Aqil, A.; Jerôme, C.; Lerner, D. A.; Gérardin, C., Physicochemical Properties of pH-Controlled Polyion Complex (PIC) Micelles of Poly(acrylic acid)-Based Double Hydrophilic Block Copolymers and Various Polyamines. *Analytical and Bioanalytical Chemistry* **2012,** *403* (5), 1395-1404.
31. Gohy, J.-F.; Varshney, S. K.; Jérôme, R., Morphology of Water-Soluble Interpolyelectrolyte Complexes Formed by Poly(2-vinylpyridinium)-*block*-Poly(ethylene oxide) Diblocks and Poly(4-styrenesulfonate) Polyanions. *Macromolecules* **2001,** *34* (9), 2745-2747.
32. Zhang, L.; Eisenberg, A., Multiple Morphologies of "Crew-Cut" Aggregates of Polystyrene-*b*-Poly(acrylic acid) Block Copolymers. *Science* **1995,** *268* (5218), 1728-1731.
33. Lefèvre, N.; Fustin, C.-A.; Varshney, S. K.; Gohy, J.-F., Self-Assembly of Block Copolymer Complexes in Organic Solvents. *Polymer* **2007,** *48* (8), 2306-2311.
34. Hameed, N.; Guo, Q., Nanostructure and Hydrogen Bonding in Interpolyelectrolyte Complexes of Poly(ε-caprolactone)-*block*-Poly(2-vinyl pyridine) and Poly(acrylic acid). *Polymer* **2008,** *49* (24), 5268-5275.
35. Gohy, J.-F.; Khousakoun, E.; Willet, N.; Varshney, S. K.; Jérôme, R., Segregation of Coronal Chains in Micelles Formed by Supramolecular Interactions. *Macromolecular Rapid Communications* **2004,** *25* (17), 1536-1539.
36. Zhang, W.; Shi, L.; Miao, Z. J.; Wu, K.; An, Y., Core–Shell–Corona Micellar Complexes between Poly(ethylene glycol)-*block*-Poly(4-vinyl pyridine) and

Polystyrene-*block*-Poly(acrylic acid). *Macromolecular Chemistry and Physics* **2005,** *206* (23), 2354-2361.

37. Gohy, J.-F.; Varshney, S. K.; Jérôme, R., Water-Soluble Complexes Formed by Poly(2-vinylpyridinium)-*block*-Poly(ethylene oxide) and Poly(sodium methacrylate)-*block*-Poly(ethylene oxide) Copolymers. *Macromolecules* **2001,** *34* (10), 3361-3366.
38. Sfika, V.; Tsitsilianis, C.; Kiriy, A.; Gorodyska, G.; Stamm, M., pH Responsive Heteroarm Starlike Micelles from Double Hydrophilic ABC Terpolymer with Ampholitic A and C Blocks. *Macromolecules* **2004,** *37* (25), 9551-9560.
39. Wang, Y.; Wei, G.; Wen, F.; Zhang, X.; Zhang, W.; Shi, L., Adsorption of Poly(*N*-isopropylacrylamide-*co*-4-vinylpyridine) onto Core–Shell Poly(styrene-*co*-methylacrylic acid) Microspheres. *European Polymer Journal* **2008,** *44* (4), 1175-1182.
40. Xiong, D. a.; He, Z.; An, Y.; Li, Z.; Wang, H.; Chen, X.; Shi, L., Temperature-Responsive Multilayered Micelles Formed from the Complexation of PNIPAM-*b*-P4VP Block-Copolymer and PS-*b*-PAA Core–Shell Micelles. *Polymer* **2008,** *49* (10), 2548-2552.
41. Vargün, E.; Usanmaz, A., Polymerization of 2-Hydroxyethyl Acrylate in Bulk and Solution by Chemical Initiator and by ATRP Method. *Journal of Polymer Science Part A: Polymer Chemistry* **2005,** *43* (17), 3957-3965.
42. Lin, M.; Xu, P.; Zhong, W., Preparation, Characterization, and Release Behavior of Aspirin-Loaded Poly(2-hydroxyethyl acrylate)/Silica Hydrogels. *Journal of Biomedical Materials Research Part B: Applied Biomaterials* **2012,** *100B* (4), 1114-1120.
43. Hoogenboom, R.; Popescu, D.; Steinhauer, W.; Keul, H.; Möller, M., Nitroxide-Mediated Copolymerization of 2-Hydroxyethyl Acrylate and 2-Hydroxypropyl Acrylate: Copolymerization Kinetics and Thermoresponsive Properties. *Macromolecular Rapid Communications* **2009,** *30* (23), 2042-2048.
44. Arun, A.; Reddy, B. S. R., *In Vitro* Drug Release Studies of 2-Hydroxyethyl Acrylate or 2-Hydroxypropyl Methacrylate-4-{(1E,4E)-5-[4-(acryloyloxy)phenyl]-3-oxopenta-1,4-dienyl}phenyl Acrylate Copolymer Beads. *Journal of Biomedical Materials Research Part B: Applied Biomaterials* **2005,** *73B* (2), 291-300.
45. Khutoryanskaya, O. V.; Mayeva, Z. A.; Mun, G. A.; Khutoryanskiy, V. V., Designing Temperature-Responsive Biocompatible Copolymers and Hydrogels Based on 2-Hydroxyethyl(meth)acrylates. *Biomacromolecules* **2008,** *9* (12), 3353-3361.
46. Gauthier, M.; Munam, A., Arborescent Polystyrene-*graft*-Poly(2-vinylpyridine) Copolymers: Solution Polyelectrolyte Behavior. *RSC Advances* **2012,** *2* (7), 3100-3108.
47. Davis, K. A.; Matyjaszewski, K., Atom Transfer Radical Polymerization of *tert*-Butyl Acrylate and Preparation of Block Copolymers. *Macromolecules* **2000,** *33* (11), 4039-4047.
48. Kirby, B. J., *Micro- and Nanoscale Fluid Mechanics: Transport in Microfluidic Devices*. Cambridge University Press: Cambridge 2009.

49. Hunter, R. J., Chapter 3 - The Calculation of Zeta Potential. In *Zeta Potential in Colloid Science*, Hunter, R. J., Ed. Academic Press: 1981; pp 59-124.
50. Sze, A.; Erickson, D.; Ren, L.; Li, D., Zeta-Potential Measurement Using the Smoluchowski Equation and the Slope of The Current–Time Relationship in Electroosmotic Flow. *Journal of Colloid and Interface Science* **2003,** *261* (2), 402-410.
51. Matyjaszewski, K.; Pintauer, T.; Gaynor, S., Removal of Copper-Based Catalyst in Atom Transfer Radical Polymerization Using Ion Exchange Resins. *Macromolecules* **2000,** *33* (4), 1476-1478.
52. Matyjaszewski, K.; Xia, J., Atom Transfer Radical Polymerization. *Chemical Reviews* **2001,** *101* (9), 2921-2990.
53. Matyjaszewski, K., Atom Transfer Radical Polymerization (ATRP): Current Status and Future Perspectives. *Macromolecules* **2012,** *45* (10), 4015-4039.
54. Mühlebach, A.; Gaynor, S. G.; Matyjaszewski, K., Synthesis of Amphiphilic Block Copolymers by Atom Transfer Radical Polymerization (ATRP). *Macromolecules* **1998,** *31* (18), 6046-6052.
55. Bloch, D. R., *Polymer Handbook*. Wiley: New York: 1999; p 536.
56. Choi, J.; Rubner, M. F., Influence of the Degree of Ionization on Weak Polyelectrolyte Multilayer Assembly. *Macromolecules* **2004,** *38* (1), 116-124.
57. Bromberg, L., Properties of Aqueous Solutions and Gels of Poly(ethylene oxide)-*b*-Poly(propylene oxide)-*b*-Poly(ethylene oxide)-*g*-Poly(acrylic acid). *The Journal of Physical Chemistry B* **1998,** *102* (52), 10736-10744.
58. Philippova, O. E.; Hourdet, D.; Audebert, R.; Khokhlov, A. R., pH-Responsive Gels of Hydrophobically Modified Poly(acrylic acid). *Macromolecules* **1997,** *30* (26), 8278-8285.
59. Petrov, A. I.; Antipov, A. A.; Sukhorukov, G. B., Base−Acid Equilibria in Polyelectrolyte Systems: From Weak Polyelectrolytes to Interpolyelectrolyte Complexes and Multilayered Polyelectrolyte Shells. *Macromolecules* **2003,** *36* (26), 10079-10086.
60. Perin, D. D., *Dissociation Constants of Inorganic Acids and Bases in Aqueous Solution*. Buttersworth: London, 1965.
61. Mori, H.; Müller, A. H. E.; Klee, J. E., Intelligent Colloidal Hybrids via Reversible pH-Induced Complexation of Polyelectrolyte and Silica Nanoparticles. *Journal of the American Chemical Society* **2003,** *125* (13), 3712-3713.
62. Zhao, H.; Liu, S.; Jiang, M.; Yuan, X. f.; An, Y.; Liu, L., Acid Terminated PS: not Polyion Micelle-like Particles Formed by Carboxylic Acid-Terminated Polystyrene and Poly(4-vinyl pyridine) in Chloroform/Methanol Mixed Solution. *Polymer* **2000,** *41* (7), 2705-2709.
63. Wichterle, O.; Lim, D., Hydrophilic Gels for Biological Use. *Nature* **1960,** *185* (4706), 117-118.
64. McAllister, K.; Sazani, P.; Adam, M.; Cho, M. J.; Rubinstein, M.; Samulski, R. J.; DeSimone, J. M., Polymeric Nanogels Produced via Inverse Microemulsion

Polymerization as Potential Gene and Antisense Delivery Agents. *Journal of the American Chemical Society* **2002,** *124* (51), 15198-15207.

65. Takakura, Y.; Mahato, R. I.; Hashida, M., Extravasation of Macromolecules. *Advanced Drug Delivery Reviews* **1998,** *34* (1), 93-108.
66. Bally, M. B.; Harvie, P.; Wong, F. M. P.; Kong, S.; Wasan, E. K.; Reimer, D. L., Biological Barriers to Cellular Delivery of Lipid-Based DNA Carriers. *Advanced Drug Delivery Reviews* **1999,** *38* (3), 291-315.
67. Pouton, C. W.; Seymour, L. W., Key Issues in Non-Viral Gene Delivery. *Advanced Drug Delivery Reviews* **2001,** *46* (1–3), 187-203.
68. Sheiko, S. S.; Gauthier, M.; Möller, M., Monomolecular Films of Arborescent Graft Polystyrenes. *Macromolecules* **1997,** *30* (8), 2343-2349.
69. Choi, S.; Briber, R. M.; Bauer, B. J.; Topp, A.; Gauthier, M.; Tichagwa, L., Small-Angle Neutron Scattering of Solutions of Arborescent Graft Polystyrenes. *Macromolecules* **1999,** *32* (23), 7879-7886.
70. Yun, S. I.; Briber, R. M.; Kee, R. A.; Gauthier, M., Small-Angle Neutron Scattering of Arborescent Polystyrene-*graft*-Poly(2-vinylpyridine) Copolymers. *Polymer* **2003,** *44* (21), 6579-6587.
71. Förster, S.; Zisenis, M.; Wenz, E.; Antonietti, M., Micellization of Strongly Segregated Block Copolymers. *The Journal of Chemical Physics* **1996,** *104* (24), 9956-9970.
72. Yamakawa, H., *Modern Theory of Polymer Solutions*. Harper and Row, New York: 1971.
73. Schmidt, M.; Burchard, W., Translational Diffusion and Hydrodynamic Radius of Unperturbed Flexible Chains. *Macromolecules* **1981,** *14* (1), 210-211.
74. Antonietti, M.; Bremser, W.; Schmidt, M., Microgels: Model Polymers for the Crosslinked State. *Macromolecules* **1990,** *23* (16), 3796-3805.
75. Qin, A.; Tian, M.; Ramireddy, C.; Webber, S. E.; Munk, P.; Tuzar, Z., Polystyrene-Poly(methacrylic acid) Block Copolymer Micelles. *Macromolecules* **1994,** *27* (1), 120-126.
76. Guo, Y.; Moffitt, M. G., Semiconductor Quantum Dots with Environmentally Responsive Mixed Polystyrene/Poly(methyl methacrylate) Brush Layers. *Macromolecules* **2007,** *40* (16), 5868-5878.
77. Pavlov, A. S.; Khalatur, P. G.; Eskin, V. E., Some New Properties of the Dilute Polymer Solutions II. Study of Thermodynamic Properties of Dilute Polymer Solutions by the Monte Carlo Method. *Polymer Journal* **1986,** *18* (11), 803-808.
78. Gauthier, M.; Chung, J.; Choi, L.; Nguyen, T. T., Second Virial Coefficient of Arborescent Polystyrenes and Its Temperature Dependence. *The Journal of Physical Chemistry B* **1998,** *102* (17), 3138-3142.
79. Babcock, K. L.; Parter, C. B., Phase Imaging: Beyond Topography. *Veeco Application Note* **1995,** (1995).
80. Eaton, P.; West, P., *Atomic Force Microscopy*. Oxford University Press Inc.: New York, 2010; p 248.

References

81. García, R.; Pérez, R., Dynamic Atomic Force Microscopy Methods. *Surface Science Reports* **2002,** *47* (6–8), 197-301.
82. Nagao, E.; Dvorak, J. A., Phase Imaging by Atomic Force Microscopy: Analysis of Living Homoiothermic Vertebrate Cells. *Biophysical Journal* **1999,** *76* (6), 3289-3297.
83. Raghavan, D.; Gu, X.; Nguyen, T.; VanLandingham, M.; Karim, A., Mapping Polymer Heterogeneity Using Atomic Force Microscopy Phase Imaging and Nanoscale Indentation. *Macromolecules* **2000,** *33* (7), 2573-2583.
84. Schmitz, I.; Schreiner, M.; Friedbacher, G.; Grasserbauer, M., Phase Imaging as an Extension to Tapping Mode AFM for the Identification of Material Properties on Humidity-Sensitive Surfaces. *Applied Surface Science* **1997,** *115* (2), 190-198.
85. Tamayo, J.; García, R., Deformation, Contact Time, and Phase Contrast in Tapping Mode Scanning Force Microscopy. *Langmuir* **1996,** *12* (18), 4430-4435.
86. Xu, L.-C.; Runt, J.; Siedlecki, C. A., Dynamics of Hydrated Polyurethane Biomaterials: Surface Microphase Restructuring, Protein Activity and Platelet Adhesion. *Acta Biomaterialia* **2010,** *6* (6), 1938-1947.
87. Salmerón Sánchez, M.; Molina Mateo, J.; Romero Colomer, F. J.; Gómez Ribelles, J. L., Nanoindentation and Tapping Mode AFM Study of Phase Separation in Poly(ethyl acrylate-*co*-hydroxyethyl methacrylate) Copolymer Networks. *European Polymer Journal* **2006,** *42* (6), 1378-1383.

References

4. Chapter 4

1. Ferrari, M., Cancer Nanotechnology: Opportunities and Challenges. *Nat Rev Cancer* **2005,** *5* (3), 161-171.
2. Sanvicens, N.; Marco, M. P., Multifunctional Nanoparticles – Properties and Prospects for Their Use in Human Medicine. *Trends in Biotechnology* **2008,** *26* (8), 425-433.
3. Gupta, A. K.; Gupta, M., Synthesis and Surface Engineering of Iron Oxide Nanoparticles for Biomedical Applications. *Biomaterials* **2005,** *26* (18), 3995-4021.
4. Veiseh, O.; Gunn, J. W.; Zhang, M., Design and Fabrication of Magnetic Nanoparticles for Targeted Drug Delivery and Imaging. *Advanced Drug Delivery Reviews* **2010,** *62* (3), 284-304.
5. TrinhThang, T.; Shinya, M.; Nguyen Thi Kim, T., Next Generation Magnetic Nanoparticles for Biomedical Applications. In *Magnetic Nanoparticles*, CRC Press: 2012; pp 99-126.
6. Lewinski, N.; Colvin, V.; Drezek, R., Cytotoxicity of Nanoparticles. *Small* **2008,** *4* (1), 26-49.
7. Wang, Y.-X.; Hussain, S.; Krestin, G., Superparamagnetic Iron Oxide Contrast Agents: Physicochemical Characteristics and Applications in MR Imaging. *European Radiology* **2001,** *11* (11), 2319-2331.
8. Gupta, A. K.; Naregalkar, R. R.; Vaidya, V. D.; Gupta, M., Recent Advances on Surface Engineering of Magnetic Iron Oxide Nanoparticles and Their Biomedical Applications. *Nanomedicine* **2007,** *2* (1), 23-39.
9. Laurent, S.; Forge, D.; Port, M.; Roch, A.; Robic, C.; Vander Elst, L.; Muller, R. N., Magnetic Iron Oxide Nanoparticles: Synthesis, Stabilization, Vectorization, Physicochemical Characterizations, and Biological Applications. *Chemical Reviews* **2008,** *108* (6), 2064-2110.
10. Massart, R., Preparation of Aqueous Magnetic Liquids in Alkaline and Acidic Media. *Magnetics, IEEE Transactions on* **1981,** *17* (2), 1247-1248.
11. Molday, R. S.; Mackenzie, D., Immunospecific ferromagnetic iron-dextran reagents for the labeling and magnetic separation of cells. *Journal of Immunological Methods* **1982,** *52* (3), 353-367.
12. Corot, C.; Robert, P.; Idée, J.-M.; Port, M., Recent Advances in Iron Oxide Nanocrystal Technology for Medical Imaging. *Advanced Drug Delivery Reviews* **2006,** *58* (14), 1471-1504.
13. Massart, R.; Cabuil, V., Effect of Some Parameters on the Formation of Colloidal Magnetite in Alkaline Medium: Yield and Particle Size Control. *Journal de Chimie Physique et de Physico-Chimie Biologique* **1987,** *84*, 967-973.
14. Jolivet, J.-P.; Chaneac, C.; Tronc, E., Iron Oxide Chemistry. From Molecular Clusters to Extended Solid Networks. *Chemical Communications* **2004,** (5), 481-483.

References

15. Etienne, D.; Marie-Hélène, D.; Stéphane, M., Synthesis and Characterisation of Iron Oxide Ferrite Nanoparticles and Ferrite-Based Aqueous Fluids. In *Magnetic Nanoparticles*, CRC Press: 2012; pp 47-72.
16. Schwertmann, U.; Cornell, R. M., General Preparative Techniques. In *Iron Oxides in the Laboratory*, Wiley-VCH Verlag GmbH: 2007; pp 19-25.
17. Schwarzer, H.-C.; Peukert, W., Combined Experimental/Numerical Study on the Precipitation of Nanoparticles. *AIChE Journal* **2004,** *50* (12), 3234-3247.
18. Sugimoto, T., Formation of Monodispersed Nano- and Micro-Particles Controlled in Size, Shape, and Internal Structure. *Chemical Engineering & Technology* **2003,** *26* (3), 313-321.
19. Boistelle, R.; Astier, J. P., Crystallization Mechanisms in Solution. *Journal of Crystal Growth* **1988,** *90* (1–3), 14-30.
20. LaMer, V. K.; Dinegar, R. H., Theory, Production and Mechanism of Formation of Monodispersed Hydrosols. *Journal of the American Chemical Society* **1950,** *72* (11), 4847-4854.
21. Jolivet, J.-P.; Tronc, E.; Chanéac, C., Iron Oxides: From Molecular Clusters to Solid. A Nice Example of Chemical Versatility. *Comptes Rendus Geoscience* **2006,** *338* (6–7), 488-497.
22. Vayssières, L.; Chanéac, C.; Tronc, E.; Jolivet, J. P., Size Tailoring of Magnetite Particles Formed by Aqueous Precipitation: An Example of Thermodynamic Stability of Nanometric Oxide Particles. *Journal of Colloid and Interface Science* **1998,** *205* (2), 205-212.
23. Babes, L.; Denizot, B.; Tanguy, G.; Le Jeune, J. J.; Jallet, P., Synthesis of Iron Oxide Nanoparticles Used as MRI Contrast Agents: A Parametric Study. *Journal of Colloid and Interface Science* **1999,** *212* (2), 474-482.
24. Jolivet, J.-P., *De la Solution à L'oxyde*. InterEditions et CNRS Editions: Paris, France, 1994.
25. Tronc, E.; Belleville, P.; Jolivet, J. P.; Livage, J., Transformation of Ferric Hydroxide into Spinel by Iron(II) Adsorption. *Langmuir* **1992,** *8* (1), 313-319.
26. Sjogren, C. E.; Briley-Saebo, K.; Hanson, M.; Johansson, C., Magnetic Characterization of Iron Oxides for Magnetic Resonance Imaging. *Magn Reson Med* **1994,** *31* (3), 268-72.
27. Bee, A.; Massart, R.; Neveu, S., Synthesis of Very Fine Maghemite Particles. *Journal of Magnetism and Magnetic Materials* **1995,** *149* (1–2), 6-9.
28. Pillai, V.; Kumar, P.; Hou, M. J.; Ayyub, P.; Shah, D. O., Preparation of Nanoparticles of Silver Halides, Superconductors and Magnetic Materials Using Water-in-Oil Microemulsions as Nano-Reactors. *Advances in Colloid and Interface Science* **1995,** *55*, 241-269.
29. Zhi, J.; Wang, Y.; Lu, Y.; Ma, J.; Luo, G., *In Situ* Preparation of Magnetic Chitosan/Fe_3O_4 Composite Nanoparticles in Tiny Pools of Water-in-Oil Microemulsion. *Reactive and Functional Polymers* **2006,** *66* (12), 1552-1558.

30. Nguyen, V. T. A.; Gauthier, M.; Sandre, O., Templated Synthesis of Magnetic Nanoparticles Through the Self-Assembly of Polymers and Surfactants. *Nanomaterials* **2014,** *4* (3), 628-685.
31. Singh, N.; Jenkins, G. J. S.; Asadi, R.; Doak, S. H., Potential Toxicity of Superparamagnetic Iron Oxide Nanoparticles (SPION). *Nano Reviews* **2010**.
32. Kim, J. S.; Yoon, T. J.; Yu, K. N.; Kim, B. G.; Park, S. J.; Kim, H. W.; Lee, K. H.; Park, S. B.; Lee, J. K.; Cho, M. H., Toxicity and Tissue Distribution of Magnetic Nanoparticles in Mice. *Toxicological Sciences* **2006,** *89* (1), 338-47.
33. Stroh, A.; Zimmer, C.; Gutzeit, C.; Jakstadt, M.; Marschinke, F.; Jung, T.; Pilgrimm, H.; Grune, T., Iron Oxide Particles for Molecular Magnetic Resonance Imaging Cause Transient Oxidative Stress in Rat Macrophages. *Free Radical Biology and Medicine* **2004,** *36* (8), 976-984.
34. Fauconnier, N.; Bee, A.; Roger, J.; Pons, J. N., Adsorption of Gluconic and Citric Acids on Maghemite Particles in Aqueous Medium. In *Trends in Colloid and Interface Science X*, Solans, C.; Infante, M. R.; García-Celma, M. J., Eds. Steinkopff: 1996; Vol. 100, pp 212-216.
35. Fauconnier, N.; Bee, A.; Roger, J.; Pons, J. N., Adsorption of Gluconic and Citric Acids on Maghemite Particles in Aqueous Medium. In *Progress in Colloid and Polymer Science*, 1996; Vol. 100, pp 212-216.
36. Fauconnier, N.; Pons, J. N.; Roger, J.; Bee, A., Thiolation of Maghemite Nanoparticles by Dimercaptosuccinic Acid. *Journal of Colloid and Interface Science* **1997,** *194* (2), 427-433.
37. Sahoo, Y.; Pizem, H.; Fried, T.; Golodnitsky, D.; Burstein, L.; Sukenik, C. N.; Markovich, G., Alkyl Phosphonate/Phosphate Coating on Magnetite Nanoparticles: A Comparison with Fatty Acids. *Langmuir* **2001,** *17* (25), 7907-7911.
38. Mohapatra, S.; Pramanik, N.; Ghosh, S. K.; Pramanik, P., Synthesis and Characterization of Ultrafine Poly(vinylalcohol phosphate) Coated Magnetite Nanoparticles. *Journal of Nanoscience and Nanotechnology* **2006,** *6* (3), 823-829.
39. Roberts, D.; Zhu, W. L.; Frommen, C. M.; Rosenzweig, Z., Synthesis of Gadolinium Oxide Magnetoliposomes for Magnetic Resonance Imaging. *Journal of Applied Physics* **2000,** *87* (9), 6208-6210.
40. Cabuil, V., Phase Behavior of Magnetic Nanoparticles Dispersions in Bulk and Confined Geometries. *Current Opinion in Colloid & Interface Science* **2000,** *5* (1–2), 44-48.
41. Cousin, F.; Dubois, E.; Cabuil, V., Approach of the Critical Point of Gas–Liquid Transitions in an Electrostatically Stabilized Colloidal Suspension. *The Journal of Chemical Physics* **2001,** *115* (13), 6051-6057.
42. Cousin, F.; Dubois, E.; Cabuil, V.; Boué, F.; Perzynski, R., Overview of the Phase Diagram of Ionic Magnetic Colloidal Dispersions. *Brazilian Journal of Physics* **2001,** *31*, 350-355.
43. Dubois, E.; Perzynski, R.; Boué, F.; Cabuil, V., Liquid−Gas Transitions in Charged Colloidal Dispersions: Small-Angle Neutron Scattering Coupled with Phase Diagrams of Magnetic Fluids. *Langmuir* **2000,** *16* (13), 5617-5625.

44. Cousin, F.; Dubois, E.; Cabuil, V., Tuning the Interactions of a Magnetic Colloidal Suspension. *Physical Review E* **2003,** *68* (2), 021405.
45. Napper, D. H., *Polymeric Stabilization of Colloidal Dispersions*. Academic Press London: 1983; Vol. 7.
46. Odenbach, S., Ferrofluids- Magnetisable Liquids and Their Application in Density Separation. *Magnetic and Electrical Separation* **1998,** *9* (1), 1-25.
47. Wilhelm, C.; Billotey, C.; Roger, J.; Pons, J. N.; Bacri, J. C.; Gazeau, F., Intracellular Uptake of Anionic Superparamagnetic Nanoparticles as a Function of Their Surface Coating. *Biomaterials* **2003,** *24* (6), 1001-1011.
48. Jain, T. K.; Reddy, M. K.; Morales, M. A.; Leslie-Pelecky, D. L.; Labhasetwar, V., Biodistribution, Clearance, and Biocompatibility of Iron Oxide Magnetic Nanoparticles in Rats. *Molecular Pharmaceutics* **2008,** *5* (2), 316-27.
49. Sadeghiani, N.; Barbosa, L. S.; Silva, L. P.; Azevedo, R. B.; Morais, P. C.; Lacava, Z. G. M., Genotoxicity and Inflammatory Investigation in Mice Treated with Magnetite Nanoparticles Surface Coated with Polyaspartic Acid. *Journal of Magnetism and Magnetic Materials* **2005,** *289*, 466-468.
50. Park, J.; Yu, M. K.; Jeong, Y. Y.; Kim, J. W.; Lee, K.; Phan, V. N.; Jon, S., Antibiofouling Amphiphilic Polymer-Coated Superparamagnetic Iron Oxide Nanoparticles: Synthesis, Characterization, and Use in Cancer Imaging *In Vivo*. *Journal of Materials Chemistry* **2009,** *19* (35), 6412-6417.
51. Berry, C. C.; Wells, S.; Charles, S.; Curtis, A. S. G., Dextran and Albumin Derivatised Iron Oxide Nanoparticles: Influence on Fibroblasts *In Vitro*. *Biomaterials* **2003,** *24* (25), 4551-4557.
52. Gupta, A. K.; Wells, S., Surface-Modified Superparamagnetic Nanoparticles for Drug Delivery: Preparation, Characterization, and Cytotoxicity Studies. *NanoBioscience, IEEE Transactions on* **2004,** *3* (1), 66-73.
53. Gupta, A. K.; Gupta, M., Cytotoxicity Suppression and Cellular Uptake Enhancement of Surface Modified Magnetic Nanoparticles. *Biomaterials* **2005,** *26* (13), 1565-1573.
54. William, W. Y.; Emmanuel, C.; Christie, M. S.; Rebekah, D.; Vicki, L. C., Aqueous Dispersion of Monodisperse Magnetic Iron Oxide Nanocrystals Through Phase Transfer. *Nanotechnology* **2006,** *17* (17), 4483.
55. Allen, C.; Maysinger, D.; Eisenberg, A., Nano-Engineering Block Copolymer Aggregates for Drug Delivery. *Colloids and Surfaces B: Biointerfaces* **1999,** *16* (1–4), 3-27.
56. Gref, R.; Domb, A.; Quellec, P.; Blunk, T.; Müller, R. H.; Verbavatz, J. M.; Langer, R., The Controlled Intravenous Delivery of Drugs Using PEG-Coated Sterically Stabilized Nanospheres. *Advanced Drug Delivery Reviews* **1995,** *16* (2-3), 215-233.
57. Wan, S.; Huang, J.; Guo, M.; Zhang, H.; Cao, Y.; Yan, H.; Liu, K., Biocompatible Superparamagnetic Iron Oxide Nanoparticle Dispersions Stabilized with Poly(ethylene glycol)–Oligo(aspartic acid) Hybrids. *Journal of Biomedical Materials Research Part A* **2007,** *80A* (4), 946-954.
58. Torrisi, V.; Graillot, A.; Vitorazi, L.; Crouzet, Q.; Marletta, G.; Loubat, C.; Berret, J. F., Preventing Corona Effects: Multiphosphonic Acid Poly(ethylene glycol)

Copolymers for Stable Stealth Iron Oxide Nanoparticles. *Biomacromolecules* **2014,** *15* (8), 3171-3179.

59. Liu, X.; Xing, J.; Guan, Y.; Shan, G.; Liu, H., Synthesis of Amino-Silane Modified Superparamagnetic Silica Supports and Their Use for Protein Immobilization. *Colloids and Surfaces A: Physicochemical and Engineering Aspects* **2004,** *238* (1–3), 127-131.
60. Liu, X.; Ma, Z.; Xing, J.; Liu, H., Preparation and Characterization of Amino–Silane Modified Superparamagnetic Silica Nanospheres. *Journal of Magnetism and Magnetic Materials* **2004,** *270* (1–2), 1-6.
61. Santra, S.; Tapec, R.; Theodoropoulou, N.; Dobson, J.; Hebard, A.; Tan, W., Synthesis and Characterization of Silica-Coated Iron Oxide Nanoparticles in Microemulsion: The Effect of Nonionic Surfactants. *Langmuir* **2001,** *17* (10), 2900-2906.
62. Tartaj, P.; González-Carreño, T.; Serna, C. J., Synthesis of Nanomagnets Dispersed in Colloidal Silica Cages with Applications in Chemical Separation. *Langmuir* **2002,** *18* (12), 4556-4558.
63. Zhang, C.; Wängler, B.; Morgenstern, B.; Zentgraf, H.; Eisenhut, M.; Untenecker, H.; Krüger, R.; Huss, R.; Seliger, C.; Semmler, W.; Kiessling, F., Silica- and Alkoxysilane-Coated Ultrasmall Superparamagnetic Iron Oxide Particles: A Promising Tool To Label Cells for Magnetic Resonance Imaging. *Langmuir* **2007,** *23* (3), 1427-1434.
64. Hahn, P. F.; Stark, D. D.; Lewis, J. M.; Saini, S.; Elizondo, G.; Weissleder, R.; Fretz, C. J.; Ferrucci, J. T., First Clinical Trial of a New Superparamagnetic Iron Oxide for Use as an Oral Gastrointestinal Contrast Agent in MR Imaging. *Radiology* **1990,** *175* (3), 695-700.
65. Johnson, W. K.; Stoupis, C.; Torres, G. M.; Rosenberg, E. B.; Ros, P. R., Superparamagnetic Iron Oxide (SPIO) as an Oral Contrast Agent in Gastrointestinal (GI) Magnetic Resonance Imaging (MRI): Comparison with State-of-the-Art Computed Tomography (CT). *Magnetic Resonance Imaging* **1996,** *14* (1), 43-49.
66. Zhou, W. L.; Carpenter, E. E.; Lin, J.; Kumbhar, A.; Sims, J.; O'Connor, C. J., Nanostructures of Gold Coated Iron Core-Shell Nanoparticles and The Nanobands Assembled under Magnetic Field. *The European Physical Journal D - Atomic, Molecular, Optical and Plasma Physics* **2001,** *16* (1), 289-292.
67. Lin, J.; Zhou, W.; Kumbhar, A.; Wiemann, J.; Fang, J.; Carpenter, E. E.; O'Connor, C. J., Gold-Coated Iron (Fe@Au) Nanoparticles: Synthesis, Characterization, and Magnetic Field-Induced Self-Assembly. *Journal of Solid State Chemistry* **2001,** *159* (1), 26-31.
68. Lyon, J. L.; Fleming, D. A.; Stone, M. B.; Schiffer, P.; Williams, M. E., Synthesis of Fe Oxide Core/Au Shell Nanoparticles by Iterative Hydroxylamine Seeding. *Nano Letters* **2004,** *4* (4), 719-723.
69. Kim, J.; Park, S.; Lee, J. E.; Jin, S. M.; Lee, J. H.; Lee, I. S.; Yang, I.; Kim, J.-S.; Kim, S. K.; Cho, M.-H.; Hyeon, T., Designed Fabrication of Multifunctional Magnetic Gold Nanoshells and Their Application to Magnetic Resonance Imaging

and Photothermal Therapy. *Angewandte Chemie International Edition* **2006,** *45* (46), 7754-7758.
70. Chen, M.; Yamamuro, S.; Farrell, D.; Majetich, S. A., Gold-Coated Iron Nanoparticles for Biomedical Applications. *Journal of Applied Physics* **2003,** *93* (10), 7551-7553.
71. Xu, H. K.; Sorensen, C. M.; Klabunde, K. J.; Hadjipanayis, G. C., Aerosol Synthesis of Gadolinium Iron Garnet Particles. *Journal of Materials Research* **1992,** *7* (03), 712-716.
72. Morawski, A. M.; Winter, P. M.; Crowder, K. C.; Caruthers, S. D.; Fuhrhop, R. W.; Scott, M. J.; Robertson, J. D.; Abendschein, D. R.; Lanza, G. M.; Wickline, S. A., Targeted Nanoparticles for Quantitative Imaging of Sparse Molecular Epitopes with MRI. *Magnetic Resonance in Medicine* **2004,** *51* (3), 480-486.
73. Jung, C. W., Surface Properties of Superparamagnetic Iron Oxide MR Contrast Agents: Ferumoxides, Ferumoxtran, Ferumoxsil. *Magnetic Resonance Imaging* **1995,** *13* (5), 675-691.
74. McCarthy, J. R.; Weissleder, R., Multifunctional Magnetic Nanoparticles for Targeted Imaging and Therapy. *Advanced Drug Delivery Reviews* **2008,** *60* (11), 1241-1251.
75. Longmire, M.; Choyke, P. L.; Kobayashi, H., Clearance Properties of Nano-sized Particles and Molecules as Imaging Agents: Considerations and Caveats. *Nanomedicine (London, England)* **2008,** *3* (5), 703-717.
76. Munam, A.; Gauthier, M., Large-Scale Synthesis of Arborescent Polystyrenes. *Journal of Polymer Science Part A: Polymer Chemistry* **2008,** *46* (17), 5742-5751.
77. Gauthier, M.; Munam, A., Arborescent Polystyrene-*graft*-Poly(2-vinylpyridine) Copolymers: Solution Polyelectrolyte Behavior. *RSC Advances* **2012,** *2* (7), 3100-3108.
78. Bekturov, E. A.; Bakauova, Z. K., *Synthetic Water-Soluble Polymers in Solution: Polymeric Acids And Their Salts - Cationic Polyelectrolytes - Non-Ionic Water-Soluble Polymers - Water-Soluble Polymers*. Huthig & Wepf Verlag, Basel: Heidelberg: New York: 1986; p 241.
79. Elias, A.; Tsourkas, A., Imaging Circulating Cells and Lymphoid Tissues with Iron Oxide Nanoparticles. *Hematology Am Soc Hematol Educ Program* **2009**, 720.
80. Gayer, K. H.; Woontner, L., The Solubility of Ferrous Hydroxide and Ferric Hydroxide in Acidic and Basic Media at 25°. *The Journal of Physical Chemistry* **1956,** *60* (11), 1569-1571.
81. Senior, J.; Crawley, J. C.; Gregoriadis, G., Tissue Distribution of Liposomes Exhibiting Long Half-lives in the Circulation after Intravenous Injection. *Biochimica et Biophysica Acta* **1985,** *839* (1), 1-8.
82. Gonzales-Weimuller, M.; Zeisberger, M.; Krishnan, K. M., Size-Dependant Heating Rates of Iron Oxide Nanoparticles for Magnetic Fluid Hyperthermia. *Journal of Magnetism and Magnetic Materials* **2009,** *321* (13), 1947-1950.
83. de la Presa, P.; Luengo, Y.; Multigner, M.; Costo, R.; Morales, M. P.; Rivero, G.; Hernando, A., Study of Heating Efficiency as a Function of Concentration, Size, and

Applied Field in γ-Fe_2O_3 Nanoparticles. *The Journal of Physical Chemistry C* **2012,** *116* (48), 25602-25610.

84. Hervault, A.; Thanh, N. T. K., Magnetic Nanoparticle-Based Therapeutic Agents for Thermo-Chemotherapy Treatment of Cancer. *Nanoscale* **2014,** *6* (20), 11553-11573.
85. Tsourkas, A.; Josephson, L., Magnetic Nanoparticles. In *Molecular imaging : principles and practice*, Weissleder, R.; Ross, B. D.; Rehemtulla, A.; Gambhir, S. S., Eds. People's Madical Publishing House-USA: 2010; pp 523-541.
86. Daniel, O., Structure and Magnetism in Magnetic Nanoparticles. In *Magnetic Nanoparticles*, CRC Press: 2012; pp 3-44.
87. Somayeh, M.; Gholamreza, K.; Bahareh, A.; Amin, R., Synthesis and Application of Magnetic Nanoparticle Supported Ephedrine as a New Sorbent for Preconcentration of Trace Amounts of Pb and Cu in Water Samples. *Journal of the Brazilian Chemical Society* **2014,** *25*, 2039-2047.
88. Zhu, R.; Jiang, W.; Pu, Y.; Luo, K.; Wu, Y.; He, B.; Gu, Z., Functionalization of Magnetic Nanoparticles with Peptide Dendrimers. *Journal of Materials Chemistry* **2011,** *21* (14), 5464-5474.
89. Alonso, A.; Bastos-Arrieta, J.; Davies, G. L.; Gun'ko, Y. K.; Vigués, N.; Muñoz-Berbel, X.; Macanás, J.; Mas, J.; Muñoz, M.; Muraviev, D. N., *Ecologically Friendly Polymer-Metal and Polymer-Metal Oxide Nanocomposites for Complex Water Treatment*. 2012.
90. Ghorbani, Z.; Baharvand, H.; Nezhati, M.; Panahi, H., Magnetic Polymer Particles Modified with β-Cyclodextrin. *Journal of Polymer Research* **2013,** *20* (7), 1-8.
91. Shang, H.; Chang, W.-S.; Kan; Majetich, S. A.; Lee, G. U., Synthesis and Characterization of Paramagnetic Microparticles through Emulsion-Templated Free Radical Polymerization. *Langmuir* **2006,** *22* (6), 2516-2522.
92. Zhang, Q.; Wang, C.; Qiao, L.; Yan, H.; Liu, K., Superparamagnetic Iron Oxide Nanoparticles Coated with a Folate-Conjugated Polymer. *Journal of Materials Chemistry* **2009,** *19* (44), 8393-8402.
93. Huang, J.; Wan, S.; Guo, M.; Yan, H., Preparation of Narrow or Mono-Disperse Crosslinked Poly((meth)acrylic acid)/Iron Oxide Magnetic Microspheres. *Journal of Materials Chemistry* **2006,** *16* (46), 4535-4541.
94. Wang, L.; Luo, J.; Maye, M. M.; Fan, Q.; Rendeng, Q.; Engelhard, M. H.; Wang, C.; Lin, Y.; Zhong, C.-J., Iron Oxide-Gold Core-Shell Nanoparticles and Thin Film Assembly. *Journal of Materials Chemistry* **2005,** *15* (18), 1821-1832.
95. Arosio, P.; Thevenot, J.; Orlando, T.; Orsini, F.; Corti, M.; Mariani, M.; Bordonali, L.; Innocenti, C.; Sangregorio, C.; Oliveira, H.; Lecommandoux, S.; Lascialfari, A.; Sandre, O., Hybrid Iron Oxide-Copolymer Micelles and Vesicles as Contrast Agents for MRI: Impact of the Nanostructure on the Relaxometric Properties. *Journal of Materials Chemistry B* **2013,** *1* (39), 5317-5328.
96. Rad, A. M.; Janic, B.; Iskander, A. S.; Soltanian-Zadeh, H.; Arbab, A. S., Measurement of Quantity of Iron In Magnetically Labeled Cells: Comparison among Different UV/VIS Spectrometric Methods. *Biotechniques* **2007,** *43* (5), 627-8, 630, 632 passim.

97. Bar, G.; Thomann, Y.; Brandsch, R.; Cantow, H. J.; Whangbo, M. H., Factors Affecting the Height and Phase Images in Tapping Mode Atomic Force Microscopy. Study of Phase-Separated Polymer Blends of Poly(ethene-*co*-styrene) and Poly(2,6-dimethyl-1,4-phenylene oxide). *Langmuir* **1997,** *13* (14), 3807-3812.
98. Magonov, S. N.; Elings, V.; Whangbo, M. H., Phase Imaging and Stiffness in Tapping-Mode Atomic Force Microscopy. *Surface Science* **1997,** *375* (2–3), L385-L391.

5. Chapter 5

1. Chikazumi, S., *Physics of Ferromagnetism*. Oxford University Press: Oxford, MI, 2009.
2. Kittel, C., *Introduction to Solid State Physics*. Wiley: Hoboken, NJ, 2005.
3. Laurent, S.; Forge, D.; Port, M.; Roch, A.; Robic, C.; Vander Elst, L.; Muller, R. N., Magnetic Iron Oxide Nanoparticles: Synthesis, Stabilization, Vectorization, Physicochemical Characterizations, and Biological Applications. *Chemical Reviews* **2008,** *108* (6), 2064-2110.
4. Dormann, J. L., Le Phénomène de Superparamagnétisme. *Rev. Phys. Appl. (Paris)* **1981,** *16* (6), 275-301.
5. Stoner, E. C.; Wohlfarth, E. P., *A Mechanism of Magnetic Hysteresis in Heterogeneous Alloys*. 1948; Vol. 240, p 599-642.
6. Demortiere, A.; Panissod, P.; Pichon, B. P.; Pourroy, G.; Guillon, D.; Donnio, B.; Begin-Colin, S., Size-Dependent Properties of Magnetic Iron Oxide Nanocrystals. *Nanoscale* **2011,** *3* (1), 225-232.
7. Dormann, J. L.; D'Orazio, F.; Lucari, F.; Tronc, E.; Prené, P.; Jolivet, J. P.; Fiorani, D.; Cherkaoui, R.; Noguès, M., Thermal Variation of the Relaxation Time of the Magnetic Moment of γ-Fe_2O_3 Nanoparticles with Interparticle Interactions of Various Strengths. *Physical Review B* **1996,** *53* (21), 14291-14297.
8. Tournus, F.; Bonet, E., Magnetic Susceptibility Curves of a Nanoparticle Assembly, I: Theoretical Model and Analytical Expressions for a Single Magnetic Anisotropy Energy. *Journal of Magnetism and Magnetic Materials* **2011,** *323* (9), 1109-1117.
9. Daniel, O., Structure and Magnetism in Magnetic Nanoparticles. In *Magnetic Nanoparticles*, CRC Press: 2012; pp 3-44.
10. Foner, S., Versatile and Sensitive Vibrating Sample Magnetometer. *Review of Scientific Instruments* **1959,** *30* (7), 548-557.
11. Graham, C. D., High-Sensitivity Magnetization Measurements. *J. Mater. Sci. Technol.* **2000,** *16* (2), 97-101.
12. Chantrell, R. W.; Popplewell, J.; Charles, S., Measurements of Particle Size Distribution Parameters in Ferrofluids. *Magnetics, IEEE Transactions on* **1978,** *14* (5), 975-977.

References

13. Popplewell, J.; Sakhnini, L., The Dependence of the Physical and Magnetic Properties of Magnetic Fluids on Particle Size. *Journal of Magnetism and Magnetic Materials* **1995,** *149* (1–2), 72-78.
14. Bacri, J. C.; Perzynski, R.; Salin, D.; Cabuil, V.; Massart, R., Magnetic Colloidal Properties of Ionic Ferrofluids. *Journal of Magnetism and Magnetic Materials* **1986,** *62* (1), 36-46.
15. Storey, P., Introduction to Magnetic Resonance Imaging and Spectroscopy. In *Magnetic Resonance Imaging*, Prasad, P., Ed. Humana Press: 2006; Vol. 124, pp 3-57.
16. Geraldes, C. F. G. C.; Laurent, S., Classification and Basic Properties of Contrast Agents for Magnetic Resonance Imaging. *Contrast Media & Molecular Imaging* **2009,** *4* (1), 1-23.
17. Corot, C.; Robert, P.; Idée, J.-M.; Port, M., Recent Advances in Iron Oxide Nanocrystal Technology for Medical Imaging. *Advanced Drug Delivery Reviews* **2006,** *58* (14), 1471-1504.
18. Muller, R. N.; Vander Elst, L.; Roch, A.; Peters, J. A.; Csajbok, E.; Gillis, P.; Gossuin, Y., Relaxation by Metal-Containing Nanosystems. In *Advances in Inorganic Chemistry*, Academic Press: 2005; Vol. Volume 57, pp 239-292.
19. Gossuin, Y.; Gillis, P.; Hocq, A.; Vuong, Q. L.; Roch, A., Magnetic Resonance Relaxation Properties of Superparamagnetic Particles. *Wiley Interdisciplinary Reviews: Nanomedicine and Nanobiotechnology* **2009,** *1* (3), 299-310.
20. Hervault, A.; Thanh, N. T. K., Magnetic Nanoparticle-Based Therapeutic Agents for Thermo-Chemotherapy Treatment of Cancer. *Nanoscale* **2014,** *6* (20), 11553-11573.
21. Suto, M.; Hirota, Y.; Mamiya, H.; Fujita, A.; Kasuya, R.; Tohji, K.; Jeyadevan, B., Heat Dissipation Mechanism of Magnetite Nanoparticles in Magnetic Fluid Hyperthermia. *Journal of Magnetism and Magnetic Materials* **2009,** *321* (10), 1493-1496.
22. Atsumi, T.; Jeyadevan, B.; Sato, Y.; Tohji, K., Heating Efficiency of Magnetite Particles Exposed to AC Magnetic Field. *Journal of Magnetism and Magnetic Materials* **2007,** *310* (2, Part 3), 2841-2843.
23. Michael, L.; Claire, W.; Jean-Michel, S.; Olivier, H.; Jean-Claude, B.; Florence, G., Magnetically Induced Hyperthermia: Size-Dependent Heating Power of γ-Fe_2O_3 Nanoparticles. *Journal of Physics: Condensed Matter* **2008,** *20* (20), 204133.
24. Fortin, J.-P.; Gazeau, F.; Wilhelm, C., Intracellular Heating of Living Cells through Néel Relaxation of Magnetic Nanoparticles. *European Biophysics Journal* **2008,** *37* (2), 223-228.
25. Rosensweig, R. E., Heating Magnetic Fluid with Alternating Magnetic Field. *Journal of Magnetism and Magnetic Materials* **2002,** *252*, 370-374.
26. Hergt, R.; Dutz, S., Magnetic Particle Hyperthermia—Biophysical Limitations of a Visionary Tumour Therapy. *Journal of Magnetism and Magnetic Materials* **2007,** *311* (1), 187-192.

References

27. Sharifi, I.; Shokrollahi, H.; Amiri, S., Ferrite-Based Magnetic Nanofluids Used in Hyperthermia Applications. *Journal of Magnetism and Magnetic Materials* **2012,** *324* (6), 903-915.
28. Giri, J.; Pradhan, P.; Sriharsha, T.; Bahadur, D., Preparation and Investigation of Potentiality of Different Soft Ferrites for Hyperthermia Applications. *Journal of Applied Physics* **2005,** *97* (10), 10Q916.
29. Hergt, R.; Andra, W.; d'Ambly, C. G.; Hilger, I.; Kaiser, W. A.; Richter, U.; Schmidt, H. G., Physical Limits of Hyperthermia Using Magnetite Fine Particles. *Magnetics, IEEE Transactions on* **1998,** *34* (5), 3745-3754.
30. Hergt, R.; Hiergeist, R.; Zeisberger, M.; Glöckl, G.; Weitschies, W.; Ramirez, L. P.; Hilger, I.; Kaiser, W. A., Enhancement of AC-Losses of Magnetic Nanoparticles for Heating Applications. *Journal of Magnetism and Magnetic Materials* **2004,** *280* (2–3), 358-368.
31. Wang, X.; Gu, H.; Yang, Z., The Heating Effect of Magnetic Fluids in an Alternating Magnetic Field. *Journal of Magnetism and Magnetic Materials* **2005,** *293* (1), 334-340.
32. Mornet, S.; Vasseur, S.; Grasset, F.; Veverka, P.; Goglio, G.; Demourgues, A.; Portier, J.; Pollert, E.; Duguet, E., Magnetic Nanoparticle Design for Medical Applications. *Progress in Solid State Chemistry* **2006,** *34* (2–4), 237-247.
33. Brezovich, I. A., Low Frequency Hyperthermia: Capacitive and Ferromagnetic Thermoseed Methods. *Med. Phys. Monogr.* **1988,** *16*, 82-111.
34. Arulmurugan, R.; Jeyadevan, B.; Vaidyanathan, G.; Sendhilnathan, S., Effect of Zinc Substitution on Co–Zn and Mn–Zn Ferrite Nanoparticles Prepared by Co-precipitation. *Journal of Magnetism and Magnetic Materials* **2005,** *288*, 470-477.
35. Jang, J.-t.; Nah, H.; Lee, J.-H.; Moon, S. H.; Kim, M. G.; Cheon, J., Critical Enhancements of MRI Contrast and Hyperthermic Effects by Dopant-Controlled Magnetic Nanoparticles. *Angewandte Chemie International Edition* **2009,** *48* (7), 1234-1238.
36. Pollert, E.; Knížek, K.; Maryško, M.; Kašpar, P.; Vasseur, S.; Duguet, E., New - Tuned Magnetic Nanoparticles for Self-Controlled Hyperthermia. *Journal of Magnetism and Magnetic Materials* **2007,** *316* (2), 122-125.
37. Kolhatkar, A.; Jamison, A.; Litvinov, D.; Willson, R.; Lee, T., Tuning the Magnetic Properties of Nanoparticles. *International Journal of Molecular Sciences* **2013,** *14* (8), 15977.
38. Grasset, F.; Mornet, S.; Demourgues, A.; Portier, J.; Bonnet, J.; Vekris, A.; Duguet, E., Synthesis, Magnetic Properties, Surface Modification and Cytotoxicity Evaluation of $Y_3Fe_{5-x}Al_xO_{12}$ ($0<x<2$) Garnet Submicron Particles for Biomedical Applications. *Journal of Magnetism and Magnetic Materials* **2001,** *234* (3), 409-418.
39. Barati, M. R.; Suzuki, K.; Selomulya, C.; Garitaonandia, J. S., New-Tuned Manganese Ferrite-Based Magnetic Implant for Hyperthermia Therapy Application. *Magnetics, IEEE Transactions on* **2013,** *49* (7), 3460-3463.

40. Yao, A.; Ai, F.; Wang, D.; Huang, W.; Zhang, X., Synthesis, Characterization and *In Vitro* Cytotoxicity of Self-Regulating Magnetic Implant Material for Hyperthermia Application. *Materials Science and Engineering: C* **2009,** *29* (8), 2525-2529.
41. Ferk, G.; Drofenik, M.; Lisjak, D.; Hamler, A.; Jagličić, Z.; Makovec, D., Synthesis and Characterization of $Mg_{1+x}Fe_{2-2x}Ti_xO_4$ Nanoparticles with an Adjustable Curie Point. *Journal of Magnetism and Magnetic Materials* **2014,** *350*, 124-128.
42. Chung, S. H.; Hoffmann, A.; Bader, S. D.; Liu, C.; Kay, B.; Makowski, L.; Chen, L., Biological Sensors Based on Brownian Relaxation of Magnetic Nanoparticles. *Applied Physics Letters* **2004,** *85* (14), 2971-2973.
43. Jeun, M.; Lee, S.; Kyeong Kang, J.; Tomitaka, A.; Wook Kang, K.; Il Kim, Y.; Takemura, Y.; Chung, K.-W.; Kwak, J.; Bae, S., Physical Limits of Pure Superparamagnetic Fe_3O_4 Nanoparticles for a Local Hyperthermia Agent in Nanomedicine. *Applied Physics Letters* **2012,** *100* (9), 092406.
44. Lartigue, L.; Innocenti, C.; Kalaivani, T.; Awwad, A.; Sanchez Duque, M. d. M.; Guari, Y.; Larionova, J.; Guérin, C.; Montero, J.-L. G.; Barragan-Montero, V.; Arosio, P.; Lascialfari, A.; Gatteschi, D.; Sangregorio, C., Water-Dispersible Sugar-Coated Iron Oxide Nanoparticles. An Evaluation of their Relaxometric and Magnetic Hyperthermia Properties. *Journal of the American Chemical Society* **2011,** *133* (27), 10459-10472.
45. Gonzales-Weimuller, M.; Zeisberger, M.; Krishnan, K. M., Size-Dependant Heating Rates of Iron Oxide Nanoparticles for Magnetic Fluid Hyperthermia. *Journal of Magnetism and Magnetic Materials* **2009,** *321* (13), 1947-1950.
46. de la Presa, P.; Luengo, Y.; Multigner, M.; Costo, R.; Morales, M. P.; Rivero, G.; Hernando, A., Study of Heating Efficiency as a Function of Concentration, Size, and Applied Field in γ-Fe_2O_3 Nanoparticles. *The Journal of Physical Chemistry C* **2012,** *116* (48), 25602-25610.
47. Carrey, J.; Mehdaoui, B.; Respaud, M., Simple Models for Dynamic Hysteresis Loop Calculations of Magnetic Single-Domain Nanoparticles: Application to Magnetic Hyperthermia Optimization. *Journal of Applied Physics* **2011,** *109* (8), 083921.
48. Khandhar, A.; Ferguson, R. M.; Simon, J. A.; Krishnan, K. M., Tailored Magnetic Nanoparticles for Optimizing Magnetic Fluid Hyperthermia. *Journal of Biomedical Materials Research. Part a* **2012,** *100* (3), 728-737.
49. Garaio, E.; Sandre, O.; Collantes, J.-M.; Garcia, J. A.; Mornet, S.; Plazaola, F., Specific Absorption Rate Dependence on Temperature in Magnetic Field Hyperthermia Measured by Dynamic Hysteresis Losses (AC Magnetometry). *Nanotechnology* **2015,** *26* (1), 015704.
50. Fortin, J.-P.; Wilhelm, C.; Servais, J.; Ménager, C.; Bacri, J.-C.; Gazeau, F., Size-Sorted Anionic Iron Oxide Nanomagnets as Colloidal Mediators for Magnetic Hyperthermia. *Journal of the American Chemical Society* **2007,** *129* (9), 2628-2635.
51. Dutz, S.; Clement, J. H.; Eberbeck, D.; Gelbrich, T.; Hergt, R.; Müller, R.; Wotschadlo, J.; Zeisberger, M., Ferrofluids of Magnetic Multicore Nanoparticles for Biomedical Applications. *Journal of Magnetism and Magnetic Materials* **2009,** *321* (10), 1501-1504.

52. Boskovic, M.; Goya, G. F.; Vranjes-Djuric, S.; Jovic, N.; Jancar, B.; Antic, B., Influence of Size Distribution and Field Amplitude on Specific Loss Power. *Journal of Applied Physics* **2015,** *117* (10), 103903.
53. Guardia, P.; Di Corato, R.; Lartigue, L.; Wilhelm, C.; Espinosa, A.; Garcia-Hernandez, M.; Gazeau, F.; Manna, L.; Pellegrino, T., Water-Soluble Iron Oxide Nanocubes with High Values of Specific Absorption Rate for Cancer Cell Hyperthermia Treatment. *ACS Nano* **2012,** *6* (4), 3080-3091.
54. Noh, S.-h.; Na, W.; Jang, J.-t.; Lee, J.-H.; Lee, E. J.; Moon, S. H.; Lim, Y.; Shin, J.-S.; Cheon, J., Nanoscale Magnetism Control *via* Surface and Exchange Anisotropy for Optimized Ferrimagnetic Hysteresis. *Nano Letters* **2012,** *12* (7), 3716-3721.
55. Song, M.; Zhang, Y.; Hu, S.; Song, L.; Dong, J.; Chen, Z.; Gu, N., Influence of Morphology and Surface Exchange Reaction on Magnetic Properties of Monodisperse Magnetite Nanoparticles. *Colloids and Surfaces A: Physicochemical and Engineering Aspects* **2012,** *408*, 114-121.
56. Hugounenq, P.; Levy, M.; Alloyeau, D.; Lartigue, L.; Dubois, E.; Cabuil, V.; Ricolleau, C.; Roux, S.; Wilhelm, C.; Gazeau, F.; Bazzi, R., Iron Oxide Monocrystalline Nanoflowers for Highly Efficient Magnetic Hyperthermia. *The Journal of Physical Chemistry C* **2012,** *116* (29), 15702-15712.
57. Walter, A.; Billotey, C.; Garofalo, A.; Ulhaq-Bouillet, C.; Lefèvre, C.; Taleb, J.; Laurent, S.; Vander Elst, L.; Muller, R. N.; Lartigue, L.; Gazeau, F.; Felder-Flesch, D.; Begin-Colin, S., Mastering the Shape and Composition of Dendronized Iron Oxide Nanoparticles to Tailor Magnetic Resonance Imaging and Hyperthermia. *Chemistry of Materials* **2014,** *26* (18), 5252-5264.
58. Bellizzi, G.; Bucci, O. M., On the Optimal Choice of the Exposure Conditions and the Nanoparticle Features in Magnetic Nanoparticle Hyperthermia. *International Journal of Hyperthermia* **2010,** *26* (4), 389-403.
59. Larumbe, S.; Gómez-Polo, C.; Pérez-Landazábal, J. I.; Pastor, J. M., Effect of a SiO_2 Coating on the Magnetic Properties of Fe_3O_4 Nanoparticles. *Journal of Physics: Condensed Matter* **2012,** *24* (26), 266007.
60. Liu, X. L.; Fan, H. M.; Yi, J. B.; Yang, Y.; Choo, E. S. G.; Xue, J. M.; Fan, D. D.; Ding, J., Optimization of Surface Coating on Fe_3O_4 Nanoparticles for High Performance Magnetic Hyperthermia Agents. *Journal of Materials Chemistry* **2012,** *22* (17), 8235-8244.
61. Shete, P. B.; Patil, R. M.; Thorat, N. D.; Prasad, A.; Ningthoujam, R. S.; Ghosh, S. J.; Pawar, S. H., Magnetic Chitosan Nanocomposite for Hyperthermia Therapy Application: Preparation, Characterization and *In Vitro* Experiments. *Applied Surface Science* **2014,** *288*, 149-157.
62. Thorat, N. D.; Khot, V. M.; Salunkhe, A. B.; Ningthoujam, R. S.; Pawar, S. H., Functionalization of $La_{0.7}Sr_{0.3}MnO_3$ Nanoparticles With Polymer: Studies on Enhanced Hyperthermia and Biocompatibility Properties for Biomedical Applications. *Colloids and Surfaces B: Biointerfaces* **2013,** *104*, 40-47.
63. Thorat, N. D.; Khot, V. M.; Salunkhe, A. B.; Prasad, A. I.; Ningthoujam, R. S.; Pawar, S. H., Surface Functionalized LSMO Nanoparticles with Improved Colloidal

Stability for Hyperthermia Applications. *Journal of Physics D: Applied Physics* **2013,** *46* (10), 105003.

64. Di Corato, R.; Espinosa, A.; Lartigue, L.; Tharaud, M.; Chat, S.; Pellegrino, T.; Ménager, C.; Gazeau, F.; Wilhelm, C., Magnetic Hyperthermia Efficiency in the Cellular Environment for Different Nanoparticle Designs. *Biomaterials* **2014,** *35* (24), 6400-6411.
65. Kallumadil, M.; Tada, M.; Nakagawa, T.; Abe, M.; Southern, P.; Pankhurst, Q. A., Suitability of Commercial Colloids for Magnetic Hyperthermia. *Journal of Magnetism and Magnetic Materials* **2009,** *321* (10), 1509-1513.
66. Roch, A.; Muller, R. N.; Gillis, P., Theory of Proton Relaxation Induced by Superparamagnetic Particles. *The Journal of Chemical Physics* **1999,** *110* (11), 5403-5411.
67. Gillis, P.; Roch, A.; Brooks, R. A., Corrected Equations for Susceptibility-Induced T_2-Shortening. *Journal of Magnetic Resonance* **1999,** *137* (2), 402-407.
68. Boutry, S.; Forge, D.; Burtea, C.; Mahieu, I.; Murariu, O.; Laurent, S.; Vander Elst, L.; Muller, R. N., How to Quantify Iron in an Aqueous or Biological Matrix: A Technical Note. *Contrast Media & Molecular Imaging* **2009,** *4* (6), 299-304.
69. Arosio, P.; Thevenot, J.; Orlando, T.; Orsini, F.; Corti, M.; Mariani, M.; Bordonali, L.; Innocenti, C.; Sangregorio, C.; Oliveira, H.; Lecommandoux, S.; Lascialfari, A.; Sandre, O., Hybrid Iron Oxide-Copolymer Micelles and Vesicles as Contrast Agents for MRI: Impact of the Nanostructure on the Relaxometric Properties. *Journal of Materials Chemistry B* **2013,** *1* (39), 5317-5328.
70. LaMer, V. K.; Dinegar, R. H., Theory, Production and Mechanism of Formation of Monodispersed Hydrosols. *Journal of the American Chemical Society* **1950,** *72* (11), 4847-4854.
71. Baaziz, W.; Pichon, B. P.; Fleutot, S.; Liu, Y.; Lefevre, C.; Greneche, J.-M.; Toumi, M.; Mhiri, T.; Begin-Colin, S., Magnetic Iron Oxide Nanoparticles: Reproducible Tuning of the Size and Nanosized-Dependent Composition, Defects, and Spin Canting. *The Journal of Physical Chemistry C* **2014,** *118* (7), 3795-3810.
72. Meledandri, C. J.; Stolarczyk, J. K.; Ghosh, S.; Brougham, D. F., Nonaqueous Magnetic Nanoparticle Suspensions with Controlled Particle Size and Nuclear Magnetic Resonance Properties. *Langmuir* **2008,** *24* (24), 14159-14165.
73. Jana, N. R.; Chen, Y.; Peng, X., Size- and Shape-Controlled Magnetic (Cr, Mn, Fe, Co, Ni) Oxide Nanocrystals via a Simple and General Approach. *Chemistry of Materials* **2004,** *16* (20), 3931-3935.
74. Chen, Z., Size and Shape Controllable Synthesis of Monodisperse Iron Oxide Nanoparticles by Thermal Decomposition of Iron Oleate Complex. *Synthesis and Reactivity in Inorganic, Metal-Organic, and Nano-Metal Chemistry* **2012,** *42* (7), 1040-1046.
75. Zhu, Y.; Jiang, F. Y.; Chen, K.; Kang, F.; Tang, Z. K., Size-Controlled Synthesis of Monodisperse Superparamagnetic Iron Oxide Nanoparticles. *Journal of Alloys and Compounds* **2011,** *509* (34), 8549-8553.

76. Bee, A.; Massart, R.; Neveu, S., Synthesis of Very Fine Maghemite Particles. *Journal of Magnetism and Magnetic Materials* **1995,** *149* (1–2), 6-9.
77. Morales, M. P.; Serna, C. J.; Bødker, F.; Mørup, S., Spin Canting Due to Structural Disorder in Maghemite. *Journal of Physics: Condensed Matter* **1997,** *9* (25), 5461.
78. Rodríguez-Carvajal, J., Recent Advances in Magnetic Structure Determination by Neutron Powder Diffraction. *Physica B: Condensed Matter* **1993,** *192* (1–2), 55-69.
79. Vichery, C.; Maurin, I.; Bonville, P.; Boilot, J.-P.; Gacoin, T., Influence of Protected Annealing on the Magnetic Properties of γ-Fe_2O_3 Nanoparticles. *The Journal of Physical Chemistry C* **2012,** *116* (30), 16311-16318.
80. Casula, M. F.; Floris, P.; Innocenti, C.; Lascialfari, A.; Marinone, M.; Corti, M.; Sperling, R. A.; Parak, W. J.; Sangregorio, C., Magnetic Resonance Imaging Contrast Agents Based on Iron Oxide Superparamagnetic Ferrofluids. *Chemistry of Materials* **2010,** *22* (5), 1739-1748.
81. Tromsdorf, U. I.; Bruns, O. T.; Salmen, S. C.; Beisiegel, U.; Weller, H., A Highly Effective, Nontoxic T1 MR Contrast Agent Based on Ultrasmall PEGylated Iron Oxide Nanoparticles. *Nano Letters* **2009,** *9* (12), 4434-4440.
82. Ninjbadgar, T.; Brougham, D. F., Epoxy Ring Opening Phase Transfer as a General Route to Water Dispersible Superparamagnetic Fe_3O_4 Nanoparticles and Their Application as Positive MRI Contrast Agents. *Advanced Functional Materials* **2011,** *21* (24), 4769-4775.
83. Hannecart, A.; Stanicki, D.; Vander Elst, L.; Muller, R. N.; Lecommandoux, S.; Thevenot, J.; Bonduelle, C.; Trotier, A.; Massot, P.; Miraux, S.; Sandre, O.; Laurent, S., Nano-Thermometers with Thermo-Sensitive Polymer Grafted USPIOs Behaving as Positive Contrast Agents in Low-Field MRI. *Nanoscale* **2015,** *7* (8), 3754-3767.
84. Roch, A.; Gossuin, Y.; Muller, R. N.; Gillis, P., Superparamagnetic Colloid Suspensions: Water Magnetic Relaxation and Clustering. *Journal of Magnetism and Magnetic Materials* **2005,** *293* (1), 532-539.
85. Jung, C. W.; Jacobs, P., Physical and Chemical Properties of Superparamagnetic Iron Oxide MR Contrast Agents: Ferumoxides, Ferumoxtran, Ferumoxsil. *Magnetic Resonance Imaging* **1995,** *13* (5), 661-674.
86. Wang, Y.; Ng, Y. W.; Chen, Y.; Shuter, B.; Yi, J.; Ding, J.; Wang, S. c.; Feng, S. S., Formulation of Superparamagnetic Iron Oxides by Nanoparticles of Biodegradable Polymers for Magnetic Resonance Imaging. *Advanced Functional Materials* **2008,** *18* (2), 308-318.
87. Koenig, S. H.; Kellar, K. E.; Fujii, D. K.; Gunther, W. H.; Briley-Saebo, K.; Spiller, M., Three Types of Physical Measurements Needed to Characterize Iron Oxide Nanoparticles for MRI and MRA: Magnetization, Relaxometry, and Light Scattering. *Acad Radiol* **2002,** *9 Suppl 1*, S5-10.
88. Vuong, Q. L.; Berret, J.-F.; Fresnais, J.; Gossuin, Y.; Sandre, O., A Universal Scaling Law to Predict the Efficiency of Magnetic Nanoparticles as MRI T_2-Contrast Agents. *Advanced Healthcare Materials* **2012,** *1* (4), 502-512.

References

89. Laurent, S.; Bridot, J.-L.; Elst, L. V.; Muller, R. N., Magnetic Iron Oxide Nanoparticles for Biomedical Applications. *Future Medicinal Chemistry* **2010,** *2* (3), 427-449.
90. Carron, S.; Bloemen, M.; Vander Elst, L.; Laurent, S.; Verbiest, T.; Parac-Vogt, T. N., Potential Theranostic and Multimodal Iron Oxide Nanoparticles Decorated with Rhenium-Bipyridine and -Phenanthroline Complexes. *Journal of Materials Chemistry B* **2015**.
91. Miguel, O. B.; Gossuin, Y.; Morales, M. P.; Gillis, P.; Muller, R. N.; Veintemillas-Verdaguer, S., Comparative Analysis of the 1H NMR Relaxation Enhancement Produced by Iron Oxide And Core-Shell Iron–Iron Oxide Nanoparticles. *Magnetic Resonance Imaging* **2007,** *25* (10), 1437-1441.
92. Pinho, S. L. C.; Laurent, S.; Rocha, J.; Roch, A.; Delville, M.-H.; Mornet, S.; Carlos, L. D.; Vander Elst, L.; Muller, R. N.; Geraldes, C. F. G. C., Relaxometric Studies of γ-Fe_2O_3@SiO_2 Core Shell Nanoparticles: When the Coating Matters. *The Journal of Physical Chemistry C* **2012,** *116* (3), 2285-2291.
93. Laurent, S.; Nicotra, C.; Gossuin, Y.; Roch, A.; Ouakssim, A.; Vander Elst, L.; Cornant, M.; Soleil, P.; Muller, R. N., Influence of the Length of the Coating Molecules on the Nuclear Magnetic Relaxivity of Superparamagnetic Colloids. *physica status solidi (c)* **2004,** *1* (12), 3644-3650.
94. Sharifi, S.; Daghighi, S.; Motazacker, M. M.; Badlou, B.; Sanjabi, B.; Akbarkhanzadeh, A.; Rowshani, A. T.; Laurent, S.; Peppelenbosch, M. P.; Rezaee, F., Superparamagnetic Iron Oxide Nanoparticles Alter Expression of Obesity and T2D-Associated Risk Genes in Human Adipocytes. *Sci. Rep.* **2013,** *3*.
95. Laurent, S.; Elst, L.; Roch, A.; Muller, R., Structure, Synthesis and Characterization of Contrast Agents for Magnetic Resonance Molecular Imaging. In *NMR-MRI, μSR and Mössbauer Spectroscopies in Molecular Magnets*, Springer Milan: 2007; pp 71-87.
96. Ouakssim, A.; Fastrez, S.; Roch, A.; Laurent, S.; Gossuin, Y.; Piérart, C.; Vander Elst, L.; Muller, R. N., Control of the Synthesis of Magnetic Fluids by Relaxometry and Magnetometry. *Journal of Magnetism and Magnetic Materials* **2004,** *272–276, Supplement*, E1711-E1713.
97. Iacob, N.; Schinteie, G.; Palade, P.; Ticos, C. M.; Kuncser, V., Stepped Heating Procedure for Experimental SAR Evaluation of Ferrofluids. *The European Physical Journal E* **2015,** *38* (6), 1-6.
98. Bordelon, D. E.; Cornejo, C.; Grüttner, C.; Westphal, F.; DeWeese, T. L.; Ivkov, R., Magnetic Nanoparticle Heating Efficiency Reveals Magneto-Structural Differences When Characterized with Wide Ranging and High Amplitude Alternating Magnetic Fields. *Journal of Applied Physics* **2011,** *109* (12), 124904.
99. Hergt, R.; Hiergeist, R.; Hilger, I.; Kaiser, W. A.; Lapatnikov, Y.; Margel, S.; Richter, U., Maghemite Nanoparticles with Very High AC-Losses for Application in RF-Magnetic Hyperthermia. *Journal of Magnetism and Magnetic Materials* **2004,** *270* (3), 345-357.

References

100. Hiergeist, R.; Andrä, W.; Buske, N.; Hergt, R.; Hilger, I.; Richter, U.; Kaiser, W., Application of Magnetite Ferrofluids for Hyperthermia. *Journal of Magnetism and Magnetic Materials* **1999,** *201* (1–3), 420-422.
101. Sadat, M. E.; Patel, R.; Sookoor, J.; Bud'ko, S. L.; Ewing, R. C.; Zhang, J.; Xu, H.; Wang, Y.; Pauletti, G. M.; Mast, D. B.; Shi, D., Effect of Spatial Confinement on Magnetic Hyperthermia *via* Dipolar Interactions in Fe_3O_4 Nanoparticles for Biomedical Applications. *Materials Science and Engineering: C* **2014,** *42*, 52-63.
102. Lartigue, L.; Hugounenq, P.; Alloyeau, D.; Clarke, S. P.; Lévy, M.; Bacri, J.-C.; Bazzi, R.; Brougham, D. F.; Wilhelm, C.; Gazeau, F., Cooperative Organization in Iron Oxide Multi-Core Nanoparticles Potentiates Their Efficiency as Heating Mediators and MRI Contrast Agents. *ACS Nano* **2012,** *6* (12), 10935-10949.
103. Materia, M. E.; Guardia, P.; Sathya, A.; Pernia Leal, M.; Marotta, R.; Di Corato, R.; Pellegrino, T., Mesoscale Assemblies of Iron Oxide Nanocubes as Heat Mediators and Image Contrast Agents. *Langmuir* **2015,** *31* (2), 808-816.
104. Dennis, C. L.; Jackson, A. J.; Borchers, J. A.; Hoopes, P. J.; Strawbridge, R.; Foreman, A. R.; Lierop, J. v.; Grüttner, C.; Ivkov, R., Nearly Complete Regression of Tumors *via* Collective Behavior of Magnetic Nanoparticles in Hyperthermia. *Nanotechnology* **2009,** *20* (39), 395103.
105. Maity, D.; Chandrasekharan, P.; Yang, C.-T.; Chuang, K.-H.; Shuter, B.; Xue, J.-M.; Ding, J.; Feng, S.-S., Facile Synthesis of Water-Stable Magnetite Nanoparticles for Clinical MRI and Magnetic Hyperthermia Applications. *Nanomedicine* **2010,** *5* (10), 1571-1584.
106. Yuan, Y.; Borca-Tasciuc, D., Anomalously High Specific Absorption Rate in Bioaffine Ligand-Coated Iron Oxide Nanoparticle Suspensions. *Magnetics, IEEE Transactions on* **2013,** *49* (1), 263-268.
107. de la Presa, P.; Luengo, Y.; Velasco, V.; Morales, M. P.; Iglesias, M.; Veintemillas-Verdaguer, S.; Crespo, P.; Hernando, A., Particle Interactions in Liquid Magnetic Colloids by Zero Field Cooled Measurements: Effects on Heating Efficiency. *The Journal of Physical Chemistry C* **2015,** *119* (20), 11022-11030.
108. Pineiro-Redondo, Y.; Banobre-Lopez, M.; Pardinas-Blanco, I.; Goya, G.; Lopez-Quintela, M. A.; Rivas, J., The influence of colloidal parameters on the specific power absorption of PAA-coated magnetite nanoparticles. *Nanoscale Research Letters* **2011,** *6* (1), 383.

References

6. Chapter 6

1. Oberdörster, G.; Oberdörster, E.; Oberdörster, J., Nanotoxicology: An Emerging Discipline Evolving from Studies of Ultrafine Particles. *Environmental Health Perspectives* **2005,** *113* (7), 823-839.
2. Prasad, G. L., Biomedical Applications of Nanoparticles. In *Safety of Nanoparticles*, Webster, T. J., Ed. Springer New York: 2009; pp 89-109.
3. Pouton, C. W.; Seymour, L. W., Key Issues in Non-Viral Gene Delivery. *Advanced Drug Delivery Reviews* **2001,** *46* (1–3), 187-203.
4. Bally, M. B.; Harvie, P.; Wong, F. M. P.; Kong, S.; Wasan, E. K.; Reimer, D. L., Biological Barriers to Cellular Delivery of Lipid-Based DNA Carriers. *Advanced Drug Delivery Reviews* **1999,** *38* (3), 291-315.
5. Freshney, R. I., Cytotoxicity. In *Culture of Animal Cells*, John Wiley & Sons, Inc.: 2010; pp 365-381.
6. Cory, A. H.; Owen, T. C.; Barltrop, J. A.; Cory, J. G., Use of an Aqueous Soluble Tetrazolium/Formazan Assay for Cell Growth Assays in Culture. *Cancer communications* **1991,** *3* (7), 207-212.
7. Berridge, M. V.; Herst, P. M.; Tan, A. S., Tetrazolium Dyes as Tools in Cell Biology: New Insights into Their Cellular Reduction. In *Biotechnology Annual Review*, El-Gewely, M. R., Ed. Elsevier: 2005; Vol. Volume 11, pp 127-152.
8. Riss, T.; Moravec, R.; Niles, A.; Benink, H.; Worzella, T.; Minor, L., *Cell Viability Assays*. Bethesda (MD): Eli Lilly & Company and the National Center for Advancing Translational Sciences: 2013.
9. Jin, H.; Heller, D. A.; Sharma, R.; Strano, M. S., Size-Dependent Cellular Uptake and Expulsion of Single-Walled Carbon Nanotubes: Single Particle Tracking and a Generic Uptake Model for Nanoparticles. *ACS Nano* **2009,** *3* (1), 149-158.
10. Nel, A. E.; Madler, L.; Velegol, D.; Xia, T.; Hoek, E. M. V.; Somasundaran, P.; Klaessig, F.; Castranova, V.; Thompson, M., Understanding Biophysicochemical Interactions at the Nano-Bio Interface. *Nat Mater* **2009,** *8* (7), 543-557.
11. Verma, A.; Stellacci, F., Effect of Surface Properties on Nanoparticle–Cell Interactions. *Small* **2010,** *6* (1), 12-21.
12. Mailänder, V.; Landfester, K., Interaction of Nanoparticles with Cells. *Biomacromolecules* **2009,** *10* (9), 2379-2400.
13. Liu, Y.; Jiao, F.; Qiu, Y.; Li, W.; Lao, F.; Zhou, G.; Sun, B.; Xing, G.; Dong, J.; Zhao, Y.; Chai, Z.; Chen, C., The Effect of $Gd@C_{82}(OH)_{22}$ Nanoparticles on the Release of Th1/Th2 Cytokines and Induction of TNF-α Mediated Cellular Immunity. *Biomaterials* **2009,** *30* (23–24), 3934-3945.
14. Harush-Frenkel, O.; Debotton, N.; Benita, S.; Altschuler, Y., Targeting of Nanoparticles to the Clathrin-Mediated Endocytic Pathway. *Biochemical and Biophysical Research Communications* **2007,** *353* (1), 26-32.

References

15. Rappoport, J. Z., Focusing on Clathrin-Mediated Endocytosis. *Biochemmical Journal* **2008,** *412*, 415-423.
16. Chithrani, B. D.; Chan, W. C. W., Elucidating the Mechanism of Cellular Uptake and Removal of Protein-Coated Gold Nanoparticles of Different Sizes and Shapes. *Nano Letters* **2007,** *7* (6), 1542-1550.
17. Gratton, S. E. A.; Ropp, P. A.; Pohlhaus, P. D.; Luft, J. C.; Madden, V. J.; Napier, M. E.; DeSimone, J. M., The Effect of Particle Design on Cellular Internalization Pathways. *Proceedings of the National Academy of Sciences* **2008,** *105* (33), 11613-11618.
18. Dasgupta, S.; Auth, T.; Gompper, G., Shape and Orientation Matter for the Cellular Uptake of Nonspherical Particles. *Nano Letters* **2014,** *14* (2), 687-693.
19. Zhang, L. W.; Monteiro-Riviere, N. A., Mechanisms of Quantum Dot Nanoparticle Cellular Uptake. *Toxicological Sciences* **2009,** *110* (1), 138-155.
20. Asin, L.; Goya, G. F.; Tres, A.; Ibarra, M. R., Induced Cell Toxicity Originates Dendritic Cell Death Following Magnetic Hyperthermia Treatment. *Cell Death Dis* **2013,** *4*, e596.
21. Sanchez, C.; El Hajj Diab, D.; Connord, V.; Clerc, P.; Meunier, E.; Pipy, B.; Payré, B.; Tan, R. P.; Gougeon, M.; Carrey, J.; Gigoux, V.; Fourmy, D., Targeting a G-Protein-Coupled Receptor Overexpressed in Endocrine Tumors by Magnetic Nanoparticles To Induce Cell Death. *ACS Nano* **2014,** *8* (2), 1350-1363.
22. Connord, V.; Clerc, P.; Hallali, N.; El Hajj Diab, D.; Fourmy, D.; Gigoux, V.; Carrey, J., Real-Time Analysis of Magnetic Hyperthermia Experiments on Living Cells under a Confocal Microscope. *Small* **2015,** *11* (20), 2437-2445.
23. LifeTechnologies, L929 Cells. Cell Line database: LifeTechnologies: 2014; Vol. Technical resources/Cell Lines/L/L929 Cells.
24. Jamur, M.; Oliver, C., Permeabilization of Cell Membranes. In *Immunocytochemical Methods and Protocols*, Oliver, C.; Jamur, M. C., Eds. Humana Press: 2010; Vol. 588, pp 63-66.
25. Fortin, J.-P.; Gazeau, F.; Wilhelm, C., Intracellular Heating of Living Cells through Néel Relaxation of Magnetic Nanoparticles. *European Biophysics Journal* **2008,** *37* (2), 223-228.
26. Hermanson, G. T., Chapter 2 - The Chemistry of Reactive Groups. In *Bioconjugate Techniques (Second Edition)*, Hermanson, G. T., Ed. Academic Press: New York, 2008; pp 169-212.
27. Sjöback, R.; Nygren, J.; Kubista, M., Absorption and Fluorescence Properties of Fluorescein. *Spectrochimica Acta Part A: Molecular and Biomolecular Spectroscopy* **1995,** *51* (6), L7-L21.
28. Margulies, D.; Melman, G.; Shanzer, A., Fluorescein as a Model Molecular Calculator with Reset Capability. *Nature Materials* **2005,** *4* (10), 768-771.
29. Imhof, A.; Megens, M.; Engelberts, J. J.; de Lang, D. T. N.; Sprik, R.; Vos, W. L., Spectroscopy of Fluorescein (FITC) Dyed Colloidal Silica Spheres. *The Journal of Physical Chemistry B* **1999,** *103* (9), 1408-1415.

30. Hungerford, G.; Benesch, J.; Mano, J. F.; Reis, R. L., Effect of the Labelling Ratio on the Photophysics of Fluorescein Isothiocyanate (FITC) Conjugated to Bovine Serum Albumin. *Photochemical & Photobiological Sciences* **2007,** *6* (2), 152-158.
31. Monti, D. M.; Guarnieri, D.; Napolitano, G.; Piccoli, R.; Netti, P.; Fusco, S.; Arciello, A., Biocompatibility, Uptake and Endocytosis Pathways of Polystyrene Nanoparticles in Primary Human Renal Epithelial Cells. *Journal of Biotechnology* **2015,** *193*, 3-10.
32. Li, G.; Shen, J.; Zhu, Y., Study of Pyridinium-type Functional Polymers. II. Antibacterial Activity of Soluble Pyridinium-type Polymers. *Journal of Applied Polymer Science* **1998,** *67* (10), 1761-1768.
33. Stratton, T. R.; Applegate, B. M.; Youngblood, J. P., Effect of Steric Hindrance on the Properties of Antibacterial and Biocompatible Copolymers. *Biomacromolecules* **2010,** *12* (1), 50-56.
34. Stratton, T. R.; Howarter, J. A.; Allison, B. C.; Applegate, B. M.; Youngblood, J. P., Structure−Activity Relationships of Antibacterial and Biocompatible Copolymers. *Biomacromolecules* **2010,** *11* (5), 1286-1290.
35. Phillips, R., Era of New Biomaterials in Esthetic Dentistry. *Journal of the American Dental Association* **1987,** *Dec*, 7E-12E.
36. Prati, C.; Pashley, D. H.; Montanari, G., Hydrostatic Intrapulpal Pressure and Bond Strength of Bonding Systems. *Dental Materials* **1991,** *7* (1), 54-58.
37. Pergande, G.; Keipert, S.; Klatt, A., Antiglaucoma Ophthalmic Agents with Prolonged Action Based on Macromolecular Excipients. 2. *In Vivo* Studies. *Die Pharmazie* **1990,** *45* (8), 587-91.
38. Pergande, G.; Keipert, S., Antiglaucoma Ophthalmic Agents with Prolonged Action Based on Macromolecular Adjuncts. 1. *In Vitro* Studies. *Pharmazie* **1990,** *45* (8), 582-586.
39. Lasser, A., Use of a Keratolytic Formulation in a Polyacrylic Vehicle to Treat Warts in Children and Adolescents. *Cutis* **1987,** *39* (4), 354.
40. Morimoto, K.; Iwamoto, T.; Morisaka, K., Possible Mechanisms for the Enhancement of Rectal Absorption of Hydrophilic Drugs and Polypeptides by Aqueous Polyacrylic Acid Gel. *Journal of Pharmacobio-Dynamics* **1987,** *10*, 85-91.
41. Bhanja, R.; Pal, T., *In Vitro* Diffusion Kinetics of Salbutamol Sulphate from Microcapsules Coated with Eudragit RS 100. *Bollettino Chimico Farmaceutico* **1989,** *128* (9), 281-283.
42. Seldon, H. L.; Dahm, M. C.; Clark, G. M.; Crowe, S., Silastic with Polyacrylic Acid Filler: Swelling Properties, Biocompatibility and Potential Use in Cochlear Implants. *Biomaterials* **1994,** *15* (14), 1161-1169.
43. Mahmoudi, M.; Simchi, A.; Imani, M., Recent Advances in Surface Engineering of Superparamagnetic Iron Oxide Nanoparticles for Biomedical Applications. *Journal of the Iranian Chemical Society* **2010,** *7* (2), S1-S27.
44. Burugapalli, K.; Koul, V.; Dinda, A. K., Effect of Composition of Interpenetrating Polymer Network Hydrogels Based on Poly(acrylic acid) and Gelatin on Tissue Response: A Quantitative *In Vivo* Study. *Journal of Biomedical Materials Research Part A* **2004,** *68A* (2), 210-218.

45. Yu, W. W.; Qu, L.; Guo, W.; Peng, X., Experimental Determination of the Extinction Coefficient of CdTe, CdSe, and CdS Nanocrystals. *Chemistry of Materials* **2003,** *15* (14), 2854-2860.
46. Safi, M.; Sarrouj, H.; Sandre, O.; Mignet, N.; Berret, J. F., Interactions Between Sub-10-nm Iron and Cerium Oxide Nanoparticles and 3T3 Fibroblasts: The Role of the Coating and Aggregation State. *Nanotechnology* **2010,** *21* (14), 145103.
47. Hoogenboom, R.; Popescu, D.; Steinhauer, W.; Keul, H.; Möller, M., Nitroxide-Mediated Copolymerization of 2-Hydroxyethyl Acrylate and 2-Hydroxypropyl Acrylate: Copolymerization Kinetics and Thermoresponsive Properties. *Macromolecular Rapid Communications* **2009,** *30* (23), 2042-2048.
48. Lin, M.; Xu, P.; Zhong, W., Preparation, Characterization, and Release Behavior of Aspirin-Loaded Poly(2-hydroxyethyl acrylate)/Silica Hydrogels. *Journal of Biomedical Materials Research Part B: Applied Biomaterials* **2012,** *100B* (4), 1114-1120.
49. McAllister, K.; Sazani, P.; Adam, M.; Cho, M. J.; Rubinstein, M.; Samulski, R. J.; DeSimone, J. M., Polymeric Nanogels Produced via Inverse Microemulsion Polymerization as Potential Gene and Antisense Delivery Agents. *Journal of the American Chemical Society* **2002,** *124* (51), 15198-15207.
50. Martínez-Ramos, C.; Lainez, S.; Sancho, F.; García Esparza, M. A.; Planells-Cases, R.; García Verdugo, J. M.; Gómez Ribelles, J. L.; Salmerón Sánchez, M.; Monleón Pradas, M.; Barcia, J. A.; Soria, J. M., Differentiation of Postnatal Neural Stem Cells into Glia and Functional Neurons on Laminin-Coated Polymeric Substrates. *Tissue Engineering Part A* **2008,** *14* (8), 1365-1375.
51. Vallés Lluch, A.; Campillo Fernández, A.; Gallego Ferrer, G.; Monleón Pradas, M., Bioactive Scaffolds Mimicking Natural Dentin Structure. *Journal of Biomedical Materials Research Part B: Applied Biomaterials* **2009,** *90B* (1), 182-194.
52. Arun, A.; Reddy, B. S. R., *In Vitro* Drug Release Studies of 2-Hydroxyethyl Acrylate or 2-Hydroxypropyl Methacrylate-4-{(1E,4E)-5-[4-(acryloyloxy)phenyl]-3-oxopenta-1,4-dienyl}phenyl Acrylate Copolymer Beads. *Journal of Biomedical Materials Research Part B: Applied Biomaterials* **2005,** *73B* (2), 291-300.
53. Gupta, A. K.; Wells, S., Surface-Modified Superparamagnetic Nanoparticles for Drug Delivery: Preparation, Characterization, and Cytotoxicity Studies. *NanoBioscience, IEEE Transactions on* **2004,** *3* (1), 66-73.
54. Gupta, A. K.; Gupta, M., Cytotoxicity Suppression and Cellular Uptake Enhancement of Surface Modified Magnetic Nanoparticles. *Biomaterials* **2005,** *26* (13), 1565-1573.
55. Hussain, S. M.; Hess, K. L.; Gearhart, J. M.; Geiss, K. T.; Schlager, J. J., *In Vitro* Toxicity of Nanoparticles in BRL 3A Rat Liver Cells. *Toxicology in Vitro* **2005,** *19* (7), 975-983.
56. Cheng, F.-Y.; Su, C.-H.; Yang, Y.-S.; Yeh, C.-S.; Tsai, C.-Y.; Wu, C.-L.; Wu, M.-T.; Shieh, D.-B., Characterization of Aqueous Dispersions of Fe_3O_4 Nanoparticles and Their Biomedical Applications. *Biomaterials* **2005,** *26* (7), 729-738.
57. Häfeli, U. O.; Riffle, J. S.; Harris-Shekhawat, L.; Carmichael-Baranauskas, A.; Mark, F.; Dailey, J. P.; Bardenstein, D., Cell Uptake and *In Vitro* Toxicity of Magnetic

Nanoparticles Suitable for Drug Delivery. *Molecular Pharmaceutics* **2009,** *6* (5), 1417-1428.

58. Jeng, H. A.; Swanson, J., Toxicity of Metal Oxide Nanoparticles in Mammalian Cells. *Journal of Environmental Science and Health, Part A* **2006,** *41* (12), 2699-2711.
59. Stroh, A.; Zimmer, C.; Gutzeit, C.; Jakstadt, M.; Marschinke, F.; Jung, T.; Pilgrimm, H.; Grune, T., Iron Oxide Particles for Molecular Magnetic Resonance Imaging Cause Transient Oxidative Stress in Rat Macrophages. *Free Radical Biology and Medicine* **2004,** *36* (8), 976-984.
60. Sadeghiani, N.; Barbosa, L. S.; Silva, L. P.; Azevedo, R. B.; Morais, P. C.; Lacava, Z. G. M., Genotoxicity and Inflammatory Investigation in Mice Treated with Magnetite Nanoparticles Surface Coated with Polyaspartic Acid. *Journal of Magnetism and Magnetic Materials* **2005,** *289*, 466-468.
61. Singh, N.; Jenkins, G. J. S.; Asadi, R.; Doak, S. H., Potential Toxicity of Superparamagnetic Iron Oxide Nanoparticles (SPION). *Nano Reviews* **2010**.
62. Bulte, J. W. M.; Douglas, T.; Witwer, B.; Zhang, S.-C.; Strable, E.; Lewis, B. K.; Zywicke, H.; Miller, B.; van Gelderen, P.; Moskowitz, B. M.; Duncan, I. D.; Frank, J. A., Magnetodendrimers Allow Endosomal Magnetic Labeling and *In Vivo* Tracking of Stem Cells. *Nat Biotech* **2001,** *19* (12), 1141-1147.
63. Veranth, J. M.; Kaser, E. G.; Veranth, M. M.; Koch, M.; Yost, G. S., Cytokine Responses of Human Lung Cells (BEAS-2B) Treated with Micron-Sized and Nanoparticles of Metal Oxides Compared to Soil Dusts. *Particle and Fibre Toxicology* **2007,** *4*, 2-2.
64. Ankamwar, B.; Lai, T. C.; Huang, J. H.; Liu, R. S.; Hsiao, M.; Chen, C. H.; Hwu, Y. K., Biocompatibility of Fe_3O_4 Nanoparticles Evaluated by *In Vitro* Cytotoxicity Assays Using Normal, Glia and Breast Cancer *Nanotechnology* **2010,** *21* (7), 075102.
65. Stevens, R. G.; Jones, D. Y.; Micozzi, M. S.; Taylor, P. R., Body Iron Stores and the Risk of Cancer. *New England Journal of Medicine* **1988,** *319* (16), 1047-1052.
66. Toyokuni, S., Iron-Induced Carcinogenesis: The Role of Redox Regulation. *Free Radical Biology and Medicine* **1996,** *20* (4), 553-566.
67. Toyokuni, S., Iron and Carcinogenesis: From Fenton Reaction to Target Genes. *Redox Report* **2002,** *7* (4), 189-197.
68. Valko, M.; Leibfritz, D.; Moncol, J.; Cronin, M. T. D.; Mazur, M.; Telser, J., Free Radicals and Antioxidants in Normal Physiological Functions and Human Disease. *The International Journal of Biochemistry & Cell Biology* **2007,** *39* (1), 44-84.
69. Halliwell, B.; Gutteridge, J. M. C., *Free Radicals in Biology and Medicine*. Oxford University Press: New York, 2007.
70. Cedervall, T.; Lynch, I.; Lindman, S.; Berggård, T.; Thulin, E.; Nilsson, H.; Dawson, K. A.; Linse, S., Understanding the Nanoparticle–Protein Corona Using Methods to Quantify Exchange Rates and Affinities of Proteins for Nanoparticles. *Proceedings of the National Academy of Sciences* **2007,** *104* (7), 2050-2055.
71. Xia, X. R.; Monteiro-Riviere, N. A.; Riviere, J. E., An Index for Characterization of Nanomaterials in Biological Systems. *Nature Nanotechnology* **2010,** *5* (9), 671-675.

72. Lundqvist, M.; Stigler, J.; Elia, G.; Lynch, I.; Cedervall, T.; Dawson, K. A., Nanoparticle Size and Surface Properties Determine the Protein Corona with Possible Implications for Biological Impacts. *Proceedings of the National Academy of Sciences* **2008,** *105* (38), 14265-14270.
73. Maiorano, G.; Sabella, S.; Sorce, B.; Brunetti, V.; Malvindi, M. A.; Cingolani, R.; Pompa, P. P., Effects of Cell Culture Media on the Dynamic Formation of Protein-Nanoparticle Complexes and Influence on the Cellular Response. *ACS Nano* **2010,** *4* (12), 7481-7491.
74. Wang, F.; Yu, L.; Monopoli, M. P.; Sandin, P.; Mahon, E.; Salvati, A.; Dawson, K. A., The Biomolecular Corona is Retained during Nanoparticle Uptake And Protects the Cells from the Damage Induced by Cationic Nanoparticles until Degraded in the Lysosomes. *Nanomedicine: Nanotechnology, Biology and Medicine* **2013,** *9* (8), 1159-1168.
75. Bexiga, M. G.; Varela, J. A.; Wang, F.; Fenaroli, F.; Salvati, A.; Lynch, I.; Simpson, J. C.; Dawson, K. A., Cationic Nanoparticles Induce Caspase 3-, 7- and 9-Mediated Cytotoxicity in a Human Astrocytoma Cell Line. *Nanotoxicology* **2010,** *5* (4), 557-567.
76. Naha, P. C.; Davoren, M.; Lyng, F. M.; Byrne, H. J., Reactive Oxygen Species (ROS) Induced Cytokine Production and Cytotoxicity of Pamam Dendrimers in J774A.1 Cells. *Toxicology and Applied Pharmacology* **2010,** *246* (1-2), 91-99.
77. Salmaso, S.; Caliceti, P., Stealth Properties to Improve Therapeutic Efficacy of Drug Nanocarriers. *Journal of Drug Delivery* **2013,** *2013*, 19.
78. Moghimi, S. M.; Hunter, A. C.; Murray, J. C., Long-Circulating and Target-Specific Nanoparticles: Theory to Practice. *Pharmacological Reviews* **2001,** *53* (2), 283-318.
79. Moghimi, S. M.; Muir, I. S.; Illum, L.; Davis, S. S.; Kolb-Bachofen, V., Coating Particles with a Block Co-Polymer (Poloxamine-908) Suppresses Opsonization but Permits the Activity of Dysopsonins in the Serum. *Biochimica et Biophysica Acta (BBA) - Molecular Cell Research* **1993,** *1179* (2), 157-165.
80. Van Butsele, K.; Morille, M.; Passirani, C.; Legras, P.; Benoit, J. P.; Varshney, S. K.; Jérôme, R.; Jérôme, C., Stealth Properties of Poly(ethylene oxide)-based Triblock Copolymer Micelles: A Prerequisite for a pH-triggered Targeting System. *Acta Biomaterialia* **2011,** *7* (10), 3700-3707.
81. Allard-Vannier, E.; Cohen-Jonathan, S.; Gautier, J.; Hervé-Aubert, K.; Munnier, E.; Soucé, M.; Legras, P.; Passirani, C.; Chourpa, I., Pegylated Magnetic Nanocarriers for Doxorubicin Delivery: A Quantitative Determination of Stealthiness *In Vitro* and *In Vivo*. *European Journal of Pharmaceutics and Biopharmaceutics* **2012,** *81* (3), 498-505.
82. Aqil, A.; Vasseur, S.; Duguet, E.; Passirani, C.; Benoît, J. P.; Roch, A.; Müller, R.; Jérôme, R.; Jérôme, C., PEO Coated Magnetic Nanoparticles for Biomedical Application. *European Polymer Journal* **2008,** *44* (10), 3191-3199.
83. William, W. Y.; Emmanuel, C.; Christie, M. S.; Rebekah, D.; Vicki, L. C., Aqueous Dispersion of Monodisperse Magnetic Iron Oxide Nanocrystals Through Phase Transfer. *Nanotechnology* **2006,** *17* (17), 4483.

84. Petri-Fink, A.; Chastellain, M.; Juillerat-Jeanneret, L.; Ferrari, A.; Hofmann, H., Development of Functionalized Superparamagnetic Iron Oxide Nanoparticles for Interaction with Human Cancer Cells. *Biomaterials* **2005,** *26* (15), 2685-2694.
85. Wan, S.; Huang, J.; Guo, M.; Zhang, H.; Cao, Y.; Yan, H.; Liu, K., Biocompatible Superparamagnetic Iron Oxide Nanoparticle Dispersions Stabilized with Poly(ethylene glycol)–Oligo(aspartic acid) Hybrids. *Journal of Biomedical Materials Research Part A* **2007,** *80A* (4), 946-954.
86. Iversen, T.-G.; Skotland, T.; Sandvig, K., Endocytosis and Intracellular Transport of Nanoparticles: Present Knowledge and Need for Future Studies. *Nano Today* **2011,** *6* (2), 176-185.
87. Lu, C.-W.; Hung, Y.; Hsiao, J.-K.; Yao, M.; Chung, T.-H.; Lin, Y.-S.; Wu, S.-H.; Hsu, S.-C.; Liu, H.-M.; Mou, C.-Y.; Yang, C.-S.; Huang, D.-M.; Chen, Y.-C., Bifunctional Magnetic Silica Nanoparticles for Highly Efficient Human Stem Cell Labeling. *Nano Letters* **2006,** *7* (1), 149-154.
88. Bertorelle, F.; Wilhelm, C.; Roger, J.; Gazeau, F.; Ménager, C.; Cabuil, V., Fluorescence-Modified Superparamagnetic Nanoparticles: Intracellular Uptake and Use in Cellular Imaging. *Langmuir* **2006,** *22* (12), 5385-5391.
89. Reich, D. H.; Tanase, M.; Hultgren, A.; Bauer, L. A.; Chen, C. S.; Meyer, G. J., Biological Applications of Multifunctional Magnetic Nanowires (Invited). *Journal of Applied Physics* **2003,** *93* (10), 7275-7280.
90. Soenen, S. J. H.; Himmelreich, U.; Nuytten, N.; Pisanic, T. R.; Ferrari, A.; De Cuyper, M., Intracellular Nanoparticle Coating Stability Determines Nanoparticle Diagnostics Efficacy and Cell Functionality. *Small* **2010,** *6* (19), 2136-2145.
91. Arbab, A. S.; Wilson, L. B.; Ashari, P.; Jordan, E. K.; Lewis, B. K.; Frank, J. A., A Model of Lysosomal Metabolism of Dextran Coated Superparamagnetic Iron Oxide (SPIO) Nanoparticles: Implications for Cellular Magnetic Resonance Imaging. *NMR in Biomedicine* **2005,** *18* (6), 383-389.
92. Soenen, S. J. H.; Nuytten, N.; De Meyer, S. F.; De Smedt, S. C.; De Cuyper, M., High Intracellular Iron Oxide Nanoparticle Concentrations Affect Cellular Cytoskeleton and Focal Adhesion Kinase-Mediated Signaling. *Small* **2010,** *6* (7), 832-842.
93. Song, C. W., Effect of Local Hyperthermia on Blood Flow and Microenvironment: A Review. *Cancer Res* **1984,** *44* (10 Suppl), 4721s-4730s.
94. Schweiger, C.; Hartmann, R.; Zhang, F.; Parak, W.; Kissel, T.; Rivera_Gil, P., Quantification of the Internalization Patterns of Superparamagnetic Iron Oxide Nanoparticles with Opposite Charge. *Journal of Nanobiotechnology* **2012,** *10* (1), 28.
95. van der Zee, J., Heating the Patient: A Promising Approach? *Annals of Oncology* **2002,** *13* (8), 1173-1184.
96. Issels, R. D., Hyperthermia Adds to Chemotherapy. *Eur J Cancer* **2008,** *44* (17), 2546-54.
97. Harmon, B. V.; Takano, Y. S.; Winterford, C. M.; Gobe, G. C., The Role of Apoptosis in the Response of Cells and Tumours to Mild Hyperthermia. *International Journal of Radiation Biology* **1991,** *59* (2), 489-501.

98. Kerr, J. F.; Winterford, C. M.; Harmon, B. V., Apoptosis. Its Significance in Cancer and Cancer Therapy. *Cancer* **1994,** *73* (8), 2013-26.
99. Hildebrandt, B.; Wust, P.; Ahlers, O.; Dieing, A.; Sreenivasa, G.; Kerner, T.; Felix, R.; Riess, H., The Cellular and Molecular Basis of Hyperthermia. *Crit Rev Oncol Hematol* **2002,** *43* (1), 33-56.
100. Lepock, J. R., Cellular Effects of Hyperthermia: Relevance to the Minimum Dose for Thermal Damage. *Int J Hyperthermia* **2003,** *19* (3), 252-66.
101. Song, C. W.; Rhee, J. G.; Levitt, S. H., Blood Flow in Normal Tissues and Tumors during Hyperthermia. *J Natl Cancer Inst* **1980,** *64* (1), 119-24.
102. Hervault, A.; Thanh, N. T. K., Magnetic Nanoparticle-Based Therapeutic Agents for Thermo-Chemotherapy Treatment of Cancer. *Nanoscale* **2014,** *6* (20), 11553-11573.
103. Kolosnjaj-Tabi, J.; Di Corato, R.; Lartigue, L.; Marangon, I.; Guardia, P.; Silva, A. K. A.; Luciani, N.; Clément, O.; Flaud, P.; Singh, J. V.; Decuzzi, P.; Pellegrino, T.; Wilhelm, C.; Gazeau, F., Heat-Generating Iron Oxide Nanocubes: Subtle "Destructurators" of the Tumoral Microenvironment. *ACS Nano* **2014,** *8* (5), 4268-4283.
104. Creixell, M.; Bohórquez, A. C.; Torres-Lugo, M.; Rinaldi, C., EGFR-Targeted Magnetic Nanoparticle Heaters Kill Cancer Cells without a Perceptible Temperature Rise. *ACS Nano* **2011,** *5* (9), 7124-7129.
105. Ota, S.; Yamazaki, N.; Tomitaka, A.; Yamada, T.; Takemura, Y., Hyperthermia Using Antibody-Conjugated Magnetic Nanoparticles and Its Enhanced Effect with Cryptotanshinone. *Nanomaterials* **2014,** *4* (2), 319-330.
106. Qu, Y.; Li, J.; Ren, J.; Leng, J.; Lin, C.; Shi, D., Enhanced Magnetic Fluid Hyperthermia by Micellar Magnetic Nanoclusters Composed of $Mn_xZn_{1-x}Fe_2O_4$ Nanoparticles for Induced Tumor Cell Apoptosis. *ACS Applied Materials & Interfaces* **2014,** *6* (19), 16867-16879.
107. Di Corato, R.; Espinosa, A.; Lartigue, L.; Tharaud, M.; Chat, S.; Pellegrino, T.; Ménager, C.; Gazeau, F.; Wilhelm, C., Magnetic Hyperthermia Efficiency in the Cellular Environment for Different Nanoparticle Designs. *Biomaterials* **2014,** *35* (24), 6400-6411.
108. Brulé, S.; Levy, M.; Wilhelm, C.; Letourneur, D.; Gazeau, F.; Ménager, C.; Le Visage, C., Doxorubicin Release Triggered by Alginate Embedded Magnetic Nanoheaters: A Combined Therapy. *Advanced Materials* **2011,** *23* (6), 787-790.
109. Oliveira, H.; Pérez-Andrés, E.; Thevenot, J.; Sandre, O.; Berra, E.; Lecommandoux, S., Magnetic Field Triggered Drug Release from Polymersomes for Cancer Therapeutics. *Journal of Controlled Release* **2013,** *169* (3), 165-170.
110. Yanase, M.; Shinkai, M.; Honda, H.; Wakabayashi, T.; Yoshida, J.; Kobayashi, T., Antitumor Immunity Induction by Intracellular Hyperthermia Using Magnetite Cationic Liposomes. *Japanese Journal of Cancer Research* **1998,** *89* (7), 775-82.
111. Le, B.; Shinkai, M.; Kitade, T.; Honda, H.; Yoshida, J. U. N.; Wakabayashi, T.; Kobayashi, T., Preparation of Tumor-Specific Magnetoliposomes and Their Application for Hyperthermia. *Journal of Chemical Engineering of Japan* **2001,** *34* (1), 66-72.

112. Tanaka, K.; Ito, A.; Kobayashi, T.; Kawamura, T.; Shimada, S.; Matsumoto, K.; Saida, T.; Honda, H., Intratumoral Injection of Immature Dendritic Cells Enhances Antitumor Effect of Hyperthermia Using Magnetic Nanoparticles. *Int J Cancer* **2005,** *116* (4), 624-33.
113. Archer, S. G.; Gray, B. N., Vascularization of Small Liver Metastases. *Br J Surg* **1989,** *76* (6), 545-8.
114. Jones, S. K.; Winter, J. G.; Gray, B. N., Treatment of Experimental Rabbit Liver Tumours by Selectively Targeted Hyperthermia. *Int J Hyperthermia* **2002,** *18* (2), 117-28.
115. Thiesen, B.; Jordan, A., Clinical Applications of Magnetic Nanoparticles for Hyperthermia. *Int J Hyperthermia* **2008,** *24* (6), 467-74.
116. Maier-Hauff, K.; Ulrich, F.; Nestler, D.; Niehoff, H.; Wust, P.; Thiesen, B.; Orawa, H.; Budach, V.; Jordan, A., Efficacy and Safety of Intratumoral Thermotherapy Using Magnetic Iron-Oxide Nanoparticles Combined with External Beam Radiotherapy on Patients with Recurrent Glioblastoma Multiforme. *Journal of Neuro-Oncology* **2011,** *103* (2), 317-324.
117. Markkanen, A.; Juutilainen, J.; Naarala, J., Pre-exposure to 50 Hz Magnetic Fields Modifies Menadione-Induced Dna Damage Response in Murine L929 Cells. *International Journal of Radiation Biology* **2008,** *84* (9), 742-51.
118. Riedinger, A.; Guardia, P.; Curcio, A.; Garcia, M. A.; Cingolani, R.; Manna, L.; Pellegrino, T., Subnanometer Local Temperature Probing and Remotely Controlled Drug Release Based on Azo-Functionalized Iron Oxide Nanoparticles. *Nano Letters* **2013,** *13* (6), 2399-2406.
119. Huang, H.; Delikanli, S.; Zeng, H.; Ferkey, D. M.; Pralle, A., Remote Control of Ion Channels and Neurons Through Magnetic-Field Heating of Nanoparticles. *Nat Nano* **2010,** *5* (8), 602-606.
120. Carrey, J.; Connord, V.; Respaud, M., Ultrasound Generation and High-Frequency Motion of Magnetic Nanoparticles in an Alternating Magnetic Field: Toward Intracellular Ultrasound Therapy? *Applied Physics Letters* **2013,** *102* (23), 232404.
121. Villanueva, A.; de la Presa, P.; Alonso, J. M.; Rueda, T.; Martínez, A.; Crespo, P.; Morales, M. P.; Gonzalez-Fernandez, M. A.; Valdés, J.; Rivero, G., Hyperthermia HeLa Cell Treatment with Silica-Coated Manganese Oxide Nanoparticles. *The Journal of Physical Chemistry C* **2010,** *114* (5), 1976-1981.
122. Domenech, M.; Marrero-Berrios, I.; Torres-Lugo, M.; Rinaldi, C., Lysosomal Membrane Permeabilization by Targeted Magnetic Nanoparticles in Alternating Magnetic Fields. *ACS Nano* **2013,** *7* (6), 5091-5101.

References

7. Chapter 7

1. Warnant, J.; Marcotte, N.; Reboul, J.; Layrac, G.; Aqil, A.; Jerôme, C.; Lerner, D. A.; Gérardin, C., Physicochemical Properties of pH-Controlled Polyion Complex (PIC) Micelles of Poly(acrylic acid)-Based Double Hydrophilic Block Copolymers and Various Polyamines. *Analytical and Bioanalytical Chemistry* **2012,** *403* (5), 1395-1404.
2. Mori, H.; Müller, A. H. E.; Klee, J. E., Intelligent Colloidal Hybrids via Reversible pH-Induced Complexation of Polyelectrolyte and Silica Nanoparticles. *Journal of the American Chemical Society* **2003,** *125* (13), 3712-3713.
3. Laurent, S.; Forge, D.; Port, M.; Roch, A.; Robic, C.; Vander Elst, L.; Muller, R. N., Magnetic Iron Oxide Nanoparticles: Synthesis, Stabilization, Vectorization, Physicochemical Characterizations, and Biological Applications. *Chemical Reviews* **2008,** *108* (6), 2064-2110.
4. Oh, J. K.; Park, J. M., Iron Oxide-Based Superparamagnetic Polymeric Nanomaterials: Design, Preparation, and Biomedical Application. *Progress in Polymer Science* **2011,** *36* (1), 168-189.
5. Akbarzadeh, A.; Samiei, M.; Davaran, S., Magnetic Nanoparticles: Preparation, Physical Properties, and Applications in Biomedicine. *Nanoscale Research Letters* **2012,** *7* (1), 144.
6. Gupta, A. K.; Gupta, M., Synthesis and Surface Engineering of Iron Oxide Nanoparticles for Biomedical Applications. *Biomaterials* **2005,** *26* (18), 3995-4021.
7. Wu, W.; He, Q.; Jiang, C., Magnetic Iron Oxide Nanoparticles: Synthesis and Surface Functionalization Strategies. In *Nanoscale Research Letters*, Springer New York: 2008; Vol. 3, pp 397-415.
8. Vékás, L.; Bica, D.; Avdeev, M. V., Magnetic Nanoparticles and Concentrated Magnetic Nanofluids: Synthesis, Properties and Some Applications. *China Particuology* **2007,** *5* (1–2), 43-49.
9. Mahmoudi, M.; Simchi, A.; Imani, M., Recent Advances in Surface Engineering of Superparamagnetic Iron Oxide Nanoparticles for Biomedical Applications. *Journal of the Iranian Chemical Society* **2010,** *7* (2), S1-S27.
10. Hervault, A.; Thanh, N. T. K., Magnetic Nanoparticle-Based Therapeutic Agents for Thermo-Chemotherapy Treatment of Cancer. *Nanoscale* **2014,** *6* (20), 11553-11573.
11. Obaidat, I.; Issa, B.; Haik, Y., Magnetic Properties of Magnetic Nanoparticles for Efficient Hyperthermia. *Nanomaterials* **2015,** *5* (1), 63-89.
12. Deatsch, A. E.; Evans, B. A., Heating Efficiency in Magnetic Nanoparticle Hyperthermia. *Journal of Magnetism and Magnetic Materials* **2014,** *354*, 163-172.
13. Mornet, S.; Vasseur, S.; Grasset, F.; Duguet, E., Magnetic Nanoparticle Design for Medical Diagnosis and Therapy. *Journal of Materials Chemistry* **2004,** *14* (14), 2161-2175.

14. Gossuin, Y.; Gillis, P.; Hocq, A.; Vuong, Q. L.; Roch, A., Magnetic Resonance Relaxation Properties of Superparamagnetic Particles. *Wiley Interdisciplinary Reviews: Nanomedicine and Nanobiotechnology* **2009,** *1* (3), 299-310.
15. Stanicki, D.; Elst, L. V.; Muller, R. N.; Laurent, S., Synthesis and Processing of Magnetic Nanoparticles. *Current Opinion in Chemical Engineering* **2015,** *8*, 7-14.
16. Qiao, R.; Yang, C.; Gao, M., Superparamagnetic Iron Oxide Nanoparticles: From Preparations to *In Vivo* MRI Applications. *Journal of Materials Chemistry* **2009,** *19* (35), 6274-6293.
17. Pankhurst, Q. A.; Thanh, N. T. K.; Jones, S. K.; Dobson, J., Progress in Applications of Magnetic Nanoparticles in Biomedicine. *Journal of Physics D: Applied Physics* **2009,** *42* (22), 224001.
18. Liu, T.-Y.; Hu, S.-H.; Liu, D.-M.; Chen, S.-Y.; Chen, I. W., Biomedical Nanoparticle Carriers with Combined Thermal And Magnetic Responses. *Nano Today* **2009,** *4* (1), 52-65.
19. Yoo, D.; Lee, J.-H.; Shin, T.-H.; Cheon, J., Theranostic Magnetic Nanoparticles. *Accounts of Chemical Research* **2011,** *44* (10), 863-874.
20. Shang, H.; Chang, W.-S.; Kan; Majetich, S. A.; Lee, G. U., Synthesis and Characterization of Paramagnetic Microparticles through Emulsion-Templated Free Radical Polymerization. *Langmuir* **2006,** *22* (6), 2516-2522.
21. Wang, L.; Luo, J.; Maye, M. M.; Fan, Q.; Rendeng, Q.; Engelhard, M. H.; Wang, C.; Lin, Y.; Zhong, C.-J., Iron Oxide-Gold Core-Shell Nanoparticles and Thin Film Assembly. *Journal of Materials Chemistry* **2005,** *15* (18), 1821-1832.
22. Huang, J.; Wan, S.; Guo, M.; Yan, H., Preparation of Narrow or Mono-Disperse Crosslinked Poly((meth)acrylic acid)/Iron Oxide Magnetic Microspheres. *Journal of Materials Chemistry* **2006,** *16* (46), 4535-4541.
23. Vuong, Q. L.; Berret, J.-F.; Fresnais, J.; Gossuin, Y.; Sandre, O., A Universal Scaling Law to Predict the Efficiency of Magnetic Nanoparticles as MRI T_2-Contrast Agents. *Advanced Healthcare Materials* **2012,** *1* (4), 502-512.
24. Kadlecova, Z.; Baldi, L.; Hacker, D.; Wurm, F. M.; Klok, H.-A., Comparative Study on the *In Vitro* Cytotoxicity of Linear, Dendritic, and Hyperbranched Polylysine Analogues. *Biomacromolecules* **2012,** *13* (10), 3127-3137.
25. Kadlecova, Z.; Rajendra, Y.; Matasci, M.; Baldi, L.; Hacker, D. L.; Wurm, F. M.; Klok, H.-A., DNA Delivery with Hyperbranched Polylysine: A Comparative Study with Linear and Dendritic Polylysine. *Journal of Controlled Release* **2013,** *169* (3), 276-288.
26. Choi, J. S.; Lee, E. J.; Choi, Y. H.; Jeong, Y. J.; Park, J. S., Poly(ethylene glycol)-*block*-Poly(L-lysine) Dendrimer: Novel Linear Polymer/Dendrimer Block Copolymer Forming a Spherical Water-Soluble Polyionic Complex with DNA. *Bioconjugate Chemistry* **1999,** *10* (1), 62-65.
27. Kadlecova, Z.; Rajendra, Y.; Matasci, M.; Hacker, D.; Baldi, L.; Wurm, F. M.; Klok, H.-A., Hyperbranched Polylysine: A Versatile, Biodegradable Transfection Agent for the Production of Recombinant Proteins by Transient Gene Expression and the Transfection of Primary Cells. *Macromolecular Bioscience* **2012,** *12* (6), 794-804.

28. Chen, X.; Tian, H.; Guan, X., Polymeric Gene Carriers. In *Bioinspired and Biomimetic Polymer Systems for Drug and Gene Delivery*, Wiley-VCH Verlag GmbH & Co. KGaA: 2014; pp 171-202.
29. Tian, H.; Deng, C.; Lin, H.; Sun, J.; Deng, M.; Chen, X.; Jing, X., Biodegradable Cationic PEG–PEI–PBLG Hyperbranched Block Copolymer: Synthesis and Micelle Characterization. *Biomaterials* **2005,** *26* (20), 4209-4217.
30. Mavrogiorgis, D.; Bilalis, P.; Karatzas, A.; Skoulas, D.; Fotinogiannopoulou, G.; Iatrou, H., Controlled Polymerization of Histidine and Synthesis of Well-Defined Stimuli Responsive Polymers. Elucidation of the Structure-Aggregation Relationship of this Highly Multifunctional Material. *Polymer Chemistry* **2014,** *5* (21), 6256-6278.
31. Lewinski, N.; Colvin, V.; Drezek, R., Cytotoxicity of Nanoparticles. *Small* **2008,** *4* (1), 26-49.
32. Wang, Y.-X.; Hussain, S.; Krestin, G., Superparamagnetic Iron Oxide Contrast Agents: Physicochemical Characteristics and Applications in MR Imaging. *European Radiology* **2001,** *11* (11), 2319-2331.
33. Gupta, A. K.; Naregalkar, R. R.; Vaidya, V. D.; Gupta, M., Recent Advances on Surface Engineering of Magnetic Iron Oxide Nanoparticles and Their Biomedical Applications. *Nanomedicine* **2007,** *2* (1), 23-39.
34. Veiseh, O.; Gunn, J. W.; Zhang, M., Design and Fabrication of Magnetic Nanoparticles for Targeted Drug Delivery and Imaging. *Advanced Drug Delivery Reviews* **2010,** *62* (3), 284-304.
35. TrinhThang, T.; Shinya, M.; Nguyen Thi Kim, T., Next Generation Magnetic Nanoparticles for Biomedical Applications. In *Magnetic Nanoparticles*, CRC Press: 2012; pp 99-126.
36. Gould, P., Nanomagnetism Shows *In Vivo* Potential. *Nano Today* **2006,** *1* (4), 34-39.
37. Sun, C.; Lee, J. S. H.; Zhang, M., Magnetic Nanoparticles in MR Imaging and Drug Delivery. *Advanced Drug Delivery Reviews* **2008,** *60* (11), 1252-1265.
38. Wohlfarth, E. P., Chapter 1 Iron, Cobalt and Nickel. In *Handbook of Ferromagnetic Materials*, Wohlfarth, E. P., Ed. Elsevier: 1980; Vol. Volume 1, pp 1-70.
39. Lu, C.-W.; Hung, Y.; Hsiao, J.-K.; Yao, M.; Chung, T.-H.; Lin, Y.-S.; Wu, S.-H.; Hsu, S.-C.; Liu, H.-M.; Mou, C.-Y.; Yang, C.-S.; Huang, D.-M.; Chen, Y.-C., Bifunctional Magnetic Silica Nanoparticles for Highly Efficient Human Stem Cell Labeling. *Nano Letters* **2006,** *7* (1), 149-154.
40. Tuma, P. L.; Hubbard, A. L., Transcytosis: Crossing Cellular Barriers. *Physiological Reviews* **2003,** *83* (3), 871-932.
41. Levy, A.; Dayan, A.; Ben-David, M.; Gannot, I., A New Thermography-Based Approach to Early Detection of Cancer Utilizing Magnetic Nanoparticles Theory Simulation and *In Vitro* Validation. *Nanomedicine: Nanotechnology, Biology and Medicine* **2010,** *6* (6), 786-796.
42. DeNardo, S. J.; DeNardo, G. L.; Miers, L. A.; Natarajan, A.; Foreman, A. R.; Gruettner, C.; Adamson, G. N.; Ivkov, R., Development of Tumor Targeting Bioprobes ((111)In-chimeric L6 Monoclonal Antibody Nanoparticles) for Alternating Magnetic Field Cancer Therapy. *Clin Cancer Res* **2005,** *11* (19 Pt 2), 7087s-7092s.

43. Shinkai, M.; Le, B.; Honda, H.; Yoshikawa, K.; Shimizu, K.; Saga, S.; Wakabayashi, T.; Yoshida, J.; Kobayashi, T., Targeting Hyperthermia for Renal Cell Carcinoma Using Human MN Antigen-Specific Magnetoliposomes. *Japanese Journal of Cancer Research* **2001,** *92* (10), 1138-45.
44. Creixell, M.; Bohórquez, A. C.; Torres-Lugo, M.; Rinaldi, C., EGFR-Targeted Magnetic Nanoparticle Heaters Kill Cancer Cells without a Perceptible Temperature Rise. *ACS Nano* **2011,** *5* (9), 7124-7129.
45. Presta, L. G., Engineering of Therapeutic Antibodies to Minimize Immunogenicity and Optimize Function. *Advanced Drug Delivery Reviews* **2006,** *58* (5–6), 640-656.
46. Hansel, T. T.; Kropshofer, H.; Singer, T.; Mitchell, J. A.; George, A. J. T., The Safety and Side Effects of Monoclonal Antibodies. *Nat Rev Drug Discov* **2010,** *9* (4), 325-338.
47. Descotes, J., Immunotoxicity of Monoclonal Antibodies. *mAbs* **2009,** *1* (2), 104-111.
48. Shubayev, V. I.; Pisanic Ii, T. R.; Jin, S., Magnetic Nanoparticles for Theragnostics. *Advanced Drug Delivery Reviews* **2009,** *61* (6), 467-477.
49. Arash, K.; Roger, L.; Aleksander, N.; Roland, P.; Azeem, S.; Didier, A. D.; Kenneth, J. D.; Isaac, R.; Benjamin, S., Putting Therapeutic Nanoparticles Where They Need to Go by Magnet Systems: Design and Control. In *Magnetic Nanoparticles*, CRC Press: 2012; pp 419-448.
50. Kumar, C. S. S. R.; Mohammad, F., Magnetic Nanomaterials for Hyperthermia-Based Therapy and Controlled Drug Delivery. *Advanced Drug Delivery Reviews* **2011,** *63* (9), 789-808.
51. Riedinger, A.; Guardia, P.; Curcio, A.; Garcia, M. A.; Cingolani, R.; Manna, L.; Pellegrino, T., Subnanometer Local Temperature Probing and Remotely Controlled Drug Release Based on Azo-Functionalized Iron Oxide Nanoparticles. *Nano Letters* **2013,** *13* (6), 2399-2406.
52. McGill, S. L.; Cuylear, C. L.; Adolphi, N. L.; Osinski, M.; Smyth, H. D., Magnetically Responsive Nanoparticles for Drug Delivery Applications Using Low Magnetic Field Strengths. *IEEE Trans Nanobioscience* **2009,** *8* (1), 33-42.
53. Nappini, S.; Al Kayal, T.; Berti, D.; Nordèn, B.; Baglioni, P., Magnetically Triggered Release from Giant Unilamellar Vesicles: Visualization by Means of Confocal Microscopy. *The Journal of Physical Chemistry Letters* **2011,** *2* (7), 713-718.
54. Sanson, C.; Diou, O.; Thévenot, J.; Ibarboure, E.; Soum, A.; Brûlet, A.; Miraux, S.; Thiaudière, E.; Tan, S.; Brisson, A.; Dupuis, V.; Sandre, O.; Lecommandoux, S., Doxorubicin Loaded Magnetic Polymersomes: Theranostic Nanocarriers for MR Imaging and Magneto-Chemotherapy. *ACS Nano* **2011,** *5* (2), 1122-1140.
55. Bilalis, P.; Chatzipavlidis, A.; Tziveleka, L.-A.; Boukos, N.; Kordas, G., Nanodesigned Magnetic Polymer Containers for Dual Stimuli Actuated Drug Controlled Release and Magnetic Hyperthermia Mediation. *Journal of Materials Chemistry* **2012,** *22* (27), 13451-13454.
56. Louguet, S.; Rousseau, B.; Epherre, R.; Guidolin, N.; Goglio, G.; Mornet, S.; Duguet, E.; Lecommandoux, S.; Schatz, C., Thermoresponsive Polymer Brush-Functionalized

Magnetic Manganite Nanoparticles for Remotely Triggered Drug Release. *Polymer Chemistry* **2012,** *3* (6), 1408-1417.

57. Hawkins, A. M.; Bottom, C. E.; Liang, Z.; Puleo, D. A.; Hilt, J. Z., Magnetic Nanocomposite Sol–Gel Systems for Remote Controlled Drug Release. *Advanced Healthcare Materials* **2012,** *1* (1), 96-100.
58. Peiris, P. M.; Bauer, L.; Toy, R.; Tran, E.; Pansky, J.; Doolittle, E.; Schmidt, E.; Hayden, E.; Mayer, A.; Keri, R. A.; Griswold, M. A.; Karathanasis, E., Enhanced Delivery of Chemotherapy to Tumors Using a Multicomponent Nanochain with Radio-Frequency-Tunable Drug Release. *ACS Nano* **2012,** *6* (5), 4157-4168.
59. Oliveira, H.; Pérez-Andrés, E.; Thevenot, J.; Sandre, O.; Berra, E.; Lecommandoux, S., Magnetic Field Triggered Drug Release from Polymersomes for Cancer Therapeutics. *Journal of Controlled Release* **2013,** *169* (3), 165-170.
60. Carregal-Romero, S.; Guardia, P.; Yu, X.; Hartmann, R.; Pellegrino, T.; Parak, W. J., Magnetically Triggered Release of Molecular Cargo from Iron Oxide Nanoparticle Loaded Microcapsules. *Nanoscale* **2015,** *7* (2), 570-576.